UNIVERSITÉ DE STRASBOURG

ÉCOLE DOCTORALE DES SCIENCES CHIMIQUES

Institut de Chimie UMR 7177

THÈSE

présentée par :

Julien ENG

soutenue le : **25 septembre 2015**

pour obtenir le grade de : **Docteur de l'université de Strasbourg**
Discipline/ Spécialité : Chimie / Chimie Théorique

Dynamics of Ultrafast Processes in Excited States of Organic and Inorganic Compounds

THÈSE dirigée par :

Mme. DANIEL Chantal	Directrice de Recherche au CNRS, Université de Strasbourg

RAPPORTEURS :

Mme. DEMACHY Isabelle	Professeure des Universités, Université Paris-Sud 11
M. GATTI Fabien	Directeur de Recherche au CNRS, Université de Montpellier 2

EXAMINATEURS :

M. KÖPPEL Horst	Professeur, Universität Heidelberg
M. LÉONARD Jérémie	Chargé de Recherche au CNRS, Université de Strasbourg

CO-ENCADRANT :

M. GINDENSPERGER Etienne	Chargé de Recherche au CNRS, Université de Strasbourg

«Emancipate yourself from mental slavery,
None but ourselves can free our minds. »
~Robert Nesta Marley

Remerciements

Ce manuscrit est le fruit de trois longues années de thèse passées au Laboratoire de Chimie Quantique de Strasbourg. La thèse a été pour moi une aventure tant scientifique qu'humaine. C'est donc pour moi l'occasion d'adresser mes remerciements à toutes les personnes qui m'ont cotoyé. Je m'excuse d'ores et déjà pour ceux et celles que je vais oublier, et je suis sûr qu'il y en aura.

En tout premier lieu, j'aimerai remercier Chantal Daniel et Etienne Gindensperger qui m'ont encadré et conseillé pendant toute cette période et sans qui tout celà n'aurait pu aboutir. Ils m'ont permis de m'épanouir scientifiquement et m'ont apporté une méthode de travail qui m'accompagnera pendant mes, j'espère longues, années de recherche à venir. C'est grâce à eux que j'ai appris à aimer le monde de la recherche et que je peux désormais continuer sereinement mon chemin. Merci à vous.

Je n'oublie pas aussi tous les autres membres du Laboratoire. Vincent Robert, grand manitou, qui malgré toutes ses obligations a su être présent tout au long de ma thèse. Merci aussi à mon collègue de bureau, Christophe Gourlaouen, pour les conseils, pour la bonne humeur et pour le soutient. Merci à Paola Sager et Sylvie Fersing pour tout l'encadrement administratif et logistique. Je n'oublierai pas les cafés et les fous rires partagés tout au long de ces trois années. Merci aussi à Emmanuel Fromager et Roberto Marquardt pour toutes les discussions que nous avons pu avoir et qui eux aussi ont contribué à ma bonne intégration au laboratoire. Pour rester l'ordre hiérarchique, voilà le tour de tous les thésards, post-docs, stagiaires que j'ai croisés au labo. Merci à vous pour tout, vous avez apporté votre pierre d'une façon ou d'une autre à cette thèse. Merci à Alex, Ben, Benji, Bruno, Corentin, David, Etienne Gaines, Erika, Julia, Killian, Louise, Marco, Mehboob, Murali, Odile, Sergi S., Sergi V., Thiago, Tim, Yann C., Yann S.. Ce fut un plaisir, et j'espère à bientôt !

Et comme une thèse, ce n'est pas que de la science, et que sans les ami(e)s je n'aurais pas fini en si bonne état je tiens à les remercier eux aussi en tachant de ne pas en oublier !

Merci aux membres d'ALCANES, j'espère que je n'ai pas été trop dur en TD. Je vous souhaite le meilleur pour la poursuite de vos études (qu'elles soient pleines de quantique !). Vous citer tous serait bien long et donc, si je vous ai oublié, ne m'en voulez pas. Merci à Alex, Aurélien, Balthazar, Corentin, Elodie, Francky, Fred, Guiguifoot, Gwen, Ian, Laura, Lisa, Lucie, Lucy, Maël, Manon K., Marine S., Mathieu, Morgane, Steuh, Thibault, Valentin, Vicky, Yannick, tous les primos/otes, et tous les autres ! Je n'oublie pas les vieux de la fac, Antoine (binôme), Joy, Laura, Manon C., Manu I, Manu II, Marine A., Renaud, Sexy Sebi, Stephen, Syla, Pinouze, Tom Pouce,

Thomas G., ceux qui ont encadré ma pré-rentrée, ...
Merci à tous ceux qui ont fait du Hand avec moi, que ce soit au SUAPS: Allan, Alex, Alice, Arwen, Benjamin, Bérénice, Claire, Clém, Charlou, Christine, Eric, Hélène, Juliane, Julien M., Julien G., Karo, Kévin, Leslie, Adrien le Lorrain, Louis, Meryem, MichMich, Nina, Quentin, Rémi, Rhian, Saroun, Seb, Théo, Thomas L., Thomas V., Yannick M.. Grand merci à Benoît, gourou du SUAPS !
... ou à Brumath: Président, Henry, Youri, Loic, Arnaud, tous les vieux, tous les moins vieux !
Spécial dédicace à la team Romain, Guillaume et Alex Boué, Max, Mathilde, Jéééréééémie, Bérangère, Nico, Maxime, ... Merci à l'équipe de l'O'brien's pour m'avoir accueilli en ces temps de disette. Merci spécial à Anaëlle, Yann, Laurent, Jen, mes serveurs préférés (soyez pas jaloux les autres.).

Merci à ma famille. Mes parents, Maryse et Michel, mon frêre Nicolas. Pour m'avoir épaulé et soutenu dans mes choix. Une pensée à mes grands-parents qui pas pu vivre tout cela avec moi. Je vous aime.

Merci également à l'Ecole Doctorale de Sciences Chimiques de Strasbourg pour le financement de thèse sans lequel cette aventure aurait été impossible. Je tiens à remercier, Isabelle Demachy, Fabien Gatti, Horst Köppel ainsi que Jérémie Léonard d'avoir accepté de faire partie de mon jury et d'avoir lu ce manuscrit.

Bonne lecture.

TABLE OF CONTENTS

LIST OF FIGURES

LIST OF TABLES

Glossary

ADT	Adiabatic to diabatic transformation
BLA	Bond length alternation
BO	Born Oppenheimer
bpy	2,2'-Bipyridine
CASPT2	Complete active space - Perturbation theory: 2nd order
CASSCF	Complete active space self consistent field
CI	Conical intersection
DFT	Density functional theory
ES	Excited state
FC	Franck-Condon
GS	Ground state
HF	Hartree Fock
HOMO	Highest occupied molecular orbital
HOOP	Hydrogens out of plane
IC	Interaction configurations
IL	Intra-ligand
ILCT	Intra-ligand charge transfer
irrep	Irreducible representation
ISC	Intersystem crossing
LLCT	Ligand to ligand charge transfer
LUMO	Lowest unoccupied molecular orbital
LVC	Linear vibronic coupling
MC	Metal-centred
MLCT	Metal to ligand charge transfer
MS-CASPT2	Multistate complete active space - Perturbation theory: 2nd order
PES	Potential energy surface
PSB3	Protonated Schiff base - 3 double bonds
SA-CASSCF	State averaged complete active space self consistent field
SC	Semi-classical

SCF	Self consistent field
SE	Schrödinger Equation
SO	Spin-orbit
SOC	Spin-orbit coupling
TD-DFT	Time-dependent density functional theory
TDSE	Time Dependent Schrödinger Equation
TISE	Time Independent Schrödinger Equation
XLCT	Halide to ligand charge transfer

FRENCH ABSTRACT/RÉSUMÉ EN FRANÇAIS

Méthodes

La première partie n'a pas pour ambition de détailler la totalité de la théorie impliquée pour les calculs présentés dans la thèse, mais uniquement d'exposer le principe et l'intérêt des méthodes utilisées. Ainsi, un premier chapitre expose quelques principes de structure électroniques, alors qu'un deuxième traite des approches de dynamique nucléaire.
La chimie quantique repose en partie sur la résolution de l'équation de Schrödinger dépendente du temps :

$$\hat{\mathcal{H}} \left|\psi(\mathbf{r}, \mathbf{R}, t)\right\rangle = i\hbar \frac{\partial}{\partial t} \left|\psi(\mathbf{r}, \mathbf{R}, t)\right\rangle$$

Où $\hat{\mathcal{H}}$ est l'opérateur Hamiltonien tel que

$$\hat{\mathcal{H}} = \hat{T} + \hat{V}$$

Avec $\hat{T}$ l'opérateur d'énergie cinétique, et $\hat{V}$ l'opérateur d'énergie potentielle.
Dans le cas où l'opérateur d'énergie potentielle est constant en fonction du temps, il est possible de considérer uniquement l'équation de Schrödinger indépendante du temps

$$\hat{\mathcal{H}} \left|\psi_\alpha(\mathbf{r}, \mathbf{R})\right\rangle = E_\alpha \left|\psi_\alpha(\mathbf{r}, \mathbf{R})\right\rangle$$

Dans un système a plusieurs corps, contenant n electrons ainsi que N noyeaux, l'Hamiltonien moléculaire prend la forme :

$$\hat{\mathcal{H}} = \hat{T}_e + \hat{V}_{eN} + \hat{V}_{ee} + \hat{V}_{NN} + \hat{T}_N$$

Avec $\hat{T}_e$ et $\hat{T}_N$ respectivement les opérateur d'énergie cinétique des électrons et des noyaux, $\hat{V}_{eN}$ l'attraction Coulombienne électron-noyeau et, $\hat{V}_{ee}$ et $\hat{V}_{NN}$, les répulsions électron-électron d'une part, et noyeau-noyeau d'autre part.

Approximation de Born-oppenheimer.

La fonction d'onde exacte d'un système Ψ_{tot} peut être écrite comme une combinaison linéaires d'états dits de Born-Oppenheimer ou adiabatiques :

$$\Psi_{tot}(\boldsymbol{r}, \boldsymbol{R}) = \sum_i \chi_i^a(\boldsymbol{R})\psi_i^a(\boldsymbol{r}, \boldsymbol{R})$$

Où ψ_i^a sont les fonctions d'ondes électroniques qui dépendent paramétriquement des coordonnées nucléaires et χ_i^a représentent les fonctions d'ondes nucléaires solutions de l'équation de Schrödinger pour les noyaux. Les fonctions d'ondes électroniques sont quant à elles solutions de l'Hamiltonien électronique à géométrie nucléaire fixe :

$$\hat{\mathcal{H}}_e \left|\psi_i^a(\boldsymbol{r}, \boldsymbol{R})\right\rangle = V_i(\boldsymbol{R}) \left|\psi_i^a(\boldsymbol{r}, \boldsymbol{R})\right\rangle$$

Où $V_i(\boldsymbol{R})$ est l'énergie potentielle dite adiabatique à une position donnée des noyaux. La résolution de l'équation de Schrödinger pour toutes les positions $\boldsymbol{R}$ des noyeaux, définit la surface d'énergie potentielle.
En injectant la fonction d'onde totale Ψ_{tot} dans l'équation de Schrödinger, nous obtenons un jeu d'équations couplées :

$$\left[V_j(\boldsymbol{R}) + \hat{T}_N - E\right] \chi_j^a(\boldsymbol{R}) = -\sum_i \hat{\Lambda}_{ij}\chi_i^a(\boldsymbol{R})$$

Où apparaissent les couplages non-adiabatiques $\hat{\Lambda}_{ij}$. Négliger ces couplages constitue l'approximation de Born-Oppenheimer. On peut alors considérer que les noyaux se meuvent sur un potentiel donnés par les électrons. Cette approximation est valable lorsque la différence d'énergie entre les états électroniques est importante. Quand plusieurs états électroniques se rapprochent ces termes de couplages deviennent non-négligeables est présentent même une singularité à la dégénérescence entre deux (ou plus) états électroniques.
Cette singularité rend les calculs de dynamique quantique très ardus, il est donc nécessaire d'utiliser une autre représentation des SEP qui minimisera cette singularité. Pour ce faire, plusieurs méthodes existent, dont deux sont présentées dans cette thèse.

Diabatisation

Le processus de diabatisation consiste à transformer les états dits adiabatiques dans une nouvelle représentation dite diabatiques, où les couplages cinétiques seront faibles et ne présenteront plus de singularité. En effectuant cette transformation, il est possible de négliger les reliquats de couplages cinétiques. Cette transformation fait apparaître des couplages inter-états de type potentiel qui ne présenteront pas de singularités.
Deux méthodes de diabatisation sont largement utilisées :

– La méthode dite des états régularisés, qui permet de construire un jeu d'états électroniques diabatiques à partir des énergies adiabatiques. Cette méthode peut être vue comme une interpolation entre deux limites : (1) un point de d'intersection, autour duquel les états électroniques diabatiques seront modélisés par un développement de Taylor. Et (2) une zone très éloignée de l'intersection où les états diabatiques et adiabatiques seront confondus.
– La méthode dite par « Ansatz », qui consiste a déterminer les états électroniques diabatiques, ainsi que les couplage par une procédure auto-cohérente d'optimisation de ces derniers à partir d'une forme analytique initiale en comparaison aux états électroniques adiabatiques calculés.

Surfaces d'énergie potentielle

Les surfaces d'énergie potentielle traduisent l'évolution de l'énergie des états électroniques en fonctions des déplacements nucléaire, de ce fait, elles représentent le paysage chimique du système et sont utilisées pour comprendre et modéliser la réactivité chimique et physique d'un système moléculaire.
L'étude de la topologie de ces surfaces est donc primordiale puisqu'elle permet de déterminer les points critiques qui dirigeront la réactivité. Parmi ceux-ci se trouvent les minima et maxima (à la fois locaux et globaux) qui sont caractérisés par un gradient nul selon tous les déplacements nucléaires.
Néanmoins, le gradient seul ne permet pas de différencier les minima des maxima, il est donc nécessaire de calculer la dérivée seconde de l'énergie en fonction des déplacements nucléaires (le Hessien). Si toutes les valeurs propres de ce dernier sont positives, alors le point stationnaire est un minimum. Au contraire, si une ou plusieurs valeurs propres du Hessien sont imaginaires, alors le point stationnaire est un point selle.

Un croisement peut avoir lieu entre deux ou plusieurs états électroniques. Ces croisements sont très importants pour la dynamique dans les états excités des systèmes moléculaires. Ils sont appelés « intersections coniques » et permettent la transition ultra-rapide entre deux états électroniques.
Ces objets topologiques sont des objets de dimensionnalité 3N-8 (N étant les nombres d'atomes) et sont caractérisés par les deux vecteurs qui lèvent la dégénérescence entre les états électroniques au premier ordre. Ces vecteurs sont appelés (1) vecteur de différence de gradient et (2) vecteur de couplage dérivatif. Ils forment le sous espace communément appelé espace de branchement.
Les intersections coniques jouant un rôle majeur dans la photochimie et photophysique des molécules, de grands efforts ont été fourni afin d'explorer et de caractériser leur topologie. En effet, c'est la topologie de ces « sillons » d'intersection qui auront une influence sur le rendement et la vitesse de certains processus comme par exemple la photoisomérisation.

Méthodes de Chimie Quantique

Diverses approches sont possibles afin de calculer l'énergie des états électroniques. Nous aborderons ici principalement les méthodes post Hartree-Fock que nous avons utilisées ainsi que l'approche de la fonctionnelle de la densité.

L'approximation Hartree-Fock

Résoudre l'équation de Schrödinger électronique n'est pas possible exactement, à cause du terme de répulsion électron-électron présent dans l'Hamiltonien moléculaire. L'approximation de Hartree-Fock consiste à traiter cette répulsion comme une interaction moyenne entre un électron et un champ-moyen (ν^{HF}) constitué par tous les autres électrons. L'Hamiltonien électronique prend alors la forme

$$\hat{\mathcal{H}}_e = \sum_i^n \left(\hat{h}(i) + \nu^{HF}(i)\right) + \hat{V}_{NN}$$

où $\hat{h}(i)$ est l'Hamiltonien mono-électronique associé à l'électron i et $v^{HF}(i)$ le champ moyen ressenti par l'électron i, et formé par les n-1 électrons restants. D'autre part, la fonction d'onde électronique du système (Ψ) est exprimée comme un déterminant de Slater d'orbitales moléculaires φ_p tel que

$$\psi(x_1, x_2, \cdots, x_N) = \frac{1}{\sqrt{N!}} |\varphi_1(x_1)\varphi_2(x_2)\cdots\varphi_N(x_N)| .$$

Ces orbitales moléculaires sont elles-même construites comme des combinaison linéaires de fonctions de base ζ_i (*i.e*, les orbitales atomiques) :

$$\varphi_p(x) = \sum_{i=1}^{M} c_{pi}\zeta_i(x)$$

L'énergie est ensuite minimisée, et les orbitales molécules optimisées de manière auto-cohérente pour obtenir l'énergie électronique du système.

L'Interaction de Configurations

Afin de décrire l'intéraction électron-électron de manière plus correcte, il est possible d'exprimer la fonction d'onde électronique du système comme une combinaison linéaire de fonctions d'état de configuration construites à partir d'un unique déterminant de Slater ψ_0

$$\Psi^{CI} = c_0\psi_0 + \sum_{a,r} c_a^r\psi_a^r + \sum_{\substack{a<b \\ r<s}} c_{a,b}^{r,s}\psi_{a,b}^{r,s} + \cdots$$

où ψ_a^r et $\psi_{a,b}^{r,s}$ correspondent respectivement à des déterminants mono- et bi-excités en promouvant un électron de l'orbital a(b) vers l'orbital r(s). $c_{a,\cdots}^{r,\cdots}$ sont les coefficients des fonctions d'états de configuration.
L'énergie est alors minimisée en developpant la fonction d'onde sur tout les déterminants excités, en en optimisant les coefficients $c_{a,\cdots}^{r,\cdots}$. Cette méthode étant variationnelle, si l'on considère tous les déterminants excités possibles dans une base d'orbitales infinie, elle donne la valeur exacte de l'énergie.

Les méthodes MCSCF

Certains systèmes ne peuvent être décrit par un seul déterminant de référence (benzène, ...). Il faut alors employer des méthodes dites multi-configurationnelles (MCSCF). La description de la fonction d'onde est alors basée sur une combinaison linéaire de déterminant de Slater

$$\Psi^{MCSCF} = \sum_{I}^{M} c_I \Psi_I^{SD}.$$

L'énergie est ensuite déterminée en optimisant à la fois les coefficients c_I et les orbitales moléculaires avec lesquelles sont construits les déterminants de Slater. La relaxation des orbitales permet de mieux décrire la corrélation électronique.

La méthode CASSCF/CASPT2

La méthode CASSCF (Complete Active Space Self Consistent) est une des méthodes MCSCF les plus répandues. Les déterminants de Slater contribuant à la fonction d'onde MCSCF sont choisis comme tous les déterminants M possibles dans un nombre restreint d'orbitales, appelé « espace actif » :

$$\Psi^{CASSCF} = \sum_{I}^{M} c_I \Psi_I \qquad \forall I \in \text{espace actif}.$$

Une amélioration de cette approche, est la méthode CASPT2. Elle consiste à appliquer la théorie de la perturbation à une fonction d'onde de type CASSCF. L'Hamiltonian électronique prend alors la forme

$$\hat{\mathcal{H}}_e = \hat{\mathcal{H}}^{(0)} + \lambda \hat{V}$$

où $\hat{\mathcal{H}}^{(0)}$ est l'Hamiltonian d'ordre zéro, dont la fonction propre est la fonction d'onde CASSCF (Ψ^{CASSCF}) telle que

$$\hat{\mathcal{H}}^{(0)} \Psi^{CASSCF} = E^{(0)} \Psi^{CASSCF}$$

et où la perturbation $\lambda\hat{V}$ est faible devant $\hat{\mathcal{H}}^{(0)}$. Il est alors possible d'écrire l'énergie comme un developpement de Taylor :

$$E = E^{(0)} + \lambda E^{(1)} + \lambda^2 E^{(2)} + \cdots$$

limiter ce développement au deuxième ordre correspond à la méthode CASPT2, qui est une extension de la théorie Moller-Plesset au second ordre (MP2).
Les méthodes CASSCF et CASPT2 sont devenues des méthodes standard en calculs de chimie quantique et sont utilisées dans cette thèse.

Dynamique Nucléaire.

Dans cette partie, deux méthodes sont exposées afin de traiter de la dynamique des noyaux.

MCTDH.

La première de ces méthodes consiste à résoudre l'équation de schrödinger dépendante du temps pour les noyaux. Pour ce faire nous utilisons le programme de dynamique quantique MCTDH de Heidelberg.
Cette méthode permet de calculer l'évolution temporelle d'un paquet d'onde sur des surfaces d'énergie potentielle diabatique en tenant compte des couplages inter-états.
L'intérêt de cette méthode réside en sa capacité à séparer les variables, permettant ainsi de réduire le temps de calcul tout en tenant compte des effets quantiques.

La dynamique moléculaire semi-classique.

Contrairement à la méthode MCTDH, la dynamique semi-classique ne traite pas la totalité du système de manière quantique. En effet, la trajectoire des noyeaux est propagée de manière classique (*i.e*, selon les équations de Newton) grâce aux forces issues d'un calcul de chimie quantique. Les trajectoires sont propagées par l'algorithme Verlet. Les couplages non-adiabatiques n'étant pas pris en compte jusque lors, il est nécessaire d'utiliser un algorithme de saut qui estimera la probabilité de transition d'un état électronique vers un autre selon des critères extraits des calculs de structure électronique.

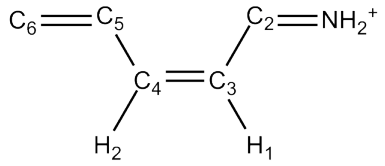

FIGURE 1 – Le modèle minimal du chromophore du rétinal étudie, le PSB3.

Etude du PSB3 : Un modèle minimal du rétinal.

Le processus de photoisomérisation du rétinal au sein de sa protéine, la Rhodopsine, est le premier évènement du processus de vision. Après absorption de lumière, le chromophore du rétinal isomérise spécifiquement autour d'une liaison C-C de manière très rapide (~ 200 fs) et avec un rendement quantique élevé ($\sim 67\%$). Ces propriétés exceptionnelles font du chromophore du rétinal un système de grand intérêt et très étudié, autant de manières expérimentales que théoriques. Afin d'effectuer une étude de dynamique quantique, il est nécessaire d'étudier un modèle minimal du chromophore du rétinal, le PSB3 (« Protonated Schiff Base 3 double liaisons »), voir FIG. 1. La petite taille de ce modèle ainsi que sa structure électronique qui reproduit les traits caractéristiques du chromophore du rétinal l'ont amenés à être un système modèle pour l'étude de différents méthodes de calculs de structure électronique. Dans ce travail, nous souhaitons faire de ce modèle, un système modèle pour les méthodes de dynamiques nucléaire. Pour ce faire, il est nécessaire de construire des surfaces d'énergie potentielle dites diabatiques à partir de calculs ab initio adiabatiques.

Structure électronique

L'état absorbant est le premier état électronique, et est l'état électronique dans lequel aura lieu la photoisomérisation. Cet état est caractérisé par une transition HOMO $\rightarrow$ LUMO et par un transfert de charge d'un bout (NH_2^+) de la molécule vers l'autre (CH_2) comme dans le chromophore du rétinal. La nature même de cette excitation déverrouille la torsion autour de la double liaison centrale. En effet, un électron est promu d'une orbital avec de la densité électronique π sur la double liaison centrale $\mathrm{C}_4 - \mathrm{C}_3$ à une orbital n'en ayant pas. Afin d'effectuer des calculs de dynamique quantique, il est nécessaire de réduire davantage la dimensionnalité du système. Afin d'analyser et d'extraire les coordonnées

jouant un rôle majeur dans la photoisomérisation du PSB3, nous avons effectué une série de calculs préliminaires.

Calculs préliminaires

Dans un premier temps, nous avons effectué des calculs de dynamique semi-classique en partant de la géométrie d'équilibre dans l'état électronique fondamental. L'analyse de l'évolution de l'énergie deux premiers états électroniques ainsi que l'évolution des longueurs de liaison et des angles dièdres du squelette carboné nous ont permis de déterminer trois phases lors de la photoisomérisation. Dans un premier temps, la réorganisation ultra-rapide des longueurs de liaison, qui intervient dans les dix premières femtoseconde. Vient ensuite, une zone où les états électroniques se rapprochent. Dans cette zone, on observe majoritairement une déformation des angles dièdres. Finalement la trajectoire atteint un point du sillon d'intersection conique est « saute » du premier état électronique à l'état électronique fondamental pour ensuite relaxer en forme trans. Dans cette zone, on observe principalement une déformation des angles dièdres $\mathrm{C}_5 - \mathrm{C}_4 - \mathrm{C}_3 - \mathrm{C}_2$, définissant la torsion autour de la double liaison centrale, et $\mathrm{H}_2 - \mathrm{C}_4 - \mathrm{C}_3 - \mathrm{H}_1$, définissant le mouvement hors du plan des hydrogènes. Ce dernier est appelé HOOP et est connu pour influencer l'issue de la photoisomérisation. Dans un deuxième temps, nous avons optimisé la géométrie du minimum du sillon d'intersection. Cette optimisation nous permet d'obtenir l'espace de branchement, composé des deux vecteurs qui lèvent la dégénérescence. Dans le cas du PSB3, la géométrie du minimum d'intersection est une structure où les angles dièdres $\mathrm{C}_5 - \mathrm{C}_4 - \mathrm{C}_3 - \mathrm{C}_2$ et $\mathrm{H}_2 - \mathrm{C}_4 - \mathrm{C}_3 - \mathrm{H}_1$ sont de $90°$. L'espace de branchement associé à cette géométrie comprend d'un côté un mouvement d'élongation de la liaison $\mathrm{C}_3 - \mathrm{C}_2$ et de contraction de la liaison C-N. Les trois autres liaisons sont impliquées à moindre mesure. D'un autre côté, l'espace de branchement comprend des mouvements hors du plan des atomes C_5, C_2, H_1 et H_2. Ces mouvements représentent la torsion de la double liaison centrale et les mouvements HOOP. La présence d'une intersection conique à cette géométrie (i.e. la dégénérescence entre les deux premiers états électroniques) peut être expliquée par une simple représentation orbitalaires. En effet à cette géométrie, les deux orbitales impliquées dans le premier état électroniques passent d'une nature liante et anti-liante respectivement à un caractère non-liant sur la liaison centrale.

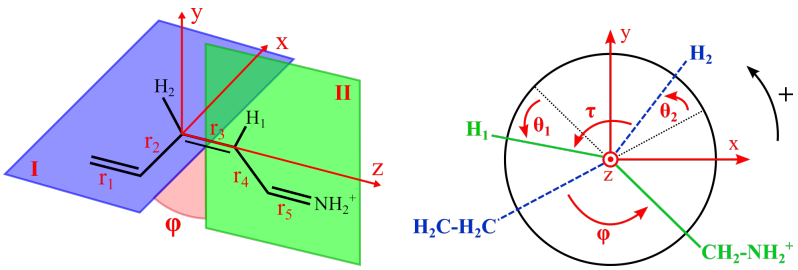

FIGURE 2 – Le modèle minimal du chromophore du rétinal étudie, le PSB3.

Coordonnées actives.

Afin de représenter les déformations mises en évidence par les calculs préliminaires, c'est-à-dire la réorganisation des longueurs de liaison, la torsion autour de la double liaison centrale ainsi que le mouvement HOOP, nous avons choisi un jeu de huit coordonnées actives (FIG. 2) : - L'angle dièdre autour de la liaison central φ dans le but de décrire l'isomérisation. - Un angle de déformation hors du plan pour chacun des hydrogènes H_1 et H_2, θ_1 et θ_2 pour décrire les mouvements HOOP. - Cinq longueurs de liaisons r_1, r_2, r_3, r_4 et r_5 pour décrire respectivement les liaisons $C_6 - C_5$, $C_5 - C_4$, $C_4 - C_3$, $C_3 - C_2$ et $C_2 - N$. Dans le but de construire les surfaces d'énergie potentielle diabatique, il est important de convenablement étudier l'influence des différentes coordonnées sur l'énergie totale du système. En comprenant la physique derrière ces déformations, il sera plus aisé de trouver des formes analytiques pour la construction des surfaces d'énergie potentielle ayant un sens physique.

La torsion autour de la double liaison centrale.

En observant l'évolution de l'énergie des états électroniques selon la seule torsion φ (toutes les autres dimensions considérées comme fixes), on peut de but en blanc observer qu'à $90°$ nous observons un point du sillon d'intersection. Ceci n'est pas évident, puisque dans d'autres systèmes, à l'instar de l'éthylène, la torsion autour de la double liaison centrale seule n'est pas suffisante pour observer une intersection conique.
Une autre caractéristique peut être observée. En effet, entre les formes planes cis et trans (i.e. $\varphi = 0°$ et $\varphi = 180°$ respectivement) et l'intersection conique ($\varphi = 90°$) nous pouvons observer deux barrières d'énergie. En étudiant la nature des états électroniques, il devient évident que cette barrière est due à un couplage entre le premier et le deuxième

état électronique excité. A $\varphi = 0°$ et $\varphi = 180°$ le premier état électronique excité est composé d'une faible pourcentage d'une excitation HOMO $\rightarrow$ LUMO+1. Or l'orbitale LUMO+1 (à la différence de l'orbitale LUMO) contient de la densité électronique π sur la double liaison centrale, stabilisant les formes planes. Au fur et à mesure que l'on effectue une rotation autour de la liaison centrale, cette contribution électronique au premier état électronique excité diminue, créant la barrière d'énergie.

Les mouvements HOOP

Le mouvement HOOP est défini dans notre système de coordonnées par les deux angles hors du plan θ_1 et θ_2 des hydrogènes H1 et H2 respectivement. L'angle dièdre entre ces deux hydrogènes (τ) peut donc être écrit en fonction des angles φ, θ_1 et θ_2 tel que

$$\tau = \varphi + \theta_1 - \theta_2. \tag{1}$$

Dans un premier temps, afin principalement de réduire la dimensionnalité du système, nous définissons deux nouvelles coordonnées (θ^- et θ^+) à partir de θ_1 et θ_2 :

$$\begin{aligned} \theta^- &= \frac{\theta_1 - \theta_2}{2} \\ \theta^+ &= \frac{\theta_1 + \theta_2}{2}. \end{aligned} \tag{2}$$

Alors que θ^- rend compte de l'angle dièdre entre les deux hydrogènes, θ^+ permet de quantifier la déformation des deux hydrogènes par rapport à leur position initiale. De plus, θ^- est inclus dans l'espace de branchement, alors que θ^+ non. Il nous est donc possible, dans un premier temps, de considérer uniquement les valeurs de θ^- pour une valeur de θ^+ minimale, i.e. de moindre déformation.
Une analyse détaillée de la surface d'énergie potentielle selon φ et θ^- pour les trois premiers états électroniques nous a permis de déterminer une condition géométrique à la présence d'une intersection conique entre les deux premiers états électroniques. En effet, le sillon d'intersection est observé le long d'une ligne d'équation :

$$\varphi + \theta^- = 90°. \tag{3}$$

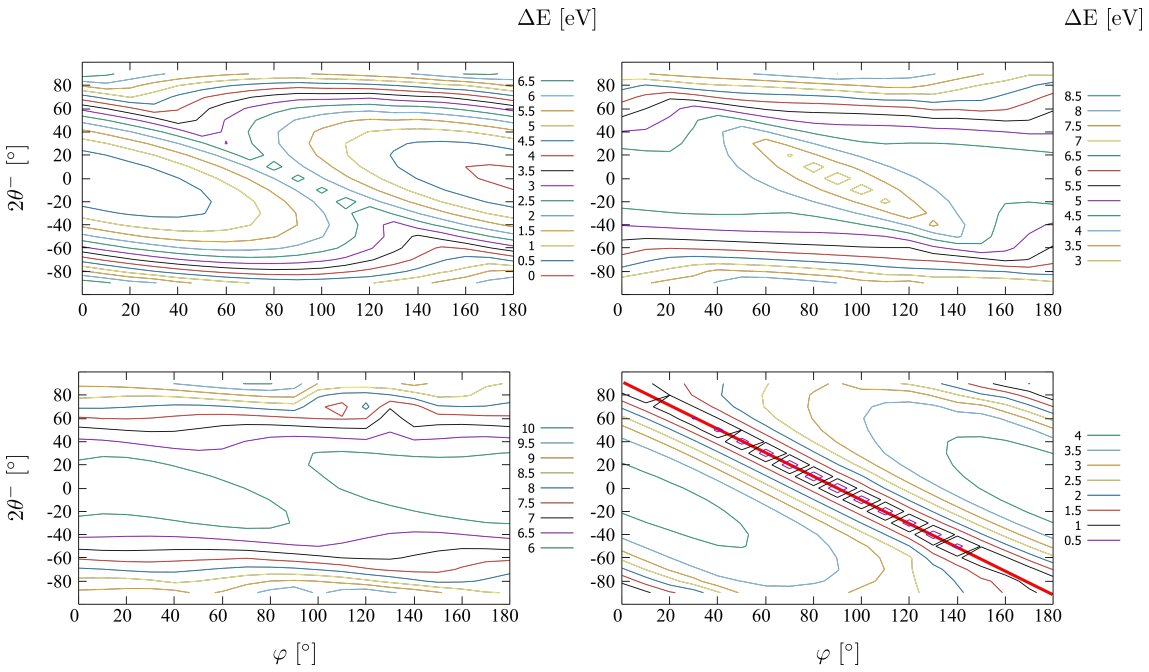

FIGURE 3 – Surfaces d'énergie potentielle en fonction de φ et θ^- ($\theta_1 = -\theta_2$ tel que $\theta^+ = 0$). Haut, gauche : Etat fondamental. Haut, droite : Premier état excité. Bas, Gauche : Deuxième état excité. Bas, Droite : Différence d'énergie entre le premier état excité et l'état fondamental.

Cette observation est appuyé par son sens physique qu'il est possible de comprendre par une explication orbitalaire. En effet, une déformation des angles θ_1 et θ_2 modifie l'orientation des orbitales p portées par les carbones C3 et C4. Ces orbitales pourront donc être orthogonales entre elles pour des valeurs de φ différentes de $90°$, moyennant une déformation suffisante des angles θ_1 et θ_2.
Les mouvements HOOP joue donc un rôle clé dans le photoisomérisation, puisqu'en plus d'influer sur l'issue de la photoisomérisation, ils permettent également de moduler le sillon d'intersection, et de le rendre accessible à des valeurs de φ inférieures à $90°$.
C'est en tenant compte de ces considérations que des premières tentatives de construction des surfaces d'énergie potentielle diabatique ont été effectuées. Bien que les surfaces d'énergie potentielle diabatiques obtenues à ce jour ne soient pas satisfaisantes, elles reproduisent néanmoins certaines caractéristiques comme la position du sillon d'intersection ou la présence des barrières d'énergie entre Franck-Condon et le-dit sillon.

Directionalité de la dynamique de photoisomérisation d'une double liaison induite par un seul centre stéréogène.

Comme mentionné précédemment, le processus de photoisomérisation du rétinal est très efficace et très rapide. Ces propriétés font du rétinal une modèle de base pour la construction de photo-commutateurs. De plus, la nature asymétrique de la poche peptidique de la Rhodopsine, dans laquelle est localisé le chromophore du rétinal, induit une directionalité dans l'isomérisation. Cette dernière propriété est très intéressante pour l'élaboration de photo-moteurs moléculaires.
Dans ce travail, nous nous intéressons à un modèle de moteur dont le design a été basé sur le modèle minimal de rétinal présenté précédemment. L'ajout de carbone sp3 à ce modèle, permet une méthylation d'un de ces centres stéréogènes, induisant la chiralité.
La propagation de 200 trajectoires semi-classiques dont les conditions initiales (positions et vitesses) représentent une distribution thermique, a mis en évidence l'unidirectionalité du modèle chiral de photo-moteur. L'origine de cette directionalité a été étudiée en comparaison au modèle de photo-commutateur achiral, totalement symétrique vis-à-vis de la torsion de la double liaison.
Deux hypothèses ont été avancées. La première est que la directionalité est induite par

la déformation de la géométrie initiale due à la fonctionnalisation du carbone sp3. La deuxième est que cette directionalité est causée par la masse du groupement méthyl en comparaison à celle de l'hydrogène.
Afin de confirmer ou d'infirmer ces suppositions, davantage de trajectoires ont été propagées avec pour conditions initiales celles du modèle achiral, et vice-versa. Ces investigations ont montré que les déformations de la géométrie initiale ainsi que l'effet inertiel du méthyle ne sont pas suffisant pour expliquer l'unidirectionalité du modèle de photomoteur étudié.
Cependant, le modèle chirale a une surface d'énergie potentielle asymétrique en fonction de la torsion autour de la double liaison. Après excitation, la courbe d'énergie potentielle du premier état électronique excité présente une barrière d'énergie de part et d'autre de Franck-Condon. Contrairement au modèle PSB3, ces barrières ne sont pas égales. Après relaxation des longueurs de liaison, ces barrières disparaissent et laissent place à une courbe d'énergie potentielle inclinée vers le sens de rotation correspondant à la position du méthyl.

Propriétés structurelles et spectroscopie d'absorption UV-Visible d'un complexe de Retinal-pyridyl-CN Re(I) Carbonyl Bipirydine : Etude théorique.

La coordination d'un ligand isomérisant à un complexe de rhénium, permet l'isomérisation par lumière dans le domaine du visible. Dans cette partie, nous avons effectué une étude préliminaire d'un ligand de type rétinal lié à un atome de Rhenium (FIG. 4).

Propriétés structurales et electronic de l'état électronique fondamental.

La conformère tout-trans a ainsi que les conformères cis autour d'une liaison à la fois. On définit les conformères 1c, 2c, 3c, 4c, et 5c comme étant les conformères cis autour des liaisons $C_{16}C_{15}$, $C_{14}C_{13}$, $C_{12}C_{11}$, $C_{10}C_9$ et C_8C_7 respectivement. Pour chaque conformère un angle de torsion τ est définit. Il est égal à 0° pour le conformère cis, et 180° pour le

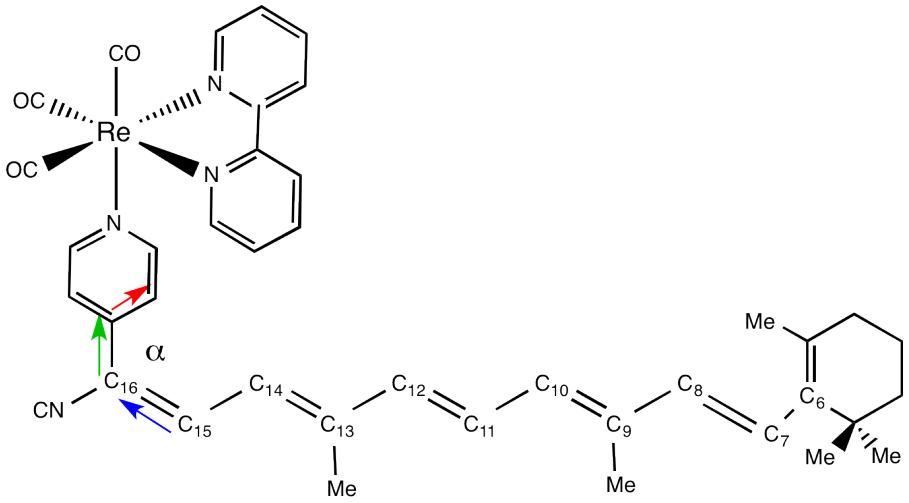

FIGURE 4 – Le complexe $[Re(CO)_3(bpy)(L)]^+$, L=Ret-pyr-CN

conformère trans.

Chaque conformère présente une alternance de liaisons courtes et de liaisons plus longues de longueurs caractéristiques intermédiaires entre simple et double liaisons, comme dans le chromophore du rétinal. Pour des raisons stériques, le conformère le plus stable est le conformère 1c, quasi-dégénéré avec le conformère tout trans a. Les conformères où la liaison isomérisante est substituée par un groupement méthyl (i.e. 2c, 4c) sont moins déstabilisés que les conformères où la liaison n'est pas substituée. (i.e. 3c, 5c).

Les orbitales Kohn-Sham sont semblables pour tous les conformères. Les orbitales HOMO et HOMO-1 sont des orbitales π sur le rétinal alors que les orbitales HOMO-2, HOMO-3 et HOMO-4 sont principalement des orbitales d du métal. Les orbitales virtuelles les plus basses sont soit des orbitales π^* sur le rétinal (LUMO, LUMO+2), soit des orbitales π^* sur le ligand bipyridine (LUMO+1, LUMO+3, LUMO+4). Ces orbitales donnent lieu aux états électroniques les plus bas en énergies, et qui seront susceptibles d'être peuplés par absorption de lumière.

Diagrammes de corrélation des états.

Afin de construire les diagrammes de corrélation des états entre le conformère tout-trans a et chacun des conformère cis, nous avons optimisé chacun des conformères à en contraignant l'angle de torsion τ autour de la liaison isomérisante à 90° dans l'état fondamental. Cette méthode nous permet d'obtenir une limite haute de la barrière d'isomérisation. En

effet, contrairement au chromophore seul ou dans son environnement peptidique où la photoisomérisation est un processus concerté autour de plusieurs liaisons, nous ne considérons ici qu'un mouvement de rotation autour d'une unique liaison C=C.

Spectre d'absorption en TD-DFT.

Les spectres d'absorption des différents conformères sont très semblables et consistent en une bande très intense vers 700nm due à une transition intra-ligand sur le rétinal (HOMO $\rightarrow$ LUMO). Vient ensuite une bande moins intense, représentant à nouveau une transition intra-ligand sur le rétinal (HOMO-1 $\rightarrow$ LUMO). L'orbitale HOMO-1 étant localisée en partie sur le métal, l'intensité d'absorption est plus faible. Les pics suivants sont des mélanges entre des transitions MLCT et LLCT. La plupart de ces états bas en énergies pourront être peuplés directement ou indirectement après irradiation à 400nm.
Cette étude préliminaire se veut être le précurseur d'études expérimentales actuellement

en cours. Pour le moment, il serait imprudent d'aller au-delà de cette analyse qualitative du système.
Néanmoins, les résultats des expériences nous permettront de comparer nos résultats théoriques à l'expérience et nous aidera à orienter et approfondir notre étude.

Croisement intersystèmes ultra-rapides dans des complexes de Re(I).

La dernière partie de cette thèse présente une méthode permettant d'effectuer une simulation de dynamique quantique sur des complexes métalliques à haute dimensionnalité tout en prenant compte, non seulement des couplages vibroniques, mais également des couplages spin-orbite intervenant entre états de multiplicité de spin différente. A la différence des systèmes présentés jusque lors, une grande variété de complexes métalliques sont rigides et n'implique pas de mouvements de grandes amplitudes (torsion, dissociation,...). Il est alors possible modéliser les états ainsi que les couplages diabatiques par

des formes analytiques approchées. Pour ce faire, nous avons développé dans un premier temps un Hamiltonien modèle diabatique permettant d'estimer à la fois les états diabatiques et les couplages à partir d'un nombre limité de calculs de structure électronique. Dans un deuxième temps, nous avons confronté notre Hamiltonien à l'étude de la dynamique de désexcitation d'un complexe de [Re(X)$(CO)_3$(bpy)] (X= F, Cl, Br, I ; bpy= bipyridine). Ce complexe, étudié expérimentalement par fluorescence résolue en temps présente un comportement contre-intuitif vis-à-vis de l'évolution du temps de désexcitation par rapport à la masse de l'Halogène. En effet, il a été observé que plus la masse de l'Halogène augmente, et donc plus les couplages spin-orbite sont important, plus la désexcitation est lente.

Construction de l'Hamiltonien

Notre Hamiltonien modèle est basé sur l'approche « Linear Vibronic Coupling ». Ainsi les états diabatiques ainsi que les couplages vibroniques sont approximés par des developpements de Taylor. La force de cette approche est qu'il est nécessaire de connaître très peu de paramètres pour pouvoir construire les états diabatiques. En effet, seuls la fréquence selon chaque mode normal, ainsi que le gradient à Franck-Condon et pour chaque état électronique, sont nécessaires. L'estimation du couplage vibronique est moins directe. Dans ce modèle nous nous restreignons à l'étude des couplages vibroniques entre deux états uniquement. Dans ce cas particulier, le couplage vibronique peut être estimé à partir de la dérivée seconde de la différence d'énergie entre les deux états électroniques.
Le système traité requiert l'inclusion des couplages spin-orbit dans l'Hamiltonien modèle. Ici, nous choisissons, en première approximation, de les considérer comme constant et égaux à leur valeur à Franck-Condon. Pour intégrer ces couplages dans notre Hamiltonien, nous considérons explicitement chaque composante de spin des états électroniques. Afin d'extraire les données nécessaires à la construction de l'Hamiltonien ; un programme fait-maison à été codé et pourra être appliqué à tous types de calcul de structure électroniques.

Etude de la structure électronique de complexes de [Re(X)(CO_3(bpy)].

Afin de tester la robustesse de l'Hamiltonien modèle, nous avons souhaité l'utiliser pour l'étude de dynamique quantique du processus de désexcitation des complexes de [Re(X)(CO_3(bpy)]. Une étude de structure électronique préalable est nécessaire pour déterminer les degrés de liberté électroniques à inclure nécessairement dans l'Hamiltonien.
Expérimentalement, l'absorption des complexes étudiés a lieu aux alentours de 400nm. Le deuxième état singulet $S2$ est l'état absorbant. Il est donc nécessaire de considérer au minimum cet état ainsi que tout les états inférieurs. Néanmoins, un calcul de type spin-orbit, a montré que cet état électronique $S2$ contribue à un état spin-orbite plus en énergie et nécessite l'inclusion de l'état triplet $T3$ (plus haut en énergie que $S2$).
Une fois la dimensionalité électronique déterminée, il est nécessaire de réduire la dimensionalité nucléaire du problème en sélectionnant un nombre limité de modes normaux ayant le plus d'impact dans la dynamique. Nous avons donc choisi un jeu de six modes normaux. Pour des raisons de symétrie, quatre d'entre eux vont modifier les états diabatiques, et les deux restant vont induire un couplage vibronique entre états.
Cette étape a été effectuée pour le complexe de Brome et les conclusions ont été reportées sur les trois complexes. Ainsi nous avons selectionné les même états électroniques ainsi que les même modes normaux pour chaque complexe. L'Hamiltonien défini, il est alors possible d'effectuer les simulations de dynamique quantique.

Dynamique quantique de complexes de [Re(X)(CO_3(bpy)].

Dans un premier temps, nous avons effectué uniquement la simulation de dynamique sur le complexe de Brome. Une simulation préliminaire en ne considérant pas les couplages vibroniques (uniquement les couplages de type spin-orbite) a été effectuée, et nous a permis de montrer que le spin-orbite seul ne permet pas d'expliquer les observations expérimentales. Il est donc nécessaire d'inclure les couplages vibroniques.
Une deuxième simulation (FIG. 5), incluant cette fois tout les couplages a été effectuée, et l'étude de l'évolution des populations dans les états spin-orbit est en accord avec les constantes de temps observées expérimentalement. Cet accord tend à valider notre modèle. La même méthode a donc été appliquée aux autres complexes (X=F, Cl, I).
L'évolution des populations, et notamment la décroissance de la population dans l'état initial, dans ces complexes sont en accord avec l'expérience. En effet, nous avons extrait

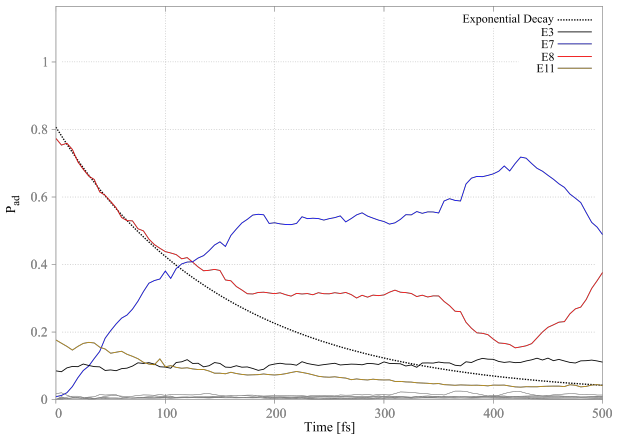

FIGURE 5 – Evolution des populations adiabatiques lors de la simulation de dynamique quantique pour le complexe de Brome.

des constantes de décroissantes du même ordre de grandeur que celle observées expérimentalement. De plus, la tendance dans ces constantes de temps et en accord avec les observations contre-intuitives mentionnées précédemment.
Néanmoins, l'application de cette méthode au complexe d'Iode, s'est révélée moins fructueuse. En effet, la constante de temps obtenue au travers de notre méthode est beaucoup trop faible, et ne correspond pas à la tendance observée. Ceci est dû au fait que les couplages spin-orbit sont beaucoup plus important dans ce complexe, et que la nature des états électroniques est différente. Une solution pour améliorer notre méthode, et pouvoir espérer traiter le complexe d'Iode serait de propager la dynamique non pas sur les états dits spin-diabatiques mais sur les états spin-adiabatiques.
En conclusion, notre méthode s'est revélée être suffisament robuste pour traiter les complexes de fluor, chlore et brome. Néanmoins, nous atteignons à ce jour, une limite de notre modèle lorsque les couplages spin-orbit sont trop importants.

GENERAL INTRODUCTION

Advanced methods of quantum chemistry are able to describe accurately and to predict chemical reactivity [6, 7, 8], molecular and electronic structures [9], magnetic [10] and optical properties [11, 12, 13, 14], in organic molecules as well as in inorganic complexes. Realistic models can treat various types of environment effects, either by means of polarized continuum models [15, 16] for standard solvents or based on hybrid quantum mechanics/molecular mechanics methods [17, 18, 19] for complex bio-environments such as DNA. The field of computational chemistry has expanded tremendously in the past twenty years thanks to the development of density functional theory, more particularly adapted to the electronic ground state properties. However still a number of challenges remain to be addressed not only in the field of relativistic chemistry [20].

The interpretation of electronic excited states properties, such as multi-photon absorption [21, 22, 23], two-dimension electronic spectra [24, 25], transient absorption spectroscopy, pump-probe experiments and ultra-fast time-resolved spectroscopies [26, 26, 27, 28, 29] are some of these defies. The bottleneck is not necessary the size of the molecular system to be investigated but its electronic complexity. Indeed, the determination of electronic excited states properties needs not only accurate quantum chemical methods able to describe near-degenerate states and/or multi-configurational wavefunctions, but also developments in semi-classical and quantum dynamics capable of providing excited states decays as function of time and branching ratio between concurrent pathways such as luminescence, non-radiative decays, isomerization, electron/energy transfers processes... All these channels activated mainly by UV light in organic chromophores and by visible irradiation in metal complexes open the route to important functions such as vision, photosynthesis, energy conversion, phototherapy, diagnostic or pollution probes.

For this ambitious purpose it is mandatory to determine accurately the character and properties of the electronic excited states and to investigate the coupling phenomena between them and with the ground state. This is the task of electronic structure methods, such as multi-configuration self consistent field wave functions methodologies and time-dependent density functional theory based on linear response approach. Whereas organic

chromophores are characterized by a few low-lying photo-active singlet electronic excited states, metal complexes present a high density and variety of excited states in a limited domain of energy (within 1.0 eV). However the electronic complexity in metal complexes is compensated by a less dramatic nuclear flexibility as compared to organic molecules. This is due to the presence of coordinated ligands that prevent in general significant rearrangements of the system within a short time-scale after irradiation. Finally relativistic effects, and more importantly for photochemical and photophysical processes, spin-orbit coupling between states of different multiplicities, cannot be circumvented in metal complexes. Indeed these effects control the kinetics of intersystem crossing processes that could become concurrent to internal conversions and fluorescent decays as illustrated by recent ultra-fast time-resolved experiments [30, 31, 32]. Ultrafast processes have been extensively observed with the development of LASER based techniques such as time-resolved spectroscopies. Femtosecond LASERs allow for the generation of light pulses short enough to probe the motions of the nuclei. In the future, we may even be able to observe the electrons motion with attosecond experiments.

The interpretation of these sophisticated experiments needs robust theoretical tools able to simulate the molecular electronic excited states dynamics during the first picoseconds following the absorption of light. The purpose of the thesis is the study and the interpretation of ultra-fast processes occurring in organic chromophores, models for active isomerizable molecules in the vision process, as well as in third-row transition metal complexes, seat of ultra-fast luminescent decay measured experimentally.

In our quest to understand and predict isomerization mechanisms in rhenium complexes coordinated to isomerizable ligands [33, 34, 35] and to compare organic and inorganic photoreactivity, we have undertaken the study of the isomerization of a pyridyl cyanoretinal ligand coordinated to a rhenium (I) bipyridine carbonyl complex for which only few experimental data are available.

The work presented in the thesis is based on various methods of quantum chemistry, semiclassical and quantum dynamics adapted to the molecular systems of interest and explicit problematics. Specific model Hamiltonians have been developed for treating vibronic and spin-orbit couplings on the same footing in the simulation of ultra-fast intersystem crossing processes in rhenium compounds.

The sticking point common to the studies performed within the context of this thesis is the nuclear dimensionality and more specifically the selection of active nuclear coordinates relevant to the investigated processes (isomerization, ISC). The electronic problem being

less tricky in organic chromophores than in transition metal complexes it is then possible to include all degrees of freedom in semi-classical dynamics simulations as illustrated in the minimal photoswitch model. Moreover, on the basis of electronic properties and preliminary semi-classical trajectories important nuclear coordinates (up to a few tens) can be selected and injected into quantum dynamics accurate simulation. However, the bottleneck is the construction of realistic multidimensional diabatic potential energy surfaces, as illustrated by the study of photoisomerization in the minimal model of retinal. In contrast, the electronic problem is more complicated in transition metal complexes because of the high density of states. In this case, approximate methods that avoid the computation of multidimensional potential energy surfaces are necessary to describe the evolution of the system as function of time. The development and application of such approaches is at the heart of the work dedicated to the ultrafast system crossings in rhenium complexes.
This work is organized into three sections. The first one, part A, is devoted to the concepts and theory useful for a comprehensive reading of the next sections, part B and C are dedicated to isomerization processes in organic and inorganic chromophore and ultrafast intersystem crossing in Re(I) complex, respectively.
The first part is divided into two chapters. In the first chapter, we develop key notions about electronic structure theory, such as the Born-Oppenheimer approximation and its limitation, the theory about the diabatic representation as well as methods to build the so-called diabatic states, and finally we present two kinds of quantum chemistry methods that we use in the rest of the thesis, namely methods relying on wavefunction and density functional theories. The second chapter concerns methods to treat nuclear dynamics. On one side, a fully quantum based methods: the MCTDH methodology, that allows to treat accurately small systems in reduced dimensionality, and on the other side, a mix of classical dynamics and quantum chemistry called semi-classical dynamics that allows to treat large systems including all degrees of freedom.
Part B of the thesis, which focuses on the study of the photoisomerization processes, is subdivided into three chapters that describe the study of three distinct molecular systems. The first chapter concerns the investigation of a minimal model for the retinal chromophore. Its goal is to bring our contribution to a better understanding of the photoisomerization process occurring in the first event of vision. For performing quantum dynamics we are required to select the most relevant coordinates describing the process in order to build the diabatic potential energy surfaces. In a first step, we perform static electronic structure analysis on critical geometries (minima and conical intersection struc-

tures). In a second step, semi-classical dynamics methods are used for selecting active coordinates. The last step is dedicated to the exploration of the potential energy surfaces as function of the selected active coordinates in order to extract the data relevant for the construction of diabatic electronic states. A tentative fitting procedure is proposed for the building of the diabatic states.

The second chapter, treats a minimal chiral molecular motor, the design of which is based on the 2,4-pentadieniminium cation. The unidirectional rotary motion of the system is investigated by means of semi-classical trajectories.

The third chapter is dedicated to the study of a retinal-like ligand coordinated to a rhenium(I) atom. This static study aims at investigating the effect of the coordination to a transition metal on the photoisomerization mechanism. For this purpose the structural, electronic and optical properties of the all-*trans* and various *cis* conformers of the complex are investigated by time-dependent density functional theory.

The third part of the thesis is devoted to ultrafast intersystem crossing processes in transition metal complexes. Since such systems are too large to be treated by means of semi-classical dynamics, we have developed a diabatic model Hamiltonian that includes both vibronic and spin-orbit coupling though being simple enough to be used on large systems. In a first chapter, we will present the development of the diabatic model Hamiltonian and the approximations on which it relies to describe diabatic electronic states and both spin-orbit and vibronic couplings. Then, we present the tools developed for extracting the required electronic structure data and the method used in the model Hamiltonian. In the second chapter, we study the [Re(X)$(CO)_3$(bpy)] complexes, where X is an halogen (F, Cl, Br, I). This study is motivated by experimental observations that seem *a priori*, conterintuitive to the relativistic representation we have of heavy atoms. Indeed, the decay time after absorption increases with the mass of the halogen instead of decreasing due to the awaited increasing spin-orbit couplings. In the third chapter, we test our diabatic model Hamiltonian for cases studies applied to the rhenium complexes. On the basis of time-dependent density functional theory and wavepacket simulations, we propose a detailed mechanism of the ultrafast decay in this class of molecules that allows a detailed interpretation of the experiments within the first picosecond.

PART A

Theory and Concepts

The goal of this section is to introduce the concepts and methods mainly used in the applications presented in the course of the manuscript. Rather to be exhaustive it pretends to be useful for a comprehensive reading of the subsequent results dedicated to the molecular properties and processes described in the thesis. The methods and developments performed within the context of the present work are explicitly described in the relevant chapters.

CHAPTER 1

ELECTRONIC STRUCTURE THEORY

1.1 The Schrödinger Equation

In quantum chemistry, the state of a system is entirely defined by its wavefunction. How the system is evolving as a function of time is given by the Time-Dependent Schrödinger Equation (TDSE):

$$\hat{\mathcal{H}} \left|\psi(\mathbf{r}, \mathbf{R}, t)\right\rangle = i\hbar \frac{\partial}{\partial t} \left|\psi(\mathbf{r}, \mathbf{R}, t)\right\rangle \tag{1.1}$$

where $\psi(\mathbf{r}, \mathbf{R}, t)$ is the wavefunction of the system, function of time t, $\mathbf{r}$, position of the electrons, and $\mathbf{R}$ position of the nuclei. $\hat{\mathcal{H}}$ is the Hamiltonian operator which characterizes the energy of the system. For a non-relativistic system, the Hamiltonian can be decomposed as a sum of kinetic energy ($\hat{T}$) and potential energy $\hat{V}(\mathbf{r}, \mathbf{R}, t)$ operators.

$$\mathcal{H} = \hat{T} + \hat{V}(\mathbf{r}, \mathbf{R}, t) \tag{1.2}$$

For a potential energy operator $\hat{V}(\mathbf{r}, \mathbf{R}, t)$ constant in time, EQ. (1.1) can be solved by introducing the set of eigenfunctions

$$\left|\psi(\mathbf{r}, \mathbf{R}, t)\right\rangle = \sum_{\alpha} C_{\alpha}(t) \left|\psi_{\alpha}(\mathbf{r}, \mathbf{R})\right\rangle \tag{1.3}$$

where $\left|\psi_{\alpha}(\mathbf{r}, \mathbf{R})\right\rangle$ are the eigenfunctions of the time-independent Scrödinger equation (TISE)

$$\hat{\mathcal{H}} \left|\psi_{\alpha}(\mathbf{r}, \mathbf{R})\right\rangle = E_{\alpha} \left|\psi_{\alpha}(\mathbf{r}, \mathbf{R})\right\rangle \tag{1.4}$$

and where E_{α} is the total energy of the system.

1.2 The many body molecular Hamiltonian

In a system containing i electrons of mass m_e, charge e and of position $\boldsymbol{r_i}$ and A nuclei of mass M_A, charge Z_A and of position $\boldsymbol{R_A}$, the molecular Hamiltonian reads

$$\begin{aligned}\hat{\mathcal{H}} = &-\sum_{A=1}^{N}\frac{\hbar^2}{2M_A}\nabla^2_{R_A}-\sum_{i=1}^{n}\frac{\hbar^2}{2m_e}\nabla^2_{r_i}-\sum_{i=1}^{n}\sum_{A=1}^{N}\frac{Z_A e^2}{4\pi\epsilon_0|\boldsymbol{R_A}-\boldsymbol{r_i}|}+\sum_{i=1}^{n}\sum_{j>i}^{n}\frac{e^2}{4\pi\epsilon_0|\boldsymbol{r_i}-\boldsymbol{r_j}|}\\ &+\sum_{A=1}^{N}\sum_{B>A}^{N}\frac{Z_A Z_B e^2}{4\pi\epsilon_0|\boldsymbol{R_A}-\boldsymbol{R_B}|}\end{aligned} \tag{1.5}$$

where $\hat{T}_N$ and $\hat{T}_e$ are the kinetic energy operators of the nuclei and of the electrons, respectively, and $\hat{V}_{eN}$, $\hat{V}_{ee}$ and $\hat{V}_{NN}$ are the potential energy operators corresponding to the Coulomb nucleus-electron attraction, electron-electron and nucleus-nucleus repulsion, respectively. $\nabla^2 = \boldsymbol{\nabla}\cdot\boldsymbol{\nabla}$ with $\boldsymbol{\nabla}$ the gradient operator. In order to lighten the writing, one can express the Hamiltonian in atomic units (au). The Hartree: $E_h = \frac{\hbar^2}{m_e a_0^2}$, is the atomic unit of energy where $a_0 = \frac{\hbar^2}{4\pi^2 m_e e^2}$ is the Bohr radius (atomic unit of length), m_e is the mass of electron (atomic unit of mass). In this unit system, $4\pi\epsilon_0 = 1$, $\hbar = 1$, $m_e = 1$ and $e = 1$ is the unit of charge. (In the rest of the thesis we will use atomic units). In atomic units the Hamiltonian EQ. (1.5) is expressed as

$$\begin{aligned}\hat{\mathcal{H}} = &-\sum_{A=1}^{N}\frac{1}{2M_A}\nabla^2_{R_A}-\sum_{i=1}^{n}\frac{1}{2}\nabla^2_{r_i}-\sum_{i=1}^{n}\sum_{A=1}^{N}\frac{Z_A}{r_{Ai}}+\sum_{i=1}^{n}\sum_{j<i}^{n}\frac{1}{r_{ij}}\\ &+\sum_{A=1}^{M}\sum_{B<A}^{M}\frac{Z_A Z_B}{r_{AB}}\end{aligned} \tag{1.6}$$

where

$$\hat{V}_{NN} = \sum_{A=1}^{M}\sum_{B<A}^{M}\frac{Z_A Z_B}{r_{AB}} \tag{1.7}$$

where r_{Ai}, r_{ij} and r_{AB} are the distances between nucleus A and electron i, between electrons i and j and between nuclei A and B, respectively. The nuclear potential $\hat{V}_{NN}$ is constant for a given set of nuclear coordinates. For the hydrogen atom EQ. (1.4) can be solved analytically [36]. However it is not the case any more for larger systems. In quan-

tum chemistry, nuclei are often considered as fixed; the nuclear kinetic energy as well as the nucleus-nucleus repulsion are then invariant and can be treated as parameters. Nevertheless, the positions of the electrons cannot be exactly known making the evaluation of the repulsive electron-electron interaction impossible. Several methods can be used to evaluate the electron-electron repulsion among which, those that have been used in this thesis and discussed in SECTION 1.6.
The molecular Hamiltonian (1.6) is composed of two components, the nuclear one

$$\hat{T}_N = -\sum_{A=1}^{N} \frac{1}{2M_A} \nabla^2_{R_A} = \nabla^2_N \tag{1.8}$$

and the electronic one $\hat{\mathcal{H}}_e$ such as

$$\hat{\mathcal{H}}_e = \hat{\mathcal{H}} - \hat{T}_N \tag{1.9}$$

with

$$\hat{\mathcal{H}}_e = \hat{T}_e + \hat{V}_{eN} + \hat{V}_{ee} + \hat{V}_{NN} \tag{1.10}$$

where

$$\hat{T}_e = -\sum_{i=1}^{n} \frac{1}{2} \nabla^2_{r_i} \tag{1.11}$$

$$\hat{V}_{eN} = -\sum_{i=1}^{n} \sum_{A=1}^{N} \frac{Z_A}{r_{Ai}} \tag{1.12}$$

$$\hat{V}_{ee} = \sum_{i=1}^{n} \sum_{j<i}^{n} \frac{1}{r_{ij}} \tag{1.13}$$

1.3 Born-Oppenheimer Approximation

The exact eigenstates of the molecular system Ψ_{tot} can be expanded in the Born Oppenheimer or adiabatic electronic states i:

$$\Psi_{tot}(\boldsymbol{r}, \boldsymbol{R}) = \sum_i \chi_i^a(\boldsymbol{R}) \psi_i^a(\boldsymbol{r}, \boldsymbol{R}) \tag{1.14}$$

where $\psi_i^a(\boldsymbol{r}, \boldsymbol{R})$ are the electronic wavefunctions that depends parametrically on the nuclear coordinates $\boldsymbol{R}$ and $\chi_i^a(\boldsymbol{R})$ represent the nuclear wavefunctions of the system which are eigenfunctions of the Schrödinger equation. The electronic wavefunctions are the solutions of the electronic Hamiltonian at fixed nuclear geometry:

$$\hat{\mathcal{H}}_e \left|\psi_i^a(\boldsymbol{r}, \boldsymbol{R})\right\rangle = V_i(\boldsymbol{R}) \left|\psi_i^a(\boldsymbol{r}, \boldsymbol{R})\right\rangle \tag{1.15}$$

where $V_i(\boldsymbol{R})$ represents the electronic potential energy for a given nuclear geometry. Solving the electronic Schrödinger equation EQ. (1.15) for all possible nuclear positions $\boldsymbol{R}$ defines the potential energy surface (PES). By injecting the wavefunction Ψ_{tot} in the Schrödinger equation (EQ. (1.4)) we get [37]

$$\begin{aligned}\hat{\mathcal{H}}\Psi_{tot}(\boldsymbol{r}, \boldsymbol{R}) =&(\hat{\mathcal{H}}_e + \hat{T}_N) \sum_i \chi_i^a(\boldsymbol{R})\psi_i^a(\boldsymbol{r}, \boldsymbol{R}) = E_{tot} \sum_i \chi_i^a(\boldsymbol{R})\psi_i^a(\boldsymbol{r}, \boldsymbol{R}) \\ =&\sum_i \big[(\nabla_N^2\psi_i^a(\boldsymbol{r}, \boldsymbol{R}))\chi_i^a(\boldsymbol{R}) + 2(\nabla_N\psi_i^a(\boldsymbol{r}, \boldsymbol{R}))(\nabla_N\chi_i^a(\boldsymbol{R})) \\ &+\psi_i^a(\boldsymbol{r}, \boldsymbol{R})(\nabla_N^2\chi_i^a(\boldsymbol{R}))\big] + \sum_i \hat{\mathcal{H}}_e\psi_i^a(\boldsymbol{r}, \boldsymbol{R})\chi_i^a(\boldsymbol{R}).\end{aligned} \tag{1.16}$$

If we project EQ. (1.16) onto a specific adiabatic electronic state j by multiplying from the left by its wavefunction $\langle\psi_j^a|$, EQ. (1.16) becomes:

$$\begin{aligned}\langle\psi_j^a(\boldsymbol{r}, \boldsymbol{R})|\hat{\mathcal{H}}|\Psi_{tot}(\boldsymbol{r}, \boldsymbol{R})\rangle =& \langle\psi_j^a(\boldsymbol{r}, \boldsymbol{R})|\hat{\mathcal{H}} \sum_i \psi_i^a(\boldsymbol{r}, \boldsymbol{R})\chi_i^a(\boldsymbol{R})\rangle \\ =&\nabla_N^2\chi_j^a(\boldsymbol{R}) + V_j(\boldsymbol{R})\chi_j^a(\boldsymbol{R}) + \sum_i \big[\langle\psi_j^a(\boldsymbol{r}, \boldsymbol{R})|\nabla_N^2|\psi_i^a(\boldsymbol{r}, \boldsymbol{R})\rangle \chi_i^a(\boldsymbol{R}) \\ &+ 2\langle\psi_j^a(\boldsymbol{r}, \boldsymbol{R})|\nabla_N|\psi_i^a(\boldsymbol{r}, \boldsymbol{R})\rangle (\boldsymbol{\nabla}_N\chi_i^a(\boldsymbol{R}))\big] \\ =&\nabla_N^2\chi_j^a(\boldsymbol{R}) + V_j(\boldsymbol{R})\chi_j^a(\boldsymbol{R}) + \sum_i \left[\tau_{ji}^{(2)}\chi_i^a(\boldsymbol{R}) + \boldsymbol{\tau}_{\boldsymbol{ji}}^{(1)}(\nabla_N\chi_i^a(\boldsymbol{R}))\right]\end{aligned} \tag{1.17}$$

where $\boldsymbol{\tau}_{\boldsymbol{ji}}^{(1)} = 2\langle\psi_j^a|\nabla_N|\psi_i^a\rangle$ and $\tau_{ji}^{(2)} = \langle\psi_j^a|\nabla_N^2|\psi_i^a\rangle$ are a vector and scalar, respectively called the first- and second-order non-adiabatic coupling terms (NACTs) [38]. Since the nuclear wavefunctions χ_j^a are solution of EQ. (1.4),

$$\hat{\mathcal{H}}\chi_j^a = E\chi_j^a(\boldsymbol{R}) \tag{1.18}$$

hence EQ. (1.17) leads to the set of coupled equations

$$\left[V_j(\boldsymbol{R}) + \hat{T}_N - E\right] \chi_j^a(\boldsymbol{R}) = -\sum_i \hat{\Lambda}_{ij} \chi_i^a(\boldsymbol{R}) \tag{1.19}$$

where $\hat{\Lambda}_{ij} = \boldsymbol{\tau}_{\mathbf{ji}}^{(1)}.\nabla_N + \tau_{ji}^{(2)}$ are the non-adiabatic operators. The $\tau_{ji}^{(2)}$ scalar coupling terms are often neglected as considered small in comparison to the $\boldsymbol{\tau}_{\mathbf{ji}}^{(1)}$ terms. The Born-Oppenheimer approximation [39] consists of neglecting the non-adiabatic coupling operators $\hat{\Lambda}_{ij}$ based on the assumption that the kinetic energy operator of the nuclei $\hat{T}_N$ is considered as a small perturbation with respect to the electronic motion. This assumption can be easily understood as the nuclei are several order of magnitude heavier than the electrons. In the Born-Oppenheimer approximation, EQ. (1.19) can thus be rewritten as:

$$\left[V_j(\boldsymbol{R}) + \hat{T}_N - E\right] \chi_j^a(\boldsymbol{R}) = 0 \tag{1.20}$$

and the nuclear motions proceeds on the potential energy surface $V_j(\boldsymbol{R})$ associated to the electronic state j. This approximation is correct as long as the electronic wavefunction varies smoothly as function of the nuclear coordinates. In case of close-lying electronic states which can become degenerate at some critical geometries this approximation is not valid. Indeed, in the adiabatic representation $\boldsymbol{\tau}_{\mathbf{ji}}^{(1)}$ is proportional to the inverse of the energy difference. According to the Hellmann-Feynmann theorem we can write

$$\frac{\boldsymbol{\tau}_{\mathbf{ji}}^{(1)}}{2} = \langle \psi_j^a(\boldsymbol{r}, \boldsymbol{R}) | \nabla_N | \psi_i^a(\boldsymbol{r}, \boldsymbol{R}) \rangle = \frac{\langle \psi_j^a(\boldsymbol{r}, \boldsymbol{R}) | \nabla_N \hat{\mathcal{H}} | \psi_i^a(\boldsymbol{r}, \boldsymbol{R}) \rangle}{V_j(\boldsymbol{R}) - V_i(\boldsymbol{R})}. \tag{1.21}$$

This equation shows that when the energy gap is small, i.e. $V_j - V_i \approx 0$, the NACTs $\boldsymbol{\tau}_{\mathbf{ji}}^{(1)}$ are large and can no longer be neglected. At a point of degeneracy between two adiabatic electronic states, i.e. $V_j - V_i = 0$, the NACTs will even diverge. This will make the use of adiabatic PES cumbersome to study the quantum dynamics. It is thus necessary to use another representation of the PES, so-called diabatic representation, which minimizes the singularity. Several methods exist for the construction of diabatic states. We present two of them in the next section.

1.4 Diabatization

In order to get rid of the divergence of the NACTs, the total wavefunction can be expressed as an expansion of diabatic electronic ψ_i^d and nuclear χ_i^d states

$$\Psi_{tot}(\boldsymbol{r}, \boldsymbol{R}) = \sum_i \chi_i^d(\boldsymbol{R})\psi_i^d(\boldsymbol{r}, \boldsymbol{R}) \tag{1.22}$$

In matrix notation, the vectors $\boldsymbol{\chi^d}$ and $\boldsymbol{\psi^d}$ are obtained by rotation of the electronic adiabatic vectors $\boldsymbol{\chi^a}$ and $\boldsymbol{\psi^a}$

$$\boldsymbol{\chi^d} = \boldsymbol{\chi^a}\boldsymbol{U}^\dagger \tag{1.23}$$

$$\text{and} \quad \boldsymbol{\psi^d} = \boldsymbol{\psi^a}\boldsymbol{U}^\dagger \tag{1.24}$$

The adiabatic to diabatic transformation (ADT) $\boldsymbol{U}$ matrix is chosen so that the NACTs vanish

$$\boldsymbol{\tau}_{ji}^{(1)} = \langle \psi_j^d(\boldsymbol{r}, \boldsymbol{R}) | \nabla_N | \psi_i^d(\boldsymbol{r}, \boldsymbol{R}) \rangle = 0 \tag{1.25}$$

where $\boldsymbol{\tau}_{ji}^{(1)}$ are the NACTs in the diabatic representation. For EQ. (1.25) to be true, the ADT matrix $\boldsymbol{U}$ is chosen such as:

$$\nabla_N \boldsymbol{U} + \boldsymbol{\tau}_{ji}^{(1)} \boldsymbol{U} = 0. \tag{1.26}$$

For diatomic molecules, this matrix can be computed and the NACTs completely vanish. In this case ψ_i^d are called diabatic states and EQ. (1.19) becomes:

$$\left[(\boldsymbol{W} - E) + \hat{T}_N^d \right] \boldsymbol{\chi}^d(\boldsymbol{R}) = 0 \tag{1.27}$$

where $\hat{T}_N^d$ is the kinetic energy operator in the diabatic representation which is now diagonal. $\boldsymbol{W}$ is the potential matrix

$$\begin{pmatrix} W_{11} & \cdots & W_{1,i} \\ \vdots & \ddots & \vdots \\ W_{i,1} & \cdots & W_{i,i} \end{pmatrix} \tag{1.28}$$

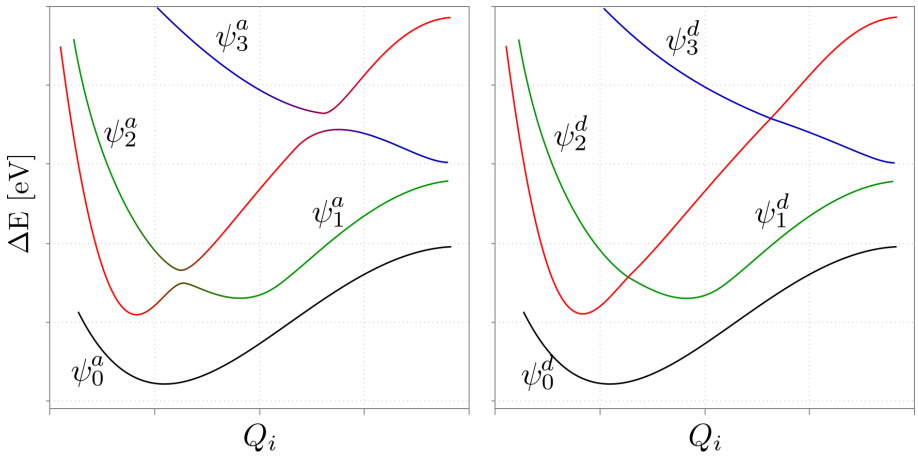

Figure 1.1: Left: Adiabatic representation. Right: Associated diabatic representation.

containing the diabatic PES: $W_{ii} = \langle \psi_i^d(\boldsymbol{r}, \boldsymbol{R}) | \hat{\mathcal{H}}_e | \psi_i^d(\boldsymbol{r}, \boldsymbol{R}) \rangle$ are the diagonal elements and the potential coupling $W_{ij} = \langle \psi_i^d(\boldsymbol{r}, \boldsymbol{R}) | \hat{\mathcal{H}}_e | \psi_j^d(\boldsymbol{r}, \boldsymbol{R}) \rangle$ are the off-diagonal elements.

However for systems with more degrees of freedom, the exact ADT matrix does not exist and thus the kinetic coupling will not entirely vanish [40]. In such a case, a ADT matrix $\boldsymbol{U}$ can however be determined so that the remaining kinetic coupling is as small as possible and can be neglected. Importantly, the divergence of the kinetic coupling is removed. The resulting electronic states are then called quasi-diabatic states.

Several methods to generate "quasi-diabatic" states exist. Here we will focus on only two of them, the regularized diabatic states approach and the diabatization by "ansatz".

1.4.1 The regularized diabatic state method

The regularized diabatic state method [41],[42],[43] is based on the reverse engineering process. We will here focus on only two electronic states that are coupled together and considered well separated in energy from all the other electronic states. We assume a diabatic potential energy matrix $\boldsymbol{W}$ EQ. (1.28) that can be written as:

$$\boldsymbol{W} = \Sigma(\boldsymbol{R})1 + \tilde{\boldsymbol{W}} \tag{1.29}$$

where $\mathbf{1}$ is the identity matrix and

$$\Sigma(\boldsymbol{R}) = \frac{V_1(\boldsymbol{R}) + V_2(\boldsymbol{R})}{2} \tag{1.30}$$

and where

$$\tilde{\boldsymbol{W}} = \begin{pmatrix} d(\boldsymbol{R}) & c(\boldsymbol{R}) \\ c(\boldsymbol{R}) & -d(\boldsymbol{R}) \end{pmatrix} \tag{1.31}$$

$V_1(\boldsymbol{R})$ and $V_2(\boldsymbol{R})$ are the adiabatic electronic potential energies defined in EQ. (1.15), of the adiabatic states 1 and 2, respectively. EQ. (1.31) can be diagonalized using the ADT matrix expressed for two states as

$$\boldsymbol{U} = \begin{pmatrix} \cos\alpha(\boldsymbol{R}) & -\sin\alpha(\boldsymbol{R}) \\ \sin\alpha(\boldsymbol{R}) & \cos\alpha(\boldsymbol{R}) \end{pmatrix} \tag{1.32}$$

which gives the adiabatic potential matrix $\boldsymbol{V}$:

$$\boldsymbol{V} = \begin{pmatrix} V_1(\boldsymbol{R}) & 0 \\ 0 & V_2(\boldsymbol{R}) \end{pmatrix} = \Sigma\mathbf{1} + \boldsymbol{U}^\dagger \tilde{\boldsymbol{W}} \boldsymbol{U} = \Sigma\mathbf{1} + \begin{pmatrix} \sqrt{c(\boldsymbol{R})^2 + d(\boldsymbol{R})^2} & 0 \\ 0 & -\sqrt{c(\boldsymbol{R})^2 + d(\boldsymbol{R})^2} \end{pmatrix}. \tag{1.33}$$

For EQ. (1.33) to be true, we have:

$$\sqrt{c(\boldsymbol{R})^2 + d(\boldsymbol{R})^2} = \frac{V_1 - V_2}{2}. \tag{1.34}$$

The adiabatic-diabatic mixing angle can be estimated from EQ. (1.33) as

$$\alpha(\boldsymbol{R}) = \frac{1}{2} \arctan \frac{c(\boldsymbol{R})}{d(\boldsymbol{R})}. \tag{1.35}$$

Due to its form, $\tilde{\boldsymbol{W}}$ EQ. (1.31) is found to vanish at a point of intersection ($\boldsymbol{Q}_0$). We can thus express it as a Taylor expansion around this geometry. We define $\tilde{\boldsymbol{W}}^{(n)}$ as this Taylor expansion to the n-th order. The order of the expansion is chosen accordingly to the type of intersection (see SECTION 1.5.2). We can thus write

$$\boldsymbol{U}^{(n)\dagger} \tilde{\boldsymbol{W}}^{(n)} \boldsymbol{U}^{(n)} = \begin{pmatrix} \sqrt{c^{(n)}(\boldsymbol{R})^2 + d^{(n)}(\boldsymbol{R})^2} & 0 \\ 0 & -\sqrt{c^{(n)}(\boldsymbol{R})^2 + d^{(n)}(\boldsymbol{R})^2} \end{pmatrix} \tag{1.36}$$

with:

$$\boldsymbol{U}^{(\mathrm{n})} = \begin{pmatrix} \cos\alpha^{(\mathrm{n})}(\boldsymbol{R}) & -\sin\alpha^{(\mathrm{n})}(\boldsymbol{R}) \\ \sin\alpha^{(\mathrm{n})}(\boldsymbol{R}) & \cos\alpha^{(\mathrm{n})}(\boldsymbol{R}) \end{pmatrix}. \tag{1.37}$$

Now that the ADT matrix has been determined, we can apply the inverse operation to the adiabatic potential energy matrix to obtain the regularized diabatic potential energy matrix $\boldsymbol{W}^{\mathrm{reg}}$

$$\boldsymbol{W}^{\mathrm{reg}} = \boldsymbol{U}^{(\mathrm{n})}\boldsymbol{V}\boldsymbol{U}^{(\mathrm{n})\dagger} \tag{1.38}$$

which gives the expression of the regularized diabatic potential matrix [43]:

$$\boldsymbol{W}^{\mathrm{reg}} = \Sigma\mathbf{1} + \frac{\mathrm{V}_1(\boldsymbol{R}) - \mathrm{V}_2(\boldsymbol{R})}{\sqrt{\mathrm{c}^{(\mathrm{n})}(\boldsymbol{R})^2 + \mathrm{d}^{(\mathrm{n})}(\boldsymbol{R})^2}}\tilde{\boldsymbol{W}}^{(\mathrm{n})}. \tag{1.39}$$

EQ. (1.39) can be seen as an interpolation between two limits. (1) when $\boldsymbol{R} \to \boldsymbol{R}_0$, then the Taylor expansion is valid and

$$\frac{\mathrm{V}_1(\boldsymbol{R}) - \mathrm{V}_2(\boldsymbol{R})}{\sqrt{\mathrm{c}^{(\mathrm{n})}(\boldsymbol{R})^2 + \mathrm{d}^{(\mathrm{n})}(\boldsymbol{R})^2}} \to 1 \tag{1.40}$$

so the regularized diabatic energy matrix is $\boldsymbol{W}^{\mathrm{reg}} = \tilde{\boldsymbol{W}}$. (2) far away from the intersection, the Born-oppenheimer approximation is valid, thus $\mathrm{c}^{(\mathrm{n})} \to 0$ and

$$\frac{1}{\sqrt{\mathrm{c}^{(\mathrm{n})}(\boldsymbol{R})^2 + \mathrm{d}^{(\mathrm{n})}(\boldsymbol{R})^2}}\tilde{\tilde{\boldsymbol{W}}}^{(\mathrm{n})} = \mathbf{1}. \tag{1.41}$$

The regularized diabatic electronic states are then the same as the adiabatic electronic states. The elements of $\tilde{\tilde{\boldsymbol{W}}}^{(\mathrm{n})}$ can be estimated by a numerical derivation of the adiabatic energy. The building of the regularized diabatic states requires the knowledge of the adiabatic electronic potentials only.

1.4.2 Diabatization by "ansatz"

The diabatization by "ansatz" is a fitting procedure.

1. The first step consists in building a physical guess for the diabatic potential energy matrix $\boldsymbol{W}^{(0)}$.

2. The guess matrix is numerically diagonalized, and the resulting diagonal matrix is then compared to the reference adiabatic PESs obtained by means of electronic structure calculations. The least square deviations between the guess adiabatic and these PESs is computed. If they are found to be larger than a convergence threshold, then:

3. The guess parameters are optimized by a non-linear optimization algorithm and a new diabatic potential energy matrix guess $\boldsymbol{W}^{(1)}$ is constructed.

The optimization scheme is then repeated from step 2 until convergence.
The difficulty of this procedure lies in the plurality of the solutions of the diabatic potential energy matrix $\boldsymbol{W}$. Indeed, different combinations of the $\boldsymbol{W}$ elements can give adiabatic PESs that fit correctly to the reference PESs, but lack of physical meaning (for example, flat diabatic states with huge diabatic coupling). This is why, it is needed to correctly investigate the reference PESs beforehand in order to elaborate a physically meaningful guess for the diabatic potential energy matrix. This procedure will be used in CHAPTER 3.

1.5 Potential Energy Surfaces

As seen in EQ. (1.15) PESs give the variation of the potential energy of the electronic states as function of the nuclear coordinates. They thus represent the chemical landscape of a system and are used to study the chemical reactions that can be undergone by the system. Indeed, it is needed to considered not only the ground state PES, but also a set of electronic excited states PESs that can be reached upon absorption. The shape of the PES associated to the electronic excited states will control the elementary processes (internal conversions, intersystem crosssings, radiationless decays, ...) responsible for the spectroscopic, photophysical and photochemical properties of the molecular system.

1.5.1 Potential Energy Surfaces Topology

The topology of the electronic PES describing a molecular system shows important features, such as energy minima or local maxima. Two minima, corresponding to the reagents

and the products respectively will be linked through a so-called saddle point, i.e. transition state. These features being either minima or maxima on the global PES, they are characterized by a zero gradient along all the nuclear coordinates R_i:

$$\frac{\partial V}{\partial R_i} = 0 \ \forall i \tag{1.42}$$

where V is the electronic electronic potential energy.
The gradient alone is not sufficient to fully characterize the stationary points. The second derivative of the potential along the 3N-6 (N being the number of atoms) nuclear coordinates R_i gives informations about the curvature of the PES at the stationary point along each coordinate. This matrix is the Hessian matrix (**F**) with elements:

$$F_{i,j} = \frac{\partial^2 V}{\partial R_i \partial R_j} \tag{1.43}$$

If all eigenvalues of the Hessian matrix **F** are positive, then the stationary point is a minimum on the PES. This means that any displacement from the point will induce a rise of the potential energy. On the opposite, if all eigenvalues are negative, the stationary point is a maximum and every displacements will lower the energy.
However, if only n eigenvalues of the Hessian matrix are negative, the stationary point is called a saddle points and is a minimum along all displacements but n. Saddle point of the first and second order (*i.e.* the point is respectively a minimum along one or two nuclear coordinates) are chemically and kinetically very important as they may occur on the path between two minima thus affecting the outcome of the reaction. Higher order saddle points exist but are very high in energy and will usually not be relevant for chemical reactions.

1.5.2 Crossing between two adiabatic PES

Crossing between two (or more) adiabatic PES is of great importance for the excited state dynamics of a molecular system. Indeed, NACTs are proportional to the inverse of the energy gap between two states, and therefore are huge in the vicinity of an intersection between two adiabatic electronic states. This point is called conical intersection (CI). These huge couplings allow an ultrafast radiationless transfer of electronic population.
Let us consider two electronic states. In the diabatic representation, the potential energy

matrix $\boldsymbol{W}(\boldsymbol{R})$ EQ. (1.28) may be written:

$$\boldsymbol{W}(\boldsymbol{R}) = \begin{pmatrix} W_{11}(\boldsymbol{R}) & W_{12}(\boldsymbol{R}) \\ W_{21}(\boldsymbol{R}) & W_{22}(\boldsymbol{R}) \end{pmatrix} \tag{1.44}$$

and the adiabatic PES, i.e. the eigenvalues of the diabatic potential matrix ($\boldsymbol{W}(\boldsymbol{R})$) are obtained from

$$\begin{aligned} \mathrm{V}_1(\boldsymbol{R}) &= \frac{W_{11}(\boldsymbol{R}) + W_{22}(\boldsymbol{R})}{2} - \sqrt{\left(\frac{W_{11}(\boldsymbol{R}) - W_{22}(\boldsymbol{R})}{2}\right)^2 + W_{12}^2(\boldsymbol{R})} \\ \mathrm{V}_2(\boldsymbol{R}) &= \frac{W_{11}(\boldsymbol{R}) + W_{22}(\boldsymbol{R})}{2} + \sqrt{\left(\frac{W_{11}(\boldsymbol{R}) - W_{22}(\boldsymbol{R})}{2}\right)^2 + W_{12}^2(\boldsymbol{R})} \end{aligned} \tag{1.45}$$

Thus the difference of energy between $\mathrm{V}_1(\boldsymbol{R})$ and $\mathrm{V}_2(\boldsymbol{R})$ is:

$$\Delta \mathrm{V} = \mathrm{V}_2(\boldsymbol{R}) - \mathrm{V}_1(\boldsymbol{R}) = 2\sqrt{\left(\frac{W_{11}(\boldsymbol{R}) - W_{22}(\boldsymbol{R})}{2}\right)^2 + W_{12}^2(\boldsymbol{R})} \tag{1.46}$$

EQ. (1.46) shows that two conditions are necessary for the two states to be degenerate, i.e. to have the intersection at $\boldsymbol{R}_{\mathrm{CI}}$:

$$\begin{aligned} &(1)\ W_{11}(\boldsymbol{R}_{\mathrm{CI}}) = W_{22}(\boldsymbol{R}_{\mathrm{CI}}) \\ &(2)\ W_{12}(\boldsymbol{R}_{\mathrm{CI}}) = 0 \end{aligned} \tag{1.47}$$

For small nuclear displacements, the diabatic potential matrix elements $W_{\mathrm{ij}}(\boldsymbol{R})$ ($\mathrm{i}, \mathrm{j} = 1, 2$) (EQ. (1.44)) can be written as a Taylor expansion of the first-order around the point of conical intersection $\boldsymbol{R}_{\mathrm{CI}}$ as:

$$W_{\mathrm{ij}}(\boldsymbol{R} - \boldsymbol{R}_{\mathrm{CI}}) = W_{\mathrm{ij}}(\boldsymbol{R}_{\mathrm{CI}}) + \boldsymbol{\nabla} W_{\mathrm{ij}}(\boldsymbol{R})|_{\mathrm{R_{CI}}} \boldsymbol{R} \tag{1.48}$$

where $\boldsymbol{\nabla}$ is the gradient operator. Taking into account the two conditions on the diabatic potential energy elements (EQ. (1.47) at the conical intersection), EQ. (1.46) can be rewritten as function of the first-order Taylor development (EQ. (1.48)) [44]:

$$\Delta \mathrm{V} = 2\sqrt{\left(\frac{\boldsymbol{\nabla} W_{11}(\boldsymbol{R})|_{\mathrm{R_{CI}}} \cdot \boldsymbol{R} - \boldsymbol{\nabla} W_{22}(\boldsymbol{R})|_{\mathrm{R_{CI}}} \cdot \boldsymbol{R}}{2}\right)^2 + (\boldsymbol{\nabla} W_{12}(\boldsymbol{R})|_{\mathrm{R_{CI}}} \cdot \boldsymbol{R})^2}. \tag{1.49}$$

We can extract from EQ. (1.49) the two vectors $\boldsymbol{g}$ and $\boldsymbol{h}$ defined as follows:

$$\boldsymbol{g} = \boldsymbol{\nabla}\left(W_{22}(\boldsymbol{R}) - W_{11}(\boldsymbol{R})\right)|_{\mathrm{R_{CI}}} \tag{1.50}$$

$$\boldsymbol{h} = \boldsymbol{\nabla} W_{12}(\boldsymbol{R})|_{\mathrm{R_{CI}}} \tag{1.51}$$

and that lift the degeneracy of the conical intersection at the first-order [44]. As the diabatic states and adiabatic states are the same at the intersection ($\boldsymbol{R}_{\mathrm{CI}}$), EQ. (1.50) and (1.51) can be rewritten as a function of the adiabatic electronic states ψ_1^a and ψ_2^a[45] such as:

$$\boldsymbol{h} = \langle \psi_1(\boldsymbol{r},\boldsymbol{R})|\boldsymbol{\nabla}\hat{\mathcal{H}}_e|\psi_2(\boldsymbol{r},\boldsymbol{R})\rangle\,|_{\mathrm{R_{CI}}} \tag{1.52}$$

and

$$\boldsymbol{g} = \boldsymbol{\nabla}\left(\Delta \mathrm{E}(\boldsymbol{r},\boldsymbol{R})\right)|_{\mathrm{R_{CI}}} \tag{1.53}$$

where

$$\Delta \mathrm{E} = \langle \psi_2^a(\boldsymbol{r},\boldsymbol{R})|\hat{\mathcal{H}}_e|\psi_2^a(\boldsymbol{r},\boldsymbol{R})\rangle - \langle \psi_1^a(\boldsymbol{r},\boldsymbol{R})|\hat{\mathcal{H}}_e|\psi_1^a(\boldsymbol{r},\boldsymbol{R})\rangle \tag{1.54}$$

$\hat{\mathcal{H}}_e$ is the electronic Hamiltonian (EQ. (1.15)) and $\boldsymbol{g}$ and $\boldsymbol{h}$ are called gradient difference and derivative coupling vectors, respectively. They define the so-called branching space which is a two dimensional subspace where the degeneracy is lifted along nuclear displacements. The subspace of 3N-8 dimensions (N being the number of atoms of the system) orthogonal to the branching space is called the intersection seam space [46] and is the space in which the degeneracy is not lifted, at least, at the first-order [47],[48]. Indeed, the linear approximation made in EQ. (1.48) is valid only for small nuclear displacements. For important nuclear distortions the degeneracy is still lifted [45]. In the case of symmetric molecular systems, the dimension of the intersection seam space can be lower. This happens when two electronic states belong to different irreducible representations (irreps). In such a case only the $W_{11}(\boldsymbol{R}) = W_{22}(\boldsymbol{R})$ condition remains and the dimension of the seam space will be 3N-7. The two conditions (EQ. (1.47)) imply that CIs between electronic states belonging to the same irrep in a diatomic molecules do not exist because the number of degrees of freedom (namely 1 for diatomic molecules) is not sufficient to fulfil both conditions. In this case, two electronic states will avoid each other instead of crossing. This is called an avoided crossing. However, if the two electronic states belong to two different irreps, then they may intersect at a point. The dimension of the intersection space is then 6-6=0. Thus the conical intersection is an hypersurface

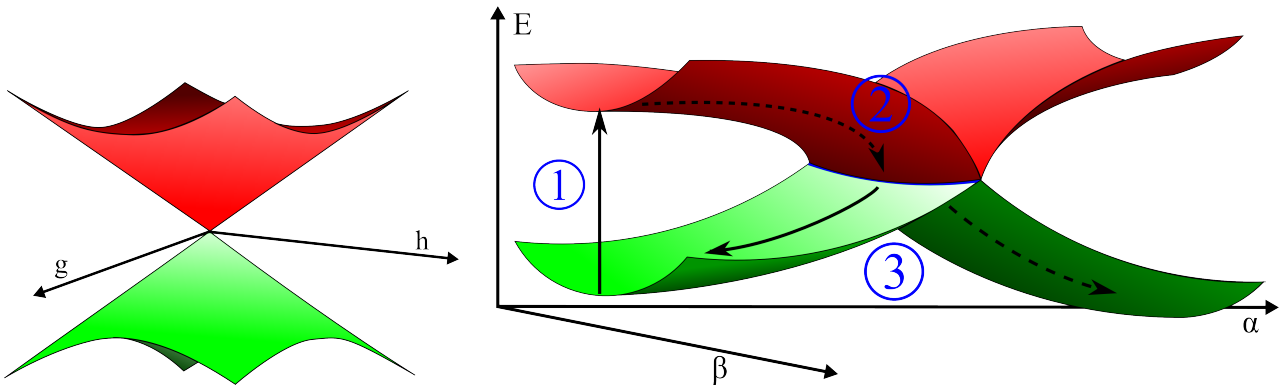

Figure 1.2: Left: Two PESs around a CI as a function of the two branching space vectors ($\boldsymbol{g}$ and $\boldsymbol{h}$). Right: Seam of intersection along one vector of the branching space $\boldsymbol{\alpha}$ and one vector of the intersection space $\boldsymbol{\beta}$.

of intersection, exhibiting all the critical PES points described above, rather than a single point.

Conical intersections act as an ultrafast funnel and allow an ultrafast electronic population transfer between two electronic states. They play a key role in the photochemistry and the photophysics of many electronic systems. These past years, a number of methodological developments have been performed to detect and characterize CIs [49]. Most of the time the optimization of CI (i.e., finding the lowest intersection point in energy) is supplemented by the search for critical points of the intersection hypersurface.

As we shall see in CHAPTER 3, during excited state dynamics, the seam of intersection can be reached before getting to the point of miniminal intersection. That is, the seam topology will generally play a key role in excited state processes. While the double cone of conical intersection can be obtained by computing PES along both vectors from the branching space ($\boldsymbol{g}$ and $\boldsymbol{h}$) (FIG. 1.2, left), the seam of intersection can be determined by computing PES along one vector of the branching space and one vector of the seam space (FIG. 1.2, right). Other types of intersection exist and are characterized by $\boldsymbol{g} = \boldsymbol{h} = 0$ by symmetry, and both $\nabla^2 \left(W_{11}(\boldsymbol{R}) - W_{22}(\boldsymbol{R})\right) \neq 0$ and $\nabla^2 W_{12}(\boldsymbol{R}) \neq 0$ (i.e. the same conditions as EQ. (1.47) but for a Taylor development to the second order), then degeneracy is only lifted quadratically and the intersection belongs to another class relevant to the Renner-Teller effect [50].

The CI is a funnel from one electronic state to another and its shape or topology drives the chemical reaction undergone by a molecule. The shape of a CI is defined by the gradient of the two states involved in the vicinity of the CI. If the gradient vector of both

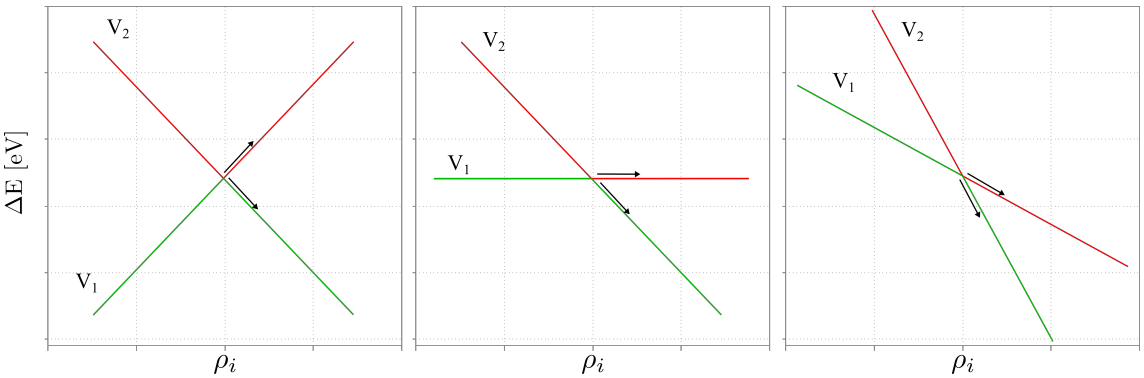

Figure 1.3: Different topologies of a CI between two adiabatic states (V_1 and V_2). The gradient vector $\frac{\partial V}{\partial \rho_i}$ is shown as a black arrow. Left: A "peaked" CI. Middle: a "flat" CI. Right: a "sloped" CI.

electronic states are pointing in opposite directions, the CI is called "peaked". On the opposite, if the gradient vector of both electronic states are pointing in the same direction, the CI is called "sloped" (FIG. 1.3). The intermediate situation, i.e. the gradient vector of one of the electronic state is null, then the CI is called "flat". A "peaked" CI allows for a relaxation in the lower electronic states by multiple channels because the point of intersection is a maximum on the lower electronic PES. On the contrary, "sloped" CI promotes one channel because the intersection point is no longer an extremum of the lower PES. This kind of CI (i.e. "sloped") are important for example in the photostability of molecules[51],[52]. Indeed, photochemical reactions (i.e. photodissociation, polymerisation, ...) can be quenched due to the presence of conical intersections that allow ultrafast relaxation of the molecule back to its ground state conformation. Not only the shape of the CI itself, but also the topology of the PES between the Franck-Condon (FC) region and the seam of CI, especially the presence of a saddle point, play a key role in the excited state dynamics. This aspect will be discussed more in CHAPTER 3.

1.5.3 Spin-Orbit Coupling

The electron being a charged particle, its motion induces a magnetic field, proportional to its orbital momentum $\hat{L}$. This magnetic field interacts with the intrinsic magnetic moment of the electron, the spin $\hat{S}$. This interaction is called the spin-orbit coupling (SOC). In case of transition metals complexes, relativistic effects, including SOC, have to be taken into account in the electronic structure calculations. A proper treatment of the relativistic

effects would require the use of the 4-component Dirac equation [53]. However, this theory is very costly and is still limited to small molecular systems. Other methods, based on a 2-component simplification of the Dirac equation have been developed. Amongst them, are the Douglas-Kroll-Hess [54] and the zero order regular approximation (ZORA) [55] Hamiltonians. In PART 6, we will use the ZORA approximation with DFT calculations to treat SOC. The ZORA Hamiltonian then reads

$$\hat{\mathcal{H}}^{\mathrm{ZORA}} = V^{\mathrm{KS}} + (\boldsymbol{\sigma}\cdot\boldsymbol{p})\,\frac{c^2}{2c^2 - V^{\mathrm{KS}}}\,(\boldsymbol{\sigma}\cdot\boldsymbol{p}) \tag{1.55}$$

which can be expanded as

$$\hat{\mathcal{H}}^{\mathrm{ZORA}} = V^{\mathrm{KS}} + \boldsymbol{p}\frac{c^2}{2c^2 - V^{\mathrm{KS}}}\boldsymbol{p} + \frac{c^2}{(2c^2 - V^{\mathrm{KS}})^2}\boldsymbol{\sigma}\cdot(\nabla\times\boldsymbol{p}) \tag{1.56}$$

where $\boldsymbol{\sigma}$ and $\boldsymbol{p}$ are the spin and the momentum of the electron and V^{KS} is the local Kohn-Sham potential that will be defined in SECTION 1.6.2. In EQ. (1.56),we can note that two terms appear which are the scalar relativistic Hamiltonian $\hat{\mathcal{H}}_{\mathrm{SR}}^{\mathrm{ZORA}}$ and the spin-orbit Hamiltonian $\hat{\mathcal{H}}_{\mathrm{SO}}^{\mathrm{ZORA}}$ such as

$$\begin{aligned} &\hat{\mathcal{H}}_{\mathrm{SR}}^{\mathrm{ZORA}} = V^{\mathrm{KS}} + \boldsymbol{p}\frac{c^2}{2c^2 - V^{\mathrm{KS}}}\boldsymbol{p} \\ \text{and}\quad &\hat{\mathcal{H}}_{\mathrm{SO}}^{\mathrm{ZORA}} = \frac{c^2}{(2c^2 - V^{\mathrm{KS}})^2}\boldsymbol{\sigma}\cdot(\nabla\times\boldsymbol{p})\,. \end{aligned} \tag{1.57}$$

1.6 Quantum Chemical Methods

1.6.1 Wavefunction Theory

In order to solve the electronic Schrödinger equation EQ. (1.15), one has to find both the eigenfunctions and eigenvalues of the system. In a non-relativistic approach, the electrons are described by their spatial coordinates ($\boldsymbol{r}$) and their spin coordinate (ms). In order to simplify the notation, we will denote the coordinates of the electron as : $\mathbf{x} = \mathbf{r}, ms$. The mono-electronic solution of the Schrödinger equation for a one-electron one-nucleus system, the spin-orbital, can then be written as $\Xi(\mathbf{x}) = \phi(\mathbf{r})s(ms)$, where $s(ms)$ is the spin function and $\phi(\mathbf{r})$ is the spatial function (note that in most quantum chemical methods the

calculation is performed within a manifold of electronic states of a given spin multiplicity, thus the spin coordinate of the wavefunction may be omitted).
For poly-electronic systems, the exact eigenfunctions and eigenvalues can no longer be determined. As a first approximation, the electronic wavefunction can be considered as a product of monoelectronic spin-orbitals. This is the orbital approximation. In order to ensure the indiscernibility of the electrons and the anti symmetry of the poly-electronic wavefunction, arising from the Pauli exclusion principle, one can express the wavefunction of N electrons as a Slater determinant:

$$\psi(x_1, x_2, \cdots, x_N) = \frac{1}{\sqrt{N!}} \begin{vmatrix} \Xi_1(x_1) & \Xi_2(x_1) & \cdots & \Xi_N(x_1) \\ \Xi_1(x_2) & \Xi_2(x_2) & \cdots & \Xi_N(x_2) \\ \vdots & \vdots & \ddots & \vdots \\ \Xi_1(x_N) & \Xi_2(x_N) & \cdots & \Xi_N(x_N) \end{vmatrix} \tag{1.58}$$

$$= \frac{1}{\sqrt{N!}} |\Xi_1(x_1)\Xi_2(x_2)\cdots\Xi_N(x_N)|$$

where $\Xi_j(x_i)$ is the spin-orbital. In the columns are the N occupied spin-orbitals, and in the rows are the N electrons. Thus the inversion of two electrons, i.e the inversion of two rows, results in the determinant changing sign. Moreover, putting two different electrons in the same spin-orbital results in two rows being equals and thus in a null determinant.

1.6.1.1 The Hartree-Fock Approximation

The main problem occurring while solving the electronic time independent Schrödinger equation is the treatment of the two electron interaction. Indeed, computing exactly the $\frac{1}{r_{ij}}$ terms is not possible. The Hartree-Fock (HF) approximation is the first and is at the origin of more accurate methods. The HF approximation states that the electronic wavefunction of a system can be described by a single Slater determinant. According to the variational principle, the best wavefunction will lead to the lowest energy.

$$E^{HF} = \min_{\psi} \langle \psi | \hat{\mathcal{H}} | \psi \rangle \tag{1.59}$$

The optimization of the spin-orbitals is therefore mandatory.
We can compute the energy of a Slater determinant by introducing $\psi(x_1, x_2, \cdots, x_N)$ into the electronic Schrödinger equation EQ. (1.15):

$$\hat{\mathcal{H}}_e \psi(x_1, x_2, \cdots, x_N) = E^{SD} \psi(x_1, x_2, \cdots, x_N) \tag{1.60}$$

where E^{SD} is the energy of the Slater determinant. It is convenient to express the electronic Hamiltonian as a sum

$$\hat{\mathcal{H}}_e = \sum_i^n \hat{h}_i + \sum_i^n \sum_{j<i}^n \frac{1}{r_{ij}} + \hat{V}_{NN} \tag{1.61}$$

where $\hat{h}_i$ is a monoelectronic Hamiltonian such as:

$$\hat{h}_i = -\frac{1}{2}\nabla^2_{r_i} - \sum \frac{Z_A}{r_{Ai}}. \tag{1.62}$$

The energy of a single Slater determinant can then be written as

$$\begin{aligned} E^{SD} &= \langle \psi(x_1, x_2, \cdots, x_N) | \hat{\mathcal{H}}_e | \psi(x_1, x_2, \cdots, x_N) \rangle \\ &= V_{NN} + \sum_a^n \langle \Xi_a(x_i) | \hat{h}_i | \Xi_a(x_i) \rangle + \sum_a^n \sum_{b<a}^n \left[\langle \Xi_a(x_1)\Xi_b(x_2) | \frac{1}{r_{12}} | \Xi_a(x_1)\Xi_b(x_2) \rangle \right] \\ &- \sum_a^n \sum_{b<a}^n \left[\langle \Xi_a(x_1)\Xi_b(x_2) | \frac{1}{r_{12}} | \Xi_b(x_1)\Xi_a(x_2) \rangle \right] \end{aligned} \tag{1.63}$$

where $\mathcal{J}_{ab} = \langle \Xi_a(x_1)\Xi_b(x_2) | \frac{1}{r_{12}} | \Xi_a(x_1)\Xi_b(x_2) \rangle$ is called the bielectronic Coulomb integral which represents the repulsion between the electronic density induced by electron 1 in the spinorbital a and the one induced by electron 2 in the spinorbital b. Summing this interaction over all occupied spinorbital b ($b \neq a$) gives the average interaction between electron 1 and the effective Coulomb potential of the (N-1) remaining electrons.
$\mathcal{K}_{ab} = \langle \Xi_a(x_1)\Xi_b(x_2) | \frac{1}{r_{12}} | \Xi_b(x_1)\Xi_a(x_2) \rangle$ is called the bielectronic exchange integral and is a correction to the coulomb potential due do the antisymmetric nature of the Slater determinant.
We can therefore write the Coulomb and exchange operators as mono-electronic operators

defined as:

$$\begin{aligned} \hat{J}_b(x_1) &= \int |\Xi_b(x_2)|^2 \frac{1}{r_{12}} dx_2 \\ \text{and} \qquad \hat{K}_b(x_1)\Xi_a(x_1) &= \left[\int \Xi_b^*(x_2)\frac{1}{r_{12}}\Xi_a(x_2)dx_2\right]\Xi_b^*(x_1) \end{aligned} \tag{1.64}$$

We can then define HF equation as a sum of mono-electronic Schrödinger equations:

$$\hat{\mathcal{H}}^{HF}\psi = \sum_i \hat{F}(i)\Xi_a(\mathbf{x}_i) = \sum_i \epsilon_a \Xi_a(\mathbf{x}_i) \tag{1.65}$$

$\hat{F}(i)$ is a one electron operator called the Fock operator composed of the kinetic energy of the electron, the electron-nuclei attraction and a screening constant:

$$\hat{F}(1) = \hat{h}(1) + v^{HF}(1) \tag{1.66}$$

Where $v^{HF}(i)$ is the screening constant (also called the Hartree-Fock potential) and is the average field of the $N-1$ electrons felt by electron i. This average field is expressed as : $v^{HF}(i) = \sum_{b\neq a} \hat{J}_b(x_i) - \hat{K}_b(x_i)$. In this approach, we do not neglect the $\frac{1}{r_{ij}}$ interaction, but we treat it in the average way. As the Coulomb and Exchange operators depend explicitly on the spin-orbitals, the problem has to be treated self-consistently. This means that each time the spin-orbitals are minimized, the Coulomb and exchange operators must be computed, and so on until convergence.

For molecular systems, we can express the Slater determinant in terms of molecular orbitals (MO) $\varphi(x)$. MOs are mono-electronic functions defined as a linear combination of atomic orbital (LCAO):

$$\varphi_p(x) = \sum_{i=1}^{M} c_{pi}\zeta_i(x) \tag{1.67}$$

where $\zeta_i(x)$ is a basis set of atomic orbitals and c_{pi} are the variational parameters of the HF calculation for a molecule. This is the molecular orbital approximation. The Slater determinant then reads:

$$\psi(x_1, x_2, \cdots, x_N) = \frac{1}{\sqrt{N!}} \left|\varphi_1(x_1)\varphi_2(x_2)\cdots\varphi_N(x_N)\right|. \tag{1.68}$$

1.6.1.2 Configuration Interaction

The HF wavefunction based on a single determinant describes each electron in an approximate mean field created by the other electrons. This mono-determinantal representation of the wavefunction is not sufficient to correctly describe the instantaneous motion of the electrons, so-called electronic correlation. The exact wavefunction is given by a linear combination of configuration state functions (CSFs) built from a single Slater determinant reference wavefunction ψ_0 (EQ. (1.68)).

$$\Psi^{\mathrm{CI}} = c_0\psi_0 + \sum_{a,r} c_a^r \psi_a^r + \sum_{\substack{a<b \\ r<s}} c_{a,b}^{r,s} \psi_{a,b}^{r,s} + \cdots \tag{1.69}$$

where a and b are occupied orbitals and r and s are unoccupied orbitals. ψ_a^r is the mono-excited determinant where the electron occupying orbital a is promoted to the orbital r. Likewise, $\psi_{a,b}^{r,s}$ is the doubly-excited determinant where the electrons occupying orbitals a and b are promoted to orbitals r and s respectively. $c_{a,\cdots}^{r,\cdots}$ are the respective CSF coefficients.

The energy is minimized by expanding the wavefunction over all the excited determinants and by optimizing the CSF coefficient $c_{a,\cdots}^{r,\cdots}$.

In an infinite basis set, and if we consider all excitations, the CI approach gives the exact energy of the system (due to this method being variational). Nevertheless, an infinite basis set can't be used, thus the number of excited determinants will be limited. Moreover to reduce the computational cost, we often truncate the linear combination. CIS, CISD, ... refers to the CI method where we consider only the single excitations, the single and the double excitations, etc. If the linear combination is not truncated, then the method is called full-CI (FCI) and is a CI in which all possible excitations are considered.

As we have seen SECTION 1.6.1.1, the electron-electron interaction is treated as a mean field in the HF method; and so electronic correlation is not described. The correlation energy can thus be defined as the difference of energy between the FCI energy E^{FCI} and the HF energy E^{HF}

$$E^{\mathrm{corr}} = E^{\mathrm{FCI}} - E^{\mathrm{HF}}. \tag{1.70}$$

1.6.1.3 MCSCF

Many different methods based on the HF method exist that allow us to recover a part of the correlation energy. These are called post Hartree Fock methods. Some systems cannot be described using only one reference determinant as their electronic wavefunction is composed of several electronic configurations. This is the case for example, when two states are coupled (e.g. close to an avoided crossing or a conical intersection) or for aromatic molecules (e.g. the benzene, where it is needed to represent all the Kekule configurations in the electronic wavefunction to describe correctly the electronic state). Multi-configurational self-consistent field (MCSCF) methods are used to overcome these difficulties and thus will have to be used in CHAPTER 3. The MCSCF wavefunction is based on a linear combination of slater determinants

$$\Psi^{MCSCF} = \sum_{I}^{M} c_I \Psi_I^{SD} \tag{1.71}$$

where each Ψ_I^{SD} is a Slater determinant, see EQ. (1.68). Instead of optimizing only the c_I coefficients (as it is the case in the CI approach where only the $c_{a,\dots}^{r,\dots}$ are optimized), the orbitals used to build the reference Slater determinants are optimized as well. This is done by optimizing the c_{pi} coefficient in EQ. (1.67). The orbital relaxation (i.e. optimization) allows to describe part of the electronic correlation.

1.6.1.4 CASSCF

One of the most widely used MCSCF method is the complete active space self-consistent field (CASSCF) method [56]. The Slater determinants contributing to the total MCSCF wavefunction correspond to all possible M electronic configurations within a limited number of orbitals, which is called the active space:

$$\Psi^{CASSCF} = \sum_{I}^{M} c_I \Psi_I \qquad \forall I \in \text{active space} \tag{1.72}$$

In a CASSCF calculation, the space is divided into three part (FIG. 1.4): (1) the inactive orbitals, which will remain doubly occupied; (2) the active orbitals, whose occupations vary between 0 and 2 and (3) the virtual orbitals, which remain empty at all times. A

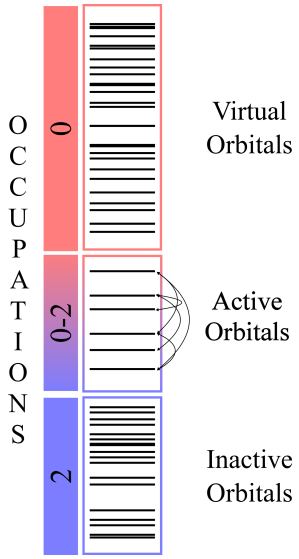

Figure 1.4: The CASSCF subdivision of the total orbital space.

CASSCF calculation is equivalent to a FCI calculation within a limited set of orbitals. Various protocols are used nowadays for giving more flexibility to the subdivision of the orbital space (generalized active space (GAS) [57], occupation restricted multiple active space (ORMAS) [58],...). Whereas CASSCF techniques take into account the static electronic correlation, generally associated to nearly degenerate configurations, they do not include dynamical correlation effects.

1.6.1.5 CASPT2

In order to include dynamical correlation effect, electronic high-order excitations have to be included. One way is to use perturbation theory applied to the zeroth order reference CASSCF wavefunction. The perturbed electronic Hamiltonian is partitioned as follows:

$$\hat{\mathcal{H}}_e = \hat{\mathcal{H}}^{(0)} + \lambda\hat{V} \tag{1.73}$$

where $\hat{\mathcal{H}}^{(0)}$ is the zeroth order Hamiltonian for which the zeroth order wavefunction Ψ_0 is an eigenfunction. In the case of CASPT2, the zeroth order wavefunction is the CASSCF wavefunction Ψ^{CASSCF} such as:

$$\hat{\mathcal{H}}^{(0)}\Psi^{CASSCF} = E^{(0)}\Psi^{CASSCF} \tag{1.74}$$

λ being a small parameter, $\lambda\hat{V}$ can thus be considered as a small perturbation to the zeroth order Hamiltonian. In such a case, the electronic wavefunction as well as the energy can be expressed as a Taylor expansion:

$$\Psi = \Psi^{CASSCF} + \lambda\Psi^{(1)} + \lambda^2\Psi^{(2)} + \cdots \tag{1.75}$$

$$E = E^{(0)} + \lambda E^{(1)} + \lambda^2 E^{(2)} + \cdots \tag{1.76}$$

truncating this expansion at the second-order gives the CASPT2 method which is an extension of the Moller-Plesset second order theory (MP2) that defines both the unperturbed Hamiltonian $\hat{\mathcal{H}}^{(0)}$ and the perturbation $\hat{V}$, to the multideterminental case.
CASPT2 [59][60] (and its multi-state extension MS-CASPT2) has become a standard *ab initio* method to study photochemistry and will be used in CHAPTER 3.

1.6.2 Density Functional Theory

1.6.2.1 The first Hohenberg-Kohn theorem

The first theorem of Hohenberg and Kohn states that the ground state energy of a system in its electronic ground state can be completely determined by its electronic density $\rho(\boldsymbol{r})$ [61]. For a "fully interacting" electrons system, the electronic Hamiltonian can be written:

$$\hat{\mathcal{H}} = -\frac{1}{2}\sum_i \nabla_i + \sum_{j<i}\frac{1}{r_{ij}} + \sum_i v_i^{ext}(\mathbf{r}_i) \tag{1.77}$$

with:

$$\sum_i v_i^{ext}(\mathbf{r}_i) = \sum_i \sum_A \frac{Z_A}{R_{Ai}} \tag{1.78}$$

where Z_A is the atomic charge of atom A ($A = 1, \cdots, N$, where N is the total number of nuclei) and R_{Ai} is the distance between nucleus A and electron i. v_i^{ext} is the external potential of electron i. The energy function of the density can be decomposed as follows:

$$E[\rho] = T[\rho] + E_{ee}[\rho] + E_{Ne}[\rho] \tag{1.79}$$

where $T[\rho]$ is the kinetic energy of the electrons and with the nucleus-electron attraction:

$$E_{Ne}[\rho] = -\sum_{A=1}^{N} \int \frac{Z_A \rho(\boldsymbol{r})}{\boldsymbol{r} - \boldsymbol{r}_A} d\boldsymbol{r} \tag{1.80}$$

By including explicitely the electronic correlation in the energy, we obtain:

$$E_{ee}[\rho] = J[\rho] + K[\rho] \tag{1.81}$$

where

$$J[\rho] = \frac{1}{2} \int\int \frac{\rho(\boldsymbol{r})\rho(\boldsymbol{r'})}{|\boldsymbol{r} - \boldsymbol{r'}|} d\boldsymbol{r} d\boldsymbol{r'} + \Delta J[\rho] \tag{1.82}$$

is the Coulomb potential and $K[\rho]$ is the exchange potential. Hence

$$E_{ee}[\rho] = \frac{1}{2} \int\int \frac{\rho(\boldsymbol{r})\rho(\boldsymbol{r'})}{|\boldsymbol{r} - \boldsymbol{r'}|} d\boldsymbol{r} d\boldsymbol{r'} + \Delta J[\rho] + K[\rho] \tag{1.83}$$

(1.79) can be rewritten as

$$E[\rho] = T[\rho] + E_{Ne}[\rho] + J[\rho] + K[\rho] \tag{1.84}$$

1.6.2.2 The Kohn-Sham DFT

Since the kinetic energy $T[\rho]$ of the system is not known, Kohn and Sham have introduce a fictive system of non interacting electrons [62] of kinetic energy $T_{NI}[\rho]$ that has the same density than the real system. Then the total energy can be expressed as:

$$E[\rho] = T_{NI}[\rho] + E_{Ne}[\rho] + J[\rho] + E_{xc}[\rho] \tag{1.85}$$

where the exchange correlation energy functional $E_{xc}[\rho]$ is defined as [63]:

$$E_{xc}[\rho] = \Delta T[\rho] + \Delta J[\rho] + K[\rho] \tag{1.86}$$

By solving the Kohn-Sham equations where the density $\rho(\boldsymbol{r})$ is expressed on the basis of Kohn-Sham orbitals

$$\rho(\boldsymbol{r}) = \sum_{i}^{N} |\phi_i(\boldsymbol{r})|^2 \tag{1.87}$$

the exact energy of the system described by one Slater determinant can be obtained following a variational protocol as in HF theory. However the analytical expression of $E_{xc}[\rho]$ is not known and needs to be approximated. Non-exact functionals, so-called "local", "non-local", and "hybrids" are developed everyday in order to describe a variety of molecular systems and properties [64].

1.6.2.3 Time-dependent density functional theory

The extension of the electronic ground state DFT to the electronic excited states is the time-dependent DFT (TDDFT) based on the linear response of the electronic density $\rho(\boldsymbol{r}, t)$ to a time-dependent electric field, namely the dynamical polarisability. This method has been developed especially for optical properties and excited-states calculations. In this latter case the excitation energies and oscillator strengths are given by the pole ω_n and residues f_n of the sum over eigenstates n on the basis of eigenfunctions generated by the linear response theory, where:

$$\omega_n = E_n - E_0 \tag{1.88}$$

$$f_n = \frac{2}{3}(E_n - E_0)(|\langle 0|\hat{x}|n\rangle|^2 + |\langle 0|\hat{y}|n\rangle|^2 + |\langle 0|\hat{z}|n\rangle|^2). \tag{1.89}$$

This theory is exact within the limit of an exact functional. The choice of the functional is even more dramatic in the case of excited states calculations, especially because of long-range charge transfer phenomena, occurrence of Rydberg states and double excitations contributions. At large distances electronic density is especially sensitive to the exchange correlation potential. In the present work, standard functionals have been tested and used.

CHAPTER 2

NUCLEAR DYNAMICS

2.1 Quantum molecular dynamics

Nowadays several methods based on the resolution of the nuclear Schrödinger equation are able to perform accurate quantum dynamics to simulate the evolution of small molecular systems as function of time and to control its behaviour after light absorption. The initial nuclear wavefunction in the electronic ground state can be approximated by a simple Morse function, constructed on the basis of a Fourier grid Hamiltonian [65], or determined from vibrational spectroscopic states [66],[67]. Both time-independent and time-dependent approaches are available and should lead in principle to the same solutions of the nuclear Schrödinger equation. However time-dependent methods are more appropriate to describe and interpret photophysical and photochemical processes especially those occurring within ultra-short time scales. Indeed, they are able to treat continuum states and are adapted to time dependent Hamiltonians necessary to introduce the effect of laser field for instance. After absorption of light and population of the electronic excited states, the initial nuclear wavefunction, eigenstate for the electronic ground state, becomes a nuclear wavepacket $\Phi(\boldsymbol{R}, t)$ defined as a coherent superposition of stationary states $\chi_j(\boldsymbol{R}, E)$ (or vibrational states solutions of the time-independent nuclear Schrödinger equation)

$$\Phi(\boldsymbol{R}, t) = \int dE \sum_j c_j(E)\chi_j(\boldsymbol{R}, E)e^{\frac{-iEt}{\hbar}} \tag{2.1}$$

The nuclear wavepacket is not eigenfunction for the electronic excited-state and consequently evolves as a function of time on the associated PES. It is solution of the time-

dependent nuclear Schrödinger equation

$$\hat{\mathcal{H}}\,|\Phi(\mathbf{R},t)\rangle = i\hbar\frac{\partial}{\partial t}\,|\Phi(\mathbf{R},t)\rangle\,. \tag{2.2}$$

Several expressions of the temporal evolution operator $e^{\frac{-i\hat{H}t}{\hbar}}$ are available [68] (linearized operator, Chebychev polynomials, split operator technique, Taylor series, ...) for easily calculating the time dependence of the nuclear wavepacket. Recent applications on small molecules such as scattering [69], laser control of unimolecular processes, vibrational relaxation of atoms or diatomics at metal surfaces [70],[71] illustrate the power of quantum dynamics. Coherent control of photodissociation processes has been proposed already in the lates 80s [72],[73], [74], [75] eventually with manipulation of the laser fields with parameters. More recently, optimal control based on a numerical optimisation of the laser field [76], [77], [78] has been applied with success to radiationless decay in pyrazine [79],[80] and to quantum dynamics of small molecules [81]. Whereas these methods are difficult and very demanding, they may provide a good starting point for more approximate methods. The MCTDH theory, using time-dependent basis functions and the variational principle to derive equations of motion, is one example of these methods able to treat large molecular systems with a reasonable accuracy [82],[83],[84]. The next section is dedicated to this method.

2.1.1 Equations of motion

The nuclear wavefunction is expressed as a sum of Hartree products of basis functions:

$$\Psi(R_1,\cdots,R_N,t) = \sum_{j_1=1}^{n_1}\cdots\sum_{j_N=1}^{n_N} A_{j_1,\cdots,j_N}(t)\prod_{k=1}^{N}\varphi_{j_k}^{(k)}(R_k,t) \tag{2.3}$$

where R_k, $i = 1,\cdots,N$ denotes the nuclear coordinates. $A_{j_1,\cdots,j_N}(t)$ are the time-dependent expansion coefficients of the Hartree product $\prod_{k=1}^{N}\varphi_{j_i}^{(k)}(R_i,t)$ where $\varphi_{j_i}^{(k)}$ are the n_k basis functions for each degree of freedom R_k. These basis functions are called single-particle functions (SPFs). By increasing the number of SPFs, the propagation of the wavefunction will be more accurate. The MCTDH wavefunction converges, in principle, to the numerically exact one. EQ. (2.3) can be simplified using composite

indices,

$$\Psi(R_1, \cdots, R_N, t) = \sum_J A_J \Phi_J \tag{2.4}$$

where

$$A_J = A_{j_1,\cdots,j_N} \quad \text{and} \quad \Phi_J = \prod_{k=1}^{N} \varphi_{j_k}^{(k)}. \tag{2.5}$$

The single hole function $\Psi_l^{(k)}$ is defined as the linear combination of Hartree products of (N-1) SPFs that do not include the SPF for R_k:

$$\Psi_l^{(k)} = \sum_{j_1} \cdots \sum_{j_{k-1}} \sum_{j_{k+1}} \cdots \sum_{j_N} A_{j_1 \cdots j_{k-1} l_{j_{k+1} \cdots j_N}} \varphi_{j_1}^{(1)} \cdots \varphi_{j_{k-1}}^{(k-1)} \varphi_{j_{k+1}}^{(k+1)} \cdots \varphi_{j_N}^{(N)} \tag{2.6}$$

From the single hole function, one can define the density matrices

$$\rho_{jl}^{(k)} = \langle \Psi_j^{(k)} | \Psi_l^{(k)} \rangle \tag{2.7}$$

and the mean-field acting on the k-th degree of freedom:

$$\langle H \rangle_{jl}^{(k)} = \langle \Psi_j^{(k)} | \hat{H} | \Psi_l^{(k)} \rangle \tag{2.8}$$

with a separable form of the Hamiltonian

$$\hat{H} = \sum_{k}^{N} \hat{h}^{(k)} + \hat{H}_R \tag{2.9}$$

$\hat{H}_R$ being the residual terms that include the correlation between all degrees of freedom and $\hat{h}^{(k)}$ the single particle operator. An inefficient multi-dimensional integration is avoided by writing the residual Hamiltonian as a sum of products of single particle operators

$$H_R = \sum_{r=1}^{s} C_r \prod_{k=1}^{N} h_r^{(k)}. \tag{2.10}$$

Ψ, $\dot{\Psi}$ and the variation of Ψ ($\delta\Psi$) may be defined as follows:

$$\Psi = \sum_{J} A_J \Phi_J = \sum_{j_k=1}^{n_k} \varphi_{j_k}^{(k)} \Psi_{j_k}^{(k)} \tag{2.11}$$

$$\dot{\Psi} = \sum_{k=1}^{N} \sum_{j=1}^{n_k} \dot{\varphi}_j^{(k)} \Psi_j^{(k)} + \sum_{J} \dot{A}_J \Phi_J \tag{2.12}$$

$$\frac{\delta\Psi}{\delta A_J} = \Phi_J \quad \text{and} \quad \frac{\delta\Psi}{\delta \varphi_j^{(k)}} = \Psi_j^{(k)} \tag{2.13}$$

Applying the Dirac-Frenkel variational principle [85],[86] gives a set of non-linear coupled equations of motion for the A_{ji} time-dependent expansion coefficients

$$i\dot{A}_J = \sum_{L} \mathcal{K}_{JL} A_L \tag{2.14}$$

and one for the SPFs

$$i\dot{\boldsymbol{\varphi}}^{(k)} = (\mathbf{1} - \boldsymbol{P}^{(k)})(\boldsymbol{\rho}^{(k)})^{-1} \langle \boldsymbol{H}^{(k)} \rangle \boldsymbol{\varphi}^{(k)} \tag{2.15}$$

where $\mathcal{K}_{JL}$ is the matrix element of the Hamiltonian in the basis of the Hartree products, such as:

$$\mathcal{K}_{JL} = \langle \Phi_J | \hat{H} | \Phi_L \rangle \tag{2.16}$$

and $P^{(k)}$ is the projector on the space spanned by the SPF for the degree of freedom k:

$$P^{(k)} = \sum_{j=1}^{n_k} |\varphi_j^{(k)}\rangle \langle \varphi_j^{(k)}| \,. \tag{2.17}$$

2.1.2 Representation of the single particle functions and operators

The coupled equations of motions EQ. (2.14),(2.15), are solved numerically by means of a finite representation of the wavefunction and operators. An efficient way to compute these elements is to expand the SPFs ($\varphi_j^{(k)}$) in a time-independent discrete variable

representation [87],[88] (DVR) basis of size N_k:

$$\varphi_j^{(k)}(R_k) = \sum_{k=1}^{N_k} \alpha_{kj}^{(k)}(t)\chi_k^{(k)}(R_k) \tag{2.18}$$

The time-independent functions $\chi_k^{(k)}$ form a set of orthonormal primitive basis functions. The coefficients are the components of the time-dependent vector which solve the time-dependent Schrödinger equation. The DVR is a grid representation used to build the wavefunctions and the operators. Time propagation methods using DVR refer as grid methods [88] and increase the efficiency by avoiding the computation of multidimensional integrals.

2.1.3 Multistate calculations

For photochemical and photophysical problems, several electronic states may be involved. To treat this problem, the multi-set formulation of MCTDH is applied. In this approach, a different set of SPFs is used for each electronic states n ($n = 1, \cdots, \sigma$). The wavefunction as well as the Hamiltonian are expanded in the set $\{|n\rangle\}$ of electronic states

$$|\Psi\rangle = \sum_{n=1}^{\sigma} \Psi^n |n\rangle \tag{2.19}$$

and

$$H = \sum_{n,m=1}^{\sigma} |n\rangle H^{nm} \langle m| \tag{2.20}$$

where each state function Ψ^n is in turn expanded as in EQ. (2.3).
EQ. (2.19) and (2.20) lead to a set of coupled equations of motions:

$$i\dot{A}_J^n = \sum_{m=1}^{\sigma} \sum_L \mathcal{K}_{JL}^{nm} A_L^{(m)} \tag{2.21}$$

$$i\dot{\boldsymbol{\varphi}}^{(n,k)} = (\mathbf{1} - \boldsymbol{P}^{(n,k)})(\boldsymbol{\rho}^{(n,k)})^{-1} \sum_{m=1}^{\sigma} \langle \boldsymbol{H}^{(n,m,k)} \rangle \, \boldsymbol{\varphi}^{(m,k)} \tag{2.22}$$

where $\mathcal{K}_{JL}^{nm}$ are the Hamiltonian matrix elements:

$$\mathcal{K}_{JL}^{nm} = \langle \Phi_J^{(n)} | H^{(nm)} | \Phi_L^{(m)} \rangle \tag{2.23}$$

and $\langle \boldsymbol{H}^{(n,m,k)} \rangle$ is the mean-field acting on the k-th degree of freedom:

$$\langle H^{(n,m,k)} \rangle = \langle \Psi_j^{(n,k)} | H^{(n,m)} | \Psi_l^{(m,k)} \rangle \tag{2.24}$$

2.2 Semi-classical molecular dynamics

Accurate quantum dynamical simulations are restricted only to a few degrees of freedom. An alternative to quantum dynamics is the semi-classical (SC) molecular dynamics. In this approach, the motion of the nuclei is propagated on PES according to the Newton laws.

$$\sum_i \mathbf{F}_i = m \cdot \mathbf{a} \tag{2.25}$$

were $\mathbf{F}_i$ are the forces applied to the particle, m is its mass, and $\boldsymbol{a}$ is the acceleration resulting from the applied forces. The advantage of this method is that all degrees of freedom can be included in the simulation. Moreover, the PES and non-adiabatic coupling can be computed "on-the-fly" and do not require preliminary heavy electronic structure calculations. The gradient of the potential energy $V(\boldsymbol{R})$ gives the force that acts on the system:

$$\mathbf{F} = -\nabla V(\mathbf{R}) \tag{2.26}$$

Knowing the initial position R and velocity $\boldsymbol{v}$ at $t = 0$ EQ. (2.26) can be integrated to yield the movement of the nuclei. The position of the nuclei as a function of time is called a trajectory. In order to mimic an initial wavepacket of a quantum dynamics simulation, a statistically relevant number of trajectories that sample the initial conditions has to be used.

2.2.1 Integration of Newton equations of motion

Several algorithms such as the Euler [89] or the Euler-Cromer [90] can be used to prop-

agate trajectories. The most popular numerical integration scheme is the Velocity-Verlet algorithm [91],[92],[93].
The second-order Taylor expansion of the position at a time $t + \Delta t$ gives:

$$\mathbf{R}(t + \Delta t) = \mathbf{R}(t) + \boldsymbol{v}(t)\Delta t + \boldsymbol{a}(t)\Delta t^2 + \mathcal{O}(\Delta t^3) \tag{2.27}$$

and for the position at a time $t - \Delta t$:

$$\mathbf{R}(t - \Delta t) = \mathbf{R}(t) - \boldsymbol{v}(t)\Delta t + \boldsymbol{a}(t)\Delta t^2 + \mathcal{O}(\Delta t^3) \tag{2.28}$$

Summing EQ. (2.27) and EQ. (2.28) gives:

$$\mathbf{R}(t + \Delta t) = 2\mathbf{R}(t) - \mathbf{R}(t - \Delta t) + 2\boldsymbol{a}(t)\Delta t^2 + \mathcal{O}(\Delta t^4) \tag{2.29}$$

where $\boldsymbol{a}(t)$ is the acceleration deduced from the gradient by the relation:

$$\boldsymbol{a}(t) = -\frac{1}{m}\nabla V(\mathbf{R}(t)) \tag{2.30}$$

Whereas the velocity $\mathbf{v}(t)$ is not needed to determine the position $\mathbf{R}(t + \Delta t)$, velocities are needed to compute the kinetic energy and ensure the conservation of the total energy. They are obtained by a simple numerical derivation

$$\mathbf{v}(t + \Delta t) = \frac{\boldsymbol{R}(t + \Delta t) - \boldsymbol{R}(t - \Delta t)}{2\Delta t}. \tag{2.31}$$

Since the errors on the velocities and positions are of the order of Δt^2 and Δt^4, respectively, the accuracy is improved when small time steps are used in the propagation.

2.2.2 Surface hopping

Applying SC dynamics to photochemical or photophysical problems proves to be more complex. Indeed the SC dynamics methodology does not account for the quantum effects, *i.e.* interferences, tunnelling effects, non-adiabatic coupling. In the vicinity of a crossing of the PES, the NACT become important, and a transfer between the two electronic states can occur. To simulate this effect with SC dynamics, a surface hopping scheme is used [94]. In regions where two electronic states are close to each other in energy, their nature

may vary abruptly resulting in a huge amount of hops. To solve this problem, Tully has proposed a fewest switch algorithm [95].

The probability of transition $P_{m\to n}$ between two electronic states n and m is approximated as:

$$P_{m\to n} = \frac{2\Re\{c_m^*(t)c_n(t)\,[i/\hbar \mathbf{H}_{mn} + \mathbf{K}_{mn}]\}}{c_m^*(t)c_n(t)}\Delta t \tag{2.32}$$

where $\Re$ indicates that we consider only the real part of the argument, and the c coefficients being defined by the linear combination of the adiabatic states in the total electronic wavefunction.

$$|\Psi_e\rangle = \sum_n c_n\,|\Psi_e^n\rangle \tag{2.33}$$

with

$$\mathbf{H}_{mn} = \langle\Psi_e^m|\hat{H}_e|\Psi_e^n\rangle \tag{2.34}$$

and

$$\mathbf{K}_{mn} = \langle\Psi_e^m|\frac{\partial}{\partial t}|\Psi_e^n\rangle = \frac{\partial \mathbf{R}(t)}{\partial t}\,\langle\Psi_e^m|\frac{\partial}{\partial \mathbf{R}}|\Psi_e^n\rangle \tag{2.35}$$

$\mathbf{K}_{mn}$ is then the product between the velocities and the non-adiabatic coupling elements, the latter being evaluated by quantum chemical computations.

Quantum decoherence can be included in the surface hopping scheme by taking into account an overlap decoherence correction (ODC) as developed recently by Granucci *et al.* [96].

For our preliminary studies, we have used a simple hopping algorithm implemented in the quantum chemistry package MolCAS [97, 98, 99]. In this algorithm the hop control is based on two properties: (1) the energy gap magnitude ($\Delta E < 3.00 \cdot 10^{-3} E_h$), and (2) the exchange of adiabatic states. This is estimated by computing the scalar product between the c_n coefficients of both states from one time step to the other, which gives two conditions:

$$\begin{aligned} c_n(t)\cdot c_m(t+\Delta t) &> 0.25 \\ c_m(t)\cdot c_n(t+\Delta t) &> 0.25 \end{aligned} \tag{2.36}$$

If both conditions are fulfilled, then the transition between the two PES is activated.

PART B

The Photoisomerization Processes

This part is dedicated to photo-induced isomerization processes in small organic chromophores, either isolated, as in penta-3,4-dieniminium minimal model for the active chromophore of the visual pigment rhodopsin, the retinal, and in pentenylidene-pyrrolinium, minimal model for the indanylidene-pyrrolinium, a synthetic mimic of the retinal, or as the cyano-pyridyl retinal coordinated to a rhenium bipyridine carbonyl fragment. Whereas the dynamical aspects of the photoisomerization are investigated in the first two applications (CHAPTER 3, 4) devoted to the isolated organic chromophores, the last section (CHAPTER 5) is restricted to the structural and electronic properties only. It is worth noting that the study devoted to the directionality of double-bond photoisomerization dynamics in a minimal photoswitch (CHAPTER 4 presented as a published article) has been performed within the context of the post-doc period of Gabriel Marchand at the Laboratoire de Chimie Quantique and should be taken as a contribution of the author of the present thesis to this work.

CHAPTER 3

STUDY OF THE PSB3: A MINIMAL MODEL OF RETINAL

3.1 Introduction

A C=C photoisomerization process is a change of conformation of a double bond after absorption of a photon. The molecule evolves on its excited state PES and eventually decays back into the ground state through a CI. In the vicinity of the CI, the electronic states are close in energy allowing for a radiationless relaxation. This radiationless decay is called internal conversion (IC) and results from the vibronic (non-adiabatic) coupling between two electronic states of same spin multiplicity. On the contrary, a transition between two electronic states of different spin multiplicity is called intersystem crossing (ISC) and results from spin-orbit coupling between the two states. However, in organic molecules, SOC are generally weak and the ISC process can be neglected. Thus the photochemistry and photophysics of the molecule will take place only in the singlet manifold as observed experimentally.

During the decay to the electronic ground state, it may either relax to its initial conformation (before absorption of light), in this case, the photoisomerization is said to be aborted; or in the other conformation, in which case the isomerization is successful. Upon excitation of a solution, the proportion of successful isomerizations defines the isomerization yield of the reaction. As mentioned in SECTION 1.5.2, the shape of the CI will modulate this quantum yield.

The paradigm of photoisomerization is the retinal chromophore (FIG. 3.1) which is the primary event of the vision. The retinal chromophore is embedded in a protein called Rhodopsin (FIG. 3.1) which is located in the membrane of photoreceptor cells in the

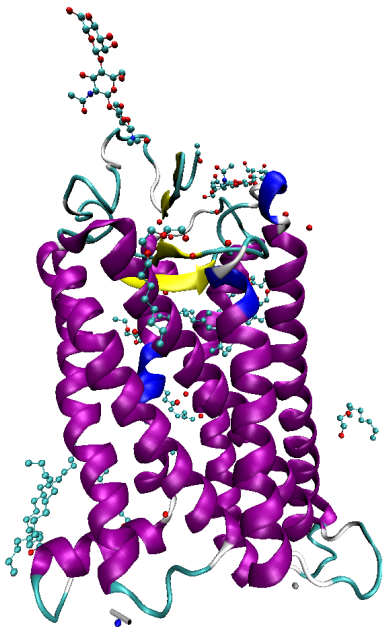

Figure 3.1: Schematic representation of the Rhodopsin protein.

retina. Vertebrates have two types of photoreceptor cells, namely the rods and the cones. The first ones are very sensitive and allow to detect as few as a single photon [100]. However, the rods are not capable of detecting colors but allows for a detection of the light intensity. It is the cones photoreceptors that allow us to see colors. Indeed, there are three types of cones that absorb light in three distinct regions. The combination of these three kinds of photoreceptors translates all colors into nerve signal.

Upon absorption of light in the lowest electronic excited state, the retinal chromophore undergoes a *cis* to *trans* isomerization around the $C_{11} - C_{12}$ bond (see FIG. 3.2). The peptidic cavity is shaped to accommodate the *cis* conformer of the retinal chromophore, but not its *trans* conformer. Thus, the isomerization will induce a geometrical change of the protein. This deformation will in turn trigger the transduction signal.

This photoisomerization is very fast, it occurs within 200fs [101],[102] and is particularly efficient, with an isomerization yield of 65% [103],[104]. It is also selective around one double bond, namely the 11-12 bond. These exceptional properties are due to the interaction with the peptide cavity. Indeed this nature leads to a pre-twist of the $C_{11} - C_{12}$ double bond of the retinal chromophore [105]. This is emphasized by the fact that the retinal chromophore in solution has an isomerization yield of approximately 30% [106] and is no longer selective.

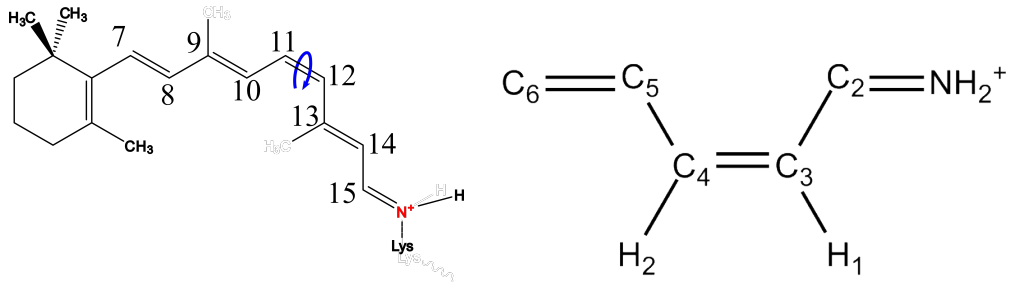

Figure 3.2: Left: retinal chromophore in its "active" 11-*cis* conformation; the blue arrow points to the isomerizable double bond. Right: the minimal model of the retinal chromophore: 3,4-pentadieniminium (PSB3).

In order to try to understand why this system is so efficient, many experimental studies [107, 108, 109, 110, 111, 112], and theoretical studies [113, 114, 115, 116] have been performed.

However, this system is large and limits the computational level of the calculations. This is why, many protonated Schiff bases (PSBs) of different backbone length, that aim at modelling the retinal chromophore are extensively studied. These models have to reproduce key features of the retinal chromophore such as the charge transfer nature of the lowest electronic excited state [107], the alternation of double and single bonds,... Among those model systems, one of the most studied is the PSB3 [117] (see FIG. 3.2), which is a protonated Schiff base containing three double bonds C=C. The small size of this system as well as its interesting electronic features (charge transfer nature, the presence of a conical intersection, multiconfigurational nature of the electronic states,...) makes it a benchmark system for quantum chemistry methods [118, 119, 120, 121].

The PSB3 has also been studied by means of semi-classical dynamics methods in order to grasp the dynamical behavior of the system around the seam of conical intersection [122, 123, 124]. However, quantum dynamics methods have not been applied yet to the PSB3. The goal of the present work is to make of the PSB3 model a benchmark for quantum dynamical methods too. To achieve this, we will construct an eight dimension adiabatic PES that includes the most important degrees of freedom that drive the photoisomerization process.

In the present chapter, we will first present a preliminary analysis of the nature of the electronic states at critical nuclear geometries. We will then use a semi-classical method to extract the important degrees of freedom involved along the trajectories. A complementary static study of low dimension PES cuts along the chosen active coordinates will

then be performed to analyze and understand key features of these PES. The information gathered from these calculations will then be used to build an initial guess for the diabatic electronic states and potential diabatic coupling, which are needed to perform quantum dynamics, see SECTION 1.4. The diabatic electronic states and potential coupling are then fitted to the adiabatic ab initio PES.

3.2 Computational Details

The structures have been optimized with the quantum chemistry software MolCAS 7.8 [97, 98, 99] using both the SA-CASSCF and SA-CASSCF//MS-CASPT2 methods using the 6-31+G* Pople's basis set [125, 126, 127] with an active space of 6 electrons in 6 π orbitals (FIG. 3.3) and averaged over 3 electronic states. In order to avoid the intruder states problem, an imaginary shift of 0.2 has been added at the MS-CASPT2 level. MolCAS IPEA shift (ionization potential, electron affinity shift) has been taken at its default value (IPEA=0.25). Single points of the adiabatic electronic PES have been computed using the same protocol. Around 70,000 single points have been computed over a wide range of nuclear distortions thus requiring a robust quantum chemical methodology.
Conical intersections have been optimized and branching spaces have been computed using the Gaussian 09 package [128] at the SA-CASSCF level (with the same basis set, and the same active space) including the highest electronic state involved in the conical intersection as well as every electronic states lying lower in energy.
Electronic density analysis has been performed through the Dgrid package [129].
The fitting procedure of the adiabatic electronic PES has been performed by means of the NL-FIT software developed in Montpellier (group of F. Gatti).

3.3 System at Franck-Condon geometry

The *cis* conformation of the retinal chromophore in Rhodopsin is the most stable in the ground state [130]. As a consequence, we choose to use the *cis* isomer of the PSB3 (FIG. 3.4, left) as starting point of our study. Its optimized geometry in the ground state is found to be planar, *i.e.* of C_s symmetry. The electronic ground state (S0) is characterized by an electronic configuration were orbitals I, II and III are doubly occupied (TAB. 3.1,

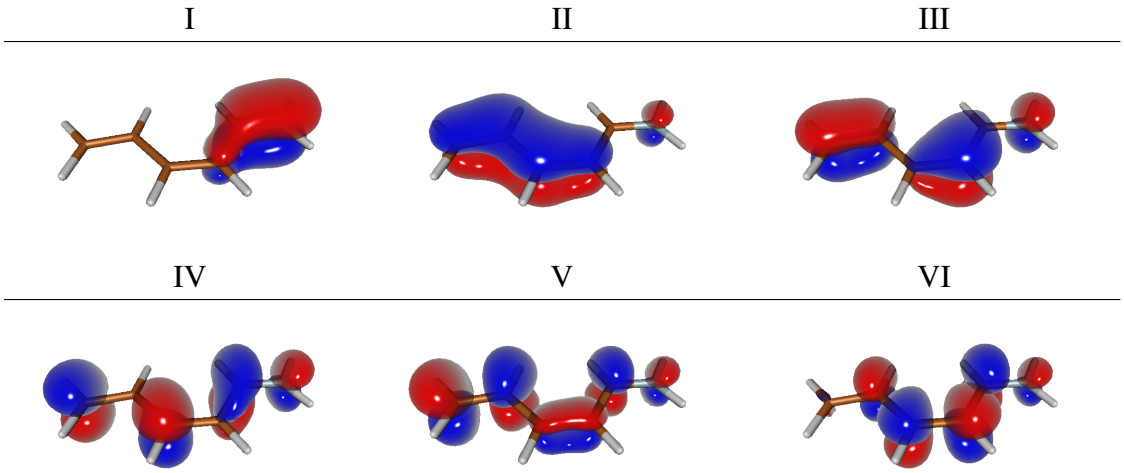

Figure 3.3: CASSCF active space containing the whole π system of the PSB3. Orbitals are numbered from I to VI for the sake of clarity. Orbital III is the HOMO and orbital IV is the LUMO.

FIG. 3.3). The resulting π electronic density is localized around the $C_6 - C_5$,$C_4 - C_3$ and $C_2 - N$ bonds (FIG. 3.4). The first electronic excited state (S1) consists mainly of a III $\rightarrow$ IV (HOMO$\rightarrow$LUMO) transition and is the absorbing state with an oscillator strength of $f = 0.86$ (TAB. 3.1). The III $\rightarrow$ IV excitation leads to two important changes in the electronic structure: (1) an electron is promoted from a π orbital (III) with electronic density on the central double bond ($C_3 - C_4$) to an orbital (IV) exhibiting an π^* anti-bonding character on this bond. This leads to a decrease of the double bond nature and unlocks the torsion around the $C_4 - C_3$ weakened bond. (2) the first excited state (S1) is a charge transfer state like in the retinal chromophore [107]. The Mulliken charge of each halves of the PSB3 has been computed and is reported TAB. 3.2. In S0, the positive charge is mainly localized on the NH_2^+ moiety ($Z^{GS}_{NH_2^+} = 0.73$), whereas in S1, this charge is reduced down to $Z^{S1}_{NH_2^+} = 0.48$. This charge transfer is highlighted by the difference of π electronic density between S1 and S0 (FIG. 3.4). A small contribution of the III$\rightarrow$V is found in S1 at FC (7%), its role in the description of the photoisomerization process will be discussed later.

The second excited state (S2) corresponds to a II$\rightarrow$IV and a III$\rightarrow$V excitation. It involves also a III$\rightarrow$IV double excitation. In S2, the charge is located on the NH_2 moiety (TAB. 3.2) as in S0. TAB. 3.1 shows the comparison between the electronic states computed at the SA-CASSCF and the MS-CASPT2 level. S0 being of the same electronic nature as S2,

SA-CASSCF

State	ΔE / eV	Configuration	%	f
S0		G.S	88	
S1	4.82	III → IV	67	0.82
		III → V	11	
S2	5.91	II → IV	25	0.17
		D.E.: III → IV	27	
		III → V	9	

MS-CASPT2

State	ΔE / eV	Configuration	%	f
S0		G.S	89	
S1	4.16	III → IV	75	0.79
		III → V	7	
S2	5.82	II → IV	32	0.08
		D.E.: III → IV	25	
		III → V	13	

Table 3.1: Electronic nature of the first three electronic states of the *cis* isomer of PSB3 at Franck-Condon optimized at the MS-CASPT2 level; *G.S*: corresponds to the configuration where the orbitals I, II and III are doubly occupied; *D.E*: stands for "double excitation". f: is the oscillator strength.

it will induce a bias in the set of orbitals used to build the wavefunction. Indeed, they are averaged over the three electronic states, equally weighted in our calculations, and will be better suited to describe the covalent electronic states (S0 and S2), thus overestimating the energy of S1. Including the dynamic correlation using the MS-CASPT2 approach allows to partially compensate that bias. The overestimated energy gap between S1 and S0 at the SA-CASSCF level (ΔE=4.82 eV) is reduced using the MS-CASPT2 approach (ΔE=4.16 eV) (Se TAB. 3.1). Moreover, the energy gap between the two electronic states S2 and S0 for which the orbitals are suited, does not significantly change using MS-CASPT2. This

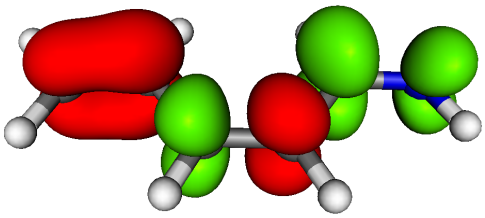

Figure 3.4: π electronic density difference between the first and ground states. *(In green: increase of electronic density; in red: decrease.)*

State	NH_2^+	CH_2
S0	0.73	0.27
S1	0.48	0.52
S2	0.78	0.22

Table 3.2: Mulliken charges summed all over each half of PSB3. The NH_2^+ half contains the atoms C_3,C_2, N, and the hydrogen atoms carried by them.

	cis (Ref: [4])	*trans* (Ref: [4])
$C_6 - C_5$	1.358 (1.354)	1.358 (1.354)
$C_5 - C_4$	1.440 (1.439)	1.434 (1.435)
$C_4 - C_3$	1.381 (1.374)	1.380 (1.371)
$C_3 - C_2$	1.413 (1.413)	1.410 (1.411)
$C_2 - N$	1.316 (1.313)	1.317 (1.314)
$C_6 - C_5 - C_4 - C_3$	180 (-)	180 (-)
$C_5 - C_4 - C_3 - C_2$	0 (0)	180 (180.0)
$C_4 - C_3 - C_2 - N$	180 (-)	180 (-)
$H_2 - C_4 - C_3 - H_1$	0 (-)	180 (-)

Table 3.3: Geometries of the *cis* and *trans* conformers optimized at the MS-CASPT2 level in the ground electronic state S0. (distances in Åand dihedral angles in °). Values at the 2-states(6,6)SA-CASSCF//CASPT2 level of theory from Ref [4] are given for comparison.

is not surprising since S0 and S2 are mainly of the same nature.

3.4 Equilibrium geometries of the *cis* and *trans* conformers.

The ground state geometry of the *trans* isomer has been optimized and also found to be of Cs symmetry. It is lower in energy than the *cis* isomer by 0.22 eV (at the MS-CASPT2 level). The geometries of the two isomers are similar, except for the central double bond torsion (0° vs 180°), see TAB. 3.3. *Trans* and *cis* isomers have the same electronic structure, see TAB. 3.4. Indeed, the excited states have the same nature and the energy gaps are basically the same. It is important to note that the III→V contribution is lower in S1 (3% instead of 7%) for the *trans* isomer. This will have to be taken into account later, in the fitting process of the PES. The gradient in S1 at both the *cis* and *trans* optimized geometries is zero except along the in plane motions (i.e. stretching of the backbone).

MS-CASPT2				
State	ΔE / eV	Configuration	%	f
S0		G.S	89	
S1	4.02	III → IV	78	1.15
		III → V	3	
S2	5.53	II → IV	30	0.02
		D.E.: III → IV	32	
		III → V	14	

Table 3.4: Electronic configuration of the three lowest electronic states of PSB3 at the equilibrium geometry of the *trans* conformer optimized at the MS-CASPT2 level; *G.S*: corresponds to a configuration where the orbitals I, II and III are doubly occupied; *D.E*: stands for "double excitation". f: is the oscillator strength.

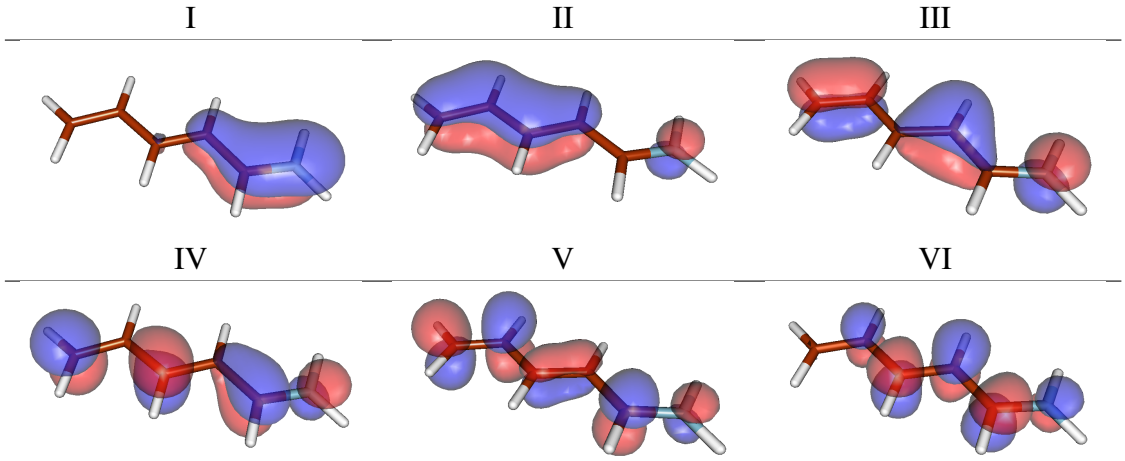

Figure 3.5: CASSCF active space for the *trans* PSB3

This corroborates the hypothesis that the first motion after excitation is a rearrangement of the bond lengths. The optimized geometries at our level of calculation are similar to those obtained by Gozem *et al.* [4]. Given that, we can assume that the geometry of the minimum of conical intersection, at our level of calculation, is the same as found in ref [4]. This will be assumed as we optimized the CI only at the SA-CASSCF level.
The minimum of CI seam is found at a central double bond ($C_3 - C_4$) torsion of $90°$.
As discussed in SECTION 1.5.2, this point of conical intersection is part of a space of dimensionality 3N-8 (where N is the number of atoms, here N=14). In order to get the vectors characterizing this point of intersection, we performed an optimization of the conical intersection geometry with Gaussian, using the same basis set as in MolCAS,

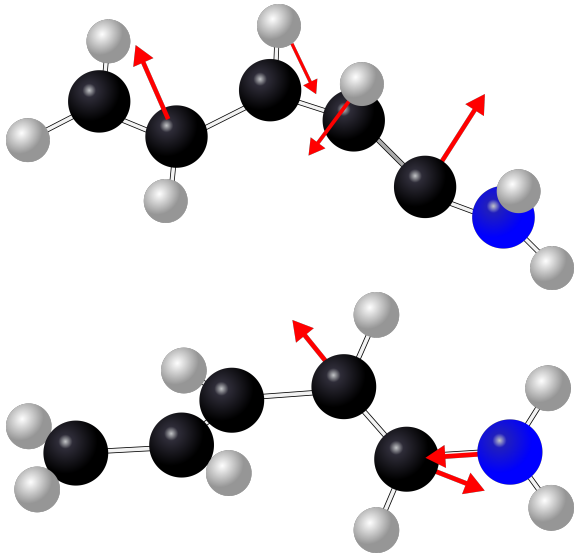

Figure 3.6: Branching space at the minimum of the conical intersection seam between the ground and the first excited state. Top: derivative coupling vector. Bottom: gradient difference vector.

but taking only into account the two lowest states at the CASSCF level. This allows to determine the branching space (see SECTION 1.5.2) in which the degeneracy is lifted at first order. The gradient difference vector (FIG. 3.6, bottom) is composed, at this point, mainly of distortions of the $C_3 - C_2$ and $C_2 - N$ bond lengths, but also of the $C_6 - C_5$, $C_5 - C_4$ and $C_4 - C_3$ bond lengths at lower extend. The derivative coupling vector (FIG. 3.6, top) is composed of the out of plane motions of the carbon atoms C_2 and C_5, inducing a torsion around the central $C_4 - C_3$ bond, and also the out of plane motions of the hydrogen H_1 and H_2. We can note that the torsions around $C_6 - C_5 - C_4 - C_3$ and $C_4 - C_3 - C_2 - N$ dihedral angles shall play a role at lifting the degeneracy at this point.

The explanation of the occurrence of a CI at this geometry follows; looking at the two orbitals mainly involved in the electronic transition from S0 to S1 (see FIG. 3.7), we can see that at $\varphi = 90°$ the π systems of each half are orthogonal, thus preventing the π communication over the whole molecule. Both bonding and anti-bonding orbitals become non-bonding leading to the degeneracy between the two states.

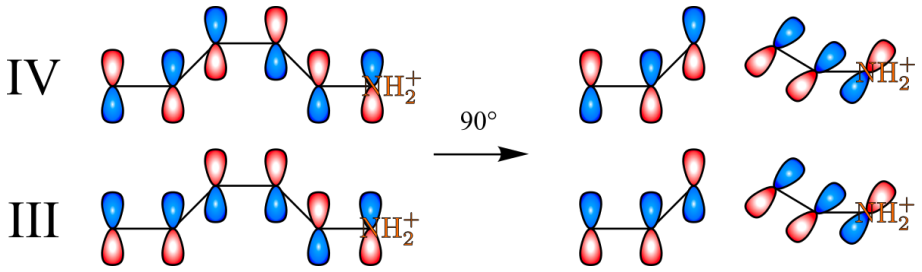

Figure 3.7: Explanation of the CI at $\varphi = 90°$ from a simple orbital point of view: the two orbitals involved in the electronic transition to S1 (namely orbitals III and IV) are represented as a combination of the p orbitals of each atom of the backbone.

3.5 Semi-Classical dynamics

In order to select the most relevant degrees of freedom for the construction of reduced dimensionality diabatic PES for quantum dynamics, a study of the dynamics using semi-classical trajectories has been performed. The goal of these simulations is to investigate qualitatively which "path" the molecule follows after light absorption, namely which deformations are primarily involved in the photoisomerization process, apart from the $C_3 - C_4$ torsion.

3.5.1 Trajectory from the FC point in S1

In a first step, we have propagated a single semi-classical trajectory at the SA-CASSCF level over two electronic states using an active space including the whole π system. The basis used was the Pople's 6-31G* basis set. The trajectory was propagated up to 242 fs with a time-step of $\delta t = 0.24$fs at 0K. Starting from the Franck-Condon region, after excitation in S1 the molecule evolves on a rather flat potential for about 150fs (FIG. 3.9). The first significant geometrical change is the ultrafast rearrangement of the bond lengths. Bonds $C_6 - C_5$, $C_3 - C_4$ and $C_2 - N$ stretch within 10 fs whereas the $C_5 - C_4$ and $C_3 - C_2$ bond lengths shrink (FIG. 3.8). This motion is called the bond length alternation (BLA) [131, 132] and is the result of the ultrafast reorganisation of the π electronic system leading to the excited state charge redistribution.
At around 150 fs, the central double bond starts twisting resulting in a change of the $C_2 - C_3 - C_4 - C_5$ and $H_1 - C_3 - C_4 - H_2$ dihedral angles (FIG. 3.8). This motion

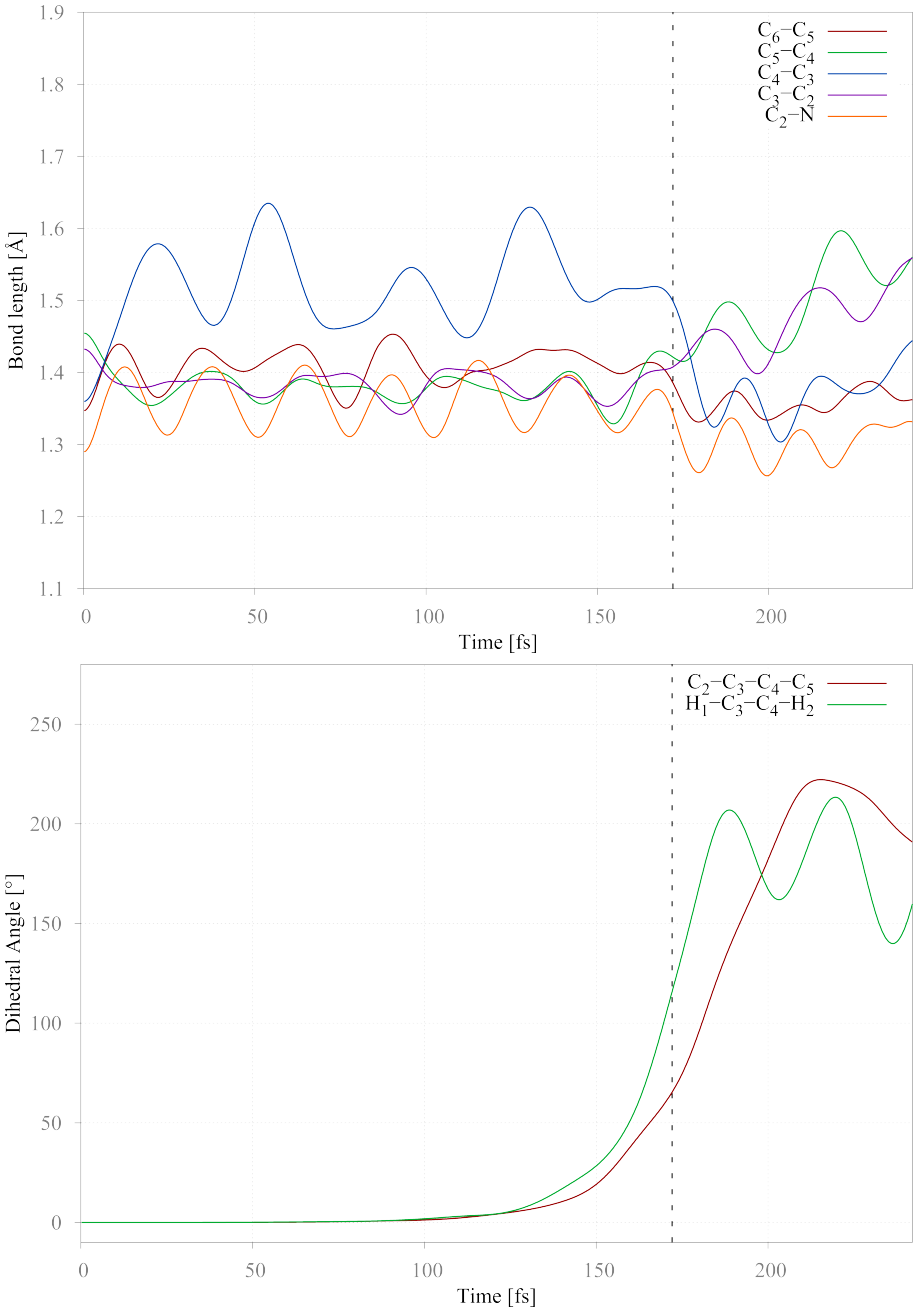

Figure 3.8: Top: evolution of the C − C bond lengths as function of time. Bottom: evolution of two dihedral angles involved in the central double bond torsion as function of time.

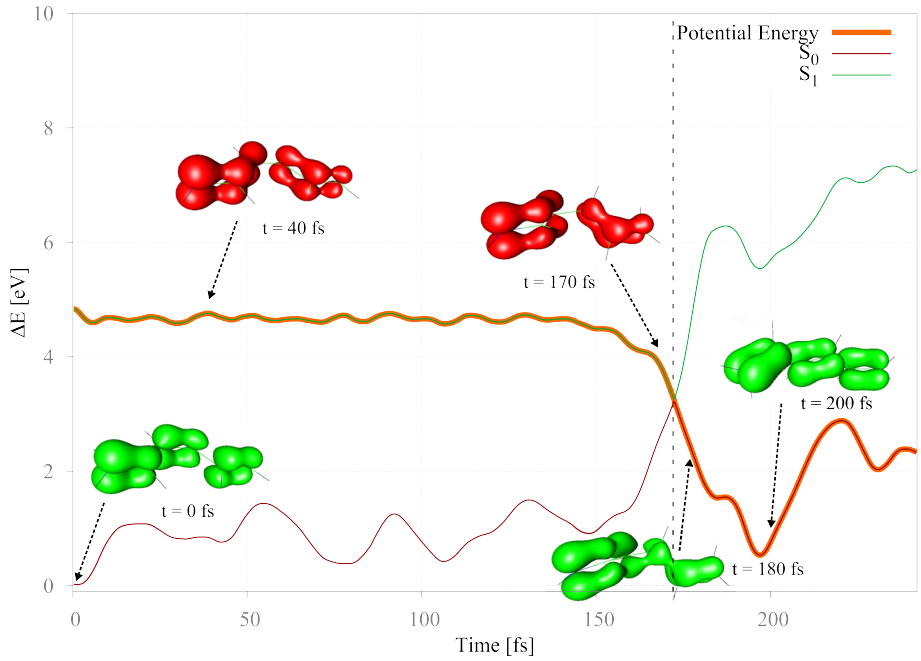

Figure 3.9: Evolution of the first two electronic states energies as function of time (the trajectory is following the red curve potential). Snapshots of the π electronic densities are given for both states at different times.

leads the trajectory toward a region where the two electronic states S1 and S2 are close in energy.

It is important to note that the $H_1 - C_3 - C_4 - H_2$ torsion precedes the $C_2 - C_3 - C_4 - C_5$ one. This motion is called Hydrogen Out Of Plane motion (HOOP) and has been extensively studied by means of semi-classical trajectories performed on several PSB of various lengths [131, 133, 134, 135]. It has been shown that at the moment of hopping from the excited state to the ground state surface, the HOOP motion determines the outcome of the photoisomerization. Works by Weingart *et al.* [123],[124] have shown that if the HOOP angle ($H_1 - C_3 - C_4 - H_2$) is opening when a trajectory hops to the ground state, then the isomerization is successful and the molecule reaches the *trans* conformation in the ground state. However, if the hop happens as the HOOP angle is closing, then the isomerization is aborted and the molecule goes back in its original conformation, i.e. *cis*.
HOOP "effect" has been discussed in Rhodopsin too [131]. Moreover, preliminary calculations on a model of molecular photoswitch (CPP) have shown that carbon atoms may play the same role as the HOOP motion. This system will be presented in details and will

be discussed later in CHAPTER 4.
After this step, the trajectory reaches a conical intersection at 172 fs and hops to the ground state. In this particular trajectory the HOOP angle value is $115°$ and the $C_2 - C_3 - C_4 - C_5$ angle is $65°$ (FIG. 3.8), which is lower than the $90°$ observed at the minimum of conical intersection geometry (see SECTION 3.4). At the hop, the first derivative of the HOOP angle is positive, meaning that the angle is opening. The final HOOP and $C_2 - C_3 - C_4 - C_5$ angles of the trajectory are about 180°, i.e. in *trans* conformation, as expected.
After the hop, the dynamics can no longer be exploited as, we have no way of dissipating the excess of kinetic energy in the "hot" ground state. A solvent would be needed to dissipate this energy.
It is clear that the central double bond torsion is the key coordinate of the photoisomerization, but it is also mandatory to include other dimensions in our study in order to be able to reach the seam of conical intersection at different values of the central double bond torsion. We saw that the HOOP motion is crucial to determine the outcome of the isomerization, and also to reach the intersection seam for a value of the $C_2 - C_3 - C_4 - C_5$ dihedral angle lower that $90°$ (i.e. the minimum of intersection). The BLA motion is the first one to happen and also plays a key role by stretching the central $C_3 - C_4$ bond thus allowing for the subsequent isomerization.

However, this trajectory can only be used to guide us in the determination of the active coordinates. Indeed, the initial geometry (i.e. the *cis* conformer) is totally planar and is not representative of the initial geometrical distribution.

3.5.2 Repartition of the kinetic energy

The analysis of the evolution of the kinetic energy during the propagation of the trajectory, has been performed by projecting the kinetic energy on the set of normal modes of the electronic ground state S0. The repartition of kinetic energy among the normal modes and along the trajectory is shown in FIG. 3.10. We will focus here on the four normal modes represented in FIG. 3.11. The first three (8, 10 and 21) are normal modes involving out of plane motions. Normal mode 8 involves all the atoms of the backbone, normal modes 10 and 21 involve mainly out of plane motions of the carbon atoms C_3, C_4 and the hydrogen atoms H_1 and H_2. The only selected in-plane motion is normal mode 33,

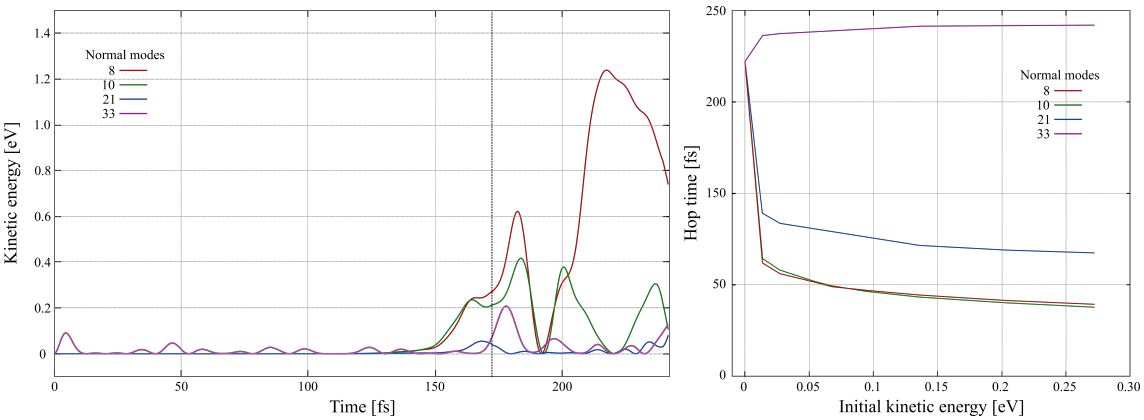

Figure 3.10: Left: distribution of the kinetic energy among normal modes all along the propagation time (only four normal modes are shown). Right: evolution of the hop time as a function of the initial amount of kinetic energy in each selected normal mode.

which is a stretching motion, mainly of the $C_3 - C_4$ bond. We can see that in the first femtoseconds, normal mode 33 gains kinetic energy. This amount of kinetic energy oscillates with time but remains quite small. This is due to the ultrafast reorganisation of the π electronic density along the backbone. On the contrary, out of plane normal modes, i.e. modes 8, 10 and 21, gain only kinetic energy while the trajectory is in the vicinity of the conical intersection. These observations are just another representation of the geometrical deformation shown in FIG. 3.8.

To qualitatively explain the role of the different motions, we have propagated new semi-classical trajectories with initial kinetic energy in one selected normal mode. The initial geometry as well as the propagation methodology are the same as before. FIG. 3.10 right, sums up the hop time of each trajectory as function of its initial kinetic energy. We can see that, very little initial kinetic energy in out of plane normal modes, i.e. 8, 10, and 21, causes a huge acceleration of the isomerization process, see FIG. 3.10. However, more kinetic energy will not accelerate the process much more. This is not surprising since the initial geometry is totally planar. In order to reach the conical intersection, the molecule has to gain energy in its out-of plane motions so that it will be able to leave this pathological area of the PES. Once the molecule is out of the planar area, it may reach the CI and isomerize. The difference of hop time between trajectories with initial kinetic energies in the out of plane modes and the trajectories with no kinetic energy is due to the fact that trajectories with initial kinetic energy will not wander on the flat PES observed in FIG. 3.9 for as long. It is important to note that normal mode 21 will not accelerate

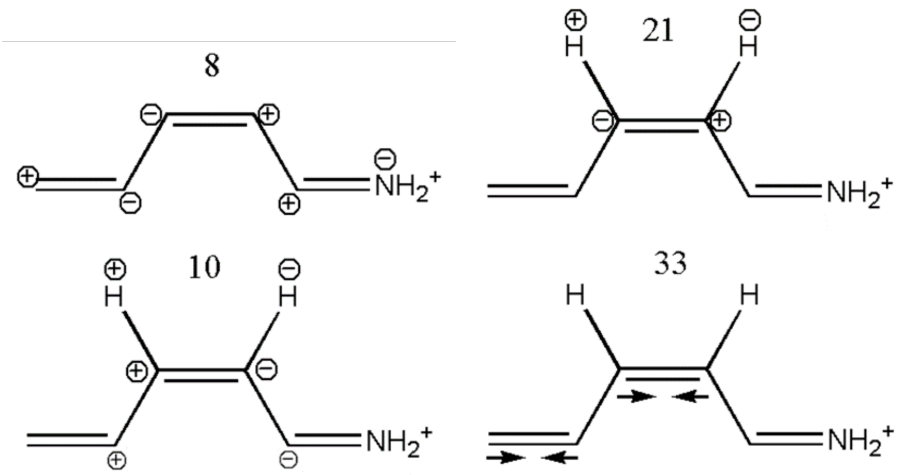

Figure 3.11: Representation of the four selected normal modes in S0.

the isomerization as much as modes 8 and 10. This is because this normal mode involves mainly motions of the hydrogen atoms which are much lighter that the carbon atoms. However, it seems that normal mode 33 which represents partially the reorganisation of the π system will not accelerate the dynamics. This is rather intuitive as this mode will not lead to out of plane distortions. Importantly, we can see that no matter the initial kinetic energy there is in normal mode 33, the isomerization will never occur faster. This means that the stretching motions of the backbone are not coupled with out plane motions. The stretch motion is thus just needed to unlock the way to the CI by allowing the torsion around the $C_3 - C_4$ bond.

3.6 Active coordinates

From the preliminary semi-classical dynamics and static results study as well as the branching space analysis of the minimum of intersection, we can extract three types of geometrical deformations which play a key role in the photoisomerization process, namely:

- The central bond torsion.
- The HOOP motions.
- The BLA.

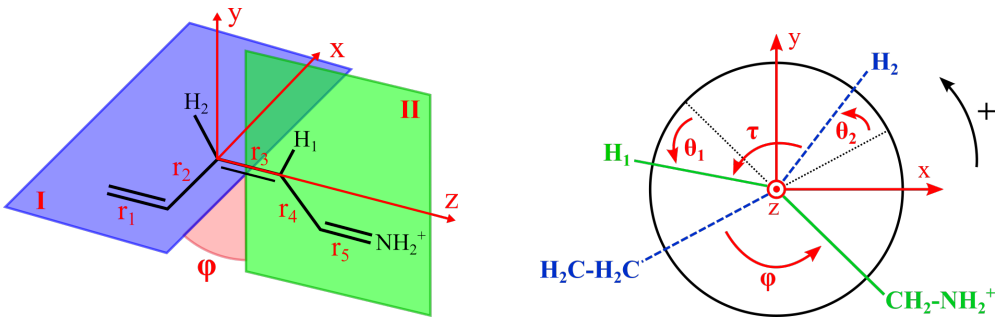

Figure 3.12: Definition of the active coordinates used to represent the photoisomerization process of PSB3.

We choose to describe these three motions by a set of eight active coordinates shown in FIG. 3.12:

- The central bond dihedral angle: φ to describe the isomerization.
- Out of plane angles of the hydrogen atoms H_1 and H_2 θ_1 and θ_2 to describe the HOOP motions
- Five bond lengths $C_6 - C_5$, $C_5 - C_4$, $C_4 - C_3$, $C_3 - C_2$ and $C_2 - N$: r_1, r_2, r_3, r_4 and r_5, respectively, to describe the BLA motion.

3.6.1 The central double bond torsion

The central double bond torsion is designed by the coordinate φ. It is defined as the $C_5 - C_4 - C_3 - C_2$ dihedral angle. As we consider only eight dimensions, both the $C_6 - C_5 - C_4 - C_3$ and $C_4 - C_3 - C_2 - N$ dihedral angles are considered fixed and equal to $180°$. We can then define two planes formed by C_6, C_5, C_4 on one hand, and C_3, C_2, N on the other hand. We will call these planes I and II respectively. φ is then the angle between planes I and II, see FIG. 3.12.
In its equilibrium geometry, the *cis* conformer of PSB3 is planar and so, the system is symmetrical along the torsion alone. This is why, in the following study, as long as we look at potential energy curves along φ only, assuming all other dimensions to be at their ground state equilibrium values, we will only compute *ab initio* points from $0°$ (*cis*) to $180°$ (*trans*), and then use the mirror symmetry. The results of the one dimension cut of the adiabatic PES along φ is shown in FIG. 3.13 at both the SA-CASSCF and MS-

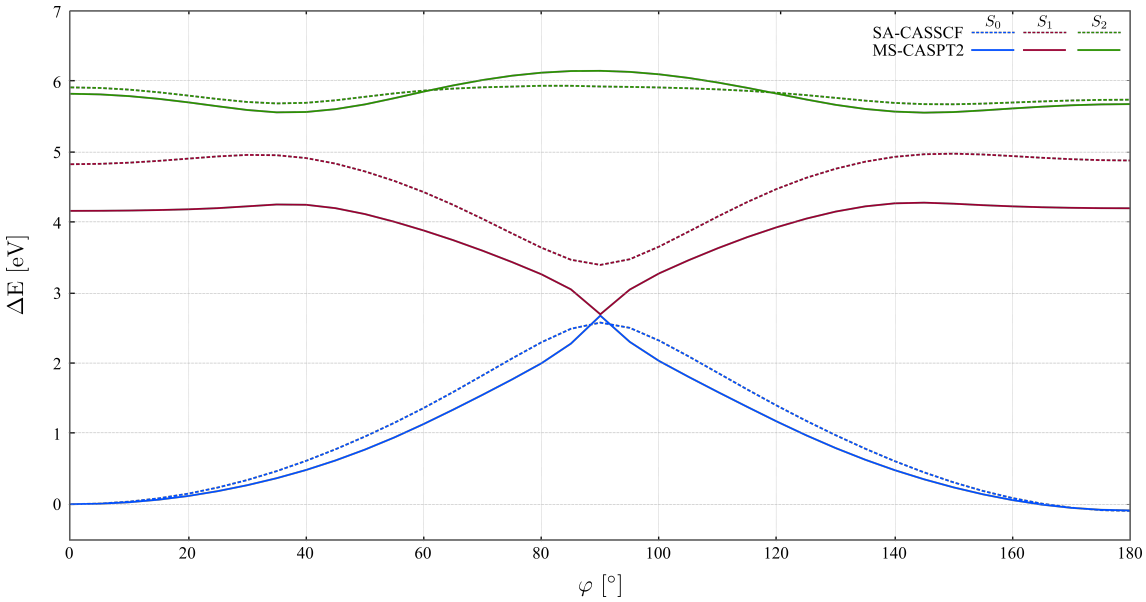

Figure 3.13: Cut of PES associated to the first three electronic states of the PSB3 model along the central double bond torsion at the SA-CASSCF level (dashed lines) and at the MS-CASPT2 level (full lines). All other geometrical parameters are frozen to the electronic ground state geometry.

CASPT2 level. If we focus on the first excited state S1, we notice at around $40°$ and $140°$ slight energy barriers. Those barriers come from a coupling between the first and the second excited states. This barrier is bigger at the SA-CASSCF level. This is not surprising as the energy gap between S1 and S2 is smaller at the SA-CASSCF level. Hence the coupling between S1 and S2 will be larger.

At Franck-Condon, the first excited state is mainly a III $\rightarrow$ IV excitation, but contains also a small contribution of the III $\rightarrow$ V excitation which main component is in the second excited state S2, see TAB. 3.1. To qualitatively explain these energy barriers, one has to look at the evolution of the electronic configurations in each electronic states, which are shown in FIG. 3.14 and are to be looked together with FIG. 3.13. As soon as we move, along φ, away from the planar geometries (*cis* and *trans*), this III $\rightarrow$ IV contribution decreases and is slowly transferred from S1 to S2. Orbital V having π density on the central double bond, this excitation leads to a stabilization of planar geometries, thus creating the energy barriers (FIG. 3.13) around $\varphi = 40°$. This effect can also be seen by looking at the evolution of the Mulliken charge on each half along the torsion, see FIG. 3.15. The charge on the NH_2^+ half in S1 decreases rapidly between $0°$ and $40°$ while, in the same time, the charge on NH_2^+ in S2 increases. This shows the coupling between the

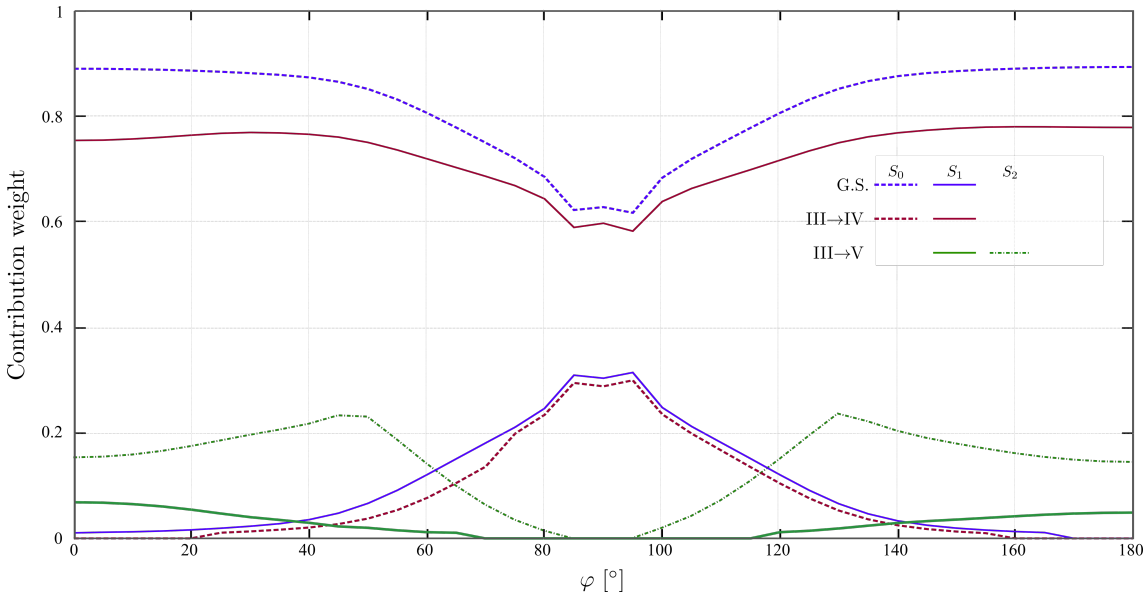

Figure 3.14: Evolution of the main electronic contributions (reference: FC; see TAB. 3.1) for each electronic state as function of φ .

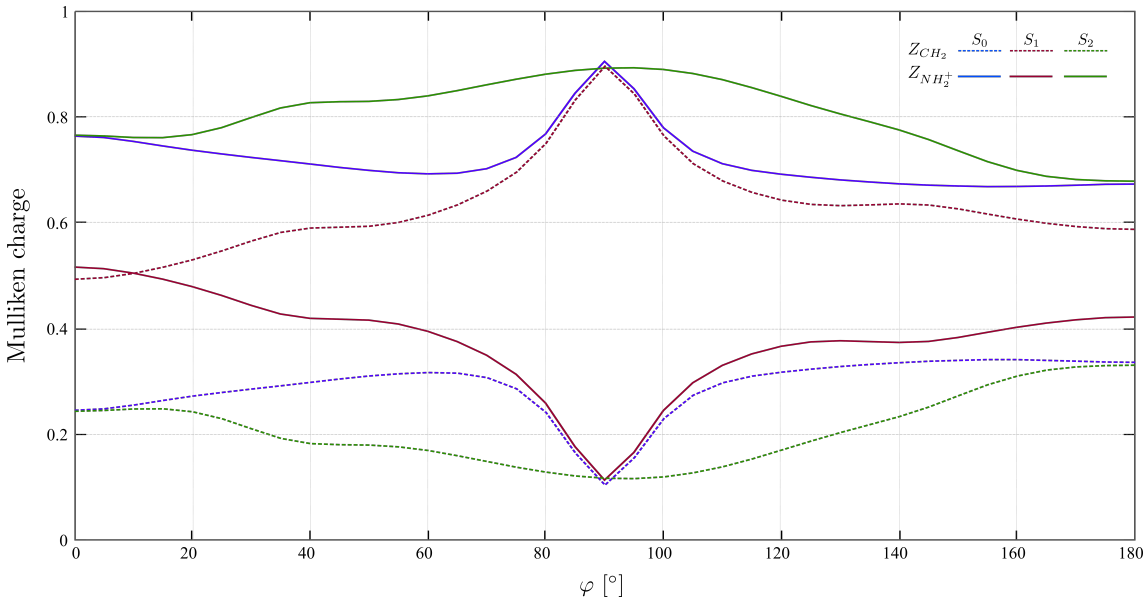

Figure 3.15: Evolution of the Mulliken charge of each half of PS3 along φ for the three first electronic states.

two states S1 and S2. Indeed, S2 being of the same nature as S0, the small contribution of S2 excitation in S1 lowers the charge transfer character of S1. The same phenomenon is observed near $180°$, in the *trans* region.
Getting closer to $90°$, the two first electronic states get closer to each other and at $\varphi = 90°$, the system reaches a conical intersection between the first two electronic states at the MS-CASPT2 level. We note that the CI can't be reached along the torsion φ alone at the SA-CASSCF level. This means that the PES topology changes dramatically going from the SA-CASSCF to the MS-CASPT2 level [4, 132]. The fact that we can reach the CI along the torsion alone in PSB3 is an important feature of the family of the protonated Schiff bases. Indeed, this is not often the case. An illustration is given by the isomerization of ethylene where the torsion around the $C = C$ bond is not sufficient for describing the process. Indeed the carbon atoms must be pyramidalized in order to reach the CI [136, 137, 138].
We can also note that at this point ($\varphi = 90°$) the π communication over the whole molecule is broken, as the p orbitals of carbon atoms C_3 and C_4 are orthogonal. This implies that the positive charge is either on one part of the molecule or on the other, namely the NH_2^+ half in S0 and S2, and the CH_2 half in S1 and that is no longer delocalized over the π system.
Moreover, at this point, S0 and S1 are degenerate and of strong multi-configurational character.

3.6.2 The HOOP motion.

The HOOP motion is described by two angles. θ_2 and θ_1 are defined as the angles between the planes described by $C_5 - C_4 - C_3$ (plane II) and $H_2 - C_4 - C_3$ and those described by $C_4 - C_3 - C_2$ (plane I) and $C_4 - C_3 - H_1$ respectively (see FIG. 3.12).

The HOOP angles define the $H_1 - C_3 - C_4 - H_2$ dihedral angle as following:

$$\tau = \varphi + \theta_1 - \theta_2 \tag{3.1}$$

The effect of both θ_1 and θ_2 angles on the potential energy surfaces are more or less the same (FIG. 3.16, FIG. 3.17). Their contribution to the total energy is quasi quadratic as both directions are equivalent for small displacements. Nevertheless, displacements with

respect to these two angles allow to reach the seam of conical intersection at values of φ different than $90°$. In fact, the seam of conical intersection is observed all along a line of equation

$$\varphi + \theta_i = 90° \qquad \text{for} \quad \theta_j = 0° \qquad i, j = 1, 2 \tag{3.2}$$

Out of plane motions of both hydrogens are thus very important to describe the seam of conical intersection correctly and should be taken into account for the building of the PESs.

In order to lower the energy of the seam of conical intersection, and to gain access to other area of the seam around the minimal energy CI, we choose to look at the concerted effects of θ_1 and θ_2. To do so, we fix φ at 90°, the lowest point of conical intersection, and vary θ_1 and θ_2 independently (FIG. 3.18). We find that both angles lift the degeneracy between $S0$ and $S1$ except along the line of equation

$$\varphi + \theta_1 - \theta_2 = 90°. \tag{3.3}$$

As a consequence, we can reach the seam of conical intersection more easily with a collective motion of both θ angles: the two hydrogen atoms will preferentially move in a concerted way.

As a first approximation, and to reduce the dimensionality of the problem for preliminary observations we can then define two new angles, which are a linear combination of θ_1 and θ_2:

$$\theta^- = \frac{\theta_1 - \theta_2}{2}$$

$$\theta^+ = \frac{\theta_1 + \theta_2}{2}$$

In itself, this decomposition does not reduce the dimensionality of the system. However only θ^- contributes to the branching space (FIG. 3.19); The θ^+ coordinate will not lift the degeneracy and lie within the intersection seam. Thus we decided to study only the influence of θ^- over the PES, and took only the lowest possible value of θ^+, i.e, $\theta^+ = 0$ when $\theta_1 = -\theta_2$ in order to minimize the energy (FIG. 3.20). Unlike the φ torsion, the θ_1 and θ_2 coordinates will not have to be periodic, because of steric hindrance. By computing a small surface as a function of θ_1 and θ_2, at a reference point of the conical intersection, we can see that both dimensions lift the degeneracy. But if we plot the PES according to θ^+ and θ^-, the degeneracy is only lifted along θ^-, confirming that θ^+ does not belong to the branching space.

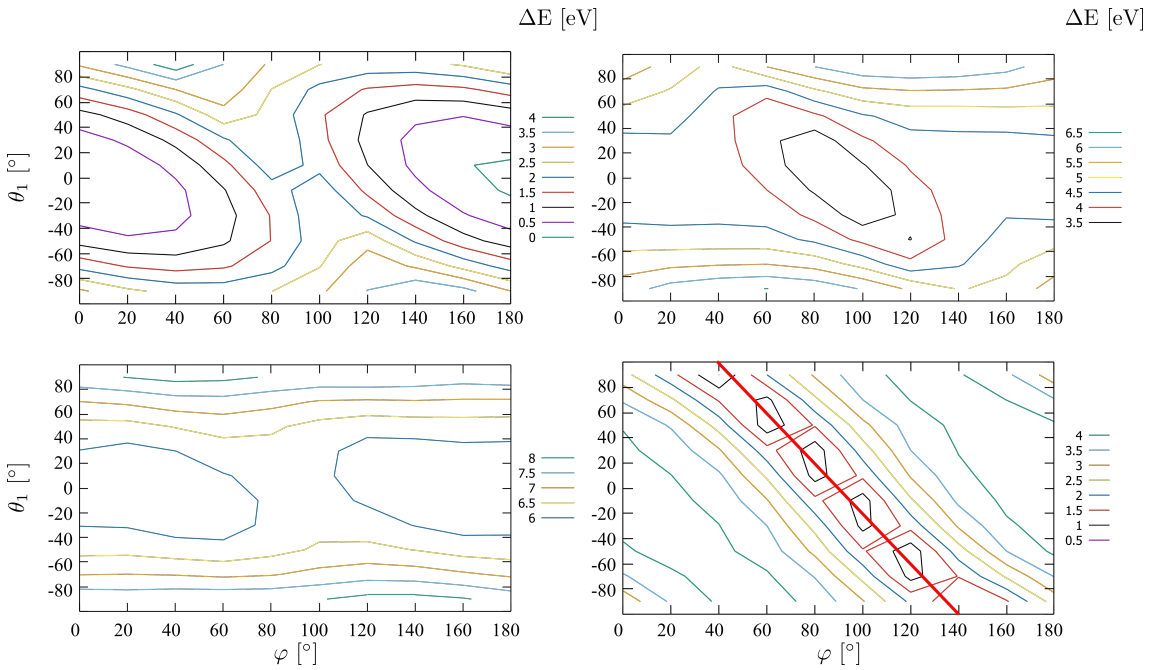

Figure 3.16: PES as function of the φ and θ_1 coordinates. Top, left: for the ground state. Top, right: first excited state. Bottom, left: second excited state. Bottom, right: Energy difference between the first excited state and the ground state. (The conical intersection is emphasized by the red line)

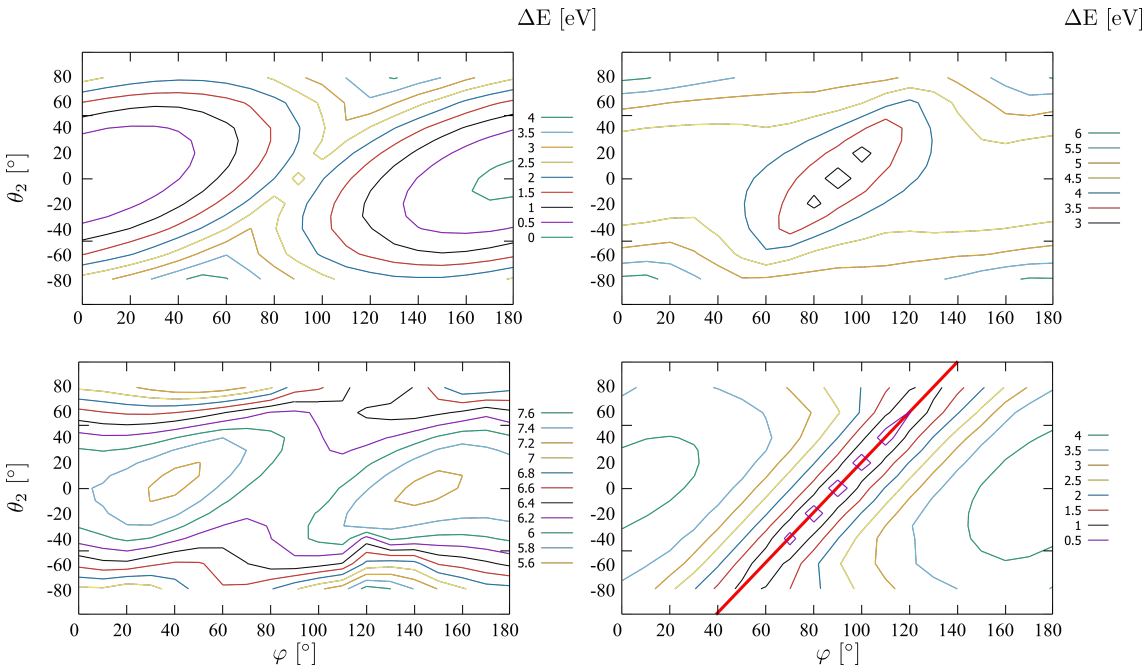

Figure 3.17: PES as function of the φ and θ_2 coordinates. Top, left: for the ground state. Top, right: first excited state. Bottom, left: second excited state. Bottom, right: Energy difference between the first excited state and the ground state. (The conical intersection is emphasized by the red line)

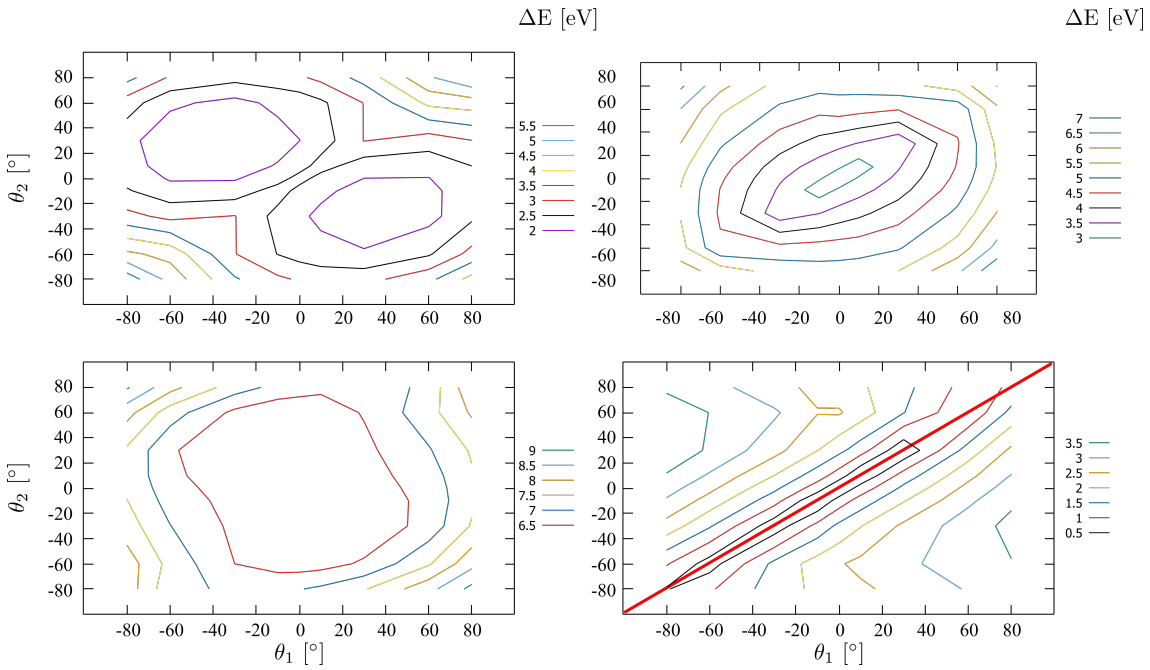

Figure 3.18: PES as function of the θ_1 and θ_2 coordinates ($\varphi = 90°$). Top, left: for the ground state. Top, right: first excited state. Bottom, left: second excited state. Bottom, right: Energy difference between the first excited state and the ground state. (The conical intersection is emphasized by the red line)

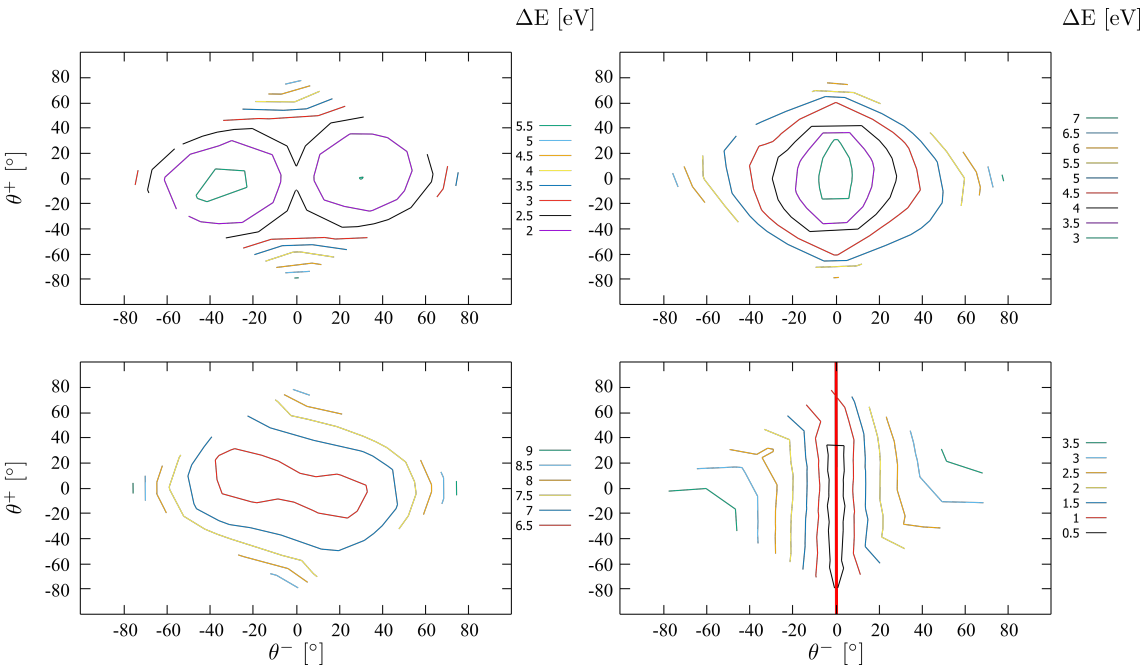

Figure 3.19: PES as function of linear combinations of the θ_1 and θ_2 coordinates, θ^- and θ^+ ($\varphi = 90°$). Top, left: for the ground state. Top, right: first excited state. Bottom, left: second excited state. Bottom, right: Energy difference between the first excited state and the ground state. (The conical intersection is emphasized by the red line)

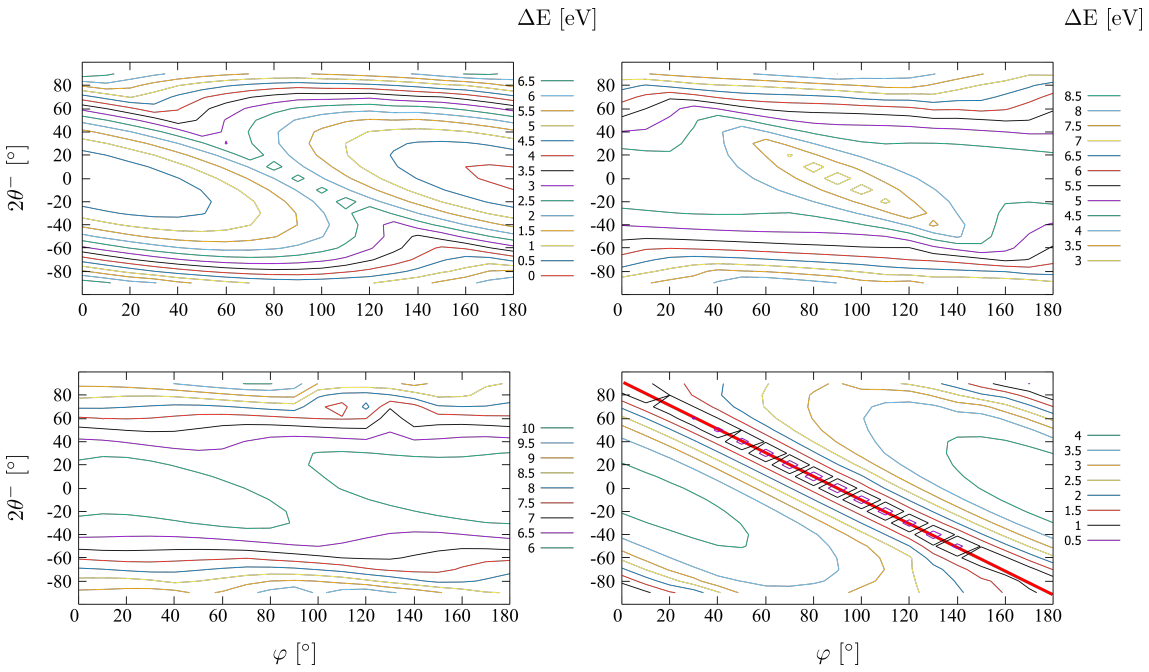

Figure 3.20: PES as function of the φ and θ^- coordinates ($\theta_1 = -\theta_2$ such as $\theta^+ = 0$). Top, left: for the ground state. Top, right: first excited state. Bottom, left: second excited state. Bottom, right: Energy difference between the first excited state and the ground state. (The conical intersection is emphasized by the red line)

3.6.3 The bond lengths

As discussed above, the bond length motion in PSB systems is often taken into account as a collective motion called BLA [131, 132]. In this study, the choice of taking into account each bond length separately has been made. Indeed the kinetic energy operator to be used in the QD of a sum of independent stretching is easier to write down than the one of a linear combination of five stretching motions. The drawback of such a choice, is that the potential energy hypersufface goes from one so called "BLA" dimension to five dimension. We will see in the following that there is another reason to consider the bond lengths separately.
Bond lengths can usually be modelled by Morse potentials. The potential energy curves of the first three electronic states have been computed along each bond length: r_1,r_2,r_3,r_4,r_5. For each bond length, the four other ones are considered at their point of equilibrium. This has been done for values of $\varphi = 0°, 90°, 180°$ (*cis*, a point of the seam of conical intersection, and *trans* respectively), see FIG. 3.21, 3.22 and 3.23. FIG. 3.22 especially shows the contribution of each bond length to the lifting of degeneracy at the minimum of conical intersection. Indeed, we can see that mainly r_5 and r_4 will lift the degeneracy. On the contrary, r_1, r_2 and r_3 will only contribute very lightly to the branching space (FIG. 3.6)

3.6.3.1 Conical intersection between $S1$ and $S2$.

An avoided crossing can be observed between $S1$ and $S2$ at approximately 1.8Åfor r_1 in the *cis* conformation, and 1.7Å in the *trans*. These values of r_1 are far from the Franck-Condon area, although a change in the other bond length, may lead to an avoided crossing, or even a conical intersection closer to the Frank-Condon region.
In fact, two points of conical intersection between $S1$ and $S2$ can be found close to the *cis* conformation, and to the *trans* conformation. Optimizing these points gives us the minimum of the conical intersection as well as the branching space at each point (FIG. 3.24). In both cases, the derivative coupling and the gradient difference vectors are in plane motions involving all $C-C$ and $C-N$ bonds. Only the C_6 carbon is involved in a small out-of-plane motion in the gradient difference vector. The fact that the combination of the bond elongation is different in the two vectors (TAB. 3.5) is a good reason for taking into account all bond lengths separately. Indeed, a unique BLA coordinate would be

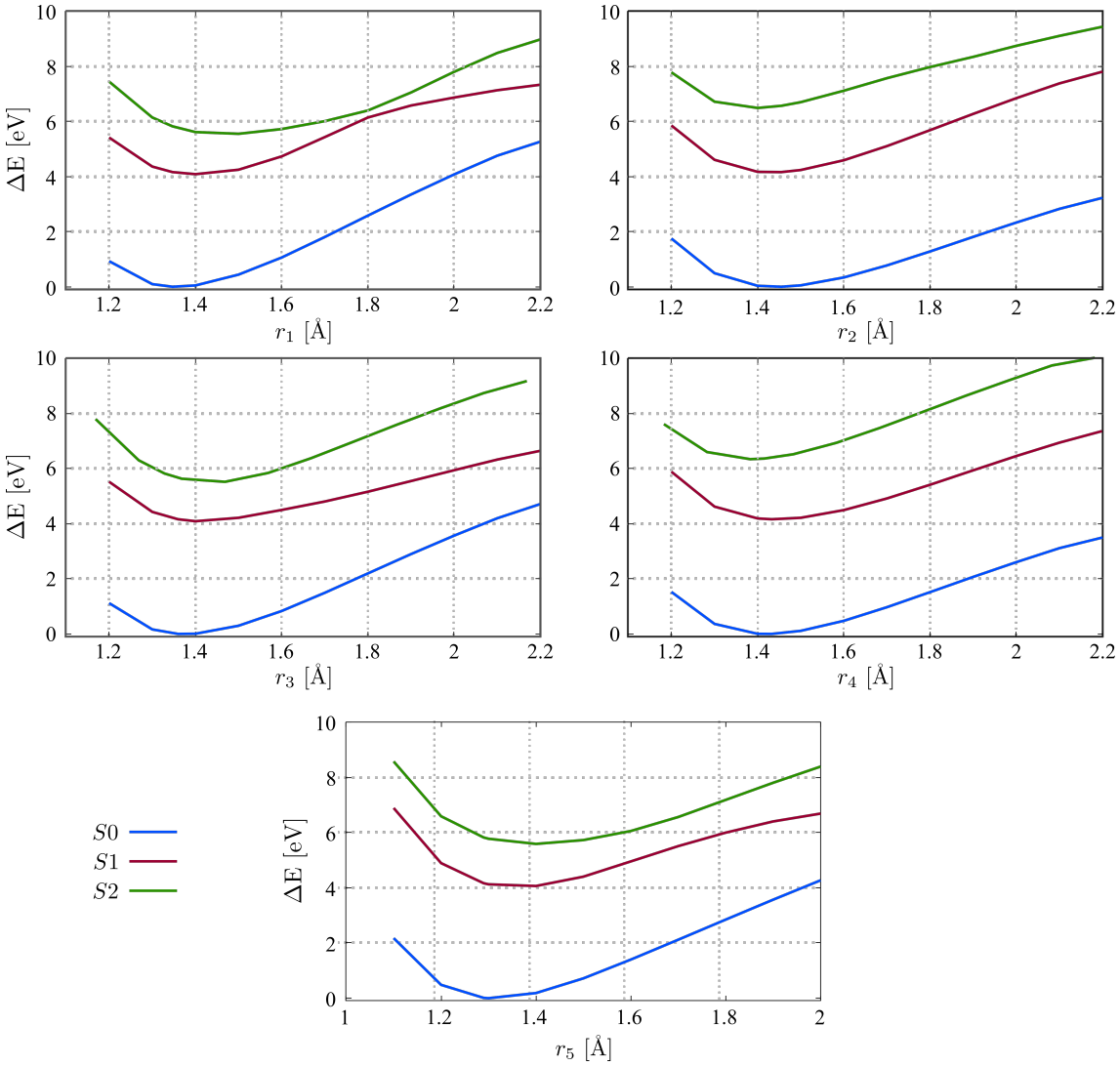

Figure 3.21: Potential energy curves associated to the *cis* geometry as function of bond lengths: r_1,r_2,r_3,r_4,r_5.

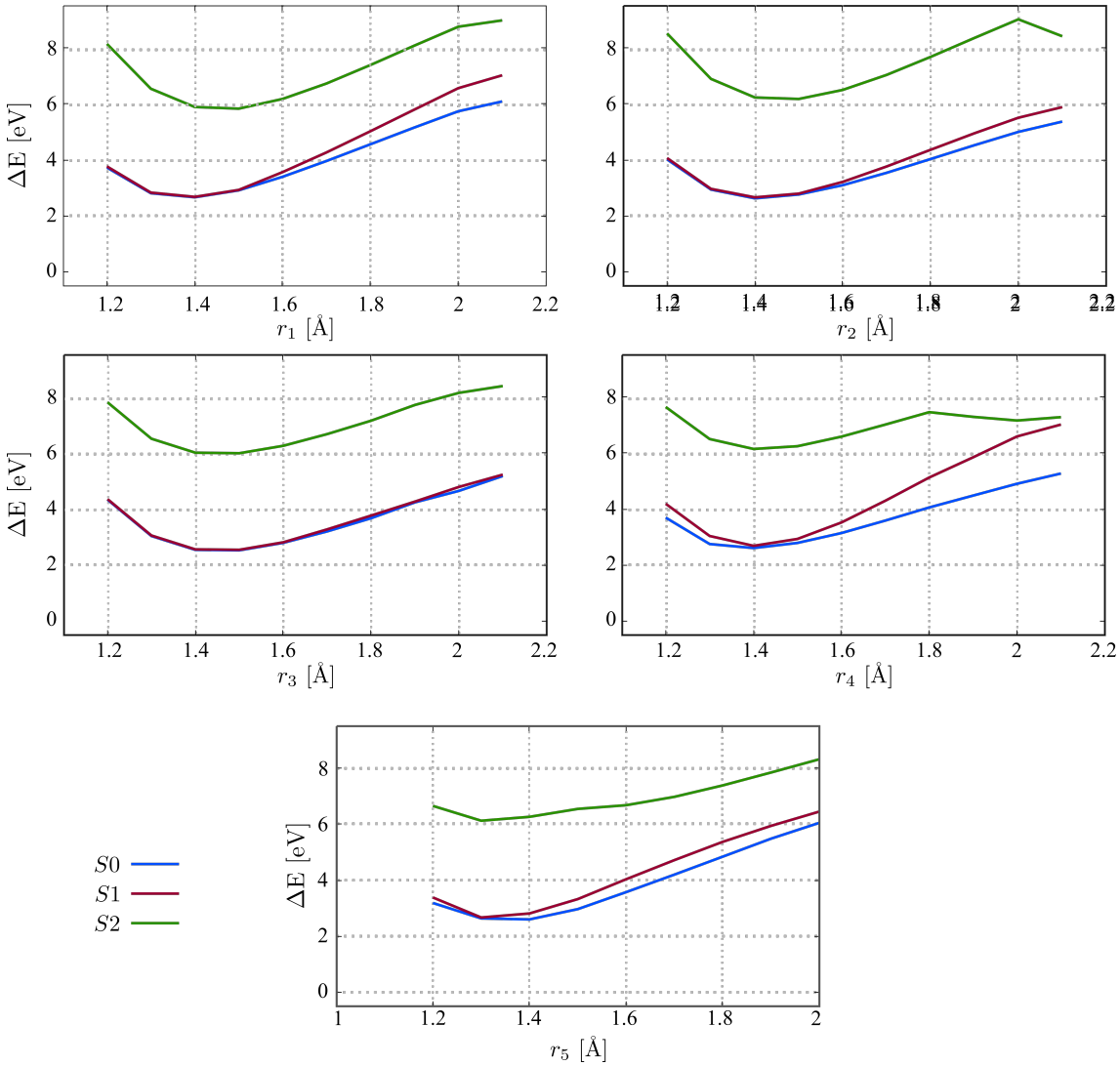

Figure 3.22: Potential energy curves at a point of the seam of CI ($\varphi = 90°$) as function of bond lengths: r_1,r_2,r_3,r_4,r_5. .

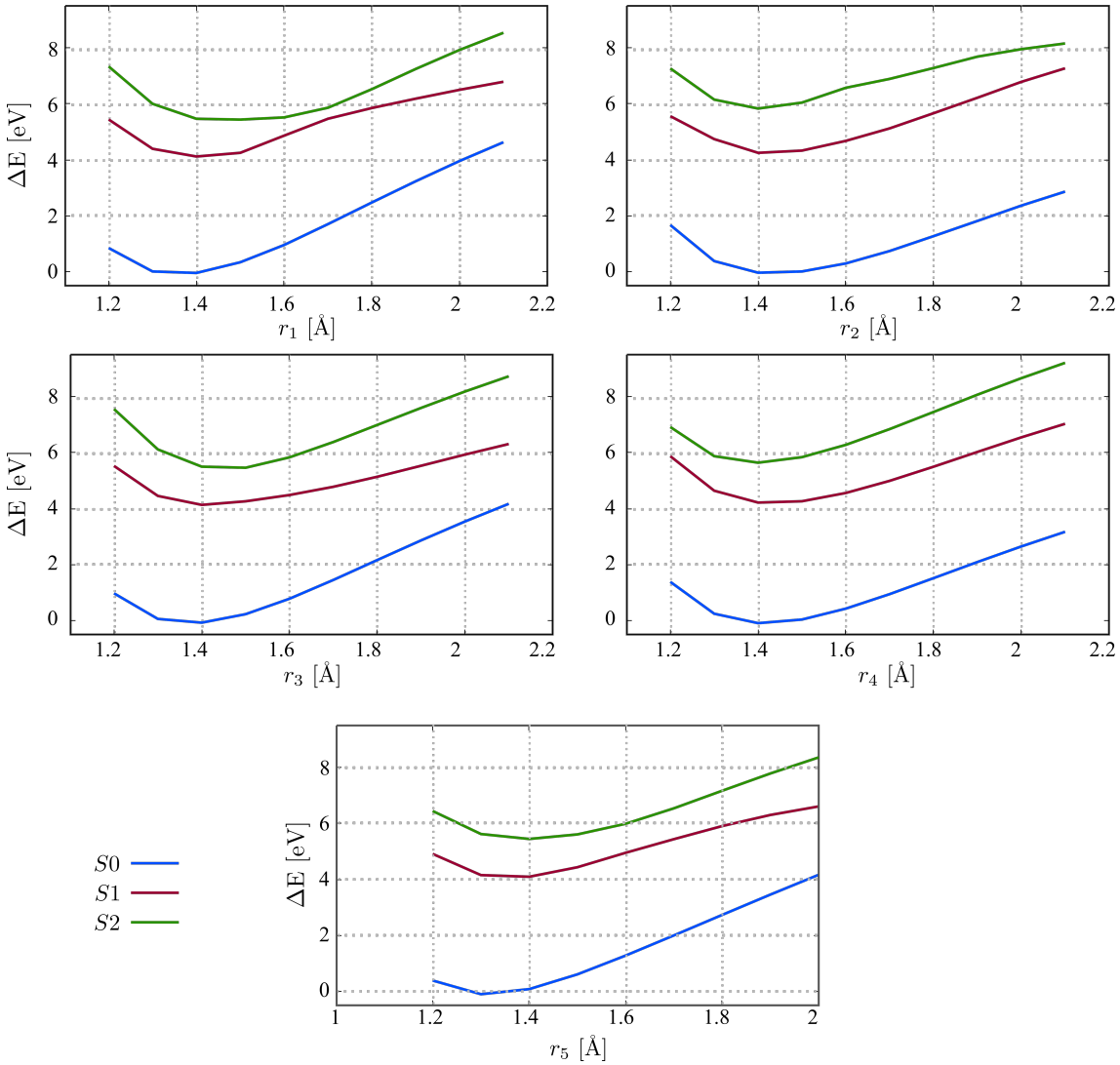

Figure 3.23: Potential energy curves associated to the *trans* geometry as function of bond lengths: r_1,r_2,r_3,r_4,r_5.

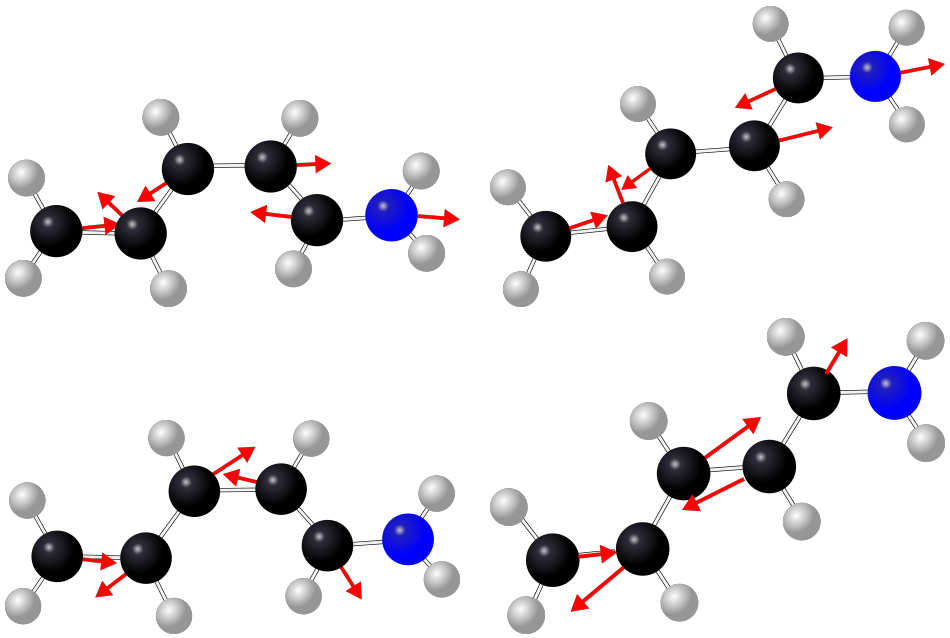

Figure 3.24: Branching space at the minimum of conical intersection between S1 and S2 at the SA-CASSCF level for both the *cis* (left) and *trans* (right) conformers. (Derivative coupling vectors are shown at the top and gradient difference vectors at the bottom)

Bond lengths motions

	r_1	r_2	r_3	r_4	r_5
Derivative coupling	$\ominus$	$\ominus$	$\oplus$	$\ominus$	$\oplus$
Gradient difference	$\ominus$	$\oplus$	$\ominus$	$\oplus$	$\ominus$

Table 3.5: Collective motions of the bond lengths r_1,r_2,r_3,r_4,r_5 for both vectors of the branching space ($\oplus$ symbolizes the elongation of a bond, $\ominus$ the shortening).

able to describe well enough only one dimension, therefore neglecting the others. These conical intersections being close in geometries to the *cis* and *trans* conformations, one has to correctly describe them.

3.6.3.2 Effect of the energy barrier along the torsion.

As seen in SECTION 3.5, the reorganization of the bond lengths is the first dynamical step of the photoisomerization [117, 139, 140, 141, 142]. As the π electronic densities are modified upon absorption, the bond lengths change and unlock the rotation around the central double bond. The barrier seen at c.a $40°$ along the torsion (FIG. 3.13) is due

to a coupling with the second excited state in energy. By looking at the orbital involved in the $III \rightarrow V$ excitation (see TAB. 3.1), we can see that the orbital V is composed of a π bonding interaction in the $C_3 - C_4$ bond, and π anti-bonding interaction in all the others. Thus, this contribution tends to prevent the torsion around $C_3 - C_4$ but promotes the rotations around $C_2 - C_3$ and $C_4 - C_5$.
In order to remove the barrier, i.e. remove the stabilization of the planar geometries, a stretch of the $C_3 - C_4$ and a squeeze the $C_2 - C_3$ and $C_4 - C_5$ bonds may occur. This way, the bonding interaction on the $C_3 - C_4$ and the anti-bonding interactions on $C_5 - C_4$ and $C_2 - C_3$ induced by orbital V decrease, whereas the bonding interaction in $C_5 - C_4$ and $C_2 - C_3$ and the anti-bonding interaction in $C_3 - C_4$ from orbital IV increase. The second excited state is then destabilized in energy and the coupling with the first excited state decreases, as well as the energy barrier near planar geometries.
As seen earlier, each r_1, r_2, r_3, r_4 and r_5 dimension is part of the branching space. A change in the bond lengths modifies not only the barrier near Franck-Condon, but also the gaps in energy between the electronic ground state and the first two excited states.
The promotion of the rotations around $C_2 - C_3$ and $C_4 - C_5$, which we call γ_1 and γ_2 could be problematic as we do not take into account those motions in our system of coordinates. Indeed, we choose to consider both halves of the PSB3 as planar except for H_1 and H_2. To build a more complete PES, these two angles should be included as well. Their impact seem however less important than the other selected degrees of freedom[4]. Minimum energy paths computed by Olivucci *et al.* at the CASPT2 level show torsion around $C_2 - C_3$ between the Franck-Condon region and the seam of conical intersection. However, as the branching space (see FIG. 3.6) does not include motions of carbon atoms C_1 and N we assume that γ_1 and γ_2 will have no effect on the degeneracy at the conical intersection.

3.7 Building of the PES

Once all active coordinates have been selected, the 8 dimension (8D) PES can be build for each of the electronic states. To achieve this, we define a grid to explore the 8D nuclear geometry space. The coordinates outside of this space, i.e. the inactive coordinates, are fixed at their value for the equilibrium geometry of the *cis* conformer. As the number of points that need to be computed grows very fast, we restricted the grid to eleven points

Coordinate	Points	Values
φ	11	$0, 20, 40, \cdots, 160, 180$
θ_1, θ_2	5	$-90, -45, 0, 45, 90$
r_1, r_2, r_3, r_4	3	$1.30, 1.45, 1.60$
r_5	3	$1.20, 1.29, 1.40$
Total:	66825	

Table 3.6: Points along each dimensions of the 8-dimensions grid.

for the central torsion φ, five points for each hydrogen angle θ_1 and θ_2 and three points for each bond length. The details are reported in TAB. 3.6.

This grid definition of the electronic PESs may not be the most efficient one, as it will generate a lot of nuclear geometries that are very high in energy and will describe regions of the PESs that will not be explored by the dynamics. To ensure the stability of the active space, as well as the fast convergence of the *ab initio* calculations we cannot compute the energy of each geometry independently. Doing so may result in discontinuities in the PES as one point may have the good active space, i.e. the π electronic systems, and the neighbour may have undergone an orbital rotation in its active space, and contain for example σ orbitals. This is why we chose to use the set of orbitals of the *cis* conformer as starting guess for each SA-CASSCF//MS-CASPT2 calculations. However, if the geometry between a given point and the *cis* conformer is too different, such method will not help as the initial guess orbitals are too far from the converged ones. To work around this issue, we used these initial guess orbitals only to compute points close in geometry to the *cis* isomer. These orbitals are then used to compute neighbour geometries on the grid, and so on until the grid is totally computed. This scheme is represented FIG. 3.25.

This way of computing the grid ensures that most of the *ab initio* points are computed with the good active space while still keeping a massively parallel process.

The submission and the analysis of the grid points were automatized using home-made bash and FORTRAN scripts.

3.8 Fit of the Adiabatic PES.

In order to perform a quantum dynamics study of PSB3, it is mandatory to transform the adiabatic PES for which the non-adiabatic coupling diverge at the conical intersection,

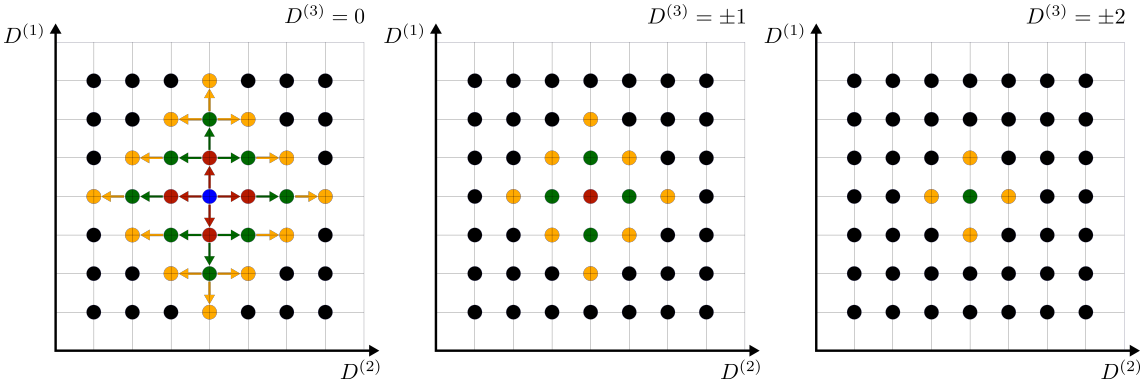

Figure 3.25: Representation of the method of computation of the total grid of geometries for a 3D-space ($D^{(1)}$, $D^{(2)}$ and $D^{(3)}$). The point in blue represents the geometry of the *cis* conformer. The points in red correspond to the geometries computed in the second step, those in green computed in the third step and those in orange computed in the fourth step.

see SECTION 1.3, into diabatic PES. This has been done using the NL-FIT software developed in Montpellier (group of F. Gatti) and based on diabatization by "ansatz" scheme (described in SECTION 1.4.2). The fitting procedure of the adiabatic electronic PES is one of the most tedious step. As mentioned in SECTION 1.4.2, it is crucial to have an initial guess for the diabatic PESs that contains physical meaning.
In this section, we will focus on the fit of the two dimensions PES along φ and θ^{-}.

3.8.1 Mathematical conditions and analytical guess functions.

We would like to build the diabatic potential matrix

$$\boldsymbol{W} = \begin{pmatrix} W_{11} & W_{12} & W_{13} \\ W_{21} & W_{22} & W_{23} \\ W_{31} & W_{32} & W_{33} \end{pmatrix} \tag{3.4}$$

where $W_{ij} = W_{ji}$ as we will consider only real coupling elements.

3.8.1.1 Analysis along φ

As a first crude approximation for the diagonal elements, i.e. the diabatic states, we can consider sinusoidal functions. As the periodicity of the φ torsion is 2π we can estimate the

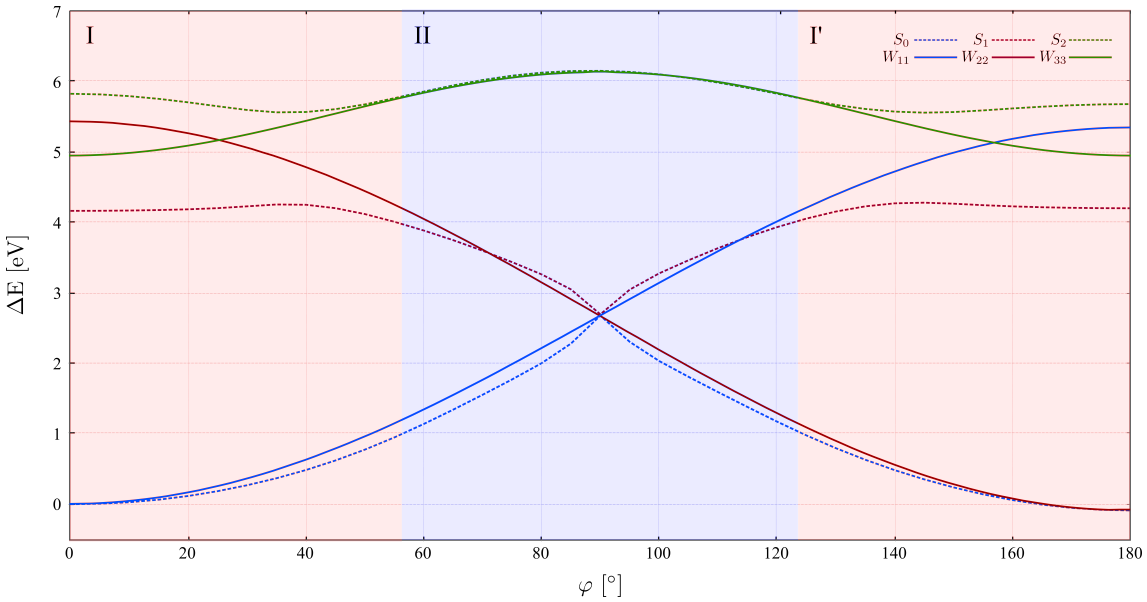

Figure 3.26: The initial guess of diabatic states along φ (full lines); adiabatic electronic states (dash lines) at the MS-CASPT2 level.

amplitude of the sine function from the energy difference between the points at $\varphi = 0°$, $\varphi = 180°$ and the point of conical intersection at $\varphi = 90°$. The assumption that W_{11} and W_{22} coincide with $S0$ at $\varphi = 0°$ and $\varphi = 180°$ respectively is supported by the fact that $S0$ is (1) very far in energy from the other states, and (2) consists of only one electronic configuration (see SECTION 3.3). The nonadiabatic coupling at these geometries can thus be considered as null. These initial guesses are shown FIG. 3.26. They are supported by previous studies of the non-adiabatic coupling of the retinal chromophore [143].

Looking at the electronic states, both diabatic and adiabatic, along φ only, we can define two regions. One that includes I and I', in red in FIG. 3.26, around the planar geometries, i.e. $\varphi = 0°$ and $\varphi = 180°$. And the other one around the conical intersection, in blue in FIG. 3.26.

Near the planar conformations, we have seen that the adiabatic electronic states $S1$ and $S2$ were close-lying to each other. We have also noticed that there was a small coupling between those two states. In the diabatic picture, the W_{22} (in red) and W_{33} (in green) states cross in the region I. Thus in order to retrieve the adiabatic states, the coupling element W_{23} has to be large. Moreover, as stated earlier, the diabatic state W_{11} is energetically well separated from the other ones. Hence we can estimate the coupling elements W_{12} and W_{13} to be very small. We can rewrite the diabatic potential matrix in the region I as:

$$\boldsymbol{W}^{\mathrm{I}} = \begin{pmatrix} W_{11} & \approx 0 & \approx 0 \\ \approx 0 & W_{22} & W_{23} \\ \approx 0 & W_{32} & W_{33} \end{pmatrix} \tag{3.5}$$

in the region I' however, it is the diabatic state W_{11} that crosses W_{33}. The same observations as in region I can be made. Thus the diabatic potential matrix in I' can be written as:

$$\boldsymbol{W}^{\mathrm{I}'} = \begin{pmatrix} W_{11} & \approx 0 & W_{13} \\ \approx 0 & W_{22} & \approx 0 \\ W_{31} & \approx 0 & W_{33} \end{pmatrix}. \tag{3.6}$$

A feature we want to reproduce is the difference of energy between the *cis* and the *trans* conformers. Using sine functions this difference in energy is naturally described using two sine functions of different amplitudes.

Our choice of diabatic states is upheld by two factors: (1) S2 is higher in energy in the *cis* conformer than in the *trans*. And (2) the III→V contribution resulting from the mixing between S2 and S1 is larger (7%) in the cis conformer than in the trans (3%).

In the region II, i.e. around the conical intersection, the two lowest diabatic electronic states must be degenerate ($W_{11} = W_{22}$) and the coupling between them has to be null ($W_{12} = 0$) at $\varphi = 90°$. However the coupling elements with the electronic diabatic state W_{33} can be non-zero as long as both coupling are the same, i.e. $W_{13} = W_{23}$. If this is not the case, the conical intersection will be shifted from $\varphi = 90°$. Thus at the point of CI ($\varphi = 90°$), the diabatic potential matrix reads

$$\boldsymbol{W}^{\mathrm{II}}(\varphi = 90°) = \begin{pmatrix} W_{11} & 0 & W_{13} \\ 0 & W_{22} & W_{23} \\ W_{31} & W_{32} & W_{33} \end{pmatrix}. \tag{3.7}$$

From all conditions on the diabatic states and nonadiabatic coupling in each region, we can build the initial guess functions. For convenience in the fitting procedure, we introduce a new coordinate φ' such as the minimum of conical intersection is at $\varphi' = 0$, i.e. $\varphi' = \varphi - 90°$.

The diabatic states can thus be described with simple sine functions

$$\begin{aligned} W_{11}(\varphi') &= \alpha \sin(\varphi') \\ W_{22}(\varphi') &= -\alpha' \sin(\varphi') \\ W_{33}(\varphi') &= \gamma \sin(2\varphi' + 90) + \epsilon \end{aligned} \tag{3.8}$$

where β is the energy of the conical intersection at $\varphi' = 0$ ($\varphi = 90°$) and ϵ is the vertical energy of S2 at $\varphi' = 0$.
The initial guess for the coupling is a bit more complicated, as the functions must decrease rapidly in order to be zero at certain points. The initial guess of the coupling elements are

$$\begin{aligned} W_{12}(\varphi') &= a \sin^2(\varphi') + b \sin^4(\varphi') \\ W_{13}(\varphi') &= c \sin^4(1/2\varphi' + d) \\ W_{23}(\varphi') &= c' \sin^4(1/2\varphi' + d') \end{aligned} \tag{3.9}$$

.

The coupling elements W_{13} and W_{23} must have a frequency two times slower than the coupling element W_{12} because the diabatic states W_{11} and W_{22} exchange at the CI, see FIG. 3.26.

3.8.1.2 Inclusion of the θ^- coordinate

As a first approximation, we consider the potential energy due to the distortion of the hydrogens H_1 and H_2 along θ^- to be an harmonic potential. This assumption can be justified as the rotation energy barrier of the hydrogen atoms around the central double bond is very high, thus preventing the rotation. We can then consider a harmonic potential instead of a periodic function.
The addition of the θ^- coordinate also modulates the position of the seam of intersection. We have seen in SECTION 3.6.2 that the intersection is present all along the line of equation $\varphi + 2\theta^- = 90°$. It imposes W_{11} and W_{22} to be degenerate and W_{12} to be null all along this line. Moreover we postulate the maximum of S2 to be aligned at all time with the seam of conical intersection.
To satisfy these conditions, we modify the initial diabatic guess by including θ^- such as:

$$
\begin{aligned}
W_{11}(\varphi', \theta^-) &= \alpha \sin(\varphi' + 1/2\theta^-) + \beta\theta^{-2} \\
W_{22}(\varphi', \theta^-) &= -\alpha' \sin(\varphi' + 1/2\theta^-) + \beta'\theta^{-2} \\
W_{33}(\varphi', \theta^-) &= \gamma \sin(2\varphi' + 1/2\theta^- + 90) + \zeta\theta^{-2} + \epsilon
\end{aligned}
\tag{3.10}
$$

and

$$
\begin{aligned}
W_{12}(\varphi') &= a \sin^2(\varphi' + 1/2\theta^-) + b \sin^4(\varphi' + 1/2\theta^-) \\
W_{13}(\varphi') &= c \sin^4(1/2\varphi' + 1/2\theta^- + d) \\
W_{23}(\varphi') &= c' \sin^4(1/2\varphi' + 1/2\theta^- + d')
\end{aligned}
\tag{3.11}
$$

.

3.8.2 The fitted surface along φ' and θ^-

The results of the fitting procedure of the initial guess functions (3.10) and 3.11 are shown in FIG. 3.27 (note that the new coordinate φ' is used for the representation) and the optimized parameters are gathered in TAB. 3.7. We will now focus on the analysis of the first excited-surface $S1$ which will determine the major part of the dynamics. We can see that the relative height of the energy barrier between FC and the CI with respect to the planar geometries are rather well described. Looking at the second excited-state PES, one can see that the coupling W_{13} at $\varphi' = -90°$ and W_{23} at $\varphi' = 90°$ is not strong enough to induce the formation of a local maximum at this geometry as we would expect.
Another key aspect to analyze is the shape of the path from FC in $S1$ to the CI. This path is reproduced pretty well by the fitted functions, indeed, the MEP on this reduced dimensionality PES involves a motion of the hydrogen atoms to reach the intersection seam. Moreover the accessible region of the CI is found to be around $\varphi' = -30°$ ($\varphi = 60°$) as expected. These aspects will be better described by refining the coupling functions W_{13} and W_{23}. However, two problems occur: (1) the region around the conical intersection is very poorly described because the adiabatic PES are not steep enough in its vicinity, and (2) the amplitude of the sine functions of the diabatic states W_{11} and W_{22} are too low, thus lacking of physical meaning, i.e. we do not recover the fact that W_{11} should coincide with $S1$ at $\varphi' = -90°$ and W_{22} with $S2$ at $\varphi' = 90°$. These problems are due to the bad guess functions describing the coupling W_{12}, indeed, this coupling is not equal to zero at both $\varphi' = -90°$ and $\varphi' = 90°$, and also does not vary fast enough around the point of

Diabatic states		Potential coupling	
Parameter	Opt. value	Parameter	Opt. value
α	1.363	a	4.743
α'	-1.30	b	-3.608
β	22.735	c	-1.912
β'	23.476	c$'$	-1.827
γ	0.721	d	-45
ϵ	2.499	d$'$	45
ζ	14.390		

Table 3.7: The optimized parameters of EQ. (3.10) and 3.11.

conical intersection. This fit of the adiabatic PES and the initial diabatic guess functions are not satisfying. Nevertheless, the fitted adiabatic PES exhibit the required key features, thus confirming the general form of the initial guess functions. The next step will be to refine the guess functions, especially the coupling W_{12} between W_{11} and W_{22}. Moreover, the coupling terms with the third excited state W_{33} need to be further investigated.

3.9 Conclusion and outlook

The construction of a diabatic PES is a tedious task. It is thus of the utmost importance to conduct carefully preliminary quantum chemical investigations. The important nuclear displacements involved in the photisomerization process have been extracted by means of semi-classical dynamics. In addition to the obvious coordinate φ that defines the torsion around the isomerizing bond, it is needed to consider the out of plane motions of the hydrogen atoms of the central double bond. Indeed, they have two major effects on the process: (1) they govern the outcome of the photoisomerization and (2) they modulate the seam of intersection and allow the seam to be reached before the minimal energy point. The bond lengths of the backbone of PSB3 also play a key role in the process. Indeed, they are part of the branching space, with the HOOP and φ motions, and by such will lift the degeneracy at the point of conical intersection. The bond rearrangement is the first ultrafast nuclear displacement to occur upon absorption of a photon. The π electronic density is modified and the alternation of single and double bond change too, unlocking the rotation around the weakened central bond.

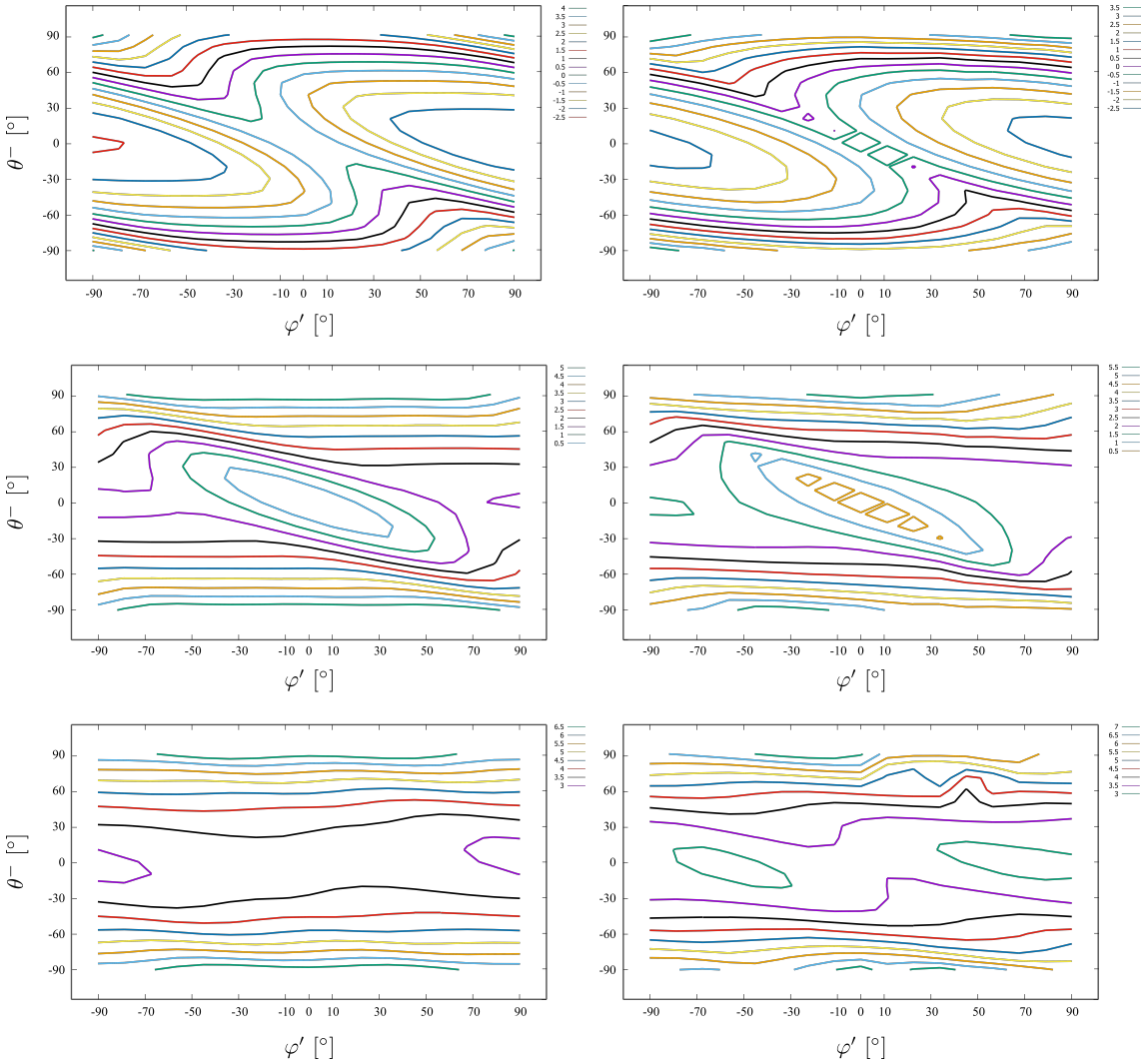

Figure 3.27: Left: fitted adiabatic PES, from top to bottom: $S0$, $S1$, $S2$. Right: computed adiabatic PES, from top to bottom: $S0$, $S1$, $S2$.

A more careful investigation of the effect of the chosen coordinates along low dimensional cut of the eight dimension PES allowed us to determine geometrical condition that proved to be useful for the construction of the guess diabatic functions. Indeed, we have found that the seam of conical intersection follows a line of equation $\varphi + 2\theta^{-} = 90°$. This condition is even more useful as it has a physical meaning that can be explained with simple orbital argument. Indeed, all along this line, the p orbitals of the carbon atoms of the central double bond $C_3 - C_4$ are orthogonal.

We have also been able to qualitatively explain the origin of the stabilisation of the planar structure in S1 resulting in energy barriers between FC and the seam of intersection. Indeed, this stabilisation is due to a strong coupling with the higher electronic excited-state S2. This coupling manifests itself by a small contribution of an electronic configuration present both in S2 and S1. By simply looking at the orbitals involved in this transition, we have proposed a way to overcome this barrier. Such consideration is crucial to estimate the behaviour of the diabatic potential coupling in the building of the diabatic PES.

Many clues, such as the difficulty to express the kinetic energy operator of a linear combination of bond lengths or their various effects on the photoisomerization process, lead us to use independent coordinates to model the bond rearrangement instead of the BLA coordinate that is often used. Moreover, the strong coupling between S1 and S2 in the vicinity of planar structures makes it mandatory to consider three electronic states instead of two, even if the absorbing state is S1.

Gathering all these informations, we have proposed an initial guess of diabatic functions that contains the physical meaning we had previously investigated. For now, only the out of plane motions φ and θ^{-} have been considered. Further development of the diabatic guess functions have to be done in order to obtain a satisfying PES surface. However, we have seen that with simple functions, we were able to reproduce key features of the photoisomerization process.

In the future, we will have to include explicitly the dependence on θ_1 and θ_2 (instead of a collective motion θ^{-}) as well as the bond length contribution to the PES. In the meantime, the determination of the kinetic energy operator will have to be done using polyspherical coordinates [144].

Once both the potential and kinetic energy operators have been determined, it will be possible to propagate quantum wavepackets on the eight dimension fitted diabatic PES which will hopefully give us new insights about the mechanism of the photoisomerization process in the PSB3 and in the rhodopsin protein.

CHAPTER 4

DIRECTIONALITY OF DOUBLE-BOND PHOTOISOMERIZATION DYNAMICS INDUCED BY A SINGLE STEREOGENIC CENTER

As mentioned before, the photoisomerization of the retinal in the Rhodopsin is the paradigm of the isomerizations processes. Its high quantum yield make it natural to design photoswitches based on a model of the retinal, especially PSBs. Indanylidene-pyrrolinium (IP) derivatives are synthesized to aim at reproducing the efficiency of the thodopsin. Its chemical structure is based on a pentanylidene-pyrrolinium (CPP) molecular basis that is similar to the PSB3 model. Indeed, it is also constituted of a sp^2 system containing five carbon and one nitrogen atoms. The difference is that the central double bond carbon atoms do no longer carry hydrogen atoms, but instead carry sp^3 carbons that form a five-atom rings. However, a fast and efficient photoisomerization is not enough to provide the basis of a powerful molecular motor. Indeed to efficiently convert light energy into mechanical work, it is mandatory that the rotary motion undergone by the motor is unidirectional.

In this chapter, we focus on the study of minimal CPP photoswitches that are made chiral by addition of a methyl on one of the sp^3 carbon atom of the five-atoms ring. The aim of this work is to explain the origin of the unidirectionality of the chiral photoswitch isomerization by means of semi-classical trajectories and CASSCF electronic structure calculations.

THE JOURNAL OF PHYSICAL CHEMISTRY Letters

Letter

pubs.acs.org/JPCL

Directionality of Double-Bond Photoisomerization Dynamics Induced by a Single Stereogenic Center

Gabriel Marchand,[†,‡,⊗] Julien Eng,[‡] Igor Schapiro,[†] Alessio Valentini,[§,⊥] Luis Manuel Frutos,[⊥] Elisa Pieri,[§] Massimo Olivucci,*[,§,∥] Jérémie Léonard,*[,†] and Etienne Gindensperger*[,‡]

[†]Institut de Physique et Chimie des Matériaux de Strasbourg & Labex NIE, Université de Strasbourg, CNRS UMR 7504, 23 rue du Loess, Strasbourg 67034, France

[‡]Institut de Chimie, Université de Strasbourg, CNRS UMR 7177, 1 rue Blaise Pascal, Strasbourg 67008, France

[§]Department of Biotechnology, Chemistry and Pharmacy, University of Siena, via Aldo Moro, 2, Siena 53100, Italy

[∥]Chemistry Department, Bowling Green State University, 141 Overman Hall, Bowling Green, Ohio 43403, United States

[⊥]Unidad Docente de Química Física, Universidad de Alcalá, E-28871 Alcalá de Henares, Madrid, Spain

Supporting Information

ABSTRACT: In light-driven single-molecule rotary motors, the photoisomerization of a double bond converts light energy into the rotation of a moiety (the rotor) with respect to another (the stator). However, at the level of a molecular population, an effective rotary motion can only be achieved if a large majority of the rotors rotate in the same, specific direction. Here we present a quantitative investigation of the directionality (clockwise vs counterclockwise) induced by a single stereogenic center placed in allylic position with respect to the reactive double bond of a model of the biomimetic indanylidene-pyrrolinium framework. By computing ensembles of nonadiabatic trajectories at 300 K, we predict that the photoisomerization is >70% unidirectional for the Z → E and E → Z conversions. Most importantly, we show that such directionality, resulting from the asymmetry of the excited state force field, can still be observed in the presence of a small (ca. 2°) pretwist or helicity of the reactive double bond. This questions the validity of the conjecture that a significant double-bond pretwist (e.g., >10°) in the ground state equilibrium structure of synthetic or natural rotary motors would be required for unidirectional motion.

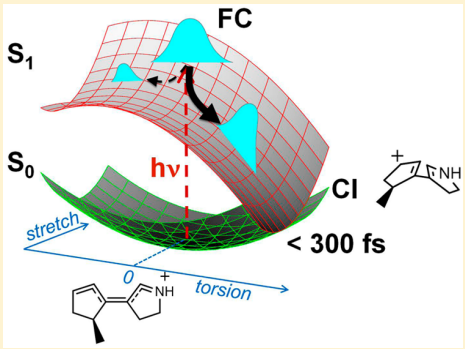

The "physical" ingredients of a (molecular) motor are (i) a source of energy, (ii) a periodic potential energy, and (iii) a structural asymmetry, as was pointed out in very simple words by Feynman.[1] At the single-molecule level, the photoisomerization of a double bond provides the first two ingredients: the light energy is converted into rotary motion around the bond axis and the potential energy changes periodically along the coordinate describing the rotation. The third ingredient is provided by a chiral "environment", which has the function of breaking the local symmetry and, ultimately, prompting a unidirectional (clockwise or counterclockwise) rotary motion.

Synthetic indanylidene-pyrrolinium (IP) molecular frameworks, originally prepared[2] to mimic the outstanding photoisomerization properties of the visual pigment rhodopsin (Rh),[3−5] could potentially yield a novel class of molecular motors. In Rh and related microbial rhodopsins a retinal protonated Schiff base embedded in the chiral environment provided by the protein cavity, undergoes a regiospecific, subpicosecond, and unidirectional double-bond photoisomerization with high quantum yield. IP compounds have been shown, experimentally and computationally,[6−9] to be able to reproduce the dynamical properties of Rh, also including the vibrational coherence observed in the photoisomerization primary photoproduct.[4] Besides, the IP framework (see Chart 1, left) should be made chiral to mimic the effect of the protein cavity to replicate the directionality of the Rh photoisomerization.[10] Under these conditions, IP compounds would provide a

Chart 1. Z Isomers of the IP Framework, Chiral (1) and Achiral (2) Model Compounds

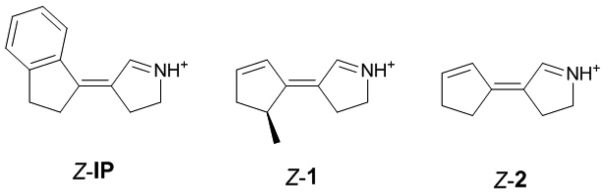

Received: December 15, 2014
Accepted: January 23, 2015
Published: January 23, 2015

DOI: 10.1021/jz502644h
J. Phys. Chem. Lett. 2015, 6, 599−604

basis for the development of biomimetic single-molecule rotary motors.

A chiral IP framework can be obtained by insertion of one or more stereogenic centers. Indeed, unlike retinal and related model systems,[5,11−14] the cyclic structure of IP contains sp^3 carbons that can be made stereogenic. Synthetic single-molecule rotary motors featuring one or two stereogenic centers have been experimentally demonstrated using diarylethene frameworks.[15] These frameworks feature one overcrowded C═C bond displaying a substantial (ca. 10−20°) pretwist reflecting the helicity of the surrounding environment.[16−18] Furthermore, a computationally designed protonated Schiff base system with two stereogenic centers and featuring a ca. 8° pretwisted C═C bond imposed via hydrogen bonding was found to display strong unidirectional motion.[19] These systems feature pretwisting values not far from the ca. 5−10° reported for the reactive C═C bond of Rh. In the later case and in other retinal proteins, the pretwist of the reactive double bond of the ground-state chromophore is held responsible for the enhanced photoreaction speed and yield of PSBR[20−22] and also for the full directionality of the isomerization.[10,12,23−26] This leads to the conjecture that significant ground-state C═C bond pretwisting is required for an effective photoisomerization directionality (i.e., this would implicitly inform on the degree of asymmetry of the excited state force field). It is presently not clear what would be the minimal requirements for such a unidirectional rotary motion. In other words, with the idea of uncovering rules for the design of effective single-molecule rotary motors, it appears to be important to find out how much the ground-state planar symmetry of a C═C bond should be perturbed to achieve a unidirectional photoisomerization. The present report addresses some of the aspects of this basic question in the context of the design of IP-based motors.

Here we focus on the pentenylidene-pyrrolinium compounds **1** and **2** (see Chart 1) as minimal models of IPs.[27] While **2** is planar and therefore achiral, **1** is made chiral by inserting a methyl group in an allylic position with respect to the exocyclic (central) double bond. This allows us to investigate: (a) whether the inserted single stereogenic center would be sufficient to induce a unidirectional photoisomerization of the exocyclic bond and (b) what is the exact mechanism prompting the unidirectional twisting and in particular the putative role of a C═C bond pretwist. We compute statistical ensembles of gas-phase, ab initio nonadiabatic molecular trajectories to show that the stereogenic center of **1**, imposing very limited symmetry breaking (i.e., a pretwist of ca. 2°), is enough to generate a significant unidirectional motion in a room-temperature molecular population. We show that the mere geometrical distortions of the untwisted C═C bond of **2** or the inertial motion of the methyl substituent of the stereogenic center of **1** are not contributing to the directionality significantly.

All computations are performed using the ab initio CASSCF method[28] and the 6-31G* basis set with six electrons in six π-type orbitals. (See the SI for details.) Ab initio nonadiabatic trajectories (see, e.g., refs 5,13,14,19,29,30) are computed here using the recent implementation[19] in Molcas 7.8[31] of Tully's surface hopping algorithm[32] with quantum decoherence correction.[33] The computed singlet ground-state (S_0) equilibrium structures of **1** and **2** are found to be very similar irrespective of the isomer (Z or E) actually compared. (See Figure 1 and Table S1 in the SI.) The main differences are

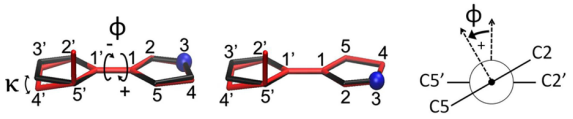

Figure 1. Superimposed structures of the chiral **1** (red) and achiral **2** (black) Z (left) and E (right) ground-state equilibrium geometries. An unconventional numbering is used for facilitating the discussion. Hydrogen atoms are not shown; nitrogen atoms are represented with a blue sphere. Carbons 4, 4′, 5, and 5′ have sp^3 hybridization. The counterclockwise (+) direction of rotation implies an increase in the value of the twisting angle ϕ defined in the Newman projection. The largest out-of-plane deformation in **1** is along the dihedral angle κ.

found in the out-of-plane deformation of the pentenylidene ring, best characterized by the dihedral angle κ = C1−C1′−C5′−C4′. For compounds *Z*-**1** and *E*-**1**, κ = −15.7 and −13.9° respectively, while κ = 0° for the planar compound **2**. To characterize the twisting of the central double bond, we introduce the internal coordinate ϕ = (C2′−C1′−C1−C2 + C5′−C1′−C1−C5)/2, which approximately measures the alignment of the two p-orbital axes of the C1′ and C1 sp^2 centers defining the reactive π bond. While ϕ = 0° (180°) for both isomers of the planar achiral compound **2**, we note that in the chiral compound **1** the double bond is twisted by as little as +1.3° (ϕ = +1.3°) and +2.2° (ϕ = +182.2°) for the Z and E isomers, respectively. Here the (+) sign in the twist angle refers to the counterclockwise direction of rotation of the pyrrolinium moiety ("rotor") with respect to the fixed cyclopentenylidene ring ("stator"), as illustrated in the Newman projection of Figure 1 and in the movie in the SI. Because **1** and **2** have nearly untwisted C1═C1′ double bonds, one should expect to see no difference between these two compounds and therefore little isomerization directionality, if any. We shall see that this is not the case.

Starting from the computed equilibrium structures of each Z and E isomer of **1** and **2**, 200 initial conditions (positions and velocities) are generated using the classical thermal sampling with a Boltzmann distribution at temperature 300 K. (See the details in the SI.) The histograms of initial values of ϕ and κ angles (and corresponding initial velocities) are shown in Figures 2 and 3 respectively. (Notice that the full width at half-maximum of the ϕ distribution is ca. five times larger than the S_0 pretwist.) These initial conditions define an ensemble of trajectories released in the first singlet excited state (S_1), the spectroscopically allowed $\pi \rightarrow \pi^*$ transition in these systems. Among all trajectories ∼10% do not react (i.e., do not decay to S_0) within 600 fs of propagation time and are disregarded in our analysis. The reactive trajectories evolve in S_1 until a conical intersection seam is approached where the trajectories hop to S_0 when ϕ is approaching a ±90° value. Hopping times are distributed between 100 and 500 fs, with a maximum probability at ∼200 fs (see the SI), with no significant differences between **1** and **2**. After the decay to S_0, further twisting along the same direction leads to successful isomerization. However, twisting in the reverse direction may also be observed, leading to an aborted isomerization. Irrespective of clockwise or counterclockwise twisting directions in S_1, ∼80% of the reactive trajectories lead to a successful isomerization. (See the SI.)

We now define the directionality *D* of a population as the percentage of the reactive trajectories traveling in the counterclockwise (+) direction. Uncertainties in *D* due to the finite number of trajectories are estimated to be ∼4%. (See the

DOI: 10.1021/jz502644h
J. Phys. Chem. Lett. 2015, 6, 599−604

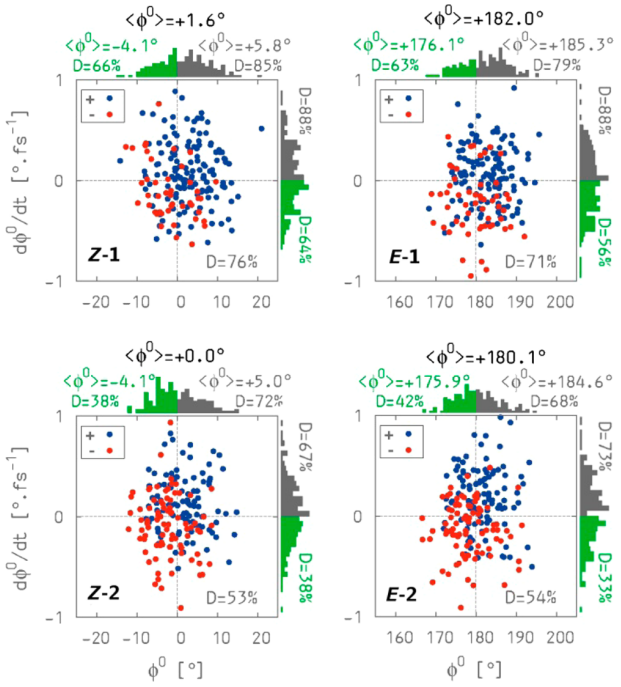

Figure 2. Correlation between the initial average twisting $\langle\phi^0\rangle$ and the photoisomerization directionality (±). Differences between the initial average value $\langle\phi^0\rangle$ and the ground-state optimized ϕ^0 value of the central double-bond twisting angles in **2** must be due to the limited size of the populations. The differences in **1** may also be due to the anharmonicity of the potential energy well.

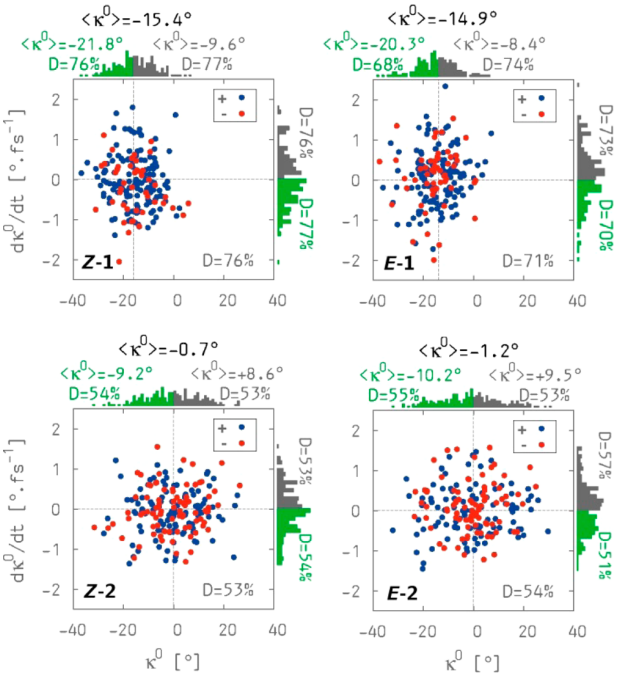

Figure 3. Correlation between the initial deformation κ° and the photoisomerization direction (±).

SI.) As expected for the planar, achiral compound **2**, the obtained D values of 53 and 54% for isomers Z and E, respectively, are consistent within the statistical uncertainty with a pure nondirectional (D = 50%) behavior. Instead, and despite the very limited C1′═C1 pretwist, the chiral molecule **1** displays a significant directionality with D = 76% for the Z isomer and D = 71% for the E isomer. This appears to be in contrast with the conjecture previously mentioned that a chiral force field inducing a significant S_0 double-bond pretwist and therefore helicity is required for an effective unidirectional rotation, as other systems including Rh would suggest.

To inspect the influence of the initial pretwist in these compounds, we analyze the ensemble of trajectories in subsets (subpopulations) corresponding to positive (gray bars in Figure 2) and negative (green bars in Figure 2) initial values of the pretwist (ϕ^0) and of their corresponding velocities ($d\phi^0/dt$). The average pretwist $\langle\phi^0\rangle$ and directionality D computed over each subpopulation are given in Figure 2. Consistent with the pretwist conjecture for the achiral compound **2**, positive (respectively negative) pretwists and velocities favor the motion in the "+" (respectively "−") direction (blue and red points in the 2D map). Indeed, with respect to the directionality D of the entire population, the directionality computed for the positively (negatively) pretwisted subpopulations increases (decreases) nearly symmetrically and proportionally to the average pretwist of each subpopulation, as shown in Table 1. This mirror-symmetry unidirectional dynamics is observed for both isomers of the achiral compound **2**.

Table 1. Analysis of the Ensembles of Trajectories Displayed in Figure 2 in Two Subpopulations[a]

	total population	subpopulation with >0 pretwist		subpopulation with <0 pretwist	
	D	$D_+ - D$	$\Delta\langle\phi^0\rangle$	$D_- - D$	$\Delta\langle\phi^0\rangle$
Z-**2**	53	+19	+5.0°	−15	−4.1°
E-**2**	54	+14	+4.6°	−12	−4.1°
Z-**1**	76	+9	+5.8°	−10	−4.1°
E-**1**	71	+8	+5.3°	−8	−3.9°

[a] $D_+ - D$ (resp. $D_- - D$) is the change in directionality of the positively (resp. negatively) pretwisted subpopulation with respect to the total population and $\Delta\langle\phi^0\rangle$ the average pretwist of the subpopulations.

In contrast, a substantial inconsistency with the pretwist conjecture is obtained when performing the same analysis for **1**. Indeed, despite a similar quasi-symmetric displacement in the $\langle\phi^0\rangle$ values of the two subpopulations, the corresponding D values vary less than in **2**. Most importantly, the D values remain significantly above 50% for both subpopulations, thus indicating a mirror-symmetry breaking at a dynamical level for both isomers. Notice that the analysis of the average $d\phi^0/dt$ leads to conclusions similar to that of $\langle\phi^0\rangle$. Thus, although an initial positive or negative pretwist may induce a significant directionality in the achiral molecule in the corresponding direction, a similar negative pretwist of −4.1° (respectively, 176.1° = 180−3.9) is not enough to suppress the directionality in **1**, which remains as large as 66% (respectively, 63%) for the Z (respectively E) isomer. We conclude that a substantial geometrical pretwist in S_0 is not, by itself, required for leading to the directionality observed in **1**.

As **1** exhibits large deformations in the pentenylidene ring, we also examine (see Figure 3) the influence of κ (which represents the deformation of the ring) on the value of D. The same analysis inspecting subpopulations characterized by initial values of κ° or $d\kappa^\circ/dt$ larger or smaller than the average over the entire population reveals that there is no correlation

DOI: 10.1021/jz502644h
J. Phys. Chem. Lett. 2015, 6, 599−604

between κ and the directionality of the reaction. Therefore, also a distorted S_0 equilibrium value of κ cannot explain the directionality computed for **1**.

To further test the effect of the initial geometrical deformations on the directionality, we computed an additional set of 200 trajectories for the achiral compound *Z*-**2** forced to the initial distorted geometry of the chiral *Z*-**1**. The result (details in Figures S3 and S4 of the SI) is D = 48%, close to the value of D = 53% obtained for the nondistorted *Z*-**2** population. This confirms that the mere geometrical deformation generated by the stereogenic center does not determine the directionality when imposed on a system with a symmetric force field in both S_0 and S_1.

The larger mass of the methyl substituent in **1** compared with the hydrogen in **2** may also affect the dynamics by modulating the velocity of each single atom or group and is therefore a potential origin of directionality through an inertial effect. To investigate this effect, a new run of 200 trajectories of *Z*-**2** with its original set of positions and velocities is computed imposing the mass of a methyl group to the pro-S hydrogen in position C5′. Thus, such a "heavy" *Z*-**2** molecule evolves on the same potential energy surfaces as the original "light" compound. This ensemble (see details in Figures S3 and S4 of the SI) yields a directionality of D = 56%, which is marginally different from D = 53% obtained with the natural hydrogen mass, and significantly smaller than the >70% directionality computed for compound **1**. Hence, the heavier mass of the methyl substituent does not affect the directionality when imposed on a system with a symmetric force field in both S_0 and S_1.

The results above show that neither an initial geometrical deformation nor an inertial effect are at the origin of a net directionality in the dynamics of the chiral compound **1**. Therefore, the observed large directionality (i.e., not a full directionality) must be induced by the stereogenic center imposing the asymmetry of the S_1 potential energy surface driving the dynamics. This concept is illustrated and demonstrated in Figure 4 for the Z isomer of the chiral compound **1**. (See the same figure for the E isomer in the SI.) The minimum energy path, computed in terms of the intrinsic reaction coordinate starting from the Franck−Condon (FC) region of the isomer, reveals that the C_1═$C_{1'}$ immediately elongates (relaxation along the stretch coordinate), as is common to all N-protonated or N-alkylated Schiff bases. This motion "unlocks" the central double bond and initiates the twisting around the bond in a specific direction. Such twisting direction is imposed by the S_1 potential energy surface asymmetry along ϕ. (See the inset in Figure 4.) This asymmetry is present in the FC region and persists while the central bond stretches, thus triggering the twisting in the counterclockwise direction preferentially. Notice that in our prototype system such small asymmetry goes in the same direction for both isomers of **1**. (See the SI.) This may not occur in more complicated systems where the directionality of the potential energy surface may be opposite in the E and Z isomers[27] due to contrasting effects. Conversely, in **2** the S_1 potential energy surface is symmetric along ϕ and κ (see the SI) and the population is symmetrically accelerated in either the clockwise and counterclockwise directions, depending on the initial conditions, leading to a mirror-symmetry dynamics.

In conclusion, our comparative study reveals that a significant photoisomerization directionality can be achieved by placing a stereogenic center in an allylic position with respect to the

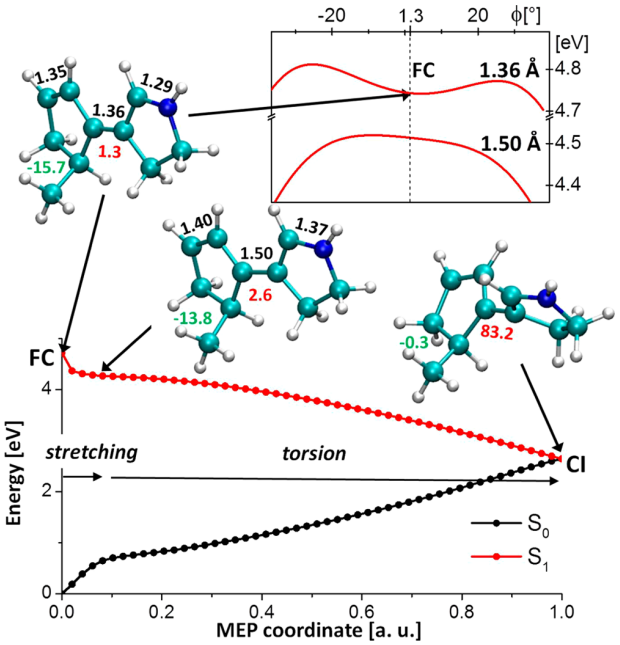

Figure 4. Excited-state reaction of Z-**1**. Minimum energy path (MEP) computed from the Franck−Condon (FC) state to the S_1/S_0 conical intersection (CI). Three structures are displayed along this path showing the direction of rotation. The lengths of the three C═C bonds are given in black, the twisting angle ϕ in red, and the dihedral κ in green. (Inset) S_1 potential energy computed as a function of the twisting angle ϕ with the central C1−C1′ bond length fixed at 1.36 or 1.50 Å, and all other coordinates fixed at their FC values.

isomerizing C═C bond, despite an almost negligible pretwist/helicity. In contrast with the conjecture that a pretwist of the S_0 equilibrium structure is required for a substantial directionality, the latter is mostly the result of the asymmetry of the S_1 force field on the initial population. In other words, even a limited symmetry breaking of the S_1 potential energy surface seems to have a large effect on the way the population branches between clockwise and counterclockwise twisting. This is supported by the reported analysis showing that the almost planar compound **1** displays a significant directionality, even in the subpopulation showing an opposite average pretwist (three to four times larger in amplitude than the equilibrium pretwist). Furthermore, the same initial deformation of **1** imposed on **2** does not yield a directionality.

The above conclusions may be important for the design of IP-based single-molecule molecular motors, since in these and other retinal-related compounds photoisomerization dynamics (e.g., photoreaction speed, yield, vibrational coherence, or directionality) are commonly rationalized or predicted by discussing ground-state equilibrium geometries. The presented compound **1** appears to be a borderline prototype featuring a high, but not full, directionality. For this IP-model system, the documented 76 and 71% directionalities of **1** in the Z → E and E → Z isomerization steps, respectively, predict that ca. 54% of the initially thermalized and reactive population (76% × 71%) will perform a full Z → E → Z rotation by absorbing two photons sequentially. In the same conditions 39% of the population (24% × 71% + 76% × 29%) would have not rotated and 7% (24% × 29%) would have rotated in opposite direction. This allows us to conclude that on average 47% (= 54−7%) of

DOI: 10.1021/jz502644h
J. Phys. Chem. Lett. 2015, 6, 599−604

the mechanical work produced by an isomerizing molecule over one full turn could be exploited.

■ ASSOCIATED CONTENT

Supporting Information

Computational method; CASSCF molecular orbitals and occupation numbers; geometries of the optimized structures; trajectory movies showing photoisomerizations in the positive and negative directions; quantum yields; S_1 lifetimes. This material is available free of charge via the Internet at http://pubs.acs.org.

■ AUTHOR INFORMATION

Corresponding Authors

*E.G.: E-mail: egindensperger@unistra.fr.
*J.L.: E-mail: leonard@ipcms.unistra.fr.
*M.O.: E-mail: molivuc@bgsu.edu.

Present Address

⊗(G.M.) Chemistry Department, Université de Nantes - CNRS UMR 6230, Nantes, France.

Notes

The authors declare no competing financial interest.

■ ACKNOWLEDGMENTS

We thank Lutz Greb for sharing unpublished information. This work was supported by the French Agence Nationale de la Recherche (ANR) through the grant ANR-11-JS04-0010 and the High-Performance Computing center (pôle HPC) at Université de Strasbourg. L.M.F. and A.V. acknowledge support from grants CTQ-2012-36966 of the Spanish Secretariá de Estado de Investigacion Desarrollo e Innovacion, and CCG2013/EXP-089 of the University of Alcala. M.O. acknowledges funding from the Italian MIUR (PRIN 2012-2014) and partial funding from the EU-FP7 (Marie-Curie PIOF-GA-2012-332233), the National Science Foundation under grant no. CHE-1152070 and the Human Frontier Science Program Organization under grant RGP0049/2012CHE09-56776.

■ REFERENCES

(1) Feynman, R. P. Leighton, R.; Sands, M. L. *The Feynman Lectures on Physics*; Basic Books: New York, 1963; Vol. *1*.

(2) Lumento, F.; Zanirato, V.; Fusi, S.; Busi, E.; Latterini, L.; Elisei, F.; Sinicropi, A.; Andruniów, T.; Ferré, N.; Basosi, R.; et al. Quantum Chemical Modeling and Preparation of a Biomimetic Photochemical Switch. *Angew. Chem., Int. Ed.* **2007**, *46*, 414−420.

(3) Kandori, H.; Shichida, Y.; Yoshizawa, T. Photoisomerization in Rhodopsin. *Biochemistry (Moscow)* **2001**, *66*, 1197−1209.

(4) Wang, Q.; Schoenlein, R. W.; Peteanu, L. A.; Mathies, R. A.; Shank, C. V. Vibrationally Coherent Photochemistry in the Femtosecond Primary Event of Vision. *Science* **1994**, *266*, 422−424.

(5) Polli, D.; Altoe, P.; Weingart, O.; Spillane, K. M.; Manzoni, C.; Brida, D.; Tomasello, G.; Orlandi, G.; Kukura, P.; Mathies, R. A.; et al. Conical Intersection Dynamics of the Primary Photoisomerization Event in Vision. *Nature* **2010**, *467*, 440−443.

(6) Briand, J.; Braem, O.; Rehault, J.; Léonard, J.; Cannizzo, A.; Chergui, M.; Zanirato, V.; Olivucci, M.; Helbing, J.; Haacke, S. Coherent Ultrafast Torsional Motion and Isomerization of a Biomimetic Dipolar Photoswitch. *Phys. Chem. Chem. Phys.* **2010**, *12*, 3178−3187.

(7) Léonard, J.; Schapiro, I.; Briand, J.; Fusi, S.; Paccani, R. R.; Olivucci, M.; Haacke, S. Mechanistic Origin of the Vibrational Coherence Accompanying the Photoreaction of Biomimetic Molecular Switches. *Chem.—Eur. J.* **2012**, *18*, 15296−15304.

(8) Léonard, J.; Briand, J.; Fusi, S.; Zanirato, V.; Olivucci, M.; Haacke, S. Isomer-Dependent Vibrational Coherence in Ultrafast Photoisomerization. *New J. Phys.* **2013**, *15*, 105022.

(9) Sinicropi, A.; Martin, E.; Ryazantsev, M.; Helbing, J.; Briand, J.; Sharma, D.; Léonard, J.; Haacke, S.; Cannizzo, A.; Chergui, M.; et al. An Artificial Molecular Switch That Mimics the Visual Pigment and Completes Its Photocycle in Picoseconds. *Proc. Natl. Acad. Sci. U.S.A.* **2008**, *105*, 17642−17647.

(10) Strambi, A.; Durbeej, B.; Ferré, N.; Olivucci, M. Anabaena Sensory Rhodopsin Is a Light-Driven Unidirectional Rotor. *Proc. Natl. Acad. Sci. U.S.A.* **2010**, *107*, 21322−21326.

(11) Garavelli, M.; Celani, P.; Bernardi, F.; Robb, M. A.; Olivucci, M. The $C_5H_6NH_2^+$ Protonated Shiff Base: An Ab Initio Minimal Model for Retinal Photoisomerization. *J. Am. Chem. Soc.* **1997**, *119*, 6891−6901.

(12) Weingart, O.; Schapiro, I.; Buss, V. Photochemistry of Visual Pigment Chromophore Models by Ab Initio Molecular Dynamics. *J. Phys. Chem. B* **2007**, *111*, 3782−3788.

(13) Klaffki, N.; Weingart, O.; Garavelli, M.; Spohr, E. Sampling Excited State Dynamics: Influence of Hoop Mode Excitations in a Retinal Model. *Phys. Chem. Chem. Phys.* **2012**, *14*, 14299−14305.

(14) Ruckenbauer, M.; Barbatti, M.; Müller, T.; Lischka, H. Nonadiabatic Photodynamics of a Retinal Model in Polar and Nonpolar Environment. *J. Phys. Chem. A* **2013**, *117*, 2790−2799.

(15) Koumura, N.; Zijlstra, R. W. J.; van Delden, R. A.; Harada, N.; Feringa, B. L. Light-Driven Monodirectional Molecular Rotor. *Nature* **1999**, *401*, 152−155.

(16) Kazaryan, A.; Kistemaker, J. C. M.; Schäfer, L. V.; Browne, W. R.; Feringa, B. L.; Filatov, M. Understanding the Dynamics Behind the Photoisomerization of a Light-Driven Fluorene Molecular Rotary Motor. *J. Phys. Chem. A* **2010**, *114*, 5058−5067.

(17) Unidirectional motion has also been recently demonstrated to occur in an imine featuring an overcrowded N═C bond.[18]

(18) Greb, L.; Lehn, J.-M. Light-Driven Molecular Motors: Imines as Four-Step or Two-Step Unidirectional Rotors. *J. Am. Chem. Soc.* **2014**, *136*, 13114−13117.

(19) García-Iriepa, C.; Marazzi, M.; Zapata, F.; Valentini, A.; Sampedro, D.; Frutos, L. M. Chiral Hydrogen Bond Environment Providing Unidirectional Rotation in Photoactive Molecular Motors. *J. Phys. Chem. Lett.* **2013**, *4*, 1389−1396.

(20) Schoenlein, R. W.; Peteanu, L. A.; Wang, Q.; Mathies, R. A.; Shank, C. V. Femtosecond Dynamics of *Cis-Trans* Isomerization in a Visual Pigment Analog: Isorhodopsin. *J. Phys. Chem.* **1993**, *97*, 12087−12092.

(21) Kochendoerfer, G. G.; Mathies, R. A. Spontaneous Emission Study of the Femtosecond Isomerization Dynamics of Rhodopsin. *J. Phys. Chem.* **1996**, *100*, 14526−14532.

(22) Kukura, P.; McCamant, D. W.; Yoon, S.; Wandschneider, D. B.; Mathies, R. A. Structural Observation of the Primary Isomerization in Vision with Femtosecond-Stimulated Raman. *Science* **2005**, *310*, 1006−1009.

(23) Altoè, P.; Cembran, A.; Olivucci, M.; Garavelli, M. Aborted Double Bicycle-Pedal Isomerization with Hydrogen Bond Breaking Is the Primary Event of Bacteriorhodopsin Proton Pumping. *Proc. Natl. Acad. Sci. U.S.A.* **2010**, *107*, 20172−20177.

(24) Okada, T.; Sugihara, M.; Bondar, A.-N.; Elstner, M.; Entel, P.; Buss, V. The Retinal Conformation and Its Environment in Rhodopsin in Light of a New 2.2 Å Crystal Structure. *J. Mol. Biol.* **2004**, *342*, 571−583.

(25) Struts, A. V.; Salgado, G. F. J.; Tanaka, K.; Krane, S.; Nakanishi, K.; Brown, M. F. Structural Analysis and Dynamics of Retinal Chromophore in Dark and Meta I States of Rhodopsin from 2h Nmr of Aligned Membranes. *J. Mol. Biol.* **2007**, *372*, 50−66.

(26) Hayashi, S.; Tajkhorshid, E.; Schulten, K. Molecular Dynamics Simulation of Bacteriorhodopsin's Photoisomerization Using Ab Initio Forces for the Excited Chromophore. *Biophys. J.* **2003**, *85*, 1440−1449.

(27) Sampedro, D.; Migani, A.; Pepi, A.; Busi, E.; Basosi, R.; Latterini, L.; Elisei, F.; Fusi, S.; Ponticelli, F.; Zanirato, V.; et al. Design and

DOI: 10.1021/jz502644h
J. Phys. Chem. Lett. 2015, 6, 599−604

Photochemical Characterization of a Biomimetic Light-Driven Z/E Switcher. *J. Am. Chem. Soc.* **2004**, *126*, 9349−9359.
(28) Roos, B. O. The Complete Active Space Self-Consistent Field Method and Its Applications in Electronic Structure Calculations. In *Advances in Chemical Physics*; John Wiley & Sons, Inc., 2007; pp 399−445.
(29) Groenhof, G.; Bouxin-Cademartory, M.; Hess, B.; de Visser, S. P.; Berendsen, H. J. C.; Olivucci, M.; Mark, A. E.; Robb, M. A. Photoactivation of the Photoactive Yellow Protein: Why Photon Absorption Triggers a Trans-to-Cis Isomerization of the Chromophore in the Protein. *J. Am. Chem. Soc.* **2004**, *126*, 4228−4233.
(30) Barbatti, M. Nonadiabatic Dynamics with Trajectory Surface Hopping Method. *Wiley Interdiscip. Rev. Comput. Mol. Sci.* **2011**, *1*, 620−633.
(31) Aquilante, F.; De Vico, L.; Ferré, N.; Ghigo, G.; Malmqvist, P.-å.; Neogrády, P.; Pedersen, T. B.; Pitoňák, M.; Reiher, M.; Roos, B. O.; et al. Molcas 7: The Next Generation. *J. Comput. Chem.* **2010**, *31*, 224−247.
(32) Tully, J. C. Molecular Dynamics with Electronic Transitions. *J. Chem. Phys.* **1990**, *93*, 1061−1071.
(33) Granucci, G.; Persico, M.; Zoccante, A. Including Quantum Decoherence in Surface Hopping. *J. Chem. Phys.* **2010**, *133*, 134111.

DOI: 10.1021/jz502644h
J. Phys. Chem. Lett. 2015, 6, 599−604

Directionality of the Double-bond Photoisomerization Dynamics Induced by a Single Stereogenic Center

Supporting Information

Gabriel Marchand, Julien Eng, Igor Schapiro, Alessio Valentini, Luis Manuel Frutos, Elisa Pieri, Massimo Olivucci,* Jérémie Léonard,* and Etienne Gindensperger*

To simulate the photodynamics of the chiral **1** (in gas phase) and compare to the achiral compound **2**, we use *ab initio* non-adiabatic molecular dynamics by generating entire ensembles (populations) of semi-classical trajectories based on the Tully's surface hopping algorithm[1] and including the quantum decoherence correction [2]. This method uses classical mechanics for the nuclear motion and allows the trajectories to hop from one electronic state to another, by taking into account non-adiabatic couplings. All computations are performed using the *ab initio* CASSCF method and the 6-31G* atomic basis set for the electronic structure with 6 electrons in 6 orbitals comprising the π system, and two states equally-weighted are considered in the state-average procedure.

The conformation of both compounds in either their *Z* or *E* isomers are optimized in their singlet electronic ground state (S_0), see the resulting equilibrium bond lengths and dihedral angles in Table S1. The Cartesian coordinates of the optimized ground state geometries are provided at the end of the SI. Starting from these equilibrium structures, 200 initial conditions (positions and velocities) are generated at 300 K using the classical thermal sampling scheme in Gaussian 09[3] for each compound and *Z/E* isomer (Boltzmann distribution along normal modes.) Only the initial conditions were generated with Gaussian 09, all subsequent calculations have been done using Molcas 7.8.[4]

Table S1. Equilibrium bond lengths and dihedral angles of molecules **1** and **2**. ϕ = (2'-1'-1-2 + 5'-1'-1-5) / 2, κ=1-1'-5'-4'. The labels refer to Figure 1 of the main text.

	Z-**1**	*E*-**1**	*Z*-**2**	*E*-**2**
1'-1 (Å)	1.36	1.36	1.36	1.36
1'-2' (Å)	1.46	1.46	1.46	1.46
1-2 (Å)	1.44	1.43	1.43	1.43
2'-3' (Å)	1.35	1.35	1.35	1.35
2-3 (Å)	1.29	1.29	1.29	1.29
3'-4' (Å)	1.51	1.51	1.51	1.51
3-4 (Å)	1.48	1.48	1.48	1.48
4'-5' (Å)	1.55	1.55	1.55	1.55
4-5 (Å)	1.54	1.54	1.54	1.55
5'-1' (Å)	1.52	1.53	1.52	1.52
5-1 (Å)	1.53	1.53	1.52	1.53
2'-1'-1-2 (°)	+0.8	+183.1	0.0	+180.0
5'-1'-1-5 (°)	+1.8	+181.2	0.0	+180.0
ϕ (°)	+1.3	+182.2	0.0	+180.0
1-1'-2'-3' (°)	-10.5	-9.0	0.0	0.0
κ (°)	-15.7	-13.9	0.0	0.0
1'-1-2-3 (°)	-3.3	-0.6	0.0	0.0
1'-1-5-4 (°)	-4.7	0.0	0.0	0.0

The initial conditions define an ensemble of trajectories which are initially released in the first singlet excited state S_1 corresponding to a π→π* transition (see the molecular orbitals in Figure S1 and occupation numbers in Table S2). The trajectories are propagated using the velocity Verlet scheme for the nuclear motion with a fixed integration time step of 1 fs.

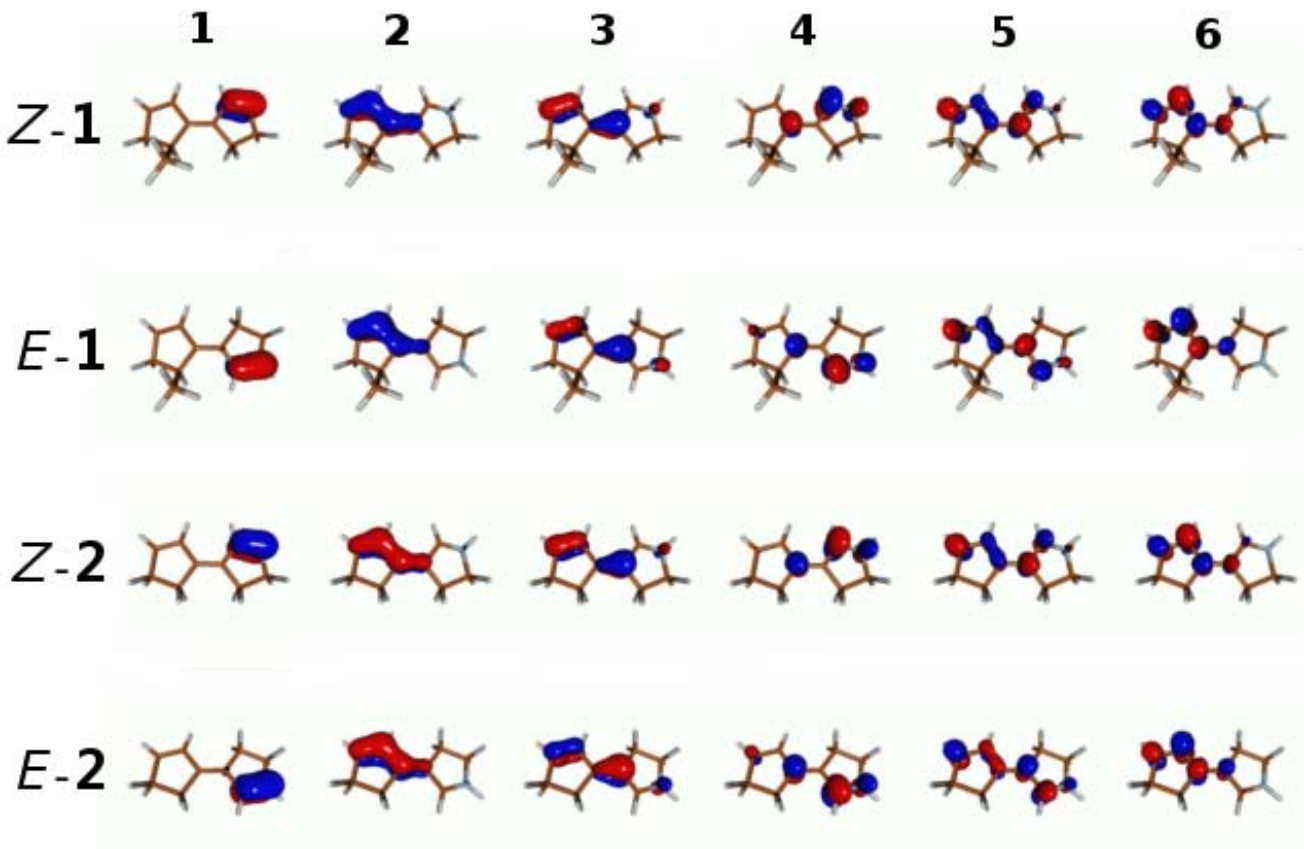

Figure S1. State-average (S_0 and S_1) molecular π-orbitals of the active space, for the ground state optimized structures of **1** and **2**.

Table S2. Electronic occupation numbers of the CAS orbitals of S_0 and S_1, for the optimized geometries of **1** and **2**.

molecule	state	1	2	3	4	5	6
Z-**1**	S_0	1.97	1.94	1.91	0.10	0.03	0.05
	S_1	1.97	1.91	1.10	0.90	0.03	0.09
E-**1**	S_0	1.97	1.94	1.91	0.10	0.05	0.03
	S_1	1.96	1.91	0.92	1.08	0.03	0.08
Z-**2**	S_0	1.97	1.94	1.91	0.10	0.05	0.03
	S_1	1.97	1.91	0.92	1.08	0.03	0.08
E-**2**	S_0	1.97	1.94	1.91	0.10	0.05	0.03
	S_1	1.96	1.92	1.01	0.99	0.04	0.07

In the analysis, the trajectories have been split according to the product of the photoisomerization reaction, i.e. trajectories for which the isomerization torsion coordinate ϕ reached $\phi^0 \pm \pi$ or went back to values close to ϕ^0 have been accounted as successful or aborted photoisomerizations, respectively, after decay in the ground electronic state. This decay is represented by a hop from the excited to the ground state. Trajectories that did not decay to S_0 within 600 fs have been accounted as non-reactive events (<

10%). The S_1-S_0 hopping times are representative of the S_1 lifetimes and are found to lie in the 100-500 fs range, with a maximum probability at about 200 fs as shown in Figure S2. With these ensembles of trajectories we obtain a yield of isomerization of ca. 80% in all cases, independently of the clockwise or counterclockwise rotational direction, see Table S3.

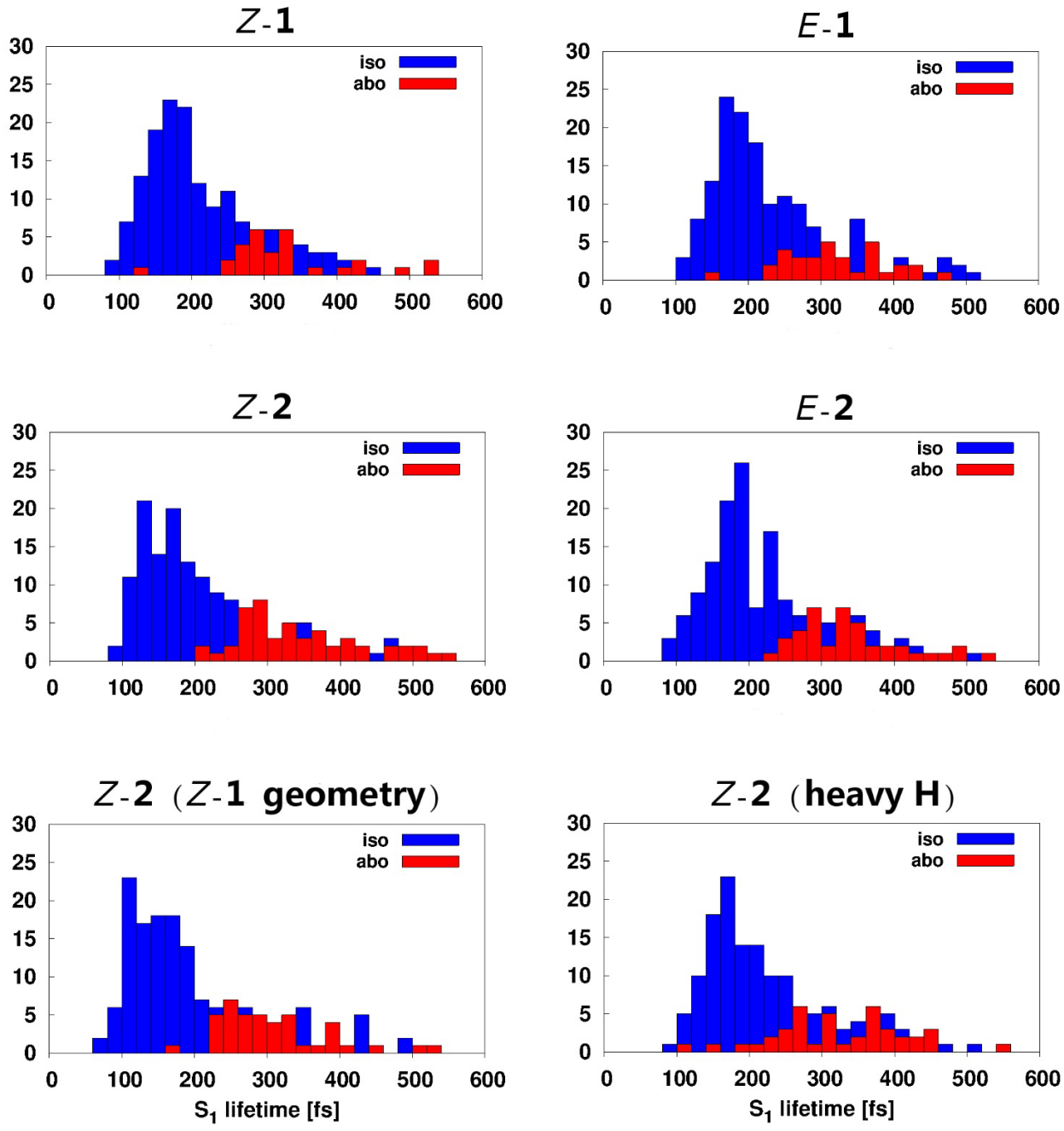

Figure S2. Distribution of the S_1 lifetimes (hopping times), for all computed ensembles of trajectories.

Table S3. For each ensemble of trajectories, number of successful (iso) and aborted (abo) photoisomerizations in the positive (+) and negative (-) directions, number of non-reactive (nr) events, and isomerization quantum yield (Q, defined as iso / (iso + abo)).

Ensemble	iso+	iso-	abo+	abo-	nr	Q
Z-**1**	117	39	24	5	15	0.84
E-**1**	109	44	23	10	14	0.82
Z-**2**	73	64	27	23	13	0.73
E-**2**	82	65	20	21	12	0.78
Z-**2 (**Z-**1** geometry)	73	67	14	28	18	0.77
Z-**2** (heavy H)	80	64	23	18	15	0.78

In order to examine the effect of the geometrical deformations induced by the introduction of the chiral center, we generated an ensemble of 200 trajectories of *Z*-**2** but with the geometry of *Z*-**1** by imposing on the *Z*-**2** geometries the difference in each element of the internal coordinate matrix between the *Z*-**2** and *Z*-**1** optimized structures. In addition, to investigate the effect of the large mass of the methyl substituent in **1 (**compared to the hydrogen substituent in **2**) on the directionality *D*, we performed a run of 200 trajectories of *Z*-**2** with the original set of positions and velocities, but imposing the mass of a methyl group to the pro-S hydrogen. The results are shown in Figure S3 and S4. The corresponding *D* values for all ensembles of trajectories are provided in Table S4. We estimate the RMS uncertainty on *D* by considering the values corresponding to 4 sets of 200 trajectories: 53%, 54%, 48% and 56% for the *Z*-**2**, *E*-**2**, *Z*-**2** (Z-1 geometry), *Z*-**2** (heavy H), respectively: This gives 4% RMS. This may already be overestimated because we implicitly assume that the 4 ensembles would converge to the same directionality (for infinite number of trajectories) which may not be exactly true. The RMS uncertainty on *D* is thus estimated to be ~4% due to the finite amount of trajectories (200) in each population.

Table S4. *D* values for the different ensembles of trajectories. The RMS uncertainty on *D* is estimated to be ~4°.

Ensemble	*D* (%)
Z-**1**	76
E-**1**	71
Z-**2**	53
E-**2**	54
Z-**2 (***Z*-**1** geometry)	48
Z-**2** (heavy H)	56

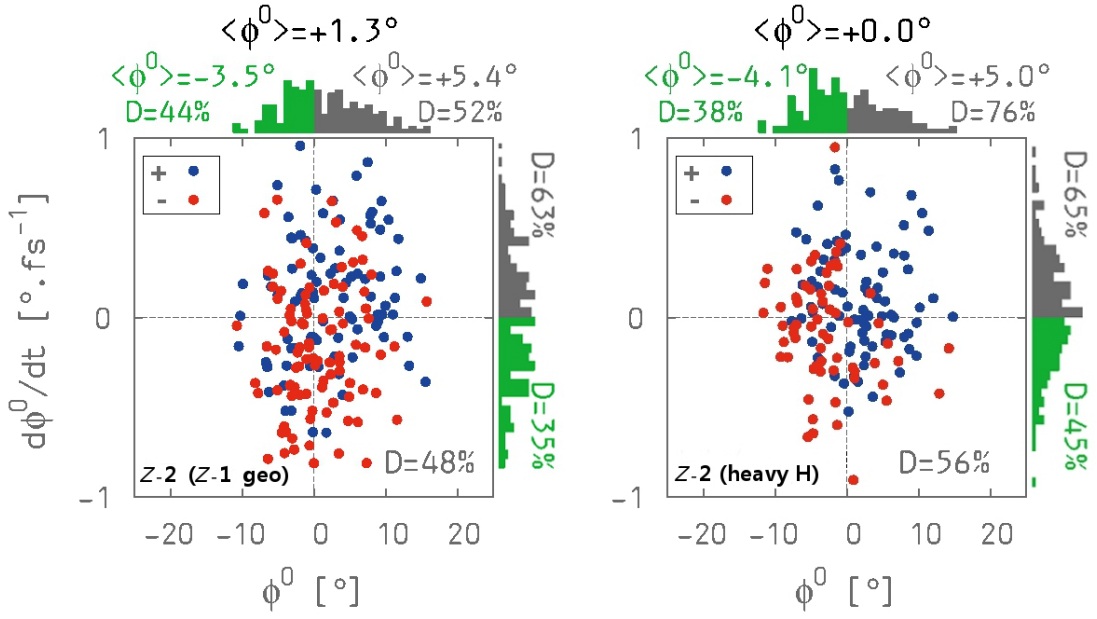

Figure S3. Influence of the pre-twist ϕ^0 and the pre-twist velocity $d\phi^0/dt$ (defined as $\phi(t=1\text{ fs}) - \phi^0$) on the photoisomerization direction (+/-), for the ensembles of trajectories of *Z*-**2** with the (distorted) geometry of *Z*-**1** (left) and *Z*-**2** with the mass of a methyl imposed on the pro-S hydrogen~(right). The global directionality *D* is shown at the bottom right corner of the main frame. On top and at right of the main frame: distributions of ϕ^0 and $d\phi^0/dt$, average ϕ^0-values, and *D* after splitting the trajectories according to the sign (relatively to the mean value) of ϕ^0 and $d\phi^0/dt$. For the ensemble of trajectories of *Z*-**2** with the heavy hydrogen substituent, the initial velocities of the heavy hydrogen have been divided by $(m_{CH3} / m_H)^{1/2}$ to ensure conservation of the total linear momentum.

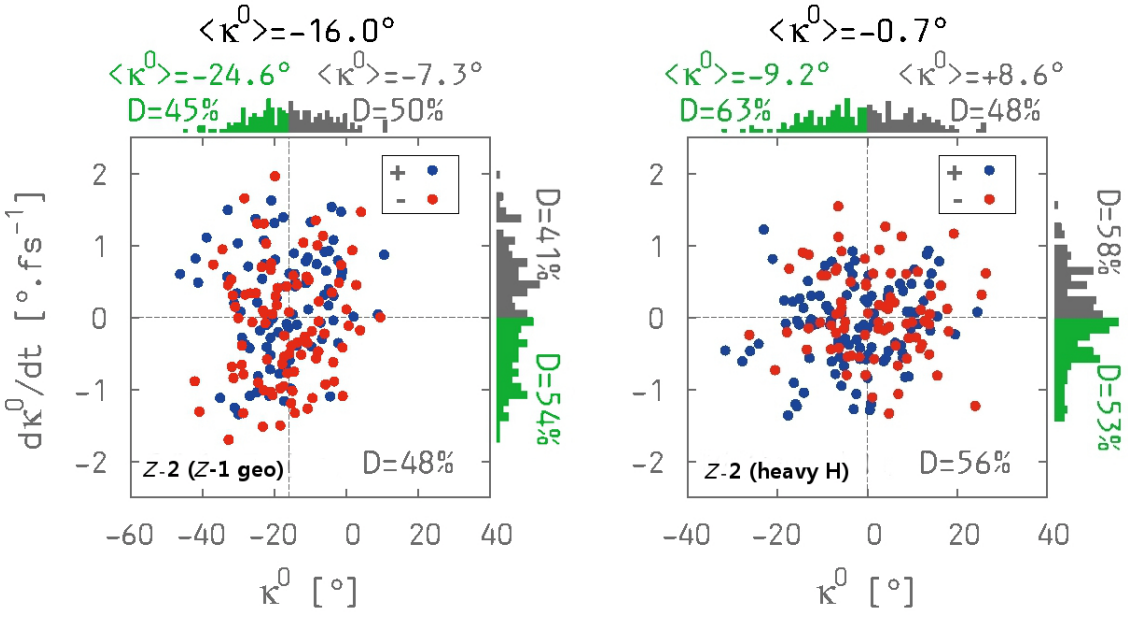

Figure S4. Influence of the largest ring initial deformation κ^0 and the velocity $d\kappa^0/dt$ (defined as $\kappa(t=1\text{ fs}) - \kappa^0$) on the photoisomerization direction (+/-), for the additional ensembles of trajectories. See caption of Figure S3 for more details.

The influence of the asymmetry for the *E*-**1** compound is depicted in Figure S5. It corresponds to Figure 4 of the main text for *Z*-**1**. We do observe an asymmetry in the excited state as a function of the torsion angle, see the inset. Similar curves have been computed for the achiral molecule and are shown in Figure S6. As expected for the planar, achiral system, no asymmetry in S_1 is observed. Figure S7 shows the slight asymmetry of the ground electronic state of the chiral compound as compared to the fully symmetric achiral one.

The asymmetry with respect to the torsion present in the S_1 state of the chiral compound is evaluated as the slope of the S_1 potential energy curve with respect toϕ. It amounts to -0.6 meV/° at a C1-C1' distance of 1.50 Å, for both isomers. Note that the sign of the asymmetry is the same for both isomers, explaining why they both lead to motion in the "+" direction. Importantly, this asymmetry may be expected to lead to a faster decay of the excited state, i.e. shorter hopping time, by providing a kick to the torsional motion. In fact, this asymmetry is so small that the hopping times of the chiral and achiral compounds are almost identical (see Figure S2). Nevertheless, it is enough to lead to a substantial directionality.

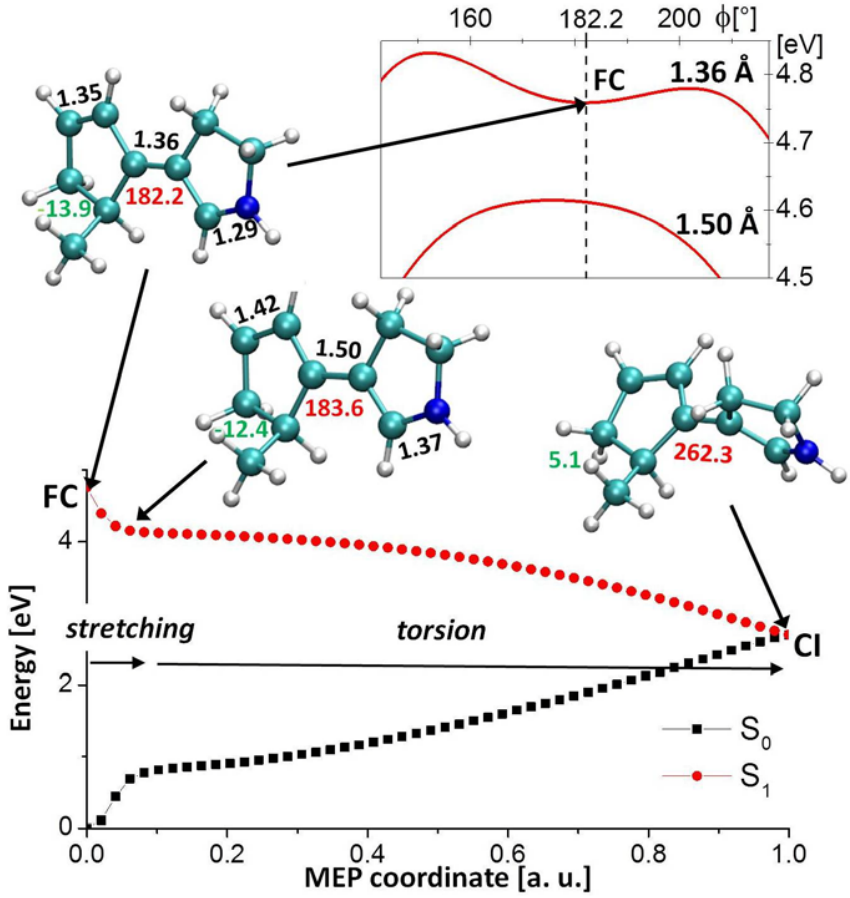

Figure S5. Excited-state reaction of *E*-**1**. Minimum Energy Path (MEP) computed from the Franck-Condon (FC) state to the S_1/S_0 conical intersection (CI). Three structures are displayed along this path showing the sense of rotation. The length of the three C=C bonds is given in black, the torsion angle ϕ in red, and the dihedral κ in green. (Inset) S_1 potential energy computed as a function of the torsion

angle ϕ with the central C1-C1' bond length fixed at 1.36 Å or 1.50 Å, and all other coordinates fixed at their FC values.

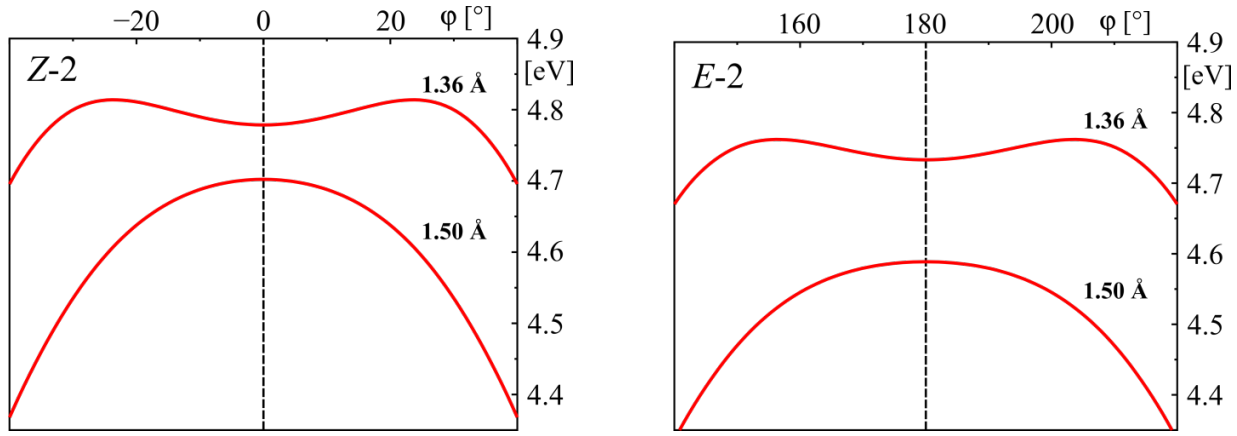

Figure S6. S_1 potential energy curves for the achiral compound 2 computed as a function of the torsion angle ϕ with the central C1-C1' bond length fixed at 1.36 Å or 1.50 Å, and all other coordinates fixed at their FC values. Left: *Z*-2; Right *E*-2. No asymmetry is present in the S_1 state of the achiral compound.

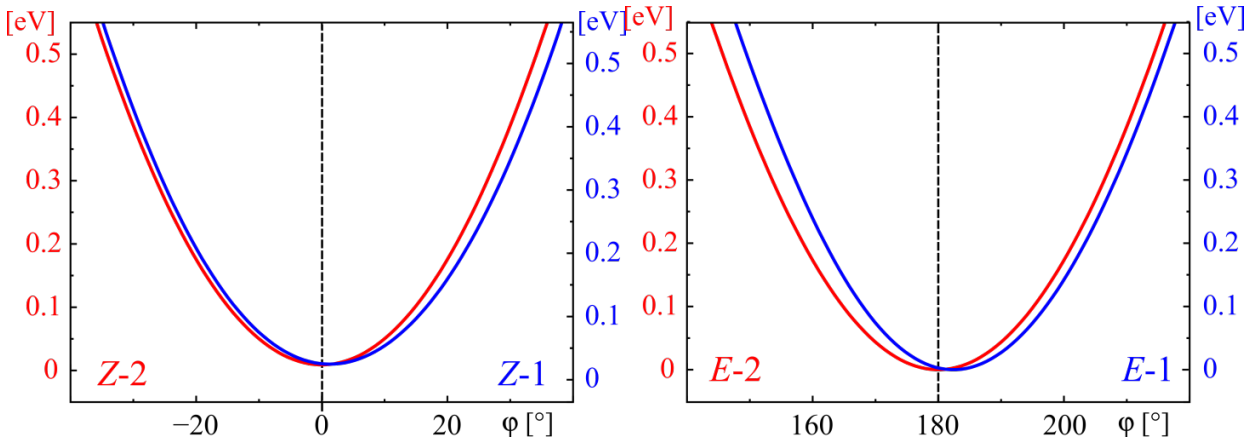

Figure S7. S_0 potential energy curves computed as a function of the torsion angle φ with all other coordinates fixed at their FC values, for the chiral (1, blue) and achiral (2, red) and compounds. Left: *Z* isomers; Right *E* isomers.

Caption of the movie. The movie shows an example of two trajectories, one rotating in the counter-clockwise "+" (left) and one rotating in the clockwise "-" (right) direction. The time is indicated for the counterclockwise reaction: in red, evolution in the excited state; in green evolution in the ground state after the hop.

Optimized Cartesian coordinates (Å) of the electronic ground state.

Z-**1**

C	4.41830177	-0.07826905	1.58123442
C	3.40311604	-0.11069365	0.44522964
C	4.14760481	-0.15740541	-0.81379169
C	5.45785158	0.04629347	-0.58488933
C	5.75368707	0.26691778	0.87463036
C	2.05530271	-0.07353409	0.59759027
C	1.23941612	0.04342138	1.88132585
C	-0.22353227	0.15570712	1.39778561
N	-0.09938384	0.02172891	-0.07146040
C	1.11367813	-0.09011865	-0.48668350
H	1.32512527	-0.17794590	-1.53441216
H	1.52332048	0.91458391	2.45666778
H	-0.68086256	1.11035878	1.61351174
H	4.14866745	0.68743227	2.30076040
H	6.57092004	-0.35399197	1.22337350
H	6.21273585	0.08408628	-1.34725687
H	3.70847290	-0.30613178	-1.78206249
H	-0.89102550	0.03758314	-0.68523610
H	1.36240046	-0.82538048	2.51287690
H	-0.86437480	-0.63331831	1.76218797
C	4.49631949	-1.43475900	2.29952074
H	6.04513258	1.29848765	1.04773904
H	5.23955457	-1.39238995	3.08703176
H	3.55208801	-1.71267642	2.75326509
H	4.78241463	-2.22090105	1.60876549

E-**1**

C	1.08125781	-0.06539740	-0.48871748
C	2.04552454	-0.02785350	0.57321562
C	1.25933106	0.07913576	1.87654481
C	-0.21835068	0.13309473	1.42905195
N	-0.12456448	0.01352199	-0.04424786
C	3.38924068	-0.10506046	0.40812697
C	4.15282221	-0.18643800	-0.91335480
C	5.58089202	-0.61318665	-0.48364089
C	5.59110221	-0.40743164	1.00734992
C	4.36549806	-0.13169038	1.49186071
C	4.16606917	1.16698471	-1.64035631
H	1.27128421	-0.15616360	-1.54039474
H	1.52460114	0.96981565	2.43027184
H	-0.70979116	1.06584064	1.66401363
H	3.71345319	-0.93567159	-1.56334959
H	6.34551825	-0.02723797	-0.98121149
H	6.47860306	-0.50579922	1.60322174
H	4.12087178	0.02100299	2.52539267
H	-0.93110436	-0.00158244	-0.63828052
H	1.43504141	-0.77619894	2.51566542
H	-0.81698803	-0.68514767	1.80105576
H	5.77648152	-1.65400196	-0.72279133
H	4.74128709	1.09296042	-2.55579141
H	3.16709425	1.50024870	-1.90411774
H	4.61712605	1.93386983	-1.01988387

Z-**2**

N	-0.08395628	-0.03971173	-0.03112962
C	-0.16678754	-0.05938752	1.44780156
C	1.31668012	-0.04496857	1.87868690
C	2.09061025	-0.01720987	0.56650856
C	1.11906686	-0.01720146	-0.48908660
C	3.43503558	0.00361585	0.39239276
C	4.17738217	0.03011763	-0.86591278
C	5.50221127	0.04551083	-0.62798097
C	5.82829012	0.03117851	0.84199635
C	4.44254644	0.00300011	1.52692663
H	1.30118539	-0.00119077	-1.54598852
H	1.53269457	0.82455820	2.48590952
H	-0.72218674	0.80914325	1.76976606
H	4.29003310	0.86488430	2.16777960
H	6.42701971	-0.83485281	1.10135291
H	6.25790530	0.06582121	-1.39014293
H	3.72834036	0.03638850	-1.84091806
H	-0.89555252	-0.04323161	-0.61850299
H	1.55638715	-0.92408711	2.46277846
H	-0.69873035	-0.95019164	1.74774704
H	4.31435319	-0.87910591	2.14519614
H	6.40265582	0.90667264	1.12372297

E-**2**

C	4.47131946	0.00311068	1.55091532
C	3.43621628	0.00316168	0.43257401
C	4.15010574	0.02940342	-0.83811179
C	5.48071072	0.04525548	-0.63181855
C	5.84091856	0.03149687	0.82987489
C	2.08828805	-0.01733162	0.57628915
C	1.01741095	-0.01802997	-0.50982905
C	-0.31649090	-0.04703768	0.26990456
N	0.12371594	-0.05869519	1.68437401
C	1.40229273	-0.04291740	1.83544246
H	1.83910253	-0.04938215	2.81555613
H	1.10397052	-0.88369072	-1.15306162
H	-0.90694584	-0.93320119	0.08944965
H	4.34589331	0.86777778	2.19293639
H	6.44526931	-0.83431658	1.07648090
H	6.22016116	0.06553455	-1.40972120
H	3.66702590	0.03499281	-1.79611523
H	-0.52045015	-0.07760668	2.45143411
H	1.07944497	0.86645547	-1.12987643
H	-0.93221105	0.82608827	0.11174265
H	4.37023409	-0.88104166	2.17029374
H	6.42094672	0.90722879	1.09885490

References

(1) Tully, J. C. Molecular Dynamics with Electronic Transitions. *J. Chem. Phys.* **1990,** *93*, 1061-1071.
(2) Granucci, G.; Persico, M.; Zoccante, A. Including Quantum Decoherence in Surface Hopping. *J. Chem. Phys.* **2010,** *133*, 134111.
(3) Frisch, M. J.; Trucks, G. W.; Schlegel, H. B.; Scuseria, G. E.; Robb, M. A.; Cheeseman, J. R.; Scalmani, G.; Barone, V.; Mennucci, B.; Petersson, G. A., *et al. Gaussian 09*, Gaussian, Inc.: Wallingford, CT, USA, 2009.
(4) Aquilante, F.; De Vico, L.; Ferré, N.; Ghigo, G.; Malmqvist, P.-å.; Neogrády, P.; Pedersen, T. B.; Pitoňák, M.; Reiher, M.; Roos, B. O., *et al.* Molcas 7: The Next Generation. *J. Comput. Chem.* **2010,** *31*, 224-247.

CHAPTER 5

STRUCTURAL PROPERTIES AND UV/VISIBLE ABSORPTION SPECTROSCOPY OF RETINAL-PYRIDYL-CN RE(I) CARBONYL BIPYRIDINE COMPLEX: A THEORETICAL STUDY

5.1 Introduction

The rich photochemistry of rhenium complexes, spanning eight oxidation states from Re(0) to Re(VII), coupled to their ability at binding various sites such as polymers, proteins, zeolites, DNA have made these compounds very attractive for a number of applications over the last three decades [145, 146, 147, 148, 149]. Rhenium(I) α-diimine complexes are particularly appealing because of their ability to be functionalized for probing biological environments [150, 151, 152, 153, 154], triggering electron/energy transfer in proteins [155, 156, 157, 158] or light harvesting [159]. Four elementary routes are open after irradiation of these molecules in the UV/visible energy domain, namely ligand substitution, ligand isomerization, luminescence and electron transfer. The coordinated ligands as well as the environment and experimental conditions entirely control the branching ratio between these competitive processes in the first picoseconds (ps) [146, 160, 161, 162]. Whereas Re(I) complexes with bipyridine types ligands character-

ized by low-lying metal-to-ligand-charge-transfer (MLCT) states show very intense long lived emission over a wide range of energies, complexes with aromatic dyads will favor electron transfer processes by the presence of intra-ligand (IL) or ligand-to-ligand CT (LLCT) states. Re(I) complexes with isomerizable stilbene-like ligands, seat of ^{3}IL ($\pi\pi^*$) states, will play a central role in probing complex environment and conformational changes. One advantage over organic chromophores is the activation of the isomerization process by visible light. A number of experimental [163, 164, 165, 166] and theoretical [33, 34, 35, 167, 168] studies performed on rhenium(I) isomerizable complexes have shown that ultra-fast $^1\mathrm{MLCT} \rightarrow^3 \mathrm{MLCT}$ intersystem crossing (ISC) occurs within a few tens of ps. The relative position of the ^{1}IL/^{1,3}MLCT states and the ^{3}MLCT/^{3}IL energy gap determines the mechanism of isomerization and the way its quantum yield is affected by irradiation wavelength, spin-orbit coupling effects or other experimental conditions. With some specific ligands, luminescence, electron transfer and isomerization may enter into competition at a single wavelength [163, 169].

Systems composed of pyridyl-carotenoids derivatives coordinated to Re(I) and Pt(II) complexes have been synthesized and characterized by Rillema *et al.* [170] in order to exploit the light-harvesting properties of these organic compounds when linked to metal fragments. In particular, a all-trans-retinal-pyridyl-CN Re(I) tricarbonyl bipyridine complex $[Re(CO)_3(bpy)(ret\text{-}pyr\text{-}CN)]^+$(bpy = 2,2'-bipyridine; ret-pyr-CN = pyridyl-CN-3,7-dimethyl-9-(2,6,6-trimethylcyclohex-2-en)-none-(2,4,6,8-tetraen)) has been obtained and a comparison between the UV-visible absorption properties of the isolated organic chromophore and those of the inorganic one has been proposed.

In our quest to understand the mechanism of isomerization processes in organic (see CHAPTER 3 and CHAPTER 4 of the thesis and related papers) and inorganic chromophores [33, 34, 35, 167, 168] we propose a complete investigation of the structural properties of the various Re(I) isomers generated by the retinal-like ligand. A theoretical analysis of the absorption spectra of both the organic and inorganic chromophores completes this study. The next section is dedicated to the computational details whereas the results are presented and discussed in the second section.

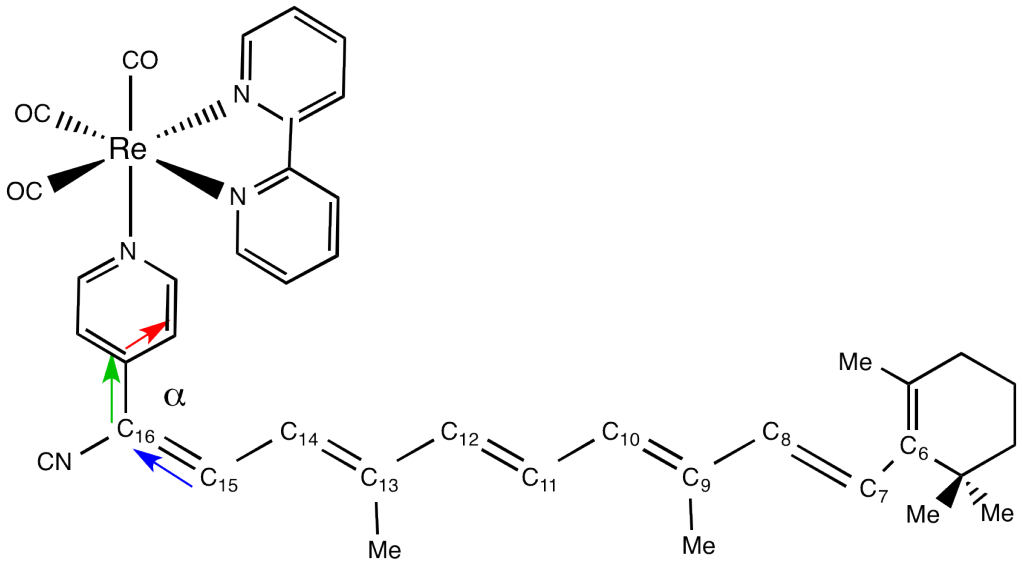

Figure 5.1: Definition of the α dihedral angle in $[Re(CO)_3(bpy)(L)]^+$ (L = Ret-pyr-CN).

5.2 Computational details

The structures of the all-*trans* conformer **a** and of the lowest *cis*-conformer **1c** (FIG. 5.2) and **2c**-**5c** (APPENDIX) of $[Re(CO)_3(bpy)(L)]^+$ (L = Ret-pyr-CN) (FIG. 5.2) have been optimized in the electronic ground state in vacuum in C_1 symmetry at the density functional theory (DFT) level using GGA PBE functional [171], including dispersion correction by Grimme [172], and with triple-ζ basis sets [173]. Five *cis* structures, generated by modifying the torsion angle around one double C=C bond at a time starting from the all-*trans* geometry, have been fully optimized. For **a** all-*trans* and **1c** *cis* structures, two additional conformers **a**-α_{opt} and **1c**-α_{opt} have been optimized by relaxing the dihedral angle α between the planes of the pyridine and retinal-CN (FIG. 5.1).

The scalar relativistic effects are taken into account within the zero-order regular approximation (ZORA) [55]. The SOC effects are introduced according to a simplified relativistic perturbational TD-DFT formalism [174, 175]. The low-lying singlet and triplet states have been calculated by means of time-dependent-DFT (TD-DFT) method using B3LYP functional [176, 177] for the lowest 80 roots. Because of the presence of low IL states, Tam-Dancoff approximation (TDA) [178] has been used for avoiding an overstabilization of the ^{3}IL state. Our tentative to calculate and correct LLCT transition energies of eventual long-range errors with the CAM-B3LYP functional [179] has failed due to technical problems. However according to our experience the performance of this functional

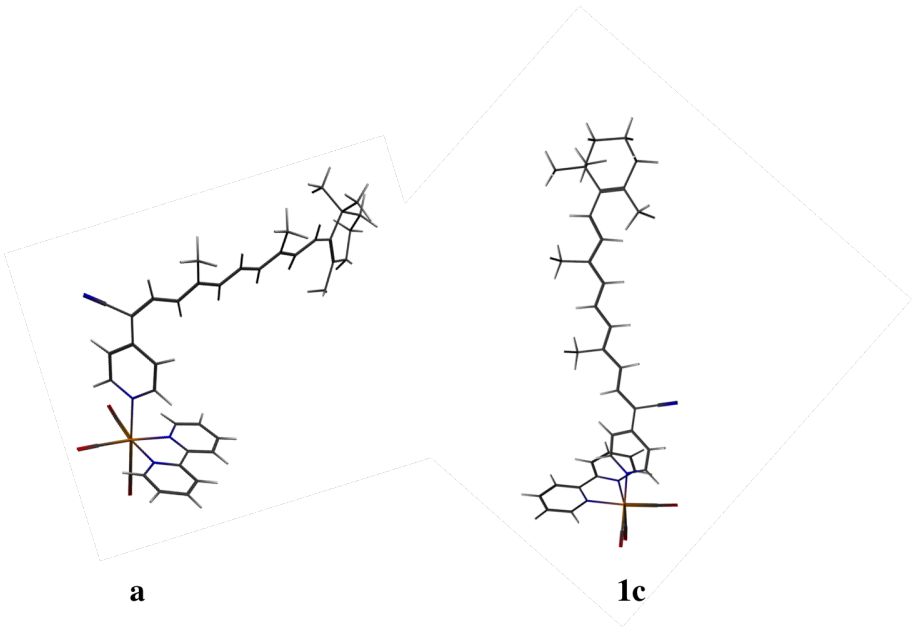

Figure 5.2: DFT optimized geometries of all-*trans*-$[Re(CO)_3(bpy)(L)]^+$ **a** ($\alpha = 8.6°$) and *cis*-$[Re(CO)_3(bpy)(L)]^+$ most stable conformer **1c** ($\alpha = 8.6°$).

for calculating transition energies of MLCT states with reasonable accuracy in this class of transition metal complexes is very poor and generally gives unrealistic blue shifted absorption spectra [180, 181]. The absorption spectra have been calculated in acetonitrile. The solvent correction is based on the conductor-like screening model (COSMO) [182, 183, 184] (with $\epsilon = 3664$ for acetonitrile) as implemented in ADF [185, 186]. The *trans-cis* isomerization potential energy profiles describing the all-*trans* conformer **a** to the *cis* structures **1c**-**5c** of $[Re(CO)_3(bpy)(L)]^+$ pathways have been estimated in acetonitrile by single point TD-DFT calculations performed on the optimized all-*trans*, *cis* and perpendicular structures (torsion angle of $90°$ around the relevant CC double bond) for the electronic ground state and the low-lying singlet and triplet excited states. This qualitative approach, that concentrates on one specific pathway only, suffers from two severe approximations: i) the neglect of other conformers that could influence the energy profiles opening the route to other isomerization channels; ii) the disregard of the excited state corresponding to the double $\pi\pi^*$ excitation. A dynamical study describing the nuclear flexibility of the retinal ligand is beyond the scope of the present investigation whereas the choice of the method (TD-DFT), dictated by the size of the system, eliminates factually the computation of the doubly excited state. Moreover current theoretical studies reported on the organic chromophore neglect the role of this state in the isomer-

ization process even though it is supposed to generate a small energy barrier for a torsion angle of $60°$ [139].
The calculations have been performed with ADF-2013 quantum chemistry softwares [187] and the electronic transitions have been analyzed with the Dgrid package [129].

5.3 Results and discussion

5.3.1 Structures and electronic ground state properties

The optimized geometries of the $[Re(CO)_3(bpy)(L)]^+$ (L = Ret-pyr-CN) all-*trans* conformers **a** ($\alpha = 8.6°$) and the *cis* conformer **1c** ($\alpha = 8.6°$) are represented in FIG. 5.2. Whereas some important bond lengths and bond angles of the **a** and **a**-α_{opt}, **1c**, **1c**-α_{opt} and **2c** to **5c** conformers are reported in TAB. 5.1. The Cartesian coordinates of the fully optimized geometries are reported in APPENDIX A.1. The electronic ground state of all-*trans*-$[Re(CO)_3(bpy)(L)]^+$ **a** is characterized by the sequence of Kohn-Sham (KS) orbitals depicted in FIG. 5.3. The low lying excited-states will be generated within this set of KS orbitals. The HOMO and HOMO-1 are both mainly localized on the ret-pyr-CN ligand with a small metal contribution in HOMO-1, whereas HOMO-2, HOMO-3 and HOMO-4 are essentially metal centred and very close in energy. The LUMO and LUMO+1 are localized on the $\pi^*_{ret-pyr-CN}$ and π^*_{bpy}, respectively. The LUMO+2 corresponds to a $\pi^*_{ret-pyr-CN}$ but is characterized by a delocalization over the pyridyl group in contrast to the LUMO which is mainly localized on the retinal. LUMO+3 and LUMO+4 correspond to π^*_{bpy} and are nearly degenerate with LUMO+2. Metal orbitals contribute essentially to higher vacant orbitals (not shown here). From the qualitative picture depicted in FIG. 5.3 we may anticipate the presence of low-lying IL excited states localized on the ret-pyr-CN ligand and of MLCT states corresponding to charge transfer to the ret-pyr-CN and bpy ligands. Metal-centred (MC) states should not contribute to the absorption spectra, as expected for this class of third row transition metal complexes. The possibility of low-lying LLCT states calls for methodological questions, devoted especially to long-range charge transfer states. However in the absence of benchmark for the complex of interest, the presence of LLCT states in the absorption spectra will have to be considered with care. The electronic configurations of the *cis* conformers are not very different (APPENDIX A.2). In **1c** for instance, the KS orbitals of which are depicted in FIG. 5.4, both HOMO and

	a	**a-α_{opt}**	**1c**	**1c-α_{opt}**	**2c**	**3c**	**4c**	**5c**
$Re-N_{bpy}$	2.182	2.181	2.183	2.184	2.182	2.181	2.182	2.182
$Re-CO_{ax}$	1.939	1.939	1.940	1.939	1.940	1.939	1.940	1.939
$Re-CO_{eq}$	1.926	1.928	1.925	1.926	1.927	1.928	1.927	1.925
$Re-N_{ret}$	2.225	2.219	2.224	2.220	2.223	2.223	2.224	2.227
$N_{bpy}ReN_{ret}$	88.5	84.0	86.7	87.6	87.9	87.8	88.3	89.0
$CO_{ax}ReCO_{eq}$	89.4	90.1	89.8	89.8	89.5	89.5	89.4	89.1
$CO_{eq}ReCO_{eq}$	90.6	90.9	90.7	90.6	90.6	90.5	90.6	90.7
$CN-C_{16}$	1.425	1.425	1.424	1.425	1.427	1.426	1.426	1.425
$C_{16}-C_{15}$	1.396	1.397	1.397	1.396	1.395	1.397	1.396	1.407
$C_{15}-C_{14}$	1.406	1.404	1.400	1.400	1.406	1.405	1.406	1.396
$C_{14}-C_{13}$	1.397	1.398	1.398	1.398	1.401	1.401	1.397	1.396
$C_{13}-C_{12}$	1.422	1.420	1.419	1.419	1.420	1.425	1.424	1.423
$C_{12}-C_{11}$	1.382	1.383	1.384	1.383	1.383	1.391	1.380	1.381
$C_{11}-C_{10}$	1.412	1.410	1.410	1.410	1.412	1.414	1.414	1.413
$C_{10}-C_{9}$	1.390	1.390	1.391	1.391	1.390	1.392	1.392	1.390
$C_{9}-C_{8}$	1.434	1.433	1.433	1.433	1.434	1.434	1.435	1.441
$C_{8}-C_{7}$	1.372	1.372	1.373	1.372	1.372	1.372	1.369	1.369
$C_{7}-C_{6}$	1.450	1.449	1.449	1.449	1.449	1.450	1.453	1.465
$C_{sp2}-Me$	1.506	1.506	1.505	1.506	1.506	1.506	1.508	1.504
$C_{sp3}-Me$	1.545	1.545	1.544	1.545	1.544	1.545	1.545	1.545

Table 5.1: DFT optimized important bond lengths (in Å) and bond angles (in °) of all-*trans*-$[Re(CO)_3(bpy)(L)]^+$ **a** ($\alpha = 8.6°$), **a-α_{opt}** ($\alpha = 22.5°$), of *cis*-$[Re(CO)_3(bpy)(L)]^+$ **1c** ($\alpha = 8.6°$), **1c-α_{opt}** ($\alpha = 1.8°$) to **5c**. (Numbering of atoms according to FIG. 5.1)

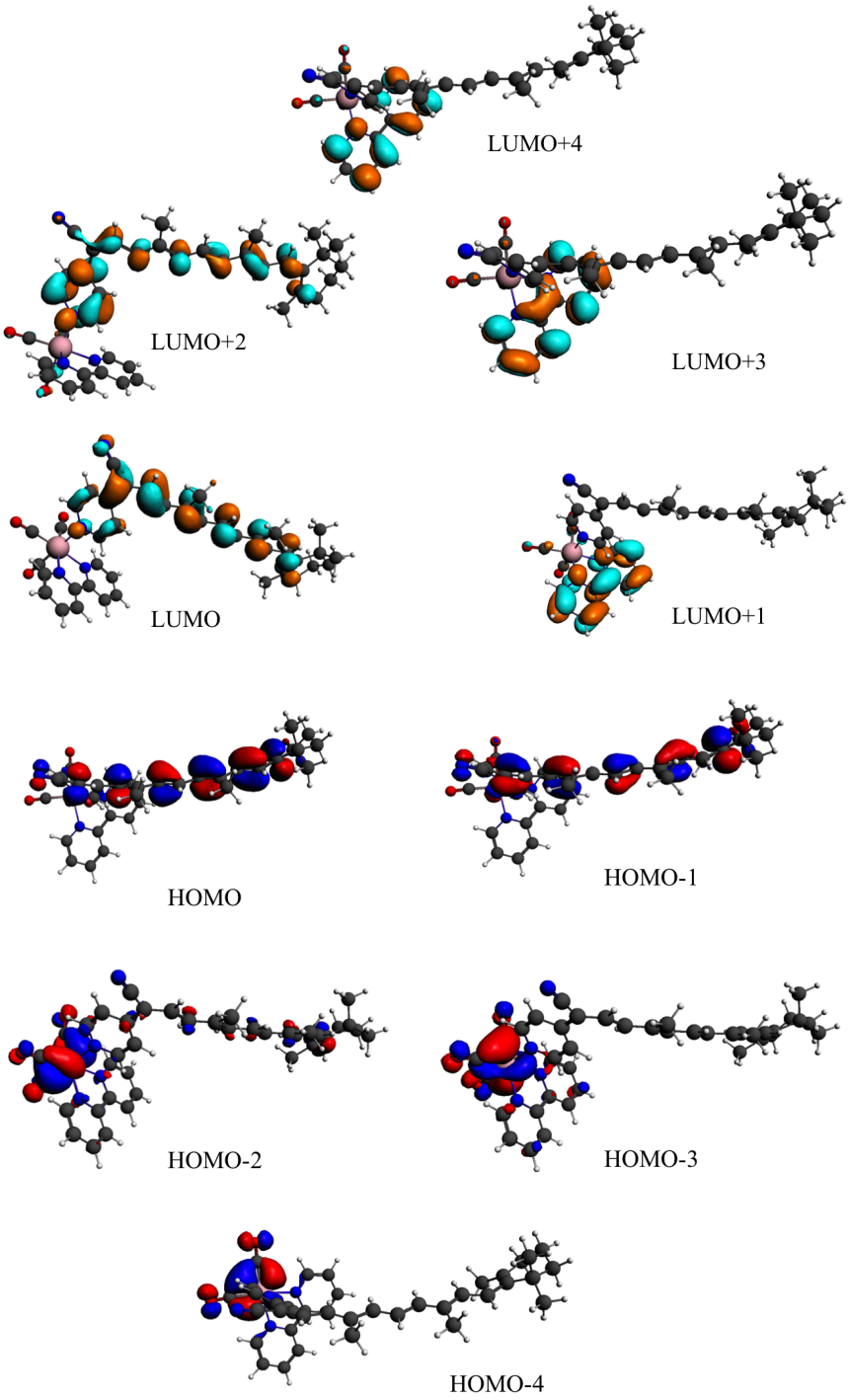

Figure 5.3: Kohn-Sham orbitals of all-**trans**-$[Re(CO)_3(bpy)(L)]^+$ **a** conformer in acetonitrile.

HOMO-1 are localized on $\pi_{\mathrm{ret-pyr-CN}}$, the HOMO-2, HOMO-3 and HOMO-4 being localized on the metal center. The position of the LUMO+2 and LUMO+3 is inverted when going from the all-*trans* **a** to the **1c** *cis* conformer but the original relative order is kept in the other *cis* conformers **2c**-**5c** (APPENDIX A.2). In all conformers we may distinguish two low-lying π^* orbitals entirely localized of the ret-pyr-CN ligand, the upper one being delocalized on the pyridyl moiety. The presence of these two different π^*_{ret} orbitals (LUMO and LUMO+2 in **a**, FIG. 5.3) will have important consequences for potential applications by irradiataion of the complex in the visible energy domain (400-450 nm) as illustrated in the section dedicated to the absorption spectroscopy.
The similitude between the electronic configurations of all-*trans* and *cis*-conformers should facilitate the correlation between the low-lying excited states of the different isomers.

As illustrated by the optimized geometrical parameters reported in TAB. 5.1 the global structures of the investigated conformers are very similar with no perturbation of the sphere of coordination of the central Re(I) metal atom from one conformer to the others. The bond lengths and bond angles are not affected by the optimization of the angle α in **a** and **1c**. The single/double bonds lengths variations in the retinal sequence are given in FIG. 5.5 for the all-*trans* **a** conformer and the five *cis* conformers **1c** to **5c**. The sequence of carbon-carbon bonds, numbered according to FIG. 5.1, alternates benzene-like/allene-like bond lengths until the second carbon ($\mathrm{C_9}$) substituted by a methyl group. Then the single/double bond character is more pronounced until $\mathrm{C_6}$ and especially for the conformer **5c** corresponding to the $\mathrm{C_7-C_8}$ double bond isomerization. The $\mathrm{C_{sp2}-Methyl}$ and $\mathrm{C_{sp3}-Methyl}$ bond lengths of the terminal cyclohexen are in the range of the usual $\mathrm{C_{sp3}-C_{sp3}}$ (1.54 Å) and $\mathrm{C_{sp3}-C_{sp2}}$ (1.50 Å) bond lengths. The relative energies of the five investigated *cis*-$[\mathrm{Re(CO)_3(bpy)(L)}]^+$ conformers **1c**-**5c, 1c-$\alpha_{\mathbf{opt}}$** are reported in TAB. 5.2 and compared to those of the all-*trans* **a** and **a-$\alpha_{\mathbf{opt}}$**.

For all conformers reported in TAB. 5.2 the dihedral angle α (FIG. 5.1) has been kept to $8.6°$, value obtained after geometry optimization in the electronic ground state of the all-*trans* conformer **a**. When α is relaxed in **a** to give the **a-$\alpha_{\mathbf{opt}}$** conformer its value increases to $22°$ and the all-*trans* conformer is stabilized by 22.2 kJ.mol^{-1} due to decrease of steric interactions between the retinal-CN and the bipyridine ligands. The relaxation of the dihedral angle α is less dramatic in the **1c** *cis* conformer with a minor stabilization of 8.7 kJ.mol^{-1} corresponding to a value of α of $1.8°$ in **1c-$\alpha_{\mathbf{opt}}$**. Indeed, the steric effects are less important in the *cis* conformers. According to the results reported in TAB. 5.2 the

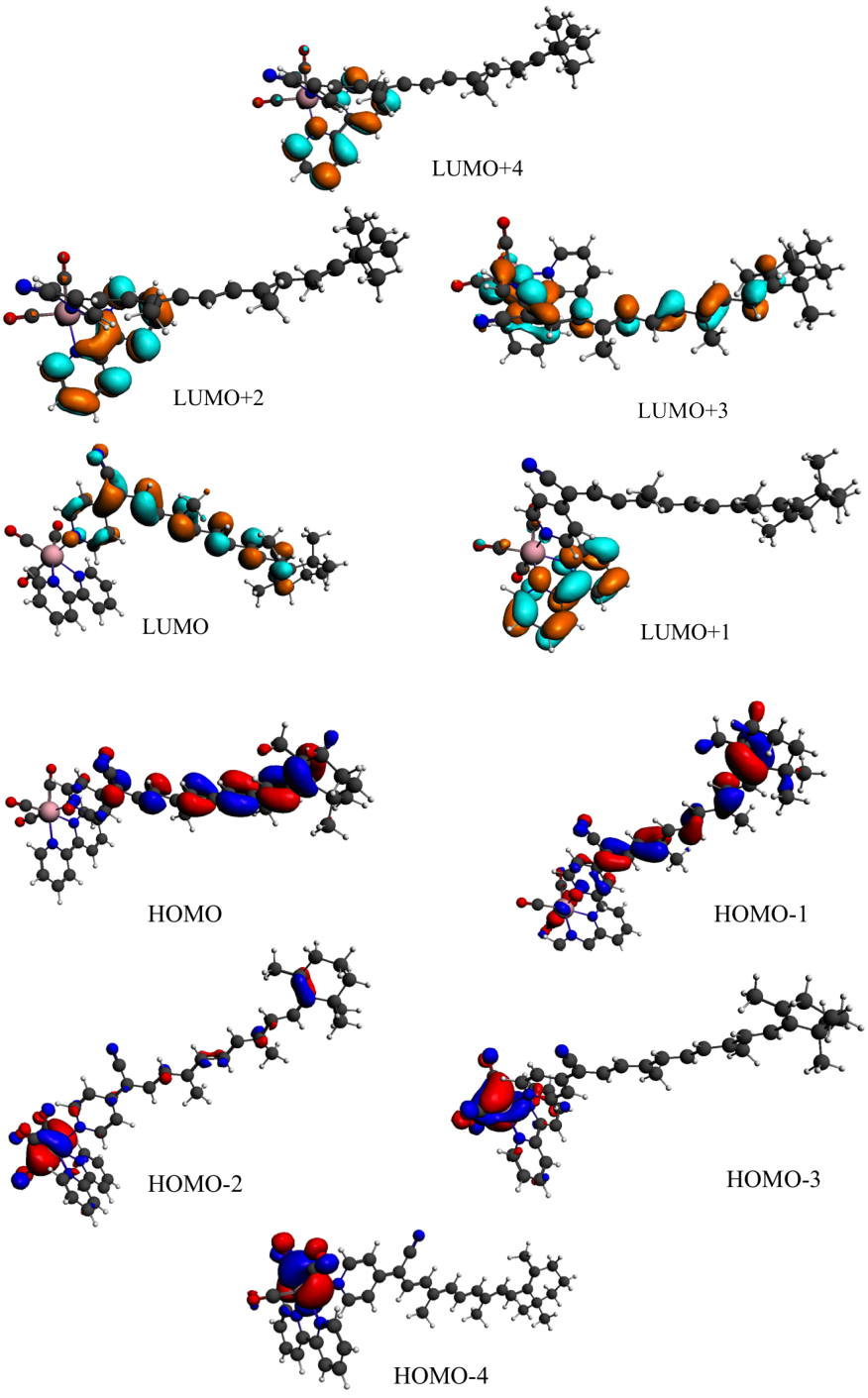

Figure 5.4: Kohn-Sham orbitals of **cis**-$[Re(CO)_3(bpy)(L)]^+$ **1c** conformer in acetonitrile.

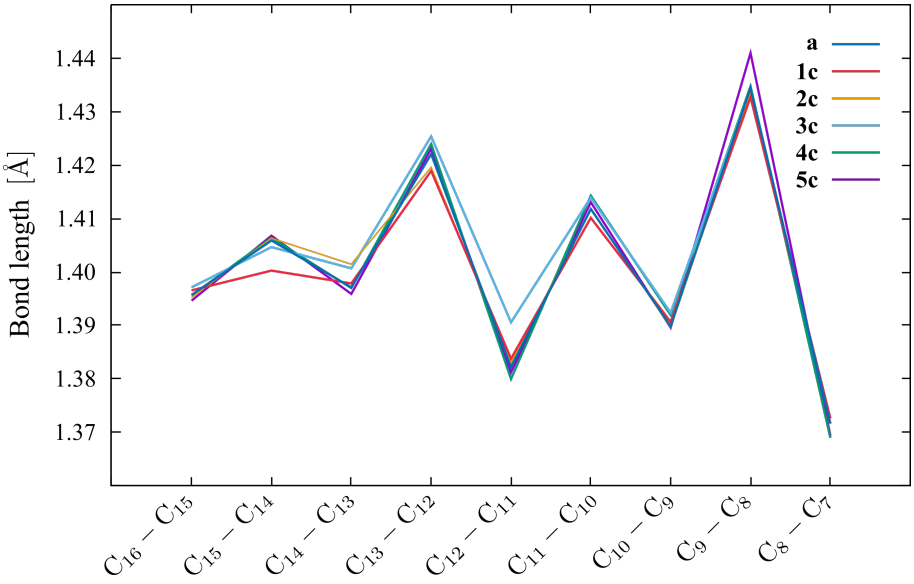

Figure 5.5: Single/double bonds lengths sequence (in Å) in the retinal-CN ligand for the all-*trans* **a** and the *cis* conformers **1c** to **5c**.

	ΔE (in kJ.mol^{-1})	ΔE (in eV)	ΔE (in cm^{-1})
a	30.9	0.32	2581
a-α_{opt}	8.7	0.09	726
1c	8.7	0.09	726
1c-α_{opt}	0.0	0.00	0
2c	32.8	0.34	2742
3c	51.1	0.53	4275
4c	34.7	0.36	2904
5c	54.0	0.56	4517

Table 5.2: Relative energies (in kJ.mol^{-1}, in eV and cm^{-1}) of the *cis*- and *trans*-[Re(CO)$_3$(bpy)(L)]$^+$ conformers.

all-*trans* and the lowest *cis* conformers are nearly degenerate. The other *cis* conformers are destabilized with respect to the most stable isomers by about 30-50 kJ.mol^{-1}. Interestingly, the *cis* **3c**, **5c** isomers corresponding to a torsion of the C=C bonds non-substituted by a methyl group, namely the central one ($C_{11} - C_{12}$) and the external one linked to the tri-methyl cyclohexen ($C_8 - C_7$) range in the same energy, namely ≈50 kJ.mol^{-1} (0.5 eV) above the most stable isomers. The *cis* isomers **2c** and **4c** corresponding to a torsion of the C=C bonds substituted by a methyl group ($C_{13} - C_{14}$ and $C_9 - C_{10}$) are more stable by about 20 kJ.mol^{-1} (or 0.2 eV) ranging at ≈30 kJ.mol^{-1} (or 0.3 eV) above the all-*trans* and *cis* **1c** isomers.

In order to get a qualitative picture of the *trans* to *cis* pathway the state correlation diagrams describing the all-*trans* [Re(CO)$_3$(bpy)(L)]$^+$ **a** to the *cis* **1c**, **2c**, **4c** isomerizations and associated to the electronic ground state and the two low-lying singlet and triplet excited states are presented in the next section. The solvent correction (acetonitrile) has been taken into account.

5.3.2 States correlation diagrams

The TD-DFT states correlation diagrams associated to the electronic ground state and to the low-lying singlet and triplet excited states of [Re(CO)$_3$(bpy)(L)]$^+$ and calculated as function of the torsion angle τ of the isomerizable C=C double bond are represented in FIG. 5.6 for the all-*trans* **a** to **1c** and in APPENDIX A.5 for the all-*trans* **a** to **2c**, **4c** isomerization pathways leading to the three most stable *cis* isomers.

Because of the crude approximation used in the computation of the potential energy profiles that does not reflect the collective torsion motion characterizing the retinal chromophore [188, 189] a comparison between the Re(I) complex and the isolated chromophore is not straightforward. The energy barrier for a single isomerization in isolated retinal has been recently measured at 0.64 eV ± 0.05 eV) [190]. The electronic ground state pathway to the **1c** and **2c** conformers is characterized by an energy barrier upper limit of 1.09 eV while a value of 1.42 eV is calculated for the isomerization to the **4c** conformer. Search for a true transition state at the perpendicular conformation ($\tau = 90°$) would certainly lower these estimated values.

All the excited electronic states correlated in FIG. 5.6 are potentially populated upon irradiation of all-*trans*-[Re(CO)$_3$(bpy)(L)]$^+$ **a** by visible light (400-450 nm), either directly by absorption (b^1IL_{ret}, c^1IL_{ret}, a^1MLCT_{ret}) or indirectly by internal conversion or

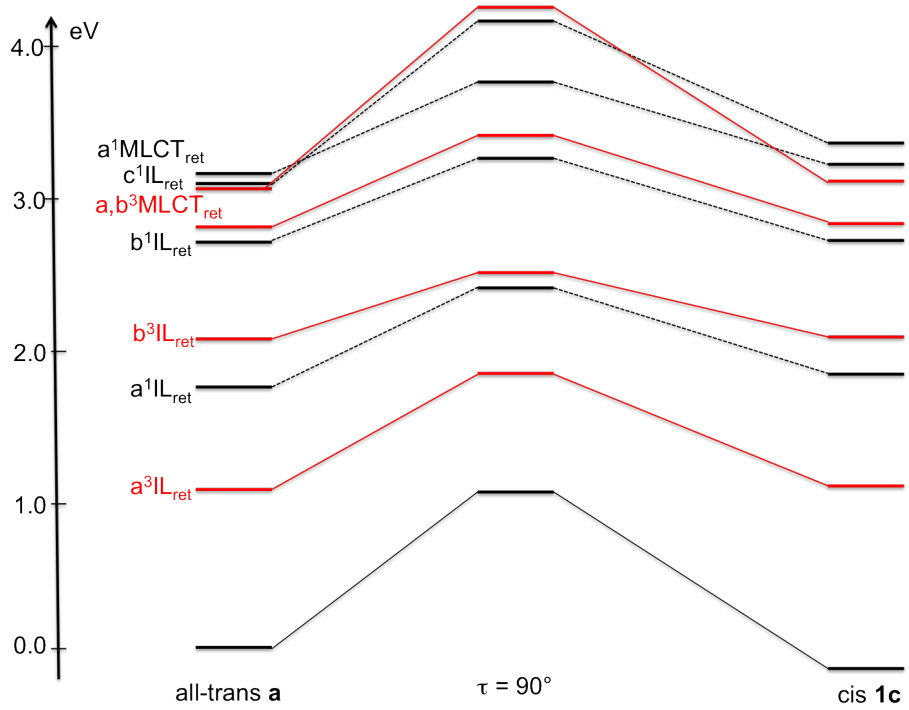

Figure 5.6: TD-DFT states correlation diagrams connecting the low-lying singlet and triplet excited states of all-*trans* $[Re(CO)_3(bpy)(L)]^+$ **a** to the corresponding states of the *cis* **1c** isomer. (energies are reported in APPENDIX TAB. A.12.)

intersystem crossing ($\mathrm{a}^3\mathrm{IL}_{\mathrm{ret}}$, $\mathrm{b}^3\mathrm{IL}_{\mathrm{ret}}$, $\mathrm{a}^1\mathrm{IL}_{\mathrm{ret}}$). All these states will play a key role in the complicated photophysics at the early stage (a few ps) and in the mechanism of the photo-induced isomerization process. The upper electronic states, initially populated, are characterized by too high-energy barriers for participating to the isomerization and will probably decay within the first ps to the three lowest $\mathrm{IL}_{\mathrm{ret}}$ states. Isomerization may proceed along the potential energy surfaces associated to these three excited states. However owning the low energy profile along the torsion angle τ also decay back to the all-*trans* electronic ground state. The high energy of the MLCT states excludes them of the mechanism, in contrast to what has been found for stilbene-like substituted Re(I) carbonyl bpy complexes [33, 34, 35]. Consequently, competitive luminescent channels are unlikely. From the relative stabilities of the *cis* conformers and states correlation diagrams depicted in FIG. 5.6 we may conclude that the all-*trans* **a** to **1c** and **2c** *cis* conformers isomerization pathways occurring at the $\mathrm{C}_{16}\mathrm{C}_{15}$ and $\mathrm{C}_{14}\mathrm{C}_{13}$ double bonds close to the [$\mathrm{Re(CO)_3(bpy)}$] fragment (FIG. 5.1) are more favorable. However no further conclusion can be achieved at this qualitative level of analysis that has to be completed by forthcoming experimental data.

5.3.3 TD-DFT absorption spectra

The transition energies to the low-lying singlet excited states of all-*trans*-$[\mathrm{Re(CO)_3(bpy)(L)}]^+$ **a** and *cis* **1c** conformers in acetonitrile are reported in TAB. 5.3 together with the wavelengths of absorption, oscillator strengths and one electron excitations in the main configuration. The corresponding data obtained for the *cis* conformers **2c**-**5c** are reported in APPENDIX A.2. The calculated absorption spectra are depicted in FIG. 5.7 and FIG. 5.8 for the all-*trans* **a** and *cis* **1c**-**5c** conformers, respectively. The visible absorption starts at about 700 nm for all conformers. Both conformers, namely the all-*trans* **a** and the *cis* **1c**, corresponding to the *trans-cis* isomerization at the $\mathrm{C}_{15} - \mathrm{C}_{16}$ double bond of **a**, are characterized by similar TD-DFT absorption spectra exhibiting one very intense peak at about 700 nm associated to the $\mathrm{IL}_{\mathrm{ret}}$ transition corresponding to HOMO$\rightarrow$LUMO excitation and localized on the retinal part of ret-pyr-CN ligand. The next visible band is calculated at 450 nm and corresponds to another IL transition corresponding to HOMO-1$\rightarrow$LUMO excitation. The HOMO-1 being slightly delocalized over the metal, the associated oscillator strength is weaker. Both conformers exhibit $\mathrm{LLCT}_{\mathrm{ret}\rightarrow\mathrm{bpy}}/\mathrm{MLCT}_{\mathrm{bpy}}$ mixed states at 415 nm with a rather small oscillator strength (0.01). The LLCT contributions has to

Conformer	State Character	One-electron excitation	ΔE [eV]	Absorption wavelengths [nm]	f
All-*trans* **a**	IL_{ret}	$\pi_{ret} \rightarrow \pi^*_{ret}$	1.79	692	2.67
	IL_{ret}	$\pi_{ret} \rightarrow \pi^*_{ret}$	2.78	450	0.36
	$LLCT_{ret\rightarrow bpy}$	61% $\pi_{ret} \rightarrow \pi^*_{bpy}$	3.01	415	0.01
	$MLCT_{bpy}$	37% $5d_{Re} \rightarrow \pi^*_{bpy}$			
	IL_{ret}	$\pi_{ret} \rightarrow \pi^*_{ret}$	3.10	403	0.49
	$MLCT_{ret}$	$5d_{Re} \rightarrow \pi^*_{ret}$	3.15	396	0.16
	$MLCT_{bpy}$	$5d_{Re} \rightarrow \pi^*_{bpy}$	3.31	378	0.09
Cis **1c**	IL_{ret}	$\pi_{ret} \rightarrow \pi^*_{ret}$	1.75	714	3.13
	IL_{ret}	$\pi_{ret} \rightarrow \pi^*_{ret}$	2.76	450	0.26
	$LLCT_{ret\rightarrow bpy}$	61% $\pi_{ret} \rightarrow \pi^*_{bpy}$	3.01	415	0.01
	$MLCT_{bpy}$	35% $5d_{Re} \rightarrow \pi^*_{bpy}$			
	$MLCT_{ret}$	$5d_{Re} \rightarrow \pi^*_{ret}$	3.13	399	0.07
	$MLCT_{ret}$	$5d_{Re} \rightarrow \pi^*_{ret}$	3.21	389	0.01
	IL_{ret}	$\pi_{ret} \rightarrow \pi^*_{ret}$	3.22	388	0.01
	$MLCT_{bpy}$	$5d_{Re} \rightarrow \pi^*_{bpy}$	3.31	377	0.13

Table 5.3: TD-DFT transition energies (in eV), wavelength of absorption (in nm) and oscillator strengths f associated to the low-lying singlet excited states of all-*trans*-$[Re(CO)_3(bpy)(L)]^+$ **a** and *cis* **1c** confomers in acetonitrile.

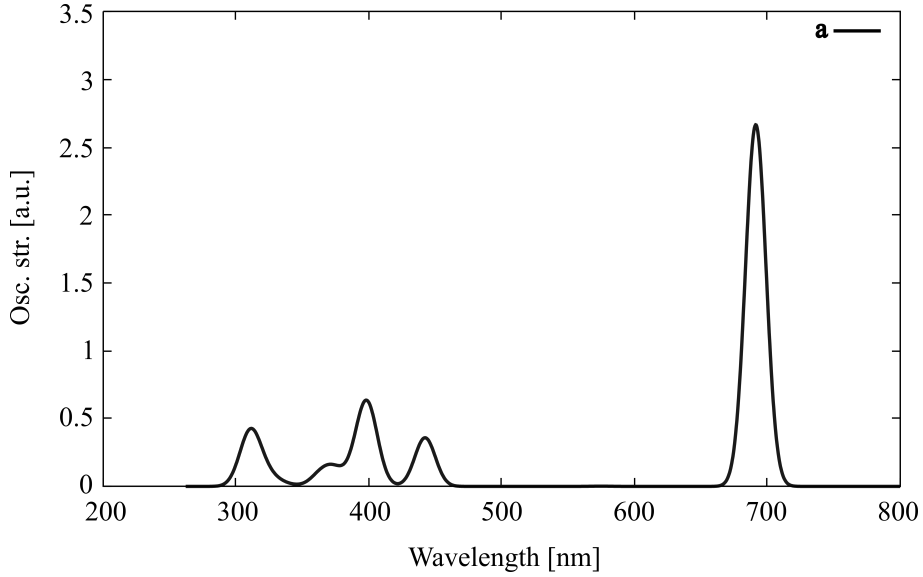

Figure 5.7: Absorption spectrum of the **a** conformer in acetonitrile.

be taken with care because of the possible underestimation of their transition energy due to erroneous treatment of long-range charge transfer interactions by B3LYP. Owning to their low oscillator strengths, these states should not participate to the photochemistry of $[Re(CO)_3(bpy)(L)]^+$.

The experimental absorption spectra of the isolated chromophore ret-pyr-CN and of the all-trans $[Re(CO)_3(bpy)(L)]^+$ conformer recorded in acetonitrile exhibit a band attributed to an IL_{ret} state at 440 nm and 464 nm, respectively [170]. These maxima are also present in the TD-DFT theoretical spectra of the all-*trans* **a** (FIG. 5.7) and **1c**-**5c** *cis* (FIG. 5.8) conformers and are indeed assigned to the second $^1IL_{ret}$ transition. This band which could play a key role after absorption at 400 nm, the usual wavelength of irradiation of Re(I) complexes, does not correspond to the HOMO-LUMO $\pi\pi^*$ excitation purely localized on the ret-pyr-CN and calculated here at 692 nm in the all-*trans* conformer **a**, transition that gives rise to a very intense peak and is probably solvatochromic as reported for a number of retinal models in various environments including proteins [191]. The lowest MLCT states correspond to charge transfer to the ret-pyr-CN ligand and are calculated above 400 nm with modest oscillator strengths as compared to the IL_{ret} states. The potentially luminescent MLCT states delocalized over the bpy ligand start at about 375 nm and will be hardly accessible by absorption in the visible energy domain.

Two low-lying triplet $^3IL_{ret}$ excited states, corresponding to the two lowest $^1IL_{ret}$ reported in TAB. 5.3, are calculated at 1.13 eV and 2.10 eV in the all-*trans* conformer **a** and at 1.09 eV and 2.06 eV in the most stable **1c** *cis* conformer. They will potentially play a key role in isomerization processes activated after absorption at 400 nm to the second $^1IL_{ret}$ state.

Finally the TD-DFT absorption spectra of the five *cis* conformers **1c**-**5c** represented in FIG. 5.8 are rather similar. We observe a significant red shift of the lowest band from **5c** (670 nm) to the most stable *cis* conformer **1c** (710 nm) due to a decrease in HOMO-LUMO energy gap. The band around 450 nm that corresponds to the second b^1IL_{ret} transition is stable within the series. The upper UV intense band gains in intensity and is slightly blue shifted in the conformer **4c** (300 nm) as compared to the other *cis* conformers (310 nm) due to a change of character from IL_{bpy} (in **1c**, **2c**, **3c** and **5c**) to IL_{ret} in **4c**.

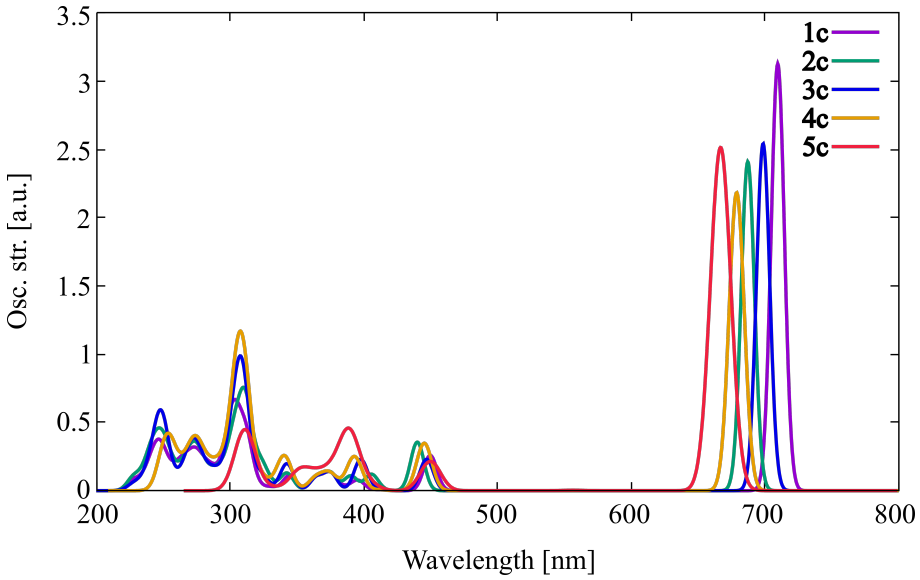

Figure 5.8: Absorption spectra of the *cis* **1c**-**5c** conformers in acetonitrile.

5.4 Conclusion

The molecular structure, electronic and optical properties of the all-*trans* and various *cis* conformers of $[Re(CO)_3(bpy)(L)]^+$ have been studied by means of DFT and TD-DFT with the aim of investigating the potential of this molecule, not yet deeply considered experimentally for photoswitches applications. Several isomerization pathways will be open upon irradiation by visible light (400-450 nm), especially to two *cis* conformers corresponding to the isomerization of the two double bonds of the retinal-like ligand close to the pyridyl group linked to the Re(I) fragment. Whereas the MLCT states localized either on the retinal group or on the bpy ligand should play a minor role in the absorption, two low-lying IL states, calculated at 450 nm and 400 nm and localized on the retinal entity can be populated efficiently. Ultra-fast decay within the first ps is expected to lead to the lowest ^{3}IL states from which isomerization may proceed. However, while these channels are unlikely quenched by luminescence processes because of the high energy of the MLCT states, their efficiency could drop by decay back to the all-*trans* electronic ground state leading to modest quantum yield. It would be hazardous to push the analysis further at this qualitative level of consideration. Indeed upcoming experimental data should complete our analysis before undertaking more quantitative investigations based on accurate potential energy surfaces associated to the key electronic states put in evidence in present study.

PART C

Intersystem Crossing Processes

CHAPTER 6

ULTRA-FAST INTERSYSTEM CROSSING PROCESSES IN RE(I) COMPLEXES

6.1 Introduction

We have seen in Chapter 3, that internal crossings (IC) play a keyrole in photochemistry and photobiology through conical intersections or more generally vibronic coupling. However IC is not the only process involving coupling between electronic states. Radiationless transition between two electronic states of different spin multiplicity, so called intersystem crossing (ISC) are at the heart of phototherapy methods where the generation of triplet states is necessary to induced oxidation of DNA by intercalated photosensitizers. This oxidation induces cell death and is used to treat cancerous cells. Moreover combustion reactions involve open-shell electronic configurations, principally oxygen [192], as well as many radicals. ISC will then play a central role in these chemical reactions.
ISC are very important in photophysics and lead to a number of applications. Indeed, the change of spin makes these processes involved in light-induced magnetism, magnetic storage, where the spin multiplicity acts as a binary system to encode data, or even in artificial photo—synthesis, organic light emitting devices and other light to electric energy (and vice-versa) conversion devices.
The importance of ISC processes in these various phenomena makes its interpretation and modelisation mandatory. The experimental estimation of the rate of ISC in simple molecules, that is to say, small molecules where the absorbing state is the first singlet state, can be performed using only fluorescence spectroscopy [193],[194]. However,

for larger and more complex systems, this method proves to be insufficient and studies based on time-resolved spectroscopy are needed. Transition metal complexes have been extensively studied especially by means of transient absorption spectroscopy and time-resolved luminescence methods [195],[3]. It has been found that ISC, even if thought as spin-forbidden and by such considered as slow processes, can occur on a large range of time-scale going from 30 fs [196],[197] up to nearly 800 ps [198]. The observation of short time-scales implies that ISC can compete not only with fluorescence, but also with IC, and is thus a process that one has to take into account in the theoretical studies.

ISC is linked to the coupling between two electronic states of different spin multiplicities. Therefore, one would think that for heavy elements, as the relativistic effects are more important, the ISC characteristic times should decrease as the SOC increase. However, it has been observed that this is not always the case [195].

In order to interpret this conterintuitive behaviour, theoretical studies may prove to be a useful complement to experiments. Several methods exist depending on the system that is treated. If the crossing point between the two electronic states of different spin multiplicities is closed to the FC region, then using the Landau-Zener theory [199],[200],[201] or the Fermi's golden rule [202],[203] may give good results. However if the FC region is far from the crossing seam, then a nuclear dynamics approach is more appropriate. It has been mentioned in CHAPTER 3 that SC dynamics are largely used to treat non-adiabatic problems involving regions of close-lying states. However these methods must be adapted by taking into account the SOC between electronic states of different spin multiplicities and not only the non-adiabatic coupling in the singlet manifold. Recent strategies are developed essentially according to two approaches: (1) The Persico-Grannuci surface hopping algorithm [204] where SOC is explicitly taken into account and applied with success to the acetone photodissociation [205] and the 6-thioguanine deexcitation [206] and (2) the SHARC methodology [207, 208, 209] which allows to include arbitrary coupling and perturbation to the SC dynamics; to study the deexcitation of cytosine, for instance [210]. These approaches are effective for medium-sized molecules but need a statistically relevant number of trajectories to be performed in order to estimate branching ratios and kinetics. Moreover, as it is mandatory to use highly accurate quantum chemical methods to properly describe the photophysics of molecules, these methods cannot pretend to be able to treat large systems such as transition metal complexes. In addition, the SC dynamics methods does not account for quantum effects.

As we have seen in the first part of the thesis, another way to study the photodynamics

is to propagate a quantum wavepacket on potential energy surfaces computed from *ab initio* calculations. Nevertheless, this methods has several drawbacks, as potential energy surfaces are fastidious to build and their complexity grows with the dimensionality of the problem, both electronic and nuclear. An alternative is to develop model Hamiltonians restricted to a few degrees of electronic and nuclear freedom. This is the aim of the present work reported in this section. Our model diabatic model Hamiltonian will have to contain not only vibronic coupling between states of the same spin multiplicity, but also SOC allowing ISC. As we have seen in CHAPTER 3, building PESs is a huge task even if we consider only three electronic states. This is why we choose to express the diabatic states as well as the coupling terms by a Taylor expansion in the model Hamiltonian. Depending on the accuracy required, we will be able to build the Hamiltonian on the basis of a limited number of electronic structure data.

In the present work, our model Hamiltonian will be tested on a [Re(X(CO)$_3$(bpy)] (bpy = 2',2-bipyridine, X=F, X=Cl, X=Br, X=I) complex [3]. It has been observed experimentally that, counter-intuitively, the speed of deexcitation decreases going from X=Cl to X=I. Indeed, one would think that SOC increases with the mass of the halogen and thus the electronic excited states become more coupled, increasing the speed of ISC. In fact, the opposite is observed. Methods of time-resolved luminescence spectroscopy are used to observe the evolution of the emission signal of the complexes after excitation at 400nm. The kinetics of deexcitation happens in three steps, characterized by three time constants. The first one τ_1 is very short, around 100fs. The second, τ_2 is around 500fs, and the last one τ_3 is more than 1ps. The study is organized in three distinct steps. The first one is the development of the model Hamiltonian and the approximation used to build it. We will also introduce in this part several parameters that will be used to check the quality of our model Hamiltonian with regard to both the computed and experimentally observed electronic states. Once the theoretical basis has been laid, we will conduct, in a second part, a preliminary static study of the electronic structure. This will have two goals: (1) either confirm the experimentally assessed deexcitation pathway or to provide another one based on *ab initio* calculations; (2) then this static study will help us to define and to select the electronic and nuclear degrees of freedom that will enter into the model Hamiltonian. This part is not to be neglected as the Hamiltonian must contain enough degrees of freedom to correctly describe the deexcitation dynamics without making the dynamics impossible to be performed. In a third part, we will build the model Hamiltonian and propagate wavepackets on all the studied complexes.

6.2 Methods and Development

Our goal is to include both spin-orbit and vibronic coupling in the model Hamiltonian. This Hamiltonian has to be simple and easy to build because systems where spin-orbit is important are generally costly to compute. Thus, the fewer calculations are needed to build the Hamiltonian, the better.

6.2.1 Construction of the Hamiltonian

In the Pauli approximation, the electronic Hamiltonian ($\mathcal{H}^{el}$) is expressed as the sum of the scalar relativistic, $\mathcal{H}^{es}$, and the "spin-orbit", $\mathcal{H}^{SO}$, Hamiltonians.

$$\mathcal{H}^{el} = \mathcal{H}^{es} + \mathcal{H}^{SO} \tag{6.1}$$

$\mathcal{H}^{es}$ contains as diagonal elements the energy of the "spin-free" states, while $\mathcal{H}^{SO}$ is composed of the Spin-Orbit coupling (SOC) off-diagonal terms. Diagonalizing $\mathcal{H}^{el}$ gives access to the energy of the "spin-orbit" states.
As the kinetic coupling between states diverge when two states are getting close to each other (see SECTION 1.3), we must use the diabatic representation. The total diabatic Hamiltonian operator can be expressed as the sum of the diagonal kinetic energy of the nuclei operator $\boldsymbol{T}_N$ and the electronic Hamiltonian $\boldsymbol{W}$.

$$\mathcal{H} = \boldsymbol{T}_N + \boldsymbol{W} \tag{6.2}$$

In this representation, the electronic Hamiltonian ($\boldsymbol{W}$) contains the diabatic electronic states on its diagonal, and the coupling term off diagonal. (see SECTION 1.4)
In a general way, the diabatic states can be expressed as a Taylor expansion of the diabatic potential. In the following development dimensionless mass and frequency weighted normal modes [211] will be used such as

$$Q_i = \sqrt{\omega_i} q_i \tag{6.3}$$

where Q_i is the frequency weighted normal mode i, μ_i and ω_i are the reduced mass and the frequency of normal mode i (q_i), respectively. The electronic diabatic Hamiltonian

elements $W_{n,m}$ can be written by expanding $\boldsymbol{W} - V_0\mathbf{1}$ as a Taylor expansion of the diabatic potential around Q_0, where V_0 is a reference potential chosen accordingly to the problem.

$$\begin{aligned} W_{n,m} - V_0\delta_{nm} = \epsilon_n\delta_{nm} + \sum_i \left.\frac{\partial W_{n,m}}{\partial Q_i}\right|_{Q_0} Q_i + \frac{1}{2!}\sum_{i,j} \left.\frac{\partial^2 W_{n,m}}{\partial Q_i \partial Q_j}\right|_{Q_0} Q_i Q_j \\ + \frac{1}{3!}\sum_{i,j,k} \left.\frac{\partial^3 W_{n,m}}{\partial Q_i \partial Q_j \partial Q_k}\right|_{Q_0} Q_i Q_j Q_k + \cdots \end{aligned} \tag{6.4}$$

where δ_{nm} is the Kronecker symbol. All summations concerning normal modes run from 1 to 3N-6, N being the number of atoms of the system. To make the notations lighter, this limit will be omitted. In the mass and frequency weighted normal modes representation, the kinetic energy operator ($\hat{T}_N$) takes the form:

$$\hat{T}_N = -\frac{1}{2}\sum_i \omega_i \frac{\partial^2}{\partial Q_i^2} \tag{6.5}$$

6.2.1.1 The linear vibronic coupling (LVC) approximation [1]

Within the LVC approximation, we truncate the Taylor expansion of $\boldsymbol{W} - V_0\mathbf{1}$ at the first order. The diagonal elements of the electronic Hamiltonian $\boldsymbol{W}$ are expressed as:

$$W_{n,n} = \epsilon_n + V_0(\boldsymbol{Q}) + \sum_i \left.\frac{\partial W_{n,n}}{\partial Q_i}\right|_{Q_0} Q_i. \tag{6.6}$$

At Q_0, by construction, both the diabatic and the adiabatic states are identical. Moreover, at this point $\left.\frac{\partial W_{n,n}}{Q_i}\right|_{Q_0} = \left.\frac{\partial V_n}{Q_i}\right|_{Q_0}$ [37] where V_n is the potential of the adiabatic state n. The vibronic instrastate coupling constant $\kappa_i^{(n)}$ induced by the normal mode i in the electronic state n is defined as:

$$\kappa_i^{(n)} = \left.\frac{\partial V_n}{Q_i}\right|_{Q_0} \tag{6.7}$$

We can then rewrite EQ. (6.6) as:

$$W_{n,n} = \epsilon_n + V_0(\boldsymbol{Q}) + \sum_i \kappa_i^{(n)} Q_i \tag{6.8}$$

The off-diagonal elements of $\boldsymbol{W}$ take the form:

$$W_{n,m} = \sum_i \left.\frac{\partial W_{n,m}}{\partial Q_i}\right|_{Q_0} Q_i. \tag{6.9}$$

The vibronic interstate coupling constant $\lambda_i^{(n),(m)}$ induced by the normal mode i between states n and m is defined as:

$$\lambda_i^{n,m} = \left.\frac{\partial W_{n,m}}{\partial Q_i}\right|_{Q_0} \tag{6.10}$$

6.2.1.1.1 The vibronic intrastate coupling constants

For the study of photophysical processes, it is convenient to consider the reference potential $V_0(\boldsymbol{Q})$ as the potential of the electronic ground state, harmonic in a first approximation EQ. (6.11), and Q_0 as the FC point ($Q_i = 0 \ \forall i$).

$$V_0(\boldsymbol{Q}) = \sum_i \frac{1}{2}\omega_i Q_i^2 \tag{6.11}$$

EQ. (6.8) can be rewritten in a canonical form:

$$W_{n,n} = \epsilon_n + \sum_i \left[\frac{1}{2}\omega_i \left(Q_i + \frac{\kappa_i^{(n)}}{\omega_i}\right)^2 - \frac{\kappa_i^{(n)^2}}{2\omega_i}\right] \tag{6.12}$$

The vibronic intrastate coupling $\kappa_i^{(n)}$ constant shifts the harmonic potential by $-\frac{\kappa_i^{(n)}}{\omega_i}$ in position, and by $-\frac{\kappa_i^{(n)^2}}{2\omega_i}$ in energy. Within the LVC approximation only normal modes which fulfil the following symmetry condition will have a non zero intra-state coupling constant.

$$\Gamma_n \otimes \Gamma_{Q_i} \otimes \Gamma_n \supset \Gamma_A \tag{6.13}$$

Γ_n being the irreducible representation of the electronic state n, Γ_{Q_i} irreducible representation of the normal mode i and Γ_A the totally symmetrical representation. In the forthcoming study, the modes fulfilling EQ. (6.13) will be referred to as tuning modes and written: Q_i^g of frequency: ω_i^g.

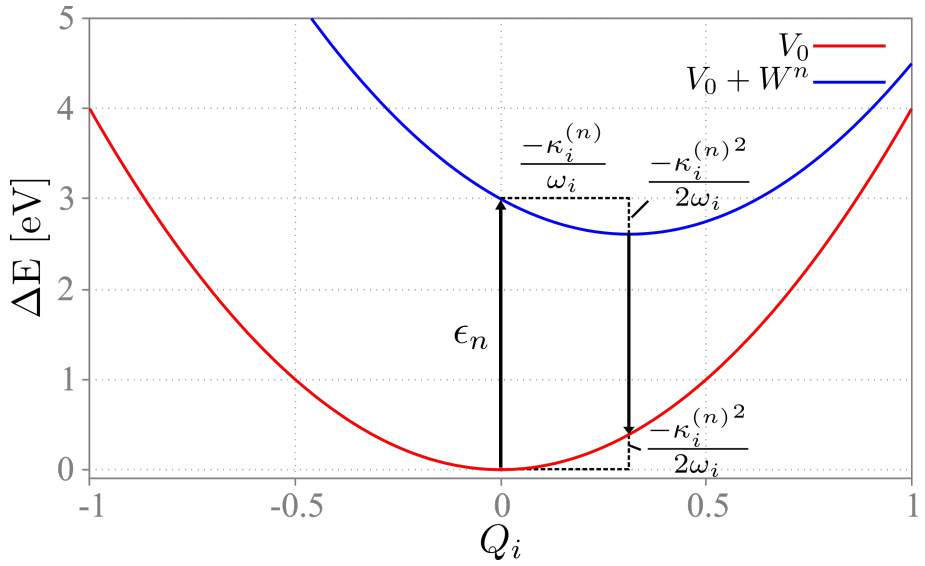

Figure 6.1: Contribution of normal mode i to the Stokes shift within the LVC approximation.

The Stokes-Shift (S.S.) is defined as the difference between the energy of the vertical absorption at Franck-Condon and the vertical emission from the minimum of the electronic excited state back to the ground state (FIG. 6.1). The normal mode i contribution to the Stokes shift is:

$$S.S._i^{(n)} = \epsilon_n - \left(\epsilon_n - 2\frac{-\kappa_i^{(n)2}}{2\omega_i}\right) = \frac{-\kappa_i^{(n)2}}{\omega_i} \tag{6.14}$$

6.2.1.1.2 The vibronic interstate coupling constant

Two states of different symmetry are vibronically coupled, and within the LVC approximation, only by normal modes that fulfil the symmetry selection rules:

$$\Gamma_n \otimes \Gamma_{Q_i} \otimes \Gamma_m \supset \Gamma_A \tag{6.15}$$

These modes will be denoted as coupling modes and from now on will be written: Q_i^u of frequency: ω_i^u. Let's consider two diabatic states within the LVC approximation. The diabatic electronic Hamiltonian reads:

$$\boldsymbol{W} = \begin{pmatrix} W_{11} & \sum_i \lambda_i^{(1),(2)} Q_i^u \\ \sum_i \lambda_i^{(1),(2)} Q_i^u & W_{22} \end{pmatrix} \tag{6.16}$$

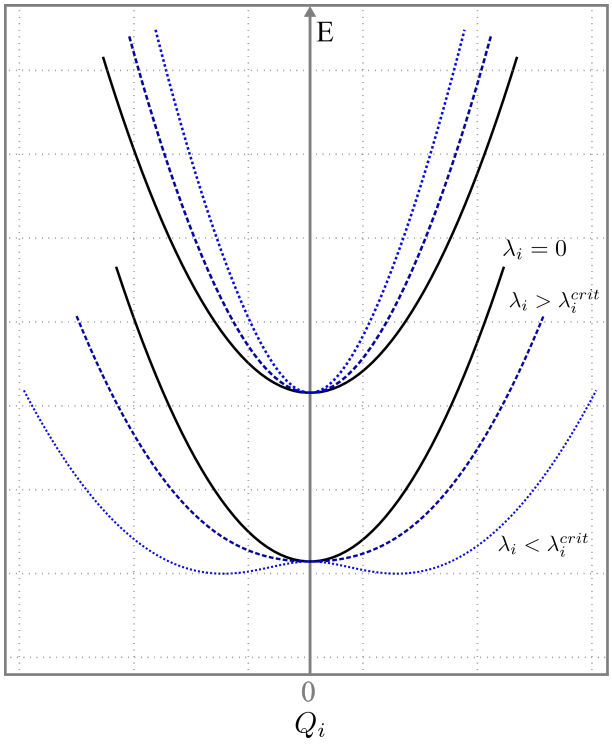

Figure 6.2: Effect of the values of the interstate coupling λ_i on the shape of the adiabatic states V_1 (EQ. (6.21)) and V_2 (EQ. (6.22)).

where:

$$W_{11} = \epsilon_1 + V_0(\boldsymbol{Q}) + \sum_i \kappa_i^{(1)} Q_i^g \tag{6.17}$$

$$W_{22} = \epsilon_2 + V_0(\boldsymbol{Q}) + \sum_i \kappa_i^{(2)} Q_i^g \tag{6.18}$$

The adiabatic electronic Hamiltonian $\boldsymbol{V}$ contains the eigenvector of $\boldsymbol{W}$ such as:

$$\boldsymbol{S}^\dagger \boldsymbol{W} \boldsymbol{S} = \boldsymbol{V} \tag{6.19}$$

where:

$$\boldsymbol{V} = \begin{pmatrix} V_1 & 0 \\ 0 & V_2 \end{pmatrix} \tag{6.20}$$

In the adiabatic representation the interstate coupling affects the shape of the potential of the electronic states (as opposed to the diabatic representation where the coupling terms appear as off-diagonal elements EQ. (6.16)). Studying the curvature of the adiabatic states gives access to the intrastate coupling constant.
Indeed, diagonalizing the 2×2 diabatic electronic Hamiltonian (EQ. (6.16)) leads to the expressions for V_1 and V_2:

$$V_1 = \frac{W_{11} + W_{22}}{2} - \sqrt{\left(\frac{W_{11} - W_{22}}{2}\right)^2 + \sum_i \left(\lambda_i^{(1),(2)} Q_i^u\right)^2} \tag{6.21}$$

$$V_2 = \frac{W_{11} + W_{22}}{2} + \sqrt{\left(\frac{W_{11} - W_{22}}{2}\right)^2 + \sum_i \left(\lambda_i^{(1),(2)} Q_i^u\right)^2} \tag{6.22}$$

Which will be rewritten for convenience:

$$V_{1,2} = V_0(Q) + \Sigma + \sum_i^N \sigma_i Q_i^g \mp W \tag{6.23}$$

where:

$$\Sigma = \frac{\epsilon_1 + \epsilon_2}{2} \tag{6.24}$$

$$\sigma_i = \frac{\kappa_1^{(1)} + \kappa_i^{(2)}}{2} \tag{6.25}$$

$$W = \sqrt{d^2 + c^2} \tag{6.26}$$

with

$$c = \sum_{j=1}^{M} \lambda_j^{(1),(2)} Q_j^u \tag{6.27}$$

$$d = \Delta + \sum_{i=1}^{N} \delta_i^{(1),(2)} Q_i^g \tag{6.28}$$

and

$$\Delta = \frac{\epsilon_1 - \epsilon_2}{2} \tag{6.29}$$

$$\delta_i = \frac{\kappa_1^{(1)} - \kappa_i^{(2)}}{2} \tag{6.30}$$

Two electronic states of different symmetry repel each other. Under certain conditions (see EQ. (6.37) and EQ. (6.38)), the repulsion along Q_i^u modes is strong enough to induce a symmetry breaking ($\lambda_i^{(1),(2)} > \lambda_i^{crit}$, see FIG. 6.2). The lower electronic state will then exhibit two minima at $Q_i^u \neq 0$, and the symmetry of the molecule will not be conserved. The position of these energy minima $\boldsymbol{Q}^{(0)}$ can be calculated. Its coordinates along each normal mode ($Q_i^{g\,(0)}$ and $Q_i^{u\,(0)}$ respectively) are expressed as:

$$Q_i^{g\,(0)} = \frac{\Delta - F}{L - D} \frac{\delta_i}{\omega_i^g} - \frac{\sigma_i}{\omega_i^g} \tag{6.31}$$

$$Q_i^{u\,(0)} = \frac{\pm\lambda_j}{\omega_j^u} \sqrt{1 - \left(\frac{\Delta - F}{L - D}\right)^2} \tag{6.32}$$

where:

$$D = \sum_i \frac{\delta_i^2}{\omega_i^g} \tag{6.33}$$

$$F = \sum_i \frac{\delta_i \sigma_i}{\omega_i^g} \tag{6.34}$$

$$L = \sum_j \frac{{\lambda_j^{(1),(2)}}^2}{\omega_j^u} \tag{6.35}$$

The stabilization of the lower PES due to the interstate vibronic coupling is defined as the difference of energy between the minimum of the PES (V_1) in the absence of interstate vibronic coupling ($\lambda_i^{(n),(m)} = 0$) and $V_1(Q^{(0)})$, namely the minimum of the lowest electronic state. The stabilization energy E_S reads:

$$E_S = \frac{(\Delta + D - L - F)^2}{2(L - D)} \tag{6.36}$$

For the stabilization energy to be positive ,i.e. for the coupling between the two electronic states to be strong enough to create two minima, two conditions must be respected at the same time:

$$L > D \tag{6.37}$$

$$\left| \frac{\Delta - F}{L - D} \right| < 1 \tag{6.38}$$

Considering only the coupling modes, the stabilization energy EQ. (6.36) can be written:

$$E_s = \frac{(1-\chi)^2}{2\chi}\Delta \quad \text{if} \quad \chi \geqslant 1 \tag{6.39}$$

where:

$$\chi = \frac{L}{\Delta} = \sum_j \chi_j \tag{6.40}$$

$$\chi_j = \frac{\lambda_j^{(1),(2)^2}}{\omega_j^u \Delta} \tag{6.41}$$

The conditional parameter χ is a sum over the contributions of each Q_i^u mode (χ_j, EQ. (6.40)). The symmetry breaking phenomenon is thus cumulative, and even if all χ_j values are lower than unity, the total χ value can be greater than unity and induce symmetry breaking.

From EQ. (6.32), one can see that, as long as $\chi \geqslant 1$, the symmetry lowering will take place on all coupling modes for which $\lambda_j^u \neq 0$. This can lead to very complex geometrical distortions.

From EQ. (6.21) and EQ. (6.22), the interstate coupling for each normal mode can be estimated by taking the second derivative of the difference of the two potentials V_1 and

V_2 along the said normal mode:

$$\lambda_i^{(1),(2)} = \left(\frac{1}{8} \frac{\partial^2}{\partial Q_i^2} \left| V_2 - V_1 \right|^2 \Big|_{Q_0} \right)^{1/2} \tag{6.42}$$

This relation can be expressed as function of the first and second derivatives of both adiabatic states along normal mode Q_i as well as the vertical transition energy of both states. The interstate coupling between states n and m can therefore be expressed as:

$$\lambda_i^{(n),(m)} = \frac{1}{2} \left((V_m - V_n) \left[\frac{\partial^2 V_n}{\partial Q_i^2} \Big|_{Q_0} - \frac{\partial^2 V_m}{\partial Q_i^2} \Big|_{Q_0} \right] \right)^{1/2} \tag{6.43}$$

where $V_m - V_n > 0$. This expression is valid within the harmonic approximation.

6.2.1.1.3 Characterization of conical intersections

We have seen SECTION 1.2 that CIs play a key role in the excited state dynamics. It is therefore important to be able to locate and characterize them. From EQ. (6.23), the minimum energy of intersection can be calculated:

$$V_{min}^{CI} = \Sigma + \frac{(F - \Delta)^2}{2D} - \frac{1}{2} \sum_i \frac{\sigma_i^2}{\omega_i^g} \tag{6.44}$$

The position of the energy minimum can be computed. Its position along each tuning mode can be expressed as

$$Q_i^{gCI} = \frac{(\delta_i / \omega_i^g)(F - \Delta)}{D} - \frac{\sigma_i}{\omega_i^g} \tag{6.45}$$

and the shortest distance between the hypersurface of intersection and FC geometry is

$$Q_0^{CI} = \Delta \sqrt{\sum_i \delta_i^2} \tag{6.46}$$

Another interesting quantity is the difference of energy between the minimum of the highest PES (V_2) and the minimum energy of intersection:

$$V_{min}^{CI} - V_{2min} = \frac{1}{2D} (\Delta - D - F)^2 \tag{6.47}$$

EQ. (6.47) shows that every tuning modes for which the intrastate vibronic coupling constants $\kappa_i^{(1)}$ and $\kappa_i^{(2)}$ have different signs will reduce the energy gap between the minimum energy of intersection and the minimum energy of V_2.

6.2.1.1.4 Spin-orbit coupling.

Two states of different spin multiplicities but of same symmetry are coupled through spin-orbit interactions. SOC ($\eta_{n,m}(\boldsymbol{Q})$) between states n and m as a function of the dimensionless normal mode displacements can be expanded as a Taylor expansion around Q_0 (*i.e.* FC):

$$\eta_{n,m}(\boldsymbol{Q}) = \eta_{n,m}(Q_0) + \sum_i \left.\frac{\partial \eta_{n,m}(\boldsymbol{Q})}{\partial Q_i}\right|_{Q_0} Q_i + \frac{1}{2}\sum_{i,j} \left.\frac{\partial^2 \eta_{n,m}(\boldsymbol{Q})}{\partial Q_i \partial Q_j}\right|_{Q_0} Q_i Q_j + \cdots \tag{6.48}$$

$\eta_{n,m}(Q)$ can have complex values and therefore can be written as:

$$\eta_{n,m}(\boldsymbol{Q}) = a(\boldsymbol{Q}) + ib(\boldsymbol{Q}) \tag{6.49}$$

N-uplet states, i.e. electronic states of a spin multiplicty of n (n=1: singlet, n=2: doublet, n=3: triplet, $\cdots$) are composed of n components of $m_s = -\frac{n-1}{2}, -\frac{n-1}{2}+1, \cdots, \frac{n-1}{2}-1, \frac{n-1}{2}$ (see SECTION 6.2.1.1.4). Considering explicitly all ms components is mandatory for a correct description of the SOC between two states of spin multiplicity $n > 1$. In the following, the spin components of each multiplet will be ordered by ascending ms values such as the SOC matrix between two multiplets with a spin multiplicity of n and m respectively, takes the form:

State:		m				
	m_s	$-\frac{m-1}{2}$	$-\frac{m-1}{2}+1$	$\cdots$	$\frac{m-1}{2}-1$	$\frac{m-1}{2}$
n	$-\frac{n-1}{2}$	$W_{1,1}$	$\cdots$	$\cdots$	$\cdots$	$W_{1,m}$
	$-\frac{n-1}{2}+1$	$\vdots$	$\ddots$			$\vdots$
	$\vdots$	$\vdots$		$\ddots$		$\vdots$
	$\frac{n-1}{2}-1$	$\vdots$			$\ddots$	$\vdots$
	$\frac{n-1}{2}$	$W_{n,1}$	$\cdots$	$\cdots$	$\cdots$	$W_{n,m}$

(6.50)

Only singlet and triplet states are considered for now, but the methodology can be expanded to states of higher spin multiplicity.

The SOC matrix between a singlet and a triplet state can be written as:

$$\mathbf{W}_{\mathbf{S_n},\mathbf{T_m}} = \begin{pmatrix} \eta^{*}_{S_m,T_n}(\boldsymbol{Q}) & -ib(\boldsymbol{Q}) & \eta_{S_m,T_n}(\boldsymbol{Q}) \end{pmatrix} \tag{6.51}$$

$\eta^{*}_{S_m,T_n}(\boldsymbol{Q})$ being the complex conjugate of the SOC.
And the SOC matrix between two triplet states is:

$$\mathbf{W}_{\mathbf{T_n},\mathbf{T_m}} = \begin{pmatrix} -ib(\boldsymbol{Q}) & \eta_{T_m,T_n}(\boldsymbol{Q}) & 0 \\ -\eta^{*}_{T_m,T_n}(\boldsymbol{Q}) & -ib(\boldsymbol{Q}) & \eta_{T_m,T_n}(\boldsymbol{Q}) \\ 0 & -\eta^{*}_{T_m,T_n}(\boldsymbol{Q}) & -ib(\boldsymbol{Q}) \end{pmatrix} \tag{6.52}$$

The total interaction matrix $\mathbf{W}$ between two triplet states can therefore be written as:

$$\mathbf{W}_{\mathbf{T_n},\mathbf{T_m}} = \begin{pmatrix} -ib(\boldsymbol{Q}) + \sum_i \lambda_i^{(n),(m)} Q_i & \eta_{T_m,T_n}(\boldsymbol{Q}) & 0 \\ -\eta^{*}_{T_m,T_n}(\boldsymbol{Q}) & -ib(\boldsymbol{Q}) + \sum_i \lambda_i^{(n),(m)} Q_i & \eta_{T_m,T_n}(\boldsymbol{Q}) \\ 0 & -\eta^{*}_{T_m,T_n}(\boldsymbol{Q}) & -ib(\boldsymbol{Q}) + \sum_i \lambda_i^{(n),(m)} Q_i \end{pmatrix} \tag{6.53}$$

$\lambda_i^{(n),(m)}$ being the interstate coupling constant between states of the same spin multiplicity (see section 6.2.1.1.2).

6.2.1.1.5 Extracting the coupling from electronic structure calculations.

Within the LVC approximation, we can build the diabatic model Hamiltonian from electronic structure data. Indeed, only the transition energies, the Hessians (i.e. second derivative of the potential as a function of the Cartesian displacements) in the GS and the ES states as well as the gradients are needed.
In order to extract these data from *ab initio* calculations, a "home-made" Fortran code was built. First,the eigenvectors and eigenvalues of the mass-weighted Hessian ($\mathbf{F^{MW}}$) of the GS whose elements are the second derivative of the potential along the mass-weighted Cartesian coordinates are computed:

$$F_{ij}^{MW} = \frac{\partial^2 V}{\partial \tilde{x}_i \partial \tilde{x}_i} \tag{6.54}$$

where $\tilde{x}_i$ is the mass-weighted Cartesian displacement such as: $\tilde{x}_i = \sqrt{m_i}x_1$, m_i being the mass of atom i.
The eigenvectors of $\mathbf{F}^{\mathbf{MW}}$ are the so-called normal mode q_i. Matrix $\mathbf{A}$ is the matrix containing all the eigenvectors of $\mathbf{F}^{\mathbf{MW}}$ as columns. The elements of $\mathbf{A}$ are thus the contributions of all mass-weighted Cartesian displacements $\tilde{x}_i$ to ground states the normal modes q_i:

$$A_{ij} = \frac{\partial \tilde{x}_i}{\partial q_j} \tag{6.55}$$

Matrix $\mathbf{A}$ is called the unitary displacements matrix and will be used as the transformation matrix to convert quantities expressed as a function of the mass-weighted Cartesian displacements $\tilde{x}_i$ into quantities functions of the normal modes q_i.
The eigenvalues of the $\mathbf{F}^{\mathbf{MW}}$ are the frequencies ω_i associated to the normal modes q_i.
Then, the Hessian and gradients matrices as a function of the mass-weighted Cartesian displacements for each electronic state n ($\mathbf{F}(\mathbf{n})^{\mathbf{MW}}$ and $\mathbf{G}(\mathbf{n})^{\mathbf{MW}}$ respectively) are expressed as a function of the GS normal modes q_i by multiplication of the unitary displacements matrix $\mathbf{A}$:

$$\tilde{\mathbf{F}}(\mathbf{n}) = \mathbf{A}^{\dagger}\mathbf{F}(\mathbf{n})^{\mathbf{MW}}\mathbf{A} \tag{6.56}$$

$$\tilde{\mathbf{G}}(\mathbf{n})^{\dagger} = \mathbf{G}(\mathbf{n})^{\mathbf{MW}^{\dagger}}\mathbf{A} \tag{6.57}$$

Finally, the normal mode coordinates q_i are scaled to become dimensionless Q_i:

$$Q_i = \sqrt{\frac{\omega_i}{\hbar}}q_i \tag{6.58}$$

Both the Hessians and gradients as a function of the normal modes displacements $\tilde{\mathbf{F}}(\mathbf{n})$ and $\tilde{\mathbf{G}}(\mathbf{n})$, respectively are scaled according to:

$$\tilde{F}(n)^0_{ij} = \tilde{F}(n)_{ij}\frac{\hbar}{\sqrt{\omega_i\omega_j}} \tag{6.59}$$

$$\tilde{G}(n)^0_i = \tilde{G}(n)_i\sqrt{\frac{\hbar}{\omega_i}} \tag{6.60}$$

where $\tilde{\mathbf{F}}(\mathbf{n})^{\mathbf{0}}_{\mathbf{ij}}$ and $\tilde{\mathbf{G}}(\mathbf{n})^{\mathbf{0}}_{\mathbf{ij}}$ are the Hessian and gradients as a function of the dimensionless normal modes displacements elements, respectively.
The intrastate vibronic coupling constants $\kappa_i^{(n),(m)}$ are the elements $\tilde{G}(n)^0_i$, and the in-

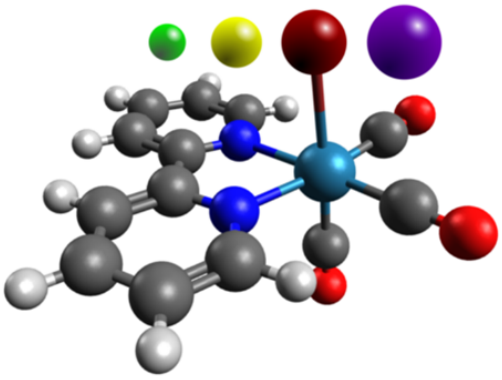

Figure 6.3: Structure of [Re(X(CO)$_3$(bpy)].

terstate vibronic coupling constant $\lambda_i^{(n),(m)}$ can be computed from $\tilde{\mathbf{F}}(\mathbf{n})^{\mathbf{0}}$ using EQ. (6.43).

6.3 Electronic structure of [Re(X)(CO)$_3$(bpy)] X=F, Cl, Br, I complexes

A pre-requisite to quantum dynamics simulations is the electronic structure study that will identify the electronic states participating to the relaxation dynamics after excitation. On the basis of the electronic structure data it will be possible to have access to energies, SOC, gradients and hessians.
Several joined experimental and theoretical studies have been performed on this class of complex [2, 3]. However, no systematic comparison has been performed inside the halide series (fluoride, chloride, bromide, iodide) in the perspective of simulating excited states dynamics.

6.3.1 Computational Details [5]

The structures of [Re(X)(CO)$_3$(bpy)] (X=F, X=Cl, X=Br, X=I) complexes have been optimized in the electronic ground state (GS) under Cs symmetry constraint. Density functional theory (DFT) method have been used with the B3LYP functional [176][177] and a triple-ζ polarized basis set [173]. All electrons were considered.

Excited electronic states were computed through time-dependent density functional theory (TD-DFT) with same functional and basis set. Scalar relativistic effect were taken into account within the zero-order relativistic approximation (ZORA) [55].
Spin-orbit coupling (SOC) were introduced according to a simplified relativistic perturbational TD-DFT formalism [174][175].
Solvent is treated implicitly, based on the conductor-like screening model (COSMO [182][183][184], $\epsilon = 33.64$ for acetonitrile) as implemented in ADF [185][186].
Electronic calculations were done using the ADF-2013 quantum chemistry software [187] and the electronic transitions were analyzed with the Dgrid package [129].
The optimization of excited states was performed in the "SOC-free" picture, using the same functional and the same basis. All optimization were carried out under C_s symmetry constraint, and frequency analysis was performed to ensure being in an energy minimum. Spin-orbit states were then computed through single points at these geometries.
Wavepacket propagations were conducted using the multi-configuration time dependent Hartree (MCTDH) method with the Heidelberg MCTDH package [82][83][84]. Details of computation are given in reference [5].

6.3.2 Description of the system at Franck-Condon

6.3.2.1 "SOC-free" description.

The complexes in their electronic GS are characterized by a Re(I) d^6 electronic configuration. All these complexes ([Re(X)$(CO)_3$(bpy)] X=F, Cl , Br, I) are found to have a ground state minimum geometry of Cs symmetry. A frequency analysis at these geometries does not show imaginary frequencies.
At Franck Condon (FC) the HOMO of [Re(X)$(CO)_3$(bpy)] X=F, X=Cl and X=Br consists of a mix of 57%d_{xz} of the rhenium and 10%p_z of the halide for X=F, 53%d_{xz} and 15%p_z for X=Cl and 47%d_{xz} and 25%p_z for X=Br. The HOMO-1 is a mix of 53%d_{yz} of the rhenium and 7%p_x of the halide for X=F, 49%d_{yz} and 17%p_x for X=Cl and 42%d_{yz} and 28%p_x for X=Br. The HOMO-2 is fully localized on the metal atom whereas the HOMO-3 orbital is a pure π orbital localized on the bipyridine ligand (π_{bpy}). The LUMO orbital is the anti-bonding counterpart of the HOMO-3 orbital, and by such is a π^* orbital local-

ized on the bipyridine ligand (π^*_{bpy}). (FIG. 6.4).
These molecular orbitals give seven low-lying excited states, 3 singlets and 4 triplets, localized around 400 nm (i.e. the experimental wavelength of excitation [3]) that are well separated from the higher electronic states.

Results from the "SOC-free" TD-DFT calculations are reported in TAB. 6.1 and TAB. 6.2. The four lowest states in energy (T1, T2, S1 and S2) have a mixed metal/halide charge transfer (MLCT/XLCT) nature (to emphasize this point, transitions in TAB. 6.1 and TAB. 6.2 are expressed according to the atomic orbital and not the molecular orbitals.) . These states work in pair, as T1 and S1 have the same nature as well as T2 and S2. The first pair, of A" symmetry, involves an excitation from the d_{xz} orbital of the rhenium and the p_z orbital of the halide to the π^*_{bpy}. Whereas the T2, S2 pair, of symmetry A', involves an excitation from the d_{xy} orbital of the rhenium and the p_x orbital of the halide to the same π^*_{bpy}. The weight of the contribution of the p_X orbital in the four lowest electronic states increases going from [Re(F)$(CO)_3$(bpy)] to [Re(I)$(CO)_3$(bpy)] in agreement with recent studies. Although the MLCT character is predominant in these four states in [Re(X)$(CO)_3$(bpy)] X=F, X=Cl, and X=Br, the XLCT contribution becomes the most important in [Re(I)$(CO)_3$(bpy)] for these states (namely, T1, T2, S1 and S2). Differences of electronic densities characterizing these transitions are shown FIG. 6.5.
The third triplet state, T3 is a A" ILCT state (FIG. 6.5) involving a $\pi \rightarrow \pi^*$ transition on the bpy ligand. T4 and S3 work together and are A' MLCT states (FIG. 6.5) involving an electronic transition from the high-lying d orbital of the Rhenium to the π^*_{bpy}.

For [Re(I)$(CO)_3$(bpy)], T3 is no longer purely ILCT but is mixed with the T1 triplet of same symmetry. Otherwise, T4 and S3 are basically unchanged.
These TD-DFT results are validated by previous MS-CASPT2 calculations. For more details, see reference [2].

6.3.2.2 "Spin-orbit" description.

Because of the presence of heavy atoms such as the halides and the rhenium metal, SOC should be taken into account. The seven "SOC-free" states considered until now will generate fifteen close-lying "spin-orbit" states. The results of TD-DFT with SOC are reported TAB. 6.3 and TAB. 6.4.
In the [Re(X$(CO)_3$(bpy)] X=F, X=Cl, and X=Br complexes (TAB. 6.3), "spin-orbit" states

State			Transition			ΔE [eV] ([cm^{-1}])	f
X=F							
T_1	a^3A''	MLCT/XLCT	$57\%d_{yz}$ $10\%p_z(F)$	$\rightarrow \pi^*_{bpy}$		2.75 (22 181)	-
T_2	a^3A'	MLCT/XLCT	$53\%d_{xy}$ $7\%p_x(F)$	$\rightarrow \pi^*_{bpy}$		2.89 (23 310)	-
S_1	a^1A''	MLCT/XLCT	$57\%d_{yz}$ $10\%p_z(F)$	$\rightarrow \pi^*_{bpy}$		2.87 (23 149)	0.011
S_2	b^1A'	MLCT/XLCT	$53\%d_{xy}$ $7\%p_x(F)$	$\rightarrow \pi^*_{bpy}$		3.04 (24 520)	0.155
T_3	b^3A''	IL	$97\%\pi_{bpy}$	$\rightarrow \pi^*_{bpy}$		3.21 (25 891)	-
T_4	b^3A'	MLCT	$73\%d_{Re}$	$\rightarrow \pi^*_{bpy}$		3.32 (26 778)	-
S_3	c^1A'	MLCT	$99\%d_{Re}$	$\rightarrow \pi^*_{bpy}$		3.36 (27 101)	0.000
X=Cl							
T_1	a^3A''	MLCT/XLCT	$53\%d_{yz}$ $15\%p_z(Cl)$	$\rightarrow \pi^*_{bpy}$		2.86 (22 880)	-
T_2	a^3A'	MLCT/XLCT	$49\%d_{xy}$ $17\%p_x(Cl)$	$\rightarrow \pi^*_{bpy}$		2.97 (23 460)	-
S_1	a^1A''	MLCT/XLCT	$53\%d_{yz}$ $15\%p_z(Cl)$	$\rightarrow \pi^*_{bpy}$		2.99 (23 920)	0.0021
S_2	b^1A'	MLCT/XLCT	$49\%d_{xy}$ $17\%p_x(Cl)$	$\rightarrow \pi^*_{bpy}$		3.18 (25 440)	0.059
T_3	b^3A''	IL	$81\%\pi_{bpy}$	$\rightarrow \pi^*_{bpy}$		3.23 (25 840)	-
T_4	b^3A'	MLCT	$63\%d_{Re}$	$\rightarrow \pi^*_{bpy}$		3.34 (26 720)	-
S_3	c^1A'	MLCT	$98\%d_{Re}$	$\rightarrow \pi^*_{bpy}$		3.38 (27 040)	0.0016
X=Br							
T_1	a^3A''	MLCT/XLCT	$47\%d_{yz}$ $25\%p_z(Br)$	$\rightarrow \pi^*_{bpy}$		2.84 (22 720)	-
T_2	a^3A'	MLCT/XLCT	$42\%d_{xy}$ $28\%p_x(Br)$	$\rightarrow \pi^*_{bpy}$		2.93 (23 440)	-
S_1	a^1A''	MLCT/XLCT	$47\%d_{yz}$ $25\%p_z(Br)$	$\rightarrow \pi^*_{bpy}$		2.96 (23 680)	0.0017
S_2	b^1A'	MLCT/XLCT	$42\%d_{xy}$ $28\%p_x(Br)$	$\rightarrow \pi^*_{bpy}$		3.13 (25 040)	0.051
T_3	b^3A''	IL	$81\%\pi_{bpy}$	$\rightarrow \pi^*_{bpy}$		3.22 (25 760)	-
T_4	b^3A'	MLCT	$63\%d_{Re}$	$\rightarrow \pi^*_{bpy}$		3.34 (26 720)	-
S_3	c^1A'	MLCT	$98\%d_{Re}$	$\rightarrow \pi^*_{bpy}$		3.37 (26 960)	0.0009

Table 6.1: TD-DFT low-lying singlet and triplet electronic excited states of [Re(X)(CO)$_3$(bpy)] X=F, X=Cl and X=Br [5]. f is the oscillator strength.

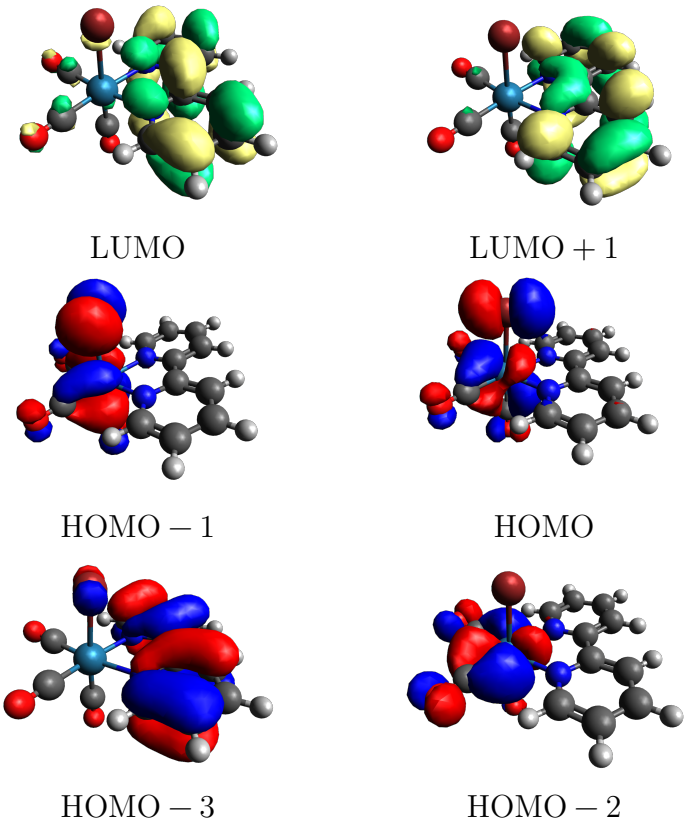

Figure 6.4: Kohn-Sham orbitals involved in the first electronic transitions of [Re(Br)$(CO)_3$(bpy)].

	State		Transition			f
X=I						
T_1	a^3A''	XLCT/MLCT	$51\%p_z(I)$ $30\%d_{yz}$	$\rightarrow \pi^*_{bpy}$	2.76 (22 080)	-
T_2	a^3A'	XLCT/MLCT	$56\%p_x(I)$ $26\%d_{xy}$	$\rightarrow \pi^*_{bpy}$	2.81 (22 480)	-
S_1	a^1A''	XLCT/MLCT	$51\%p_z(I)$ $30\%d_{yz}$	$\rightarrow \pi^*_{bpy}$	2.85 (22 800)	0.0008
S_2	b^1A'	XLCT/MLCT	$56\%p_x(I)$ $26\%d_{xy}$	$\rightarrow \pi^*_{bpy}$	2.95 (23 600)	0.029
T_3	b^3A''	IL/XLCT/MLCT	$67\%\pi_{bpy}$ $7\%p_z(I)$ $5\%d_{yz}$	$\rightarrow \pi^*_{bpy}$	3.18 (25 440)	-
T_4	b^3A'	MLCT	$64\%d_{Re}$	$\rightarrow \pi^*_{bpy}$	3.33 (26 640)	-
S_3	c^1A'	MLCT	$98\%d_{Re}$	$\rightarrow \pi^*_{bpy}$	3.37 (26 960)	0.0005

Table 6.2: TD-DFT low-lying singlet and triplet electronic excited states of [Re(I)$(CO)_3$(bpy)] [5]. f is the oscillator strength.

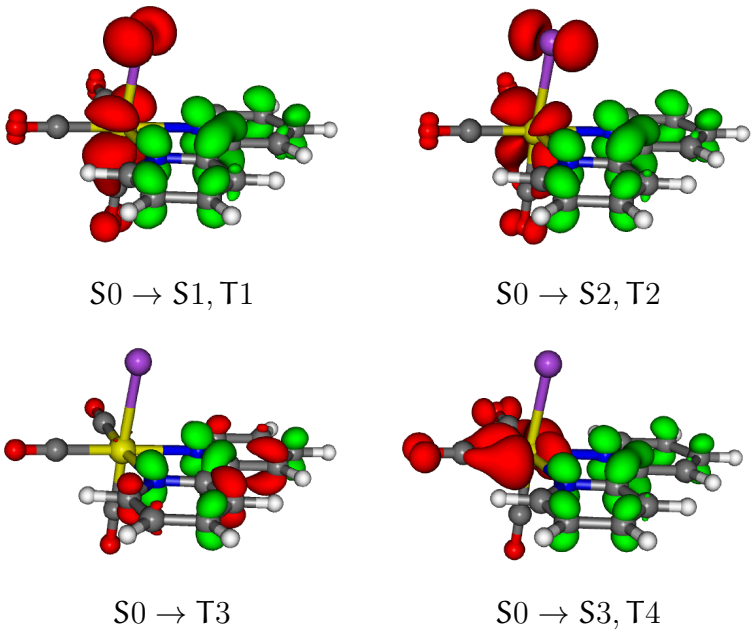

Figure 6.5: Differences in electronic densities between the electronic ground state and the lowest electronic excited "SOC-free" states of [Re(Br)$(CO)_3$(bpy)]. *(In green: increase of electronic density; in red: decrease.)*

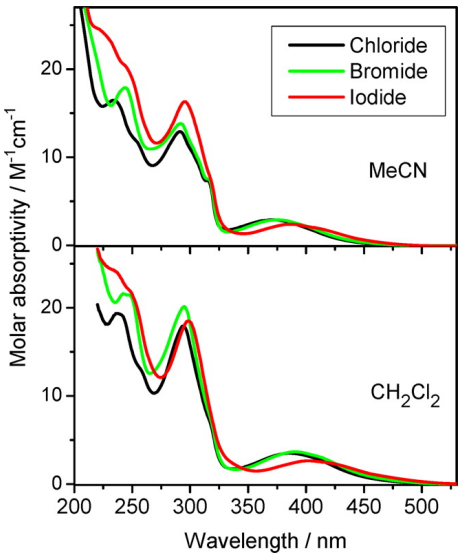

Figure 6.6: UV-Visible absorption spectra of [Re(X)$(CO)_3$(bpy)] X=Cl, Br, I in CH_3CN (upper panel). (from reference [2])

E1 to E3 as well as states E5 and E6 are mainly a mix of "SOC-free" triplet states T1 and T2. The E4 and E7 states are a nearly 50:50 mix between T2 and S1.

The S2 "SOC-free" state (i.e. the absorbing state) composes mainly the E8 state. Small contributions of S2 are also found in E3 and E11. Although these three states will absorb, E8 has the largest oscillator strength (f $= 1.3 \times 10^{-2}$ for [Re(X)$(CO)_3$(bpy)] X=F, f $= 3.5 \times 10^{-2}$ for X=Cl, f $= 3.6 \times 10^{-2}$ for X=Br) and is the closest to the excitation wavelength. Finally states E9 to E11, E12 to E14 and E15 (E12 to E15 not being reported in TAB. 6.3 and TAB. 6.4. See reference [5] for details.), are purely T3, T4 and S3 respectively.
As S2 is the absorbing state, it is mandatory to consider it for the dynamics. To do so, we must include "spin orbit" states up to E11. In addition to S2, T3 is also involved in E11. E9 and E10 are purely composed of T3. Thus, it is needed to consider the T1, T2, S1, S2 and T3 "SOC-free" states in the dynamics.
For the [Re(I)$(CO)_3$(bpy)] complex, the same observations are made (TAB. 6.4). Except that E3 and E4 are now degenerate. E12 is composed of T3 and T1 and E15 is a mix of S3 and higher lying A' triplet. Again, E8 has the greatest oscillator strength f $= 1.8 \times 10^{-2}$.

The TD-DFT "spin-orbit" results (TAB. 6.3 and TAB. 6.4) are in good agreement with

		State	Composition	ΔE [eV] ([cm^{-1}])	f
X=F					
E_1	(A")	MLCT/XLCT	$74\%a^3A''\,22\%a^3A'$	2.68(21616)	9.0×10^{-6}
E_2	(A')	MLCT/XLCT	$74\%a^3A''\,22\%a^3A'$	2.68(21616)	3.2×10^{-5}
E_3	(A')	MLCT/XLCT	$86\%a^3A'$	2.70(21777)	1.4×10^{-2}
E_4	(A")	MLCT/XLCT	$53\%a^1A''\,42\%a^3A'$	2.75(22181)	6.1×10^{-3}
E_5	(A")	MLCT/XLCT	$76\%a^3A'\,24\%a^3A''$	2.93(23633)	1.2×10^{-5}
E_6	(A')	MLCT/XLCT	$75\%a^3A'\,22\%a^3A''$	2.93(23633)	1.1×10^{-5}
E_7	(A")	MLCT/XLCT	$50\%a^3A'\,49\%a^1A''$	3.07(24036)	2.4×10^{-6}
E_8	**(A')**	**MLCT/IL/XLCT**	**$83\%b^1A'\,12\%a^3A''$**	**3.05(24600)**	**1.3×10^{-2}**
E_9	(A")	IL	$94\%b^3A''$	3.21(25891)	3.9×10^{-7}
E_{10}	(A')	IL	$96\%b^3A''$	3.21(25891)	2.7×10^{-5}
E_{11}	(A')	IL/MLCT/XLCT	$92\%b^3A''$	3.22(25972)	5.5×10^{-3}
X=Cl					
E_1	(A")	MLCT/XLCT	$71\%a^3A''\,24\%a^3A'$	2.78(22240)	2.0×10^{-6}
E_2	(A')	MLCT/XLCT	$72\%a^3A''\,24\%a^3A'$	2.78(22240)	9.9×10^{-5}
E_3	(A')	MLCT/XLCT	$88\%a^3A'$	2.81(22480)	4.0×10^{-3}
E_4	(A")	MLCT/XLCT	$48\%a^3A'\,46\%a^1A''$	2.85(22800)	9.5×10^{-4}
E_5	(A")	MLCT/XLCT	$72\%a^3A'\,26\%a^3A''$	3.01(24080)	6.8×10^{-4}
E_6	(A')	MLCT/XLCT	$72\%a^3A'\,26\%a^3A''$	3.01(24080)	1.0×10^{-4}
E_7	(A")	MLCT/XLCT	$50\%a^3A'\,49\%a^1A''$	3.07(24560)	2.4×10^{-6}
E_8	**(A')**	**MLCT/IL/XLCT**	**$58\%b^1A'\,26\%b^3A''$**	**3.17(25360)**	**3.5×10^{-2}**
E_9	(A")	IL	$94\%b^3A''$	3.23(25840)	3.9×10^{-7}
E_{10}	(A')	IL	$95\%b^3A''$	3.23(25840)	8.2×10^{-5}
E_{11}	(A')	IL/MLCT/XLCT	$72\%b^3A''\,26\%b^1A'$	3.25(26000)	1.6×10^{-2}
X=Br					
E_1	(A")	MLCT/XLCT	$66\%a^3A''\,30\%a^3A'$	2.75(22000)	2.1×10^{-6}
E_2	(A')	MLCT/XLCT	$66\%a^3A''\,30\%a^3A'$	2.75(22000)	5.1×10^{-5}
E_3	(A')	MLCT/XLCT	$86\%a^3A''\,10\%b^1A'$	2.78(22240)	5.2×10^{-3}
E_4	(A")	MLCT/XLCT	$44\%a^1A''\,50\%a^3A'$	2.80(22400)	7.4×10^{-4}
E_5	(A")	MLCT/XLCT	$66\%a^3A'\,31\%a^3A''$	2.99(23920)	5.8×10^{-6}
E_6	(A')	MLCT/XLCT	$66\%a^3A'\,31\%a^3A''$	2.99(23920)	9.3×10^{-5}
E_7	(A")	MLCT/XLCT	$51\%a^1A''\,48\%a^3A'$	3.05(24400)	8.6×10^{-4}
E_8	**(A')**	**MLCT/IL/XLCT**	**$70\%b^1A'\,14\%b^3A''$**	**3.13(25040)**	**3.6×10^{-2}**
E_9	(A")	IL	$95\%b^3A''$	3.22(25760)	1.2×10^{-6}
E_{10}	(A')	IL	$96\%b^3A''$	3.22(25760)	8.8×10^{-5}
E_{11}	(A')	IL/MLCT/XLCT	$82\%b^3A''\,16\%b^1A'$	3.23(25840)	8.0×10^{-3}

Table 6.3: Spin-Orbit coupled low-lying electronic excited states of [Re(X)(CO)$_3$(bpy)] (X=F, X=Cl, X=Br) at FC (computed at the TD-DFT level) [5]. f is the oscillator strength.

		State	Composition	ΔE [eV] ([cm^{-1}])	f
X=I					
E_1	(A")	MLCT/XLCT	$55\%a^3A''\,42\%a^3A'$	2.58(20640)	1.4×10^{-6}
E_2	(A')	MLCT/XLCT	$54\%a^3A''\,42\%a^3A'$	2.58(20640)	1.4×10^{-5}
E_3	(A")	MLCT/XLCT	$54\%a^3A'\,44\%a^1A''$	2.62(20960)	3.4×10^{-4}
E_4	(A')	MLCT/XLCT	$70\%a^3A''\,26\%b^1A'$	2.62(20960)	7.6×10^{-3}
E_5	(A")	MLCT/XLCT	$52\%a^3A'\,40\%a^3A''$	2.88(23040)	1.0×10^{-6}
E_6	(A')	MLCT/XLCT	$51\%a^3A'\,40\%a^3A''$	2.90(23200)	1.8×10^{-3}
E_7	(A")	MLCT/XLCT	$49\%a^1A''\,42\%a^3A'$	2.93(23440)	3.8×10^{-4}
E_8	**(A')**	**MLCT/IL/XLCT**	**$62\%b^1A'\,24\%a^3A''$**	**2.97(23760)**	**1.8×10^{-2}**
E_9	(A")	IL/MLCT/XLCT	$89\%b^3A''$	3.17(25360)	4.4×10^{-6}
E_{10}	(A')	IL/MLCT/XLCT	$88\%b^3A''$	3.17(25360)	1.3×10^{-4}
E_{11}	(A')	IL/MLCT/XLCT	$94\%b^3A''$	3.18(25440)	1.6×10^{-3}

Table 6.4: Spin-Orbit coupled low-lying electronic excited states of [Re(I)(CO)$_3$(bpy)] at FC (computed at the TD-DFT level) [5]. f is the oscillator strength.

the observed absorption spectra [2] (FIG. 6.6). The $S0 \rightarrow E8$ transition energy: 391 nm, 396 nm and 417 nm for [Re(X)(CO)$_3$(bpy)] X=Cl, X=Br and X=I , respectively, reproduce the position of the absorption maximum observed around 400 nm. The red shift between [Re(X)(CO)$_3$(bpy)] X=Cl, X=Br and [Re(I)(CO)$_3$(bpy)] of this absorption band is reproduced.

The SOC at FC between each states are reported in TAB. 6.5. The SOC between states of same symmetry (i.e. S1/T1, S2/T2 and T1/T3) are equal to zero due to symmetry reasons, as far as the imaginary part of SOC is neglected. This will be discussed in details in SECTION 6.4.1. SOC rises going from [Re(Cl)(CO)$_3$(bpy)] to [Re(I)(CO)$_3$(bpy)] (TAB. 6.5) due to the increase of the halide mass. The difference between [Re(F)(CO)$_3$(bpy)] and [Re(Cl)(CO)$_3$(bpy)] is less obvious. This may be due to the low weight of the Halide, in these two cases, the SOC may mainly be induced by the rhenium atom. SOC in [Re(I)(CO)$_3$(bpy)] is much stronger ($|\eta_{\mathrm{Br}}^{(S2),(T1)}| = 641\mathrm{cm}^{-1}$ and $|\eta_{\mathrm{I}}^{(S2),(T1)}| = 1088\mathrm{cm}^{-1}$ for example).

The evolution of the SOC for [Re(X)(CO)$_3$(bpy)] X=Cl, X=Br and X=I, along the stretch normal mode is shown FIG. 6.7. The maximum amplitude of the SOC for [Re(Cl)(CO)$_3$(bpy)] and [Re(Br)(CO)$_3$(bpy)] is $\approx 200\mathrm{cm}^{-1}$. On the other hand, for [Re(I)(CO)$_3$(bpy)], the amplitude of the SOC can go as high as $\approx 700\mathrm{cm}^{-1}$ and varies faster than in the other

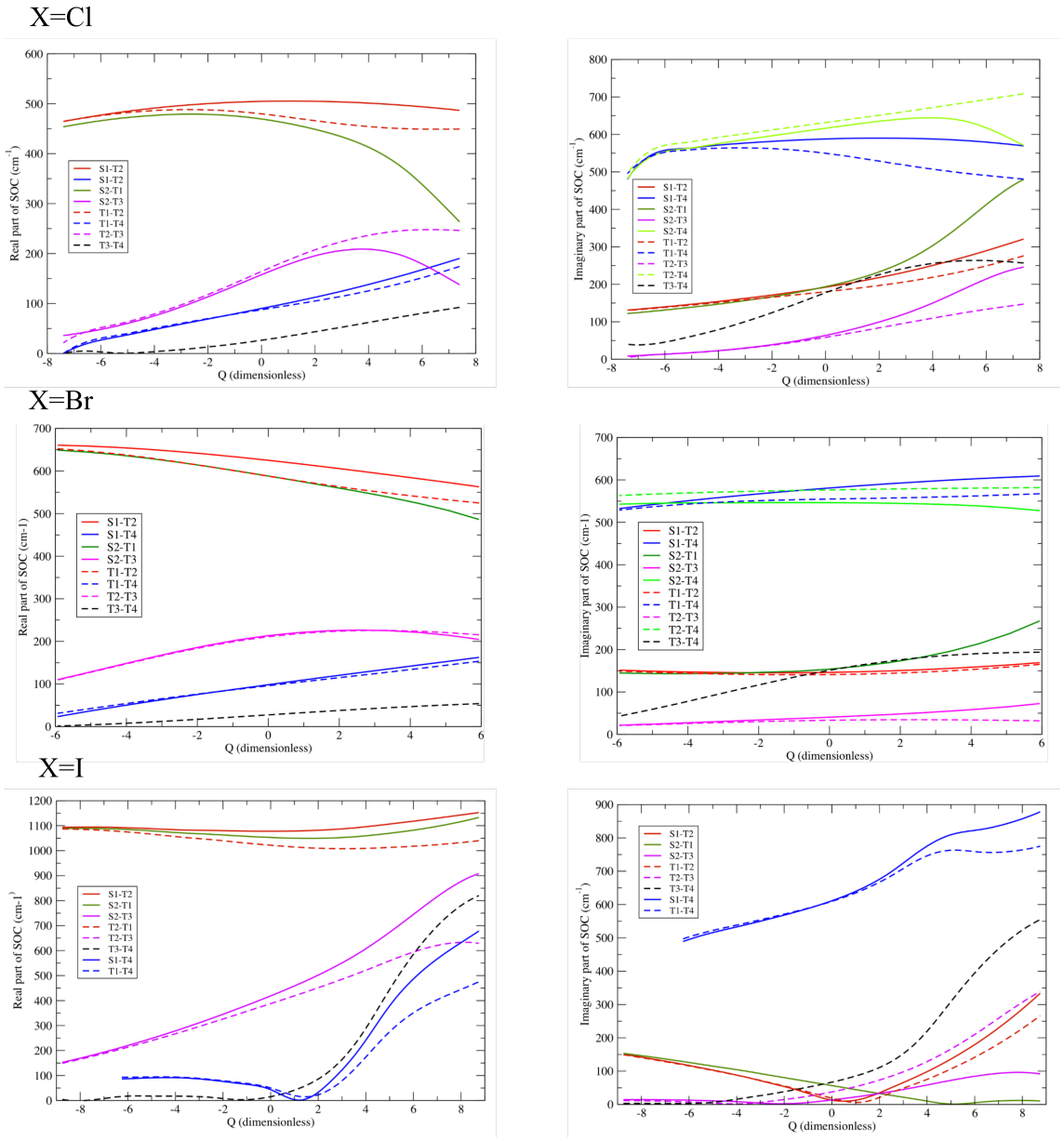

Figure 6.7: Evolution of the SOC along the normal mode of stretch for [Re(X)(CO)$_3$(bpy)] X=Cl, X=Br and X=I. The real part of the SOC is shown on the left side, the imaginary part on the right.

$\eta\,[cm^{-1}]$	F	Cl	Br	I
S1S2	0	0	0	0
S1T1	0	0	0	0
S1T2	-510 +227i (558)	-505 +192i (540)	-625 +146i (641)	-1078 +13i (1088)
S1T3	0	0	0	0
S2T1	-492 +208i (534)	469 -194i (507)	588 -154i (608)	-1053 +57i (1055)
S2T2	0	0	0	0
S2T3	-120 +52i (131)	158 -64i (170)	-214 +41i (218)	-419 -14i (419)
T1T2	-497 +218i (543)	-480 +180i (513)	588 -141i (605)	-1022 +19i (1022)
T1T3	0	0	0	0
T2T3	125 -54i (136)	164 -59i (174)	211 -33i (214)	388 +38i (390)

Table 6.5: SOC terms at Franck-Condon between the singlet and triplet electronic excited states of [Re(X)(CO)$_3$(bpy)] X=F, X=Cl, X=Br, X=I (the *modulus* is shown in parenthesis).

complexes.

6.3.3 Optimized excited states.

To explain the observed emission (FIG. 6.8, FIG. 6.9), restricting the study to the FC region is not satisfying. It is needed to find the PES minimum of the emitting excited-states in order to estimate the position of the maximum of the corresponding state emission band.

The minimum of the "SOC-free" electronic excited states T1, T2, S1, S2 and T3 were investigated for [Re(X)(CO)$_3$(bpy)] X=Cl, X=Br and X=I. The geometry of all minima are found to be of Cs symmetry. For [Re(Cl)(CO)$_3$(bpy)] and [Re(Br)(CO)$_3$(bpy)], the minimum of S2 is found at 505 nm and 522 nm, respectively (TAB. 6.6). This corresponds to the E8 "spin-orbit" state emitting at 496 nm and 505 nm respectively (TAB. 6.6). This gives rise to a Stokes shift in S2 of $S.S._{Cl}^{(S2)} = 5640\,cm^{-1}$ (0.70 eV) and $S.S._{Br}^{(S2)} = 5880\,cm^{-1}$ (0.73 eV) for [Re(Cl)(CO)$_3$(bpy)] and [Re(Br)(CO)$_3$(bpy)] respectively; which is in good agreement with the experimentally observed Stokes shift: $S.S.^{(S2)} \approx 6000\,cm^{-1}$ (≈0.74 eV) [3]. The small red-shift between the two complexes is also found in the experimental luminescence spectra [3] (see FIG. 6.8). The early signal observed right after absorption at 400 m, which covers the 500-550 nm energy range (the blue region in FIG. 6.8) and decays with a time constant of $\tau_1 = 85$ fs for

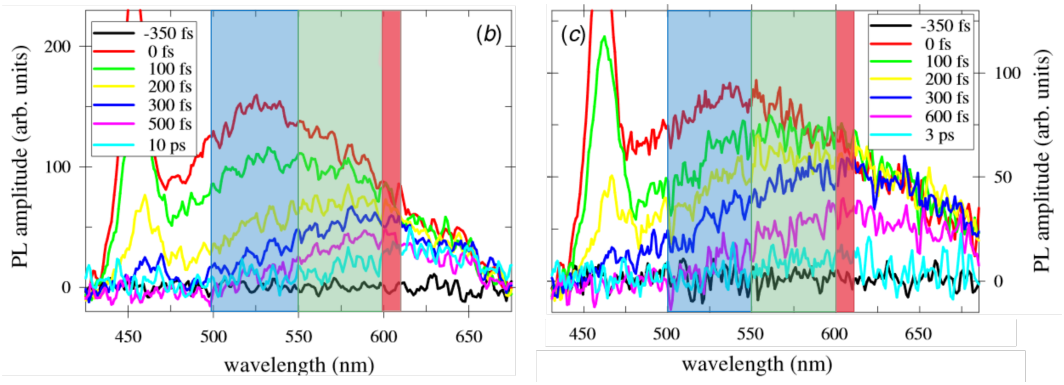

Figure 6.8: Luminescence spectra of [Re(Cl)$(CO)_3$(bpy)] (left) and [Re(Br)$(CO)_3$(bpy)] (right) in CH_3CN measured at selected time delays upon 400 nm excitation. Figure adapted from reference [3]. The three energy domains discussed are colored: in blue, the first domain associated with the time constant τ_1, in green the second domain associated with τ_2 and in red, the long-lived emission associated with τ_3.

[Re(X)$(CO)_3$(bpy)] X=Cl and 128 fs for X=Br [3] is attributed to the "spin-orbit" states E8(S2) and E9(T3) which emit at 496 nm (505 nm) and 482 nm (487 nm) (TAB. 6.6) respectively for [Re(Cl)$(CO)_3$(bpy)] ([Re(Br)$(CO)_3$(bpy)]).
At the minimum of T2, the corresponding "spin-orbit" states, E4-E6(T2), are found to emit at around 580 nm for both [Re(Cl)$(CO)_3$(bpy)] and [Re(Br)$(CO)_3$(bpy)] (TAB. 6.6). T2 couples by spin orbit with S2 and by this mean, the corresponding "spin-orbit" states gain in oscillator strength ($f = 0.2 \times 10^{-2}$). This is why E4-E6(T2) can explain the emission band between 550 nm and 600 nm (the green region in FIG. 6.8) with a time constant $\tau_2 = 340$ fs for [Re(X)$(CO)_3$(bpy)] X=Cl and τ_2 =470 fs for X=Br [3]. The "spin-orbit" state E7(S1), calculated at 557 nm for [Re(X)$(CO)_3$(bpy)] X=Cl and 553 nm for X=Br (TAB. 6.6), with an oscillator strength: $f \approx 0.2 \times 10^{-2}$, may also participate to this emission.
Finally, the long lived emission at 600-610 nm is attributed to the lowest triplet state, T1. It is computed at 596 nm for [Re(X)$(CO)_3$(bpy)] X=Cl and 592 nm for [Re(X)$(CO)_3$(bpy)] X=Br and is shifted to $\approx$ 610 nm by SOC (E1-E3(T1)) for both complexes with an oscillator strength of $f = 0.6 \times 10^{-2}$.

The effect of SOC in [Re(I)$(CO)_3$(bpy)] is more important. Indeed, the computed Stokes shift in the "SOC-free" S2 state ($S.S.^{S2} = 4944\,cm^{-1}$) is far from the experimental one ($S.S.^{exp} = 6430\,cm^{-1}$ [3]). On the other hand the stokes shift in the "spin-orbit" state E8 ($S.S.^{E8} = 6429\,cm^{-1}$) is in good agreement with experiments.

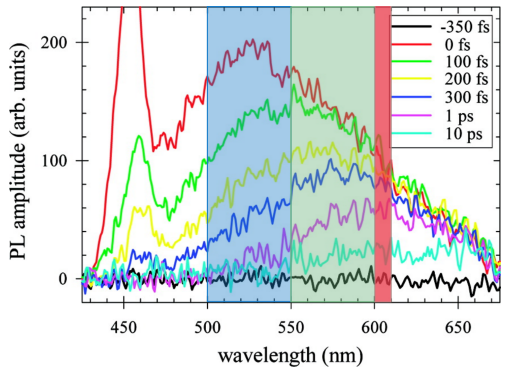

Figure 6.9: Luminescence spectra of [Re(I)$(CO)_3$(bpy)] in CH_3CN measured at selected time delays upon 400 nm excitation. Figure adapted from reference [3]. See FIG. 6.8 for the definition of the color code.

The nature of the states being different, another deexcitation mechanism has to be proposed.

The initial decay (characterized by $\tau_1 = 152fs$ [3]) is attributed to both the "spin-orbit" state E9(T3) found at 512 nm with an oscillator strength $f = 0.17 \times 10^{-1}$ and the E8(S2) state computed at 577 nm with $f = 0.4 \times 10^{-1}$ (TAB. 6.6). E7(S1) (595 nm) will contribute to the intermediate emission band (550-600 nm) characterized by a decay time constant $\tau_2 = 1180fs$ [3]. E8(S2) may also contribute to this intermediate band. E1-E3(T1) and E4-46(T2) are located close to 620 nm and are contributing to the long-lived emission band at 600-610 nm. However E1-E3(T1) acquires significant oscillator strength through SOC ($f = 0.15 \times 10^{-1}$) and is the main contribution to the band.

The two mechanisms for the decay of, on one side [Re(Cl)$(CO)_3$(bpy)] and [Re(Br)$(CO)_3$(bpy)], and on the other, of [Re(I)$(CO)_3$(bpy)], are summed up FIG. 6.10.

6.4 Quantum Dynamics of [Re(X)(bpy)$(CO)_3$] (X=F, Cl, Br, I) Complexes

This chapter will be focusing at first on the study of the bromide complex [212] in order to settle the methodology of the study. It will then be generalized to the other Re(I) halide complexes.

	State	Emission energy [eV] $S_n, T_n \rightarrow S_0$	Emission Wavelength [nm]	Emission Wavelength [nm] with SOC	"spin-orbit" state
X=Cl					
T1	a^3A''	2.10	596	610 (A")	E1(T1)
				610 (A')	E2(T1)
				607 (A')	E3(T1)
T2	a^3A'	2.24	558	575 (A")	E4(T2)
				576 (A')	E5(T2)
				570 (A")	E6(T2)
S1	a^1A''	2.25	557	575 (A")	E7(S1)
S2	b^1A'	2.47	505	496 (A')	E8(S2)
T3	b^3A''	2.64	474	482 (A')	E9(T3)
				472 (A")	E10(T3)
				466 (A")	E11(T3)
X=Br					
T1	a^3A''	2.11	592	609 (A")	E1(T1)
				608 (A')	E2(T1)
				604 (A')	E3(T1)
T2	a^3A'	2.19	571	587 (A")	E4(T2)
				587 (A')	E5(T2)
				583 (A")	E6(T2)
S1	a^1A''	2.26	553	576 (A")	E7(S1)
S2	b^1A'	2.39	522	505 (A')	E8(S2)
T3	b^3A''	2.62	477	487 (A')	E9(T3)
				467 (A")	E10(T3)
				467 (A')	E11(T3)
X=I					
T1	a^3A''	2.13	587	620 (A")	E1(T1)
				619 (A')	E2(T1)
				612 (A')	E3(T1)
T2	a^3A'	2.10	596	620 (A")	E4(T2)
				620 (A')	E5(T2)
				617 (A")	E6(T2)
S1	a^1A''	2.26	552	595 (A")	E7(S1)
S2	b^1A'	2.33	536	577 (A')	E8(S2)
T3	b^3A''	2.54	492	512 (A')	E9(T3)
				483 (A')	E10(T3)
				479 (A")	E11(T3)

Table 6.6: $S_n, T_n \rightarrow S_0$ transition energies at the geometry of the S_n, T_n minima obtained without spin-orbit. Corresponding emission wavelengths are reported with and without spin-orbit [5] (the "spin-orbit" state EX at the geometry of the minimum of state Y is labelled EX(Y)).

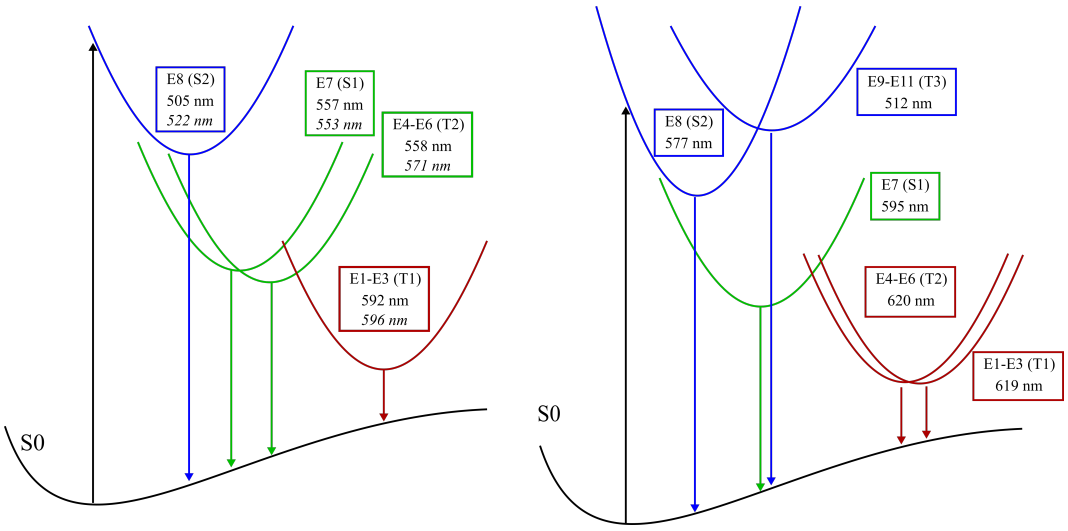

Figure 6.10: Qualitative representation of the mechanism of decay after absorption of [Re(Cl)(CO)$_3$(bpy)], [Re(Br)(CO)$_3$(bpy)] (left) and [Re(I)(CO)$_3$(bpy)] (right). The color code used is the same as in FIG. 6.8. In blue, states involved in the first emission band; in green, those involved in the second band and in red, states involved in the third emission band.

6.4.1 The Hamiltonian

On the basis of the electronic structure study, we will limit the quantum dynamics to five "SOC-free" states (namely T1, T2, S1, S2 and T3) describing eleven "spin-orbit" states. A further simplification of the diabatic model Hamiltonian is based on symmetry considerations. Within the Cs symmetry and according to the symmetry selection rules EQ. (6.13) and EQ. (6.15) only a' normal modes will contribute to the intrastate coupling ($\kappa_i^{(n)} \neq 0$), and only a" normal modes will induce interstate coupling ($\lambda_i^{(n),(m)} \neq 0$) between states of different symmetry but same spin multiplicity.
The model Hamiltonian for [Re(X)(bpy)(CO)$_3$] complexes is

$$\boldsymbol{W} = \begin{pmatrix} W^{S1} & W^{S1,S2} & 0 & \boldsymbol{W^{S1,T2}} & 0 \\ W^{*S1,S2} & W^{S2} & \boldsymbol{W^{S2,T1}} & 0 & \boldsymbol{W^{S2,T3}} \\ 0 & \boldsymbol{W^{*S2,T1}} & \boldsymbol{W^{T1}} & \boldsymbol{W^{T1,T2}} & 0 \\ \boldsymbol{W^{*S1,T2}} & 0 & \boldsymbol{W^{*T1,T2}} & \boldsymbol{W^{T2}} & \boldsymbol{W^{T2,T3}} \\ 0 & \boldsymbol{W^{*S2,T3}} & 0 & \boldsymbol{W^{*T2,T3}} & \boldsymbol{W^{T3}} \end{pmatrix} \tag{6.61}$$

where the elements written in bold are submatrices whose size will depend on the multiplicity of the states. Within the LVC approximation, the Taylor expansion of the elements of the electronic diabatic Hamiltonian W (EQ. (6.4)) will be truncated to the first order [1] (see SECTION 6.2.1.1). In addition, the Taylor expansion of the SOC terms (EQ. (6.48)) will be truncated at the zeroth order (i.e. they will be considered as constant). The "SOC-free" components of the triplets states will be degenerate; therefore the diabatic energy matrix of a triplet can be written:

$$\boldsymbol{W}^{\mathrm{T}n} = \begin{pmatrix} \epsilon_n + \sum\limits_{i\in a'} \kappa_i^{(n)} Q_i + \frac{1}{2}\sum\limits_{j\in a''} \omega_j Q_j^2 & 0 & 0 \\ 0 & \epsilon_n + \sum\limits_{i\in a'} \kappa_i^{(n)} Q_i + \frac{1}{2}\sum\limits_{j\in a''} \omega_j Q_j^2 & 0 \\ 0 & 0 & \epsilon_n + \sum\limits_{i\in a'} \kappa_i^{(n)} Q_i + \frac{1}{2}\sum\limits_{j\in a''} \omega_j Q_j^2 \end{pmatrix} \tag{6.62}$$

The interaction between the two-singlet states (S2(b^1A') and S1(a^1A'')) will be purely vibronic, and takes the form:

$$W^{S1,S2} = \sum_{j\in a''} \lambda_j^{S1,S2} Q_j \tag{6.63}$$

As for the coupling between two triplets, only the intrastate vibronic coupling between spin components of same multiplicity are considered. Thus, the coupling between T1/T2 can be expressed as:

$$W_{n,n}^{(T1),(T2)} = \sum_{j\in a''} \lambda_j^{T1,T2} Q_j \qquad n = 1,2,3 \tag{6.64}$$

Since our definition of the interstate vibronic coupling is limited to pairs of states (EQ. (6.43)), and because the energy gap is important between T2 and T3, we choose to neglect this term for T2/T3.

In order to add SOC into the model Hamiltonian, the double symmetry group has to be considered in order to apply symmetry selection rules. In the double symmetry group, the symmetry of each spin component of each electronic state will be the result of the direct product between the orbital species and the spin function species. In the Cs spatial group, the spin function species is A' for singlets and $A' + 2A''$ for triplet states. Thus, the S1 (a^1A'') state has only one A'' spin component, and S2 (b^1A') only has one A'

spin component. For T1 and T3 (a^3A'' and b^3A'' respectively, the direct products yields:

$$\Gamma_{A''} \otimes (\Gamma_{A'} + 2\Gamma_{A''}) = \Gamma_{A''} + 2\Gamma_{A'} \tag{6.65}$$

Thus, triplets T1 and T3, will be composed of two A' spin components ($ms = \pm 1$) and one A'' spin component ($ms = 0$). On the opposite, the direct product for T2 (a^3A') yields:

$$\Gamma_{A'} \otimes (\Gamma_{A'} + 2\Gamma_{A''}) = \Gamma_{A'} + 2\Gamma_{A''} \tag{6.66}$$

and thus is composed of one A' spin component ($ms = 0$) and two A'' spin components ($ms = \pm 1$).

SO couples spin components of different symmetry. Therefore the $ms = \pm 1$ spin components of T1 (T3) will couple with the $ms = 0$ spin component of T2 and *vice versa*. In addition, the $ms = \pm 1$ components of T1 couples with the $ms = \pm 1$ spin components of T3. However these coupling are null due to spin selection rules.

Following the same pattern, electronic states S2 will couple with the spin components $ms = \pm 1$ of T1 (T3) and *vice versa* but not with T2. And S1 will couple with the $ms = \pm 1$ spin components of T2 only.

We can rewrite the coupling matrices, including spin-orbit, for the interaction between a singlet (S_n) and a triplet (T_m) electronic state of different symmetry:

$$\boldsymbol{W^{Sn,Tm}} = \begin{pmatrix} \eta^*_{Sn,Tm} & 0 & \eta_{Sn,Tm} \end{pmatrix} \tag{6.67}$$

The coupling between T1 and T2, can be expressed from EQ. (6.52) as:

$$\boldsymbol{W^{T1,T2}} = \begin{pmatrix} \sum\limits_{j\in a''} \lambda_j^{T1,T2} Q_j & \eta_{T1,T2} & 0 \\ \eta_{T1,T2} & \sum\limits_{j\in a''} \lambda_j^{T1,T2} Q_j & -\eta^*_{T1,T2} \\ 0 & -\eta^*_{T1,T2} & \sum\limits_{j\in a''} \lambda_j^{T1,T2} Q_j \end{pmatrix} \tag{6.68}$$

Because the interstate vibronic coupling due to T3 is neglected, the T2/T3 interaction matrix reads:

$$\boldsymbol{W^{T2,T3}} = \begin{pmatrix} 0 & \eta_{T2,T3} & 0 \\ -\eta^*_{T2,T3} & 0 & \eta_{T2,T3} \\ 0 & -\eta^*_{T2,T3} & 0 \end{pmatrix} \tag{6.69}$$

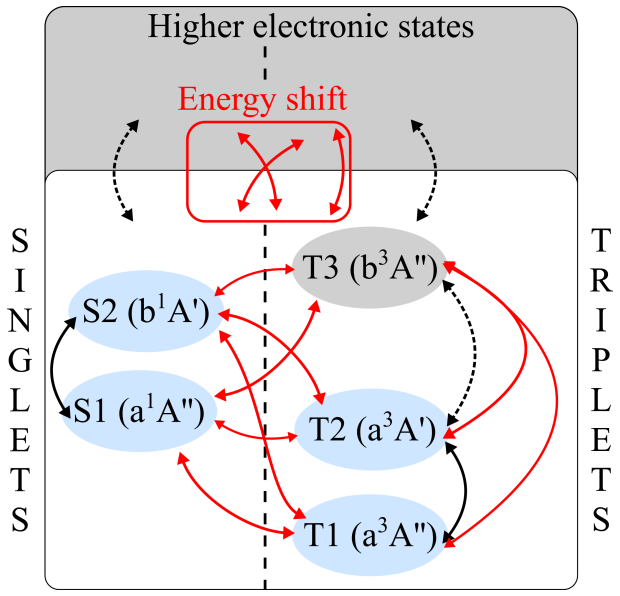

Figure 6.11: Strategy used to describe the coupling between states; black arrows mean interstate coupling, red arrows mean SOC; Full lines represent interactions that are explicitly considered whereas dotted lines show neglected interactions.

Of course, the energy obtained by diagonalization of the **W** matrix constructed on the basis of a model Hamiltonian restrained to five electronic states, cannot pretend to be quantitative. For correcting this bias we adjusted the diabatic potentials (*i.e.* the $W_{n,n}$ elements) by adding a shift in energy in order to match the adiabatic computed vertical transition energies. These considerations are reported in FIG. 6.11, the energy shift does not exceed 0.06eV.

6.4.2 The case study "[Re(CO)$_3$(bpy)Br]"

The [Re(Br)(CO)$_3$(bpy)] complex has a total of 78 degrees of freedom. In order to lower the dimensionality of the system and to allow a quantum dynamical approach, we select a set of normal modes that should mainly contribute to the excited state dynamics.

6.4.2.1 Electronic structure data

6.4.2.1.1 Intrastate coupling

As seen in EQ. (6.13), only normal modes of symmetry a' will induce intrastate coupling.

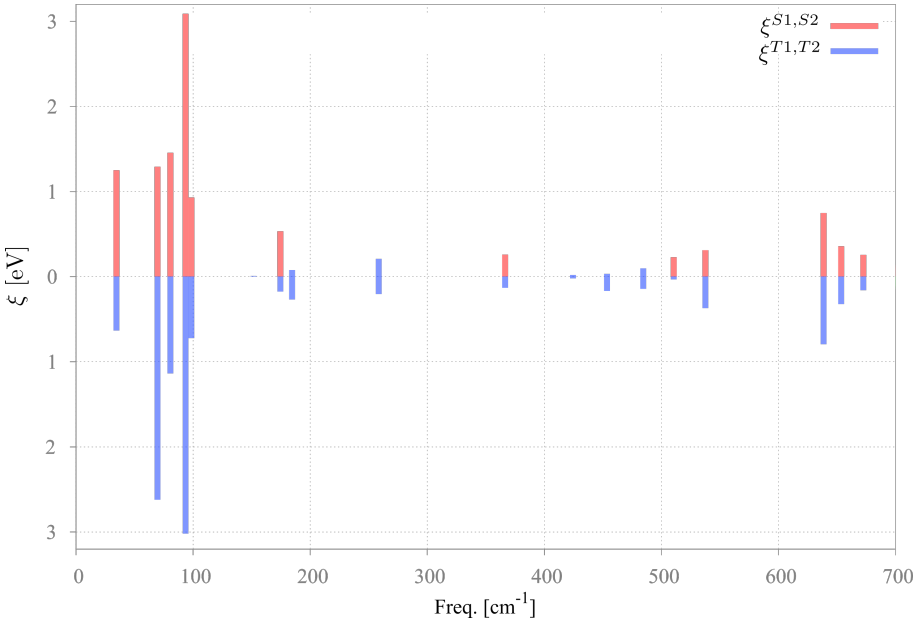

Figure 6.12: Differences in displacements between S1 and T1 and S2 and T2. For convenience high frequency normal modes are not shown.

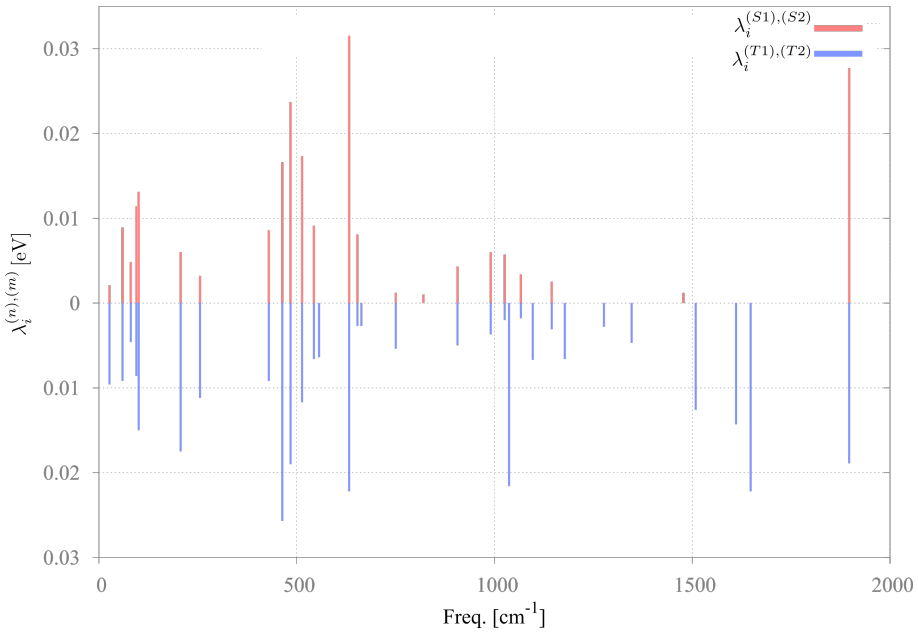

Figure 6.13: Vibronic coupling constant ($\lambda_i^{(n),(m)}$).

Mode	ω	κ				
		S1	S2	T1	T2	T3
6 (a')	0.0116	-0.0172	0.0187	-0.0161	0.0190	0.0015
17 (a')	0.0188	0.0090	0.0091	0.0002	-0.0006	0.0056
18 (a')	0.0229	-0.0289	-0.0271	-0.0261	-0.0322	0.0133
29 (a')	0.0792	-0.0187	0.0404	-0.0196	0.0433	0.0033
Mode	ω	λ^{S1S2}		λ^{T1T2}		
8 (a")	0.0118	0.0114		0.0086		
23 (a")	0.0601	0.0237		0.0190		
State	E			η		
	calculed	adjusted				
S1 (A")	2.96	2.94		S1T2	0.0769 + 0.0186i	
S2 (A')	3.13	3.11		S2T1	-0.0719 + 0.0196i	
T1 (A")	2.84	2.81		S2T3	0.0274 + 0.0056i	
T2 (A')	2.93	2.93		T1T2	0.0719 + 0.0177i	
T3 (A")	3.22	3.22		T2T3	-0.0270 + 0.0046i	

Table 6.7: List of the parameters entering the model Hamiltonian for [Re(Br)$(CO)_3$(bpy)].

A mode that shifts two states apart from each other will induce a crossing point between them. The greater the shift, the closer will be the crossing from FC. This will play a key role in the ISC process. The relative shift between two states n and m:

$$\xi^{(n),(m)} = \frac{-\left(\kappa_i^{(n)} - \kappa_i^{(m)}\right)}{\omega_i} \tag{6.70}$$

will drive our choice in the selection of modes. Two modes, namely at $\omega_7 = 94\text{cm}^{-1}$ and $\omega_{30} = 638\text{cm}^{-1}$ (FIG. 6.16), involve symmetrical motions of CO ligands. The opposite signs between the κ^{S1} and κ^{T1} constants, on the one hand, and the κ^{S2} and κ^{T2} constants (TAB. 6.7) on the other hand, arise from the fact that these motions do not have the same impact on the Re(I) d_{yz} orbital involved in S1 and T1, and the Re(I) d_{xy} involved in S2 and T2.

In order to tentatively interpret the observed correlation between the decay time τ_1 and the frequency of Re-X bond stretching motion we have to include the two normal modes at $\omega_{11} = 152\text{cm}^{-1}$ and $\omega_{13} = 185\text{cm}^{-1}$ respectively (FIG. 6.16). These are the two modes involving a stretching motion of the Re-Br bond, the main component being in the mode at $\omega = 152\text{cm}^{-1}$, and a motion of the bipyridine ligand. The vibronic intrastate coupling constants induced by these two modes shift mainly the electronic states in only one direction (i.e. the constants κ have the same sign). As seen in paragraph 6.2.1.1.3,

such modes will not bring the conical intersection closer to the origin, see EQ. (6.46). Nevertheless, they induce a large contribution to the Stokes shift in S2, $S.S._{11}^{S2} = 0.44 \times 10^{-2} eV$ and $S.S._{13}^{S2} = 0.32 \times 10^{-1} eV$ respectively (see APPENDIX B.1). This can be easily understood by looking at the difference of electronic densities for the S0 $\rightarrow$ S1, S2, T1 and T2 (FIG. 6.5). Indeed, in both cases, the p orbital of the halide is parallel to the d orbital of the metal. In that case, a shortening or a stretching of the Re-Br bond will have the same effect on the four MLCT states.

6.4.2.1.2 Vibronic coupling

Only a" normal modes will be able to couple two states of different symmetry (EQ. (6.15)). Among the a" normal modes which induce a strong coupling between both S1 and S2, and, T1 and T2, (FIG. 6.13) we select two modes at $\omega = 95\mathrm{cm}^{-1}$ and $\omega = 485\mathrm{cm}^{-1}$. These two modes involve asymmetric carbonyl motions (FIG. 6.17).

We discarded normal modes inducing imaginary interstate vibronic coupling. From EQ. (6.43), it is clear that an imaginary value of $\lambda_i^{(n),(m)}$ is due to a negative $\frac{\partial^2 V_m}{\partial Q_i^2} - \frac{\partial^2 V_n}{\partial Q_i^2}$ term. It implies that the curvature of the lowest PES (V_m) is steeper that the curvature of V_n. This would correspond to the attraction of two electronic states, which is unphysical. This coupling could be an artefact of our level of approximation: (1) considering that all normal modes have the same frequency in each electronic states; (2) as we restrict our computation of the interstate vibronic constant to a pair of electronic states. In order to investigate if a breaking of symmetry (See SECTION 6.2.1.1.2) occurs, the conditions EQ. (6.37) and (6.38)) have been computed for the pairs of states S1/S2 and T1/T2 for [Re(X)(CO)$_3$(bpy)] X=F, X=Cl, X=Br and X=I and are reported in APPENDIX B.1. For the pair of states S1/S2, both conditions are not met in all four complexes. Thus there are no a" normal modes which couple the two electronic states S1 and S2 enough to induce a symmetry breaking. However, for the pair of states T1/T2, the two conditions are both met for [Re(X)(CO)$_3$(bpy)] X=Cl, X=Br, X=I (not for X=F). Nevertheless, the stabilization energy resulting of the symmetry breaking is very low ($< 10^{-3} eV$) and can be considered as negligible. We can thus consider the total Stoke shift in S2 to be solely due to the intrastate coupling constants. As no excited state minimum were found with an a" symmetry, this result validates partially our method. This observation is in agreement with the fact that none of the optimized structures in the excited states are out of the C_s symmetry.

6.4.2.1.3 Stokes Shift

As seen previously, the TD-DFT calculations were able to reproduce very well the experiments. Within our approximations (*i.e.* taking harmonic potentials), we can compute the Stokes shift in S2 using (EQ. (6.14))

$$S.S.^{S2} = 0.72eV$$

The fact that our approximated potential energy surfaces reproduces pretty well the Stokes shift obtained through calculations ($S.S.^{TD-DFT} = 0.73$ eV), and thus obtained experimentally ($S.S.^{exp} = 0.74$ eV), comforts us in the idea that the system is rigid enough to consider only small displacements and therefore harmonic potentials.
A large difference between our Stokes Shift and the computed one, would either mean that: (1) considering the SOC as constant is not realistic (indeed, a constant SOC induces only a shift in energy in the "spin-orbit" states, whereas in fact, the SOC affects the shape of the "spin-orbit" states); (2) the normal mode approximation is not valid, and we should take into account the anharmonicity of the potentials.

6.4.2.1.4 Vertical transition energies

As we consider only the first two singlets and the first three triplets, we lack the contributions of higher lying electronic states to SOC.
While the model diabatic states we construct will have the good energy at Franck-Condon, the associated adiabatic states will be artificially shifted in energy with respect to the TD-DFT results. To ensure that the adiabatic vertical transition energies match with the computed ones, we adjust the energies of the "soc-free" states. This adjustment is minor (in the order of 10^{-2} eV) and is reported in TAB. 6.7.

6.4.2.1.5 Construction of the potentials

On the basis of the transition energies and the vibronic coupling terms we can now construct the diabatic and adiabatic potentials.

6.4.2.1.5.1 (1) Diabatic states

First, the so-called "diabatic states" (FIG. 6.14, FIG. 6.15) will be the diagonal elements of the diabatic Hamiltonian, coupled together by λ and η. In this representation we still

have two singlet (full lines) and three triplet states (dotted lines). Here we can see the shift induced by normal modes 11 and 13, i.e. the two modes involving the stretching motion of Re-Br. All states but T3 are shifted in the same direction. T3 remains centered arount $Q_i = 0$. On the opposite, modes 7 and 30 shift S1 and T1 apart from S2 and T2, thus creating a crossing between S1/S2 around $Q_7 = -5$ and $Q_{30} = -3$, and between T1/T2 at $Q_7 = -3$ and $Q_{30} = -1.5$. This will improve the population transfer between S1 and S2 and between T1 and T2. In this representation, the diabatic electronic states as function of a" modes 8 and 23 are parallel harmonic potentials as the λ coupling occurs on the off diagonal.

6.4.2.1.5.2 (2) Adiabatic states

By diagonalizing the diabatic Hamiltonian we obtain the adiabatic states (FIG. 6.14, FIG. 6.15: right). Here triplet states are split into two groups. On one side the $m_s = \pm 1$ components, and on the other side, the $m_s = 0$ component. Indeed, by looking at the Hamiltonian as we built it, the coupling with the $m_s = \pm 1$ components of each triplets are the same. In this representation, a conical intersection is observed between the E8 and E7 states at around $Q_7 = -5$, $Q_{13} = -3.5$ and $Q_{30} = -3$. A conical intersection is also observed between E3 and E2 at $Q_7 = -2.5$ and $Q_{30} = -1.5$.
According to normal modes 8 and 23, the adiabatic electronic states remain centred around $Q_i = 0$ but their frequency are slightly modified.

6.4.2.2 Wavepackets Propagations

6.4.2.2.1 Quantum dynamics with no vibronic coupling.

First, a preliminary wavepacket propagation has been performed without taking into account the vibronic interstate coupling (*i.e.* $\lambda_i = 0$, $\kappa_i \neq 0$ and $\eta_i \neq 0$). The parameters entering the Hamiltonian can be found TAB. 6.7.

The diabatic population evolution as a function of time after excitation to S2 is shown FIG. 6.18. Here, to lighten the graph, the population in all spin components of each triplet state are summed over. A transfer of population is observed within 10-20 fs between S2 and T1 on one side, and S2 and T3 on the other. This transfer is solely due to the strong spin-orbit coupling between those states.

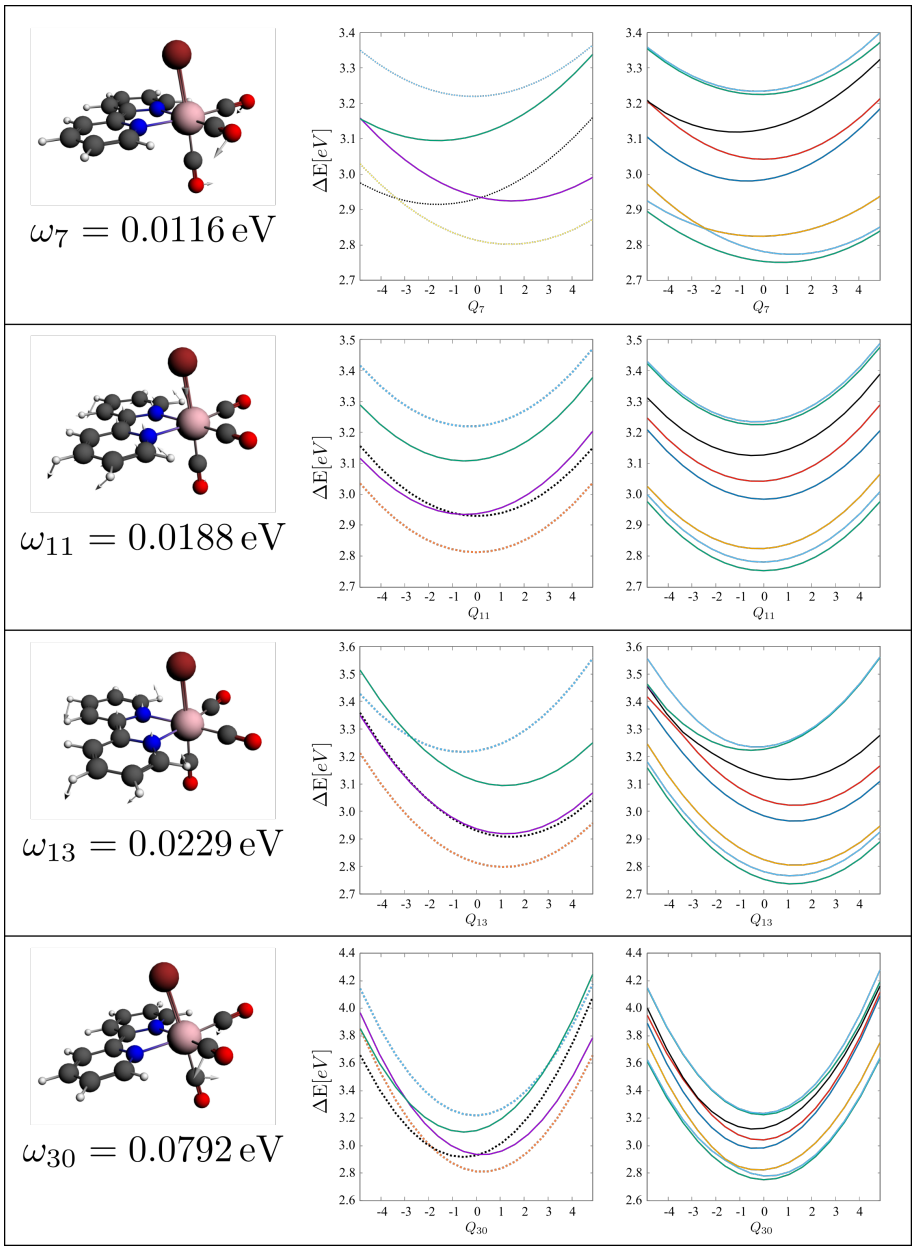

Figure 6.14: Left: Selected a' normal modes and associated frequencies in eV. Middle: diabatic states built from the *ab initio* parameters reported in TAB. 6.7 (singlet states in full lines). In increasing energy at Franck-Condon: T1, T2, S1, S2 and T1 (S2 in green). Triplet states are represented in dotted lines. Right: Adiabatic states obtained from the diagonalization of the diabatic Hamiltonian (E8 in black).

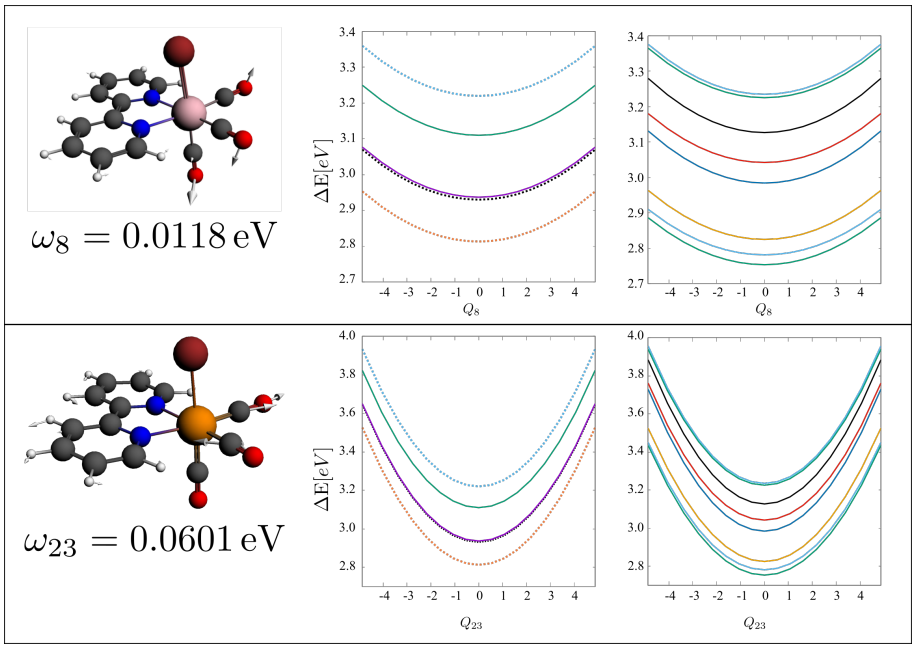

Figure 6.15: Left: Selected a" normal and associated frequencies in eV. Middle: diabatic states built from the *ab initio* parameters reported in TAB. 6.7 (singlet states in full lines). In increasing energy at Franck-Condon: T1, T2, S1, S2 and T1 (S2 in green). Triplet states are represented in dotted lines. Right: Adiabatic states obtained from the diagonalization of the diabatic Hamiltonian (E8 in black).

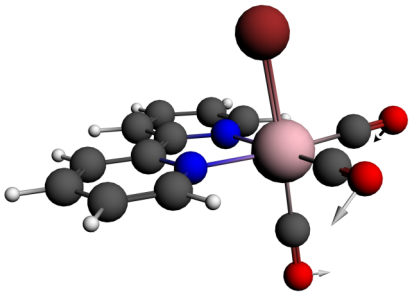

ω_7 =0.0116 eV (94 cm^{-1})

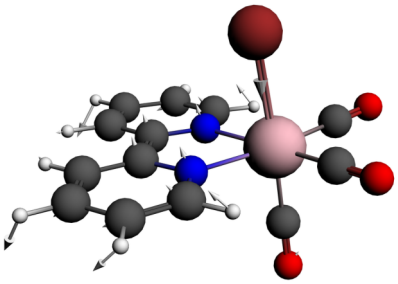

ω_{11} =0.0188 eV (152 cm^{-1})

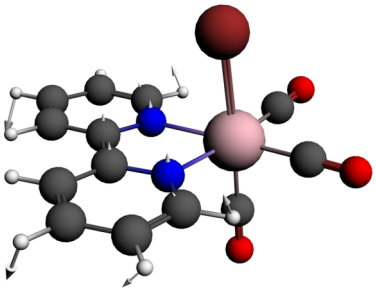

ω_{13} =0.0229 eV (185 cm^{-1})

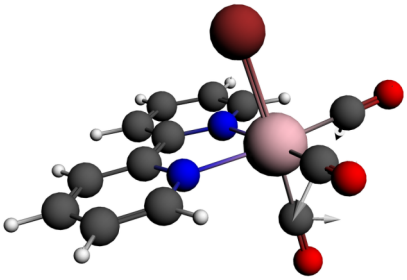

ω_{30} =0.0792 eV (638 cm^{-1})

Figure 6.16: a' normal modes selection for [Re(Br)(CO)$_3$(bpy)].

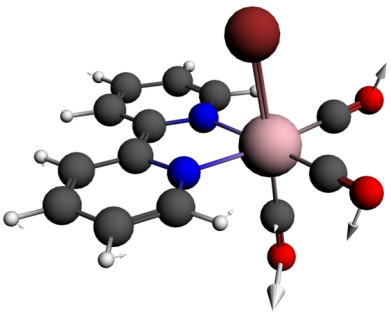

ω_8 =0.0118 eV (95 cm^{-1})

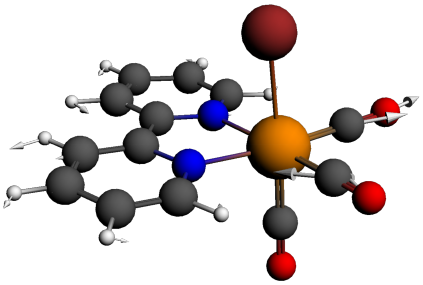

ω_{23} =0.0601 eV (485 cm^{-1})

Figure 6.17: a" normal modes selection for [Re(Br)(CO)$_3$(bpy)].

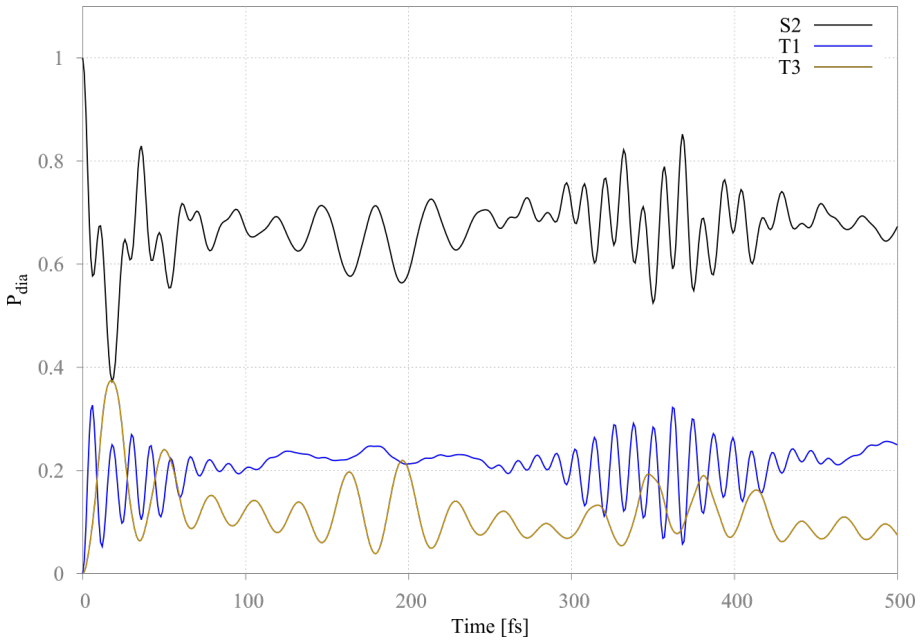

Figure 6.18: Evolution of the diabatic populations as function of time after initial excitation in S2 for the [Re(Br)$(CO)_3$(bpy)] complex without vibronic coupling (for convenience the population in all spin components of each triplet state are summed over).

The fast oscillations in those three states are directly related to the spin-orbit coupling. One can see that the oscillations in the population of T1 have a higher frequency than those in T3 as the SOC between S2 and T1 is more important as the one between S2 and T3. The oscillation pattern of the population in S2 is more complex, as it involves SOC with both T1 and T3.

Spin-orbit coupling, as considered (i.e. constant at their value at Franck-Condon), does not allow to populate S1 as it will couple only states of different spin multiplicity but of same symmetry. Thus SOC allows only a transfer of population through the A' channel (FIG. 6.19). After some time (c.a. 20 fs) the population of each state oscillates around an average population which is constant in time. Populating S1 and T2 is therefore not possible through spin-orbit coupling alone.

Recurrences are observed around 250 fs mainly in S2 and T1. These features arise from the lack of degrees of freedom to dissipate the energy.

6.4.2.2.2 Quantum dynamics with vibronic coupling.

The same dynamics is propagated with the vibronic interstate coupling switched on

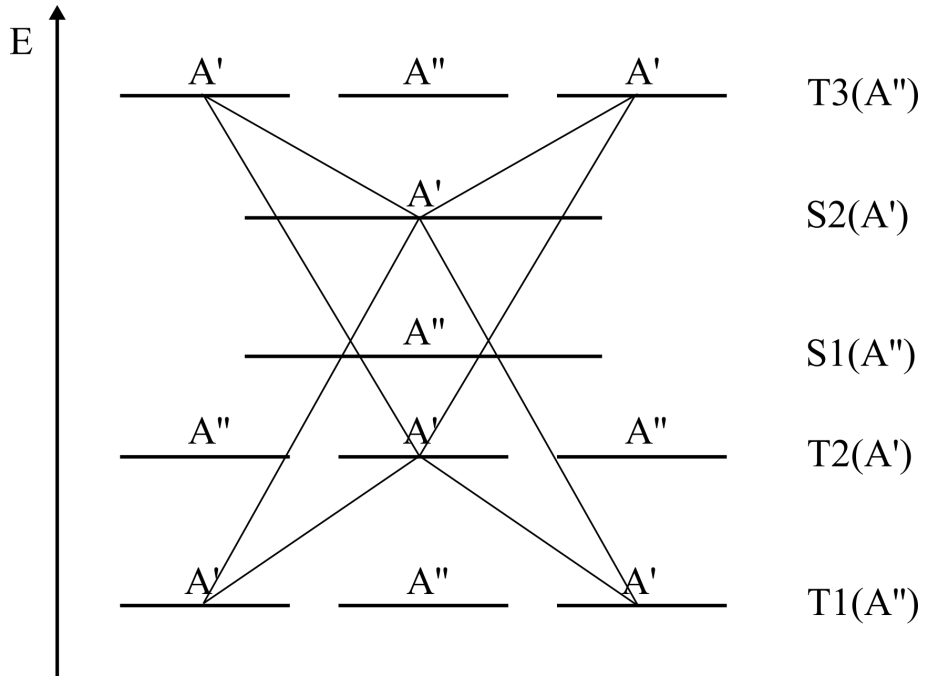

Figure 6.19: Representation of the first two singlet states and three triplet states. Here every component of each triplet state is shown with its symmetry. Black lines denote the coupling between A' states due to SOC.

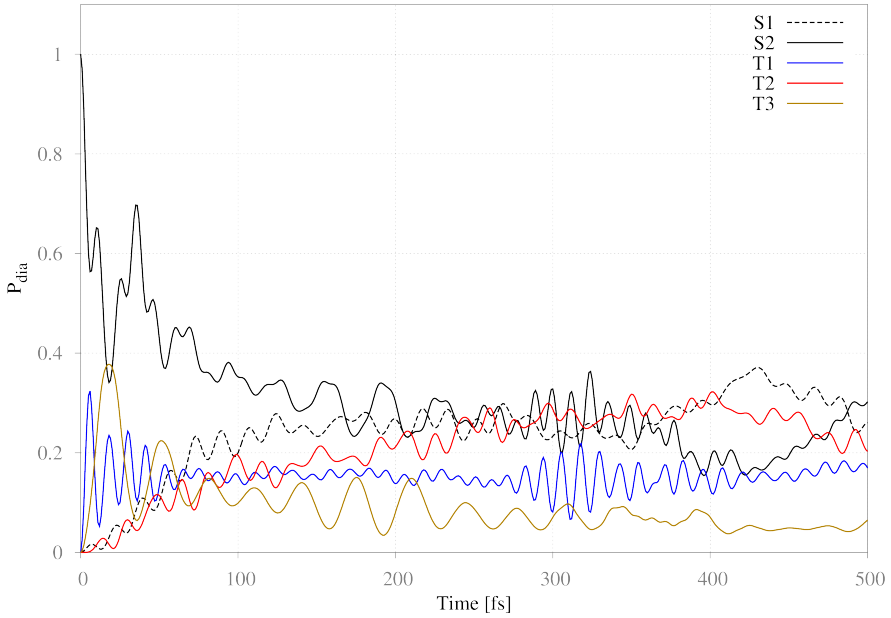

Figure 6.20: Evolution of the diabatic populations as function of time after initial excitation in S2 for the [Re(Br)$(CO)_3$(bpy)] complex including vibronic coupling (for convenience the population in all spin components of each triplet state are summed over).

(TAB. 6.7). At short time, (i.e. 10-20 fs) (FIG. 6.20) the same behavior is observed as in the dynamics with no interstate coupling (FIG. 6.18), as the SOC are stronger and occur faster than vibronic interstate coupling. A fast population transfer is observed between S2 and T1, T3, with exactly the same shape as with SOC alone. But then the population in S2 decreases, exhibiting a quasi-exponential decay on top on the SOC oscillations to finally reach at 300 fs around 25% of the total poulation.
S1 starts to be quasi immediately populated through vibronic interstate coupling with S2 and in turn populates T2 through SOC. T2 will also be populated by T1 due to the vibronic interstate coupling between them. Population in S1 and T2 slowly increases in time to reach around 25% of the population each.
Population in T3, the highest lying triplet, slowly decreases in time. And the population of T1 remains nearly constant.
Turning on the vibronic interstate coupling unlocks the A" channel by allowing a transfer between S1 and S2, and between T1 and T2 (FIG. 6.21). We can thus first slowly populate A" states by vibronic interstate coupling and then have a faster transfer between A" modes through SOC.
At around 250 fs, we can observe the same recurrences as with spin orbit alone, making it impossible to interpret the dynamics at longer time. From the diabatic states and populations, it is possible to compute the adiabatic populations, that's to say the populations in the "spin-orbit" states. This representation of the population is easiest to compare with experiments. The diabatic to adiabatic transformation has been done using the Heidelberg MCTDH package, with the Monte-Carlo integration scheme. The adiabatic populations are thus computed every 5 fs up to 1 ps (FIG. 6.22: the first 500 fs only are shown.). Initially, three A' electronic states are mainly populated, namely: E11, E8, E3. This is due to the contribution of S2, which is the diabatic populated state, in these "spin-orbit" states (16%, 70% and 10% for E11, E8 and E3 respectively). The adiabatic populations do not oscillate as the diabatic ones. Indeed, here the SOC will act as diagonal element of the Hamiltonian and will no longer induce population transfers between states. The population of the E8 "spin-orbit" state quickly decreases, and populates quasi only E7. This behaviour is in good agreement with the experimental facts; indeed at the same period of time a decrease in an emission band and the appearance of another one are observed. The E7 "spin-orbit" state is composed of 51% of S1 and 48% of T2. It is therefore populated through two different ways: first, the vibronic interstate coupling between S2 and S1; second, the strong SOC between S2 and T2. The population of E11 (83% T3)

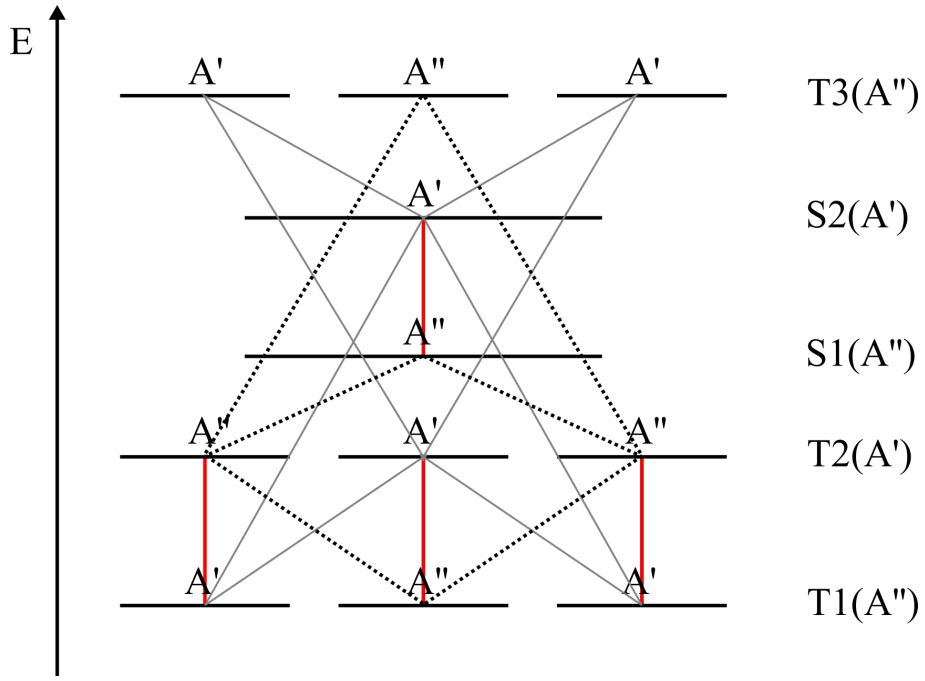

Figure 6.21: Representation of the first two singlet states and three triplet states; here every component of each triplet state is shown with its symmetry. Gray lines denote the coupling between A' states due to SOC; black dotted lines represent the coupling between A" states and red lines show the vibronic interstate coupling between states of different symmetry but same spin multiplicity.

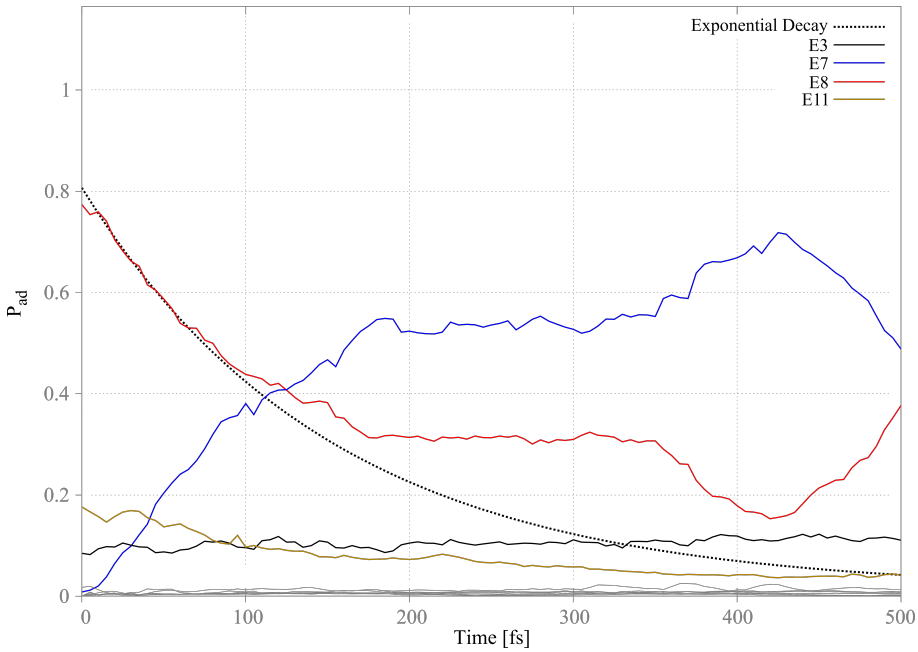

Figure 6.22: Evolution of the adiabatic populations as function of time after initial excitation in the diabatic S2 state for the [Re(Br)(CO)$_3$(bpy)] complex including virbonic coupling (low populated in gray).

decreases slowly with time to repopulate E8. The population of E3 (85% T1) remains nearly constant throughout the dynamics as the diabatic population of T1. In fact, it increases very slowly with a long time constant. To make the connection with experiments, one has to look back at the emission wavelengths of the excited state, that's to say their minima computed with TD-DFT methods (see section 6.3.3). E8 is computed to emit at $\lambda_{em}^{E8} = 503\,nm$, E3 at $\lambda_{em}^{E3} = 600\,nm$, E11 at $\lambda_{em}^{E11} = 490\,nm$ and E7 at $\lambda_{em}^{E7} = 580\,nm$. After excitation at 400nm, the E8 state is populated. Its decrease in population, together with E11, explains the disappearance of the emission band at $\simeq$ 500nm. At the same time, E7 gets more populated and is responsible for the emission band at around 580nm. Finally the E3 state, will lead to the long-lived emission signal at around 610nm. E1 and E2 should also contribute to the long-lived emission band as they are mainly composed of T1, but they are only weakly populated within our level of approximation due to the weak T1/T2 vibronic coupling constant.

The initial decay of E8, responsible for the experimentally observed τ_1 [3] time constant can be estimated by comparing the initial decay to an exponential one:

$$f(t) = P_0 e^{-t/\tau_{th}} \tag{6.71}$$

P_0 being the initial population in E8. The estimated time constant is $\tau_{th}^{Br} = 152\,fs$. This value is close to the experimentally determined time constant: $\tau_1^{Br} = 128 \pm 12\,fs$. The presence of recurrences prevents us to estimate τ_2 and τ_3 as the dynamics can no longer be exploited at such large time scales.

6.4.3 Application of the method to the other complexes (X=F, Cl, I)

6.4.3.1 Electronic structure data

Mode	ω	κ				
		S1	S2	T1	T2	T3
8 (a')	0.0115	-0.0200	0.0224	-0.0178	0.0236	0.0003
12 (a')	0.0510	0.0686	0.0595	0.0581	0.0565	0.0005
14 (a')	0.0526	-0.0094	-0.0074	-0.0072	-0.0044	-0.0026
30 (a')	0.0799	-0.0286	0.0454	-0.0272	0.0479	0.0054
Mode	ω	λ^{S1S2}		λ^{T1T2}		
8 (a")	0.0119	0.0141		0.0158		
23 (a")	0.0603	0.0190		0.0193		
State	E			η		
	calculed	adjusted				
S1 (A")	2.87	2.86		S1T2	-0.0632 + 0.0281i	
S2 (A')	3.04	3.03		S2T1	-0.0610 - 0.0258i	
T1 (A")	2.75	2.80		S2T3	-0.0155 + 0.0067i	
T2 (A')	2.89	2.89		T1T2	-0.0616 + 0.0270i	
T3 (A")	3.21	3.24		T2T3	0.0149 - 0.0064i	

Table 6.8: List of the parameters entering the model Hamiltonian for [Re(F)$(CO)_3$(bpy)].

As for the complex [Re(Br)$(CO)_3$(bpy)] the electronic structure data needed to build the Hamiltonian are extracted from TD-DFT calculations and reported in TAB. 6.8,TAB. 6.9 and TAB. 6.10 for the complexes [Re(X)$(CO)_3$(bpy)] X=F, X=Cl, X=I respectively.

6.4.3.2 Quantum dynamics

6.4.3.2.1 Diabatic populations

Looking at the evolution of the diabatic populations of [Re(X)$(CO)_3$(bpy)] X=F (FIG.

Mode	ω	κ				
		S1	S2	T1	T2	T3
7 (a')	0.0119	-0.0179	0.0040	-0.0174	-0.0001	-0.0001
11 (a')	0.0229	0.0131	0.0167	0.0140	0.0227	-0.0053
13 (a')	0.0293	-0.0315	-0.0283	-0.0190	-0.0222	0.0032
30 (a')	0.0793	-0.0227	0.0448	-0.0214	0.0469	0.0035
Mode	ω	λ^{S1S2}		λ^{T1T2}		
8 (a")	0.0118	0.0157		0.0127		
23 (a")	0.0600	0.0239		0.0182		
State	E			η		
	calculed	adjusted				
S1 (A")	2.99	2.95		S1T2	-0.0626 + 0.0238i	
S2 (A')	3.18	3.12		S2T1	0.0581 + 0.0241i	
T1 (A")	2.86	2.81		S2T3	0.0196 - 0.0079i	
T2 (A')	2.97	2.97		T1T2	-0.0595 + 0.0223i	
T3 (A")	3.23	3.22		T2T3	0.0203 - 0.0073i	

Table 6.9: List of the parameters entering the model Hamiltonian for [Re(Cl)$(CO)_3$(bpy)].

6.23, left) and X=Cl (FIG. 6.23, right) we can again observe the fast population transfer from S2 due to SOC within the first femtoseconds. In the case of [Re(X)$(CO)_3$(bpy)] X=F, the intensity of the transfer is weaker than for X=Cl, itself weaker than for X=Br. Indeed, the population of the diabatic state S2 after one full oscillation (i.e. the second minima of the oscillations in S2), is about 0.57, 0.5 and 0.35 for [Re(X)$(CO)_3$(bpy)] X=F, X=Cl (FIG. 6.23) and X=Br (FIG. 6.20) respectively.

After this initial fast transfer due to SOC, the slower decay due to vibronic interstate coupling is observed. This decay is slower going from the [Re(X)$(CO)_3$(bpy)] X=F to X=Cl and to X=Br.

The strength of the interstate coupling depends both on the coupling constant (λ) and on the energy gap between the two states. Thus, comparing only the values of the coupling constants is not satisfying.

In [Re(F)$(CO)_3$(bpy)], S1 and T2 are quickly populated and oscillate in phase with each other. The population exchanges back and forth between S2 and T2. The first triplet T1 is immediately populated by SOC and is getting more and more populated with time. On the contrary, T3 is nearly not populated at all during the dynamics. Again, recurrences are observe at 250fs, indicating that we do need more normal modes to dissipate the energy. Note in this case, that the oscillations due to the SOC are less present. This may be caused by a fortuitous cancellation of the oscillations.

Mode	ω	κ				
		S1	S2	T1	T2	T3
7 (a')	0.0115	0.0095	-0.0154	0.0108	-0.0163	-0.0035
11 (a')	0.0155	-0.0058	-0.0040	-0.0009	-0.0005	0.0029
13 (a')	0.0226	0.0202	0.0186	0.0211	0.0250	-0.0170
30 (a')	0.0787	0.0054	-0.0315	0.0095	-0.0358	-0.0036

Mode	ω	λ^{S1S2}	λ^{T1T2}
8 (a")	0.0116	0.0074	0.0057
23 (a")	0.0603	0.0188	0.0165

State	E		η	
	calculed	adjusted		
S1 (A")	2.85	2.75	S1T2	-0.1337 + 0.0016i
S2 (A')	2.95	2.85	S2T1	-0.1306 + 0.0071i
T1 (A")	2.76	2.71	S2T3	-0.0520 - 0.0017i
T2 (A')	2.81	2.73	T1T2	-0.1267 + 0.0024i
T3 (A")	3.19	3.19	T2T3	0.0481 + 0.0017i

Table 6.10: List of the parameters entering the model Hamiltonian for [Re(I)$(CO)_3$(bpy)].

For [Re(Cl)$(CO)_3$(bpy)], the dynamics look like in the bromide case. At first, both T1 and T3 are quickly populated by SOC. The population in T1 remains nearly constant all along the dynamics, while the population in T3 decreases slowly with time. Again, T2 and S1 are populated in a second step, and recurrences are observed at 250fs, just as with both other complexes.

6.4.3.2.2 Adiabatic populations

Looking at the evolution of the adiabatic populations with time allows us to estimate the time constant of decay for both [Re(X)$(CO)_3$(bpy)] X=F and X=Cl.

In [Re(F)$(CO)_3$(bpy)] and [Re(Cl)$(CO)_3$(bpy)], E11, E8 and E3 are initially populated due to the important contribution of S2.

In both cases, the population of E8 is transferred mainly to E7. For [Re(Cl)$(CO)_3$(bpy)], the population initially in S2 oscillates between E8 and E7. The population in E11 tends to slowly decrease to lower electronic states while the population in E3 remains rather constant as it is one of the lowest states.

In [Re(F)$(CO)_3$(bpy)] however, the initial population of E8 does not only oscillate between E8 and E7 but is also transferred to lower electronic states. This transfer allows the final population in E8 to reach above 20% in [Re(X)$(CO)_3$(bpy)] X=F compared to 40%

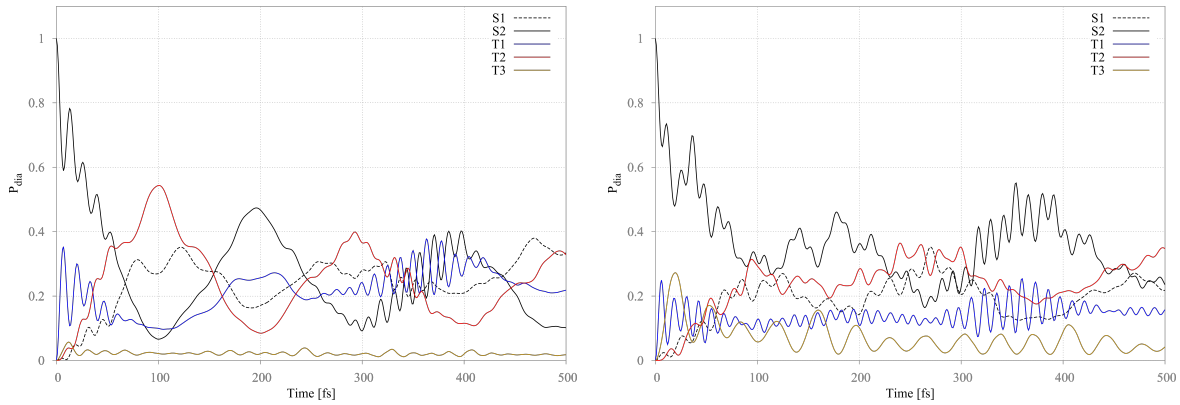

Figure 6.23: Evolution of the diabatic populations as function of time after initial excitation in S2 state for: [Re(F)(CO)$_3$(bpy)] (on the left), and [Re(Cl)(CO)$_3$(bpy)](on the right) (low populated in gray).

X=	τ_1 [fs]	τ_{th} [fs]
F	-	90
Cl	85 ± 8	125
Br	128 ± 12	152
I	152 ± 8	-

Table 6.11: Left: time-constants extracted from the experiment. Right: theoretical time-constants.

in X=Cl.

Plotting the same decay function as for [Re(Br)(CO)$_3$(bpy)] gives us access to the initial decay time constants. We find for [Re(X)(CO)$_3$(bpy)] X=F a time constant of $\tau_{th}^{F} = 90$fs, and for X=Cl: $\tau_{th}^{Cl} = 125$fs (TAB. 6.11).

The estimated time constants are of the same order magnitude and the experimental trend [3] in the series is well reproduced for the two complex [Re(Cl)(CO)$_3$(bpy)] and [Re(Br)(CO)$_3$(bpy)] (TAB. 6.11). Even though the [Re(F)(CO)$_3$(bpy)] has not been synthesized, our calculations show that it follows the same trends (i.e. $\tau_{th}^{F} < \tau_{th}^{Cl}$, TAB. 6.11)

.

6.4.3.2.3 "[Re(I)(CO)$_3$(bpy)]": a tough case.

The wavepacket propagation is done on the diabatic states built from the electronic structure data stored in TAB. 6.10. The evolution of the diabatic population with time is shown FIG. 6.25. As for the complexes [Re(X)(CO)$_3$(bpy)] X=F, X=Cl and X=Br, the first pop-

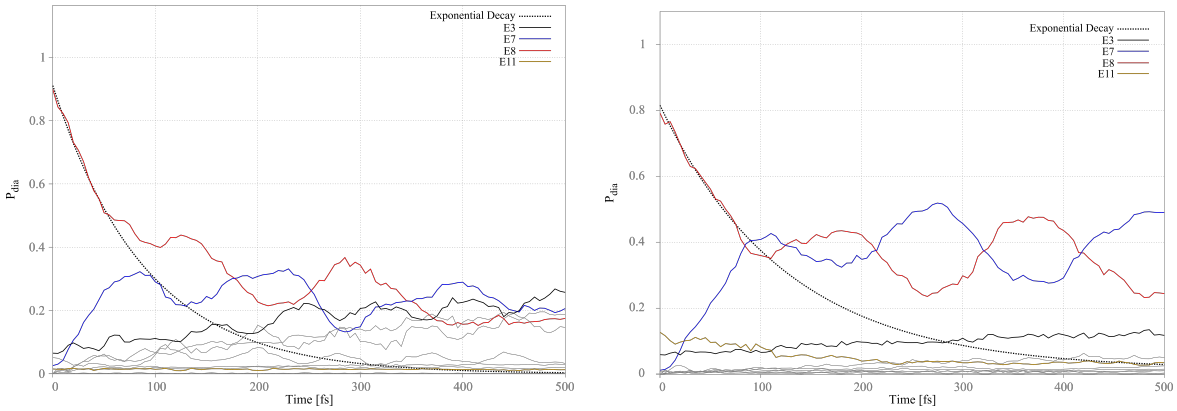

Figure 6.24: Evolution of the adiabatic populations as function of time after initial excitation in the diabatic S2 state for: [Re(F)$(CO)_3$(bpy)] (on the left), and [Re(Cl)$(CO)_3$(bpy)] (on the right) (low populated states in gray).

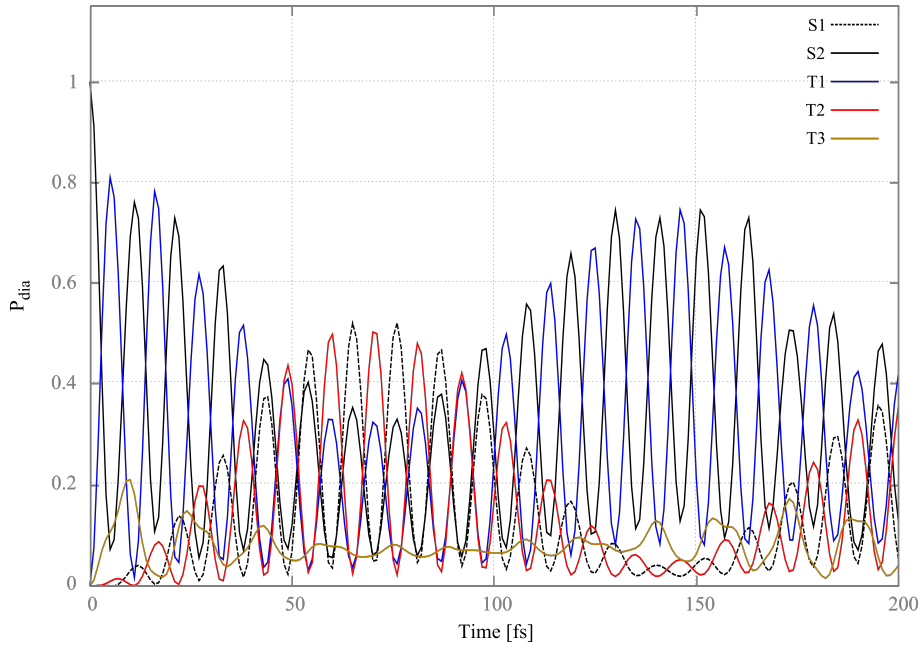

Figure 6.25: Evolution of the diabatic populations as function of time after initial excitation in S2 state for: [Re(I)$(CO)_3$(bpy)].

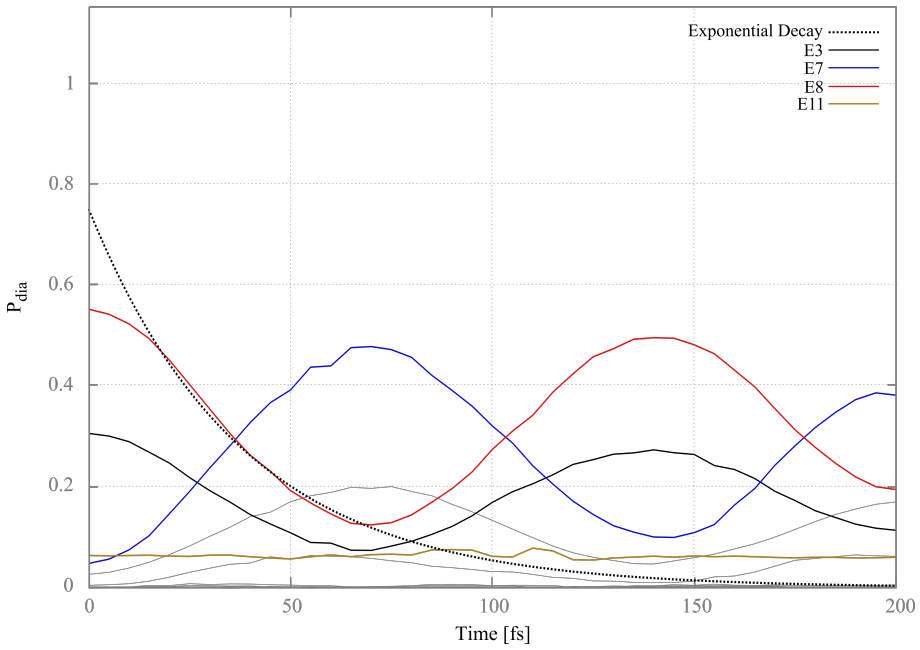

Figure 6.26: Evolution of the adiabatic populations as function of time after initial excitation in S2 state for: [Re(I)$(CO)_3$(bpy)] (very low populated states in gray).

ulation transfer is solely due to the SOC. Indeed, within the 10 first femtosecond, the S2 population is mainly transferred to T1 due to strong SOC ($|\eta_{S2T1}| = 1.3 \times 10^{-2}$ eV, TAB. 6.5). A small fraction of S2 population is also transferred to T3 (about 20% of the population after 10fs). After this first step, the population transfer due to the vibronic interstate coupling takes place. Population from S2 is transferred to S1, while population from T1 is transferred to T2. The out-of-phase oscillations between the population of S2 and T1, and between T2 and S1 respectively confirm this observation. To be able to extract a decay time constant, the adiabatic populations are computed and shown FIG. 6.26. As the SOC is more important for [Re(I)$(CO)_3$(bpy)], the initial adiabatic populations are more spread over the "spin-orbit" states (around 55% in E8, 30% in E4 and 7% in E11). The population of E8 is mainly transferred to the E7 "spin-orbit" state just like in the other complexes while the initial population in E4 is transferred to E3. The initial decay of the population of the "spin-orbit" state E8 can be represented by an exponential decay with a time constant of $\tau^{\mathrm{I}}_{\mathrm{th}} = 38\mathrm{fs}$ which is even faster than for [Re(F)$(CO)_3$(bpy)] which is meaningless. We do not recover the good trend for the time constant of decay, therefore we can assume that our method is not robust enough to treat the iodine complex which proves to be more delicate. This may come from the fact that the SOC are way more intense in this complex than in the [Re(X)$(CO)_3$(bpy)] X=F, X=Cl, X=Br complexes.

Indeed, in such case the splitting of the electronic states due to SOC is bigger and the variation of SOC is much larger along nuclear displacements. The zero order approximation for representing SOC (*i.e.* considering SOC as constant) is no longer valid. To partially correct this crude approximation, a first Taylor expansion of SOC should be used.

6.4.4 Conclusion and Outlook

We have developed a diabatic model Hamiltonian based on a limited number of electronic structure data that aims at including both vibronic coupling and SOC. It relies on a Taylor expansion of the elements of the diabatic Hamiltonian. This makes it possible to improve the description of the states as well as the coupling by computing more points. Within the LVC approximation and considering SOC constant, only a frequency analysis in each excited state is needed. The inclusion of more normal modes is possible and ought to improve the excited state dynamics but will dramatically increase the computational time. It is therefore mandatory to perform an electronic structure study beforehand in order to properly select the electronic states and normal modes describing the dynamics.
Preliminary TD-DFT calculations performed on [Re(X)$(CO)_3$(bpy)] X=F, X=Cl, X=Br and X=I are in good agreement with previous studies at a higher computational level (MS-CASPT2) as well as with experimental data. The computed emission properties match the experimental emission spectra. A new mechanism (different from Ref. [3]) of decay has been proposed: the initial population of E8 (the absorbing state, corresponding to S2) decays to E7 (which is composed of T2 and S1) and then to T1 which in turn phosphoresce back to the GS. These three steps are assumed to be responsible for the three experimentally observed time constants. To validate this guess, a quantum wavepacket was propagated using a diabatic model Hamiltonian built on TD-DFT electronic structure data.
The selection of active normal modes has been done based on two parameters: ξ, and λ that quantify the contribution of a normal mode to the dynamics. 2 a' normal modes involving the stretching mode as well as 2 a' and 2 a" normal modes involving carbonyl motions have been chosen.
The evolution of the adiabatic population validates the mechanism of decay assessed beforehand. The initially populated "spin-orbit" state E8 decays mainly to the E7 "spin-orbit" state, which is a mix of T2 and S1. The E3 "spin-orbit" state, composed mainly of

T1, is slowly populated throughout the dynamics.
The initial decay time-constant is evaluated, $\tau_{\mathrm{th}}^{\mathrm{Br}} = 152\mathrm{fs}$ and found to be in good agreement with experiments.
The study of [Re(I)$(CO)_3$(bpy)] has proven to be more tricky. The SOC are stronger and may not be described accurately enough.
The model Hamiltonian is robust enough to describe the dynamics of X=F, X=Cl, X=Br, and to recover the good ISC kinetics trends. Unfortunately it fails to describe correctly the [Re(I)$(CO)_3$(bpy)] complex. In order to correct the "spin-orbit" transition energies, we could diagonalize the diabatic model Hamiltonian at FC (i.e. $\mathrm{Q_i} = 0 \ \forall \mathrm{i}$). At this point, interstate coupling are null, and only SOC will be present as off-diagonal elements. The resulting matrix will be the adiabatic matrix ($\mathbf{V}$) containing the "spin-orbit" states on its diagonal.

$$\boldsymbol{U}^{-1}\boldsymbol{W}^{\mathrm{FC}}\boldsymbol{U} = \boldsymbol{V} \tag{6.72}$$

Applying this transformation matrix $\boldsymbol{U}$ to the diabatic model Hamiltonian gives us the "SOC-adiabatic" matrix $\boldsymbol{V}^{\mathrm{SOC-ad}}$ that contains on its diagonal the "spin-orbit" states, and the interstate coupling on the off-diagonal. An energy shift can then be applied to the "spin-orbit" states in order to recover exactly the calculated transition energies, thus providing a better description of the spin-orbit states. The wavepacket propagation would then be done on the "SOC-adiabatic" electronic states and no longer on the "SOC-free" electronic states.

In addition to being more intense, the SOC also varies more and faster as function of nuclear coordinates in [Re(I)$(CO)_3$(bpy)] (FIG. 6.7) than in the other complexes. To consider this fast change in the SOC, we could consider a Taylor expansion for the SOC truncated at an higher order. However, this approach would require more *ab initio* points in order to be able to compute the derivatives of the SOC along each normal modes. Within the Cs symmetry group, only a' normal modes contribute to the SOC . The contribution of a" normal modes to the SOC are null at FC, but as soon as the geometry is distorted their contributions will rapidly grow. Another way of approximating the contributions of a" normal modes have to be found.

GENERAL CONCLUSION

Two types of photo-induced processes have been investigated, namely the isomerization in organic and inorganic chromophores, and ultra-fast intersystem crossings in rhenium (I) carbonyl bipyridine complexes substituted by halogens. For this purpose different standard quantum chemical methods, based on wave function and density functional theories, have been used. Semi-classical trajectories and quantum dynamics simulations have completed the static study. For this purpose the nuclear dimensionality problem, inherent to dynamical studies performed on quite large molecular systems, has been explored according to different protocols depending on the molecular system under investigation. In the case of organic chromophores preliminary semi-classical trajectories have been performed for following the time-evolution of the molecule after absorption and for selecting the nuclear coordinates that control the isomerization. Adiabatic potential energy surfaces restricted to the dimensionality defined by these active coordinates have been explored in order to construct the diabatic states. Transition metal complexes being too large for semi-classical simulations including all degrees of freedom, reduced dimensionality has been introduced in a diabatic model Hamiltonian able to treat both spin-orbit and vibronic couplings. This Hamiltonian has been used for subsequent quantum dynamics simulations based on wave packet propagation on the diabatic potentials. This new strategy, which avoids the computation of multi-dimensional potential energy surfaces, can be generalized to various molecular systems and processes since it needs only a few electronic structure data easily calculated by the standard methods of quantum chemistry. Several homemade tools have been developed for extracting these data and one program has been written for exploiting them in the model Hamiltonian. In order to push the minimal PSB3 retinal model towards a benchmark of quantum dynamics simulations, we have tentatively proposed a scheme of construction of realistic diabatic potential energy surfaces. We have put in evidence the importance of the S2 excited state, on the electronic side as well as of the HOOP motions, on the nuclear side. Indeed they were already known to influence the outcome of the process by aborting the isomerization or not whether the system reaches the conical intersection while the HOOP angle closes or opens. However, we have shown

that the HOOP motions have another key role. Indeed they modulate the position of the seam of conical intersection and allow it to be reached for values of φ lower than $90°$. Our first tentative of construction of diabatic potentials, based on the central torsion of the isomerizable bond and on the HOOP motions, with five frozen bond lengths, gives reasonable energy barriers and describes rather well the energy path from Franck-Condon to the seam of conical intersection. However, these potentials do not provide a satisfactory description of the $S0/S1$ vibronic coupling. This study opened the way to several future work. First, further investigations will be needed to design better guess function for the coupling between $S0/S1$. The next task will be dedicated to the determination of the kinetic energy operator in the eight dimensional space. In parallel, one and two dimensional quantum dynamics will bring new insights as far as behaviour of the wavepacket in the vicinity of the conical intersection is concerned.

The origin of unidirectionality in the chiral CPP model photoswitch has been attributed to an asymmetry in $S1$ electronic state. Indeed, on the basis of our simulations we have discovered that the pre-twist angle is not sufficient by itself for driving the directionality. In the same way, the carbon ring deformations will not influence significantly the directionality. This fundamental theoretical study may provide hints for the synthesis of new molecular motors. Moreover, as soon as final functions will be ready for the PSB3 model, they could be used for fitting potentials for this chromophore.

Qualitative analysis based on molecular and electronic structure data obtained for $[Re(CO)_3(bpy)(L)]^+$ (L=pyr-ret-CN) has shown that possible *trans-cis* isomerization channels are open upon irradiation of this molecule in the visible energy domain (400-450 nm). Several *cis* conformers have been put in evidence. The calculated absorption spectra show the presence of low-lying singlet and triplet retinal localized intra-ligand states that will play a key role in the isomerization process.

The mechanism of ultrafast intersystem crossings in third row transition metal complexes has been deciphered on the basis of electronic structure calculations completed by quantum wavepacket propagations. The trend in the experimental decay times observed just after absorption within the series of halogen substituted complexes has been well reproduced. We have shown that in addition to spin-orbit coupling, vibronic coupling plays a central role in the intersystem crossings processes. However, our estimation of the spin-orbit coupling by perturbation theory is probably too limited for describing molecules with heavy substituents like Iodide. The emissive properties of the complexes have been well reproduced and interpreted.

This work has shown that an interplay between various methods of quantum chemistry and quantum dynamics eventually associated to semi-classical approaches, is mandatory to progress in our understanding of ultrafast excited-state processes. What is learned from fundamental studies performed on small organic chromophores should in medium-term provide the key for a better comprehension of photoinduced processes in large molecules, eventually in metal systems.

Appendices

APPENDIX A

ELECTRONIC STRUCTURE DATA OF [RE(CO)$_3$(BPY)(L)] (L=RET-PYR-CN)

A.1 Optimized geometries

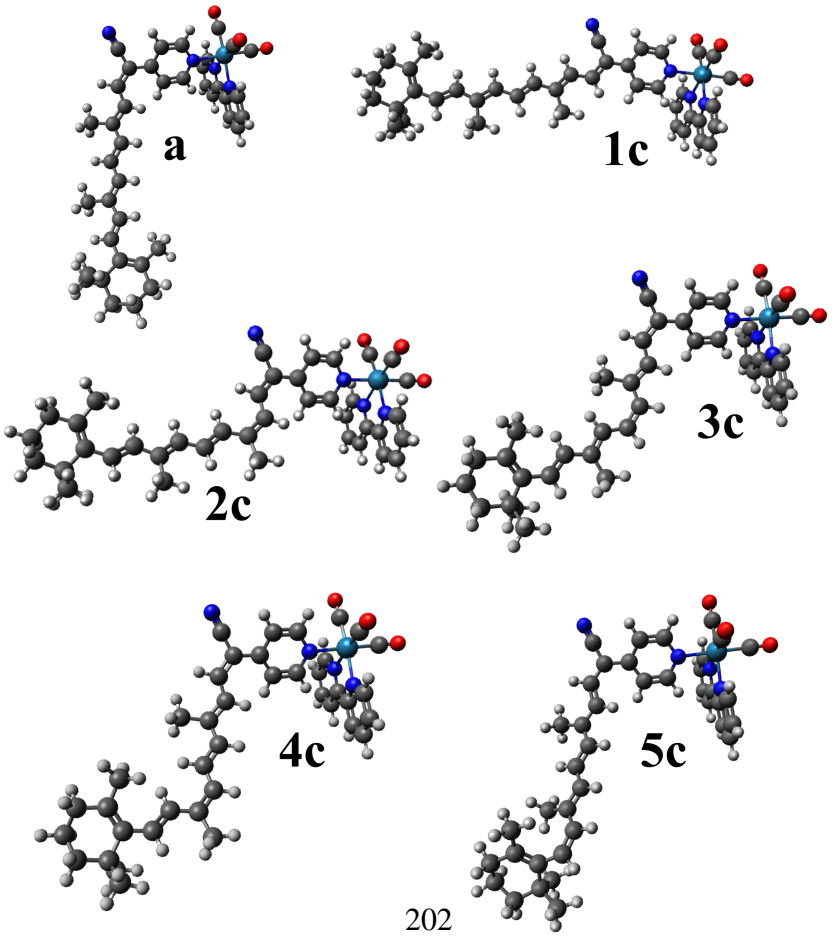

	a				1c		
Atom	X	Y	Z	Atom	X	Y	Z
Re	-0.566338	-0.074696	-0.215917	Re	-0.656400	0.128270	-0.163292
C	-1.027259	-0.330212	-2.082247	C	-1.158296	0.059423	-2.035747
O	-1.300357	-0.477825	-3.202676	O	-1.456108	0.023575	-3.159331
C	-2.429095	-0.240043	0.244790	C	-2.509980	-0.066080	0.317434
O	-3.547879	-0.389592	0.538559	O	-3.624710	-0.234847	0.618150
C	-0.766318	1.830536	-0.432112	C	-0.841629	2.047674	-0.190226
O	-0.833574	2.986324	-0.568973	O	-0.899896	3.211687	-0.212992
N	1.559829	-0.195583	-0.691281	N	1.459229	0.037126	-0.693436
C	2.318245	0.867055	-1.041870	C	2.222578	1.122239	-0.952275
C	2.127793	-1.438169	-0.698616	C	2.014306	-1.203655	-0.831206
C	3.649547	0.748140	-1.419753	C	3.546577	1.029165	-1.362206
H	1.822831	1.835298	-1.018205	H	1.737888	2.087871	-0.825400
C	3.462655	-1.619059	-1.076907	C	3.340520	-1.358398	-1.249267
C	4.232826	-0.519958	-1.443756	C	4.116254	-0.235479	-1.519963
H	4.210253	1.640430	-1.695745	H	4.112678	1.939050	-1.557984
H	3.897638	-2.616000	-1.089748	H	3.764994	-2.353064	-1.366644
H	5.272043	-0.652027	-1.745804	H	5.149373	-0.346204	-1.850228
N	-0.030859	-2.173928	0.041891	N	-0.136473	-1.989273	-0.119395
C	-0.887840	-3.125916	0.472971	C	-0.994648	-2.970778	0.236102
C	1.247696	-2.536613	-0.270494	C	1.131410	-2.330769	-0.492487
C	-0.525016	-4.460779	0.602938	C	-0.644010	-4.315060	0.228218
H	-1.894493	-2.790468	0.712887	H	-1.992309	-2.650845	0.528989
C	1.668951	-3.866317	-0.162606	C	1.539964	-3.668502	-0.523822
C	0.777253	-4.840635	0.275125	C	0.646863	-4.672766	-0.163574
H	-1.259587	-5.184318	0.954547	H	-1.379255	-5.062670	0.523617
H	2.690232	-4.140709	-0.417724	H	2.552370	-3.925852	-0.827471
H	1.094889	-5.880035	0.360697	H	0.954466	-5.718416	-0.187141
N	-0.011397	0.197632	1.921293	N	-0.055302	0.186558	1.976858

continued on next page

continued from previous page

	a				**1c**		
C	1.115699	-0.320194	2.471644	C	1.103147	-0.346863	2.446187
C	-0.844615	0.859341	2.772386	C	-0.873214	0.749979	2.910606
C	1.442676	-0.208756	3.810238	C	1.469471	-0.345996	3.776915
H	1.780495	-0.865522	1.805209	H	1.764979	-0.801113	1.712014
C	-0.599054	0.996235	4.122800	C	-0.583080	0.782495	4.257733
H	-1.744492	1.283892	2.331756	H	-1.796719	1.189310	2.538732
C	0.576876	0.462476	4.702905	C	0.621343	0.226470	4.754871
H	2.343569	-0.703636	4.165522	H	2.413047	-0.817544	4.046008
H	-1.328968	1.520407	4.740273	H	-1.296953	1.246998	4.938535
C	0.803739	0.541372	6.138467	C	0.929722	0.244338	6.170094
C	-0.355953	0.780894	6.931990	C	-0.096049	0.702622	7.045802
N	-1.324172	0.984455	7.554671	N	-0.943655	1.083335	7.754788
C	2.014081	0.408862	6.820755	C	2.157047	-0.138401	6.715581
H	1.912661	0.359196	7.906259	H	2.939315	-0.422947	6.012088
C	3.320845	0.443327	6.303364	C	2.447582	-0.168229	8.085048
H	3.450701	0.703930	5.251040	H	1.628318	0.083789	8.764756
C	4.491883	0.291005	7.049939	C	3.674452	-0.480797	8.677562
C	5.736474	0.568119	6.420281	C	3.742368	-0.483646	10.094854
H	5.699793	0.907551	5.379820	H	2.810731	-0.272845	10.629057
C	6.971720	0.493860	7.036065	C	4.877376	-0.720102	10.850284
H	7.003590	0.142344	8.068488	H	5.817216	-0.905862	10.326964
C	8.189184	0.876805	6.432509	C	4.883549	-0.727501	12.260372
H	8.129292	1.268484	5.411350	H	3.916847	-0.570327	12.750173
C	9.450285	0.844051	7.015751	C	5.981165	-0.905424	13.095527
C	10.557770	1.357320	6.262304	C	5.753351	-0.890411	14.509931
H	10.313578	1.759363	5.278373	H	4.712548	-0.786372	14.816136
C	4.475170	-0.125914	8.498593	C	4.908966	-0.797723	7.872123
H	5.108722	-1.011894	8.650466	H	5.693122	-0.049284	8.061308
H	4.874660	0.675200	9.137977	H	5.317503	-1.778925	8.154074
H	3.473633	-0.381046	8.857185	H	4.721300	-0.809539	6.793785

continued on next page

continued from previous page

	a				**1c**		
C	9.685915	0.310629	8.404886	C	7.378471	-1.098419	12.567422
H	10.086609	1.099762	9.059205	H	7.809305	-2.037619	12.945078
H	8.776851	-0.080120	8.871402	H	7.418184	-1.128021	11.474516
H	10.426506	-0.502230	8.386733	H	8.034998	-0.282268	12.903850
C	11.844491	1.428091	6.732083	C	6.735770	-1.039790	15.456804
H	11.987919	1.091769	7.760804	H	7.738552	-1.226464	15.066892
C	13.035713	1.970948	6.107685	C	6.638192	-1.073272	16.901892
C	13.222632	2.036907	4.748233	C	5.619131	-0.484913	17.614491
C	12.303061	1.415491	3.730267	C	4.568460	0.414472	17.019956
H	11.735804	0.565314	4.127150	H	4.907226	0.931000	16.114160
H	11.582064	2.155475	3.342682	H	3.656039	-0.152364	16.767801
H	12.889377	1.074326	2.863600	H	4.265133	1.168307	17.761752
C	14.109001	2.473139	7.107076	C	7.796547	-1.827795	17.603266
C	14.419018	2.712030	4.127179	C	5.476003	-0.650788	19.105494
H	15.070151	1.925279	3.697880	H	5.720496	0.319253	19.581299
H	14.071076	3.295633	3.256250	H	4.406780	-0.811993	19.330764
C	15.216556	3.583321	5.089888	C	6.338068	-1.757605	19.699456
H	16.178890	3.866585	4.639417	H	6.348710	-1.685037	20.796595
H	14.671124	4.520171	5.286343	H	5.908209	-2.741147	19.451226
C	15.431270	2.814322	6.387296	C	7.747603	-1.637621	19.134497
H	15.964680	1.875221	6.157448	H	8.142920	-0.636959	19.382529
H	16.072071	3.378576	7.082833	H	8.427201	-2.368987	19.599338
C	14.437411	1.389863	8.158888	C	9.167642	-1.295098	17.129582
H	15.305951	1.715300	8.750896	H	9.960235	-1.738953	17.750643
H	13.616682	1.218883	8.869553	H	9.394980	-1.560800	16.087672
H	14.690967	0.432058	7.681305	H	9.227646	-0.201635	17.231119
C	13.570156	3.720405	7.840990	C	7.706864	-3.329534	17.255878
H	13.377179	4.549705	7.145189	H	6.773797	-3.777150	17.627349
H	12.624008	3.496391	8.357020	H	7.735786	-3.485357	16.166620
H	14.296633	4.062303	8.594714	H	8.554104	-3.874599	17.700766

continued on next page

continued from previous page

a	**1c**

Table A.1: Cartesian coordinates for the **a** and **1c** conformers.

	2c				**3c**		
Atom	X	Y	Z	Atom	X	Y	Z
Re	-0.623546	0.231765	-0.243234	Re	-0.424056	0.343983	-0.373368
C	-1.093747	0.236984	-2.125173	C	-0.774170	0.322727	-2.280846
O	-1.374503	0.242139	-3.253486	O	-0.981957	0.312214	-3.424792
C	-2.487305	0.031162	0.203605	C	-2.321383	0.418826	-0.040401
O	-3.607070	-0.140692	0.479393	O	-3.468555	0.413136	0.168117
C	-0.799931	2.150098	-0.206965	C	-0.338525	2.269248	-0.422639
O	-0.854998	3.314909	-0.187811	O	-0.236674	3.430634	-0.449286
N	1.504805	0.152292	-0.715232	N	1.698385	-0.044777	-0.693950
C	2.282446	1.244197	-0.889727	C	2.629353	0.922683	-0.850638
C	2.057151	-1.082847	-0.902294	C	2.086054	-1.350686	-0.793847
C	3.618038	1.163760	-1.263098	C	3.963421	0.645120	-1.120430
H	1.799678	2.205462	-0.726613	H	2.273854	1.946812	-0.759273
C	3.395548	-1.224995	-1.284685	C	3.415115	-1.690084	-1.069974
C	4.185457	-0.094721	-1.470851	C	4.364398	-0.686867	-1.238567
H	4.194651	2.079011	-1.392751	H	4.668474	1.466972	-1.240162
H	3.818593	-2.215018	-1.440890	H	3.707131	-2.734420	-1.156769
H	5.227665	-0.194867	-1.774696	H	5.401271	-0.941123	-1.459828
N	-0.117917	-1.889912	-0.293853	N	-0.214484	-1.826956	-0.311539
C	-0.992606	-2.883344	-0.020098	C	-1.234605	-2.679182	-0.066653
C	1.155808	-2.220288	-0.659509	C	1.022065	-2.343214	-0.575040
C	-0.652716	-4.228090	-0.102694	C	-1.080317	-4.059852	-0.080615
H	-1.993838	-2.572004	0.269739	H	-2.199725	-2.222338	0.141452
C	1.552631	-3.557726	-0.767100	C	1.235808	-3.725489	-0.608124
C	0.643368	-4.573633	-0.488397	C	0.177778	-4.594982	-0.361456
H	-1.400168	-4.985477	0.130554	H	-1.939604	-4.697592	0.123753

continued on next page

continued from previous page

	2c				**3c**		
H	2.568667	-3.805738	-1.066086	H	2.225027	-4.122357	-0.825720
H	0.942546	-5.618886	-0.570520	H	0.333485	-5.673772	-0.387198
N	-0.065446	0.210547	1.908543	N	-0.004676	0.348585	1.809820
C	0.959985	-0.522252	2.409766	C	0.897117	-0.472585	2.403692
C	-0.787045	0.929216	2.814146	C	-0.693935	1.181786	2.639227
C	1.301487	-0.557953	3.749093	C	1.148242	-0.489469	3.763442
H	1.527216	-1.120753	1.699869	H	1.434014	-1.161497	1.754781
C	-0.514539	0.939087	4.165778	C	-0.509762	1.216071	4.004979
H	-1.614301	1.513055	2.415096	H	-1.420564	1.839023	2.165401
C	0.568768	0.195411	4.694293	C	0.445501	0.377809	4.630577
H	2.106600	-1.219487	4.056894	H	1.851716	-1.223712	4.147726
H	-1.148068	1.532997	4.825044	H	-1.112113	1.903537	4.599362
C	0.836604	0.193997	6.124888	C	0.612263	0.397091	6.075433
C	-0.235040	0.648997	6.949791	C	-0.461576	0.982879	6.808795
N	-1.125616	1.032537	7.602667	N	-1.349106	1.478460	7.386154
C	2.011395	-0.162694	6.787622	C	1.697465	-0.053063	6.831519
H	1.923519	-0.142882	7.875441	H	1.531148	0.001319	7.908481
C	3.288920	-0.436791	6.267514	C	2.977800	-0.450273	6.411993
H	3.456419	-0.292719	5.200158	H	3.227245	-0.375565	5.352749
C	4.417217	-0.764361	7.031514	C	4.027490	-0.808503	7.267407
C	4.356102	-1.033567	8.423995	C	5.310449	-1.003291	6.677702
H	3.372209	-1.078889	8.896890	H	5.309868	-0.961691	5.584135
C	5.451571	-1.212053	9.249060	C	6.565823	-1.180550	7.248930
H	6.447816	-1.163655	8.805773	H	7.370180	-1.302735	6.519006
C	5.350107	-1.405349	10.643864	C	6.961717	-1.154076	8.606049
H	4.335977	-1.469246	11.052428	H	6.196429	-1.009966	9.366916
C	6.393172	-1.460982	11.560326	C	8.265936	-1.220246	9.089079
C	6.056791	-1.575463	12.949284	C	8.447877	-1.070503	10.503931
H	4.995503	-1.693802	13.166532	H	7.530300	-0.991326	11.087886
C	5.751698	-0.805618	6.327250	C	3.810414	-0.969012	8.748825

continued on next page

continued from previous page

	2c				**3c**		
H	6.414853	-0.010637	6.700621	H	4.300377	-1.882604	9.110967
H	6.265622	-1.763086	6.493779	H	4.241493	-0.118286	9.299335
H	5.635144	-0.658819	5.246845	H	2.750627	-1.037274	9.013463
C	7.838932	-1.360693	11.149217	C	9.467200	-1.395246	8.199118
H	8.415916	-2.203429	11.557582	H	10.082851	-2.238699	8.545102
H	7.971511	-1.361796	10.062905	H	9.199139	-1.586867	7.155608
H	8.290929	-0.437376	11.541831	H	10.103332	-0.497433	8.225454
C	6.969946	-1.551337	13.973068	C	9.661865	-1.031175	11.141158
H	8.017210	-1.514750	13.665656	H	10.535675	-1.209269	10.510061
C	6.769452	-1.629496	15.406221	C	9.956310	-0.851415	12.549785
C	5.597671	-1.278728	16.035686	C	9.129169	-0.181356	13.421595
C	4.426518	-0.617819	15.358482	C	7.901376	0.591705	13.017014
H	4.716920	-0.019250	14.486661	H	7.939072	0.948330	11.980690
H	3.684775	-1.364178	15.026793	H	6.989785	-0.019002	13.135177
H	3.905777	0.034802	16.074806	H	7.776505	1.458965	13.683417
C	8.005378	-2.125655	16.199477	C	11.307035	-1.457977	13.008290
C	5.381177	-1.483992	17.513118	C	9.405333	-0.105342	14.901967
H	5.372721	-0.487352	17.996644	H	9.700281	0.936236	15.139226
H	4.358179	-1.874424	17.658094	H	8.450709	-0.255047	15.437622
C	6.414138	-2.381819	18.181716	C	10.471476	-1.076413	15.393681
H	6.327109	-2.313482	19.275743	H	10.774594	-0.820977	16.419783
H	6.225453	-3.433723	17.914299	H	10.060290	-2.098385	15.430300
C	7.802908	-1.958778	17.720747	C	11.662739	-1.018083	14.445316
H	7.954634	-0.897817	17.985952	H	12.041489	0.019329	14.417372
H	8.587133	-2.529015	18.242514	H	12.491289	-1.646718	14.807735
C	9.264719	-1.311593	15.825155	C	12.462480	-0.986612	12.095787
H	10.082117	-1.577282	16.512168	H	13.420033	-1.302544	12.536335
H	9.625063	-1.520304	14.808113	H	12.418594	-1.422916	11.087357
H	9.082668	-0.230716	15.915035	H	12.476442	0.109883	12.002025
C	8.262063	-3.609748	15.860905	C	11.219803	-2.998515	12.933630

continued on next page

continued from previous page

	2c				**3c**		
H	7.419897	-4.247329	16.166368	H	10.452628	-3.395492	13.614992
H	8.404369	-3.748331	14.778225	H	10.960963	-3.330044	11.915876
H	9.169939	-3.965705	16.372501	H	12.188325	-3.448569	13.202679

Table A.2: Cartesian coordinates for the **2c** and **3c** conformers.

	4c				**5c**		
Atom	X	Y	Z	Atom	X	Y	Z
Re	-0.655426	0.247487	-0.179912	Re	-0.491827	0.005902	-0.299725
C	-1.187712	0.227466	-2.045189	C	-0.912476	-0.200669	-2.181182
O	-1.503709	0.219984	-3.163949	O	-1.159163	-0.315930	-3.311356
C	-2.512318	0.178155	0.329238	C	-2.375980	-0.021591	0.093550
O	-3.631161	0.085385	0.644610	O	-3.513773	-0.092601	0.341731
C	-0.708868	2.174671	-0.191622	C	-0.536623	1.923513	-0.501206
O	-0.688545	3.340300	-0.203962	O	-0.507823	3.082158	-0.624221
N	1.442681	0.016774	-0.731170	N	1.629231	-0.281054	-0.730948
C	2.275734	1.050474	-0.985265	C	2.470069	0.714986	-1.089366
C	1.909569	-1.256959	-0.891723	C	2.100729	-1.563475	-0.713277
C	3.585045	0.872600	-1.413546	C	3.792595	0.489050	-1.448677
H	1.859802	2.045367	-0.841081	H	2.049401	1.718230	-1.086701
C	3.217718	-1.496726	-1.326485	C	3.421865	-1.851346	-1.072887
C	4.064946	-0.425982	-1.593640	C	4.277903	-0.819952	-1.445829
H	4.208988	1.744414	-1.606930	H	4.422735	1.331295	-1.731877
H	3.571996	-2.516437	-1.460797	H	3.778844	-2.878829	-1.067945
H	5.083768	-0.602642	-1.939179	H	5.307308	-1.035435	-1.732982
N	-0.283311	-1.901704	-0.166834	N	-0.124175	-2.126355	-0.018768
C	-1.204980	-2.826507	0.182038	C	-1.058618	-3.004952	0.406813
C	0.952959	-2.325160	-0.562651	C	1.134114	-2.585159	-0.282235
C	-0.950643	-4.191794	0.145323	C	-0.794137	-4.357647	0.582086
H	-2.173952	-2.442368	0.493413	H	-2.046358	-2.594665	0.605500

continued on next page

continued from previous page

	4c				**5c**		
C	1.264905	-3.687570	-0.623413	C	1.458383	-3.937003	-0.126105
C	0.306924	-4.632528	-0.269563	C	0.488241	-4.834912	0.308030
H	-1.733395	-4.891092	0.436765	H	-1.587915	-5.018917	0.927463
H	2.252711	-4.010257	-0.945087	H	2.465976	-4.287688	-0.338666
H	0.539155	-5.696708	-0.315949	H	0.730509	-5.890540	0.432289
N	-0.025380	0.250933	1.952964	N	0.016723	0.215279	1.858156
C	1.031105	-0.457302	2.424633	C	1.144139	-0.302736	2.407809
C	-0.735403	0.956102	2.877594	C	-0.846038	0.822179	2.720073
C	1.410480	-0.485322	3.754528	C	1.441040	-0.246920	3.756657
H	1.591493	-1.042776	1.698651	H	1.835556	-0.799665	1.731150
C	-0.429443	0.967785	4.222126	C	-0.631558	0.900484	4.081049
H	-1.582480	1.526380	2.501345	H	-1.743985	1.251585	2.280766
C	0.681618	0.244709	4.719945	C	0.541818	0.361782	4.660140
H	2.240007	-1.127247	4.040539	H	2.346075	-0.737090	4.108230
H	-1.058438	1.546105	4.899340	H	-1.384675	1.380858	4.706238
C	0.975492	0.229672	6.145753	C	0.738483	0.369200	6.103194
C	-0.102710	0.614403	6.996581	C	-0.442643	0.523996	6.885558
N	-0.999735	0.943952	7.669681	N	-1.427712	0.664466	7.499151
C	2.178928	-0.080472	6.780799	C	1.941628	0.235018	6.795612
H	2.107653	-0.096108	7.869408	H	1.829780	0.113551	7.874439
C	3.461106	-0.262414	6.232266	C	3.251874	0.349424	6.296402
H	3.598434	-0.110438	5.160606	H	3.379992	0.693375	5.267896
C	4.622866	-0.492707	6.973101	C	4.420622	0.176749	7.039856
C	5.876836	-0.458869	6.299287	C	5.660639	0.546128	6.447375
H	5.856296	-0.311096	5.214429	H	5.619731	0.979150	5.442396
C	7.103635	-0.510315	6.929083	C	6.891754	0.452695	7.066527
H	7.104076	-0.623326	8.014118	H	6.930508	0.005169	8.061525
C	8.354290	-0.362472	6.285514	C	8.103115	0.944593	6.530464
H	8.339451	-0.274053	5.194589	H	8.053508	1.451106	5.560893
C	9.589348	-0.245584	6.916732	C	9.335579	0.893713	7.170286

continued on next page

continued from previous page

	4c				**5c**		
C	9.718641	-0.315154	8.343949	C	10.446086	1.533800	6.511908
H	8.831437	-0.598058	8.905358	H	10.223548	1.857751	5.489401
C	4.599358	-0.722709	8.463828	C	4.406408	-0.357272	8.449388
H	5.190324	-1.611278	8.725800	H	5.060854	-1.237222	8.533078
H	5.041609	0.134879	8.994251	H	4.783691	0.397693	9.154842
H	3.590283	-0.876635	8.856731	H	3.409352	-0.665084	8.778017
C	10.809081	0.011195	6.070331	C	9.494939	0.141872	8.466148
H	11.594676	-0.732787	6.269727	H	9.163829	0.748767	9.323157
H	10.566060	-0.022555	5.001742	H	8.895719	-0.778031	8.460206
H	11.239953	1.000234	6.288934	H	10.542241	-0.123991	8.643882
C	10.869483	-0.057214	9.038992	C	11.731257	1.765007	6.924342
H	11.764614	0.135253	8.443403	H	12.393164	2.120154	6.127599
C	11.073484	-0.054874	10.477530	C	12.389597	1.605056	8.222914
C	10.077481	0.221785	11.382803	C	11.922533	2.199895	9.361844
C	8.698135	0.714757	11.024146	C	10.743534	3.133083	9.412935
H	8.662665	1.231847	10.058023	H	10.298740	3.335897	8.433398
H	7.971256	-0.115644	10.994507	H	9.958888	2.737421	10.078854
H	8.340896	1.403795	11.804543	H	11.058535	4.091111	9.858933
C	12.523932	-0.363831	10.925374	C	13.722258	0.816063	8.186408
C	10.285708	0.112575	12.872797	C	12.616626	2.052462	10.694707
H	10.289011	1.137794	13.292671	H	13.075918	3.026179	10.951694
H	9.392267	-0.367478	13.310603	H	11.845823	1.890605	11.468764
C	11.557611	-0.622577	13.276594	C	13.669161	0.950119	10.736038
H	11.756925	-0.477562	14.348303	H	14.287098	1.047640	11.640479
H	11.429673	-1.705982	13.122259	H	13.178751	-0.034861	10.796006
C	12.714936	-0.100731	12.434506	C	14.531274	1.033143	9.481763
H	12.807294	0.987458	12.597501	H	15.004938	2.029572	9.441671
H	13.670293	-0.548757	12.749268	H	15.348392	0.294892	9.512573
C	13.534801	0.537312	10.180986	C	14.607584	1.269237	7.005905
H	14.530609	0.408716	10.630858	H	15.595397	0.792733	7.092721

continued on next page

continued from previous page

	4c				**5c**		
H	13.632555	0.282944	9.116185	H	14.190647	0.976376	6.032033
H	13.259602	1.599178	10.262772	H	14.756848	2.359414	7.011837
C	12.849000	-1.837768	10.599970	C	13.406029	-0.685329	8.002492
H	12.198633	-2.529024	11.155416	H	12.851484	-1.093924	8.860158
H	12.710811	-2.043927	9.527457	H	12.798889	-0.850506	7.099270
H	13.895396	-2.063133	10.858613	H	14.339785	-1.259539	7.896465

Table A.3: Cartesian coordinates for the **4c** and **5c** conformers.

A.2 Electronic structure

Conformer 5c

KS orbitals

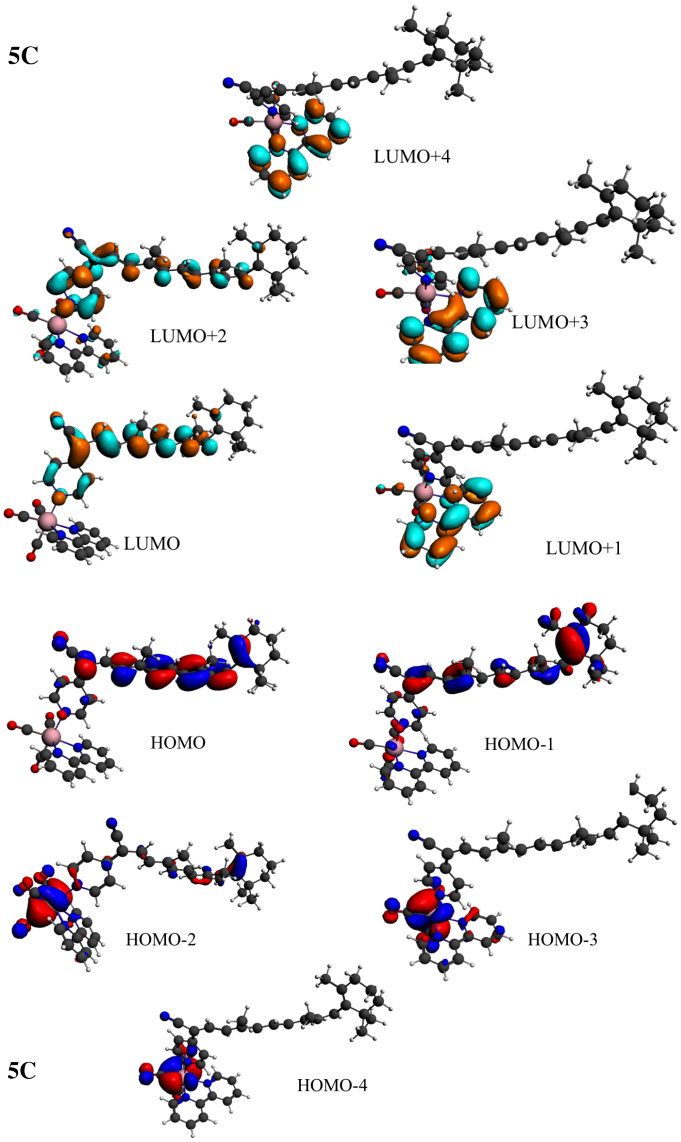

Figure A.1: Kohn-Sham orbitals of the *cis* **5c** conformer in acetonitrile.

Electronic states ($\tau = 180°$)

State	One-electron excitation	%	Energie [eV]	Energie [nm]	f	Nature
T1	HOMO $\rightarrow$ LUMO	94	1.17	1060	-	IL_{ret}
S1	HOMO $\rightarrow$ LUMO	96	1.86	667	2.51	IL_{ret}
T2	HOMO $-$ 1 $\rightarrow$ LUMO	73	2.18	569	-	IL_{ret}
	HOMO $-$ 5 $\rightarrow$ LUMO	9				IL_{ret}
	HOMO $\rightarrow$ LUMO + 2	7				IL_{ret}
T3	HOMO $\rightarrow$ LUMO + 1	97	2.22	558	-	$LLCT_{ret\rightarrow bpy}$
S2	HOMO LUMO + 1	99	2.23	556	0.00	$LLCT_{ret\rightarrow bpy}$
T4	HOMO $\rightarrow$ LUMO + 2	49	2.60	477	-	IL_{ret}
	HOMO $-$ 1 $\rightarrow$ LUMO	14				IL_{ret}
	HOMO $-$ 2 $\rightarrow$ LUMO	9				$MLCT_{ret}$
	HOMO $-$ 5 $\rightarrow$ LUMO	7				IL_{ret}
S3	HOMO $-$ 1 $\rightarrow$ LUMO	96	2.76	449	0.21	IL_{ret}
T5	HOMO $-$ 2 $\rightarrow$ LUMO	42	2.83	438	-	$MLCT_{ret}$
	HOMO $-$ 5 $\rightarrow$ LUMO	23				IL_{ret}
	HOMO $\rightarrow$ LUMO + 2	20				IL_{ret}
T6	HOMO $-$ 2 $\rightarrow$ LUMO + 1	58	2.92	425	-	$MLCT_{bpy}$
	HOMO $-$ 1 $\rightarrow$ LUMO + 1	26				$LLCT_{ret\rightarrow bpy}$
S4	HOMO $-$ 1 $\rightarrow$ LUMO + 1	47	3.04	408	0.01	$LLCT_{ret\rightarrow bpy}$
	HOMO $-$ 2 $\rightarrow$ LUMO + 1	46				$MLCT_{bpy}$
T7	HOMO $-$ 5 $\rightarrow$ LUMO	38	3.05	406	-	IL_{ret}
	HOMO $-$ 2 $\rightarrow$ LUMO	29				$MLCT_{ret}$
	HOMO $-$ 1 $\rightarrow$ LUMO	5				IL_{ret}
S5	HOMO $-$ 2 $\rightarrow$ LUMO	73	3.08	403	0.04	$MLCT_{ret}$
	HOMO $\rightarrow$ LUMO + 2	20				IL_{ret}
S6	HOMO $\rightarrow$ LUMO + 2	66	3.18	390	0.39	IL_{ret}
	HOMO $-$ 2 $\rightarrow$ LUMO	18				$MLCT_{ret}$
	HOMO $-$ 3 $\rightarrow$ LUMO	5				$MLCT_{ret}$

Table A.4: TD-DFT transition energies (in eV), wavelength of absorption (in nm) and oscillator strengths f associated to the low-lying singlet excited states of **5c** conformer in acetonitrile.

Conformer 4c

KS orbitals

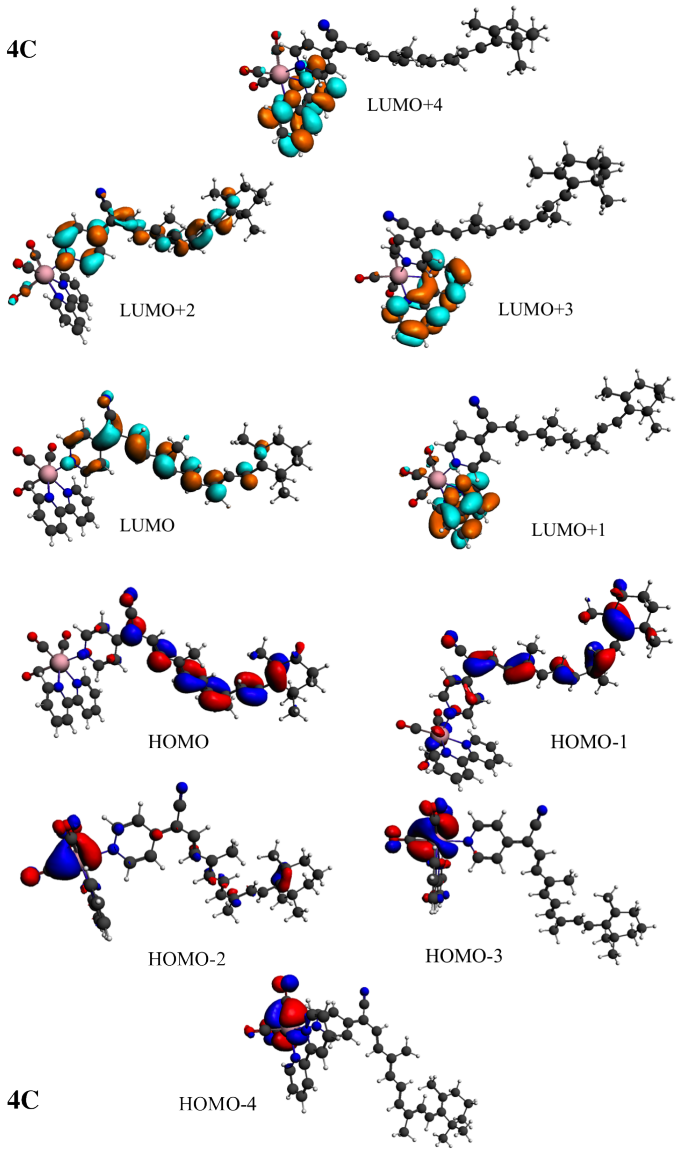

Figure A.2: Kohn-Sham orbitals of the *cis* **4c** conformer in acetonitrile.

Electronic states ($\tau = 180°$)

State	One-electron excitation	%	Energie [eV]	Energie [nm]	f	Nature
T1	HOMO $\rightarrow$ LUMO	94	1.20	1033	-	IL_{ret}
S1	HOMO $\rightarrow$ LUMO	97	1.83	677	2.18	IL_{ret}
T2	HOMO $-$ 1 $\rightarrow$ LUMO	73	2.10	590	-	IL_{ret}
	HOMO $\rightarrow$ LUMO + 2	11				IL_{ret}
	HOMO $\rightarrow$ 209	5				IL_{ret}
T3	HOMO $\rightarrow$ LUMO + 1	98	2.22	558	-	$LLCT_{ret\rightarrow bpy}$
S2	HOMO $\rightarrow$ LUMO + 1	98	2.23	556	0.00	$LLCT_{ret\rightarrow bpy}$
T4	HOMO $\rightarrow$ LUMO + 2	68	2.59	479	-	IL_{ret}
	HOMO $-$ 1 $\rightarrow$ LUMO	14				IL_{ret}
	HOMO $\rightarrow$ 209	6				IL_{ret}
S3	HOMO $-$ 1 $\rightarrow$ LUMO	95	2.80	443	0.35	IL_{ret}
T5	HOMO $-$ 2 $\rightarrow$ LUMO	41	2.82	440	-	$MLCT_{ret}$
	HOMO $-$ 5 $\rightarrow$ LUMO	25				IL_{ret}
	HOMO $-$ 1 $\rightarrow$ LUMO + 2	11				IL_{ret}
	HOMO $\rightarrow$ 209	6				IL_{ret}
T6	HOMO $-$ 2 $\rightarrow$ LUMO + 1	53	2.90	428	-	$MLCT_{bpy}$
	HOMO $-$ 1 $\rightarrow$ LUMO + 1	36				$LLCT_{ret\rightarrow bpy}$
S4	HOMO $-$ 1 $\rightarrow$ LUMO + 1	58	3.01	412	0.01	$LLCT_{ret\rightarrow bpy}$
	HOMO $-$ 2 $\rightarrow$ LUMO + 1	39				$MLCT_{bpy}$
T7	HOMO $-$ 3 $\rightarrow$ LUMO + 1	93	3.10	400	-	$MLCT_{bpy}$
S5	HOMO $\rightarrow$ LUMO + 2	53	3.13	396	0.05	IL_{ret}
	HOMO $-$ 2 $\rightarrow$ LUMO	41				$MLCT_{ret}$
S6	HOMO $-$ 2 $\rightarrow$ LUMO	53	3.16	392	0.21	$MLCT_{ret}$
	HOMO $\rightarrow$ LUMO + 2	40				IL_{ret}

Table A.5: TD-DFT transition energies (in eV), wavelength of absorption (in nm) and oscillator strengths f associated to the low-lying singlet excited states of **4c** conformer in acetonitrile.

Electronic states ($\tau = 90°$)

State	One-electron excitation	%	Energie [eV]	Energie [nm]	f	Nature
T1	HOMO $\rightarrow$ LUMO	97	0.62	2000	-	IL_{ret}

continued on next page

continued from previous page

State	One-electron excitation	%	Energie [eV]	Energie [nm]	f	Nature
S1	HOMO $\rightarrow$ LUMO	97	1.35	918	1.95	IL_{ret}
T2	HOMO $\rightarrow$ LUMO + 2	61	1.78	697	-	IL_{ret}
	HOMO $\rightarrow$ LUMO + 1	19				$LLCT_{ret\rightarrow bpy}$
	HOMO $-$ 1 $\rightarrow$ LUMO	11				IL_{ret}
T3	HOMO $\rightarrow$ LUMO + 1	79	1.8	689	-	$LLCT_{ret\rightarrow bpy}$
	HOMO LUMO + 2	14				IL_{ret}
S2	HOMO $\rightarrow$ LUMO + 1	99	1.8	689	0	$LLCT_{ret\rightarrow bpy}$
T4	HOMO $-$ 1 $\rightarrow$ LUMO	46	2.01	617	-	IL_{ret}
	HOMO $-$ 2 $\rightarrow$ LUMO	18				$MLCT_{ret}$
	HOMO $\rightarrow$ LUMO + 2	17				IL_{ret}
	HOMO $-$ 5 $\rightarrow$ LUMO	13				IL_{ret}
S3	HOMO $\rightarrow$ LUMO + 2	64	2.41	514	0.3	IL_{ret}
	HOMO $-$ 1 $\rightarrow$ LUMO	30				IL_{ret}
T5	HOMO $-$ 5 $\rightarrow$ LUMO	50	2.51	494	-	IL_{ret}
	HOMO $-$ 1 $\rightarrow$ LUMO	28				IL_{ret}
	HOMO $-$ 2 $\rightarrow$ LUMO	10				$MLCT_{ret}$
S4	HOMO $-$ 1 $\rightarrow$ LUMO	63	2.73	454	0.28	IL_{ret}
	HOMO $\rightarrow$ LUMO + 2	27				IL_{ret}
T6	HOMO $\rightarrow$ LUMO + 5	59	2.76	449	-	IL_{ret}
	HOMO $\rightarrow$ LUMO + 6	14				IL_{ret}
	HOMO $-$ 1 $\rightarrow$ LUMO + 2	6				IL_{ret}
	HOMO $\rightarrow$ LUMO + 3	6				$LLCT_{ret\rightarrow bpy}$
T7	HOMO $\rightarrow$ LUMO + 3	91	2.8	443	-	IL_{ret}
S5	HOMO $\rightarrow$ LUMO + 3	99	2.8	443	0	IL_{ret}
T8	HOMO $-$ 1 $\rightarrow$ LUMO + 1	50	2.88	430	-	$LLCT_{ret\rightarrow bpy}$
	HOMO $-$ 2 $\rightarrow$ LUMO + 1	37				$MLCT_{bpy}$
S6	HOMO $\rightarrow$ LUMO + 4	98	2.97	417	0	$LLCT_{ret\rightarrow bpy}$
S7	HOMO $-$ 2 $\rightarrow$ LUMO	68	3	413	0.05	$MLCT_{ret}$
	HOMO $-$ 1 $\rightarrow$ LUMO + 1	12				$LLCT_{ret\rightarrow bpy}$
	HOMO $\rightarrow$ LUMO + 5	8				IL_{ret}

continued on next page

continued from previous page

State	One-electron excitation	%	Energie [eV]	Energie [nm]	f	Nature
	$\mathrm{HOMO}-2 \rightarrow \mathrm{LUMO}+1$	5				$\mathrm{MLCT}_{\mathrm{bpy}}$
S8	$\mathrm{HOMO}-1 \rightarrow \mathrm{LUMO}+1$	55	3	413	0.04	$\mathrm{LLCT}_{\mathrm{ret}\rightarrow\mathrm{bpy}}$
	$\mathrm{HOMO}-2 \rightarrow \mathrm{LUMO}+1$	24				$\mathrm{MLCT}_{\mathrm{bpy}}$

Table A.6: TD-DFT transition energies (in eV), wavelength of absorption (in nm) and oscillator strengths f associated to the low-lying singlet excited states of **4c** conformer in acetonitrile. ($\tau = 90°$)

Conformer 3c

KS orbitals

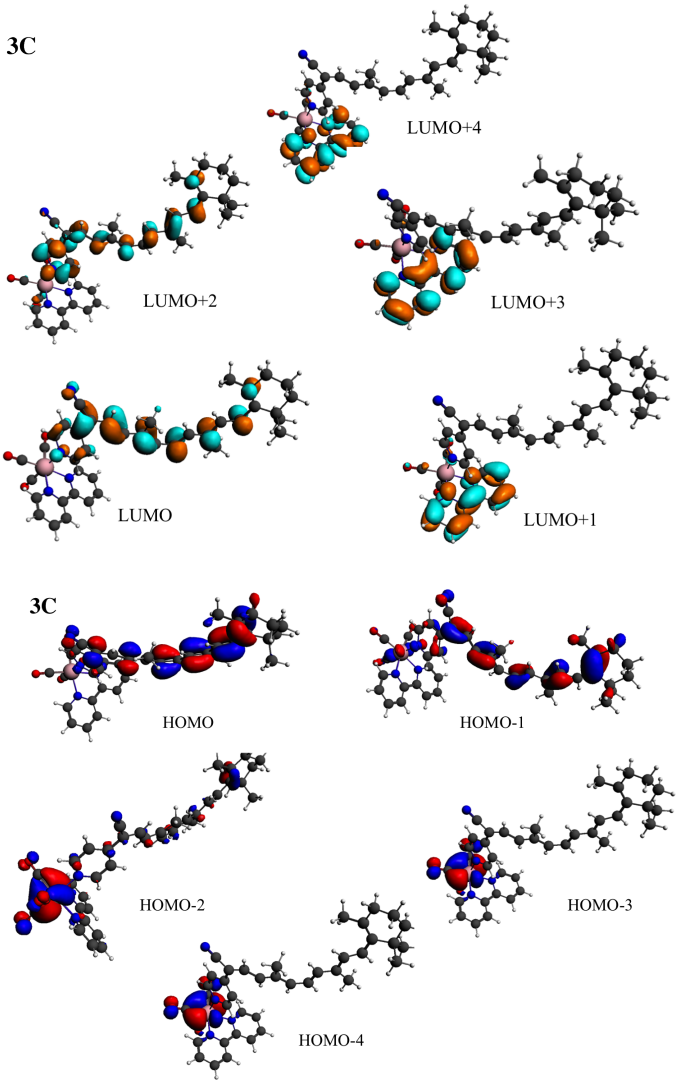

Figure A.3: Kohn-Sham orbitals of the *cis* **3c** conformer in acetonitrile.

Electronic states ($\tau = 180°$)

State	One-electron excitation	%	Energie [eV]	Energie [nm]	f	Nature
T1	HOMO $\rightarrow$ LUMO	95	1.12	1107	-	IL_{ret}
S1	HOMO $\rightarrow$ LUMO	97	1.77	700	2.54	IL_{ret}
T2	HOMO $-$ 1 $\rightarrow$ LUMO	75	2.07	599	0.00	IL_{ret}
	HOMO $\rightarrow$ LUMO + 2	11			-	IL_{ret}
T3	HOMO $\rightarrow$ LUMO + 1	98	2.18	569	-	$LLCT_{ret\rightarrow bpy}$
S2	HOMO $\rightarrow$ LUMO + 1	98	2.18	569	0.00	$LLCT_{ret\rightarrow bpy}$
T4	HOMO $\rightarrow$ LUMO + 2	72	2.55	486	-	IL_{ret}
	HOMO $-$ 1 $\rightarrow$ LUMO	13			-	IL_{ret}
S3	HOMO $-$ 1 $\rightarrow$ LUMO	93	2.77	448	0.23	IL_{ret}
T5	HOMO $-$ 2 $\rightarrow$ LUMO	47	2.82	440	-	$MLCT_{ret}$
	HOMO $-$ 5 $\rightarrow$ LUMO	25				IL_{ret}
	HOMO $-$ 1 $\rightarrow$ LUMO + 2	9				IL_{ret}
T6	HOMO $-$ 2 $\rightarrow$ LUMO + 1	52	2.90	428	-	$MLCT_{bpy}$
	HOMO $-$ 1 $\rightarrow$ LUMO + 1	36				$LLCT_{ret\rightarrow bpy}$
S4	HOMO $-$ 1 $\rightarrow$ LUMO + 1	57	3.01	412	0.01	$LLCT_{ret\rightarrow bpy}$
	HOMO $-$ 2 $\rightarrow$ LUMO + 1	40			-	$MLCT_{bpy}$
T7	HOMO $-$ 3 $\rightarrow$ LUMO + 1	63	3.10	400	-	$MLCT_{bpy}$
	HOMO $-$ 5 $\rightarrow$ LUMO	17				IL_{ret}
	HOMO $-$ 2 $\rightarrow$ LUMO	9				$MLCT_{ret}$
S5	HOMO $\rightarrow$ LUMO + 2	79	3.10	400	0.06	IL_{ret}
	HOMO $-$ 2 $\rightarrow$ LUMO	12				$MLCT_{ret}$
S6	HOMO $-$ 2 $\rightarrow$ LUMO	83	3.12	397	0.17	$MLCT_{ret}$
	HOMO $\rightarrow$ LUMO + 2	12				IL_{ret}

Table A.7: TD-DFT transition energies (in eV), wavelength of absorption (in nm) and oscillator strengths f associated to the low-lying singlet excited states of **3c** conformer in acetonitrile.

Conformer 2c

KS orbitals

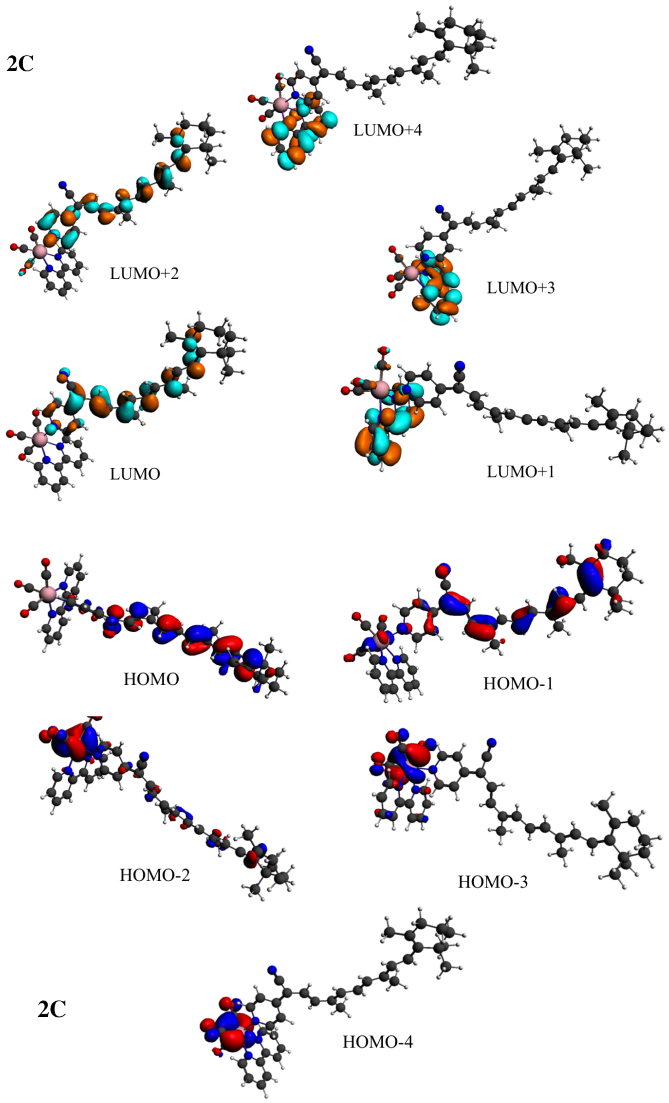

Figure A.4: Kohn-Sham orbitals of the *cis* **2c** conformer in acetonitrile.

Electronic states ($\tau = 180°$)

State	One-electron excitation	%	Energie [eV]	Energie [nm]	f	Nature
T1	HOMO $\rightarrow$ LUMO	94	1.17	1060	-	IL_{ret}
S1	HOMO $\rightarrow$ LUMO	97	1.80	689	2.41	IL_{ret}
T2	HOMO $-$ 1 $\rightarrow$ LUMO	70	2.09	593	0.00	IL_{ret}
	HOMO $\rightarrow$ LUMO + 2	16			-	IL_{ret}
T3	HOMO $\rightarrow$ LUMO + 1	98	2.20		-	$LLCT_{ret\rightarrow bpy}$
S2	HOMO $\rightarrow$ LUMO + 1	98	2.20	564	0.00	$LLCT_{ret\rightarrow bpy}$
T4	HOMO $\rightarrow$ LUMO + 2	67	2.52	492	-	IL_{ret}
	HOMO $-$ 1 $\rightarrow$ LUMO	18			-	IL_{ret}
T5	HOMO $-$ 2 $\rightarrow$ LUMO	38	2.82	440	-	$MLCT_{ret}$
	HOMO $-$ 5 $\rightarrow$ LUMO	29				IL_{ret}
	HOMO $-$ 1 $\rightarrow$ LUMO + 2	12				IL_{ret}
S3	HOMO $-$ 1 $\rightarrow$ LUMO	91	2.82	440	0.36	IL_{ret}
T6	HOMO $-$ 2 $\rightarrow$ LUMO + 1	49	2.90	428	-	$MLCT_{bpy}$
	HOMO $-$ 1 $\rightarrow$ LUMO + 1	39				$LLCT_{ret\rightarrow bpy}$
S4	HOMO $-$ 1 $\rightarrow$ LUMO + 1	60	3.01	412	0.01	$LLCT_{ret\rightarrow bpy}$
	HOMO $-$ 2 $\rightarrow$ LUMO + 1	37			-	$MLCT_{bpy}$
S5	HOMO $\rightarrow$ LUMO + 2	89	3.06	405	0.12	IL_{ret}
T7	HOMO $-$ 3 $\rightarrow$ LUMO + 1	94	3.10		-	$MLCT_{bpy}$
S6	HOMO $-$ 2 $\rightarrow$ LUMO	94	3.18	390	0.11	$MLCT_{ret}$

Table A.8: TD-DFT transition energies (in eV), wavelength of absorption (in nm) and oscillator strengths f associated to the low-lying singlet excited states of **2c** conformer in acetonitrile.

Electronic states ($\tau = 90°$)

State	One-electron excitation	%	Energie [eV]	Energie [nm]	f	Nature
T1	HOMO $\rightarrow$ LUMO	97	0.82	1512	-	IL_{ret}
S1	HOMO $\rightarrow$ LUMO	97	1.39	892	1.89	IL_{ret}
T2	HOMO $-$ 1 $\rightarrow$ LUMO	93	1.59		-	IL_{ret}
T3	HOMO $\rightarrow$ LUMO + 1	98	2.02		-	$LLCT_{ret\rightarrow bpy}$
S2	HOMO $\rightarrow$ LUMO + 1	99	2.02	614	0	$LLCT_{ret\rightarrow bpy}$
S3	HOMO $-$ 1 $\rightarrow$ LUMO	92	2.42	512	0.72	IL_{ret}

continued on next page

continued from previous page

State	One-electron excitation	%	Energie [eV]	Energie [nm]	f	Nature
T4	HOMO $\rightarrow$ LUMO + 3	84	2.46		-	IL_{ret}
T5	HOMO $-$ 5 $\rightarrow$ LUMO	49	2.61		-	IL_{ret}
	HOMO $-$ 2 $\rightarrow$ LUMO	23				$MLCT_{ret}$
	HOMO $-$ 6 $\rightarrow$ LUMO	11				$LLCT_{bpy\rightarrow ret}$
	HOMO $-$ 1 $\rightarrow$ LUMO + 5	5				IL_{ret}
T6	HOMO $-$ 2 $\rightarrow$ LUMO	68	2.78	446	-	$MLCT_{ret}$
	HOMO $-$ 5 $\rightarrow$ LUMO	18				IL_{ret}
S4	HOMO $-$ 2 $\rightarrow$ LUMO	98	2.8	443	0.06	$MLCT_{ret}$
T7	HOMO $-$ 2 $\rightarrow$ LUMO + 1	66	2.92	425	-	$MLCT_{bpy}$
	HOMO $-$ 1 $\rightarrow$ LUMO + 1	20				$LLCT_{ret\rightarrow bpy}$
S5	HOMO $-$ 3 $\rightarrow$ LUMO	99	2.94	422	0	$MLCT_{ret}$
S6	HOMO $\rightarrow$ LUMO + 2	47	3.03	409	0.01	$MLCT_{ret}$
	HOMO $-$ 2 $\rightarrow$ LUMO + 1	26				$MLCT_{bpy}$
	HOMO $-$ 1 $\rightarrow$ LUMO + 1	25				$LLCT_{ret\rightarrow bpy}$
S7	HOMO $\rightarrow$ LUMO + 2	51	3.04	408	0	$LLCT_{ret\rightarrow bpy}$
	HOMO $-$ 1 $\rightarrow$ LUMO + 1	23				$LLCT_{ret\rightarrow bpy}$
	HOMO $-$ 2 $\rightarrow$ LUMO + 1	23				$MLCT_{bpy}$
S8	HOMO $\rightarrow$ LUMO + 3	86	3.06	405	0.22	IL_{ret}

Table A.9: TD-DFT transition energies (in eV), wavelength of absorption (in nm) and oscillator strengths f associated to the low-lying singlet excited states of **2c** conformer in acetonitrile. ($\tau = 90°$)

Conformer 1c

Electronic states ($\tau = 180°$)

State	One-electron excitation	%	Energie [eV]	Energie [nm]	f	Nature
T1	HOMO $\rightarrow$ LUMO	95	1.09	1137	-	IL_{ret}
S1	HOMO $\rightarrow$ LUMO	97	1.75	708	3.13	IL_{ret}
T2	HOMO $-$ 1 $\rightarrow$ LUMO	76	2.06	602	-	IL_{ret}
	HOMO $\rightarrow$ LUMO + 3	9				IL_{ret}
T3	HOMO $\rightarrow$ LUMO + 1	98	2.17	571	-	IL_{ret}
S2	HOMO $\rightarrow$ LUMO + 1	98	2.17	571	0.00	IL_{ret}
T4	HOMO $\rightarrow$ LUMO + 3	56	2.59	479	-	IL_{ret}
	HOMO $\rightarrow$ LUMO + 2	15				$LLCT_{ret\rightarrow bpy}$
	HOMO $-$ 1 $\rightarrow$ LUMO	13				IL_{ret}
S3	HOMO $-$ 1 $\rightarrow$ LUMO	94	2.76	449	0.26	IL_{ret}
T5	HOMO $-$ 2 $\rightarrow$ LUMO	47	2.81	441	-	$MLCT_{ret}$
	HOMO $-$ 5 $\rightarrow$ LUMO	27				IL_{ret}
	HOMO $-$ 1 $\rightarrow$ LUMO + 3	7				IL_{ret}
T6	HOMO $-$ 2 $\rightarrow$ LUMO + 1	48	2.90	428	-	$MLCT_{bpy}$
	HOMO $-$ 1 $\rightarrow$ LUMO + 1	40				$LLCT_{ret\rightarrow bpy}$
S4	HOMO $-$ 1 $\rightarrow$ LUMO + 1	61	3.01	412	0.01	$LLCT_{ret\rightarrow bpy}$
	HOMO $-$ 2 $\rightarrow$ LUMO + 1	35				$MLCT_{bpy}$
T7	HOMO $-$ 3 $\rightarrow$ LUMO + 1	91	3.10	400	-	$MLCT_{bpy}$
S5	HOMO $-$ 2 $\rightarrow$ LUMO	94	3.13	396	0.07	$MLCT_{ret}$
S6	HOMO $\rightarrow$ LUMO + 2	94	3.18	390	0.00	$MLCT_{bpy}$

Table A.10: TD-DFT transition energies (in eV), wavelength of absorption (in nm) and oscillator strengths f associated to the low-lying singlet excited states of **1c** conformer in acetonitrile.

Electronic states ($\tau = 90°$)

State	One-electron excitation	%	Energie [eV]	Energie [nm]	f	Nature
T1	HOMO $\rightarrow$ LUMO	97	0.8	1550	-	IL_{ret}
S1	HOMO $\rightarrow$ LUMO	97	1.36	912	1.74	IL_{ret}

continued on next page

continued from previous page

State	One-electron excitation	%	Energie [eV]	Energie [nm]	f	Nature
T2	HOMO $-1 \rightarrow$ LUMO	92	1.41	879	-	IL_{ret}
T3	HOMO $\rightarrow$ LUMO $+1$	97	2.12	585	-	$LLCT_{ret\rightarrow bpy}$
S2	HOMO $\rightarrow$ LUMO $+1$	97	2.13	582	0	$LLCT_{ret\rightarrow bpy}$
S3	HOMO $-1 \rightarrow$ LUMO	94	2.2	564	0.65	IL_{ret}
T4	HOMO $-5 \rightarrow$ LUMO	53	2.34	530	-	IL_{ret}
	HOMO $-2 \rightarrow$ LUMO	15				$MLCT_{ret}$
	HOMO $\rightarrow$ LUMO $+2$	12				IL_{ret}
	HOMO $-1 \rightarrow$ LUMO $+2$	12				IL_{ret}
T5	HOMO $\rightarrow$ LUMO $+2$	72	2.52	492	-	IL_{ret}
	HOMO $-5 \rightarrow$ LUMO	15				IL_{ret}
T6	HOMO $-2 \rightarrow$ LUMO	75	2.66	466	-	$MLCT_{ret}$
	HOMO $-5 \rightarrow$ LUMO	15				$MLCT_{ret}$
S4	HOMO $-2 \rightarrow$ LUMO	98	2.7	459	0.05	$MLCT_{ret}$
T7	HOMO $-3 \rightarrow$ LUMO	99	2.79	444	-	$MLCT_{ret}$
S5	HOMO $-3 \rightarrow$ LUMO	99	2.79	444	0	$MLCT_{ret}$
T8	HOMO $-1 \rightarrow$ LUMO $+1$	55	2.88	430	-	$LLCT_{ret\rightarrow bpy}$
	HOMO $-2 \rightarrow$ LUMO $+1$	36				$MLCT_{bpy}$
S6	HOMO $-1 \rightarrow$ LUMO $+1$	81	2.94	422	0	$LLCT_{ret\rightarrow bpy}$
	HOMO $-2 \rightarrow$ LUMO $+1$	15				$MLCT_{bpy}$
S7	HOMO $-4 \rightarrow$ LUMO	99	2.97	417	0	$MLCT_{ret}$
S8	HOMO $\rightarrow$ LUMO $+2$	86	2.98	416	0.19	IL_{ret}
	HOMO $-5 \rightarrow$ LUMO	6				IL_{ret}
	HOMO $\rightarrow$ LUMO $+2$	7				IL_{ret}

Table A.11: TD-DFT transition energies (in eV), wavelength of absorption (in nm) and oscillator strengths f associated to the low-lying singlet excited states of **1c** conformer in acetonitrile. ($\tau = 90°$)

A.3 States-correlation diagrams

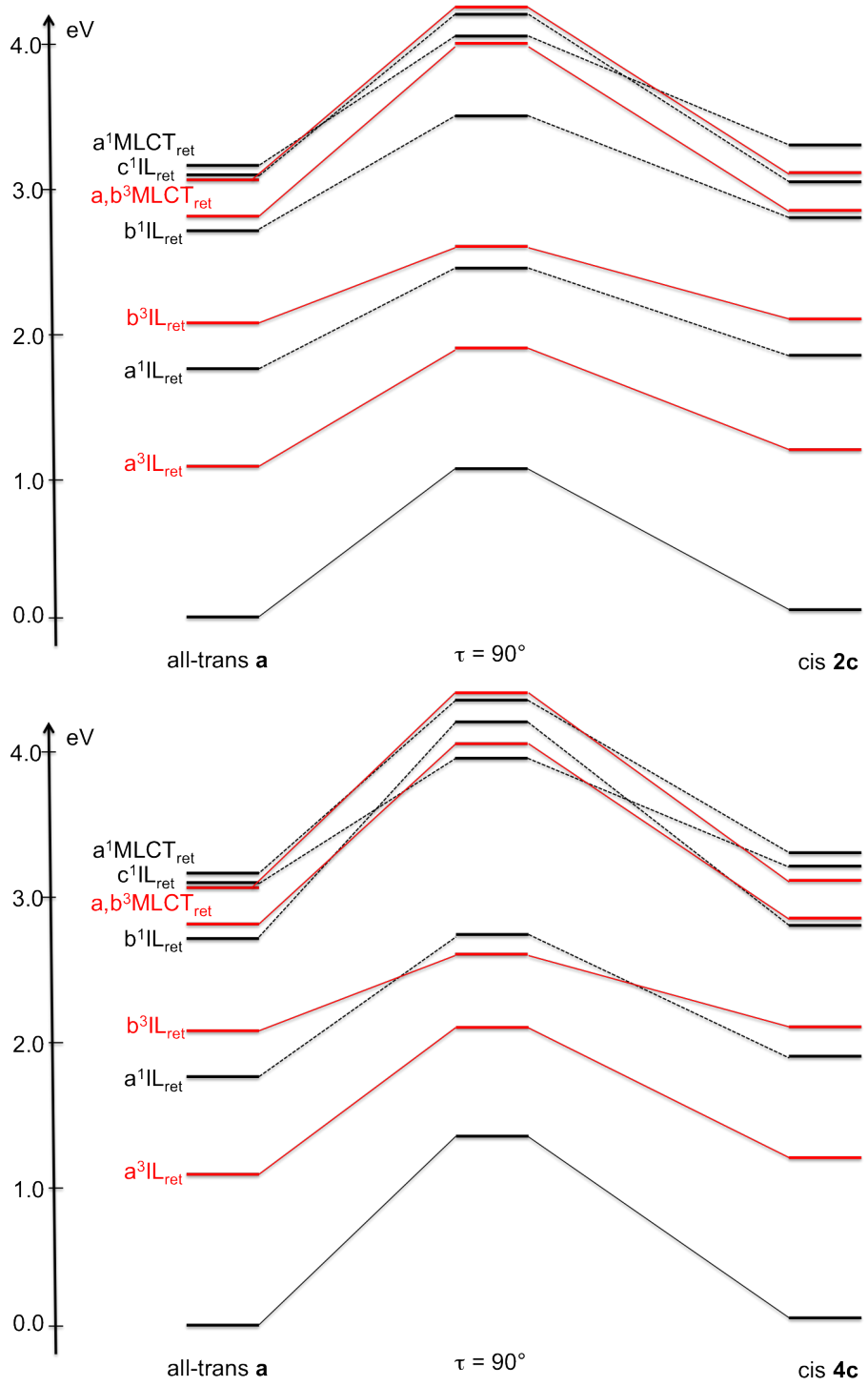

Figure A.5: TD-DFT states correlation diagrams connecting the low-lying singlet and triplet excited states of all-*trans* [Re(CO)$_3$(bpy)(L)]$^+$ **a** to the corresponding states of the *cis* **2c** (left) and **4c** (right) isomers. (energies are reported in APPENDIX TAB. A.12.)

State	$\tau = 180°$	$\tau = 90°$	$\tau = 0°$
All-*trans* **a** to **1c**			
Ground state	0.0	1.09	-0.18
a^3IL_{ret}	1.13	1.89	1.14
a^1IL_{ret}	1.79	2.45	1.80
b^3IL_{ret}	2.10	2.50	2.11
b^1IL_{ret}	2.78	3.29	2.81
a^3MLCT_{ret}	2.84	3.43	2.86
b^3MLCT_{ret}	3.10	4.15	3.15
c^1IL_{ret}	3.10	4.07	3.27
a^1MLCT_{ret}	3.15	3.79	3.18
All-*trans* **a** to **2c**			
Ground state	0.0	1.09	0.05
a^3IL_{ret}	1.13	1.91	1.22
a^1IL_{ret}	1.79	2.48	1.85
b^3IL_{ret}	2.10	2.68	2.14
b^1IL_{ret}	2.78	3.51	2.87
a^3MLCT_{ret}	2.84	3.87	2.87
b^3MLCT_{ret}	3.10	4.19	2.95
c^1IL_{ret}	3.10	4.15	3.11
a^1MLCT_{ret}	3.15	3.89	3.23
All-*trans* **a** to **4c**			
Ground state	0.0	1.42	0.05
a^3IL_{ret}	1.13	2.04	1.25
a^1IL_{ret}	1.79	2.78	1.88
b^3IL_{ret}	2.10	3.43	2.15
b^1IL_{ret}	2.78	4.15	2.85
a^3MLCT_{ret}	2.84	3.93	2.87
b^3MLCT_{ret}	3.10	4.50	3.15
c^1IL_{ret}	3.10	3.83	3.18
a^1MLCT_{ret}	3.15	4.42	3.21

Table A.12: Relative energies (in eV) of the low-lying singlet and triplet states of $[Re(CO)_3(bpy)(L)]^+$ as function of the isomerizable double CC bond torsion angle τ. (the energy of reference is the electronic ground state of the all-*trans* conformer **a**).

APPENDIX B

NORMAL MODE PARAMETERS EXTRACTED FROM ELECTRONIC STRUCTURE OF [RE(X)(CO)$_3$(BPY)]

B.1 Quantum Chemical Interpretation of Ultrafast Luminescence Decay and Intersystem Crossings in Rhenium(I) Carbonyl Bipyridine Complexes

[Re(Br)(CO)$_3$(bpy)]

Mode T [fs]	ω [eV] ω [cm^{-1}]	$\kappa_i^{(S1)}$ $\frac{-\kappa_i^{(S1)}}{\omega_i}$ $\frac{-\kappa_i^{(S1)^2}}{2\omega_i}$	$\kappa_i^{(S2)}$ $\frac{-\kappa_i^{(S2)}}{\omega_i}$ $\frac{-\kappa_i^{(S2)^2}}{2\omega_i}$	$\kappa_i^{(T1)}$ $\frac{-\kappa_i^{(T1)}}{\omega_i}$ $\frac{-\kappa_i^{(T1)^2}}{2\omega_i}$	$\kappa_i^{(T2)}$ $\frac{-\kappa_i^{(T2)}}{\omega_i}$ $\frac{-\kappa_i^{(T2)^2}}{2\omega_i}$	$\kappa_i^{(T3)}$ $\frac{-\kappa_i^{(T3)}}{\omega_i}$ $\frac{-\kappa_i^{(T3)^2}}{2\omega_i}$
2	0.004	-0.018	-0.023	-0.019	-0.017	-0.006
962	35	4.140	5.395	4.465	3.837	1.372
		-0.037	-0.063	-0.043	-0.032	-0.004
4	0.009	-0.008	-0.019	-0.008	-0.031	-0.003
481	69	0.930	2.233	0.919	3.547	0.372
		-0.004	-0.021	-0.004	-0.054	-0.001
6	0.010	0.005	-0.010	0.003	-0.009	0.002

continued on next page

continued from previous page

Mode T [fs]	ω [eV] ω [cm^{-1}]	$\kappa_i^{(S1)}$ $\frac{-\kappa_i^{(S1)}}{\omega_i}$ $\frac{-\kappa_i^{(S1)2}}{2\omega_i}$	$\kappa_i^{(S2)}$ $\frac{-\kappa_i^{(S2)}}{\omega_i}$ $\frac{-\kappa_i^{(S2)2}}{2\omega_i}$	$\kappa_i^{(T1)}$ $\frac{-\kappa_i^{(T1)}}{\omega_i}$ $\frac{-\kappa_i^{(T1)2}}{2\omega_i}$	$\kappa_i^{(T2)}$ $\frac{-\kappa_i^{(T2)}}{\omega_i}$ $\frac{-\kappa_i^{(T2)2}}{2\omega_i}$	$\kappa_i^{(T3)}$ $\frac{-\kappa_i^{(T3)}}{\omega_i}$ $\frac{-\kappa_i^{(T3)2}}{2\omega_i}$
414	81	-0.480	0.980	-0.280	0.860	-0.220
		-0.001	-0.005	0.000	-0.004	0.000
7	0.012	-0.017	0.019	-0.016	0.019	0.002
357	94	1.483	-1.612	1.388	-1.638	-0.129
		-0.013	-0.015	-0.011	-0.016	0.000
9	0.012	0.001	-0.011	-0.001	-0.009	0.003
339	98	-0.074	0.861	0.041	0.762	-0.279
		0.000	-0.005	0.000	-0.004	0.000
11	0.019	0.009	0.009	0.000	-0.001	0.006
220	152	-0.479	-0.484	-0.011	0.032	-0.298
		-0.002	-0.002	0.000	0.000	-0.001
12	0.022	-0.020	-0.009	-0.022	-0.018	0.015
191	175	0.926	0.392	1.005	0.830	-0.682
		-0.009	-0.002	-0.011	-0.008	-0.005
13	0.023	-0.029	-0.027	-0.026	-0.032	0.013
181	185	1.262	1.183	1.140	1.406	-0.581
		-0.018	-0.016	-0.015	-0.023	-0.004
16	0.032	-0.026	-0.019	-0.030	-0.024	0.006
129	259	0.813	0.604	0.938	0.735	-0.178
		-0.011	-0.006	-0.014	-0.009	-0.001
17	0.046	0.012	0.000	0.020	0.014	0.025
91	367	-0.257	0.000	-0.429	-0.297	-0.552
		-0.002	0.000	-0.004	-0.002	-0.007
18	0.053	-0.003	-0.004	-0.002	-0.001	-0.003
78	425	0.047	0.066	0.040	0.019	0.051
		0.000	0.000	0.000	0.000	0.000
20	0.056	0.002	0.004	0.003	0.012	-0.002
73	454	-0.041	-0.073	-0.046	-0.213	0.027
		0.000	0.000	0.000	-0.001	0.000
22	0.060	-0.018	-0.024	-0.018	-0.027	-0.006

continued on next page

continued from previous page

Mode T [fs]	ω [eV] ω [cm^{-1}]	$\kappa_i^{(S1)}$ $\frac{-\kappa_i^{(S1)}}{\omega_i}$ $\frac{-\kappa_i^{(S1)2}}{2\omega_i}$	$\kappa_i^{(S2)}$ $\frac{-\kappa_i^{(S2)}}{\omega_i}$ $\frac{-\kappa_i^{(S2)2}}{2\omega_i}$	$\kappa_i^{(T1)}$ $\frac{-\kappa_i^{(T1)}}{\omega_i}$ $\frac{-\kappa_i^{(T1)2}}{2\omega_i}$	$\kappa_i^{(T2)}$ $\frac{-\kappa_i^{(T2)}}{\omega_i}$ $\frac{-\kappa_i^{(T2)2}}{2\omega_i}$	$\kappa_i^{(T3)}$ $\frac{-\kappa_i^{(T3)}}{\omega_i}$ $\frac{-\kappa_i^{(T3)2}}{2\omega_i}$
69	485	0.298	0.394	0.298	0.443	0.107
		-0.003	-0.005	-0.003	-0.006	0.000
24	0.063	-0.066	-0.052	-0.064	-0.062	-0.006
65	511	1.044	0.817	1.017	0.984	0.095
		-0.035	-0.021	-0.033	-0.031	0.000
26	0.067	0.001	-0.020	0.001	-0.023	-0.009
62	538	-0.008	0.304	-0.018	0.351	0.129
		0.000	-0.003	0.000	-0.004	-0.001
30	0.079	-0.019	0.040	-0.020	0.043	0.003
52	639	0.236	-0.510	0.248	-0.547	-0.042
		-0.002	-0.010	-0.002	-0.012	0.000
31	0.081	0.022	-0.007	0.017	-0.009	-0.012
51	653	-0.270	0.085	-0.207	0.115	0.152
		-0.003	0.000	-0.002	-0.001	-0.001
34	0.083	0.009	-0.012	0.014	0.000	0.031
50	673	-0.110	0.145	-0.163	-0.004	-0.375
		-0.001	-0.001	-0.001	0.000	-0.006
36	0.093	0.007	0.013	0.006	0.007	0.008
44	751	-0.071	-0.144	-0.059	-0.073	-0.084
		0.000	-0.001	0.000	0.000	0.000
37	0.095	-0.001	0.003	-0.003	0.001	-0.005
43	767	0.005	-0.035	0.036	-0.013	0.056
		0.000	0.000	0.000	0.000	0.000
38	0.097	0.019	0.010	0.031	0.016	0.048
43	782	-0.194	-0.104	-0.318	-0.169	-0.500
		-0.002	-0.001	-0.005	-0.001	-0.012
40	0.112	0.003	0.001	0.006	0.003	-0.002
37	905	-0.030	-0.012	-0.054	-0.026	0.015
		0.000	0.000	0.000	0.000	0.000
42	0.123	0.001	-0.001	0.001	0.000	0.004

continued on next page

continued from previous page

Mode T [fs]	ω [eV] ω [cm^{-1}]	$\kappa_i^{(S1)}$ $\frac{-\kappa_i^{(S1)}}{\omega_i}$ $\frac{-\kappa_i^{(S1)2}}{2\omega_i}$	$\kappa_i^{(S2)}$ $\frac{-\kappa_i^{(S2)}}{\omega_i}$ $\frac{-\kappa_i^{(S2)2}}{2\omega_i}$	$\kappa_i^{(T1)}$ $\frac{-\kappa_i^{(T1)}}{\omega_i}$ $\frac{-\kappa_i^{(T1)2}}{2\omega_i}$	$\kappa_i^{(T2)}$ $\frac{-\kappa_i^{(T2)}}{\omega_i}$ $\frac{-\kappa_i^{(T2)2}}{2\omega_i}$	$\kappa_i^{(T3)}$ $\frac{-\kappa_i^{(T3)}}{\omega_i}$ $\frac{-\kappa_i^{(T3)2}}{2\omega_i}$
34	990	-0.009	0.011	-0.010	-0.001	-0.031
		0.000	0.000	0.000	0.000	0.000
45	0.128	-0.001	0.000	-0.001	0.000	-0.002
32	1028	0.011	0.002	0.010	0.002	0.015
		0.000	0.000	0.000	0.000	0.000
47	0.130	0.086	0.068	0.099	0.084	0.121
32	1049	-0.661	-0.525	-0.760	-0.646	-0.934
		-0.028	-0.018	-0.038	-0.027	-0.057
49	0.135	-0.002	0.005	-0.001	0.004	0.020
31	1089	0.012	-0.040	0.004	-0.032	-0.145
		0.000	0.000	0.000	0.000	-0.001
51	0.140	0.013	0.008	0.016	0.014	0.028
30	1131	-0.093	-0.060	-0.117	-0.101	-0.197
		-0.001	0.000	-0.001	-0.001	-0.003
54	0.148	-0.069	-0.059	-0.070	-0.062	-0.048
28	1190	0.464	0.399	0.477	0.418	0.324
		-0.016	-0.012	-0.017	-0.013	-0.008
56	0.160	-0.007	-0.009	-0.012	-0.008	-0.037
26	1289	0.044	0.058	0.076	0.048	0.232
		0.000	0.000	0.000	0.000	-0.004
57	0.163	0.064	0.047	0.059	0.071	-0.086
25	1312	-0.390	-0.290	-0.363	-0.436	0.526
		-0.012	-0.007	-0.011	-0.015	-0.022
58	0.166	0.107	0.096	0.107	0.099	0.130
25	1336	-0.644	-0.577	-0.647	-0.596	-0.786
		-0.034	-0.028	-0.035	-0.029	-0.051
60	0.181	-0.006	-0.002	-0.009	-0.012	0.042
23	1463	0.034	0.010	0.050	0.067	-0.229
		0.000	0.000	0.000	0.000	-0.005
63	0.189	0.165	0.143	0.171	0.151	0.159

continued on next page

continued from previous page

Mode T [fs]	ω [eV] ω [cm^{-1}]	$\kappa_i^{(S1)}$ $\frac{-\kappa_i^{(S1)}}{\omega_i}$ $\frac{-\kappa_i^{(S1)^2}}{2\omega_i}$	$\kappa_i^{(S2)}$ $\frac{-\kappa_i^{(S2)}}{\omega_i}$ $\frac{-\kappa_i^{(S2)^2}}{2\omega_i}$	$\kappa_i^{(T1)}$ $\frac{-\kappa_i^{(T1)}}{\omega_i}$ $\frac{-\kappa_i^{(T1)^2}}{2\omega_i}$	$\kappa_i^{(T2)}$ $\frac{-\kappa_i^{(T2)}}{\omega_i}$ $\frac{-\kappa_i^{(T2)^2}}{2\omega_i}$	$\kappa_i^{(T3)}$ $\frac{-\kappa_i^{(T3)}}{\omega_i}$ $\frac{-\kappa_i^{(T3)^2}}{2\omega_i}$
22	1522	-0.872	-0.759	-0.905	-0.798	-0.841
		-0.072	-0.054	-0.077	-0.060	-0.067
64	0.199	-0.116	-0.105	-0.122	-0.103	-0.122
21	1601	0.583	0.527	0.613	0.517	0.617
		-0.034	-0.028	-0.037	-0.027	-0.038
66	0.203	0.032	0.035	0.032	0.009	0.209
20	1637	-0.155	-0.170	-0.159	-0.042	-1.031
		-0.002	-0.003	-0.003	0.000	-0.110
68	0.233	0.038	0.034	0.036	0.037	0.007
18	1879	-0.164	-0.145	-0.155	-0.160	-0.031
		-0.003	-0.002	-0.003	-0.003	0.000
70	0.253	0.093	0.074	0.083	0.084	-0.004
16	2042	-0.367	-0.293	-0.328	-0.333	0.017
		-0.017	-0.011	-0.014	-0.014	0.000

Table B.1: Extracted parameters for a' normal modes of [Re(Br)(CO)$_3$(bpy)] : the intrastate coupling κ_i (eV), the induced displacement $-\frac{\kappa_i^{(n)}}{\omega_i}$ (dimensionless) and the induced shift in energy $-\frac{\kappa_i^{(n)^2}}{2\omega_i}$ (in eV). The period (in fs) and the frequency (in eV and cm^{-1}) are shown for each normal mode.

Mode T [fs]	ω [eV] ω [cm^{-1}]	$\lambda^{(S1),(S2)}$ [eV]	$\lambda^{(T1),(T2)}$ [eV]
1	0.0032	0.002	0.010
1292.38	26		
3	0.0073	0.009	0.009
566.52	59		
5	0.01	0.005	0.005
413.56	81		

continued on next page

continued from previous page

Mode T [fs]	ω [eV] ω [cm^{-1}]	$\lambda^{(S1),(S2)}$ [eV]	$\lambda^{(T1),(T2)}$ [eV]
8	0.0118	0.011	0.009
350.47	95		
10	0.0125	0.013	0.015
330.85	101		
14	0.0256	0.006	0.018
161.55	206		
15	0.0317	0.003	0.011
130.46	256		
19	0.0532	0.009	0.009
77.74	429		
21	0.0575	0.017	0.026
71.92	464		
23	0.0601	0.024	0.019
68.81	485		
25	0.0637	0.017	0.012
64.92	514		
27	0.0674	0.009	0.007
61.36	544		
28	0.069	0.000	0.006
59.94	557		
29	0.0784	0.032	0.022
52.75	632		
32	0.0811	0.008	0.003
50.99	654		
33	0.0822	0.000	0.003
50.31	663		
35	0.093	0.001	0.005
44.47	750		
39	0.1017	0.001	0.000
40.66	820		

continued on next page

continued from previous page

Mode T [fs]	ω [eV] ω [cm^{-1}]	$\lambda^{(S1),(S2)}$ [eV]	$\lambda^{(T1),(T2)}$ [eV]
41	0.1123	0.004	0.005
36.83	906		
43	0.1228	0.006	0.004
33.68	990		
44	0.1271	0.006	0.002
32.54	1025		
46	0.1285	0.000	0.022
32.18	1036		
48	0.1322	0.003	0.002
31.28	1066		
50	0.1359	0.000	0.007
30.43	1096		
52	0.1419	0.003	0.003
29.14	1145		
53	0.146	0.000	0.007
28.33	1178		
55	0.1583	0.000	0.003
26.13	1277		
59	0.1669	0.000	0.005
24.78	1346		
61	0.1832	0.001	0.000
22.57	1478		
62	0.1871	0.000	0.013
22.1	1509		
65	0.1997	0.000	0.014
20.71	1611		
67	0.2042	0.000	0.022
20.25	1647		
69	0.2351	0.028	0.019
17.59	1896		

continued on next page

continued from previous page

Mode	ω [eV]	$\lambda^{(S1),(S2)}$ [eV]	$\lambda^{(T1),(T2)}$ [eV]
T [fs]	ω [cm^{-1}]		

Table B.2: Extracted interstate vibronic coupling $\lambda_i^{(n),(m)}$ (in eV) for a" normal modes of [Re(Br)(CO)$_3$(bpy)]. The period (in fs) and the frequency (in eV and cm^{-1}) are shown for each normal mode.

[Re(F)(CO)$_3$(bpy)]

Mode T [fs]	ω [eV] ω [cm^{-1}]	$\kappa_i^{(S1)}$ $\frac{-\kappa_i^{(S1)}}{\omega_i}$ $\frac{-\kappa_i^{(S1)^2}}{2\omega_i}$	$\kappa_i^{(S2)}$ $\frac{-\kappa_i^{(S2)}}{\omega_i}$ $\frac{-\kappa_i^{(S2)^2}}{2\omega_i}$	$\kappa_i^{(T1)}$ $\frac{-\kappa_i^{(T1)}}{\omega_i}$ $\frac{-\kappa_i^{(T1)^2}}{2\omega_i}$	$\kappa_i^{(T2)}$ $\frac{-\kappa_i^{(T2)}}{\omega_i}$ $\frac{-\kappa_i^{(T2)^2}}{2\omega_i}$	$\kappa_i^{(T3)}$ $\frac{-\kappa_i^{(T3)}}{\omega_i}$ $\frac{-\kappa_i^{(T3)^2}}{2\omega_i}$
2	0.0045	-0.0077	-0.0079	-0.0096	-0.0031	-0.0009
919.02	36	1.7111	1.7556	2.1333	0.6889	0.2000
		-0.0066	0.0069	-0.0100	-0.0011	-0.0001
4	0.0097	0.0057	-0.0005	0.0057	0.0049	-0.0003
426.35	78	-0.5876	0.0515	-0.5876	-0.5052	0.0309
		-0.0017	0.0000	-0.0017	-0.0012	0.0000
6	0.0115	-0.0200	0.0224	-0.0178	0.0236	0.0003
359.62	93	1.7391	-1.9478	1.5478	-2.0522	-0.0261
		-0.0170	0.0220	-0.0140	-0.0240	0.0000
8	0.0121	0.0013	0.0185	0.0034	0.0179	-0.0023
351.79	98	-0.1074	-1.5289	-0.2810	-1.4793	0.1901
		-0.0001	0.0140	-0.0005	-0.0130	-0.0002
9	0.0162	0.0093	0.0068	0.0101	0.0150	0.0060
255.28	131	-0.5741	-0.4198	-0.6235	-0.9259	-0.3704
		-0.0027	0.0014	-0.0031	-0.0069	0.0011
11	0.0214	-0.0274	-0.0114	-0.0316	-0.0249	0.0192
193.25	173	1.2804	0.5327	1.4766	1.1636	-0.8972
		-0.0180	0.0030	-0.0230	-0.0140	0.0086
13	0.0252	-0.0262	-0.0221	-0.0273	-0.0346	0.0035
164.11	203	1.0397	0.8770	1.0833	1.3730	-0.1389
		-0.0140	0.0097	-0.0150	-0.0240	0.0002
14	0.0316	-0.0309	-0.0237	-0.0356	-0.0286	0.0055
130.87	255	0.9778	0.7500	1.1266	0.9051	-0.1741
		-0.0150	0.0089	-0.0200	-0.0130	0.0005
16	0.0452	-0.0066	0.0073	-0.0137	-0.0081	-0.0286
91.5	365	0.1460	-0.1615	0.3031	0.1792	0.6327

continued on next page

continued from previous page

Mode T [fs]	ω [eV] ω [cm^{-1}]	$\kappa_i^{(S1)}$ $\frac{-\kappa_i^{(S1)}}{\omega_i}$ $\frac{-\kappa_i^{(S1)2}}{2\omega_i}$	$\kappa_i^{(S2)}$ $\frac{-\kappa_i^{(S2)}}{\omega_i}$ $\frac{-\kappa_i^{(S2)2}}{2\omega_i}$	$\kappa_i^{(T1)}$ $\frac{-\kappa_i^{(T1)}}{\omega_i}$ $\frac{-\kappa_i^{(T1)2}}{2\omega_i}$	$\kappa_i^{(T2)}$ $\frac{-\kappa_i^{(T2)}}{\omega_i}$ $\frac{-\kappa_i^{(T2)2}}{2\omega_i}$	$\kappa_i^{(T3)}$ $\frac{-\kappa_i^{(T3)}}{\omega_i}$ $\frac{-\kappa_i^{(T3)2}}{2\omega_i}$
		-0.0005	0.0006	-0.0021	-0.0007	-0.0090
17	0.051	0.0686	0.0595	0.0581	0.0565	0.0005
81.09	411	-1.3451	-1.1667	-1.1392	-1.1078	-0.0098
		-0.0460	0.0350	-0.0330	-0.0310	0.0000
18	0.0526	-0.0094	-0.0074	-0.0072	-0.0044	-0.0026
78.62	424	0.1787	0.1407	0.1369	0.0837	0.0494
		-0.0008	0.0005	-0.0005	-0.0002	-0.0001
20	0.0565	0.0076	0.0051	0.0078	0.0125	-0.0010
73.2	456	-0.1345	-0.0903	-0.1381	-0.2212	0.0177
		-0.0005	0.0002	-0.0005	-0.0014	0.0000
23	0.061	-0.0453	-0.0468	-0.0435	-0.0508	-0.0085
67.8	492	0.7426	0.7672	0.7131	0.8328	0.1393
		-0.0170	0.0180	-0.0160	-0.0210	-0.0006
24	0.0639	-0.0695	-0.0592	-0.0676	-0.0677	-0.0064
64.72	515	1.0876	0.9264	1.0579	1.0595	0.1002
		-0.0380	0.0270	-0.0360	-0.0360	-0.0003
27	0.068	-0.0019	0.0075	-0.0023	0.0076	0.0065
60.82	548	0.0279	-0.1103	0.0338	-0.1118	-0.0956
		0.0000	0.0004	0.0000	-0.0004	0.0003
29	0.0799	-0.0286	0.0454	-0.0272	0.0479	0.0054
51.76	644	0.3579	-0.5682	0.3404	-0.5995	-0.0676
		-0.0051	0.0130	-0.0046	-0.0140	0.0002
32	0.0821	-0.0182	0.0009	-0.0125	0.0048	0.0178
50.37	662	0.2217	-0.0110	0.1523	-0.0585	-0.2168
		-0.0020	0.0000	-0.0010	-0.0001	0.0019
34	0.0835	-0.0168	0.0109	-0.0192	-0.0025	-0.0317
49.53	673	0.2012	-0.1305	0.2299	0.0299	0.3796
		-0.0017	0.0007	-0.0022	0.0000	-0.0060
36	0.0932	0.0032	0.0082	0.0022	0.0022	0.0043
44.37	752	-0.0343	-0.0880	-0.0236	-0.0236	-0.0461

continued on next page

continued from previous page

Mode T [fs]	ω [eV] ω [cm^{-1}]	$\kappa_i^{(S1)}$ $\frac{-\kappa_i^{(S1)}}{\omega_i}$ $\frac{-\kappa_i^{(S1)2}}{2\omega_i}$	$\kappa_i^{(S2)}$ $\frac{-\kappa_i^{(S2)}}{\omega_i}$ $\frac{-\kappa_i^{(S2)2}}{2\omega_i}$	$\kappa_i^{(T1)}$ $\frac{-\kappa_i^{(T1)}}{\omega_i}$ $\frac{-\kappa_i^{(T1)2}}{2\omega_i}$	$\kappa_i^{(T2)}$ $\frac{-\kappa_i^{(T2)}}{\omega_i}$ $\frac{-\kappa_i^{(T2)2}}{2\omega_i}$	$\kappa_i^{(T3)}$ $\frac{-\kappa_i^{(T3)}}{\omega_i}$ $\frac{-\kappa_i^{(T3)2}}{2\omega_i}$
		-0.0001	0.0004	0.0000	0.0000	0.0001
37	0.0952	-0.0040	-0.0008	-0.0062	-0.0018	-0.0060
43.44	768	0.0420	0.0084	0.0651	0.0189	0.0630
		-0.0001	0.0000	-0.0002	0.0000	-0.0002
38	0.0969	0.0182	0.0091	0.0278	0.0159	0.0486
42.68	782	-0.1878	-0.0939	-0.2869	-0.1641	-0.5015
		-0.0017	0.0004	-0.0040	-0.0013	0.0120
40	0.1123	0.0024	-0.0006	0.0047	0.0015	-0.0030
36.83	906	-0.0214	0.0053	-0.0419	-0.0134	0.0267
		0.0000	0.0000	-0.0001	0.0000	0.0000
42	0.1228	0.0016	-0.0005	0.0016	0.0004	0.0019
33.68	990	-0.0130	0.0041	-0.0130	-0.0033	-0.0155
		0.0000	0.0000	0.0000	0.0000	0.0000
45	0.1276	-0.0009	0.0002	-0.0007	0.0003	-0.0017
32.41	1029	0.0071	-0.0016	0.0055	-0.0024	0.0133
		0.0000	0.0000	0.0000	0.0000	0.0000
47	0.13	0.0881	0.0676	0.0977	0.0838	0.1227
31.81	1049	-0.6777	-0.5200	-0.7515	-0.6446	-0.9438
		-0.0300	0.0180	-0.0370	-0.0270	0.0580
49	0.1349	-0.0037	0.0041	-0.0030	0.0029	0.0238
30.66	1088	0.0274	-0.0304	0.0222	-0.0215	-0.1764
		-0.0001	0.0001	0.0000	0.0000	0.0021
51	0.1402	0.0130	0.0072	0.0156	0.0137	0.0286
29.5	1131	-0.0927	-0.0514	-0.1113	-0.0977	-0.2040
		-0.0006	0.0002	-0.0009	-0.0007	0.0029
54	0.1476	-0.0701	-0.0596	-0.0710	-0.0629	-0.0473
28.02	1191	0.4749	0.4038	0.4810	0.4262	0.3205
		-0.0170	0.0120	-0.0170	-0.0130	-0.0076
56	0.1599	-0.0124	-0.0127	-0.0152	-0.0106	-0.0350
25.86	1290	0.0775	0.0794	0.0951	0.0663	0.2189

continued on next page

continued from previous page

Mode T [fs]	ω [eV] ω [cm^{-1}]	$\kappa_i^{(S1)}$ $\frac{-\kappa_i^{(S1)}}{\omega_i}$ $\frac{-\kappa_i^{(S1)^2}}{2\omega_i}$	$\kappa_i^{(S2)}$ $\frac{-\kappa_i^{(S2)}}{\omega_i}$ $\frac{-\kappa_i^{(S2)^2}}{2\omega_i}$	$\kappa_i^{(T1)}$ $\frac{-\kappa_i^{(T1)}}{\omega_i}$ $\frac{-\kappa_i^{(T1)^2}}{2\omega_i}$	$\kappa_i^{(T2)}$ $\frac{-\kappa_i^{(T2)}}{\omega_i}$ $\frac{-\kappa_i^{(T2)^2}}{2\omega_i}$	$\kappa_i^{(T3)}$ $\frac{-\kappa_i^{(T3)}}{\omega_i}$ $\frac{-\kappa_i^{(T3)^2}}{2\omega_i}$
		-0.0005	0.0005	-0.0007	-0.0004	-0.0038
57	0.163	0.0567	0.0400	0.0570	0.0642	-0.1041
25.37	1315	-0.3479	-0.2454	-0.3497	-0.3939	0.6387
		-0.0099	0.0049	-0.0100	-0.0130	-0.0330
58	0.1655	0.1176	0.1020	0.1162	0.1085	0.1218
24.99	1335	-0.7106	-0.6163	-0.7021	-0.6556	-0.7360
		-0.0420	0.0310	-0.0410	-0.0360	0.0450
60	0.1814	-0.0052	-0.0002	-0.0098	-0.0115	0.0441
22.8	1463	0.0287	0.0011	0.0540	0.0634	-0.2431
		-0.0001	0.0000	-0.0003	-0.0004	0.0054
63	0.1888	0.1678	0.1438	0.1717	0.1522	0.1577
21.9	1523	-0.8888	-0.7617	-0.9094	-0.8061	-0.8353
		-0.0750	0.0550	-0.0780	-0.0610	0.0660
64	0.1987	-0.1187	-0.1070	-0.1207	-0.1045	-0.1241
20.81	1603	0.5974	0.5385	0.6074	0.5259	0.6246
		-0.0350	0.0290	-0.0370	-0.0270	-0.0390
66	0.2029	0.0299	0.0334	0.0235	0.0075	0.2173
20.38	1637	-0.1474	-0.1646	-0.1158	-0.0370	-1.0710
		-0.0022	0.0027	-0.0014	-0.0001	0.1200
68	0.23	0.0329	0.0284	0.0339	0.0344	0.0044
17.98	1855	-0.1430	-0.1235	-0.1474	-0.1496	-0.0191
		-0.0024	0.0018	-0.0025	-0.0026	0.0000
70	0.2523	0.1211	0.1033	0.1079	0.1089	-0.0042
16.39	2035	-0.4800	-0.4094	-0.4277	-0.4316	0.0166
		-0.0290	0.0210	-0.0230	-0.0240	0.0000

Table B.3: Extracted parameters for a' normal modes of [Re(F)(CO)$_3$(bpy)] : the intrastate coupling κ_i (eV), the induced displacement $-\frac{\kappa_i^{(n)}}{\omega_i}$ (dimensionless) and the induced shift in energy $-\frac{\kappa_i^{(n)^2}}{2\omega_i}$ (in eV). The period (in fs) and the frequency (in eV and cm^{-1}) are shown for each normal mode.

NORMAL MODE PARAMETERS EXTRACTED FROM ELECTRONIC STRUCTURE OF $[Re(X)(CO)_3(bpy)]$

Mode T [fs]	ω [eV] ω [cm^{-1}]	$\lambda^{(S1),(S2)}$ [eV]	$\lambda^{(T1),(T2)}$ [eV]
1	0.0035	0.0000	0.0057
1181.60	28		
3	0.0091	0.0000	0.0038
454.46	73		
5	0.0106	0.0033	0.0057
390.15	85		
7	0.0119	0.0141	0.0158
347.53	96		
10	0.0180	0.0131	0.0154
229.76	145		
12	0.0251	0.0045	0.0173
164.76	22		
15	0.0321	0.0000	0.0104
128.83	259		
19	0.0534	0.0066	0.0092
77.45	431		
21	0.0573	0.0141	0.0262
72.17	462		
22	0.0603	0.0190	0.0193
68.58	486		
25	0.0648	0.0216	0.0184
63.82	523		
26	0.0678	0.0093	0.0098
61.00	547		
28	0.0690	0.0000	0.0064
59.94	557		
30	0.0803	0.0334	0.0275
51.50	648		

continued on next page

continued from previous page

Mode T [fs]	ω [eV] ω [cm^{-1}]	$\lambda^{(S1),(S2)}$ [eV]	$\lambda^{(T1),(T2)}$ [eV]
31	0.0811	0.0093	0.0054
50.99	654		
33	0.0823	0.0000	0.0000
50.25	664		
35	0.0930	0.0000	0.0053
44.47	750		
39	0.1018	0.0000	0.0000
40.62	821		
41	0.1124	0.0040	0.0051
36.79	907		
43	0.1229	0.0065	0.0040
33.65	991		
44	0.1271	0.0060	0.0023
32.54	1025		
46	0.1285	0.0000	0.0202
32.18	1036		
48	0.1322	0.0033	0.0014
31.28	1066		
50	0.1359	0.0000	0.0069
30.43	1096		
52	0.1419	0.0030	0.0032
29.14	1145		
53	0.1458	0.0000	0.0040
28.36	1176		
55	0.1584	0.0000	0.0000
26.11	1278		
59	0.1668	0.0000	0.0042
24.79	1345		
61	0.1831	0.0000	0.0000
22.59	1477		

continued on next page

continued from previous page

Mode T [fs]	ω [eV] ω [cm^{-1}]	$\lambda^{(S1),(S2)}$ [eV]	$\lambda^{(T1),(T2)}$ [eV]
62	0.1870	0.0000	0.0120
21.12	1508		
65	0.1998	0.0000	0.0110
20.70	1612		
67	0.2042	0.0000	0.0212
20.25	1647		
69	0.2331	0.0288	0.0220
17.74	1880		

Table B.4: Extracted interstate vibronic coupling $\lambda_i^{(n),(m)}$ (in eV) for a" normal modes of [Re(F)(CO)$_3$(bpy)]. The period (in fs) and the frequency (in eV and cm^{-1}) are shown for each normal mode.

[Re(Cl)(CO)$_3$(bpy)]

NORMAL MODE PARAMETERS EXTRACTED FROM ELECTRONIC STRUCTURE OF $[Re(X)(CO)_3(bpy)]$

Mode T [fs]	ω [eV] ω [cm^{-1}]	$\kappa_i^{(S1)}$ $\frac{-\kappa_i^{(S1)}}{\omega_i}$ $\frac{-\kappa_i^{(S1)2}}{2\omega_i}$	$\kappa_i^{(S2)}$ $\frac{-\kappa_i^{(S2)}}{\omega_i}$ $\frac{-\kappa_i^{(S2)2}}{2\omega_i}$	$\kappa_i^{(T1)}$ $\frac{-\kappa_i^{(T1)}}{\omega_i}$ $\frac{-\kappa_i^{(T1)2}}{2\omega_i}$	$\kappa_i^{(T2)}$ $\frac{-\kappa_i^{(T2)}}{\omega_i}$ $\frac{-\kappa_i^{(T2)2}}{2\omega_i}$	$\kappa_i^{(T3)}$ $\frac{-\kappa_i^{(T3)}}{\omega_i}$ $\frac{-\kappa_i^{(T3)2}}{2\omega_i}$
2	0.0049	-0.0088	-0.0113	-0.0108	-0.0030	-0.0024
844	40	1.7959	2.3061	2.2041	0.6122	0.4898
		-0.0079	-0.0130	-0.0120	0.0009	0.0006
4	0.0098	0.0077	0.0020	0.0063	0.0092	0.0016
422	79	-0.7857	-0.2041	-0.6429	-0.9388	-0.1633
		-0.0030	-0.0002	-0.0020	0.0043	-0.0001
6	0.0112	0.0068	-0.0303	0.0041	-0.0364	-0.0013
369.25	90	-0.6071	2.7054	-0.3661	3.2500	0.1161
		-0.0021	-0.0410	-0.0008	0.0590	0.0001
8	0.0119	-0.0179	0.0040	-0.0174	-0.0001	-0.0001
347.53	96	1.5042	-0.3361	1.4622	0.0084	0.0084
		-0.0130	-0.0007	-0.0130	0.0000	0.0000
9	0.0123	-0.0054	0.0070	-0.0042	0.0026	-0.0043
336.23	99	0.4390	-0.5691	0.3415	-0.2114	0.3496
		-0.0012	-0.0020	-0.0007	0.0003	0.0008
11	0.0216	-0.0219	-0.0099	-0.0260	-0.0241	0.0186
191.46	174	1.0139	0.4583	1.2037	1.1157	-0.8611
		-0.0110	-0.0023	-0.0160	0.0130	-0.0080
12	0.0229	0.0131	0.0167	0.0140	0.0227	-0.0053
180.59	185	-0.5721	-0.7293	-0.6114	-0.9913	0.2314
		-0.0037	-0.0061	-0.0043	0.0110	0.0006
14	0.0293	-0.0315	-0.0283	-0.0190	-0.0222	0.0032
141.15	236	1.0751	0.9659	0.6485	0.7577	-0.1092
		-0.0170	-0.0140	-0.0062	0.0084	-0.0002
16	0.0322	-0.0352	-0.0276	-0.0361	-0.0300	0.0074
128.43	260	1.0932	0.8571	1.1211	0.9317	-0.2298
		-0.0190	-0.0120	-0.0200	0.0140	-0.0009

continued on next page

continued from previous page

Mode T [fs]	ω [eV] ω [cm^{-1}]	$\kappa_i^{(S1)}$ $\frac{-\kappa_i^{(S1)}}{\omega_i}$ $\frac{-\kappa_i^{(S1)2}}{2\omega_i}$	$\kappa_i^{(S2)}$ $\frac{-\kappa_i^{(S2)}}{\omega_i}$ $\frac{-\kappa_i^{(S2)2}}{2\omega_i}$	$\kappa_i^{(T1)}$ $\frac{-\kappa_i^{(T1)}}{\omega_i}$ $\frac{-\kappa_i^{(T1)2}}{2\omega_i}$	$\kappa_i^{(T2)}$ $\frac{-\kappa_i^{(T2)}}{\omega_i}$ $\frac{-\kappa_i^{(T2)2}}{2\omega_i}$	$\kappa_i^{(T3)}$ $\frac{-\kappa_i^{(T3)}}{\omega_i}$ $\frac{-\kappa_i^{(T3)2}}{2\omega_i}$
17	0.0455	-0.0138	-0.0006	-0.0215	-0.0149	-0.0248
90.89	367	0.3033	0.0132	0.4725	0.3275	0.5451
		-0.0021	0.0000	-0.0051	0.0024	0.0068
18	0.0527	-0.0038	-0.0039	-0.0029	-0.0012	-0.0028
78.47	425	0.0721	0.0740	0.0550	0.0228	0.0531
		-0.0001	-0.0001	-0.0001	0.0000	0.0001
20	0.0563	0.0027	0.0044	0.0030	0.0119	-0.0015
73.46	454	-0.0480	-0.0782	-0.0533	-0.2114	0.0266
		-0.0001	-0.0002	-0.0001	0.0013	0.0000
23	0.0602	-0.0221	-0.0277	-0.0214	-0.0305	-0.0063
68.7	486	0.3671	0.4601	0.3555	0.5066	0.1047
		-0.0041	-0.0064	-0.0038	0.0077	0.0003
26	0.067	0.0026	-0.0157	0.0030	-0.0180	-0.0070
61.73	540	-0.0388	0.2343	-0.0448	0.2687	0.1045
		-0.0001	-0.0018	-0.0001	0.0024	0.0004
30	0.0793	-0.0227	0.0448	-0.0214	0.0469	0.0035
52.15	640	0.2863	-0.5649	0.2699	-0.5914	-0.0441
		-0.0032	-0.0130	-0.0029	0.0140	-0.0001
32	0.0812	-0.0227	0.0044	-0.0167	0.0068	0.0108
50.93	655	0.2796	-0.0542	0.2057	-0.0837	-0.1330
		-0.0032	-0.0001	-0.0017	0.0003	-0.0007
34	0.0834	0.0103	-0.0130	0.0142	0.0004	0.0327
49.59	673	-0.1235	0.1559	-0.1703	-0.0048	-0.3921
		-0.0006	-0.0010	-0.0012	0.0000	-0.0064
35	0.093	-0.0003	-0.0002	-0.0001	-0.0002	0.0000
44.47	750	0.0032	0.0022	0.0011	0.0022	0.0000
		0.0000	0.0000	0.0000	0.0000	0.0000
37	0.0951	-0.0014	0.0022	-0.0037	0.0004	-0.0039
43.49	767	0.0147	-0.0231	0.0389	-0.0042	0.0410
		0.0000	0.0000	-0.0001	0.0000	0.0001

continued on next page

continued from previous page

Mode T [fs]	ω [eV] ω [cm^{-1}]	$\kappa_i^{(S1)}$ $\frac{-\kappa_i^{(S1)}}{\omega_i}$ $\frac{-\kappa_i^{(S1)2}}{2\omega_i}$	$\kappa_i^{(S2)}$ $\frac{-\kappa_i^{(S2)}}{\omega_i}$ $\frac{-\kappa_i^{(S2)2}}{2\omega_i}$	$\kappa_i^{(T1)}$ $\frac{-\kappa_i^{(T1)}}{\omega_i}$ $\frac{-\kappa_i^{(T1)2}}{2\omega_i}$	$\kappa_i^{(T2)}$ $\frac{-\kappa_i^{(T2)}}{\omega_i}$ $\frac{-\kappa_i^{(T2)2}}{2\omega_i}$	$\kappa_i^{(T3)}$ $\frac{-\kappa_i^{(T3)}}{\omega_i}$ $\frac{-\kappa_i^{(T3)2}}{2\omega_i}$
38	0.0969	0.0186	0.0089	0.0321	0.0159	0.0454
42.68	782	-0.1920	-0.0918	-0.3313	-0.1641	-0.4685
		-0.0018	-0.0004	-0.0053	0.0013	-0.0110
40	0.1122	0.0030	0.0003	0.0058	0.0024	-0.0016
36.86	905	-0.0267	-0.0027	-0.0517	-0.0214	0.0143
		0.0000	0.0000	-0.0002	0.0000	0.0000
42	0.1228	0.0013	-0.0014	0.0011	0.0001	0.0028
33.68	990	-0.0106	0.0114	-0.0090	-0.0008	-0.0228
		0.0000	0.0000	0.0000	0.0000	0.0000
45	0.1274	-0.0010	0.0002	-0.0007	0.0004	-0.0013
32.46	1028	0.0078	-0.0016	0.0055	-0.0031	0.0102
		0.0000	0.0000	0.0000	0.0000	0.0000
47	0.13	0.0872	0.0676	0.1016	0.0849	0.1197
31.81	1049	-0.6708	-0.5200	-0.7815	-0.6531	-0.9208
		-0.0290	-0.0180	-0.0400	0.0280	-0.0550
49	0.135	-0.0010	0.0065	0.0007	0.0057	0.0218
30.63	1089	0.0074	-0.0481	-0.0052	-0.0422	-0.1615
		0.0000	-0.0002	0.0000	0.0001	-0.0018
51	0.1402	0.0124	0.0072	0.0160	0.0135	0.0271
29.5	1131	-0.0884	-0.0514	-0.1141	-0.0963	-0.1933
		-0.0006	-0.0002	-0.0009	0.0007	-0.0026
54	0.1476	-0.0696	-0.0589	-0.0717	-0.0624	-0.0459
28.02	1191	0.4715	0.3991	0.4858	0.4228	0.3110
		-0.0160	-0.0120	-0.0170	0.0130	0.0071
56	0.1599	-0.0079	-0.0097	-0.0138	-0.0080	-0.0359
25.86	1290	0.0494	0.0607	0.0863	0.0500	0.2245
		-0.0002	-0.0003	-0.0006	0.0002	0.0040
57	0.1629	0.0613	0.0442	0.0552	0.0698	-0.0900
25.39	1314	-0.3763	-0.2713	-0.3389	-0.4285	0.5525
		-0.0120	-0.0060	-0.0094	0.0150	0.0250

continued on next page

continued from previous page

Mode T [fs]	ω [eV] ω [cm^{-1}]	$\kappa_i^{(S1)}$ $\frac{-\kappa_i^{(S1)}}{\omega_i}$ $\frac{-\kappa_i^{(S1)^2}}{2\omega_i}$	$\kappa_i^{(S2)}$ $\frac{-\kappa_i^{(S2)}}{\omega_i}$ $\frac{-\kappa_i^{(S2)^2}}{2\omega_i}$	$\kappa_i^{(T1)}$ $\frac{-\kappa_i^{(T1)}}{\omega_i}$ $\frac{-\kappa_i^{(T1)^2}}{2\omega_i}$	$\kappa_i^{(T2)}$ $\frac{-\kappa_i^{(T2)}}{\omega_i}$ $\frac{-\kappa_i^{(T2)^2}}{2\omega_i}$	$\kappa_i^{(T3)}$ $\frac{-\kappa_i^{(T3)}}{\omega_i}$ $\frac{-\kappa_i^{(T3)^2}}{2\omega_i}$
58	0.1656	0.1123	0.0990	0.1129	0.1040	0.1274
24.97	1336	-0.6781	-0.5978	-0.6818	-0.6280	-0.7693
		-0.0380	-0.0300	-0.0380	0.0330	-0.0490
60	0.1814	-0.0045	0.0003	-0.0075	-0.0110	0.0435
22.8	1463	0.0248	-0.0017	0.0413	0.0606	-0.2398
		-0.0001	0.0000	-0.0002	0.0003	-0.0052
63	0.1888	0.1666	0.1430	0.1744	0.1516	0.1542
21.9	1523	-0.8824	-0.7574	-0.9237	-0.8030	-0.8167
		-0.0740	-0.0540	-0.0810	0.0610	-0.0630
64	0.1986	-0.1180	-0.1058	-0.1253	-0.1043	-0.1179
20.82	1602	0.5942	0.5327	0.6309	0.5252	0.5937
		-0.0350	-0.0280	-0.0400	0.0270	0.0350
66	0.203	0.0318	0.0353	0.0340	0.0071	0.2099
20.31	1637	-0.1567	-0.1739	-0.1675	-0.0350	-1.0340
		-0.0025	-0.0031	-0.0028	0.0001	-0.1100
68	0.2326	0.0381	0.0329	0.0360	0.0377	0.0078
17.78	1876	-0.1638	-0.1414	-0.1548	-0.1621	-0.0335
		-0.0031	-0.0023	-0.0028	0.0031	-0.0001
70	0.2532	-0.1044	-0.0865	-0.0897	-0.0944	0.0003
16.33	2042	0.4123	0.3416	0.3543	0.3728	-0.0012
		-0.0220	-0.0150	-0.0160	0.0180	0.0000

Table B.5: Extracted parameters for a' normal modes of [Re(Cl)(CO)$_3$(bpy)] : the intrastate coupling κ_i (eV), the induced displacement $-\frac{\kappa_i^{(n)}}{\omega_i}$ (dimensionless) and the induced shift in energy $-\frac{\kappa_i^{(n)^2}}{2\omega_i}$ (in eV). The period (in fs) and the frequency (in eV and cm^{-1}) are shown for each normal mode.

NORMAL MODE PARAMETERS EXTRACTED FROM ELECTRONIC STRUCTURE OF $[Re(X)(CO)_3(bpy)]$

Mode T [fs]	ω [eV] ω [cm^{-1}]	$\lambda^{(S1),(S2)}$ [eV]	$\lambda^{(T1),(T2)}$ [eV]
1	0.0035	0.0000	0.0090
1181.60	28		
3	0.0098	0.0019	0.0079
492.33	68		
5	0.0105	0.0073	0.0064
393.87	85		
7	0.0118	0.0157	0.0127
350.47	95		
10	0.0134	0.0127	0.0156
308.63	108		
13	0.0255	0.0063	0.0190
162.18	206		
15	0.0318	0.0000	0.0109
130.05	256		
19	0.0533	0.0082	0.0081
77.59	430		
21	0.0574	0.0180	0.0278
72.05	463		
22	0.0600	0.0239	0.0182
68.93	484		
25	0.0640	0.0195	0.0130
64.62	516		
27	0.0675	0.0099	0.0077
61.27	544		
28	0.0690	0.0000	0.0079
59.94	557		
29	0.0789	0.0353	0.0246
52.42	636		

continued on next page

continued from previous page

Mode T [fs]	ω [eV] ω [cm^{-1}]	$\lambda^{(S1),(S2)}$ [eV]	$\lambda^{(T1),(T2)}$ [eV]
31	0.0811	0.0088	0.0033
50.99	654		
33	0.0822	0.0000	0.0029
50.31	663		
36	0.0930	0.0051	0.0000
44.47	750		
39	0.1017	0.0000	0.0000
40.66	820		
41	0.1124	0.0047	0.0058
36.86	907		
43	0.1228	0.0064	0.0038
33.68	990		
44	0.1271	0.0064	0.0026
32.54	1025		
46	0.1285	0.0000	0.0240
32.18	1036		
48	0.1322	0.0033	0.0019
31.28	1066		
50	0.1359	0.0000	0.0077
30.43	1096		
52	0.1419	0.0020	0.0034
29.14	1145		
53	0.1459	0.0000	0.0067
28.35	1177		
55	0.1583	0.0000	0.0000
26.13	1277		
59	0.1669	0.0000	0.0052
24.78	1336		
61	0.1831	0.0000	0.0000
22.59	1477		

continued on next page

continued from previous page

Mode T [fs]	ω [eV] ω [cm^{-1}]	$\lambda^{(S1),(S2)}$ [eV]	$\lambda^{(T1),(T2)}$ [eV]
62	0.1871	0.0000	0.0139
22.10	1509		
65	0.1997	0.0000	0.0159
20.71	1611		
67	0.2042	0.0000	0.0245
20.25	1647		
69	0.2349	0.0299	0.0195
17.61	1895		

Table B.6: Extracted interstate vibronic coupling $\lambda_i^{(n),(m)}$ (in eV) for a" normal modes of [Re(Cl)(CO)$_3$(bpy)]. The period (in fs) and the frequency (in eV and cm^{-1}) are shown for each normal mode.

[Re(I)(CO)$_3$(bpy)]

Mode T [fs]	ω [eV] ω [cm^{-1}]	$\kappa_i^{(S1)}$ $\frac{-\kappa_i^{(S1)}}{\omega_i}$ $\frac{-\kappa_i^{(S1)^2}}{2\omega_i}$	$\kappa_i^{(S2)}$ $\frac{-\kappa_i^{(S2)}}{\omega_i}$ $\frac{-\kappa_i^{(S2)^2}}{2\omega_i}$	$\kappa_i^{(T1)}$ $\frac{-\kappa_i^{(T1)}}{\omega_i}$ $\frac{-\kappa_i^{(T1)^2}}{2\omega_i}$	$\kappa_i^{(T2)}$ $\frac{-\kappa_i^{(T2)}}{\omega_i}$ $\frac{-\kappa_i^{(T2)^2}}{2\omega_i}$	$\kappa_i^{(T3)}$ $\frac{-\kappa_i^{(T3)}}{\omega_i}$ $\frac{-\kappa_i^{(T3)^2}}{2\omega_i}$
2	0.0044	0.0171	0.0261	0.0186	0.0219	0.0033
939.91	35	-3.8864	-5.9318	-4.2273	-4.9773	-0.7500
		-0.0330	-0.0770	0.0390	-0.0550	0.0012
4	0.0079	0.0045	0.0128	0.0048	0.0250	0.0032
523.49	64	-0.5696	-1.6203	-0.6076	-3.1646	-0.4051
		-0.0013	-0.0100	0.0015	-0.0400	0.0007
6	0.01	-0.0069	0.0025	-0.0045	0.0015	-0.0037
413.56	81	0.6900	-0.2500	0.4500	-0.1500	0.3700
		-0.0024	-0.0003	0.0010	-0.0001	-0.0007
7	0.0115	0.0095	-0.0154	0.0108	-0.0163	-0.0035
359.62	93	-0.8261	1.3391	-0.9391	1.4174	0.3043
		-0.0039	-0.0100	0.0051	-0.0120	-0.0005
9	0.0121	-0.0033	0.0071	-0.0025	0.0075	-0.0031
341.79	98	0.2727	-0.5868	0.2066	-0.6198	0.2562
		-0.0005	-0.0021	0.0003	-0.0023	-0.0004
11	0.0155	-0.0058	-0.0040	-0.0009	-0.0005	0.0029
266.81	125	0.3742	0.2581	0.0581	0.0323	-0.1871
		-0.0011	-0.0005	0.0000	0.0000	0.0003
12	0.0216	0.0135	0.0044	0.0175	0.0136	-0.0132
191.46	174	-0.6250	-0.2037	-0.8102	-0.6296	0.6111
		-0.0042	-0.0005	0.0071	-0.0043	-0.0040
13	0.0226	0.0202	0.0186	0.0211	0.0250	-0.0170
182.99	182	-0.8938	-0.8230	-0.9336	-1.1062	0.7522
		-0.0090	-0.0077	0.0098	-0.0140	-0.0064
16	0.0321	0.0198	0.0127	0.0236	0.0174	-0.0017
128.83	259	-0.6168	-0.3956	-0.7352	-0.5421	0.0530

continued on next page

continued from previous page

Mode T [fs]	ω [eV] ω [cm^{-1}]	$\kappa_i^{(S1)}$ $\frac{-\kappa_i^{(S1)}}{\omega_i}$ $\frac{-\kappa_i^{(S1)2}}{2\omega_i}$	$\kappa_i^{(S2)}$ $\frac{-\kappa_i^{(S2)}}{\omega_i}$ $\frac{-\kappa_i^{(S2)2}}{2\omega_i}$	$\kappa_i^{(T1)}$ $\frac{-\kappa_i^{(T1)}}{\omega_i}$ $\frac{-\kappa_i^{(T1)2}}{2\omega_i}$	$\kappa_i^{(T2)}$ $\frac{-\kappa_i^{(T2)}}{\omega_i}$ $\frac{-\kappa_i^{(T2)2}}{2\omega_i}$	$\kappa_i^{(T3)}$ $\frac{-\kappa_i^{(T3)}}{\omega_i}$ $\frac{-\kappa_i^{(T3)2}}{2\omega_i}$
		-0.0061	-0.0025	0.0087	-0.0047	0.0000
17	0.0456	0.0065	-0.0021	0.0131	0.0088	0.0259
90.69	368	-0.1425	0.0461	-0.2873	-0.1930	-0.5680
		-0.0005	0.0000	0.0019	-0.0009	0.0074
18	0.0529	-0.0003	0.0023	-0.0002	0.0009	-0.0001
78.18	427	0.0057	-0.0435	0.0038	-0.0170	0.0019
		0.0000	-0.0001	0.0000	0.0000	0.0000
20	0.0562	-0.0051	-0.0042	-0.0052	-0.0137	0.0011
73.59	453	0.0907	0.0747	0.0925	0.2438	-0.0196
		-0.0002	-0.0002	0.0002	-0.0017	0.0000
22	0.0599	-0.0104	-0.0154	-0.0104	-0.0171	-0.0070
69.04	483	0.1736	0.2571	0.1736	0.2855	0.1169
		-0.0009	-0.0020	0.0009	-0.0024	-0.0004
24	0.063	0.0477	0.0323	0.0524	0.0448	0.0008
65.64	508	-0.7571	-0.5127	-0.8317	-0.7111	-0.0127
		-0.0180	-0.0083	0.0220	-0.0160	0.0000
26	0.0661	0.0027	0.0202	0.0016	0.0259	0.0092
62.57	533	-0.0408	-0.3056	-0.0242	-0.3918	-0.1392
		-0.0001	-0.0031	0.0000	-0.0051	0.0006
30	0.0787	0.0054	-0.0315	0.0095	-0.0358	-0.0036
52.55	635	-0.0686	0.4003	-0.1207	0.4549	0.0457
		-0.0002	-0.0063	0.0006	-0.0081	-0.0001
31	0.0808	0.0198	-0.0071	0.0181	-0.0096	-0.0120
51.18	652	-0.2450	0.0879	-0.2240	0.1188	0.1485
		-0.0024	-0.0003	0.0020	-0.0006	-0.0009
33	0.0823	-0.0005	0.0000	-0.0007	-0.0002	-0.0011
50.25	664	0.0061	0.0000	0.0085	0.0024	0.0134
		0.0000	0.0000	0.0000	0.0000	0.0000
36	0.0933	-0.0063	-0.0126	-0.0054	-0.0064	-0.0082
44.33	753	0.0675	0.1350	0.0579	0.0686	0.0879

continued on next page

continued from previous page

Mode T [fs]	ω [eV] ω [cm^{-1}]	$\kappa_i^{(S1)}$ $\frac{-\kappa_i^{(S1)}}{\omega_i}$ $\frac{-\kappa_i^{(S1)2}}{2\omega_i}$	$\kappa_i^{(S2)}$ $\frac{-\kappa_i^{(S2)}}{\omega_i}$ $\frac{-\kappa_i^{(S2)2}}{2\omega_i}$	$\kappa_i^{(T1)}$ $\frac{-\kappa_i^{(T1)}}{\omega_i}$ $\frac{-\kappa_i^{(T1)2}}{2\omega_i}$	$\kappa_i^{(T2)}$ $\frac{-\kappa_i^{(T2)}}{\omega_i}$ $\frac{-\kappa_i^{(T2)2}}{2\omega_i}$	$\kappa_i^{(T3)}$ $\frac{-\kappa_i^{(T3)}}{\omega_i}$ $\frac{-\kappa_i^{(T3)2}}{2\omega_i}$
		-0.0002	-0.0009	0.0002	-0.0002	-0.0004
37	0.0952	-0.0060	-0.0088	-0.0030	-0.0068	0.0012
43.44	768	0.0630	0.0924	0.0315	0.0714	-0.0126
		-0.0002	-0.0004	0.0000	-0.0002	0.0000
38	0.097	-0.0175	-0.0115	-0.0248	-0.0163	-0.0565
42.64	782	0.1804	0.1186	0.2557	0.1680	0.5825
		-0.0016	-0.0007	0.0032	-0.0014	-0.0160
40	0.1122	0.0006	0.0004	0.0022	0.0010	-0.0019
36.86	905	-0.0053	-0.0036	-0.0196	-0.0089	0.0169
		0.0000	0.0000	0.0000	0.0000	0.0000
42	0.1227	-0.0013	-0.0026	-0.0009	-0.0015	0.0017
33.7	990	0.0106	0.0212	0.0073	0.0122	-0.0139
		0.0000	0.0000	0.0000	0.0000	0.0000
45	0.1276	0.0006	-0.0004	0.0006	0.0000	0.0020
32.41	1029	-0.0047	0.0031	-0.0047	0.0000	-0.0157
		0.0000	0.0000	0.0000	0.0000	0.0000
47	0.1299	-0.0823	-0.0693	-0.0902	-0.0810	-0.1276
31.84	1048	0.6336	0.5335	0.6944	0.6236	0.9823
		-0.0260	-0.0180	0.0310	-0.0250	-0.0630
49	0.135	-0.0020	-0.0070	-0.0017	-0.0057	-0.0191
30.63	1089	0.0148	0.0519	0.0126	0.0422	0.1415
		0.0000	-0.0002	0.0000	-0.0001	-0.0014
51	0.1402	-0.0103	-0.0074	-0.0127	-0.0118	-0.0251
29.5	1131	0.0735	0.0528	0.0906	0.0842	0.1790
		-0.0004	-0.0002	0.0006	-0.0005	-0.0022
54	0.1477	0.0662	0.0591	0.0671	0.0614	0.0545
28	1191	-0.4482	-0.4001	-0.4543	-0.4157	-0.3690
		-0.0150	-0.0120	0.0150	-0.0130	0.0100
56	0.1599	0.0001	0.0042	0.0023	0.0010	0.0449
25.86	1290	-0.0006	-0.0263	-0.0144	-0.0063	-0.2808

continued on next page

continued from previous page

Mode T [fs]	ω [eV] ω [cm^{-1}]	$\kappa_i^{(S1)}$ $\frac{-\kappa_i^{(S1)}}{\omega_i}$ $\frac{-\kappa_i^{(S1)^2}}{2\omega_i}$	$\kappa_i^{(S2)}$ $\frac{-\kappa_i^{(S2)}}{\omega_i}$ $\frac{-\kappa_i^{(S2)^2}}{2\omega_i}$	$\kappa_i^{(T1)}$ $\frac{-\kappa_i^{(T1)}}{\omega_i}$ $\frac{-\kappa_i^{(T1)^2}}{2\omega_i}$	$\kappa_i^{(T2)}$ $\frac{-\kappa_i^{(T2)}}{\omega_i}$ $\frac{-\kappa_i^{(T2)^2}}{2\omega_i}$	$\kappa_i^{(T3)}$ $\frac{-\kappa_i^{(T3)}}{\omega_i}$ $\frac{-\kappa_i^{(T3)^2}}{2\omega_i}$
		0.0000	-0.0001	0.0000	0.0000	0.0063
57	0.1629	-0.0606	-0.0479	-0.0615	-0.0655	0.0764
25.39	1314	0.3720	0.2940	0.3775	0.4021	-0.4690
		-0.0110	-0.0070	0.0120	-0.0130	0.0180
58	0.1656	-0.1027	-0.0949	-0.1024	-0.0970	-0.1306
24.97	1336	0.6202	0.5731	0.6184	0.5857	0.7886
		-0.0320	-0.0270	0.0320	-0.0280	-0.0510
60	0.1817	-0.0022	-0.0043	0.0004	0.0026	-0.0422
22.76	1466	0.0121	0.0237	-0.0022	-0.0143	0.2323
		0.0000	-0.0001	0.0000	0.0000	-0.0049
63	0.1889	-0.1566	-0.1421	-0.1588	-0.1467	-0.1696
21.89	1524	0.8290	0.7522	0.8407	0.7766	0.8978
		-0.0650	-0.0530	0.0670	-0.0570	-0.0760
64	0.1985	0.1121	0.1038	0.1132	0.1024	0.1308
20.83	1601	-0.5647	-0.5229	-0.5703	-0.5159	-0.6589
		-0.0320	-0.0270	0.0320	-0.0260	0.0430
66	0.2031	-0.0340	-0.0363	-0.0308	-0.0184	-0.2029
20.36	1638	0.1674	0.1787	0.1516	0.0906	0.9990
		-0.0028	-0.0032	0.0023	-0.0008	-0.1000
68	0.2334	-0.0421	-0.0403	-0.0406	-0.0416	-0.0079
17.72	1883	0.1804	0.1727	0.1740	0.1782	0.0338
		-0.0038	-0.0035	0.0035	-0.0037	-0.0001
70	0.253	0.0655	0.0464	0.0659	0.0599	-0.0093
16.35	2041	-0.2589	-0.1834	-0.2605	-0.2368	0.0368
		-0.0085	-0.0043	0.0086	-0.0071	-0.0002

Table B.7: Extracted parameters for a' normal modes of [Re(I)(CO)$_3$(bpy)] : the intrastate coupling κ_i (eV), the induced displacement $-\frac{\kappa_i^{(n)}}{\omega_i}$ (dimensionless) and the induced shift in energy $-\frac{\kappa_i^{(n)^2}}{2\omega_i}$ (in eV). The period (in fs) and the frequency (in eV and cm^{-1}) are shown for each normal mode.

NORMAL MODE PARAMETERS EXTRACTED FROM ELECTRONIC STRUCTURE OF $[Re(X)(CO)_3(bpy)]$

Mode T [fs]	ω [eV] ω [cm^{-1}]	$\lambda^{(S1),(S2)}$ [eV]	$\lambda^{(T1),(T2)}$ [eV]
1	0.0033	0.0072	0.0096
1253.21	27		
3	0.0067	0.0075	0.0072
617.25	54		
5	0.0099	0.0000	0.0023
417.74	80		
8	0.0116	0.0074	0.0057
356.52	94		
10	0.0126	0.0123	0.0126
341.79	102		
14	0.0255	0.0028	0.0115
162.18	206		
15	0.0317	0.0060	0.0116
130.46	256		
19	0.0534	0.0067	0.0089
77.45	431		
21	0.0577	0.0120	0.0188
71.67	465		
23	0.0603	0.0188	0.0165
68.58	486		
25	0.0633	0.0126	0.0085
65.33	511		
27	0.0674	0.0068	0.0044
61.36	544		
28	0.0693	0.0000	0.0031
59.68	559		
29	0.0776	0.0217	0.0161
53.29	626		

continued on next page

continued from previous page

Mode T [fs]	ω [eV] ω [cm^{-1}]	$\lambda^{(S1),(S2)}$ [eV]	$\lambda^{(T1),(T2)}$ [eV]
32	0.0811	0.0066	0.0009
50.99	654		
34	0.0834	0.0029	0.0013
49.59	673		
35	0.0929	0.0029	0.0032
44.52	749		
39	0.1020	0.0028	0.0000
40.55	823		
41	0.1131	0.0027	0.0024
36.57	912		
43	0.1249	0.0052	0.0022
33.11	1007		
44	0.1272	0.0038	0.0014
32.51	1026		
46	0.1284	0.0000	0.0131
32.21	1036		
48	0.1322	0.0035	0.0016
31.28	1066		
50	0.1360	0.0037	30.4100
30.41	1097		
52	0.1420	0.0019	0.0019
29.13	1145		
53	0.1458	0.0000	0.0043
28.35	1177		
55	0.1583	0.0000	0.0037
26.13	1277		
59	0.1674	0.0000	0.0037
24.7	1350		
61	0.1831	0.0005	0.0000
22.59	1477		

continued on next page

continued from previous page

Mode T [fs]	ω [eV] ω [cm^{-1}]	$\lambda^{(S1),(S2)}$ [eV]	$\lambda^{(T1),(T2)}$ [eV]
62	0.1873	0.0000	0.0077
22.08	1511		
65	0.1997	0.0000	0.0089
20.71	1611		
67	0.2043	0.0000	0.0138
20.24	1648		
69	0.2352	0.0192	0.0152
17.58	1897		

Table B.8: Extracted interstate vibronic coupling $\lambda_i^{(n),(m)}$ (in eV) for a" normal modes of [Re(I)(CO)$_3$(bpy)]. The period (in fs) and the frequency (in eV and cm^{-1}) are shown for each normal mode.

B.2 Parameters of the topology of [Re(X)(CO)$_3$(bpy)] PESs

	F		Cl		Br		I	
	S1/S2	T1/T2	S1/S2	T1/T2	S1/S2	T1/T2	S1/S2	T1/T2
L > D	T	T	T	T	T	T	F	T
$\left\lvert\frac{\Delta-\mathrm{F}}{\mathrm{L}-\mathrm{D}}\right\rvert$	F	T	F	T	F	T	F	F
E_s [eV]	7.1×10^{-3}	2.7×10^{-3}	4.5×10^{-1}	1.2×10^{-5}	2.1×10^{-1}	2.0×10^{-3}	5.6×10^{-1}	1.4×10^{-3}

Table B.9: Energetic conditions for a breaking of symmetry for [Re(X)(CO)$_3$(bpy)] (X=F, Cl, Br, I). The energy stabilization is given in eV. (see EQ. (6.37) and (6.38))

	F		Cl		Br		I	
	S1/S2	T1/T2	S1/S2	T1/T2	S1/S2	T1/T2	S1/S2	T1/T2
$V^{g}_{\mathrm{min}}{}^{\mathrm{CI}}$ [eV]	2.66	2.47	2.89	2.6	2.8	2.54	2.61	2.4
Q_0^{CI}	1.78×10^{-3}	1.51×10^{-3}	5.00×10^{-3}	2.88×10^{-3}	4.15×10^{-3}	2.23×10^{-3}	2.73×10^{-3}	2.01×10^{-3}
$V^{\mathrm{CI}}_{\mathrm{min}} - V_{2\mathrm{min}}$	1.02×10^{-3}	6.12×10^{-3}	1.85×10^{-2}	1.76×10^{-3}	7.8×10^{-3}	6.62×10^{-3}	2.66×10^{-3}	1.82×10^{-3}

Table B.10: Characterization of the CI between S1/S2 and T1/T2 for [Re(X)(CO)$_3$(bpy)] (X=F, Cl, Br, I). (see SECTION 6.2.1.1.3 for definition)

APPENDIX C

PUBLISHED PAPERS

C.1 Quantum Chemical Interpretation of Ultrafast Luminescence Decay and Intersystem Crossings in Rhenium(I) Carbonyl Bipyridine Complexes

JCTC Journal of Chemical Theory and Computation

Article

pubs.acs.org/JCTC

Quantum Chemical Interpretation of Ultrafast Luminescence Decay and Intersystem Crossings in Rhenium(I) Carbonyl Bipyridine Complexes

Christophe Gourlaouen, Julien Eng, Miho Otsuka, Etienne Gindensperger, and Chantal Daniel*

Laboratoire de Chimie Quantique, Institut de Chimie de Strasbourg UMR-7177 CNRS-UdS, 1 Rue Blaise Pascal BP 296/R8, F-67008 Strasbourg Cedex, France

Supporting Information

ABSTRACT: Ultrafast luminescence decay and intersystem crossing processes through the seven low-lying singlet and triplet excited states of [Re (X)$(CO)_3$(bpy)] (X = Cl, Br, I; bpy = 2,2′-bipyridine) are interpreted on the basis of time-dependent density functional theory (TD-DFT) electronic structure calculations performed in acetonitrile and including spin−orbit coupling (SOC) effects within the zeroth-order approximation. It is shown that the red shift of the lowest part of the spectra by SOC increases from X = Cl (0.06 eV) to X = Br (0.09 eV) and X = I (0.18 eV) due to the participation of the triplet sublevels to the absorption. The six lowest "spin−orbit" states remain largely triplet in character and the maximum of absorption is not drastically affected by SOC. While the energy of the excited states is affected by SOC, the character of these states is not significantly modified: SOC mixes states of the same nature, namely metal-to-ligand-charge-transfer/halide-to-ligand-charge-transfer (MLCT/XLCT). This mixing can be large, however, as illustrated by the S_1/T_2 (a^1A''/a^3A') mixing that amounts to about 50:50 within the series Cl > Br > I. On the basis of the optimized structures of the six lowest excited states an interpretation of the emission signals detected by ultrafast luminescence spectroscopy is proposed. It is shown that whereas the experimental Stokes shift of 6000 cm^{-1} observed for the three complexes is well reproduced without SOC correction for the Cl and Br complexes, SOC effects have to be taken into account for the iodide complex. The early signal of ultrafast luminescence detected immediately after absorption at 400 nm to the S_2 state, covering the 500−550 nm energy domain and characterized by a decay τ_1 = 85 fs (X = Cl) and 128 fs (X = Br), is attributed to S_2 calculated at 505 and 522 nm, respectively, and to some extend to T_3 by SOC. The intermediate band observed at longer time-scale between 550 and 600 nm with emissive decay time τ_2 = 340 fs (X = Cl) and 470 fs (X = Br) can be assigned to T_2 calculated at 558 and 571 nm, respectively. The S_1 state could also participate to this band by SOC. In both complexes the long-lived emission at 600−610 nm is attributed to the lowest T_1 state calculated at 596 and 592 nm for the chloride and bromide complexes, respectively, and shifted to ∼610 nm by SOC. Important SOC effects characterize the luminescence decay of [Re (I)$(CO)_3$(bpy)], the mechanism of which differs significantly of the one proposed for the two other complexes. The A′ spin−orbit sublevel of T_3 state calculated at 512 nm with an oscillator strength of 0.17×10^{-1} participates to the first signal characterized by a rapid decay (τ_1 = 152 fs) with a maximum at 525 nm. The intermediate band covering the 550−600 nm region with a decay time τ_2 = 1180 fs is assigned to the "spin−orbit" S_1 state calculated at 595 nm. The S_2 absorbing state calculated at 577 nm could contribute to these two signals. According to the spin−orbit sublevels calculated for T_1 and T_2, both states contribute to the long-lived emission detected at 600−610 nm, T_1 with two sublevels A′ of significant oscillator strengths of $\sim 10^{-1}$ being the main contributor. In order to follow the evolution of the excited states energy and SOC as a function of the Re−X stretching normal mode their potentials have been calculated without and with SOC as a function of the mass and frequency weighted Re−X stretching mode displacement from the Franck−Condon geometries. Exploratory wavepacket propagations show that SOC alone cannot account for the whole ISC process. Vibronic effects should play an important role in the ultrafast luminescence decay observed experimentally.

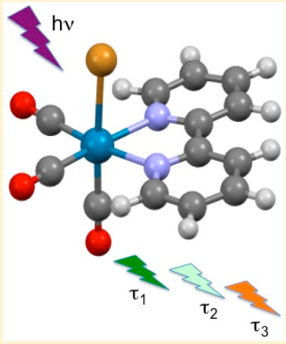

1. INTRODUCTION

The interpretation of ultrafast intersystem crossing (ISC) processes observed in transition metal complexes[1−11] by means of femtosecond luminescence experiments is very challenging for quantum chemistry. It appears that considering spin−orbit coupling (SOC) explicitly is essential to get a correct understanding of these photophysical phenomena. Whereas the use of four-component relativistic approaches is very demanding for electronic excited states calculations in molecules,[12] two component/two-step methods offer a promising option based either on wave function or on density functional theory.[13,14]

Only a few theoretical studies have been dedicated to ISC processes in transition metal complexes. The first detailed investigations of the dynamics of singlet to triplet transitions

Received: September 21, 2014
Published: December 2, 2014

dx.doi.org/10.1021/ct500846n | J. Chem. Theory Comput. 2015, 11, 99−110

have been performed to understand the photochemical reactivity of HCo $(CO)_4$[15] and HM $(CO)_3(\alpha$-diimine) (M = Mn, Re) molecules,[16−18] that undergo concurrent primary photoreactions whose branching ratio is controlled by ISC from the absorbing state to the reactive states.

More recently, review articles have discussed possible consequences of SOC on the electronic structure, excited state characters, and their deactivation pathways, and demonstrated relations between SOC, the metal-to-ligand-charge-transfer (MLCT) character of the lowest "triplet" state, its zero-field splitting and photoluminescence, that are of paramount importance for OLED applications.[19,20] Spin−orbit calculations of electronic absorption spectra consistently point to large densities of low-lying spin−orbit states and extensive singlet−triplet mixing making void the notion of pure singlet and triplet electronic states.[14,21,22]

Up to now, three types of dynamical simulations, far from being routine, have needed specific developments to be applicable to transition metal complexes and ultrafast phenomena circumscribed by spin-vibronic coupling.

(i) A recent approach, applied to the spin crossover complex $[Fe(bpy)_3]^{2+}$,[10,23,24] is based on time-dependent calculations of ISC rates in the multimode harmonic oscillator and Condon approximations and beyond, where the electronic spin−orbit matrix elements depend linearly on the nuclear coordinates within a spin-vibronic coupling scheme. The ISC rate can be decomposed into three contributions, namely direct, mixed direct vibronic, and vibronic.[25,26]

(ii) The first simulation based on TD-DFT energies and forces (gradient and Hessian) computed on-the-fly and introducing both vibronic and SO coupling effects into the Tully's trajectory surface hopping algorithm has been able to reproduce semiquantitatively the ultrafast relaxation of the photo excited ^{1}MLCT state of $[Ru(bpy)_3]^{2+}$ (bpy = 2,2′-bipyridine) followed by ISC to the lowest ^{3}MLCT state.[27]

(iii) Combined effects of Jahn−Teller (JT) and SOC on the adiabatic PES and electronic spectra of a series of first-row transition metal halides MF_3 (M = Mn, Co, Ti, Cr, and Ni) have been recently investigated from first-principles methods based on the derivation of an Hamiltonian expanded up to linear, quadratic, and higher order in normal modes displacements active for JT distortions and including SOC up to first order in these modes.[28,29] This original work has put in evidence SO induced JT distortions not detectable by the standard model in which SOC is considered as a static property independent of the nuclear motion.

The photophyics of rhenium(I) tricarbonyl complexes $[Re(X)(CO)_3(\alpha$-diimine)] (X = Cl, Br, I), recently investigated by means of ultrafast luminescence spectroscopy,[30] is still the subject of unresolved questions related to SOC. Indeed, two or three ultrafast steps follow optical excitation of their lowest allowed $Re(X)(CO)_3 \rightarrow$ diimine CT transition, the fastest one having been attributed to the $^1CT \rightarrow {}^3CT$ intersystem crossing (ISC). In the halide series, singlet excited-state lifetime counterintuitively increases on going from the chloride (85 fs) to the bromide (128 fs) and iodide (152 fs), whereas SOC between the singlet and triplet states increases in the order Cl < Br ≪ I due to an increase of both the admixture of the halide character to the excited states in question and the halide SOC constant by itself. Moreover, a correlation has been observed between the ISC kinetics and vibrational period of the Re−X stretching mode in similar complexes. In a recent study combining spectroscopic measurements and CASSCF/MS-CASPT2 and TD-DFT calculations, we have shown that whereas both spin-free and spin−orbit quantum chemical calculations simulate UV−vis electronic spectra of $[Re(X)(CO)_3(\alpha$-diimine)] (X = Cl, Br, I) complexes in a reasonable agreement with experiment, they give a very different interpretation of the absorption bands and only the SO treatment can account for the observed spectral features.[14]

The goal of the present study is to go further in our understanding of ultrafast ISC in this class of molecules on the basis of the spin−orbit coupled potential energy curves (PEC) calculated as a function of the Re−X bond stretching mode, for the electronic ground state and the lowest S_1, S_2, S_3, T_1, T_2, T_3, and T_4 excited states of $[Re(X)(CO)_3(bpy)]$ (X = Cl, Br, I; bpy = 2,2′-bipyridine) taking into account solvent effects. The choice of the method has been motivated by the theoretical results of our previous study that has put in evidence the importance of solvent effects in SO-DFT calculations and the limitation of SO-MS-CASPT2 due to restricted active-space size.[14] Moreover the geometries of the lowest six excited states were fully optimized in order to interpret on a static basis the emissive properties of the molecules. Our objective is to provide a comprehensive mechanism of deactivation of the electronic excited states leading to the time-resolved luminescence spectra observed in CH_3CN after irradiation at 400 nm[30] on the basis of a unified picture of the absorption/emission spectroscopy of the three complexes. The computation and analysis of PEC and SOC as a function of the Re−X stretching mode, prior to one-dimensional exploratory wave-packet propagations, should enable us to discuss the measured correlation between the ISC kinetics with the vibrational period of this mode in similar complexes.[30]

2. COMPUTATIONAL DETAILS

The structures of $[Re(X)(CO)_3(bpy)]$ (X = Cl, Br, I) (Figure 1) in the S_0 (a^1A') electronic ground state, the lowest S_1 (a^1A''),

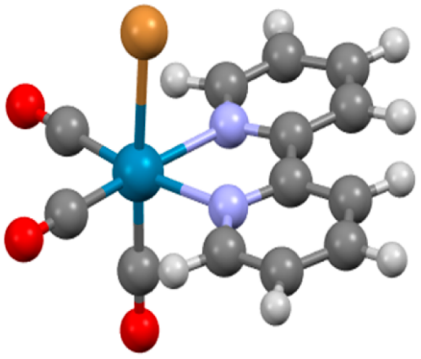

Figure 1. General structure of $[Re(X)(CO)_3(bpy)]$ (**1**: X = Cl; **2**: X = Br; **3**: X = I) complexes.

S_2 (b^1A') and S_3(c^1A') singlet excited states and the T_1 (a^3A''), T_2 (a^3A'), T_3 (b^3A''), and T_4 (b^3A') triplet excited states are optimized under the C_s symmetry constraint at the density functional theory (DFT) level, within the time-dependent approach (TD-DFT) for excited states, using the functional B3LYP[31,32] with all electrons and triple-ζ polarized basis sets.[33]

dx.doi.org/10.1021/ct500846n | J. Chem. Theory Comput. 2015, 11, 99−110

Table 1. TD-DFT Low-Lying Singlet and Triplet States of $[Re(Cl)(CO)_3(bpy)]$ 1, $[Re(Br)(CO)_3(bpy)]$ 2, and $[Re(I)(CO)_3(bpy)]$ 3

	state	assignment	vertical $S_0 \rightarrow S_n$, T_n transition energy (in eV and cm^{-1})	absorption wavelength (in nm)	oscillator strength f
X = Cl **1**					
	T_1 a^3A'' MLCT/XLCT	53% d_{yz} 15% $p_z(Cl) \rightarrow \pi^*_{bpy}$	2.86 (22 880)		
	T_2 a^3A' MLCT/XLCT	49% d_{xy} 17% $p_x(Cl) \rightarrow \pi^*_{bpy}$	2.97 (23 760)		
	S_1 a^1A'' MLCT/XLCT	53% d_{yz} 15% $p_z(Cl) \rightarrow \pi^*_{bpy}$	2.99 (23 920)	418	0.0021
	S_2 b^1A' MLCT/XLCT	49% d_{xy} 17% $p_x(Cl) \rightarrow \pi^*_{bpy}$	3.18 (25 440)	393	0.059
	T_3 b^3A'' IL	81% $\pi_{bpy} \rightarrow \pi^*_{bpy}$	3.23 (25 840)		
	T_4 b^3A' MLCT	63% $d_{Re} \rightarrow \pi^*_{bpy}$	3.34 (26 720)		
	S_3 c^1A' MLCT	98% $d_{Re} \rightarrow \pi^*_{bpy}$	3.38 (27 040)	370	0.0016
X = Br **2**					
	T_1 a^3A'' MLCT/XLCT	47% d_{yz} 25% $p_z(Br) \rightarrow \pi^*_{bpy}$	2.84 (22 720)		
	T_2 a^3A' MLCT/XLCT	42% d_{xy} 28% $p_x(Br) \rightarrow \pi^*_{bpy}$	2.93 (23 440)		
	S_1 a^1A'' MLCT/XLCT	47% d_{yz} 25% $p_z(Br) \rightarrow \pi^*_{bpy}$	2.96 (23 680)	422	0.0017
	S_2 b^1A' MLCT/XLCT	42% d_{xy} 28% $p_x(Br) \rightarrow \pi^*_{bpy}$	3.13 (25 040)	399	0.051
	T_3 b^3A'' IL	81% $\pi_{bpy} \rightarrow \pi^*_{bpy}$	3.22 (25 760)		
	T_4 b^3A' MLCT	63% $d_{Re} \rightarrow \pi^*_{bpy}$	3.34 (26 720)		
	S_3 c^1A' MLCT	98% $d_{Re} \rightarrow \pi^*_{bpy}$	3.37 (26 960)	371	0.0009
X = I **3**					
	T_1 a^3A'' XLCT/MLCT	51% $p_z(I)$ 30% $d_{yz} \rightarrow \pi^*_{bpy}$	2.76 (22 080)		
	T_2 a^3A' XLCT/MLCT	56% $p_x(I)$ 26% $d_{xy} \rightarrow \pi^*_{bpy}$	2.81 (22 480)		
	S_1 a^1A'' XLCT/MLCT	51% $p_z(I)$ 30% $d_{yz} \rightarrow \pi^*_{bpy}$	2.85 (22 800)	438	0.0008
	S_2 b^1A' XLCT/MLCT	56% $p_x(I)$ 26% $d_{xy} \rightarrow \pi^*_{bpy}$	2.95 (23 600)	424	0.029
	T_3 b^3A'' IL/XLCT/MLCT	67% π_{bpy}7% $p_z(I)$5% $d_{yz} \rightarrow \pi^*_{bpy}$	3.18 (25 440)		
	T_4 b^3A' MLCT	64% $d_{Re} \rightarrow \pi^*_{bpy}$	3.33 (26 640)		
	S_3 c^1A' MLCT	98% $d_{Re} \rightarrow \pi^*_{bpy}$	3.37 (26 960)	371	0.0005

The scalar relativistic effects are taken into account within the zero-order regular approximation (ZORA).[34] The SOC effects are introduced according to a simplified relativistic perturbational TD-DFT formalism.[35,36] The nature of the stationary state was checked through a frequency analysis. The solvent correction is based on the conductor-like screening model (COSMO)[37−39] (with ε = 36.64 for acetonitrile) as implemented in ADF.[40,41]

The "spin-free" (SF) and "spin−orbit" (SO) potential energy curves (PEC) considered for the electronic ground and excited states as a function of the mass and frequency weighted Re−X stretching mode displacements (Q, dimensionless) have been obtained by single point TD-DFT calculations of S_0, S_1, S_2, S_3, T_1, T_2, T_3, and T_4 states, as well as the variation of the SOC along this coordinate. Exploratory wavepacket propagations on the PEC coupled by spin−orbit have been performed for the three complexes using multi configuration time-dependent Hartree (MCTDH) method.[42−44] The SOC variation as a function of the Re−X stretching mode has been taken into account during the propagations.

The calculations have been performed with ADF-2013 quantum chemistry software[45] and the electronic transitions have been analyzed with the Dgrid package.[46]

3. RESULTS AND DISCUSSION

3.1. Electronic Structure. The molecules under investigation are characterized by a d^6 electronic configuration of the rhenium atom and low-lying π^* orbitals localized on the bpy ligand in the electronic ground state. Whereas the HOMO and HOMO−1 of $[Re(Cl)(CO)_3(bpy)]$ and $[Re(Br)(CO)_3(bpy)]$ are composed of about 50% of electronic density localized on the rhenium atom ($5d_{Re}$) and between 15% and 28% of density localized on the halides (p_X, X = Cl, Br), the HOMO−3 is purely localized on the metal and the HOMO−4 is localized on the bpy ligand (π_{bpy}) in both complexes. The LUMO is the π^*_{bpy} antibonding counterpart of the HOMO−4. This electronic structure leads to seven low-lying singlet and triplet-excited states potentially populated upon irradiation at 400 nm (or 25 000 cm^{-1}) (Table 1).

Representative differences of electronic densities corresponding to these $S_0 \rightarrow S_n$, T_n electronic transitions are shown in Figure 2 for illustration. The other densities maps are reported in Supporting Information Figure S1. The results reported in Table 1 show clearly that the chloride and bromide substituted complexes **1** and **2** behave similarly. They are characterized by singlet and triplet states of mixed MLCT/XLCT character with a major contribution of MLCT that decreases when going from Cl to Br.

In contrast the HOMO and HOMO−1 of the iodide complex $[Re(I)(CO)_3(bpy)]$ **3** are composed of more than 50% of p(I) localized contributions with an admixture of about 30% of d_{Re} while the HOMO−3 and HOMO−4 have the same character in the three molecules, namely purely d_{Re} and π_{bpy}, respectively. Consequently, as already pointed out in previous studies the composition of the absorption spectrum of the iodide complex **3** differs significantly from the spectra of the chloride and bromide compounds **1** and **2**.[14,30] The absorption is slightly shifted to the red and the lowest excited states are predominantly XLCT (Table 1) with MLCT contributions never exceeding 30%. Within the domain of energy of interest the three complexes exhibit seven excited states within about

dx.doi.org/10.1021/ct500846n | J. Chem. Theory Comput. 2015, 11, 99−110

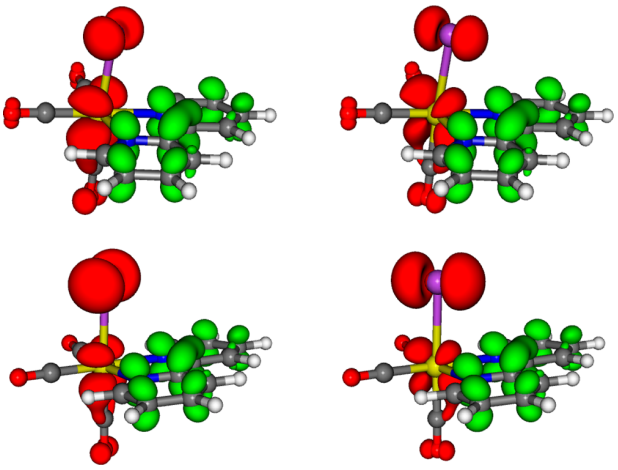

Figure 2. Differences in electronic densities when going from S_0 to S_1/T_1 (top left) and S_2/T_2 (top right) in **2** (X = Br) and from S_0 to S_1/T_1 (bottom left) and S_2/T_2 (bottom right) in **3** (X = I) at the Franck–Condon Geometry. Electronic densities for X = Cl (not shown) are similar to those for Br.

0.5 eV, three singlet's and four triplets, potentially populated either directly upon absorption at 400 nm to S_2 or through singlet–triplet ISC. The absorption wavelengths of S_2 are calculated at 393, 399, and 424 nm for X = Cl, Br, and I, respectively, in good agreement with the experimental spectra recorded in acetonitrile.[14] In order to analyze the role of the triplet states in the ultrafast decay observed after absorption at 400 nm we have calculated the spin–orbit splitting of T_1, T_2, T_3, and T_4 and the SOC between the seven excited states reported in Table 1. The SOC effects are reported in Table 2 for the three complexes.

When SOC is included the seven "spin-free" excited states described in Table 1 generate 15 "spin–orbit" states in the relevant domain of energy of the spectra of [Re(Cl)-$(CO)_3$(bpy)], [Re(Br)$(CO)_3$(bpy)] and [Re(I)$(CO)_3$(bpy)]. The results reported in Table 2 compare well to the data we have published earlier on the same systems but using different solvent and various functionals and methods.[14] The "spin–orbit" spectra of the three molecules that agree rather well with the experimental spectra recorded in CH_3CN are depicted in Supporting Information Figure S2. Within the present zeroth-order approximation the SOC perturbation has already several effects on the absorption spectroscopy of the complexes:

(i) The lowest part of the spectra is red-shifted by 0.06 eV (X = Cl), 0.09 eV (X = Br) and 0.18 eV (X = I) due to the participation of the triplet sublevels to the absorption;

(ii) The six lowest "spin–orbit" states remain largely "triplet" in character, the only significant singlet contributions being present in E_3/E_4 (X = Cl: 46% in E_4), (X = Br: 10% in E_3; 44% E_4) and (X = I: 44% in E_3; 26% in E_4);

(iii) The maximum of absorption originated from the S_2 (b^1A') state is not drastically affected by the SOC corrections, the only alterations being a decrease of the oscillator strength by mixing with the IL b^3A'' state (X = Cl, Br) or the XLCT/MLCT a^3A'' state (X = I) and a small blue shift (160 cm^{-1}) of the maximum in the iodide complex **3**;

(iv) The character of the lowest states below S_2, namely MLCT/XLCT for the chloride and bromide complexes and XLCT/MLCT for the iodide complex, is not modified by SOC interactions;

(v) The SOC splitting of the triplet states never exceeds 0.06 eV (480 cm^{-1}) leading to several sets of nearly degenerate electronic states of moderate to weak intensities.

As illustrated by the results reported in Table 2 the singlet–triplet mixing by SOC can become important and does not follow the heavy-atom rules. For instance the S_1/T_2 (a^1A''/a^3A') mixing amounts to about 50:50 within the series Cl > Br > I. Here the predominant MLCT character of these states in the chloride and bromide complexes may compensate the larger SOC effect in the iodide compound.

In order to interpret the luminescence properties of the three complexes the structures of the six low-lying singlet and triplet states, namely S_1, S_2, T_1, T_2, T_3, and T_4, have been optimized at the same level of calculation than the one of the electronic ground state. The geometries of the "spin-free" states described in this section (Table 1) have been optimized. Their energy has been corrected a posteriori by SOC perturbation. The structural properties and emissive properties of these excited states are discussed in the two next sections.

3.2. Structural Properties. Some important structural parameters extracted from the optimized geometries of complexes [Re(Cl)$(CO)_3$(bpy)] **1**, [Re(Br)$(CO)_3$(bpy)] **2**, and [Re(I)$(CO)_3$(bpy)] **3** in the electronic ground state and low-lying triplet and singlet excited states are reported in Table 3. The S_1 and T_1 geometries converged to a C_s solution, validated by a frequency analysis. However, the Cs symmetry has been retained during the optimization procedure for S_2 and T_2 states to avoid convergence problems. A single imaginary frequency (<100 cm^{-1}) remains in the C_s structures.

The structural deformations when going from the electronic ground state to the relaxed low-lying singlet and triplet exited states are quite small. After nuclear relaxation into the potential wells of the excited states S_1, S_2, T_1, T_2, and T_3 the Re–X shortening does not exceed 0.097 Å in the singlet states and 0.043 Å in the triplet states. This deformation is accompanied by an elongation of the Re–C_{ax} bonds (<3%) together with a minor shortening of the Re–N bonds in all excited states. In contrast to the MLCT/XLCT, XLCT/MLCT and IL states, the pure MLCT state T_4 is characterized by a small elongation of the Re–X bond in the bromide and iodide substituted complexes. The T_1 and T_2 triplet states in the bromide and iodide substituted complexes are the seat of a moderate bending of the XRe–C_{ax} angle complemented by an opening of the NReX angle. This effect increases with the XLCT character and is especially significant in the T_2 states where the XReC_{ax} angle decreases from 178.9° to 169° and from 177.9° to 164.1° in [Re(Br)$(CO)_3$(bpy)] and [Re(I)$(CO)_3$(bpy)], respectively. As illustrated in Table 3 the other important geometrical parameters are not drastically modified when going from the electronic ground state to the excited states whatever the halide ligand is.

In the next section, the above structural data are used to provide a qualitative interpretation of the emissive properties of the three molecules.

3.3. Emission Properties. The energy of the relaxed lowest excited states S_1, S_2, T_1, T_2, T_3, and T_4 under C_s symmetry constraint and corrected by SOC perturbation at their "spin-free" optimized geometries are summarized in Table 4 for the three complexes.

dx.doi.org/10.1021/ct500846n | J. Chem. Theory Comput. 2015, 11, 99–110

Table 2. Spin−Orbit Coupled Low-Lying Excited States of [Re(Cl)(CO)$_3$(bpy)] 1, [Re(Br)(CO)$_3$(bpy)] 2, and [Re(I)(CO)$_3$(bpy)] 3 Calculated at the TD-DFT Level

	state	composition	vertical $S_0 \rightarrow E_n$ transition energy (in eV and cm^{-1})	oscillator strength f
X = Cl **1**				
	E_1 (A″) MLCT/XLCT	71% a^3A'' 24% a^3A'	2.78 (22 240)	2.0×10^{-6}
	E_2 (A′) MLCT/XLCT	72% a^3A'' 24% a^3A'	2.78 (22 240)	0.99×10^{-4}
	E_3 (A′) MLCT/XLCT	88% a^3A'	2.81 (22 480)	0.004
	E_4 (A″) MLCT/XLCT	48% a^3A'46% a^1A''	2.85 (22 800)	0.95×10^{-3}
	E_5 (A″) MLCT/XLCT	72% a^3A' 26% a^3A''	3.01 (24 080)	0.68×10^{-3}
	E_6 (A′) MLCT/XLCT	72% a^3A' 26% a^3A''	3.01 (24 080)	0.10×10^{-3}
	E_7 (A″) MLCT/XLCT	50% a^3A' 49% a^1A''	3.07 (24 560)	0.24×10^{-5}
	E_8 (A′) MLCT/IL/XLCT	58% b^1A' 26% b^3A''	3.17 (25 360)	0.035
	E_9 (A″) IL	94% b^3A''	3.23 (25 840)	0.39×10^{-6}
	E_{10} (A′) IL	95% b^3A''	3.23 (25 840)	0.82×10^{-4}
	E_{11} (A′) IL/MLCT/XLCT	72% b^3A'' 26% b^1A'	3.25 (26 000)	0.016
	E_{12} (A″) MLCT	92% b^3A'	3.37 (26 960)	0.43×10^{-5}
	E_{13} (A″) MLCT	92% b^3A'	3.37 (26 960)	0.12×10^{-3}
	E_{14} (A′) MLCT	87% b^3A'	3.38 (27 040)	0.47×10^{-2}
	E_{15} (A′) MLCT	93% c^1A'	3.41 (27 280)	0.15×10^{-2}
X = Br **2**				
	E_1 (A″) MLCT/XLCT	66% a^3A'' 30% a^3A'	2.75 (22 000)	0.21×10^{-5}
	E_2 (A′) MLCT/XLCT	66% a^3A'' 30% a^3A'	2.75 (22 000)	0.51×10^{-4}
	E_3 (A′) MLCT/XLCT	86% a^3A'' 10% b^1A'	2.78 (22 240)	0.52×10^{-2}
	E_4 (A″) MLCT/XLCT	44% a^1A'' 50% a^3A'	2.80 (22 400)	0.74×10^{-3}
	E_5 (A″) MLCT/XLCT	66% a^3A' 31% a^3A''	2.99 (23 920)	0.58×10^{-5}
	E_6 (A′) MLCT/XLCT	66% a^3A' 31% a^3A''	2.99 (23 920)	0.93×10^{-4}
	E_7 (A″) MLCT/XLCT	51% a^1A'' 48% a^3A'	3.05 (24 400)	0.86×10^{-3}
	E_8 (A′) MLCT/XLCT/IL	70% b^1A' 14% b^3A''	3.13 (25 040)	0.036
	E_9 (A″) IL	95% b^3A''	3.22 (25 760)	0.12×10^{-5}
	E_{10} (A′) IL	96% b^3A''	3.22 (25 760)	0.88×10^{-4}
	E_{11} (A′) IL/MLCT/XLCT	82% b^3A'' 16% b^1A'	3.23 (25 840)	0.80×10^{-2}
	E_{12} (A″) MLCT	92% b^3A'	3.35 (26 800)	0.35×10^{-5}
	E_{13} (A′) MLCT	92% b^3A'	3.36 (26 880)	0.20×10^{-3}
	E_{14} (A′) MLCT	91% b^3A'	3.36 (26 880)	0.16×10^{-2}
	E_{15} (A′) MLCT	94% c^1A'	3.39 (27 120)	0.85×10^{-3}
X = I **3**				
	E_1 (A″)XLCT/MLCT	55% a^3A'' 42% a^3A'	2.58 (20 640)	0.14×10^{-5}
	E_2 (A′) XLCT/MLCT	54% a^3A'' 42% a^3A'	2.58 (20 640)	0.14×10^{-4}
	E_3 (A″) XLCT/MLCT	54% a^3A' 44% a^1A''	2.62 (20 960)	0.34×10^{-3}
	E_4 (A′) XLCT/MLCT	70% a^3A'' 26% b^1A'	2.62 (20 960)	0.76×10^{-2}
	E_5 (A″) XLCT/MLCT	52% a^3A' 40% a^3A''	2.88 (23 040)	0.10×10^{-5}
	E_6 (A′) XLCT/MLCT	51% a^3A' 40% a^3A''	2.90 (23 200)	0.18×10^{-2}
	E_7 (A″) XLCT/MLCT	49% a^1A'' 42% a^3A'	2.93 (23 440)	0.38×10^{-3}
	E_8 (A′) XLCT/MLCT	62% b^1A' 24% a^3A''	2.97 (23 760)	0.018
	E_9 (A″) IL/XLCT/MLCT	89% b^3A''	3.17 (25 360)	0.44×10^{-5}
	E_{10} (A′) IL/XLCT/MLCT	88% b^3A''	3.17 (25 360)	0.13×10^{-3}
	E_{11} (A′) IL/XLCT/MLCT	94% b^3A''	3.18 (25 440)	0.16×10^{-2}
	E_{12} (A″) MLCT/XLCT	64% b^3A' 24% a^3A'	3.28 (26 240)	0.30×10^{-4}
	E_{13} (A″) MLCT	62% b^3A'	3.28 (26 240)	0.34×10^{-4}
	E_{14} (A′) MLCT	75% b^3A'	3.31 (26 480)	0.31×10^{-2}
	E_{15} (A′) MLCT	39% c^1A' 30% c^3A'	3.46 (27 680)	0.70×10^{-3}

According to the calculations the luminescence should start from the S_2 state at 505 and 522 nm for the chloride and bromide complexes, giving Stokes shifts of 5640 and 5880 cm^{-1}, respectively, in agreement with the exprimental data (~6000 cm^{-1}). Accordingly, the two complexes behave similarly and the small calculated red-shift is also observed on the experimental luminescence spectra when going from Cl to Br.[30] On the basis of the results without SOC reported in Table 4 a qualitative interpretation of the time-resolved luminescence of [Re(Cl)(CO)$_3$(bpy)] and [Re(Br)(CO)$_3$(bpy)] spectra is proposed:

The early signal detected immediately after absorption at 400 nm, covering the 500−550 nm energy domain and characterized by a rapid decay, τ_1 = 85 fs (X = Cl) and 128 fs (X = Br), is attributed to the S_2 state in both complexes. The T_3 state could also contribute to this emission by SOC with a maximum calculated at 482 nm and a significant oscillator strength $f = 0.24 \times 10^{-1}$. The intermediate band observed at longer timescale between 550 and 600 nm with emissive decay time τ_2 =

dx.doi.org/10.1021/ct500846n | J. Chem. Theory Comput. 2015, 11, 99−110

Table 3. Optimized Representative Bond Lengths (in Å) and Bond Angles (in Degree) of [Re(Cl)(CO)$_3$(bpy)] 1, [Re(Br)(CO)$_3$(bpy)] 2, and [Re(I)(CO)$_3$(bpy)] 3 in the S_0 Electronic Ground State and Low-Lying S_1, S_2 Singlet and T_1, T_2, T_3, T_4 Triplet States Calculated in CH_3CN

	S_0	S_1	S_2	T_1	T_2	T_3	T_4
X = Cl **1**		MLCT/XLCT	MLCT/XLCT	MLCT/XLCT	MLCT/XLCT	IL	MLCT
Re−X	2.552	2.455	2.473	2.480	2.509	2.512	2.550
Re−N	2.204	2.165	2.187	2.149	2.157	2.194	2.154
Re−C_{ax}	1.907	1.968	1.946	1.961	1.939	1.928	1.914
Re−C_{eq}	1.925	1.955	1.952	1.956	1.959	1.936	1.988
C−C_{bpy}	1.472	1.415	1.426	1.411	1.421	1.396	1.418
NReN	74.1	76.2	76.0	76.6	76.0	74.4	75.9
$C_{eq}ReC_{eq}$	88.3	83.6	95.6	84.2	94.9	86.8	89.6
$XReC_{ax}$	178.0	173.4	179.0	174.1	173.3	175.1	172.3
NReX	84.1	86.4	88.2	86.7	89.8	84.2	84.1
X = Br **2**		MLCT/XLCT	MLCT/XLCT	MLCT/XLCT	MLCT/XLCT	IL	MLCT
Re−X	2.713	2.616	2.654	2.646	2.693	2.678	2.727
Re−N	2.204	2.166	2.181	2.150	2.158	2.195	2.153
Re−C_{ax}	1.907	1.965	1.936	1.958	1.930	1.934	1.912
Re−C_{eq}	1.925	1.953	1.953	1.954	1.958	1.934	1.989
C−C_{bpy}	1.471	1.415	1.426	1.411	1.422	1.397	1.418
NReN	74.0	76.1	76.0	76.6	76.1	74.4	75.8
$C_{eq}ReC_{eq}$	88.3	84.0	95.7	84.5	94.6	87.2	89.4
$XReC_{ax}$	178.9	174.5	173.9	175.3	169.0	175.8	174.3
NReX	85.0	87.9	91.6	88.2	92.9	85.2	85.8
X = I **3**		XLCT/MLCT	XLCT/MLCT	XLCT/MLCT	XLCT/MLCT	IL/XLCT/MLCT	MLCT
Re−X	2.911	2.823	2.879	2.846	2.942	2.914	2.949
Re−N	2.205	2.173	2.186	2.158	2.157	2.198	2.156
Re−C_{ax}	1.909	1.959	1.928	1.957	1.919	1.914	1.912
Re−C_{eq}	1.925	1.948	1.947	1.950	1.954	1.929	1.986
C−C_{bpy}	1.470	1.416	1.425	1.412	1.422	1.396	1.417
NReN	74.0	75.9	75.8	76.3	76.1	74.3	75.4
$C_{eq}ReC_{eq}$	88.6	85.0	95.0	85.1	94.1	88.3	91.2
$XReC_{ax}$	177.9	176.3	170.8	176.9	164.1	176.7	176.5
NReX	86.0	89.1	93.9	89.4	95.0	85.1	87.1

340 fs (X = Cl) and 470 fs (X = Br) can be assigned to the T_2 state calculated at 558 nm (X = Cl) and 571 nm (X = Br). By SOC this triplet state gains oscillator strength (0.2×10^{-3}) and becomes coupled to the S_1 state (see Table 2). To some extent the S_1 state calculated at ∼550 nm ($f = 0.2 \times 10^{-2}$) (stabilized at ∼570 nm by SOC), despite of it's A″ symmetry, should participate indirectly to this intermediate band. In both molecules, the observed long-lived emission at 600−610 nm is attributed to the lowest T_1 states calculated at 596 and 592 nm for the chloride and bromide complexes, respectively, and shifted to ∼610 nm with $f = 0.6 \times 10^{-2}$ by SOC in better agreement with experimental data.

As shown in Table 4, the SOC effects are not dramatic and can be neglected as far as the emissive properties of [Re(Cl)(CO)$_3$(bpy)] and [Re(Br)(CO)$_3$(bpy)] are concerned. Indeed, the SOC induced splitting of the lowest emissive triplet states is very small. The good agreement between experimental and theoretical Stokes shifts (about 6000 cm^{-1}) obtained for the Cl and Br substituted complexes without SOC correction confirms this assumption. Moreover, the reasonable qualitative correlation between the calculated minima of the emissive states and the energy domain of the observed luminescence time-resolved signals corroborate our interpretation. However, the SOC will be important for describing the nonadiabatic dynamics of the excited states coupled vibronically as well as by spin−orbit.[29]

In contrast, the results reported in Table 4 for [Re(I)(CO)$_3$(bpy)] indicate important SOC effects on the emissive properties of the iodide complex. The Stokes shift calculated from S_2 emission without SOC (4944 cm^{-1}) is underestimated as compared to the value obtained with SOC, namely 6430 cm^{-1} closer to the experimental data.[30] When analyzing the SOC corrected results reported in Table 4 for [Re(I)(CO)$_3$(bpy)] a qualitative interpretation of the time-resolved luminescence spectrum can be given:

The first signal characterized by a rapid decay (τ_1 = 152 fs) and a maximum at 525 nm is attributed to the "spin−orbit" A′ component of the T_3 state calculated at 512 nm with $f = 0.17 \times 10^{-1}$ and to the S2 state calculated at 577 nm with $f = 0.4 \times 10^{-1}$. The intermediate band covering the 550−600 nm region with a decay time τ_2 = 1180 fs is assigned to the "spin−orbit" S_1 state calculated at 595 nm. The S_2 state could also contribute to this intermediate band. According to the values obtained for the spin−orbit sublevels of the T_1 and T_2 states (Table 4) both states should contribute to the observed long-lived emission detected at 600−610 nm. However, T_1 that acquires significant oscillator strength by SOC ($f = 0.15 \times 10^{-1}$) is probably the main contributor to the long-lived luminescence.

Scheme 1 gives a qualitative picture of the luminescence decay through the low-lying singlet and triplet states of the three complexes on the basis of emission wavelengths collected in Table 4, namely without SOC for chloride and bromide

dx.doi.org/10.1021/ct500846n | J. Chem. Theory Comput. 2015, 11, 99−110

Table 4. TD-DFT Vertical S_n, $T_n \rightarrow S_0$ Transition Energies (in eV) and Corresponding Emission Wavelengths (in nm) of the Lowest Relaxed Singlet and Triplet States of $[Re(Cl)(CO)_3(bpy)]$ 1, $[Re(Br)(CO)_3(bpy)]$ 2, and $[Re(I)(CO)_3(bpy)]$ 3 Calculated in CH_3CN

	state	vertical S_n, $T_n \rightarrow S_0$ transition energy (in eV)	emission wavelength (in nm)	emission wavelength (in nm) with SOC
X = Cl **1**				
	T_1 (a^3A'')	2.096	596	610 (A″)
				610 (A′)
				607 (A′)
	T_2 (a_3A')	2.239	558	575 (A″)
				576 (A′)
				570 (A″)
	S_1 (a^1A'')	2.245	557	575 (A″)
	S_2 (b^1A')	2.474	505	496 (A′)
	T_3 (b^3A'')	2.637	474	482 (A′)
				472 (A″)
				466 (A″)
	T_4 (b^3A')	2.724	459	453 (A″)
				451 (A″)
				449 (A′)
X = Br **2**				
	T_1 (a^3A'')	2.113	592	609 (A″)
				608 (A′)
				604 (A′)
	T_2 (a^3A')	2.1894	571	587 (A″)
				587 (A′)
				583 (A″)
	S_1 (a^1A'')	2.260	553	576 (A″)
	S_2 (b^1A')	2.393	522	505 (A′)
	T_3 (b^3A'')	2.623	477	487 (A′)
				467 (A″)
				467 (A′)
	T_4 (b^3A')	2.722	459	454 (A″)
				452 (A″)
				447 (A′)
X = I **3**				
	T_1 (a^3A'')	2.129	587	620 (A″)
				619 (A′)
				612 (A′)
	T_2 (a^3A')	2.096	596	620 (A″)
				620 (A′)
				617 (A″)
	S_1 (a^1A'')	2.263	552	595 (A″)
	S_2 (b^1A')	2.331	536	577 (A′)
	T_3 (b^3A'')	2.539	492	512 (A′)
				483 (A′)
				479 (A″)
	T_4 (b^3A')	2.725	459	459 (A″)
				458 (A′)
				458 (A″)

substituted complexes **1** and **2** and with SOC perturbation for complex **3**.

On the basis of the static electronic and structural properties of the three complexes discussed in this section, we cannot get time scales associated with the time-resolved luminescence spectra.[30] In order to study the population of the active excited states in real time as a function of the nuclear relaxation, it is necessary to perform nonadiabatic quantum dynamics within a multimode approach applied to spin-vibronically coupled excited states. This type of simulation is very challenging for transition metal complexes[28,29,47] and is beyond the scope of the present paper. Instead, we propose here exploratory wavepacket propagations on the spin−orbit coupled PEC associated with the singlet and triplet excited states discussed above and calculated as a function of the mass and frequency weighted Re−X stretching mode. This simulation is the first step toward the analysis of the experimental evidence of a correlation between the ISC times measured for the $[Re(X)(CO)_3(bpy)]$ complexes and the vibrational period of the Re−X stretching mode in similar complexes.[30] The PEC calculated without and with SOC are presented in the next section together with the variation of the SOC as a function of this coordinate for the three complexes.

3.4. Potential Energy Curves. The gradients analysis shows an important contribution of the Re−X stretching mode around the FC region, especially for S_2 and S_1 states. This will have important consequences at the early stage of the photophysical process. A frequency analysis of the normal modes in the S_0 electronic ground state within the harmonic approximation and corrected by solvent effects has been performed for the three complexes. In each case, a stretch frequency is identified at 236, 152, and 125 cm^{-1} for $[Re(Cl)(CO)_3(bpy)]$ **1**, $Re(Br)(CO)_3(bpy)]$ **2**, and $[Re(I)(CO)_3(bpy)]$ **3**, respectively. This mode is associated with a deformation of the bpy ligand corresponding to an out-of-plane bending mode for **3** and an in-plane scissoring mode for **1** and **2** (Figure 3).

The TD-DFT and SOC corrected TD-DFT potential energy curves calculated as a function of the mass and frequency weighted Re−X stretching mode displacements (Q, dimensionless) and associated with S_1, S_2, S_3, T_1, T_2, T_3, and T_4 excited states described in Table 1 are depicted in Figure 4 for $[Re(Br)(CO)_3(bpy)]$ and in Supporting Information Figures S3 and S4 for $[Re(Cl)(CO)_3(bpy)]$ and $[Re(I)(CO)_3(bpy)]$, respectively.

The minima of the excited states are shifted to shorter Re−Br distances as compared to the FC point (Table 3) with values varying between 2.56 and 2.61 Å. The T_1 and T_2 states remain the lowest states along this coordinate and the degeneracy between the S_1 and T_2 states is left at long distances. The T_3 and T_4 states present a crossing point at long Re−Br distances that should not take part into the ultrafast decay mechanism. When SOC is applied (Figure 4 bottom) 15 potential energy curves are generated corresponding to the E_n states described in Table 2. T_1 and T_2 lead to two sets of degenerated E_1/E_2 and E_5/E_6 potentials, whereas E_3 is essentially composed of T_1. The singlet components are minor in these "spin−orbit" potentials. In contrast the E_4 and E_7 potentials correspond to a 50:50 S_1/T_2 mixing whereas E_8 and E_{11} are generated by S_2/T_1 mixing with a major contribution of S_2 in E_8 that remains the absorbing state with a minimum at short Re−Br bond distance (2.60 Å). The upper T_3 and T_4 states give rise to two sets of three nearly degenerate potentials at FC that interact nonadiabatically at longer distances as illustrated by the presence of avoided crossings in Figure 4. The S_3 potential remains nearly purely singlet (E_{15}) and does not cross the upper E_n triplet potentials. The lowest "spin−orbit" states of interest run more or less in a parallel way with no crossings around the FC region along this A′ normal mode of vibration.

The PEC associated with the low-lying excited states of $[Re(Cl)(CO)_3(bpy)]$ **1** and $[Re(I)(CO)_3(bpy)]$ **3** are

dx.doi.org/10.1021/ct500846n | J. Chem. Theory Comput. 2015, 11, 99−110

Scheme 1. Qualitative Representation of the Mechanism of Luminescent Decay of (a) [Re(Cl)(CO)$_3$(bpy)] 1, [Re(Br)(CO)$_3$(bpy)] 2, and (b) [Re(I)(CO)$_3$(bpy)] 3 after Absorption to S$_2$ at 400 nm[a]

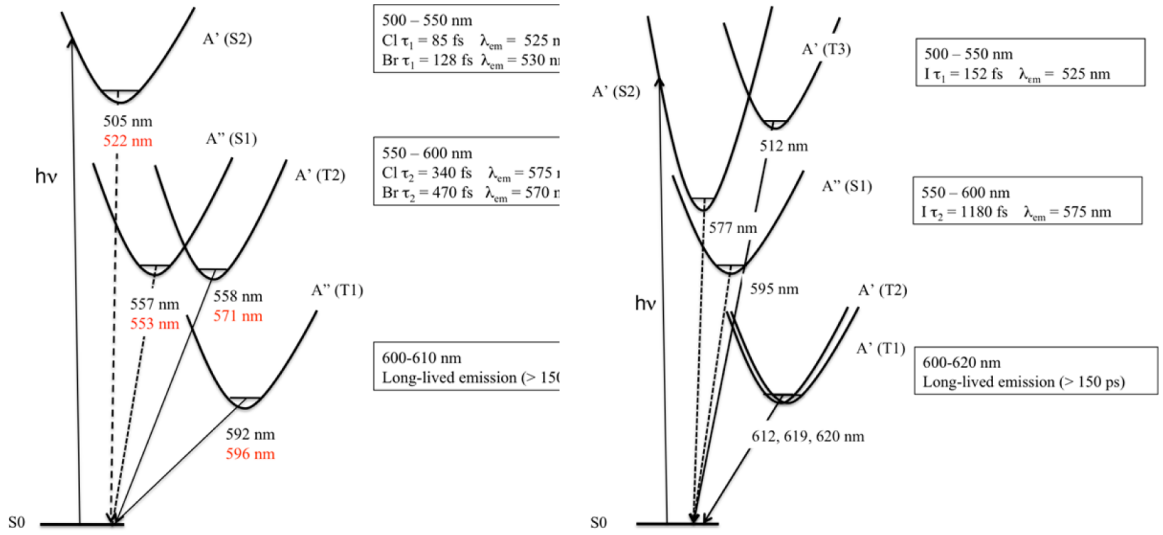

[a]The calculated emission wavelengths (in nm) are reported in black (X = Cl) and red (X = Br). The experimental data from ref 30 are reported on the right of the diagrams for comparison.

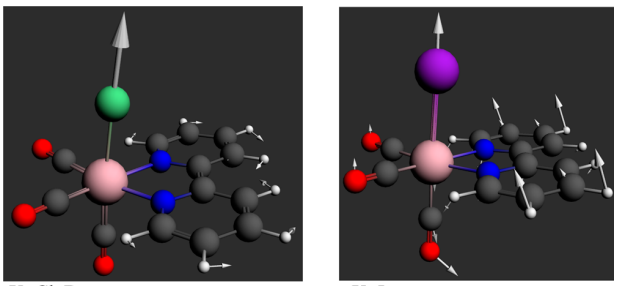

Figure 3. Representation of the Re−X stretching mode displacements in the S$_0$ electronic ground state of [Re(Cl)(CO)$_3$(bpy)] **1**, [Re(Br)(CO)$_3$(bpy)] **2**, and [Re(I)(CO)$_3$(bpy)] **3** in CH$_3$CN.

represented in Supporting Information Figures S3 and S4, respectively. Whereas only "spin-free" potentials of the chloride, bromide and iodide complexes show comparable characteristics, both "spin−orbit" and "spin-free" potentials of **1** and **2** are similar. This corroborates the common luminescent decay behavior of the two complexes upon irradiation at 400 nm and the absence of heavy atom effect into the ultrafast process when replacing Cl by Br. The "spin−orbit" potentials of the iodide complex **3** differ significantly of the others. Indeed, they are characterized by the occurrence of a number of avoided crossings when elongating the Re−I bond above 23 000 cm^{-1}. Moreover five sets of degenerate potentials coexist, namely E$_1$/E$_2$, E$_3$/E$_4$, E$_5$/E$_6$, E$_7$/E$_8$, and E$_9$/E$_{10}$ potentially populated upon irradiation at 400 nm, either directly or by spin-vibronic coupling. This picture confirms the participation of both lowest triplet states T$_1$ and T$_2$, more precisely their SOC sublevels E$_1$/E$_2$ and E$_3$/E$_4$, to the long-lived emission of [Re(I)(CO)$_3$(bpy)] as deduced from the emission properties discussed in section 3.3.

Whereas E$_8$ generated by S$_2$ remains the only absorbing state in the chloride and bromide complexes, four "spin−orbit" states, namely E$_5$/E$_6$ and E$_7$/E$_8$ and to lesser extent E$_9$/E$_{10}$/E$_{11}$ may participate to the absorption of [Re(I)(CO)$_3$(bpy)]. Similarly these two sets of sublevels generated by SOC will contribute to the 2-fold luminescence decay observed at the early time below 1 ps.[30]

The variations of SOC between the singlet and triplet electronic states calculated as a function of the Re−X stretching normal mode are represented in Figure 5 for [Re(Br)(CO)$_3$(bpy)] **2** and in Supporting Information Figures S5 and S6 for [Re(Cl)(CO)$_3$(bpy)] **1** and [Re(I)(CO)$_3$(bpy)] **3**, respectively.

The real and imaginary parts of the SOC are equally important but act differently on the calculated singlet/triplet and triplet/triplet SOC as a function of the Re−Br stretching mode. At short Re−Br distances, especially around FC, the S$_1$/T$_2$ and S$_2$/T$_1$ SOC (real contribution) are greater than 500 cm^{-1} (Figure 5 top) and remain nearly constant. In contrast, their imaginary contributions is rather small with values of ∼150 cm^{-1} (Figure 5 bottom). The T$_1$/T$_2$ interaction follows the same trends. The SOC between S$_1$, S$_2$ and the upper T$_3$ and T$_4$ triplet states does not exceed 200 cm^{-1} as far as the real part is concerned but may reach 600 cm^{-1} when imaginary contribution is considered. Globally, we may distinguish between two sets of SOC, namely a series below 200 cm^{-1} and a second one above 500 cm^{-1}. These values are not really affected by the Re−Br bond stretching mode since the character of the excited states is not strongly modified along this coordinate. The same behavior characterizes the chloride complex **1** (Supporting Information Figure S5). Again the heavy-atom effect along the halide series does not play an important role since on one hand Br is heavier than Cl but the low-lying excited states of the chloride complex have a slightly more pronounced metal character.

dx.doi.org/10.1021/ct500846n | J. Chem. Theory Comput. 2015, 11, 99−110

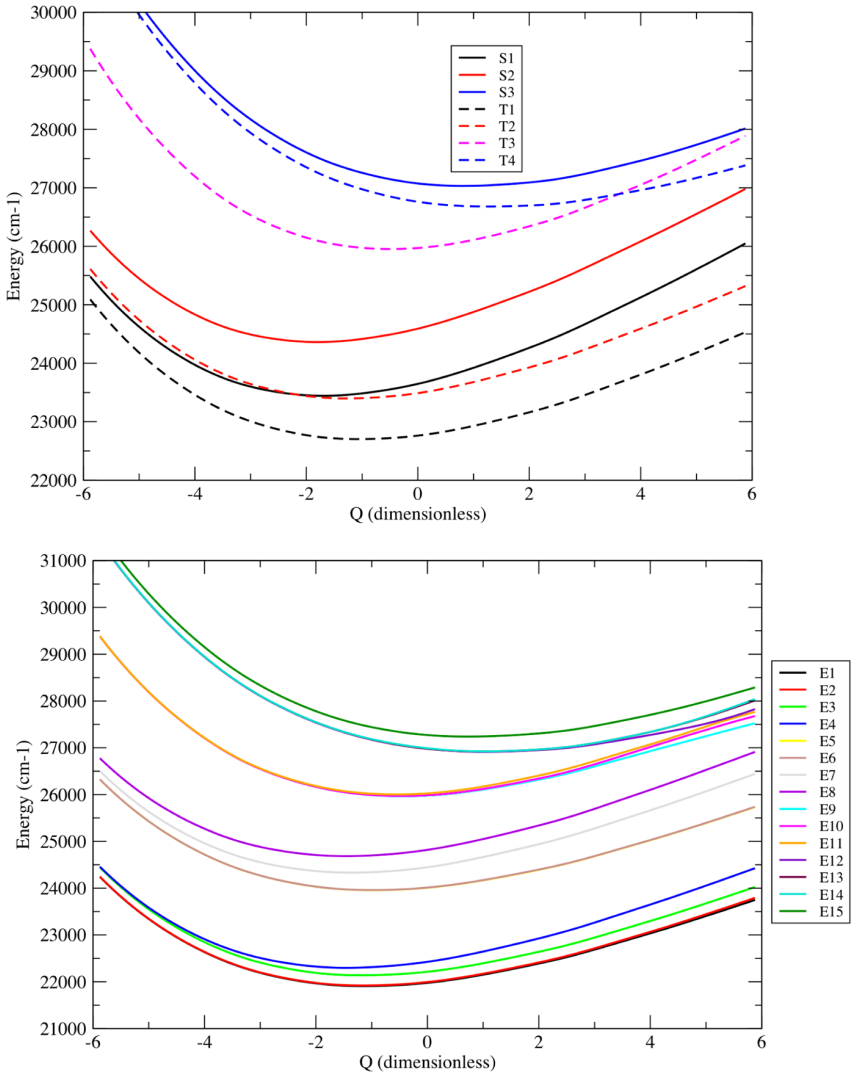

Figure 4. Potential energy curves associated with the low-lying excited states of [Re(Br)(CO)$_3$(bpy)] **2** calculated without SOC (top) and with SOC (bottom) as a function of the mass and frequency weighted Re−X stretching mode displacement from Franck−Condon (Q = 0) (in CH_3CN).

The S_1/T_2, S_2/T_1, and T_1/T_2 SOC evolve similarly in the three complexes along the Q coordinate as shown in Figure 5, Supporting Information Figures S5 and S6 but with larger real-SOC values for the iodide complex **3** greater than 1000 cm^{-1} (Supporting Information Figure S6 top). We may notice in the iodide complex **3** an important variation of S_2/T_3 and S_1/T_4 real-SOC and S_1/T_4 imaginary-SOC that increase drastically with the Re−I bond distance. The significant enhancement of S_2/T_3 real-SOC from 350 to 900 cm^{-1} in [Re(I)(CO)$_3$(bpy)] (Supporting Information Figure S6 (top)) as a function of the Re−X stretching mode displacement (Q), points to the importance of vibronic spin−orbit coupling immediately after absorption at the early stage of the photophysical process. Indeed, while the predominant XLCT character in the iodide substituted complex (see Figure 2) weakens the SOC effects it enhances the involvement of the Re−I vibrational mode in the vibronic spin−orbit coupling.

Obviously, the SOC behavior along other nuclear coordinates and other nuclear deformations around Franck−Condon has to be investigated to fully understand the mechanism of ultrafast luminescence decay in the title complexes. Moreover, calculated spin−orbit data could certainly be improved by more accurate relativistic calculations, especially for [Re(I)(CO)$_3$(bpy)] that combines two heavy atoms. Exploratory wavepacket propagations on the spin−orbit coupled PEC described above are discussed in the next section.

3.5. Wavepacket Propagations. The evolution, as a function of time, of the populations of the low-lying S_1, T_1, T_2, and T_3 excited states after absorption to S_2 has been obtained by wavepacket propagations on the "spin-free" PEC (Figure 4 (top), Supporting Information Figures S3 (top) and S4 (top)). The variation of the SOC as a function of the Re−X stretching mode (Figure 5, Supporting Information Figures S5 and S6) has been taken into account in this preliminary one-dimensional simulation. Figure 6 shows the evolution of population in [Re(Br)(CO)$_3$(bpy)] within the first 500 fs, whereas Supporting Information Figures S7, S8, and S9 exhibit the evolution of population in [Re(Cl)(CO)$_3$(bpy)], [Re(Br)-(CO)$_3$(bpy)], and [Re(I)(CO)$_3$(bpy)], respectively, within the first ps.

At the early stage SOC controls the ultrafast population of T_1 that exceeds 20% within 10 fs as illustrated in Figure 6 for

dx.doi.org/10.1021/ct500846n | J. Chem. Theory Comput. 2015, 11, 99−110

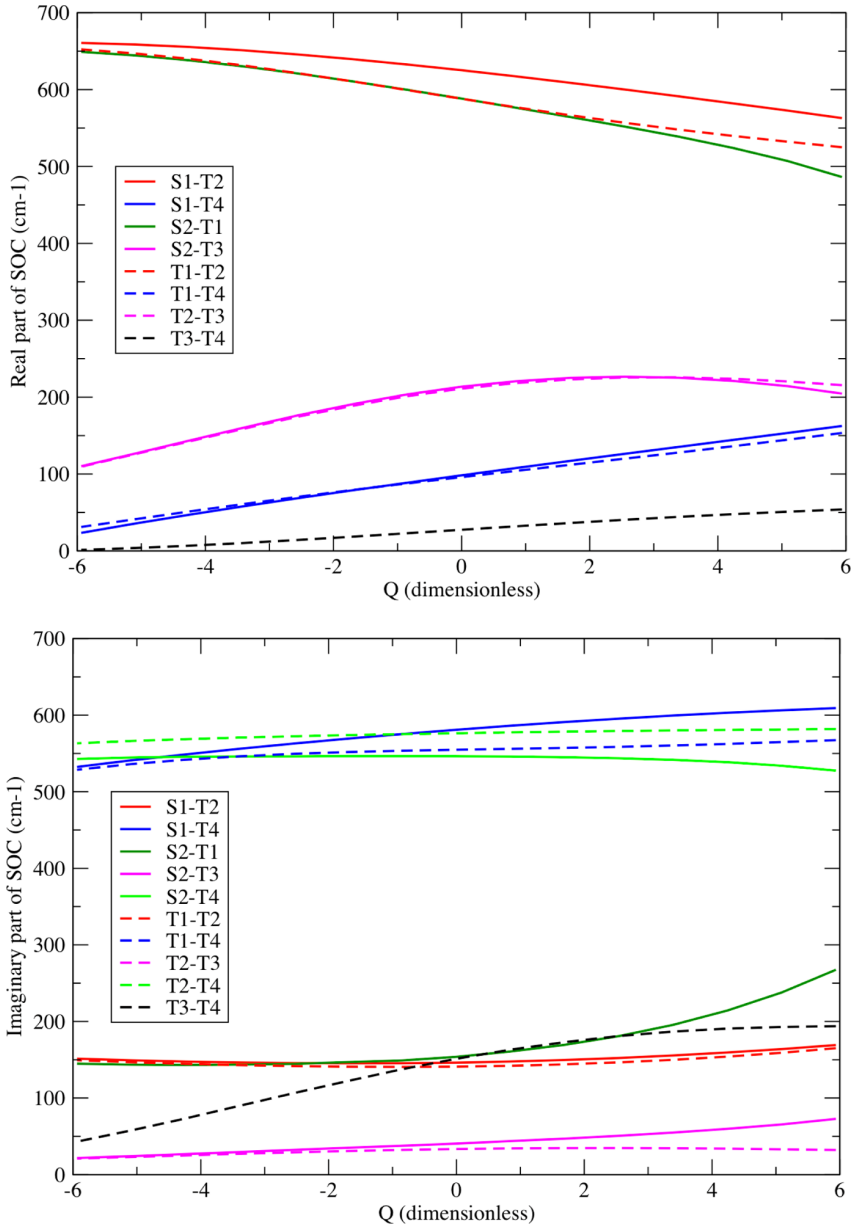

Figure 5. Variation of the SOC matrix elements between the S_1, S_2, S_3, T_1, T_2, T_3, and T_4 electronic states of [Re(Br)$(CO)_3$(bpy)] **2** calculated as a function of the mass and frequency weighted Re−X stretching mode displacement from Franck−Condon ($Q = 0$) (in CH_3CN): absolute values of real contributions (top); absolute values of imaginary contributions (bottom).

[Re(Br)$(CO)_3$(bpy)]. This is a consequence of the large SOC between S_2 (A′) and the two A′ components of T_1. The two A′ components of T_3 are populated as well but less efficiently (<10%) because of the moderate SOC with S_2. The direct $S_2 \rightarrow S_1$ transition is forbidden by symmetry and the probability of $S_2 \rightarrow T_2$ transition that involves the same orbitals excitation is low. However, at longer time-scales, as soon as T_1 and T_3 are populated, T_2 coupled to T_1 and T_3 by SOC (Figure 5) is potentially populated as long as symmetry rules are respected at the spin−orbit sublevels (Table 4). Indeed the A′ component of T_2 is marginally populated (<0.2%) within the first 25 fs by SOC with the A′ components of T_1 and T_3.

After 1 ps the total populations of S_2, T_1 and T_3 remain nearly constant with average values of 67%, 24%, and 9%, respectively (Supporting Information Figure S8). It should be pointed out that the ISC process simulated here via the $S_2 \rightarrow T_1$, T_3 and T_1,$T_3 \rightarrow T_2$ transitions excludes the A″ pathways that will be activated only by vibronic spin−orbit coupling along a″ normal modes.

At short time-scale [Re(Cl)$(CO)_3$(bpy)] behaves similarly to [Re(Br)$(CO)_3$(bpy)] showing an ultrafast population of T_1 (<20%) within less than 10 fs and population of T_3 (<10%) within 20 fs and a negligible population of T_2. Due to smaller values of SOC the ISC is less efficient in the chloride substituted complex with average populations of S_2, T_1, and T_3 of 74%, 16%, and 10%, respectively, within 1 ps (Supporting Information Figure S7).

The population exchange between S_2 and T_1 is more dramatic in [Re(I)$(CO)_3$(bpy)] due to large SOC (>1000 cm^{-1}) with an ultrafast population of T_1 within 10 fs (40%)

dx.doi.org/10.1021/ct500846n | J. Chem. Theory Comput. 2015, 11, 99−110

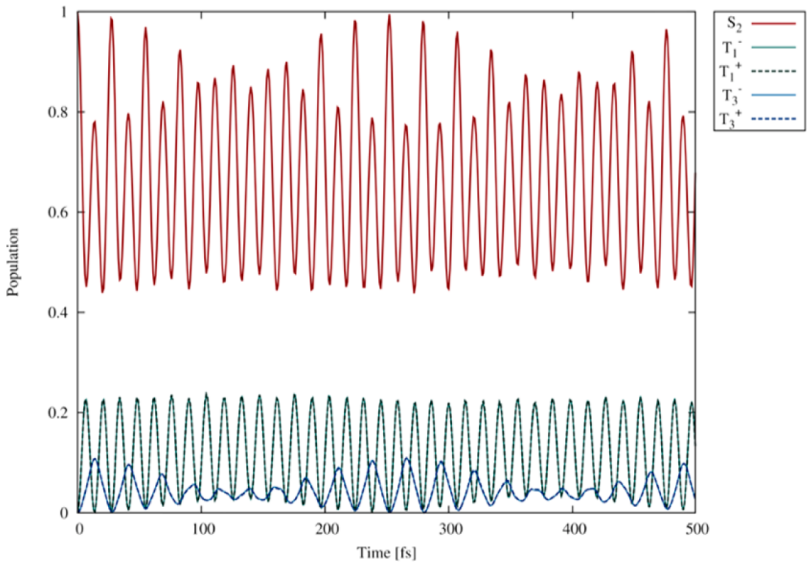

Figure 6. Time-evolution of the population of S_2, T_1, and T_3 excited states of [Re(Br)$(CO)_3$(bpy)] within 500 fs. The population of the A′ spin−orbit sublevels of T_1 and T_3 is represented.

(Supporting Information Figure S9). The population of T_3 reaches nearly 20% in the first 20 fs. The population of T_2 remains marginal, and the average populations of S_2, T_1, and T_3 amount to 46%, 41%, and 13%, respectively.

Whereas the heavy atom effect does not impact the time scale of ISC within the first picaseconds, it does influence significantly the ratio of population of the triplet states.

CONCLUSION

The first complete quantum chemical study of the electronic, structural, and emissive properties of a series of halide substituted Re(I) carbonyls α-diimine complexes investigated experimentally has enabled us to propose a qualitative mechanism for the ultrafast luminescent decay through the seven low-lying singlet and triplet excited states coupled by SOC in acetonitrile. According to our previous studies based on SOC multistate complete active space perturbation theory second order (MS-CASPT2),[14] we have shown that TD-DFT within the ZORA approximation provides realistic absorption spectra and allows the interpretation of the emissive properties of this class of molecules on a semiquantitative static basis. At least six excited states, two singlets and four triplets, are involved in the ISC processes underlying the ultrafast decay after absorption at 400 nm. In contrast to the iodide complex and in a first approximation, the time-resolved luminescence spectra of [Re(Cl)$(CO)_3$(bpy)] and [Re(Br)$(CO)_3$(bpy)] can be analyzed on the basis of the emission wavelengths calculated without SOC correction. Whereas the S_2 absorbing state is responsible for the initial signal of luminescence characterized by an ultrafast decay of a few tens of fs, the intermediate signal between 500 and 600 nm with a decay of a few hundreds of fs is attributed to both S_1 and T_2 in these two complexes. The long-lived emission at 600−610 nm originates into the deactivation of the lowest T_1 state. [Re(I)$(CO)_3$(bpy)] behaves differently because spin−orbit splitting of the triplet states and singlet/triplet mixing becomes important and cannot be ignored. Consequently the luminescence decay should be interpreted on the basis of the spin−orbit sublevels of the original singlet's and triplets. Three domains of energy may be distinguished for the iodide complex: (i) the lowest one involving three nearly degenerate A′ spin−orbit states issue from T_1 and T_2 calculated at 610−620 nm and responsible for the long-lived emission; (ii) a second one involving the spin−orbit states of S_1 (A″) and S_2 (A′) at 577−595 nm controlling the intermediate time scale of 1 ps; (iii) a third one corresponding to the A′ spin−orbit sublevel of T_3 calculated at 512 nm responsible for the early ultrafast decay of 152 fs together with S_2.

In order to investigate the nuclear deformation at Franck−Condon and to infer the interplay between SOC and nuclear relaxation for a subsequent quantum dynamical study, we have calculated the PEC (without and with SOC) and the SOC evolution of the seven lowest singlet and triplet excited states as a function of the mass and frequency weighted Re−X stretching mode displacements. Whereas the PEC are smooth, run in parallel, and very similar for [Re(Cl)$(CO)_3$(bpy] and [Re(Br)-$(CO)_3$(bpy], the shapes of the potentials are more complicated for the iodide complex with a number of avoided crossings appearing at long Re−I bond distances. This is correlated to the strong influence of the SOC that generates important mixing between states. Moreover, some SOC values, especially between the S_2 absorbing state and T_3 increase dramatically with the Re−I stretching mode pointing to a non-negligible interplay between vibronic and spin−orbit couplings.

The accuracy of the spin−orbit data, namely the singlet/triplet coupling and the triplet splitting in [Re(I)$(CO)_3$(bpy)] **3** could certainly be improved by better relativistic calculations going beyond the current level of zero-order approximation. This will be the subject of an ongoing study. The luminescence theoretical data reported in the present work have been obtained under the C_s symmetry constraint. Broken symmetry solutions, the validity of which is always uncertain within the framework of DFT especially for excited states geometry optimization, could lead to slightly different values but probably not to a different interpretation.

Exploratory wavepacket propagations on spin−orbit coupled PEC have been able to simulate partly the ultrafast ISC process observed experimentally via the A′ channels. This preliminary

one-dimensional simulation has shown the importance of vibronic spin−orbit coupling in transition metal complexes.

■ ASSOCIATED CONTENT

Supporting Information

Nuclear coordinates of the optimized structures, theoretical electronic densities and absorption spectra, potential energy and SOC curves for complexes **1** and **3**. Time evolution of the excited state's population in complexes **1** and **3**. This material is available free of charge via the Internet at http://pubs.acs.org.

■ AUTHOR INFORMATION

Corresponding Author

*E-mail: c.daniel@unistra.fr.

Notes

The authors declare no competing financial interest.

■ ACKNOWLEDGMENTS

The authors thank A. Vlček, Jr., M. Chergui, and A. Cannizzo for having motivated this work. We are grateful to S. Záliš for fruitful discussions. The European actions COST perspect-H_2O and CODEC are acknowledged. The quantum chemical calculations have been performed on the computer nodes of the LCQS, Strasbourg, and the authors thank the computer facilities of the High Performance Computing regional center of Unistra.

■ REFERENCES

(1) Juban, E. A.; Smeigh, A. L.; Monat, J. E.; McCusker, J. K. *Coord. Chem. Rev.* **2006**, *250*, 1783.
(2) McCusker, J. K. *Acc. Chem. Res.* **2003**, *36*, 876.
(3) Chergui, M. *Dalton Trans.* **2012**, *41*, 13022.
(4) Bräm, O.; Messina, F.; Baranoff, E.; Cannizzo, A.; Nazeeruddin, M. K.; Chergui, M. *J. Phys. Chem. C* **2013**, *117*, 15958.
(5) El Nahhas, A.; Consani, C.; Blanco-Rodríguez, A. M.; Lancaster, K. M.; Bräm, O.; Cannizzo, A.; Towrie, M.; Clark, I. P.; Záliš, S.; Chergui, M.; Vlček, A., Jr. *Inorg. Chem.* **2011**, *50*, 2932.
(6) Renske, M.; van der Veen, R. M.; Cannizzo, A.; van Mourik, F.; Vlček, A., Jr.; Chergui, M. *J. Am. Chem. Soc.* **2011**, *133*, 305.
(7) El Nahhas, A.; Cannizzo, A.; van Mourik, F.; Blanco-Rodríguez, A. B.; Záliš, S.; Vlček, A., Jr.; Chergui, M. *J. Phys. Chem. A* **2010**, *114*, 6361.
(8) Huse, N.; Kim, T. K.; Jamula, L.; McCusker, J. K.; de Groot, F. M. F.; Schoenlein, R. W. *J. Am. Chem. Soc.* **2010**, *132*, 6809.
(9) Huse, N.; Cho, H.; Hong, K.; Jamula, L.; de Groot, F. M. F.; Kim, T. K.; McCusker, J. K.; Schoenlein, R. W. *J. Phys. Chem. Lett.* **2011**, *2*, 880.
(10) Bressler, Ch.; Milne, C.; Pham, V.-T.; El Nahhas, A.; van der Veen, R. M.; Gawelda, W.; Johnson, S.; Beaud, P.; Grolimund, D.; Kaiser, M.; Borca, C. N.; Ingold, G.; Abela, R.; Chergui, M. *Science* **2009**, *323*, 489.
(11) Blanco-Rodríguez, A. M.; Kvapilová, H.; Sýkora, J.; Towrie, M.; Nervi, C.; Volpi, G.; Záliš, S.; Vlček, A., Jr. *J. Am. Chem. Soc.* **2014**, *136*, 5963.
(12) Visscher, L.; Saue, T.; Nieuwpoort, W. C.; Faegri, K.; Gropen, O. *J. Chem. Phys.* **1993**, *99*, 6704.
(13) Vallet, V.; Strich, A.; Daniel, C. *Chem. Phys.* **2005**, *13*, 18.
(14) Heydová, R.; Gindensperger, E.; Romano, R.; Sýkora, J.; Vlček, A., Jr.; Záliš, S.; Daniel, C. *J. Phys. Chem. A* **2012**, *116*, 11319−11329.
(15) Heitz, M. C.; Ribbing, C.; Daniel, C. *J. Chem. Phys.* **1997**, *106*, 1421.
(16) Guillaumont, D.; Daniel, C. *J. Am. Chem. Soc.* **1999**, *121*, 11733.
(17) Bruand-Cote, I.; Daniel, C. *Chem. Eur. J.* **2002**, *8*, 1361.
(18) Daniel, C.; Guillaumont, D.; Ribbing, C.; Minaev, B. *J. Phys. Chem. A* **1999**, *103*, 5766.
(19) Minaev, B.; Baryshnikov, G.; Ågren, H. *Phys. Chem. Chem. Phys.* **2014**, *16*, 1719.
(20) Daniel, C. *Coord. Chem. Rev.* **2015**, *282*−*283*, 19.
(21) Li, X.; Minaev, B.; Ågren, H.; Tian, H. *J. Phys. Chem. C* **2011**, *115*, 20724.
(22) Brahim, H.; Daniel, C. *Comp. Theor. Chem.* **2014**, *1040*−*1041*, 219.
(23) Papai, M.; Vanko, G.; de Graaf, C.; Rozgonyi, T. *J. Chem. Theory Comp.* **2013**, *9*, 509.
(24) Sousa, C.; de Graaf, C.; Rudavskyi, A.; Broer, R.; Tatchen, J.; Etinski, M.; Marian, C. M. *Chem. Eur. J.* **2013**, *19*, 17541.
(25) Etinski, M.; Tatchen, J.; Marian, C. M. *J. Chem. Phys.* **2011**, *134*, 154105.
(26) Etinski, M.; Rai-Constapel, V.; Marian, C. M. *J. Chem. Phys.* **2014**, *140*, 114104.
(27) Tavernelli, I.; Curchod, B. F. E.; Rothlisberger, U. *Chem. Phys.* **2011**, *391*, 101.
(28) Mondal, P.; Opalka, D.; Poluyanov, L. V.; Domcke, W. *Chem. Phys.* **2011**, *387*, 56.
(29) Mondal, P.; Opalka, D.; Poluyanov, L. V.; Domcke, W. *J. Chem. Phys.* **2012**, *136*, 084308.
(30) Cannizzo, A.; Blanco- Rodríguez, A. M.; El Nahhas, A.; Sebera, J.; Záliš, S.; Vlček, A., Jr.; Chergui, M. *J. Am. Chem. Soc.* **2008**, *130*, 8967.
(31) Becke, A. D. *J. Chem. Phys.* **1993**, *98*, 5648.
(32) Stephens, P. J.; Devlin, F. J.; Chabalowski, C. F.; Frisch, M. J. *J. Phys. Chem.* **1994**, *98*, 11623.
(33) van Lenthe, E.; Baerends, E. J. *J. Comput. Chem.* **2003**, *24*, 1142.
(34) van Lenthe, E.; van Leeuwen, R.; Baerends, E. J.; Snijders, J. G. *Int. J. Quantum Chem.* **1996**, *57*, 281.
(35) Runge, E.; Gross, E. K. U. *Phys. Rev. Lett.* **1984**, *52*, 997.
(36) Petersilka, M.; Gossmann, U. J.; Gross, E. K. U. *Phys. Rev. Lett.* **1996**, *76*, 1212.
(37) Klamt, A.; Schüürmann, G. J. *Chem. Soc., Perkin Trans.* **1993**, *2*, 799.
(38) Klamt, A. *J. Phys. Chem.* **1995**, *99*, 2224.
(39) Klamt, A.; Jones, V. J. *Chem. Phys.* **1996**, *105*, 9972.
(40) Rosa, A.; Baerends, E. J.; van Gisbergen, S. J. A.; van Lenthe, E.; Groeneveld, J. A.; Snijders, J. G. *J. Am. Chem. Soc.* **1999**, *121*, 10356.
(41) Pye, C.; Ziegler, T. *Theor. Chem. Acc.* **1999**, *101*, 396.
(42) Meyer, H.-D.; Manthe, U.; Cederbaum, L. S. *Chem. Phys. Lett.* **1990**, *165*, 73.
(43) Beck, M. H.; Jägle, A.; Worth, G. A.; Meyer, H.-D. *Phys. Rep.* **2000**, *324*, 1.
(44) *Multidimensional Quantum Dynamics MCTDH Theory and Applications*; Meyer, H.-D., Gatti, F., Worth, G. A., Eds.; Wiley-VCH: Weinheim, 2009.
(45) *ADF, SCM, Theoretical Chemistry*; Vrije Universiteit: Amsterdam, The Netherlands, 2013; https://www.scm.com/Downloads/2013.
(46) Kohout, M. *DGrid*, version 4.5; Springer: Radebeul, 2009.
(47) Capano, G.; Penfold, T. J.; Röthlisberger, U.; Tavernelli, I. *CHIMIA* **2014**, *68*, 227.

SUPPORTING INFORMATION

A quantum chemical study of femtosecond fluorescence and intersystem crossing in rhenium(I) carbonyl bipyridine complexes

Christophe Gourlaouen, Julien Eng, Miho Otsuka, Etienne Gindensperger, Chantal Daniel,[*]

Laboratoire de Chimie Quantique, Institut de Chimie de Strasbourg UMR-7177 CNRS- UdS 1 Rue Blaise Pascal BP 296/R8 F-67008 Strasbourg cedex France.

Nuclear oordinates at the optimized electronic ground state geometries of :

- $[Re(Cl)(CO)_3(bpy)]$ **1**

C	1.463997	0.016577	-0.735801
C	0.181190	-0.104366	-2.664504
C	1.300174	-0.055137	-3.472794
C	2.546930	0.041724	-2.875399
C	2.626662	0.075459	-1.494592
C	1.463997	0.016577	0.735801
C	0.181190	-0.104366	2.664504
C	1.300174	-0.055137	3.472794
C	2.546930	0.041724	2.875399
C	2.626662	0.075459	1.494592
H	-0.805645	-0.179336	-3.089632
H	1.186392	-0.091627	-4.543773
H	3.444711	0.087370	-3.471957
H	3.586981	0.145580	-1.014377
H	-0.805645	-0.179336	3.089632
H	1.186392	-0.091627	4.543773
H	3.444711	0.087370	3.471957
H	3.586981	0.145580	1.014377
N	0.252219	-0.066056	-1.328108
N	0.252219	-0.066056	1.328108
Re	-1.506900	-0.093729	0.000000
Cl	-1.219112	2.442006	0.000000

C	-2.887435	-0.036466	1.340545
O	-3.705047	-0.005176	2.155053
C	-2.887435	-0.036466	-1.340545
O	-3.705047	-0.005176	-2.155053
C	-1.588228	-1.999116	0.000000
O	-1.633883	-3.156260	0.000000

- [Re(Br)(CO)$_3$(bpy)] **2**

C	1.465310	0.036278	-0.735494
C	0.182041	-0.093759	-2.663405
C	1.301395	-0.057673	-3.471682
C	2.548494	0.040688	-2.875118
C	2.628104	0.085305	-1.494646
C	1.465310	0.036278	0.735494
C	0.182041	-0.093759	2.663405
C	1.301395	-0.057673	3.471682
C	2.548494	0.040688	2.875118
C	2.628104	0.085305	1.494646
H	-0.804784	-0.169454	-3.088140
H	1.187538	-0.105604	-4.542209
H	3.446509	0.077871	-3.471750
H	3.588527	0.154024	-1.014682
H	-0.804784	-0.169454	3.088140
H	1.187538	-0.105604	4.542209
H	3.446509	0.077871	3.471750
H	3.588527	0.154024	1.014682
N	0.252671	-0.042281	-1.327080
N	0.252671	-0.042281	1.327080
Re	-1.506867	-0.066894	0.000000
Br	-1.247638	2.633241	0.000000
C	-2.886714	-0.007821	1.341195
O	-3.703117	0.024314	2.156677
C	-2.886714	-0.007821	-1.341195
O	-3.703117	0.024314	-2.156677
C	-1.586902	-1.971762	0.000000
O	-1.636405	-3.128369	0.000000

- [Re(I)(CO)$_3$(bpy)] **3**

C	1.466705	0.031535	-0.735183
C	0.181826	-0.076552	-2.663127
C	1.300894	-0.045625	-3.471584
C	2.549434	0.037257	-2.875493
C	2.629535	0.074065	-1.495121
C	1.466705	0.031535	0.735183
C	0.181826	-0.076552	2.663127
C	1.300894	-0.045625	3.471584
C	2.549434	0.037257	2.875493
C	2.629535	0.074065	1.495121
H	-0.815664	-0.138935	-3.088271
H	1.185854	-0.085460	-4.542308
H	3.447548	0.069170	-3.472352
H	3.591149	0.132334	-1.016071
H	-0.805664	-0.138935	3.088271

H	1.185854	-0.085460	4.542308
H	3.447548	0.069170	3.472352
H	3.591149	0.132334	1.016071
N	0.252733	-0.034671	-1.326217
N	0.252733	-0.034671	1.326217
Re	-1.508317	-0.064567	0.000000
I	-1.302895	2.839566	0.000000
C	-2.884049	-0.003700	1.344736
O	-3.695615	0.028753	2.165091
C	-2.884049	-0.003700	-1.344736
O	-3.695615	0.028753	-2.165091
C	-1.574646	-1.972641	0.000000
O	-1.620704	-3.128707	0.000000

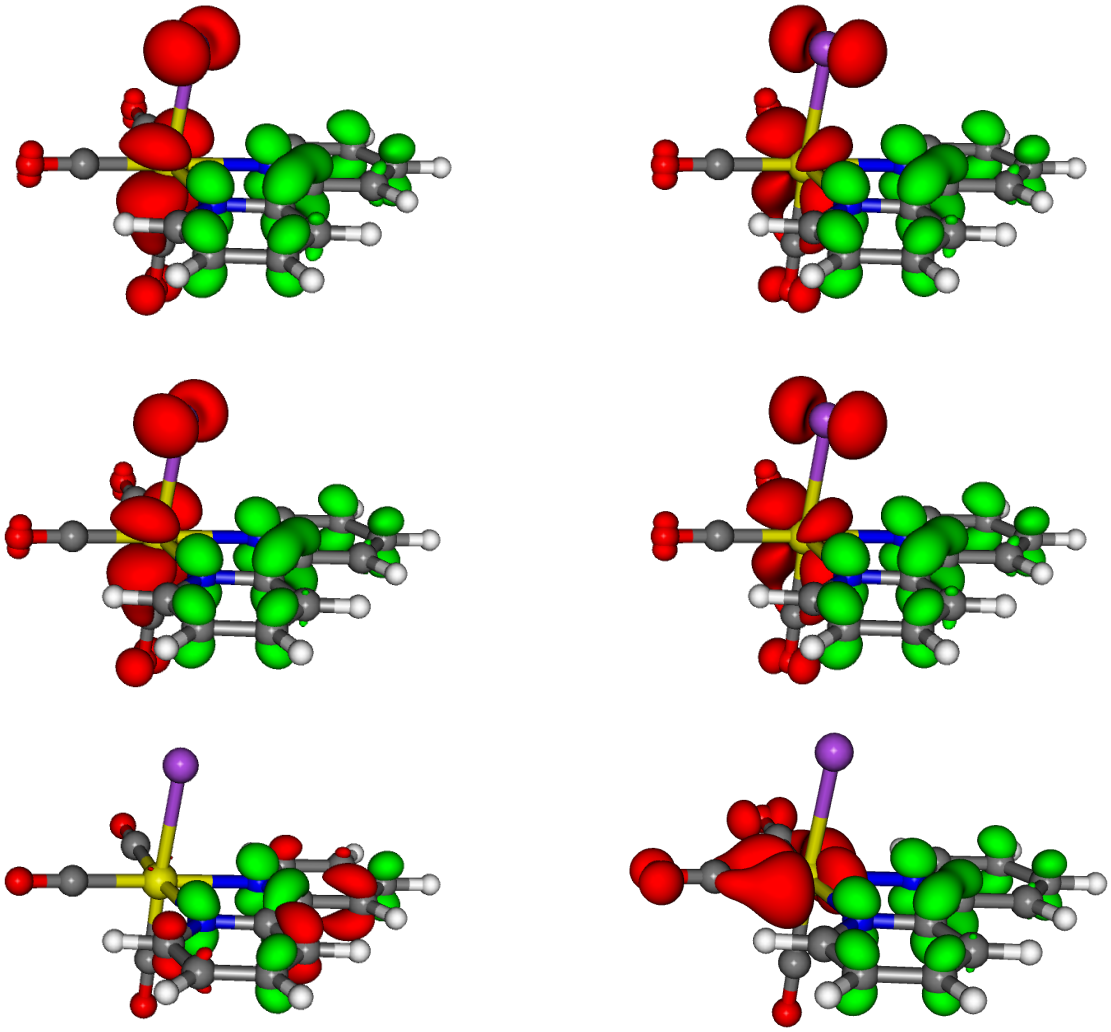

Figure S1. Differences in electronic densities when going from S_0 to S_1 (up left), S_2 (up right), T_1

(middle left), T_2 (middle right), T_3 (down left) and T_4 (down right) for complex **2**.

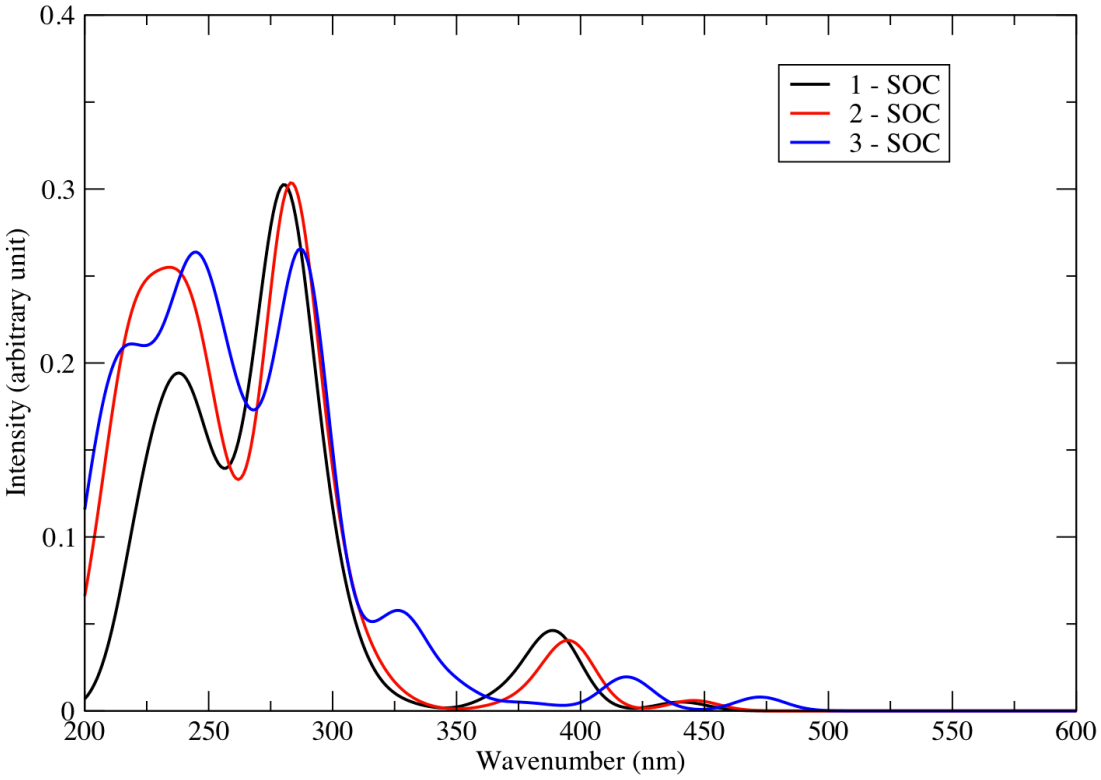

Figure S2. SOC-TD-DFT absorption spectra of complexes **1**, **2** and **3**.

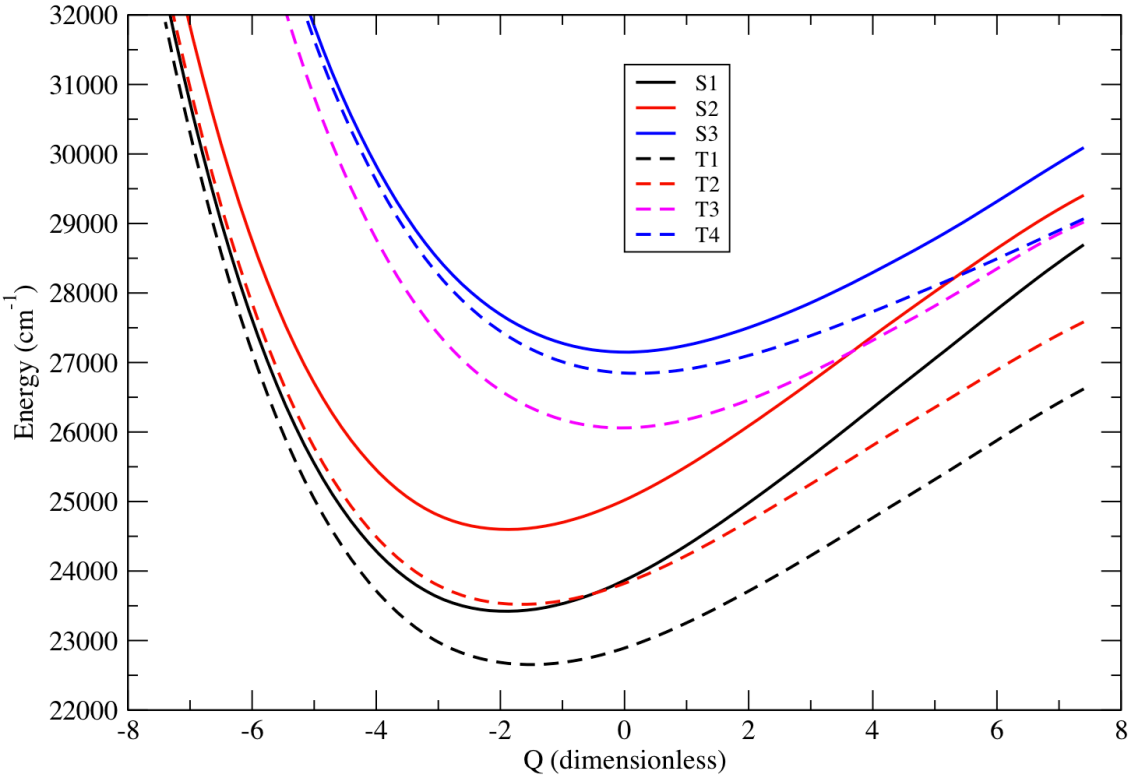
S1
S2
S3
T1
T2
T3
T4
Energy (cm-1)
Q (dimensionless)
32000
31000
30000
29000
28000
27000
26000
25000
24000
23000
22000
-8
-6
-4
-2
0
2
4
6
8

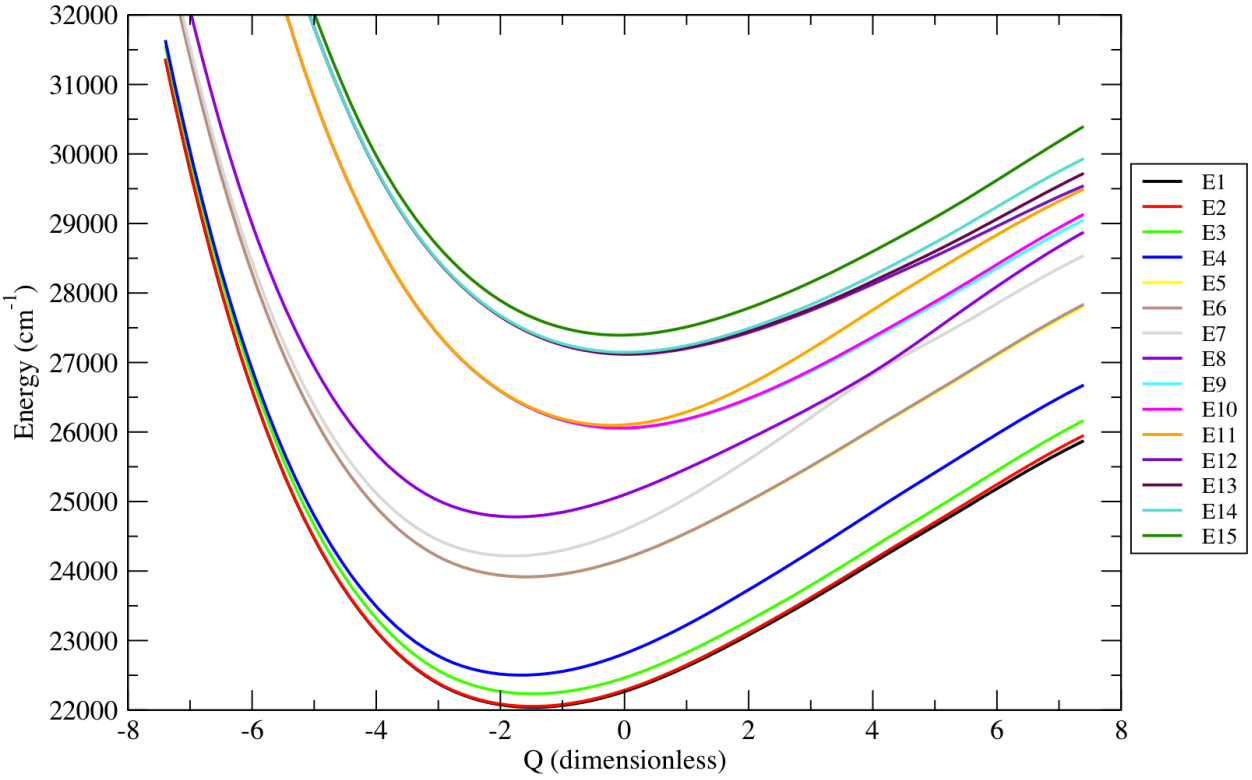

Figure S3. Potential energy curves associated to the low-lying excited states of [Re(Cl)(CO)$_3$(bpy)] **1** calculated without SOC(top) and with SOC (bottom) as function of the mass and frequency weighted Re-X stretching mode displacement from Franck-Condon (Q =0) (in CH_3CN).

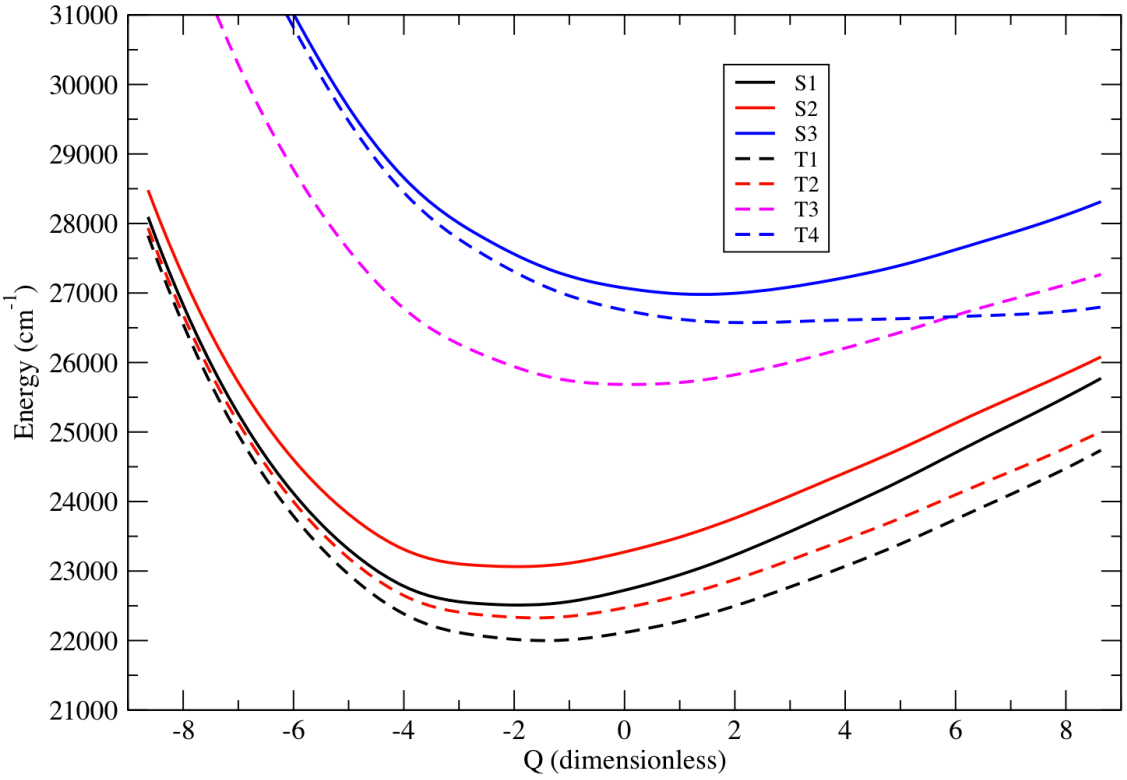
31000
30000
29000
28000
27000
26000
25000
24000
23000
22000
21000
Energy (cm-1)
-8
-6
-4
-2
0
2
4
6
8
Q (dimensionless)
S1
S2
S3
T1
T2
T3
T4

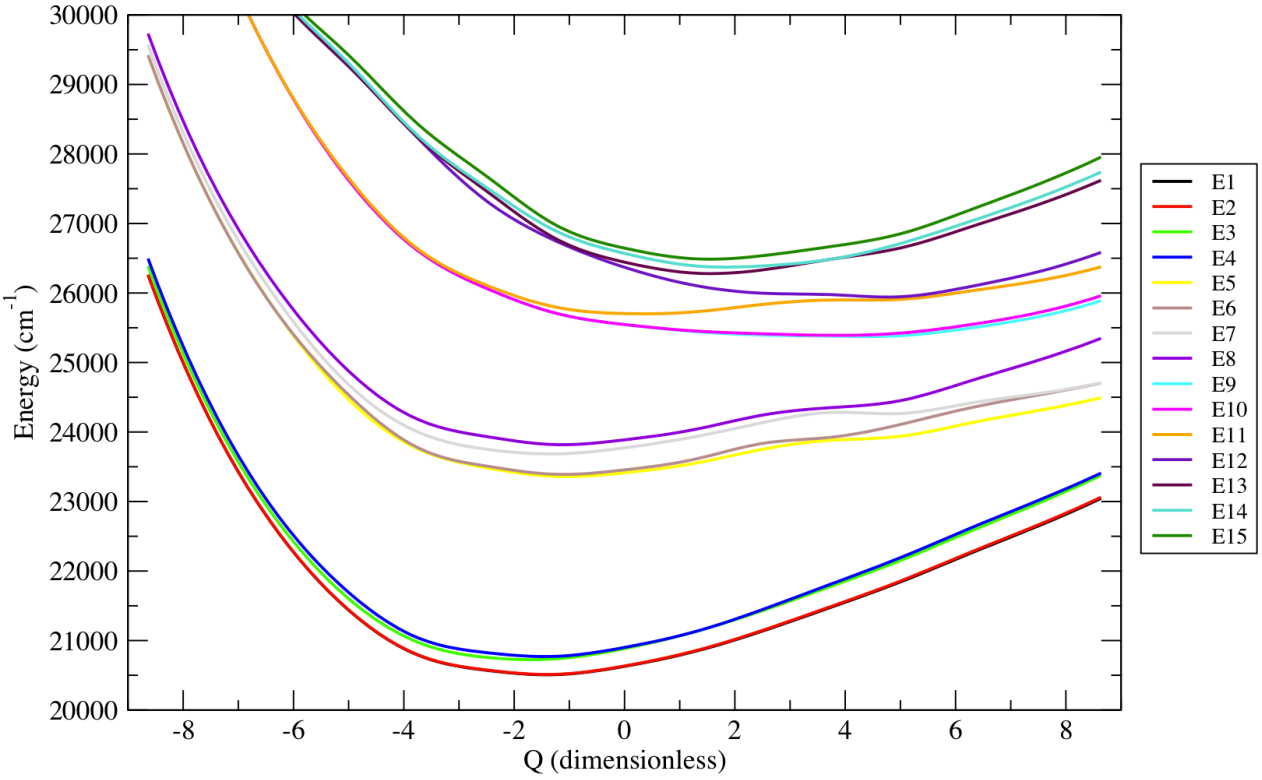

Figure S4. Potential energy curves associated to the low-lying excited states of [Re(I)$(CO)_3$(bpy)] **3** calculated without SOC(top) and with SOC (bottom) as function of the mass and frequency weighted Re-X stretching mode displacement from Franck-Condon (Q =0) (in CH_3CN)

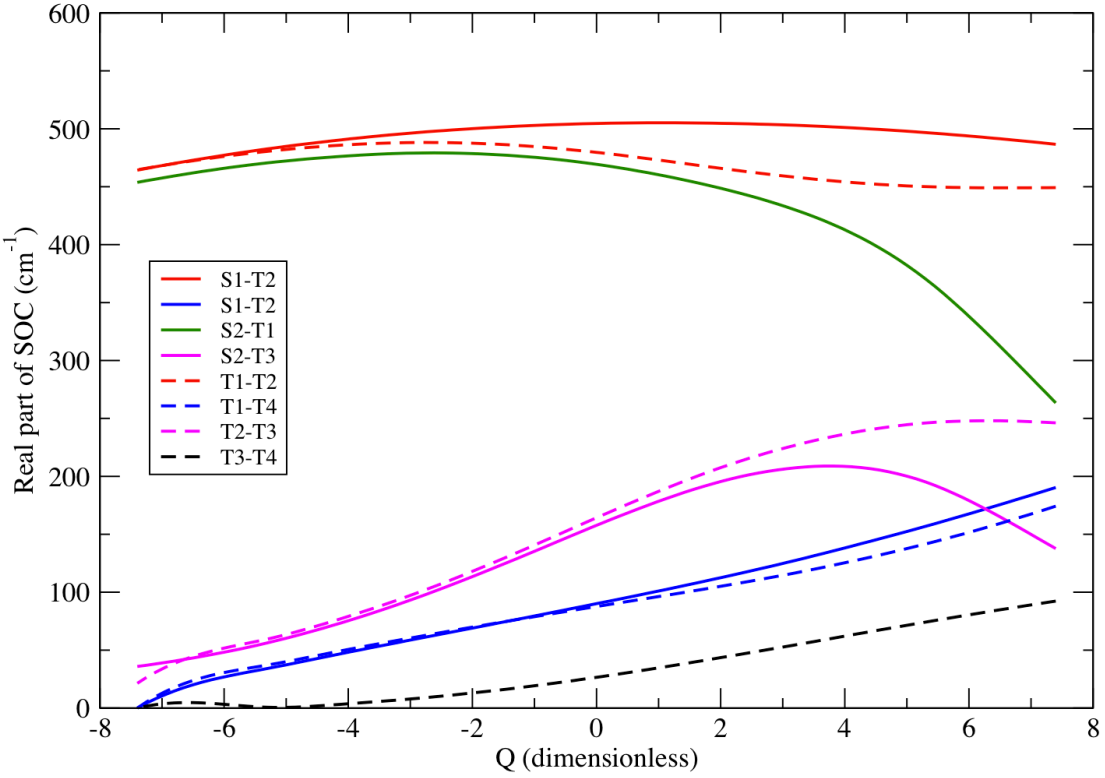
600
500
400
300
200
100
0
-8
-6
-4
-2
0
2
4
6
8
Real part of SOC (cm-1)
Q (dimensionless)
S1-T2
S1-T2
S2-T1
S2-T3
T1-T2
T1-T4
T2-T3
T3-T4

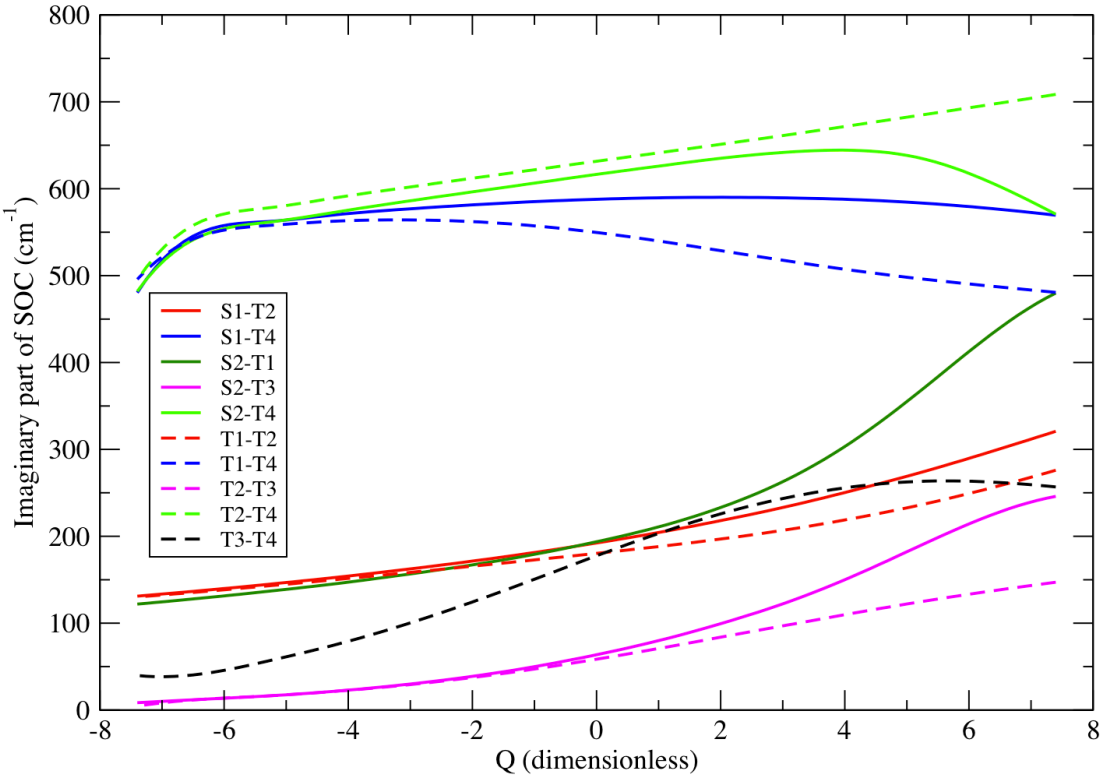

Figure S5. Variation of the SOC between the S_1, S_2, S_3, T_1, T_2, T_3 and T_4 electronic states of [Re(Cl)(CO)$_3$(bpy)] **1** calculated as a function of the mass and frequency weighted Re-X stretching mode displacement from Franck-Condon (Q =0) (in CH_3CN): absolute values of real contributions (top); absolute values of imaginary contributions (bottom).

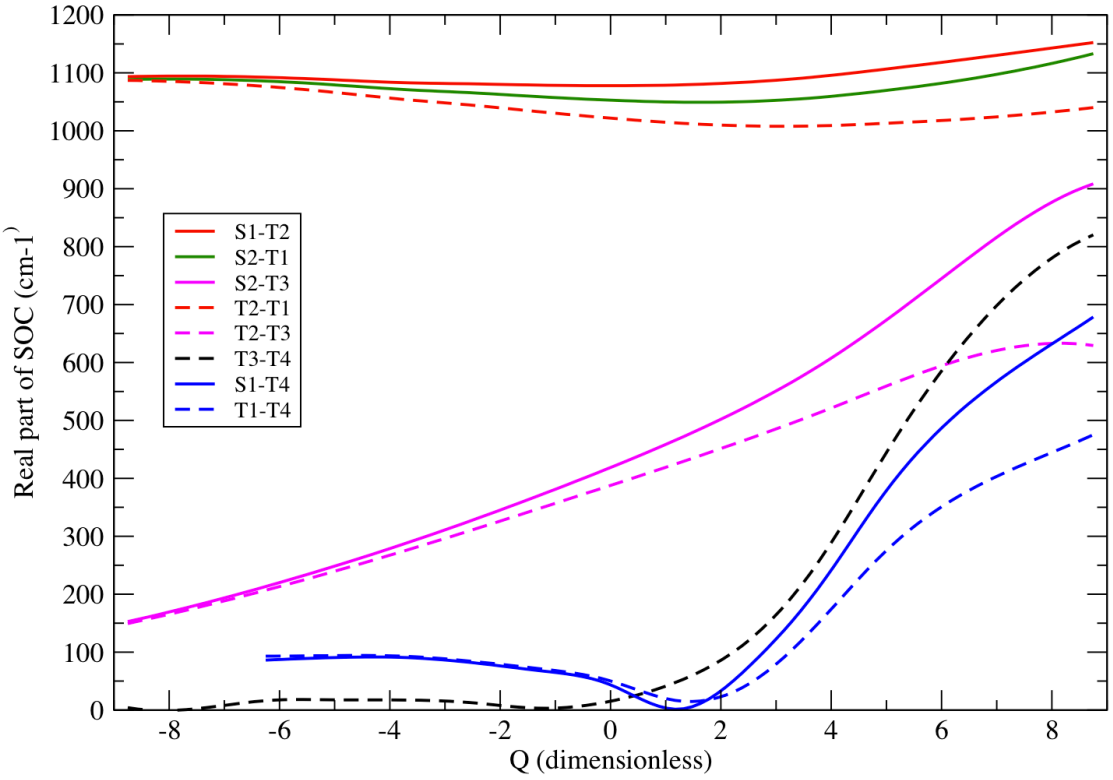
Real part of SOC (cm-1)
Q (dimensionless)
S1-T2
S2-T1
S2-T3
T2-T1
T2-T3
T3-T4
S1-T4
T1-T4
1200
1100
1000
900
800
700
600
500
400
300
200
100
0
-8
-6
-4
-2
0
2
4
6
8

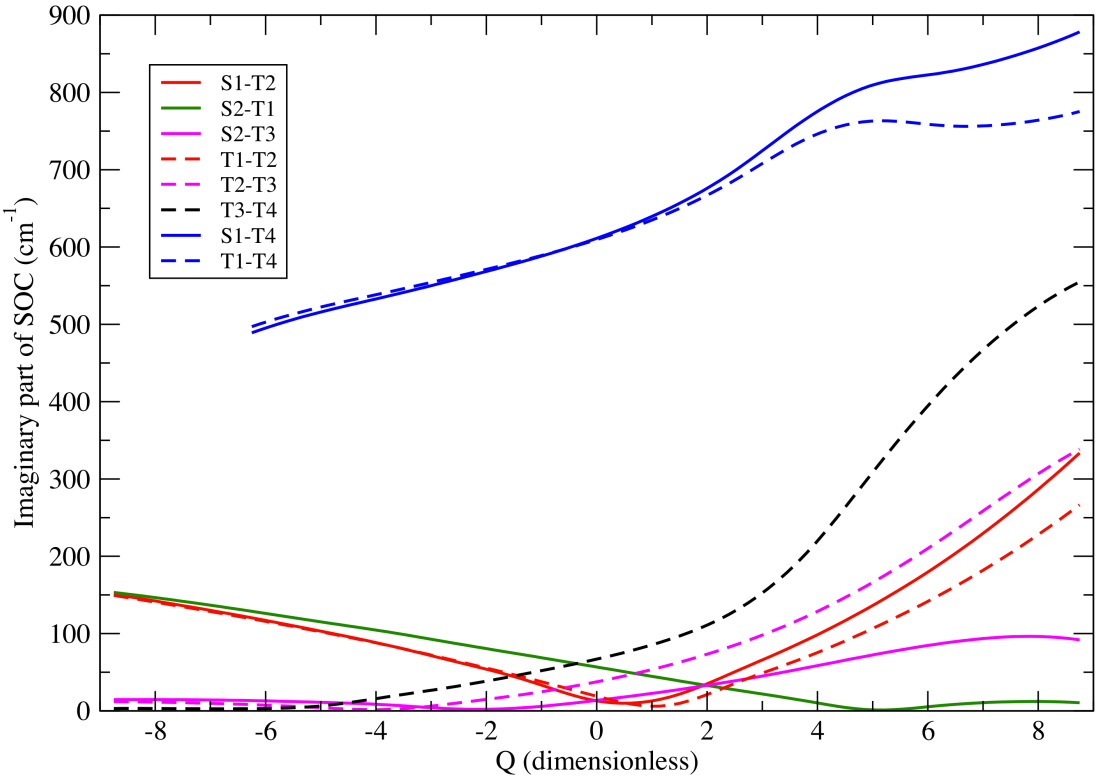

Figure S6. Variation of the SOC between the S_1, S_2, S_3, T_1, T_2, T_3 and T_4 electronic states of [Re(I)$(CO)_3$(bpy)] **3** calculated as function of the mass and frequency weighted Re-X stretching mode displacement from Franck-Condon (Q =0) (in CH_3CN): absolute values of real contributions (top); absolute values of imaginary contributions (bottom).

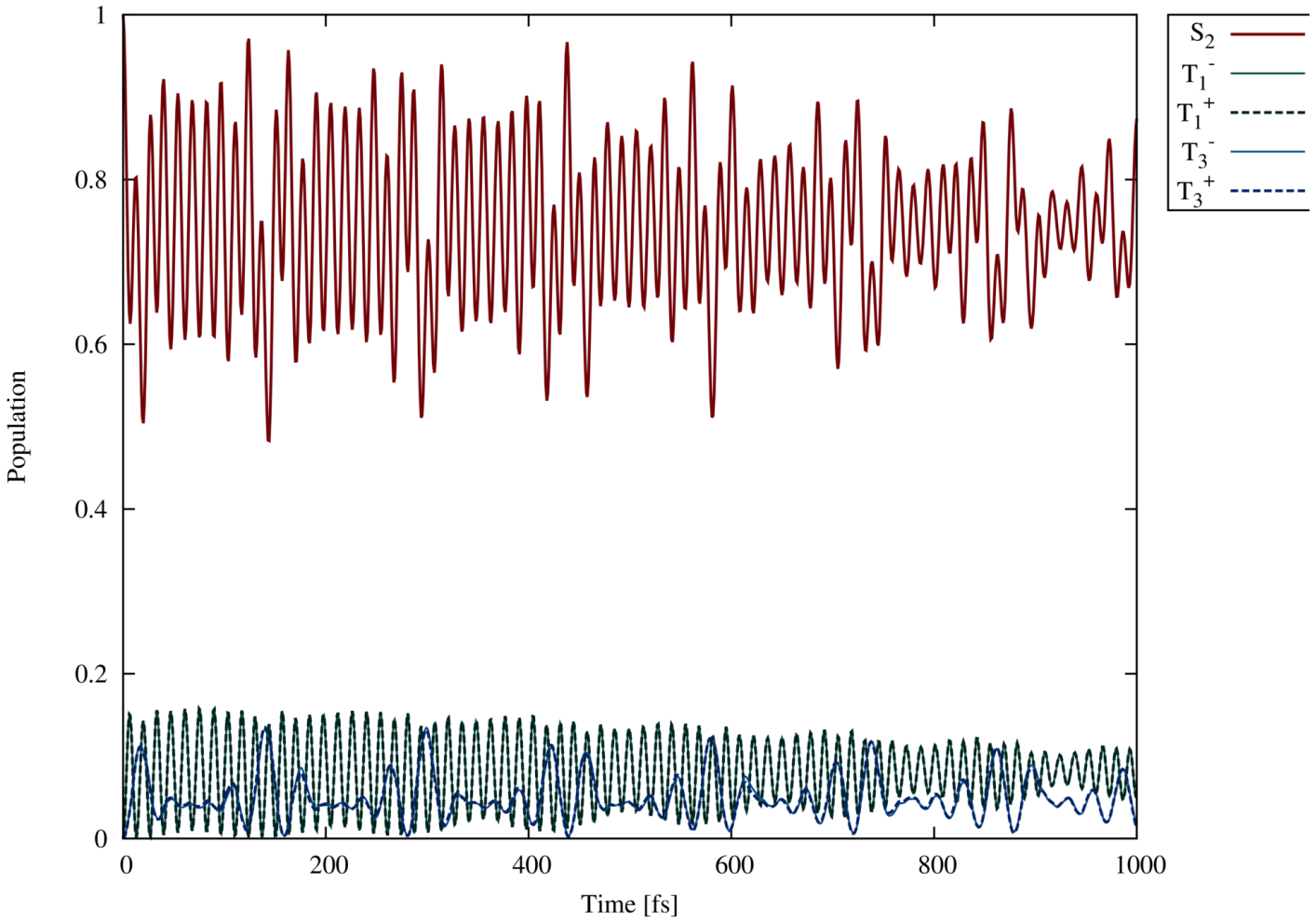

Figure S7. Time-evolution of the population of S_2, T_1 and T_3 excited states of [Re(Cl)(CO)$_3$(bpy)] within 1 ps. The population of the A' spin-orbit sub-levels of T_1 and T_3 is represented.

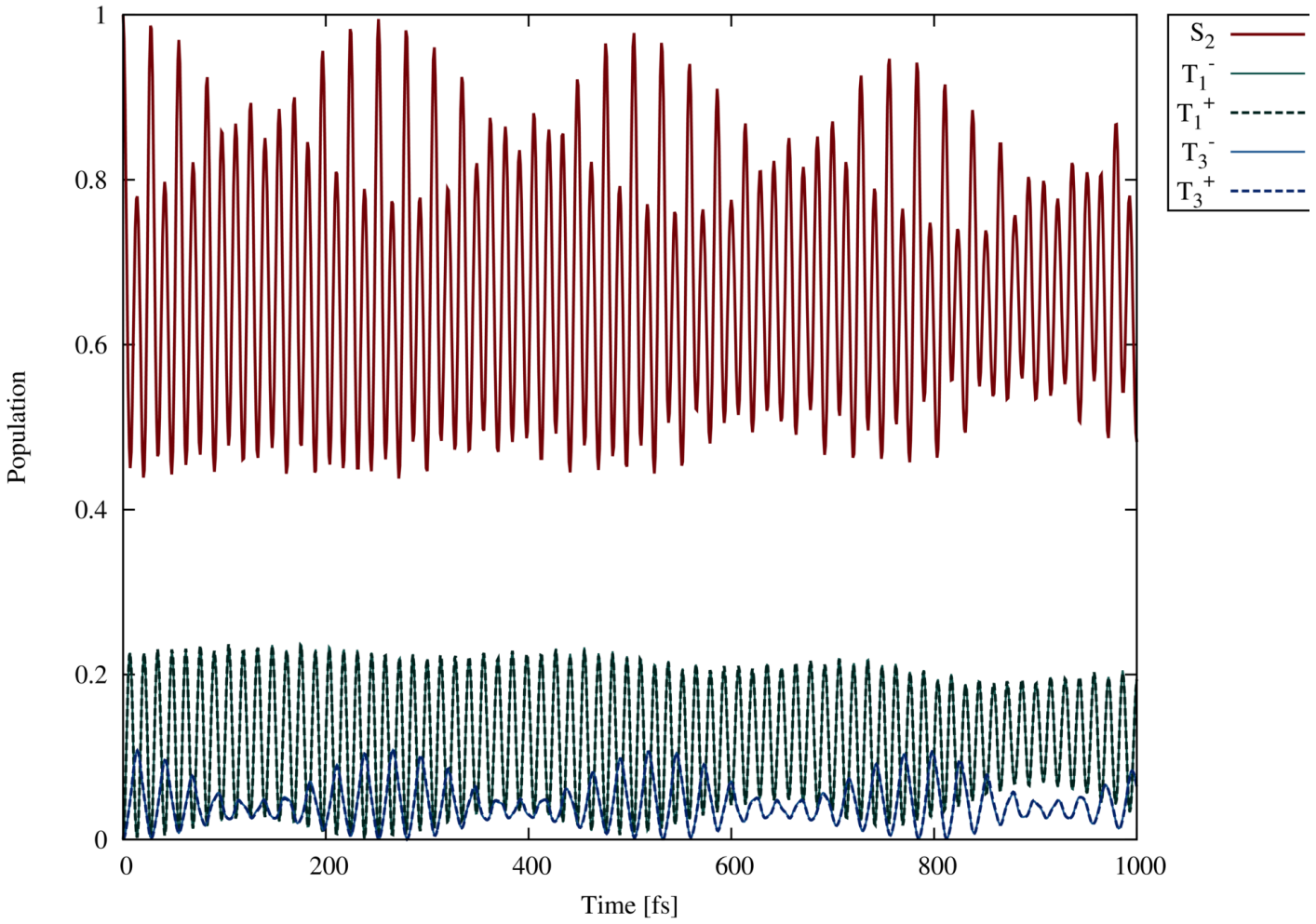

Figure S8. Time-evolution of the population of S_2, T_1 and T_3 excited states of [Re(Br)(CO)$_3$(bpy)] within 1 ps. The population of the A' spin-orbit sub-levels of T_1 and T_3 is represented.

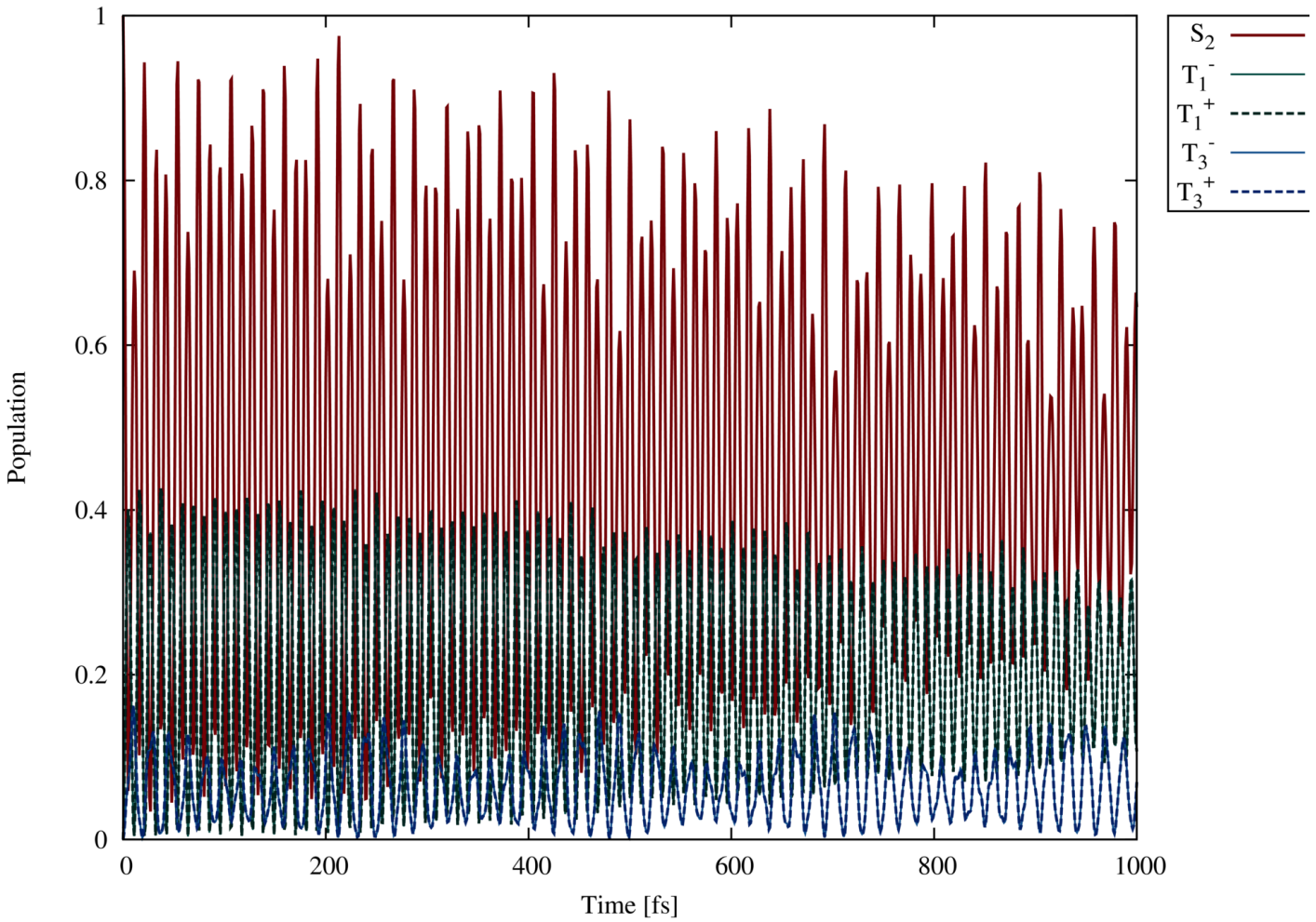

Figure S9. Time-evolution of the population of S_2, T_1 and T_3 excited states of [Re(I)$(CO)_3$(bpy)] within 1 ps. The population of the A' spin-orbit sub-levels of T_1 and T_3 is represented.

C.2 Spin-Vibronic Quantum Dynamics for Ultrafast Excited-State Processes

ACCOUNTS of chemical research

Article

pubs.acs.org/accounts

Spin-Vibronic Quantum Dynamics for Ultrafast Excited-State Processes

Published as part of the Accounts of Chemical Research special issue "Ultrafast Excited-State Processes in Inorganic Systems".

Julien Eng, Christophe Gourlaouen, Etienne Gindensperger,* and Chantal Daniel*

Laboratoire de Chimie Quantique, Institut de Chimie UMR-7177, Université de Strasbourg−CNRS, 1 Rue Blaise Pascal BP 296/R8, F-67008 Strasbourg, France

CONSPECTUS: Ultrafast intersystem crossing (ISC) processes coupled to nuclear relaxation and solvation dynamics play a central role in the photophysics and photochemistry of a wide range of transition metal complexes. These phenomena occurring within a few hundred femtoseconds are investigated experimentally by ultrafast picosecond and femtosecond transient absorption or luminescence spectroscopies, and optical laser pump−X-ray probe techniques using picosecond and femtosecond X-ray pulses. The interpretation of ultrafast structural changes, time-resolved spectra, quantum yields, and time scales of elementary processes or transient lifetimes needs robust theoretical tools combining state-of-the-art quantum chemistry and developments in quantum dynamics for solving the electronic and nuclear problems. Multimode molecular dynamics beyond the Born−Oppenheimer approximation has been successfully applied to many small polyatomic systems. Its application to large molecules containing a transition metal atom is still a challenge because of the nuclear dimensionality of the problem, the high density of electronic excited states, and the spin−orbit coupling effects.

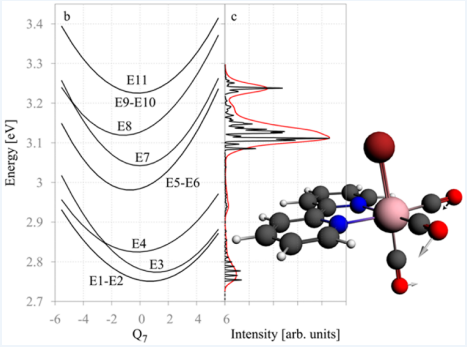

Rhenium(I) α-diimine carbonyl complexes, $[Re(L)(CO)_3(N,N)]^{n+}$ are thermally and photochemically robust and highly flexible synthetically. Structural variations of the N,N and L ligands affect the spectroscopy, the photophysics, and the photochemistry of these chromophores easily incorporated into a complex environment. Visible light absorption opens the route to a wide range of applications such as sensors, probes, or emissive labels for imaging biomolecules. Halide complexes $[Re(X)(CO)_3(bpy)]$ (X = Cl, Br, or I; bpy = 2,2′-bipyridine) exhibit complex electronic structure and large spin−orbit effects that do not correlate with the heavy atom effects. Indeed, the ^{1}MLCT → ^{3}MLCT intersystem crossing (ISC) kinetics is slower than in $[Ru(bpy)_3]^{2+}$ or $[Fe(bpy)_3]^{2+}$ despite the presence of a third-row transition metal. Counterintuitively, singlet excited-state lifetime increases on going from Cl (85 fs) to Br (128 fs) and to I (152 fs). Moreover, correlation between the Re−X stretching mode and the rate of ISC is observed.

In this Account, we emphasize on the role of spin-vibronic coupling on the mechanism of ultrafast ISC put in evidence in $[Re(Br)(CO)_3(bpy)]$. For this purpose, we have developed a model Hamiltonian for solving an 11 electronic excited states multimode problem including vibronic and SO coupling within the linear vibronic coupling (LVC) approximation and the assumption of harmonic potentials. The presence of a central metal atom coupled to rigid ligands, such as α-diimine, ensures nuclear motion of small amplitudes and *a priori* justifies the use of the LVC model. The simulation of the ultrafast dynamics by wavepacket propagations using the multiconfiguration time-dependent Hartree (MCTDH) method is based on density functional theory (DFT), and its time-dependent extension to excited states (TD-DFT) electronic structure data. We believe that the interplay between time-resolved experiments and these pioneering simulations covering the first picoseconds and including spin-vibronic coupling will promote a number of quantum dynamical studies that will contribute to a better understanding of ultrafast processes in a wide range of organic and inorganic chromophores easily incorporated in biosystems or supramolecular devices for specific functions.

1. INTRODUCTION

Ultrafast excited state processes play a central role in the photophysics and photochemistry of transition metal complexes.[1−7] Understanding and controlling the decay pathways via the low-lying singlet and triplet states manifold within the first 100 ps is key to their resourceful applications in photonics. Most of the time very short-lived metal-to-ligand-charge-transfer (MLCT) states control the kinetics of singlet−singlet and triplet−triplet internal conversion (IC) and singlet−triplet

Received: October 4, 2014
Published: February 3, 2015

DOI: 10.1021/ar500369r
Acc. Chem. Res. 2015, 48, 809−817

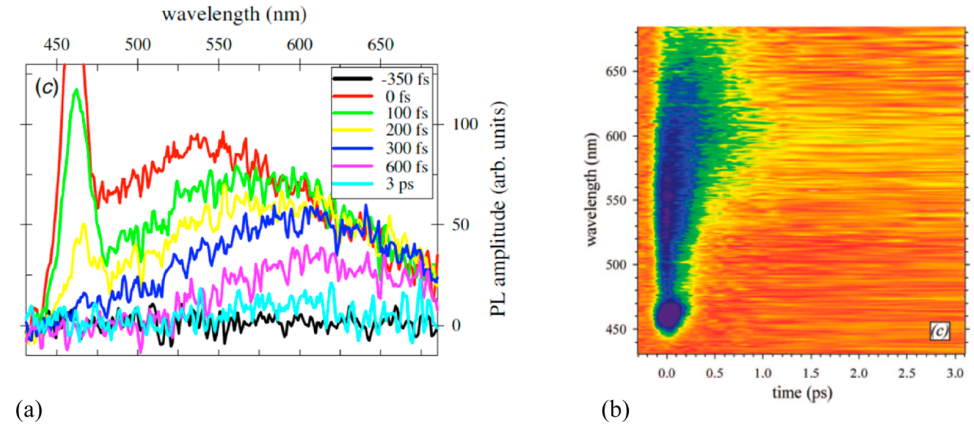

Figure 1. (a) Luminescence spectrum of $[Re(Br)(CO)_3bpy]$ in CH_3CN measured at selected time delays after 400 nm excitation. (b) Two-dimensional plot of time-resolved luminescence spectrum of $[Re(Br)(CO)_3bpy]$ in CH_3CN measured after 400 nm excitation. Adapted with permission from ref 18. Copyright 2008 American Chemical Society.

intersystem crossing (ISC) occurring immediately after light absorption within a few tens of femtseconds to a few tens of picoseconds.[8] Solvation dynamics and presence of low-lying metal-centered (MC) or intraligand (IL) charge transfer states may take part in the complicated mechanism of deactivation.[9−14]

Ultrafast picosecond and femtosecond transient absorption or luminescence spectroscopies and optical laser pump-X-ray probe techniques using picosecond and femtosecond X-ray pulses are the experiments of choice for deciphering the molecular electronic and conformational changes in real time.[15−18] Interpretation of time-resolved spectra and data from these sophisticated techniques needs solid developments in theory. Quantum chemistry has to handle high densities of various close-lying electronic excited states in a limited domain of energy (within 1.5 eV or 12 000 cm^{-1}) including relativistic effects, especially spin−orbit coupling (SOC).[19−21] Quantum dynamics has to treat dynamical processes that are not confined to a single electronic potential energy surface and that violate the Born−Oppenheimer separation of electronic and nuclear motions, taking into account nonadiabatic coupling between two or more electronic states via several vibrational modes.[22] Various methods of electronic structure theory are able to calculate electronic excited states and potential energy curves in transition metal complexes. Time-dependent density functional theory (TD-DFT)[23−25] and complete-active-space self-consistent-field (CASSCF)[26] combined with CAS-perturbation second order (CASPT2)[27,28] are among the most popular methods for computing electronic excited states and associated nuclear forces in this class of molecules with reasonable accuracy. The bottleneck is the computation of accurate multidimensional potential energy surfaces, seat of the ultrafast dynamics observed in time-resolved experiments. In order to bypass these difficulties two strategies can be considered: (i) *ab initio* molecular dynamics where efficient electronic structure methods are coupled to classical trajectory-based approaches;[29] (ii) quantum dynamics where both electronic and nuclear wave functions are treated exactly within a given level of approximation.[22,30−32] Molecular dynamics, usually coupled to DFT methods and extended recently to the nonadiabatic regime,[29,33,34] is adapted to large systems involving a restricted number of active electronic excited states in the dynamical process. The applicability of the full quantum approach is limited by the nuclear dimensionality and requires very robust electronic structure methods for excited states.[35] An additional difficulty in transition metal complexes is the simultaneous treatment of nonadiabatic and spin−orbit coupling.[36−39]

A recent promising approach, applied[5] to the spin crossover complex $[Fe(bpy)_3]^{2+}$,[5] has been developed by C. M. Marian et al.[40,41] This method is based on time-dependent calculations of ISC rates in the multimode harmonic oscillator and Condon approximations and beyond, where the electronic spin−orbit matrix elements depend linearly on the nuclear coordinates within a spin-vibronic coupling scheme. The ISC rate can be decomposed into three contributions, namely, direct, mixed direct-vibronic, and vibronic.

The first simulation based on TD-DFT energies and forces (gradient and Hessian) computed on-the-fly and introducing both vibronic and SO coupling effects into the Tully's trajectory surface hopping algorithm has been able to reproduce semiquantitatively the ultrafast relaxation of the photoexcited ^{1}MLCT state of $[Ru(bpy)_3]^{2+}$ (bpy = 2,2′-bipyridine) followed by ISC to the lowest ^{3}MLCT state.[42]

Combined effects of Jahn−Teller (JT) and SOC on the adiabatic PES and electronic spectra of a series of first-row transition metal halides MF_3 (M = Mn, Co, Ti, Cr, and Ni) have been recently investigated from first-principles methods based on the derivation of a Hamiltonian expanded up to linear, quadratic, and higher order in normal mode displacements active for JT distorsions and including SO up to first order in these modes.[36,43] This original work has put in evidence SO induced JT distorsions not detectable by the standard model in which SOC is considered as a static property independent of the nuclear motion.

These pioneering dynamical simulations performed on transition metal complexes are far from being routine and need specific developments to be applicable to a wide range of systems and ultrafast phenomena circumscribed by spin-vibronic coupling.

In order to decipher the photophysics of rhenium(I) tricarbonyl complexes, $[Re(X)(CO)_3bpy)]$ (X = Cl, Br, or I; bpy = 2,2′-bipyridine), recently investigated by means of ultrafast luminescence spectroscopy,[18] we have developed an effective matrix Hamiltonian for solving an 11 electronic excited states multimode problem including vibronic and SO coupling within the simplified linear vibronic coupling (LVC) model and

DOI: 10.1021/ar500369r
Acc. Chem. Res. 2015, 48, 809−817

Scheme 1. Change of Electronic Density Induced by Excitation of the Electronic Ground State of [Re(Br)(CO)$_3$(bpy)] in the Lowest Singlet (S1 and S2) and Triplet (T1, T2, and T3) Excited States[a]

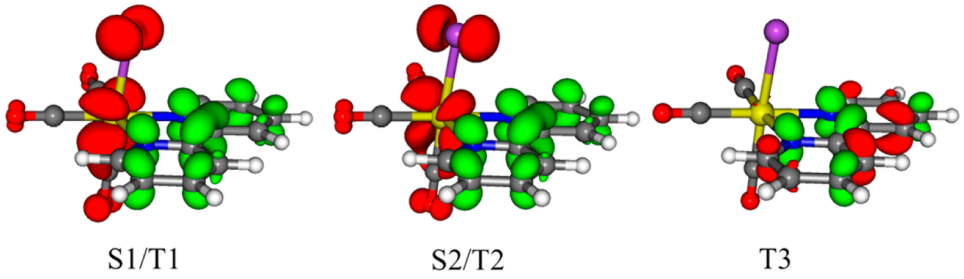

[a]In red, loss; in green, gain.

the assumption of harmonic diabatic potentials.[22,30] Our aim is to shed light on the following fundamental questions: (i) Why does the singlet excited-state lifetime counterintuitively increase on going from chloride (85 fs) to bromide (128 fs) and iodide (152 fs), whereas SOC between the singlet and triplet states increases within the series? (ii) How can we explain the correlation observed between the ISC kinetics and vibrational period of the Re−X stretching mode in similar complexes? (iii) How can we interpret the time-resolved luminescence spectra observed in CH_3CN after absorption at 400 nm, namely, a band between 500 and 550 nm (τ_1 80−150 fs), an intermediate band at about 600 nm (τ_2 0.3−1.2 ps), and a long-lived signal at 600−610 nm ($\tau_3 \approx 10$ μs) (Figure 1)?

2. QUANTUM CHEMISTRY OF [Re(Br)(CO)$_3$bpy)]

The details about the electronic properties of the series [Re(X)(CO)$_3$bpy)] (X = Cl, Br, I) can be found in recent articles by Záliš et al. and by us.[18,19,44−46] By combining spectroscopic measurements and CASSCF/MS-CASPT2 and TD-DFT calculations, we have shown that whereas both spin-free and spin−orbit quantum chemical calculations simulate UV−vis electronic spectra of [Re(X)(CO)$_3$bpy)] (X = Cl, Br, or I) complexes in a reasonable agreement with experiment, they give a very different interpretation of the absorption bands and only the SO treatment can account for the observed spectral features.[44,46] Going further we computed the spin−orbit coupled TD-DFT potential energy curves as a function of the Re−X bond elongation, as well as of the Re−X bond stretching modes, for the electronic ground state and the lowest excited states of [Re(X)(CO)$_3$(bpy)] (X = Cl, Br, or I) taking into account solvent effects.[19,46] When SOC is activated the five lowest electronic excited states, S1, S2, T1, T2, and T3, the electronic densities of which are depicted in Scheme 1 for [Re(Br)(CO)$_3$(bpy)], generate 11 "spin−orbit" states of mixed metal-to-ligand-charge-transfer MLCT/halide-LCT character within 0.5 eV, see Scheme 2 and Figure 2 further below.

According to the spin C_s double group symmetry rules, T1 and T3 (^{3}A″) states generate two A′ and one A″ "spin−orbit" states, T2 (^{3}A′) generates two A″ and one A′ "spin−orbit" states, S1 (^{1}A″) generates one A″ state, and S2 (^{1}A′) generates one A′ state. The two lowest A′ and A″ states, E1 and E2, are degenerate and composed of 66%T1 and 30%T2, whereas the next states, E3 (A′) and E4 (A″), are composed of 85%T1/11% S2 and 44%S1/50%T2, respectively. E5 and E6 of A″ and A′ symmetry, respectively, and counterparts of E1, E2, are degenerate, and are composed of 67%T2 and 31%T1. E7 (A″) is the counterpart of E4 and is composed of 51%T2 and 48%S1. The upper state E8 of symmetry A′ is characterized by

Scheme 2. Representation of the Interplay of Intersystem Crossing (ISC) and Internal Conversion (IC) Mechanisms within the Singlet and Triplet Manifolds of [Re(Br)(CO)$_3$(bpy)]

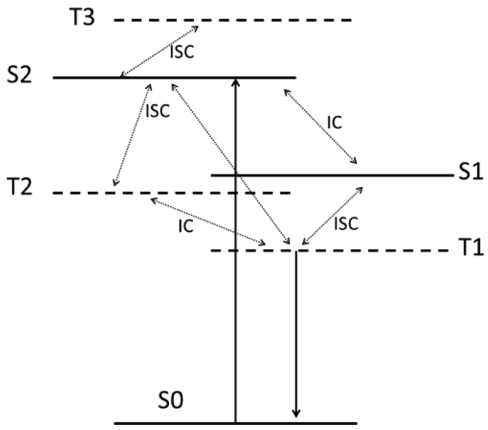

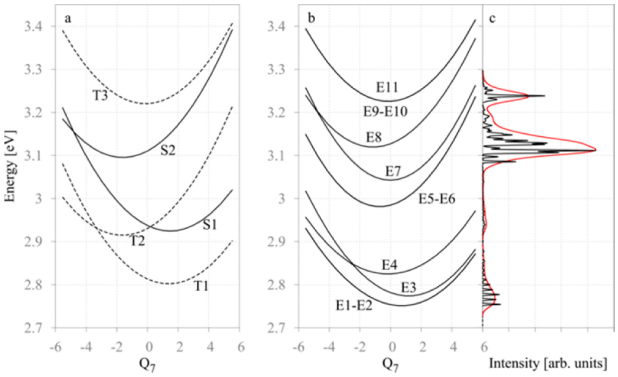

Figure 2. (a) Diabatic potential energy curves along Q_7. Each triplet state is triply degenerate. (b) Corresponding adiabatic potential energy curves. (c) Calculated absorption spectrum with its envelope after excitation of the S2 state. S2 (E8) is the strongly absorbing A′ state.

an oscillator strength of 0.036 and is described by 70% of the S2 (^{1}A′) absorbing state, with a contribution of 10% from T3 (^{3}A″). The E9 (A″) and E10 (A′) remain of quasi-pure triplet character (95% T3), while E11 (A′) is the counterpart of E8 with 82%T3/16%S2.

From the lowest electronic excited state optimized geometries, we can extract seven minima after perturbative SOC treatment of each state in its optimized structure.[46] From these electronic structure calculations performed in CH_3CN, we have

DOI: 10.1021/ar500369r
Acc. Chem. Res. 2015, 48, 809−817

proposed the following qualitative mechanism for the deactivation pathway of [Re(Br)(CO)$_3$(bpy)]. At very short time-scale, the activation of the Re−Br normal mode in S2, strongly correlated to the τ_1 time-scale (128 fs), initiates the decay to S2 minimum and S1/T2. The four upper "spin-orbit" states of A′ and A″ symmetries are potentially luminescent in the 510−550 nm energy domain. As soon as S1 and T1 are populated within the τ_2 time-scale (470 fs) correlated to SOC, the two "spin-orbit" states A″ and A′ calculated at 572 and 582 nm can luminesce as well at about 580 nm. The only purely phosphorescent state is the "spin-orbit" state calculated at 610 nm that contributes to the long time-scale decay observed at 600−620 nm. Exploratory wavepacket propagations on spin−orbit coupled potential energy curves has been able to simulate partly the ultrafast ISC process observed experimentally via the A′ channels pointing to the importance of vibronic spin−orbit coupling in transition metal complexes. This study[46] proposed a new picture for a comprehensive understanding of ultrafast ISC processes in transition metal complexes. However, the one-dimensional "spin-orbit" potential energy curves give a crude approximation of the complicated set of potential energy surfaces underlying the ultrafast decay mechanism after irradiation to S2. Indeed conical intersections may be present in the adiabatic multidimensional PES and vibronic coupling should play a role in the decay mechanism.

In this Account, we report the first quantum dynamical simulation of ultrafast nonradiative decay in the prototype transition metal complex [Re(Br)(CO)$_3$(bpy)], involving the five low-lying singlet and triplet excited states. The multimode dynamics of these five low-lying excited states are investigated on the basis of DFT and TD-DFT electronic structure data taking into account SOC in a spin-vibronic coupling model.

3. THEORETICAL BACKGROUND AND METHODOLOGY

3.1. The Model Hamiltonian

Five low-lying "spin-free" singlet and triplet excited states of [Re(Br)(CO)$_3$bpy] are in the energy domain close to the experimental 400 nm (3.10 eV) excitation energy, namely, S2 (a^1A') calculated at 3.13 eV (399 nm) with an oscillator strength $f = 5.1 \times 10^{-2}$, S1 (a^1A'') calculated at 2.96 eV ($f = 0.17 \times 10^{-2}$), and the lowest triplets T3 (b^3A''), T2 (a^3A'), and T1 (a^3A'') calculated at 3.22, 2.93, and 2.84 eV, respectively.[44,46]

In the Pauli approximation, the electronic Hamiltonian $\mathbf{H}^{el}$ is expressed as the sum of the nonrelativistic (electrostatic), $\mathbf{H}^{es}$, and the "spin−orbit", $\mathbf{H}^{SO}$, Hamiltonians:

$$\mathbf{H}^{el} = \mathbf{H}^{es} + \mathbf{H}^{SO}$$

The $\mathbf{H}^{es}$ Hamiltonian contains the energy of the "spin-free" states as diagonal elements (triply degenerate for the triplets), while the $\mathbf{H}^{SO}$ Hamiltonian is comprised of the SOC off-diagonal terms. If one diagonalizes the $\mathbf{H}^{el}$ Hamiltonian, one recovers the energy of the "spin-orbit" states.

The 11 × 11 (2 singlets + 3 × 3 triplet components) total Hamiltonian is expressed as

$$\mathbf{H} = T_N\mathbf{1} + \mathbf{H}^{el}$$

where T_N is the kinetic energy of the nuclei, $\mathbf{1}$ is the identity matrix, and $\mathbf{H}^{el}$ depends on the nuclear coordinates. Within the vibronic coupling approach,[22] the effective matrix Hamiltonian reads

$$\mathbf{H} = (T_N + V_0)\mathbf{1} + \mathbf{W}$$

where V_0 is the ground state potential energy surface, here taken to be harmonic with vibrational frequencies ω_i along dimensionless normal coordinates Q_i determined from the electronic structure calculations at the ground state equilibrium geometry (Franck−Condon point, FC). The matrix Hamiltonian $\mathbf{W}$ contains the spin−orbit coupling terms plus the vibronic coupling terms. The vibronic coupling terms are obtained from a Taylor expansion of the "spin-free" potential energy surfaces up to first order around FC.[22]

The multistate vibronic interactions within the set of the five "spin-free" electronic excited states ($n = 1-5$) are deduced from the diabatic electronic representation including all pertinent coupling terms, namely, the intrastate κ^n and interstate $\lambda^{n,m}$ vibronic coupling constants between the n and m electronic states and the (complex-valued) $\eta^{n,m}$ SOC constants deduced from the electronic structure calculations. Within the LVC approach, the nonvanishing intrastate κ^n and interstate $\lambda^{n,m}$ coupling constants are those for which the product of the irreducible representations of states n and m and of the nuclear normal mode coordinate Q_i contains the totally symmetric representation Γ_A (A′ in C_s):

$$\Gamma_n \otimes \Gamma_{Q_i} \otimes \Gamma_m \subset \Gamma_A$$

In the C_s symmetry point group, only vibrational modes of a′ symmetry can have nonvanishing κ^n coupling constant while only a″ vibrational modes will contribute to the off-diagonal coupling $\lambda^{n,m}$. The coupling constants can be obtained from the following expressions[22] evaluated at $Q_i = 0$:

$$\kappa_i^n = \frac{\partial V_n}{\partial Q_i}$$

$$\lambda_i^{n,m} = \left(\frac{1}{8}\frac{\partial^2}{\partial {Q_i}^2}(|V_m - V_n|^2)\right)^{1/2}$$

where V_n is the adiabatic potential energy surface of the "spin-free" state n. That is, only the gradients and the Hessians at FC are needed within this model. The SOC will generally also depend on the nuclear displacements. However, they are kept constant here, that is, the FC values are used. With those ingredients, the unitary potential energy matrix, $\mathbf{W}$, is

$$\mathbf{W} = \begin{pmatrix} \mathbf{W}^{T1,T1} & \mathbf{W}^{T1,T2} & 0 & \mathbf{W}^{T1,S2} & 0 \\ \mathbf{W}^{*T1,T2} & \mathbf{W}^{T2,T2} & \mathbf{W}^{T2,S1} & 0 & \mathbf{W}^{T2,T3} \\ 0 & \mathbf{W}^{*T2,S1} & \mathbf{W}^{S1,S1} & \mathbf{W}^{S1,S2} & 0 \\ \mathbf{W}^{*T1,S2} & 0 & \mathbf{W}^{*S1,S2} & \mathbf{W}^{S2,S2} & \mathbf{W}^{S2,T3} \\ 0 & \mathbf{W}^{*T2,T3} & 0 & \mathbf{W}^{*S2,T3} & \mathbf{W}^{T3,T3} \end{pmatrix}$$

where the asterisk stands for the conjugate transpose and with the submatrices

DOI: 10.1021/ar500369r
Acc. Chem. Res. 2015, 48, 809−817

Table 1. List of the Parameters Entering the Model Hamiltonian[a]

mode	ω	κ				
		S1	S2	T1	T2	T3
7 (a′)	0.0116	−0.0172	0.0187	−0.0161	0.0190	0.0015
11 (a′)	0.0188	0.0090	0.0091	0.0002	−0.0006	0.0056
13 (a′)	0.0229	−0.0289	−0.0271	−0.0261	−0.0322	0.0133
30 (a′)	0.0792	−0.0187	0.0404	−0.0196	0.0433	0.0033

mode	ω	λ^{S1S2}	λ^{T1T2}
8 (a″)	0.0118	0.0114	0.0086
23 (a″)	0.0601	0.0237	0.0190

State	E		η	
state	calcd	adjd		
S1 (A″)	2.96	2.94	S1T2	0.0769 + 0.0186i
S2 (A′)	3.13	3.11	S2T1	−0.0719 − 0.0196i
T1 (A″)	2.84	2.81	S2T3	0.0274 + 0.0056i
T2 (A′)	2.93	2.93	T1T2	0.0719 + 0.0177i
T3 (A″)	3.22	3.22	T2T3	−0.0270 + 0.0046i

[a]Values are given in eV. E is the vertical excitation energy. Calcd indicates the calculated values from ref 46. Adjd indicates the adjusted values used in this work.

$$\mathbf{W}^{n,n} = E_n + \sum_{i\in a'} \kappa_i^n Q_i; \quad \mathbf{W}^{S1,S2} = \sum_{j\in a''} \lambda_j^{S1,S2} Q_j;$$

$$\mathbf{W}^{S2,T3} = (\eta^*_{S2T3};\ 0;\ \eta_{S2T3});$$

$$\mathbf{W}^{Tn,Sm} = \begin{pmatrix} \eta_{SmTn} \\ 0 \\ \eta^*_{SmTn} \end{pmatrix}, \ n, m = 1, 2;$$

$$\mathbf{W}^{T1,T2} = \begin{pmatrix} \sum_{j\in a''} \lambda_j^{T1,T2} Q_j & \eta_{T1T2} & 0 \\ -\eta^*_{T1T2} & \sum_{j\in a''} \lambda_j^{T1,T2} Q_j & \eta_{T1T2} \\ 0 & -\eta^*_{T1T2} & \sum_{j\in a''} \lambda_j^{T1,T2} Q_j \end{pmatrix};$$

$$\mathbf{W}^{T2,T3} = \begin{pmatrix} 0 & \eta_{T2T3} & 0 \\ -\eta^*_{T2T3} & 0 & \eta_{T2T3} \\ 0 & -\eta^*_{T2T3} & 0 \end{pmatrix}$$

In each submatrix, the triplet components are ordered by ascending m_s values. E_n is the vertical excitation energy of the "spin-free" state n. Note that some of the zeros in $\mathbf{W}$ come from (C_s) symmetry constraint and others from the fact that the corresponding computed coupling constants have very small values and are thus disregarded in the present study. In addition, coupling to higher lying states, in particular S3 and T4, is not included in the study along with the T2/T3 vibronic coupling neglected here (see $\mathbf{W}^{T2,T3}$ above). Note that T3 is of IL_{bpy} nature, in contrast to all other states of MLCT/XLCT nature (see Scheme 1), and is included here mainly because it contributes to the "spin-orbit" absorbing state E8.

The proposed model Hamiltonian is probably the simplest one that can be constructed with only relatively few electronic structure data (all obtained at FC), but still treating explicitly all triplet components and thus accounting for the triplet's multiplicity.

3.2. Electronic Structure Data

The detailed data of the electronic structure calculations are reported elsewhere.[46] All the data used in the present work have been determined by means of DFT and TD-DFT methods including polarized continuum model (PCM)[47,48] solvent corrections and using the functional B3LYP[49] with all electrons and triple-ζ basis sets.[50] The scalar relativistic effects have been taken into account within the zero-order regular approximation (ZORA).[51] The SOC effects have been introduced according to a simplified relativistic perturbative TD-DFT formalism.[52] The TD-DFT calculations have been validated by accurate CASSCF/multistate-CASPT2 methods.[44]

3.3. Wavepacket Propagation by MCTDH

The time-dependent Schrödinger equation for the nuclei is solved by employing the MCTDH method.[53−55] Here, the multiconfiguration nuclear wave function is expressed as a Hartree product of time-dependent basis functions, known as single-particle functions. The wavepacket ansatz adapted to the present nonadiabatic problem corresponds to the multiset formulation.[54] The Heidelberg MCTDH Package[56] is used (version 8.4.9).

4. RESULTS

4.1. Vibrational Modes Selection

The gradients and Hessians of the energy have been computed analytically and numerically, respectively, at the FC geometry, to evaluate the κ^n and $\lambda^{n,m}$ coupling constants. The [Re(Br)-$(CO)_3$bpy]$^+$ complex possesses 78 internal degrees of freedom, among which 41 are of a′ symmetry and 37 are of a″ symmetry. All of the computed κ^n and $\lambda^{n,m}$ values are small, order of 10^{-2} to 10^{-3} eV. This is not surprising because the molecule is quite rigid, and moreover S1, S2, T1, and T2 are characterized by the same electronic structure. Based on the κ^n and $\lambda^{n,m}$ values, only six nuclear degrees of freedom, four a′ and two a″ modes, are included in the present dynamical study. The corresponding values entering the model Hamiltonian are provided in Table 1. The four a′ modes are divided in two groups. The first one includes the two vibrational modes, ν_{11} and ν_{13}, that involve stretching of the Re−Br bond; the modes are labeled according to increasing frequency. They are calculated to have frequencies

DOI: 10.1021/ar500369r
Acc. Chem. Res. 2015, 48, 809−817

of ω_{11} = 152 cm^{-1} and ω_{13} = 185 cm^{-1}. They both exhibit contributions of motion of the bpy moiety. The largest Re−Br stretch contribution is by far for the ν_{11} mode; it is relatively small for ν_{13}. These modes are included in the present treatment because of the experimentally found correlation between excited state lifetimes and the Re−Br vibrational frequency.[18] In fact, these two modes do have κ^n of the same sign for S1, T1, S2, and T2, meaning that they shift all those electronic states toward the same direction. This common sign is again not surprising, since we are dealing with charge transfer to the bpy (except T3): they all react the same if we stretch the Re−Br bond. However, the strongest nonadiabatic effect is obtained when the κ^n have opposite signs and largest absolute values. This is achieved here for two other a′ modes, ν_7 and ν_{30} of frequency ω_7 = 94 cm^{-1} and ω_{30} = 638 cm^{-1}. These modes both involve motion of the carbonyl groups. These motions of the CO groups have a different impact on the d_{xy} (involved in S0−S2/T2 transitions) and d_{yz} (involved in S0−S1/T1 transitions) orbitals of the metal, leading to the opposite sign in the coupling constants.

Among the a″ modes, a large number of them do not have a $\lambda^{n,m}$ coupling constant that leads to a coupling (the computed values are purely imaginary, meaning that S1/S2 on the one hand and T1/T2 on the other hand do not repel each other.) Interestingly, some modes are found at this level of description that couple at the same time S1 with S2 and T1 with T2. Large coupling constants are found for ν_8 (ω_8 = 95 cm^{-1}) and ν_{23} (ω_{23} = 485 cm^{-1}). These are both modes that involve symmetry breaking motions of the carbonyl groups. They are the nontotally symmetric companions of the totally symmetric ν_7 and ν_{30}.

These six modes are included for the study of the quantum dynamics of the [Re(Br)(CO)$_3$bpy] complex to gain access to the absorption spectrum and short-time electronic population dynamics.

4.2. Potential Energy Surfaces and Absorption Spectrum

The diabatic potential energy surfaces are used for the quantum dynamics. They are shown in Figure 2a along a single vibrational mode, Q_7. In Figure 2b, the 11 corresponding adiabatic potential energy curves are provided. These curves are obtained from the diagonalization of the diabatic Hamiltonian matrix. Figure 2c displays the associated absorption spectrum that is evaluated as the Fourier transform of the autocorrelation function obtained with MCTDH.[54] A total propagation time of 1 ps is used, after excitation of the S2 state.

In our calculations, we have used slightly adjusted vertical transition energies for S1, S2, and T1, see Table 1, variation of 0.03 eV at most. These values are adjusted in order to recover the computed transition energies of the "spin-orbit" states at FC. Indeed the state T4, excluded from the present study, interacts by spin−orbit with these three states. Its static effect is thus taken into account indirectly when using the adjusted values.

The diabatic potential energy curves (Figure 2a) show the intersections between S1/S2 and T1/T2. The vibronic off-diagonal term allows population transfer between these states. In contrast to the regular vibronic coupling Hamiltonian without SOC, the adiabatic energies at FC are vertically shifted by constant values here, values directly related to the SOC constants. The E1/E2 and E9/E10 states remain degenerate, and S2 contributes mainly to E8 (70%) at 3.13 eV and slightly to E11 (16%) and E3 (10%). See section 2 and ref. [46] for the description of the spin-adiabatic states.

The spectra computed after transition to the diabatic S2 state are characterized by three bands, corresponding to E1−E3 at ∼2.76 eV, E7/E8 at ∼3.10 eV, and E9−E11 at ∼3.22 eV. E4−E6 do not contribute to the absorption. Regarding the E7/E8 band, one can see that absorption occurs below the minimum of E8(A′) along Q_7. Indeed, the global minimum within our six dimensional potential is lower in energy. Furthermore, some intensity is borrowed from the A″ E7 state by vibronic coupling. The vibrational progression, which can be seen in the E1−E3 band, corresponds to the ν_7 low frequency. In the E7/E8 band, it is more intricate; ν_{11} and ν_{13} modes do contribute to the absorption band.

4.3. Excited-State Population Dynamics

The evolution of the diabatic electronic populations as a function of time is shown in Figure 3 after initial excitation of S2. For convenience, the populations of the individual triplet components are summed over. The S2 population decreases very rapidly, within 10−20 fs, to reach a value of ∼50%. This is purely due to the SOC to T1 and T3. The fast oscillations in T1 and T3 are directly related to the strength of the SOC. After this initial decay, the S2 population further decays until ∼320 fs, while the population of T1 remains rather constant. Indeed, this S2 decay is due to SOC to T2 (A′ component) in addition to vibronic coupling to S1. S1 in turn populates T2 (A″ components) due to strong S1/T2 SOC. The population of the T3 state, which lies above S2, decreases slowly after 20 fs. Around 350 fs, we do see a recurrence in the T1 (and S2) population. In fact, this corresponds to the period associated with ν_7 and twice that of ν_{13}. That is, after 350 fs our results can no longer be exploited: additional nuclear degrees of freedom would have killed those recurrences. This also goes in line with the small value of vibronic coupling with respect to the SOC (see Table 1). This strongly suggests that the population dynamics at longer time is not governed by some particular vibrational modes but rather by collective effects.

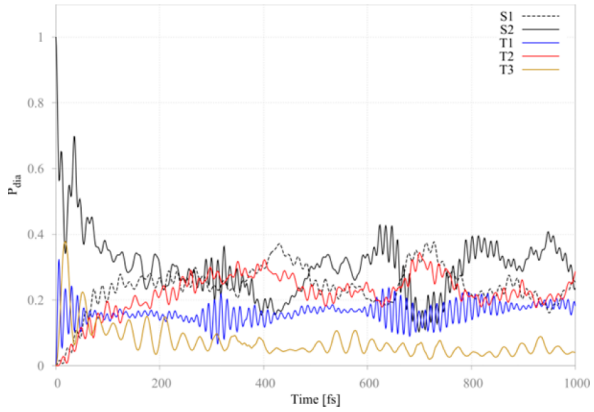

Figure 3. Diabatic electronic populations as a function of time. The triplet components are summed over. The S2 population drops very quickly due to SOC and then evolves further due to vibronic coupling.

It is also very instructive to analyze the evolution of the adiabatic populations (Figure 4). These are calculated from the diabatic ones with MCTDH by using the Monte Carlo integration scheme with default parameters.[56] At time zero, E8, E3, and E11, all of A′ symmetry, are initially populated

DOI: 10.1021/ar500369r
Acc. Chem. Res. 2015, 48, 809−817

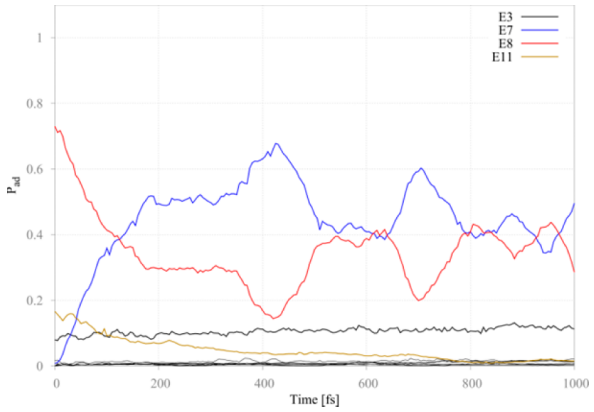

Figure 4. Adiabatic electronic populations as a function of time. The E8 (A′) population decreases to populate E7 (A″) by vibronic coupling. Only four adiatabic "spin-orbtit" states are significantly populated in the first 350 fs.

because they have contributions from the S2 state of 70%, 10%, and 16%, respectively (see section 2).[46] The first observation is that these adiabatic populations do not oscillate as the diabatic ones do. This is not surprising since the (constant) SOC acts in the adiabatic picture as diagonal contributions to the Hamiltonian: it does not induce population transfer anymore.

In Figure 4, we observe that only four "spin-orbit" states are significantly populated. In particular, we see that the population of E8 is mainly transferred to a single other "spin-orbit" state, E7 (A″). This state is composed of 51%T2 and 48%S1 and is populated because of the S1/S2 vibronic coupling and S2/T2 SOC. The E8 population drops up to 0.3 in ∼180 fs and then stays constant up to 350 fs. The E8 and E7 adiabatic population curves cross at about 130 fs. The population of E3, composed of 85% T1, remains almost constant, as the diabatic population of T1 does. In fact it increases very slowly, with a large time constant. Finally, the population of E11 (82% T3) decreases slowly to repopulate E8.

The E8 state has been calculated to emit (relaxed excited state geometry) at 505 nm, the E3 state at 600 nm, the E11 state at 490 nm, and the E7 state at 580 nm.[46] Upon absorption at 400 nm used in experiment,[18] the E8 state is populated. The nuclear relaxation within this state, together with E11, will be responsible for the ∼500 nm emission band. The population of the vibronically coupled E7 state within the first 130 fs correlates with the observed emission around 580 nm. The E3 state explains the long-lived 600−610 emission band. Of course the phosphorescent E1 and E2 states will also contribute (95% T1). They are however very weakly populated using the present model because of the very small T1/T2 vibronic coupling constant.

The time scales of the present study, for example, the ∼130−180 fs decrease (rise) time of the E8 (E7) state population, are in the same order as the τ_1 = 128 fs deduced from the time-resolved emission spectra,[18] which is satisfactory given the model used. The second measured decay time τ_2 = 470 fs cannot be studied here because of our reduced dimensionality approach, which leads to recurrences in the population dynamics. Other vibrational modes need to be included, in particular for the T1/T2 coupling, and to avoid the recurrences.

5. CONCLUSIONS

In this Account, we have shown that it is possible to construct a model Hamiltonian to study the quantum dynamics of transition metal complexes involving several electronic states and accounting for both spin−orbit and vibronic coupling. This model Hamiltonian requires limited data from electronic structure calculations. While we have applied it in its simplest form, it is possible to systematically increase its complexity to account for additional effects. The first application to the study of the ultrafast relaxation in the $[Re(Br)(CO)_3(bpy)]$ complex after excitation at 400 nm allows us to confirm that the fast decay of the initially populated electronic state is mainly due to vibronic coupling, with a time scale on the order of the experimentally found one. This study shows that, rather than important contributions of some few vibrational modes, it is collective effects that play a key role in this class of complexes. Inclusion of additional degrees of freedom and possibly higher order terms in the Hamiltonian, and comparison with the study of the $[Re(X)(CO)_3(bpy)]$, X = Cl or I, complexes will allow us to analyze in more detail the interplay between spin−orbit and vibronic coupling in transition metal complexes using a full quantum treatment.

AUTHOR INFORMATION

Corresponding Authors

*E-mail: egindensperger@unistra.fr.
*E-mail: c.daniel@unistra.fr.

Notes

The authors declare no competing financial interest.

Biographies

Julien Eng graduated in Physical Chemistry from the University of Strasbourg. Since 2012, he has been a Ph.D. student in the Laboratoire de Chimie Quantique Strasbourg. Current interests are theoretical studies of isomerization pathways in organic and inorganic systems from both the quantum chemical and quantum dynamical perspectives.

Christophe Gourlaouen received his Ph.D. (2006) from the University Pierre & Marie Curie, Paris. In 2007, he joined ICQC, Tarragona, Spain, where he performed post-doctoral research with Feliu Maseras and then moved in 2008 to the CEA. Since 2010, he has been CNRS-researcher at the Laboratoire de Chimie Quantique, Strasbourg, as Chargé de Recherche. Current interests are electronic structure in transition metal complexes, bonding in polymetallic systems, and more recently luminescent properties.

Etienne Gindensperger received his Ph.D. in 2004 from the Université Paul Sabatier, Toulouse, France. He then joined the Theoretical Chemistry group of the University of Heidelberg, Germany, as a Alexender von Humbold fellow. Since 2007, he has been CNRS-researcher at the Laboratoire de Chimie Quantique, Institut de Chimie, Université de Strasbourg. Current interests are focused on the theoretical description of ultrafast photoinduced processes in organic and inorganic systems.

Chantal Daniel received her Ph.D. in 1985 from the University of Strasbourg. She joined the group of Keiji Morokuma at IMS, Okazaki, Japan, in 1986 as JSPS fellow and then the IBM Department in Kingston, NY, USA, as postdoctoral associate of Michel Dupuis in 1988. Since 1999, she has been CNRS-researcher at the Laboratoire de Chimie Quantique as Directeur de Recherche. Current interests are excited state properties in transition metal complexes and modeling

DOI: 10.1021/ar500369r
Acc. Chem. Res. 2015, 48, 809−817

and simulation of photochemical and photophysical properties of molecules in complex environments.

■ ACKNOWLEDGMENTS

The authors thank A. Vlček Jr., M. Chergui, and A. Cannizzo for having motivated this work. The European actions COST perspect-H2O and CODEC are acknowledged. The calculations have been performed on the computer nodes of the LCQS, Strasbourg, and the High-Performance Computing center (pole HPC) at Université de Strasbourg.

■ REFERENCES

(1) Juban, E. A.; Smeigh, A. L.; Monat, J. E.; McCusker, J. K. Ultrafast dynamics of ligand-field excited states. *Coord. Chem. Rev.* **2006**, *250*, 1783−1791.

(2) McCusker, J. K. Femtosecond absorption spectroscopy of transition metal charge-transfer complexes. *Acc. Chem. Res.* **2003**, *36*, 876−887.

(3) Chergui, M. On the interplay between charge, spin and structural dynamics in transition metal complexes. *Dalton Trans.* **2012**, *41*, 13022−13029.

(4) Bräm, O.; Messina, F.; Baranoff, E.; Cannizzo, A.; Nazeeruddin, M. K.; Chergui, M. Ultrafast relaxation dynamics of osmium-polypyridine complexes in solution. *J. Phys. Chem. C* **2013**, *117*, 15958−15966.

(5) Sousa, C.; de Graaf, C.; Rudavskyi, A.; Broer, R.; Tatchen, J.; Etinski, M.; Marian, C. M. Ultrafast deactivation mechanism of the excited singlet in the light-induced spin crossover of $[Fe(2,2'\text{-bipyridine})_3]^{2+}$. *Chem.—Eur. J.* **2013**, *19*, 17541−17551.

(6) El Nahhas, A.; Consani, C.; Blanco-Rodríguez, A. B.; Lancaster, K. M.; Braem, O.; Cannizzo, A.; Towrie, M.; Clark, I. P.; Záliš, S.; Chergui, M.; Vlček, A., Jr. Ultrafast excited-state dynamics of rhenium(I) photosensitizers $[Re(Cl)(CO)_3(N,N)]$ and $[Re(imidazole)(CO)_3(N,N)]^+$: Diimine effects. *Inorg. Chem.* **2011**, *50*, 2932−2943.

(7) Renske, M.; van der Veen, R. M.; Cannizzo, A.; van Mourik, F.; Vlček, A., Jr.; Chergui, M. Vibrational relaxation and intersystem crossing of binuclear metal complexes in solution. *J. Am. Chem. Soc.* **2011**, *133*, 305−315.

(8) Damrauer, N. H.; Cerullo, G.; Yeh, A.; Boussie, T. R.; Shank, C. V.; McCusker, J. K. Femtosecond dynamics of excited-state evolution in $[Ru(bpy)_3]^{2+}$. *Science* **1997**, *275*, 54−57.

(9) El Nahhas, A.; Cannizzo, A.; van Mourik, F.; Blanco-Rodríguez, A. M.; Záliš, S.; Vlček, A., Jr.; Chergui, M. Ultrafast excited-state dynamics of $[Re(L)(CO)_3(bpy)]^{n+}$ complexes: involvement of the solvent. *J. Phys. Chem. A* **2010**, *114*, 6361−6369.

(10) Kuimova, M. K.; Alsindi, W. Z.; Blake, A. J.; Davies, E. S.; Lampus, D. J.; Matousek, P.; McMaster, J.; Parker, A. W.; Towrie, M.; Sun, X.-Z.; Wilson, C.; George, M. W. Probing the solvent dependent photophysics of *fac*-$[Re(CO)_3(dppz\text{-}X_2)Cl]$ (dppz-X_2 = 11,12-X_2-dipyrido[3,2-a:2′,3′-c]phenazine); X = CH_3, H, F, Cl, CF_3). *Inorg. Chem.* **2008**, *47*, 9857−9869.

(11) Huse, N.; Kim, T. K.; Jamula, L.; McCusker, J. K.; de Groot, F. M. F.; Schoenlein, R. W. Photo-induced spin-state conversion in solvated transition metal complexes probed via time-resolved soft X-ray spectroscopy. *J. Am. Chem. Soc.* **2010**, *132*, 6809−6816.

(12) Huse, N.; Cho, H.; Hong, K.; Jamula, L.; de Groot, F. M. F.; Kim, T. K.; McCusker, J. K.; Schoenlein, R. W. Femtosecond soft X-ray spectroscopy of solvated transition-metal complexes: Deciphering the interplay of electronic and structural dynamics. *J. Phys. Chem. Lett.* **2011**, *2*, 880−884.

(13) Bressler, Ch.; Milne, C.; Pham, V.-T.; El Nahhas, A.; van der Veen, R. M.; Gawelda, W.; Johnson, S.; Beaud, P.; Grolimund, D.; Kaiser, M.; Borca, C. N.; Ingold, G.; Abela, R.; Chergui, M. Femtosecond XANES study of the light-induced spin crossover dynamics in an iron(II) complex. *Science* **2009**, *323*, 489−492.

(14) Blanco-Rodríguez, A. M.; Kvapilová, H.; Sýkora, J.; Towrie, M.; Nervi, C.; Volpi, G.; Záliš, S.; Vlček, A., Jr. Photophysics of singlet and triplet intraligand excited states in $[ReCl(CO)_3(1\text{-}(2\text{-pyridyl})\text{-imidazo-}[1,5\text{-}\alpha]\text{pyridine})]$ complexes. *J. Am. Chem. Soc.* **2014**, *136*, 5963−5973.

(15) van der Veen, R. M.; Milne, C. J.; El Nahhas, A.; Lima, F. A.; Pham, V.-T.; Best, J.; Weinstein, J. A.; Borca, C. N.; Abela, R.; Bressler, Ch.; Chergui, M. Structural determination of a photochemically active diplatinum molecule by time-resolved EXAFS spectroscopy. *Angew. Chem., Int. Ed.* **2009**, *48*, 2711−2714.

(16) Cannizzo, A.; Milne, C. J.; Consani, C.; Gawelda, W.; Bressler, Ch.; van Mourik, F.; Chergui, M. Light-induced spin crossover in Fe(II)-based complexes: The full photocycle unraveled by ultrafast optical and X-ray spectroscopies. *Coord. Chem. Rev.* **2010**, *254*, 2677−2686.

(17) Smeigh, A. L.; Creelman, M.; Mathies, R. A.; McCusker, J. K. Femtosecond time-resolved optical and Raman spectroscopy of photoinduced spin crossover: Temporal resolution of low-to-high spin optical switching. *J. Am. Chem. Soc.* **2008**, *130*, 14105−14107.

(18) Cannizzo, A.; Blanco-Rodríguez, A. M.; El Nahhas, A.; Sebera, J.; Záliš, S.; Vlček, A., Jr.; Chergui, M. Femtosecond fluorescence and intersystem crossing in rhenium(I) carbonyl-bipyridine complexes. *J. Am. Chem. Soc.* **2008**, *130*, 8967−8974.

(19) Daniel, C. Photochemistry and photophysics of transition metal complexes: Quantum chemistry. *Coord. Chem. Rev.* **2015**, *282*−*283*, 19−32.

(20) Daniel, C. Electronic spectroscopy and photoreactivity of transition metal complexes: Quantum chemistry and wave packet dynamics. In *Transition Metal and Rare Earth Compounds: Excited States, Transitions, Interactions III* Yersin, H. Ed.; Topics in Current Chemistry; Springer-Verlag: Heidelberg, 2005; Vol. *241*, pp 119−165.

(21) González, L.; Escudero, D.; Serrano-Andrés, L. Progress and challenges in the calculation of electronic excited states. *ChemPhysChem* **2012**, *13*, 28−51.

(22) Köppel, H.; Domcke, W.; Cederbaum, L. S. Multimode molecular dynamics beyond the Born-Oppenheimer approximation. *Adv. Chem. Phys.* **1984**, *57*, 59−246.

(23) Runge, E.; Gross, E. K. U. Density-functional theory for time-dependent systems. *Phys. Rev. Lett.* **1984**, *52*, 997−1000.

(24) Petersilka, M.; Gossmann, U. J.; Gross, E. K. U. Excitation energies from time-dependent density-functional theory. *Phys. Rev. Lett.* **1996**, *76*, 1212−1215.

(25) Casida, M. E.; Huix-Rotlant, M.; Johnson, M.A.; Martinez, T. J. Progress in Time-Dependent Density-Functional Theory. *Annu. Rev. Phys. Chem.* **2012**, *63*, 287−323.

(26) Roos, B. O.; Taylor, P. R.; Siegbahn, P. E. M. A complete active space SCF method (CASSCF) using a density matrix formulated super-CI approach. *Chem. Phys.* **1980**, *48*, 157−173.

(27) Andersson, K.; Malmqvist, P. -Å.; Roos, B. O.; Sadlej, A. J.; Wolinski, K. Second-order perturbation theory with a CASSCF reference function. *J. Phys. Chem.* **1990**, *94*, 5483−5488.

(28) Andersson, K.; Malmqvist, P. -Å.; Roos, B. O. Second-order perturbation theory with a complete active space self-consistent field reference function. *J. Chem. Phys.* **1992**, *96*, 1218−1226.

(29) Curchod, B. F. E.; Rothlisberger, U.; Tavernelli, I. Trajectory-based nonadiabatic dynamics with time-dependent density functional theory. *ChemPhysChem* **2013**, *14*, 1314−1340 and references therein..

(30) Köppel, H.; Domcke, W. Vibronic dynamics of polyatomic molecules. In *Encyclopedia in Computational Chemistry*; von Ragué Schleyer, P., Ed.; Wiley: New York, 1998; p 3166.

(31) Domcke, W., Yarkony, D. R., Köppel, H., Eds. *Conical Intersections - Electronic structure, Dynamics and Spectroscopy*; Advanced Series in Physical Chemistry; World Scientific; Singapore, 2004; Vol. *15*.

(32) Baer, M. *Beyond Born-Oppenheimer: Conical Intersections and Electronic Nonadiabatic Coupling Terms*; Wiley-Interscience: Hoboken, NJ, 2006.

(33) Curchod, B. F. E.; Penfold, T. J.; Rothlisberger, U.; Tavernelli, I. Nonadiabatic *ab initio* molecular dynamics using linear-response time-

DOI: 10.1021/ar500369r
Acc. Chem. Res. 2015, 48, 809−817

dependent density functional theory. *Cent. Eur. J. Phys.* **2013**, *11*, 1059−1065.
(34) de Carvalho, F. F.; Bouduban, M. E. F.; Curchod, B. F. E.; Tavernelli, I. Nonadiabatic molecular dynamics based on trajectories. *Entropy* **2014**, *16*, 62−85.
(35) Worth, G. A.; Welch, G.; Paterson, M. J. Wavepacket dynamics of $Cr(CO)_5$ after formation by photodissociation: Relaxation through an (E⊕A)⊗e Jahn-Teller conical intersection. *Mol. Phys.* **2006**, *104*, 1095−1105.
(36) Mondal, P.; Opalka, D.; Poluyanov, L. V.; Domcke, W. Jahn-Teller and spin-orbit coupling effects in transition metal trifluorides. *Chem. Phys.* **2011**, *387*, 56−65.
(37) Ando, H.; Iuchi, S.; Sato, H. Theoretical study on ultrafast intersystem crossing of chromium (III) acetylacetonate. *Chem. Phys. Lett.* **2012**, *535*, 177−181.
(38) Baková, R.; Chergui, M.; Daniel, C.; Vlček, A.; Záliš, S. Relativistic effects in spectroscopy and photophysics of heavy-metal complexes illustrated by spin−orbit calculations of [Re (imidazole)-$(CO)_3$phen)]$^+$. *Coord. Chem. Rev.* **2011**, *255*, 975−989.
(39) Heitz, M.-C.; Ribbing, C.; Daniel, C. Spin-orbit induced radiationless transitions in organometallics: Quantum simulation of the intersystem crossing processes in the photodissociation of $HCo(CO)_4$. *J. Chem. Phys.* **1997**, *106*, 1421−1428.
(40) Etinski, M.; Tatchen, J.; Marian, C. M. Time-dependent approaches for the calculation of intersystem crossing rates. *J. Chem. Phys.* **2011**, *134*, No. 154105.
(41) Etinski, M.; Rai-Constapel, V.; Marian, C. M. Time-dependent approach to spin-vibronic coupling: Implementation and assessment. *J. Chem. Phys.* **2014**, *140*, No. 114104.
(42) Tavernelli, I.; Curchod, B. F. E.; Rothlisberger, U. Nonadiabatic molecular dynamics with solvent effects: A LR-TDDFT QM/MM study of ruthenium (II) tris (bipyridine) in water. *Chem. Phys.* **2011**, *391*, 101−109.
(43) Mondal, P.; Opalka, D.; Poluyanov, L. V.; Domcke, W. *Ab initio* study of dynamical E⊗e Jahn-Teller and spin-orbit coupling effects in the transition-metal trifluorides TiF_3, CrF_3 and NiF_3. *J. Chem. Phys.* **2012**, *136*, No. 084308.
(44) Heydová, R.; Gindensperger, E.; Romano, R.; Sýkora, J.; Vlček, A., Jr.; Záliš, S.; Daniel, C. Spin−orbit treatment of UV−vis absorption spectra and photophysics of rhenium(I) carbonyl−bipyridine complexes: MS-CASPT2 and TD-DFT Analysis. *J. Phys. Chem. A* **2012**, *116*, 11319−11329.
(45) El Nahhas, A.; van der Veen, R. M.; Penfold, T. J.; Pham, V. T.; Lima, F. A.; Abela, R.; Blanco-Rodriguez, A. M.; Záliš, S.; Vlček, A., Jr.; Tavernelli, I.; Rothlisberger, U.; Milne, C. J.; Chergui, M. X-ray absorption spectroscopy of ground and excited of rhenium-carbonyl-diimine complexes: evidence for a two-center electron Transfer. *J. Phys. Chem. A* **2013**, *117*, 361−369.
(46) Gourlaouen, C.; Eng, J.; Otsuka, M.; Gindensperger, E.; Daniel, C. A quantum chemical interpretation of ultra-fast luminescence decay and intersystem crossings in Rhenium (I) carbonyl bipyridine complexes. *J. Chem. Theory Comput.* **2015**, *11*, 99−110 DOI: 10.1021/ct500846n.
(47) J. Tomasi, J.; Persico, M. Molecular interactions in solution: An overview of methods based on continuous distributions of the solvent. *Chem. Rev.* **1994**, *94*, 2027−2094.
(48) Tomasi, J.; Mennucci, B.; Cammi, R. Quantum mechanical continuum solvation models. *Chem. Rev.* **2005**, *105*, 2999−3093.
(49) Stephens, P. J.; Devlin, F. J.; Chabalowski, C. F.; Frisch, M. J. *Ab initio* calculation of vibrational absorption and circular dichroism spectra using density functional force fields. *J. Phys. Chem.* **1994**, *98*, 11623−11627.
(50) van Lenthe, E.; Baerends, E. J. Optimized Slater-type basis sets for the elements 1−118. *J. Comput. Chem.* **2003**, *24*, 1142−1156.
(51) van Lenthe, E.; van Leeuwen, R.; Baerends, E. J.; Snijders, J. G. Relativistic regular two-component Hamiltonians. *Int. J. Quantum Chem.* **1996**, *57*, 281−293.
(52) Wang, F.; Ziegler, T. A simplified relativistic time-dependent density-functional theory formalism for the calculations of excitation energies including spin-orbit coupling effect. *J. Chem. Phys.* **2005**, *123*, No. 154102.
(53) Meyer, D.-H.; Manthe, U.; Cederbaum, L. S. The multi-configurational time-dependent Hartree approach. *Chem. Phys. Lett.* **1990**, *165*, 73−78.
(54) Beck, M. H.; Jäckle, A.; Worth, G. A.; Meyer, H.-D. The multiconfiguration time-dependent Hartree (MCTDH) method: a highly efficient algorithm for propagating wavepackets. *Phys. Rep.* **2000**, *324*, 1−105.
(55) Meyer, H.-D., Gatti, F., Worth, G. A., Eds. *Multidimensional Quantum Dynamics: MCTDH Theory and Applications*; Wiley-VCH: Weinheim, Germany, 2009.
(56) Worth, G. A.; Beck, M. H.; Jäckle, A.; Meyer, H.-D. The MCTDH Package, version 8.2, University of Heidelberg, Heidelberg, Germany, 2000. Meyer, H.-D. The MCTDH Package, version 8.3, University of Heidelberg, Heidelberg, Germany, 2002, Meyer, H.-D. The MCTDH Package, version 8.4, University of Heidelberg, Heidelberg, Germany, 2007. Vendrell, O.; Meyer, H.-D. The MCTDH Package, version 8.5, University of Heidelberg, Heidelberg, Germany, 2011. See http://mctdh.uni-hd.de.

DOI: 10.1021/ar500369r
Acc. Chem. Res. 2015, 48, 809−817

C.3 Structural Properties and UV-Visible Absorption Spectroscopy of Retinal-pyridyl-CN Re(I) Carbonyl Bipyridine Complex: A Theoretical Study

THE JOURNAL OF PHYSICAL CHEMISTRY A

Article

pubs.acs.org/JPCA

Structural Properties and UV−Visible Absorption Spectroscopy of Retinal-pyridyl-CN Re(I) Carbonyl Bipyridine Complex: A Theoretical Study

Published as part of The Journal of Physical Chemistry A virtual special issue "Spectroscopy and Dynamics of Medium-Sized Molecules and Clusters: Theory, Experiment, and Applications".

Julien Eng and Chantal Daniel*

Laboratoire de Chimie Quantique, Institut de Chimie Strasbourg, UMR-7177 CNRS/Université de Strasbourg 1 Rue Blaise Pascal BP 296/R8, F-67008 STRASBOURG, France

Supporting Information

ABSTRACT: The structural, electronic, and optical properties of the all-trans and five cis conformers of $[Re(CO)_3(bpy)(ret\text{-}pyr\text{-}CN)]^+$ (bpy = 2,2′-bipyridine; ret-pyr-CN = pyridyl-CN-3,7-dimethyl-9-(2,6,6-trimethylcyclohex-2-n)-none-(2,4,6,8-tetraen) were studied in solvent by means of density functional theory (DFT) and time-dependent DFT. The isolated retinal-like chromophore ret-pyr-CN was investigated as well for comparison. By coordination to the complex the two lowest intraligand (IL) states localized on the retinal group are slightly red-shifted from 627 to 690 nm and from 415 to 450 nm, respectively. Several isomerization pathways are open upon irradiation of the Re(I) complex by visible light (400−450 nm), especially to two cis conformers corresponding to the isomerization of the two double bonds of the retinal-like ligand close to the pyridyl group linked to the Re(I) fragment. The metal-to-ligand charge transfer states localized either on the retinal group or on the bpy ligand should play a minor role in the isomerization process itself but could improve its efficiency via ultra-fast intersystem crossing.

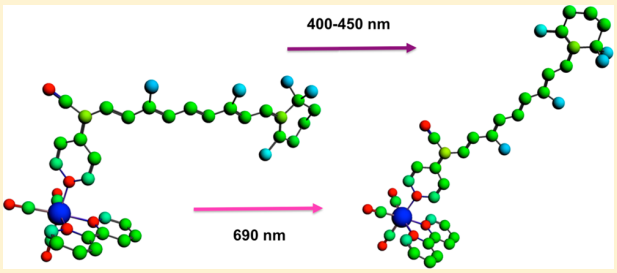

INTRODUCTION

The rich photochemistry of rhenium complexes, spanning eight oxidation states from Re(0) to Re(VII), coupled to their ability at binding various sites such as polymers, proteins, zeolites, and DNA have made these compounds very attractive for a number of applications over the last 3 decades.[1−5] Rhenium(I) α-diimine complexes are particularly appealing because of their ability to be functionalized for probing biological environments,[6−10] triggering electron/energy transfer in proteins,[11−14] or light harvesting.[15] Four elementary routes are open after irradiation of these molecules in the UV−visible energy domain, namely, ligand substitution, ligand isomerization, luminescence, and electron transfer. The coordinated ligands as well as the environment and experimental conditions entirely control the branching ratio between these competitive processes in the first picoseconds.[2,16−18] Whereas Re(I) complexes with bipyridine types ligands characterized by low-lying metal-to-ligand charge-transfer (MLCT) states show very intense long-lived emission over a wide range of energies, complexes with aromatic dyads will favor electron transfer processes by the presence of intraligand (IL) or ligand-to-ligand CT (LLCT) states. Re(I) complexes with isomerizable stilbene-like ligands, seat of ^{3}IL ($\pi\pi^*$) states, will play a central role in probing complex environment and conformational changes. One advantage over organic chromophores is the activation of the isomerization process by visible light. A number of experimental[19−22] and theoretical[23−27] studies have been performed on rhenium(I) isomerizable complexes. Some of them have shown that ultrafast ^{1}MLCT → ^{3}MLCT intersystem crossing (ISC) occurs within less than 1 ps.[20] The relative position of the ^{1}IL/^{1,3}MLCT states and the ^{3}MLCT/^{3}IL energy gap determines the mechanism of isomerization and the way its quantum yield is affected by irradiation wavelength, spin−orbit coupling effects, or other experimental conditions. With some specific ligands, luminescence, electron transfer, and isomerization may enter into competition at a single wavelength.[19,28]

Systems composed of pyridyl−carotenoids derivatives coordinated to Re(I) and Pt(II) complexes have been synthesized and characterized by Rillema et al.[29] to exploit the light-harvesting properties of these organic compounds when linked to metal fragments. In particular, an all-trans-retinal-pyridyl-CN Re(I) tricarbonyl bipyridine complex $[Re(CO)_3(bpy)(ret\text{-}pyr\text{-}CN)]^+$ (bpy = 2,2′-bipyridine; ret-pyr-CN = pyridyl-CN-3,7-dimethyl-9-(2,6,6-trimethylcyclohex-2-n)-

Received: August 18, 2015
Revised: October 2, 2015

DOI: 10.1021/acs.jpca.5b08047
J. Phys. Chem. A XXXX, XXX, XXX−XXX

none-(2,4,6,8-tetraen) was obtained, and a comparison between the UV−visible absorption properties of the isolated organic chromophore and those of the inorganic one was proposed.

In our quest to understand the mechanism of isomerization processes in organic[30] and inorganic chromophores[23−27] we propose a complete investigation of the structural properties of the various Re(I) isomers generated by the retinal-like ligand. A theoretical analysis of the absorption spectra of both the organic and inorganic chromophores completes this study. The next section is dedicated to the Computational Details, whereas the results are presented and discussed in the second section.

COMPUTATIONAL DETAILS

The structures of the all-trans conformer **a** and of the lowest cis-conformer **1c**−**5c** of $[Re(CO)_3(bpy)(L)]^+$ (L = Ret-pyr-CN) were optimized in the electronic ground state in vacuum in C_1 symmetry at the density functional theory (DFT) level using GGA PBE functional, including dispersion correction by Grimme,[31] and with triple-ζ basis sets.[32] Five cis structures, generated by modifying the torsion angle around one double C=C bond at a time starting from the all-trans geometry, were fully optimized. For **a** all-trans and **1c** cis structures, two additional conformers **a**-α_{opt} and **1c**-α_{opt} were optimized by relaxing the dihedral angle α between the planes of the pyridine and retinal-CN and defined by the three color vectors in Scheme 1. The cis conformers are defined as follows according to the numbering of Scheme 1: **1c** for C_{16}=C_{15}; **2c** for C_{14}=C_{13}; **3c** for C_{12}=C_{11}; **4c** for C_{10}=C_9; **5c** for C_8=C_7.

Scheme 1. Definition of the α Dihedral Angle in $[Re(CO)_3(bpy)(L)]^+$ (L = Ret-pyr-CN)

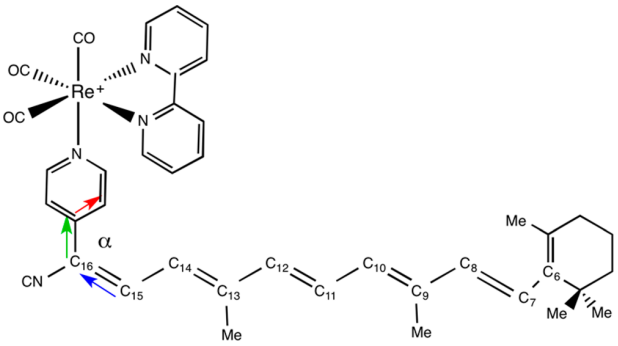

The scalar relativistic effects are taken into account within the zero-order regular approximation.[33] The spin−orbital coupling effects are introduced according to a simplified relativistic perturbational time-dependent (TD) DFT formalism.[34,35] The low-lying singlet and triplet states were calculated by means of TD-DFT method using B3LYP functional[36,37] for the lowest 80 roots. Because of the presence of low IL states, Tam−Dancoff approximation (TDA)[38] was used for avoiding an over stabilization of the ^{3}IL states. Our attempt to calculate and correct $LLCT_{ret\text{-}bpy}$ transition energies of eventual long-range errors with the CAM-B3LYP functional[39] failed due to technical problems. However, according to our experience the performance of this functional for calculating transition energies of MLCT states with reasonable accuracy in this class of transition metal complexes is very poor and gives generally unrealistic blue-shifted absorption spectra.[40,41] The absorption spectra were computed with solvent correction based on the conductor-like screening model (COSMO;[42−44] with ε = 36.64 for acetonitrile) as implemented in ADF.[45,46] The lowest singlet excited states of the isolated organic chromophore **b** were determined by the same approach for comparison.

The trans−cis isomerization potential energy profiles describing the all-trans conformer **a** to the cis structures **1c**−**5c** of $[Re(CO)_3(bpy)(L)]^+$ pathways were estimated in acetonitrile by single-point TD-DFT calculations performed on the optimized all-trans, cis, and perpendicular structures (torsion angle of 90° around the relevant CC double bond) for the electronic ground state and the low-lying singlet and triplet excited states. This qualitative approach, which concentrates on one specific pathway only, suffers from two severe approximations: (i) the neglect of other conformers that could influence the energy profiles opening the route to other isomerization channels; (ii) the disregard of the excited state corresponding to the doubly $\pi\pi^*$ excitation. A dynamical study describing the nuclear flexibility of the retinal ligand is beyond the scope of the present investigation, whereas the choice of the method (TD-DFT), dictated by the size of the system, eliminates factually the computation of the doubly excited state. Moreover current theoretical studies reported on organic chromophores neglect the role of this state in the isomerization process even though it is supposed to generate a small energy barrier for a torsion angle of 60°.[47] The calculations were performed with ADF-2013 quantum chemistry softwares,[48] and the electronic transitions were analyzed with the Dgrid package.[49]

RESULTS AND DISCUSSION

Structures and Electronic Ground-State Properties. The fully optimized geometries of the $[Re(CO)_3(bpy)(L)]^+$ (L = Ret-pyr-CN) all-trans conformers **a** (α = 8.6°) and of the cis conformers **1c** (α = 8.6°), **2c** to **5c** are represented in Figure 1, whereas some important bond lengths and bond angles of the **a** and **a**-α_{opt}, **1c**, **1c**-α_{opt} and **2c** to **5c** conformers are reported in Table 1.

The electronic ground state of all-*trans*-$[Re(CO)_3(bpy)(L)]^+$ **a** in acetonitrile is characterized by the sequence of Kohn−Sham (KS) orbitals depicted in Scheme 2. The low-lying excited states will be generated within this set of KS orbitals.

The highest occupied molecular orbital (HOMO) and HOMO−1 are both mainly localized on the ret-pyr-CN ligand with a small metal contribution in HOMO−1, whereas HOMO−2, HOMO−3, and HOMO−4 are essentially metal centered and very close in energy. The lowest unoccupied molecular orbital (LUMO) and LUMO+1 are localized on the ret-pyr-CN and bpy ligands, respectively. The LUMO+2 corresponds to a $\pi^*_{ret\text{-}pyr\text{-}CN}$ but is characterized by a delocalization over the pyridyl group in contrast to the LUMO, which is mainly localized on the retinal. LUMO+3 and LUMO+4 correspond to π^*_{bpy} and are nearly degenerate with LUMO+2. Metal orbitals contribute essentially to higher vacant orbitals (not shown here). From the qualitative picture depicted in Scheme 2 we may anticipate the presence of low-lying IL excited states localized on the ret-pyr-CN ligand and of MLCT states corresponding to charge transfer to the ret-pyr-CN and bpy ligands. Metal-centered MC states should not contribute to the absorption spectra, as expected for this class of third-row transition metal complexes.[50,51] The possibility of low-lying $LLCT_{ret\text{-}bpy}$ calls for methodological questions, devoted especially to long-range charge transfer states. However, in the absence of benchmark for the complex of

DOI: 10.1021/acs.jpca.5b08047
J. Phys. Chem. A XXXX, XXX, XXX−XXX

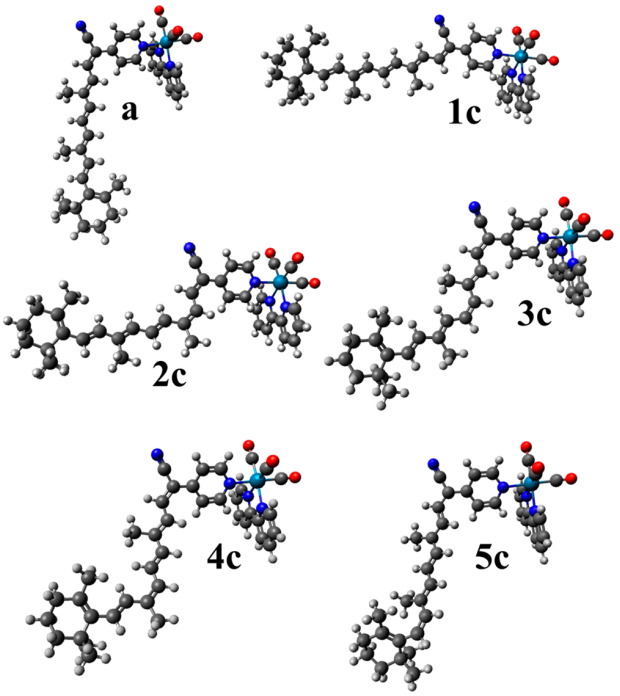

Figure 1. DFT optimized geometries of all-*trans*-$[Re(CO)_3(bpy)(L)]^+$ **a** and *cis*-$[Re(CO)_3(bpy)(L)]^+$ conformers **1c**–**5c**.

interest the presence of $LLCT_{ret\text{-}bpy}$ in the lowest part of the absorption spectra must be considered with care.

The electronic configurations of the cis conformers are not very different (see Scheme S1 in Supporting Information section). In **1c**, for instance, the Kohn–Sham orbitals of which are depicted in Scheme 3, both HOMO and HOMO−1 are localized on ret-pyr-CN, the HOMO−2, HOMO−3, and HOMO−4 being localized on the metal center. The position of the LUMO+2 and LUMO+3 is inverted when going from the all-trans **a** to the **1c** cis conformer, but the original relative order is kept in the other cis conformers **2c**–**5c** (Scheme S1 in Supporting Information). In all conformers we may distinguish two low-lying π^* orbitals entirely localized on the ret-pyr-CN ligand, the upper one being delocalized on the pyridyl part. The presence of these two different π^*_{ret} orbitals (LUMO and LUMO+2 in **a**, Scheme 2) will have important consequences for ultimate functions activated by visible light irradiation (400–450 nm) as illustrated in the section dedicated to the absorption spectroscopy.

The similitude between the electronic configurations of all-trans and cis conformers should facilitate the correlation between the low-lying excited states of the different isomers.

As illustrated by the optimized geometrical parameters reported in Table 1 the global structures of the investigated conformers are very similar without any perturbation of the sphere of coordination of the central Re(I) metal atom from one conformer to the others. The bond lengths and bond angles are not affected by the optimization of the angle α in **a** and **1c**.

The sequence of carbon–carbon bonds, numbered according to Scheme 1, alternates benzene-like/allene-like bond lengths until the second carbon (C_9) substituted by a methyl group as illustrated by the bond length alteration depicted in Figure 2 for the different conformers. Then the single/double bond character is more pronounced until C_6 and especially for the conformer **5c** corresponding to the C_7–C_8 double bond isomerization and for which a maximum of amplitude is found. The C_{sp^2}–methyl and C_{sp^3}–methyl bond lengths of the terminal cyclohexen are in the range of the usual C_{sp^3}–C_{sp^3} (1.54 Å) and C_{sp^3}–C_{sp^2} (1.50 Å) bond lengths. All together, optimized parameters are realistic, and despite the lack of experimental

Table 1. Density Functional Theory Optimized Important Bond Lengths (Å) and Bond Angles (deg) of All-*trans*-$[Re(CO)_3(bpy)(L)]^+$ a (α = 8.6°), a-α_{opt} (α = 22.5°), of *cis*-$[Re(CO)_3(bpy)(L)]^+$ 1c (α = 8.6°), 1c-α_{opt} (α = 1.8°) to 5c, and of the Isolated Organic Chromophore b[a]

	a	a-α_{opt}	1c	1c-α_{opt}	2c	3c	4c	5c	b
Re–N_{bpy}	2.182	2.181	2.183	2.184	2.182	2.181	2.182	2.182	
Re–CO_{ax}	1.939	1.939	1.940	1.939	1.940	1.939	1.940	1.939	
Re–CO_{eq}	1.926	1.928	1.925	1.926	1.927	1.928	1.927	1.925	
Re–N_{ret}	2.225	2.219	2.224	2.220	2.223	2.223	2.224	2.227	
$N_{bpy}ReN_{ret}$	88.5	84.0	86.7	87.6	87.9	87.8	88.3	89.0	
$CO_{ax}ReCO_{eq}$	89.4	90.1	89.8	89.8	89.5	89.5	89.4	89.1	
$CO_{eq}ReCO_{eq}$	90.6	90.9	90.7	90.6	90.6	90.5	90.6	90.7	
CN–C_{16}	1.425	1.425	1.424	1.425	1.427	1.426	1.426	1.425	1.427
C_{16}–C_{15}	1.396	1.397	1.397	1.396	1.395	1.397	1.396	1.407	1.383
C_{15}–C_{14}	1.406	1.404	1.400	1.400	1.406	1.405	1.406	1.396	1.415
C_{14}–C_{13}	1.397	1.398	1.398	1.398	1.401	1.401	1.397	1.396	1.386
C_{13}–C_{12}	1.422	1.420	1.419	1.419	1.420	1.425	1.424	1.423	1.433
C_{12}–C_{11}	1.382	1.383	1.384	1.383	1.383	1.391	1.380	1.381	1.375
C_{11}–C_{10}	1.412	1.410	1.410	1.410	1.412	1.414	1.414	1.413	1.422
C_{10}–C_9	1.390	1.390	1.391	1.391	1.390	1.392	1.392	1.390	1.382
C_9–C_8	1.434	1.433	1.433	1.433	1.434	1.434	1.435	1.441	1.443
C_8–C_7	1.372	1.372	1.373	1.372	1.372	1.372	1.369	1.369	1.365
C_7–C_6	1.450	1.449	1.449	1.449	1.449	1.450	1.453	1.465	1.460
C_{sp2}–Me	1.506	1.506	1.505	1.506	1.506	1.506	1.508	1.504	1.508
C_{sp3}–Me	1.545	1.545	1.544	1.545	1.544	1.545	1.545	1.545	1.544

[a]Numbering of the C atoms according to Scheme 1.

DOI: 10.1021/acs.jpca.5b08047
J. Phys. Chem. A XXXX, XXX, XXX–XXX

Scheme 2. Kohn−Sham Orbitals of the All-*trans*-$[Re(CO)_3(bpy)(L)]^+$ a Conformer in Acetonitrile

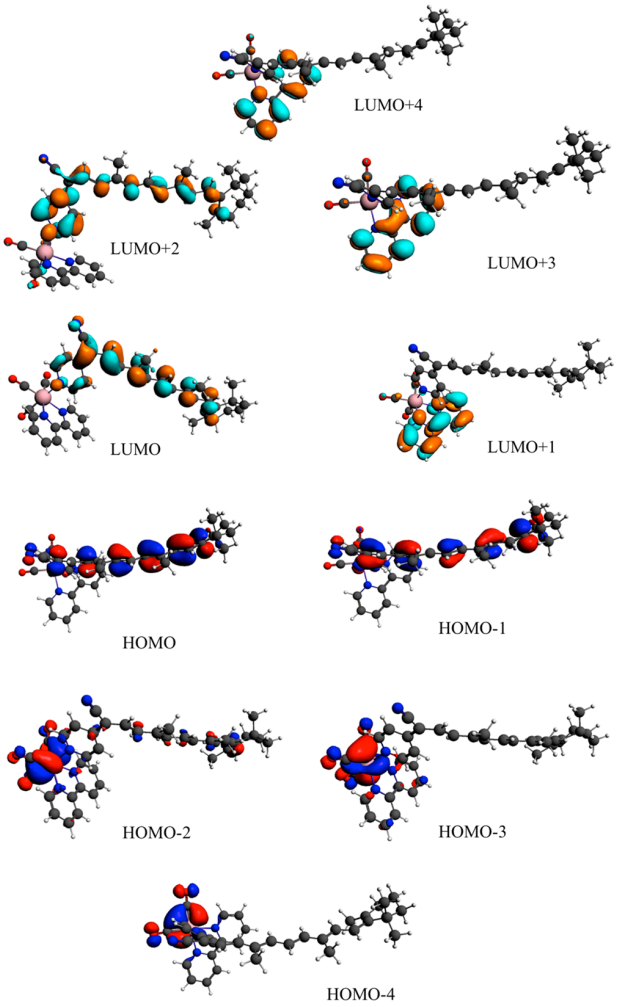

Scheme 3. Kohn−Sham Orbitals of the *cis*-$[Re(CO)_3(bpy)(L)]^+$ 1c Conformer in Acetonitrile

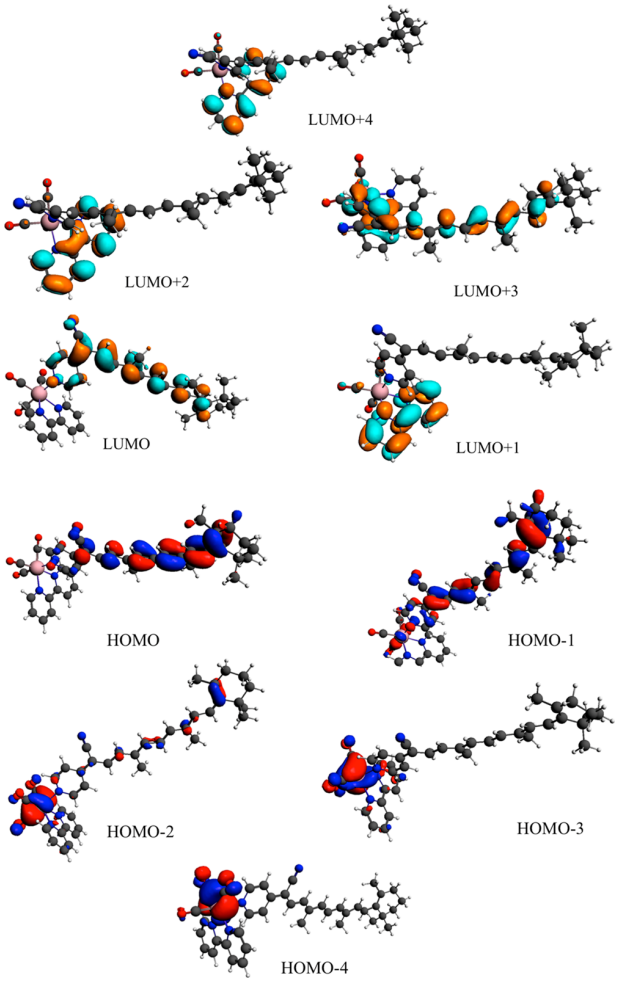

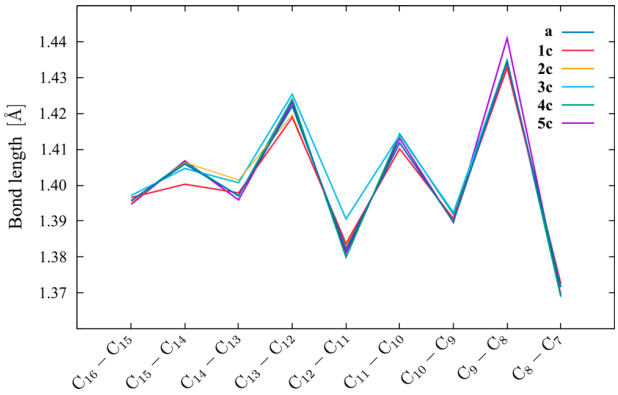

Figure 2. Bond length alteration in the retinal-like chain of carbon atoms.

structure we may consider these geometries as good starting points for subsequent excited-states calculations.

The relative energies of the five investigated *cis*-$[Re(CO)_3(bpy)(L)]^+$ conformers **1c**−**5c**, **1c**-α_{opt} are reported in Table 2 and compared to those of the all-trans **a** and **a**-α_{opt}.

For all conformers reported in Table 2 the dihedral angle α (Scheme 1) was kept to 8.6°, value obtained after geometry optimization in the electronic ground state of the all-trans conformer **a**. When α is relaxed in **a** to give the **a**-α_{opt} conformer its value increases to 22°, and the all-trans conformer is stabilized by 22.2 kJ mol^{-1} due to a decrease of steric interactions between the retinal-CN and the bipyridine ligands. The relaxation of the dihedral angle α is less dramatic in the **1c** cis conformer with a minor stabilization of 8.7 kJ mol^{-1} corresponding to a value of α of 1.8° in **1c**-α_{opt}. Indeed, the steric effects are less important in the cis conformers. According to the results reported in Table 2 the all-trans and the lowest cis conformers are nearly degenerate. The other cis conformers are destabilized with respect to the most stable isomers by ∼30−50 kJ mol^{-1}. Interestingly, the cis isomers **3c** and **5c**, corresponding to a torsion of the C═C bonds nonsubstituted by a methyl group, namely, the central one (C_{11}−C_{12}) and the external one linked to the trimethyl cyclohexen (C_8−C_7) range in the same energy, namely, ∼50 kJ mol^{-1} or 0.5 eV above the most stable isomers. The cis isomers **2c** and **4c** corresponding to a torsion of the C═C bonds substituted by a methyl group (C_{13}−C_{14} and C_9−C_{10}) are more stable by ∼20 kJ mol^{-1} or 0.2 eV ranging at ∼30 kJ mol^{-1} or 0.3 eV above the all-*trans*- and *cis*-**1c** isomers.

DOI: 10.1021/acs.jpca.5b08047
J. Phys. Chem. A XXXX, XXX, XXX−XXX

Table 2. Relative Energies (in kJ mol^{-1}, in eV, and in cm^{-1}) of the *cis*- and *trans*-$[Re(CO)_3(bpy)(L)]^+$ Conformers

	ΔE (kJ mol^{-1})	ΔE (eV)	ΔE (cm^{-1})
a	30.9	0.32	2581
a-α_{opt}	8.7	0.09	726
1c	8.7	0.09	726
1c-α_{opt}	0.0	0.0	0.0
2c	32.8	0.34	2742
3c	51.1	0.53	4275
4c	34.7	0.36	2904
5c	54.0	0.56	4517

To get a qualitative picture of the trans to cis pathway the state correlation diagrams describing the all-trans $[Re(CO)_3(bpy)(L)]^+$ **a** to the cis **1c**, **2c**, and **4c** isomerizations and associated with the electronic ground state and low-lying singlet and triplet excited states are presented in the next section. The solvent correction (acetonitrile) was taken into account.

State Correlation Diagrams. The TD-DFT state correlation diagrams associated with the electronic ground state and the low-lying singlet and triplet excited states of $[Re(CO)_3(bpy)(L)]^+$ and calculated as a function of the torsion angle τ of the isomerizable CC double bond are represented in Figure 3 for the all-trans **a** to **1c**, **2c**, and **4c** isomerization pathways leading to the three most stable cis conformers. The corresponding energy values are reported in Table 3. The overall shapes of the three states correlation diagrams depicted in Figure 3a−c are very similar.

Because of the crude approximation used in the computation of the potential energy profiles that does not reflect the collective torsion motion characterizing the retinal chromophore[52,53] a comparison between the Re(I) complex and the isolated chromophore is not straightforward. The energy barrier for a single isomerization in isolated retinal was recently measured at 0.64 ± 0.05 eV.[54] The electronic ground-state pathway to the **1c** and **2c** conformers is characterized by an energy barrier upper limit of 1.09 eV, while a value of 1.42 eV is calculated for the isomerization to the **4c** conformer. Search for a true transition state at the perpendicular conformation (τ = 90°) would certainly lower these estimated values.

All the excited electronic states correlated in Figure 3 are potentially populated upon irradiation of all-*trans*-$[Re(CO)_3(bpy)(L)]^+$ **a** by visible light (400−450 nm), either directly by absorption (b^1IL_{ret}, c^1IL_{ret}, a^1MLCT_{ret}) or indirectly by internal conversion or ISC (a^3IL_{ret}, b^3IL_{ret}, a^1IL_{ret}). All these states will play a key role in the complicated photophysics at the early stage (a few picoseconds) and in the mechanism of the photoinduced isomerization process. The upper electronic states, initially populated, are characterized by too high-energy barriers for participating to the isomerization and will probably decay within the first picosecond to the three lowest IL_{ret} states. Isomerization may proceed along the potential energy surfaces associated with these three excited states but, owing the low-energy profile along the torsion angle τ, may decay back to the all-trans as well. The high energy of the MLCT states excludes them of the mechanism, in contrast to what was found for stilbene-like substituted Re(I) carbonyl bpy complexes,[23−25] and makes competitive luminescent channels unlikely.

From the relative stabilities of the cis conformers and state correlations diagrams depicted in Figure 3 we may conclude that the all-trans **a** to **1c** and **2c** cis conformers isomerization

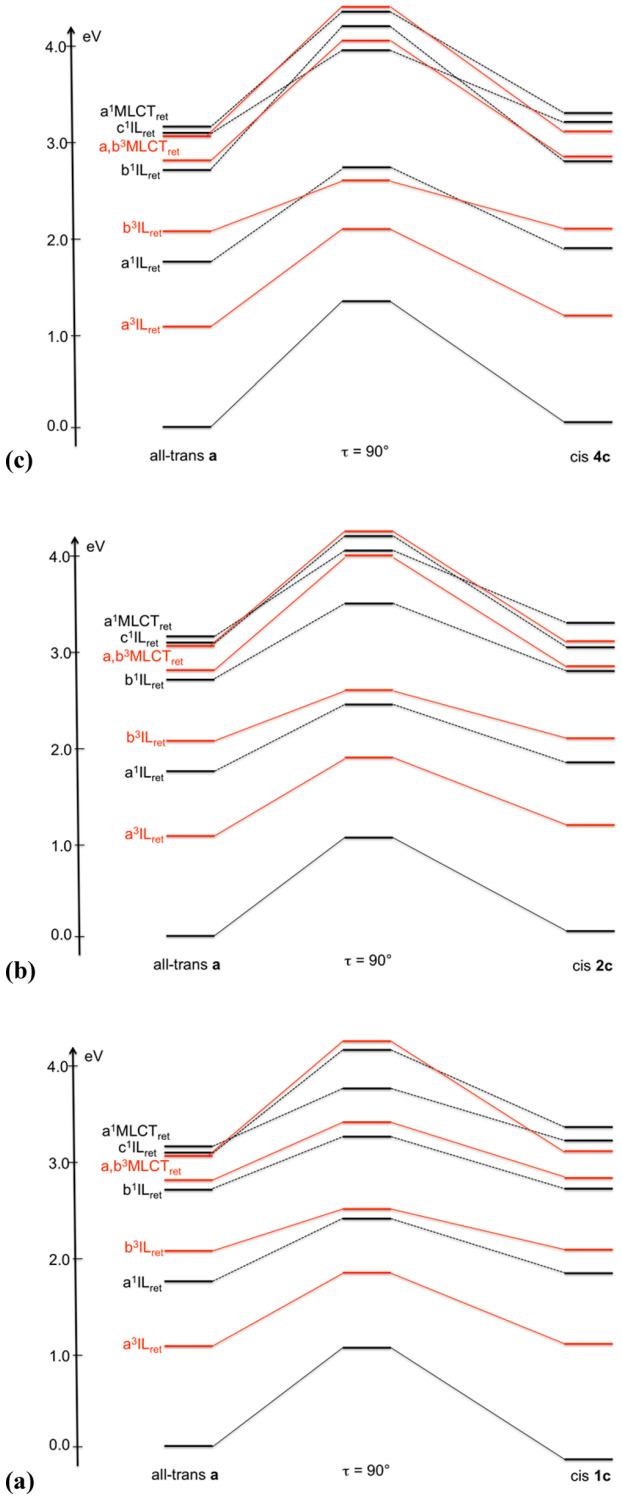

Figure 3. TD-DFT state correlation diagrams connecting the low-lying singlet and triplet excited states of all-trans $[Re(CO)_3(bpy)(L)]^+$ **a** to the corresponding states of the cis isomers (a) **1c**, (b) **2c**, and (c) **4c**. (black: singlet states; red: triplet states).

pathways occurring at the $C_{16}C_{15}$ and $C_{14}C_{13}$ double bonds close to the $[Re(CO)_3(bpy)]$ fragment (Scheme 1) are more favorable. We may anticipate that the b^3IL_{ret} is the most reactive state because of the low energy barrier characterizing this

DOI: 10.1021/acs.jpca.5b08047
J. Phys. Chem. A XXXX, XXX, XXX−XXX

Table 3. Relative Energies (eV) of the Low-Lying Singlet and Triplet States of $[Re(CO)_3(bpy)(L)]^+$ as Function of the Isomerizable Double CC Bond Torsion Angle τ[a]

state	τ = 180°	τ = 90°	τ = 0°
all-trans **a** to **1c**			
ground state	0.0	1.09	−0.18
a^3ILret	1.13	1.89	1.14
a^1ILret	1.79	2.45	1.80
b^3ILret	2.10	2.50	2.11
b^1IL_{ret}	2.78	3.29	2.81
a^3MLCT_{ret}	2.84	3.43	2.86
b^3MLCT_{ret}	3.10	4.15	3.15
c^1IL_{ret}	3.10	4.07	3.27
a^1MLCT_{ret}	3.15	3.79	3.18
all-trans **a** to **2c**			
ground state	0.0	1.09	0.05
a^3ILret	1.13	1.91	1.22
a^1ILret	1.79	2.48	1.85
b^3ILret	2.10	2.68	2.14
b^1IL_{ret}	2.78	3.51	2.87
a^3MLCT_{ret}	2.84	3.87	2.87
b^3MLCT_{ret}	3.10	4.19	2.95
c^1IL_{ret}	3.10	4.15	3.11
a^1MLCT_{ret}	3.15	3.89	3.23
all-trans **a** to **4c**			
ground state	0.0	1.42	0.05
a^3ILret	1.13	2.04	1.25
a^1ILret	1.79	2.78	1.88
b^3ILret	2.10	3.43	2.15
b^1IL_{ret}	2.78	4.15	2.85
a^3MLCT_{ret}	2.84	3.93	2.87
b^3MLCT_{ret}	3.10	4.50	3.15
c^1IL_{ret}	3.10	3.83	3.18
a^1MLCT_{ret}	3.15	4.42	3.21

[a]The energy of reference is the electronic ground state of the all-trans conformer **a**.

potential, barrier that could be overcome easily by activation energy provided by relaxation of higher excited states. Consequently, exciting at ∼400 nm to the upper group of $MLCT_{ret}$ and IL_{ret} states could be more efficient than irradiation at 700 nm to the lowest a^1IL_{ret} state that would require thermal activation because of a relatively high energy barrier along the isomerization pathway. The population of the MLCT states is particularly promising because of the efficiency of ISC within the ^{1,3}MLCT manifold. In contrast isomerization via the $a^1IL/^3IL$ states will proceed at longer time scale supposing that this set of states will be sufficiently long-lived. No further conclusion can be achieved at this qualitative level of analysis; that must be completed by forthcoming experimental data.

Time-Dependent Density Functional Theory Absorption Spectra. The transition energies to the low-lying singlet excited states of all-*trans*-$[Re(CO)_3(bpy)(L)]^+$ **a** and *cis*-**1c** conformers in acetonitrile are reported in Table 4 together with the wavelengths of absorption, oscillator strengths, and one-electron excitations in the main configuration. The corresponding data obtained for the cis conformers **2c**−**5c** are reported in Table S2 of the Supporting Information.

The calculated absorption spectra are depicted in Figures 4 and 5 for the all-*trans*-**a** and *cis*-**1c**−**5c** conformers, respectively. The visible absorption starts at ∼700 nm for all conformers.

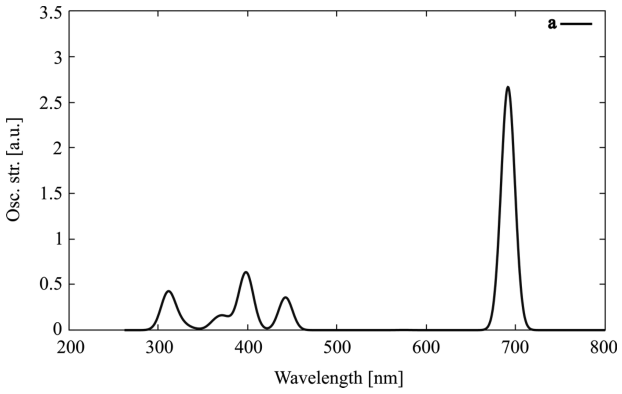

Figure 4. Calculated TD-DFT absorption spectrum of the all-*trans*-**a** conformer of $[Re(CO)_3(bpy)(L)]^+$ in acetonitrile.

Both conformers, namely, the all-*trans*-**a** and the *cis*-**1c**, corresponding to the trans−cis isomerization at the $C_{15}-C_{16}$ double bond of **a**, are characterized by similar TD-DFT absorption spectra exhibiting one very intense peak at ∼700 nm

Table 4. TD-DFT Transition Energies (eV), Wavelengths of Absorption (in nm), and Oscillator Strengths *f* Associated to the Low-Lying Singlet Excited States of All-*trans*-$[Re(CO)_3(bpy)(L)]^+$ a and cis 1c Confomers in Acetonitrile

conformer	state character	one-electron excitation[a]	transition energies (eV)	absorption wavelengths (nm)	*f*
all-*trans*-**a**	a^1IL_{ret}	$\pi_{ret} \rightarrow \pi^*_{ret}$	1.79	692	2.67
	b^1IL_{ret}	$\pi_{ret} \rightarrow \pi^*_{ret}$	2.78	450	0.36
	$^1LLCT_{ret\text{-}bpy}/\ ^1MLCT_{bpy}$	61% $\pi_{ret} \rightarrow \pi^*_{bpy}$ /37% $5d_{Re} \rightarrow \pi^*_{bpy}$	3.01	415	0.01
	c^1IL_{ret}	$\pi_{ret} \rightarrow \pi^*_{ret}$	3.10	403	0.49
	a^1MLCT_{ret}	$5d_{Re} \rightarrow \pi^*_{ret}$	3.15	396	0.16
	a^1MLCT_{bpy}	$5d_{Re} \rightarrow \pi^*_{bpy}$	3.31	378	0.09
cis-**1c**	a^1IL_{ret}	$\pi_{ret} \rightarrow \pi^*_{ret}$	1.75	714	3.13
	b^1IL_{ret}	$\pi_{ret} \rightarrow \pi^*_{ret}$	2.76	450	0.26
	$^1LLCT_{ret\text{-}bpy}/\ ^1MLCT_{bpy}$	61% $\pi_{ret} \rightarrow \pi^*_{bpy}$ /35% $5d_{Re} \rightarrow \pi^*_{bpy}$	3.01	415	0.01
	a^1MLCT_{ret}	$5d_{Re} \rightarrow \pi^*_{ret}$	3.13	399	0.07
	b^1MLCT_{ret}	$5d_{Re} \rightarrow \pi^*_{ret}$	3.21	389	0.01
	c^1IL_{ret}	$\pi_{ret} \rightarrow \pi^*_{ret}$	3.22	388	0.01
	a^1MLCT_{bpy}	$5d_{Re} \rightarrow \pi^*_{bpy}$	3.31	377	0.13

[a]For the sake of clarity the weight (%) values are omitted when they are greater than 90%.

DOI: 10.1021/acs.jpca.5b08047
J. Phys. Chem. A XXXX, XXX, XXX−XXX

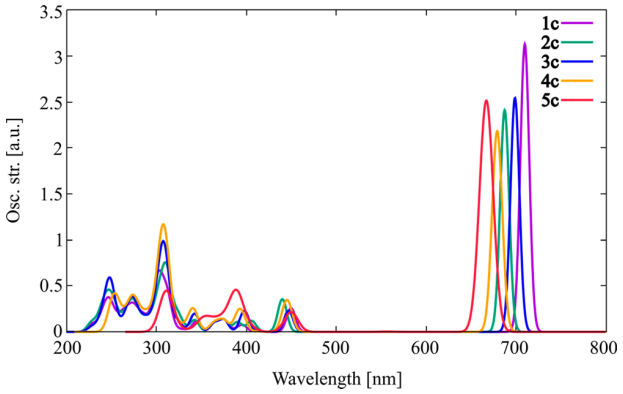

Figure 5. Calculated TD-DFT absorption spectra of the *cis*-**1c**−**5c** conformers of $[Re(CO)_3(bpy)(L)]^+$ in acetonitrile.

associated with the a^1IL_{ret} transition corresponding to a HOMO → LUMO excitation and localized on the retinal part of ret-pyr-CN ligand. The next visible band is calculated at 450 nm and corresponds to another IL transition (b^1IL_{ret}) namely a HOMO−1 → LUMO excitation. The HOMO−1 being slightly delocalized over the metal, the associated oscillator strength is weaker. Both conformers exhibit $LLCT_{ret\text{-}bpy}/MLCT_{bpy}$ mixed states at 415 nm with a rather small oscillator strength (0.01). The $LLCT_{ret\text{-}bpy}$ contributions must be taken with care because of the possible underestimation of their transition energies due to erroneous treatment of long-range charge transfer interactions by B3LYP. Owing to their low oscillator strengths, these states should not participate to the photochemistry of $[Re(CO)_3(bpy)(L)]^+$.

The experimental absorption spectra of the isolated chromophore ret-pyr-CN and of the all-*trans*-$[Re(CO)_3(bpy)(L)]^+$ conformer recorded in acetonitrile exhibit a band attributed to an IL_{ret} state at 440 and 465 nm, respectively.[29] These maxima are also present in the TD-DFT theoretical spectra of the all-trans **a** (Figure 4) and **1c**−**5c** cis (Figure 5) conformers and are indeed assigned to the b^1IL_{ret} transition. This band that could play a key role after absorption at 400−450 nm, the usual wavelength of irradiation of Re(I) complexes, does not correspond to the HOMO−LUMO $\pi\pi^*$ excitation purely localized on the ret-pyr-CN and calculated here at 692 nm in the all-trans conformer **a** transition that gives rise to a very intense peak and is probably solvatochromic as reported for a number of retinal models in various environments including proteins.[55] The lowest MLCT states correspond to charge transfer to the ret-pyr-CN ligand and are calculated above 400 nm with modest oscillator strengths as compared to the IL_{ret} states. The potentially luminescent MLCT states delocalized over the bpy ligand start at ∼375 nm and will be hardly accessible by absorption in the visible energy domain.

Two low-lying triplet $^3IL_{ret}$ excited states, corresponding to the two lowest $^1IL_{ret}$ reported in Table 3, are calculated at 1.13 and 2.10 eV in the all-trans conformer **a** and at 1.09 and 2.06 eV in the most stable **1c** cis conformer. They will potentially play a key role in isomerization processes activated after absorption at 400 nm to the second $^1IL_{ret}$ state.

The theoretical spectrum of the isolated chromophore **b** shows one intense peak calculated at 627 nm (f = 2.77) and one band at 415 nm. Whereas the lowest $^1IL_{ret\text{-}pyr\text{-}CN}$ band corresponds to the HOMO−LUMO excitation, the second less intense $^1IL_{ret\text{-}pyr\text{-}CN}$ band corresponds to the HOMO−1 to LUMO excitation and is assigned to the experimental band observed at 440 nm.[29] The character of these transitions in the isolated chromophore **b** are slightly different from the related bands found in the Re(I) complexes **a** and **c**. Indeed whereas the LUMO compares rather well in the three molecules, the HOMO and HOMO−1 differ by their delocalized features, namely, on the pyridyl coordinated to the Re atom in the metal complex and on the cyclohexene in the retinal-like isolated ligand (Scheme 4). The consequence is a red shift of the $^1IL_{ret\text{-}pyr\text{-}CN}$ bands when going from the organic ligand to the metal complex well-reproduced by the calculations. Indeed whereas the lowest $IL_{ret\text{-}pyr\text{-}CN}$ band is calculated at 627 nm in the isolated organic chromophore and shifted to 700 nm in $[Re(CO)_3(bpy)(L)]^+$ (a^1IL_{ret}), a value of 415 nm is obtained for the second $IL_{ret\text{-}pyr\text{-}CN}$ band in the isolated organic ligand as compared to 450 nm (b^1IL_{ret}) in the complex. Moreover this theoretical red shift reproduces rather well the experimental one observed in the absorption spectra recorded in acetonitrile, namely, with maxima at 440 nm (isolated chromophore) and 465 nm (metal complex).[29]

Scheme 4. Comparison between the Frontiers Kohn−Sham Orbitals of the All-*trans*-$[Re(CO)_3(bpy)(L)]^+$ a and of the Isolated Retinal-Like Ligand b

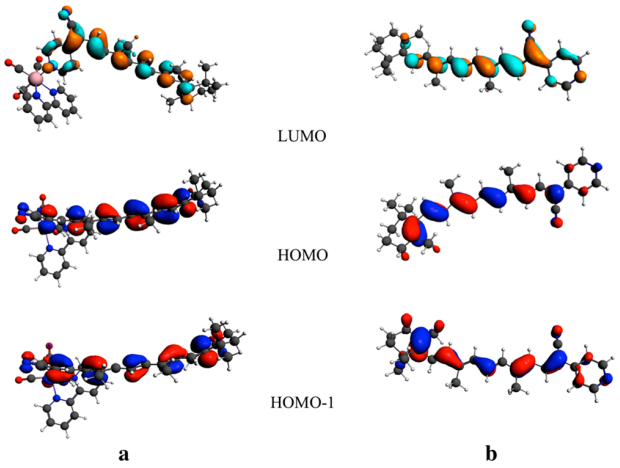

Finally the TD-DFT absorption spectra of the five cis conformers **1c**−**5c** represented in Figure 5 are rather similar. We observe a significant red shift of the lowest band from **5c** (670 nm) to the most stable cis conformer **1c** (710 nm) due to a decrease in HOMO−LUMO energy gap. The band around 450 nm that corresponds to the second b^1IL_{ret} transition is stable within the series. The upper UV intense band gains in intensity and is slightly blue-shifted in the conformer **4c** (300 nm) as compared to the other cis conformers (310 nm) due to a change of character from IL_{bpy} (in **1c**, **2c**, **3c**, and **5c**) to IL_{ret} in **4c**.

CONCLUSION

The molecular structure and electronic and optical properties of the all-trans and various cis conformers of $[Re(CO)_3(bpy)(L)]^+$ have been studied by means of DFT and TD-DFT with the aim of investigating the potential of this molecule, not yet deeply considered experimentally, in photo switches applications. Several isomerization pathways will be open upon

DOI: 10.1021/acs.jpca.5b08047
J. Phys. Chem. A XXXX, XXX, XXX−XXX

irradiation by visible light (400−450 nm), especially to two cis conformers corresponding to the isomerization of the two double bonds of the retinal-like ligand close to pyridyl group linked to the Re(I) fragment. Whereas the MLCT states localized either on the retinal group or on the bpy ligand should play a minor role in the absorption, two low-lying IL states, calculated at 450 and 400 nm and localized on the retinal entity, can be populated efficiently.

Ultrafast decay within the first picosecond is expected to lead to the lowest ^{3}IL states from which isomerization may proceed. However, while these channels are unlikely quenched by luminescence processes because of the high energy of the MLCT states, their efficiency could be affected by decay back to the all-trans electronic ground state leading to modest quantum yield.

It would be hazardous to push the analysis further at this qualitative level of consideration. Indeed upcoming experimental data should complete our analysis before undertaking more quantitative investigations based on accurate potential energy surfaces associated with the key electronic states put in evidence in the present study.

■ ASSOCIATED CONTENT

Supporting Information

The Supporting Information is available free of charge on the ACS Publications website at DOI: 10.1021/acs.jpca.5b08047.

Cartesian coordinates corresponding to the fully optimized structures, TD-DFT transition energies, absorption wavelengths, and oscillator strengths of **2c**−**5c**, Frontier Kohn−Sham orbitals of **2c**−**5c**. (PDF)

■ AUTHOR INFORMATION

Notes

The authors declare no competing financial interest.

■ ACKNOWLEDGMENTS

J.E. thanks the Doctoral School in Chemistry (Strasbourg) for funding. The authors are grateful to Dr. C. Gourlaouen for valuable and stimulating discussions. The European actions COST perspect-H_2O and CODEC are acknowledged as well as the Labex "Chimie des Systèmes Complexes" (ANR-10-LABX-0026_CSC). The quantum chemical calculations were performed on the computer nodes of the LCQS, Strasbourg, and thanks to the computer facilities of the High Performance Computing (HPC) regional center of Univ. of Strasbourg.

■ REFERENCES

(1) Kumar, A.; Sun, S.-S.; Lees, A. J. Photophysics and Photochemistry of Organometallic Rhenium Diimine Complexes. In *Topics in Organometallic Chemistry: Photophysics of Organometallics;* Springer-Verlag : Berlin Heidelberg, 2010; Vol. *29*, pp 37 − 71.

(2) Vlček, A., Jr. Ultrafast Excited-State Processes in Re(I) Carbonyl-Diimine Complexes: From Excitation to Photochemistry. In *Topics in Organometallic Chemistry: Photophysics of Organometallics;* Springer-Verlag: Berlin Heidelberg, 2010; Vol. *29*, pp 115−158.

(3) Leonidova, A.; Gasser, G. Underestimated Potential of Organometallic Rhenium Complexes as Anticancer Agents. *ACS Chem. Biol.* **2014**, *9*, 2180−2193.

(4) Kuninobu, Y.; Takai, K. Organic Reactions Catalyzed by Rhenium Carbonyl Complexes. *Chem. Rev.* **2011**, *111*, 1938−1953.

(5) Wenger, O. S. Proton-Coupled Electron Transfer with Photoexcited Ruthenium(II), Rhenium(I), and Iridium(III) complexes. *Coord. Chem. Rev.* **2015**, *282*−*283*, 150−158.

(6) Lo, K. K.-W.; Louie, M.-W.; Sze, K.-S.; Lau, J. S.-Y. Rhenium(I) Polypyridine Biotin Isothiocyanate Complexes as the First Luminescent Biotinylation Reagents: Synthesis, Photophysical Properties, Biological Labeling, Cytotoxicity, and Imaging Studies. *Inorg. Chem.* **2008**, *47*, 602−611.

(7) Lo, K. K.-W.; Tsang, K. H.-K.; Sze, K.-S. Utilization of the Highly Environment-Sensitive Emission Properties of Rhenium(I) Amidodipyridoquinoxaline Biotin Complexes in the Development of Biological Probes. *Inorg. Chem.* **2006**, *45*, 1714−1722.

(8) Choi, A. W.-T.; Louie, M.-W.; Li, S. P.-Y.; Liu, H.-W.; Chan, B. T.-N.; Lam, T. C.-Y.; Lin, A. C.-C.; Cheng, S.-H.; Lo, K. K.-W. Emissive Behavior, Cytotoxic Activity, Cellular Uptake, and PEGylation Properties of New Luminescent Rhenium(I) Polypyridine Poly(ethylene glycol) Complexes. *Inorg. Chem.* **2012**, *51*, 13289−13302.

(9) Louie, M. W.; Fong, T.-H.; Lo, K. K.-W. Luminescent Rhenium(I) Polypyridine Fluorous Complexes as Novel Trifunctional Biological Probes. *Inorg. Chem.* **2011**, *50*, 9465−9471.

(10) Chan, C. Y.; Pellegrini, P. A.; Greguric, I.; Barnard, P. J. Rhenium and Technetium Tricarbonyl Complexes of N-Heterocyclic Carbene Ligands. *Inorg. Chem.* **2014**, *53*, 10862−10873.

(11) Blanco-Rodriguez, A. M.; Di Bilio, A. J.; Shih, C.; Museth, A. K.; Clark, I. P.; Towrie, M.; Cannizzo, A.; Sudhamsu, J.; Crane, B. R.; Sykora, J.; Winkler, J. R.; Gray, H. B.; Záliš, S.; Vlček, A., Jr. Phototriggering electron flow through Re^{I}-modified Pseudomonas areruginosa Azurins. *Chem. - Eur. J.* **2011**, *17*, 5350−5361.

(12) Blanco-Rodriguez, A. M.; Towrie, M.; Sykora, J.; Záliš, S.; Vlček, A., Jr. Photoinduced Intramolecular Tryptophan Oxidation and Excited-State Behavior of $[Re(L\text{-}AA)\ (CO)_3(\alpha\text{-diimine})]^+$ (L = pyridine or imidazole, AA = tryptophan, tyrosine, phenylalanine). *Inorg. Chem.* **2011**, *50*, 6122−6134.

(13) Blanco-Rodriguez, A. M.; Busby, M.; Grădinaru, C.; Crane, B. R.; Di Bilio, A. J.; Matousek, P.; Towrie, M.; Leigh, B. S.; Richards, J. H.; Vlček, A., Jr.; Gray, H. B. Excited States Dynamics of Structurally Characterized $[Re(CO)_3(phen)HisX]^+$ (X = 83, 109) *Pseudomonas aeruginosa* Azurins in Aqueous Solution. *J. Am. Chem. Soc.* **2006**, *128*, 4365−4370.

(14) Blanco-Rodriguez, A. M.; Busby, M.; Ronayne, K.; Towrie, M.; Grădinaru, C.; Sudhamsu, J.; Sykora, J.; Hof, M.; Záliš, S.; Di Bilio, A. J.; Crane, B. R.; Gray, H. B.; Vlček, A., Jr. Relaxation Dynamics of *Pseudomonas aeruginosa* $[Re(CO)_3(\alpha\text{-diimine})HisX]^+$ (X = 83, 107, 109, 124, 126) Cu^{II} Azurins. *J. Am. Chem. Soc.* **2009**, *131*, 11788−11800.

(15) Kirgan, R. A.; Patrick Sullivan, B.; Rillema, D. P. Photochemistry and Photophysics of Coordination Compounds: Rhenium. In *Topics In Current Chemistry: Photochemistry and Photophysics of Coordination Compounds;* Springer-Verlag: Berlin Heidelberg, 2007; Vol. *281*, pp 45−100.

(16) McCusker, J. K. Femtosecond Absorption Spectroscopy of Transition Metal Charge-Transfer Complexes. *Acc. Chem. Res.* **2003**, *36*, 876−887.

(17) Chergui, M. On the Interplay Between Charge, Spin and Structural dynamics in Transition Metal Complexes. *Dalton Trans.* **2012**, *41*, 13022−13029.

(18) El Nahhas, A.; Consani, C.; Blanco-Rodríguez, A. M.; Lancaster, K. M.; Braem, O.; Cannizzo, A.; Towrie, M.; Clark, I. P.; Záliš, S.; Chergui, M.; Vlček, A., Jr. Ultrafast Excited-State Dynamics of Rhenium(I) Photosensitizers $[Re(Cl)\ (CO)_3(N,N)]$ and $[Re(imidazole)\ (CO)_3(N,N)]^+$: Diimine Effects. *Inorg. Chem.* **2011**, *50*, 2932−2943.

(19) Wenger, O. S.; Henling, L. M.; Day, M. W.; Winkler, J. R.; Gray, H. B. Rhenium(I) Tricarbonyl Complexes With Photoisomerizable Ligands. *Polyhedron* **2004**, *23*, 2955−2958.

(20) Busby, M.; Matousek, P.; Towrie, M.; Vlček, A., Jr. Ultrafast Excited-State Dynamics Preceding a Ligand Trans-Cis Isomerization of *fac*-$[Re(Cl)\ (CO)_3(t\text{-4-styrylpyridine})_2]$ and *fac*-$[Re(t\text{-4-styrylpyridine})\ (CO)_3(2,2'\text{-bipyridine})]^+$. *J. Phys. Chem. A* **2005**, *109*, 3000−3008.

DOI: 10.1021/acs.jpca.5b08047
J. Phys. Chem. A XXXX, XXX, XXX−XXX

(21) Polo, A. S.; Itokazu, M. K.; Frin, K. M.; de Toledo Patrocınio, A. O.; Murakami Iha, N. Y. Light Driven *trans*-to-*cis* Isomerization of Stilbene-like Ligands in *fac*-[Re(CO)$_3$(NN)(*trans*-L)]$^+$ and Luminescence of their Photoproducts. *Coord. Chem. Rev.* **2006**, *250*, 1669−1680.
(22) de Toledo Patrocinio, A. O.; Brennaman, M. K.; Meyer, T. J.; Murakami Iha, N. Y. Excited-State Dynamics in *fac*-[Re(CO)$_3$(Me$_4$phen)(L)]$^+$. *J. Phys. Chem. A* **2010**, *114*, 12129−12137.
(23) Kayanuma, M.; Daniel, C.; Gindensperger, E. Spectroscopic Trends in a Series of Re (I) α-diimine Complexes as a Function of the Antenna/Photoisomerizable Ligands: A TD-DFT and MS-CASPT2 study. *Can. J. Chem.* **2014**, *92*, 979−986.
(24) Kayanuma, M.; Gindensperger, E.; Daniel, C. Inorganic Photoisomerization: The Case Study of Rhenium (I) Complexes. *Dalton Trans.* **2012**, *41*, 13191−13203.
(25) Kayanuma, M.; Daniel, C.; Köppel, H.; Gindensperger, E. Photophysics of Isomerizable Re (I) Complexes: A Theoretical Analysis. *Coord. Chem. Rev.* **2011**, *255*, 2693−2703.
(26) Gindensperger, E.; Köppel, H.; Daniel, C. Mechanism of Visible-Light Photoisomerization of a Rhenium (I) Carbonyl−diimine Complex. *Chem. Commun.* **2009**, *46*, 8225−8227.
(27) Bossert, J.; Daniel, C. *Trans*−*cis* Photoisomerization of the Styrylpyridine Ligand in [Re (CO)$_3$ (2, 2′-bipyridine)(t-4-styrylpyridine)]$^+$: Role of the Metal-to-Ligand Charge-Transfer Excited States. *Chem. - Eur. J.* **2006**, *12*, 4835−4843.
(28) Vlček, A., Jr.; Busby, M. Ultrafast Ligand-to-Ligand Electron and Energy Transfer in the Complexes *fac*-[Re^{I}(L) (CO)$_3$(bpy)]n^+. *Coord. Chem. Rev.* **2006**, *250*, 1755−1762.
(29) Cruz, A. J.; Kirgan, R. A.; Siam, K.; Islam, M. R.; Moore, C.; Rillema, D. P. Synthesis, Structural Elucidation, Electrochemical and UV/Visible Absorption Studies of Pyridyl-Carotenoid Ligands to Rhenium (I) and Platinum (II). In *Proceedings of the 3rd Annual GRASP Symposium;* Eichhorn, D. M., Kovar, S.; Wichita State University: Wichita, KS, 2007; pp 169−170.
(30) Marchand, G.; Eng, J.; Schapiro, I.; Valentini, A.; Frutos, L. M.; Pieri, E.; Olivucci, M.; Léonard, J.; Gindensperger, E. On the Directionality of Double Bond Photoisomerization Dynamics Induced by a Single Stereogenic Center. *J. Phys. Chem. Lett.* **2015**, *6*, 599−604.
(31) Grimme, S. Semiempirical GGA-type Density Functional Constructed with a Long-Range Dispersion Correction. *J. Comput. Chem.* **2006**, *27*, 1787−1799.
(32) van Lenthe, E.; Baerends, E. J. Optimized Slater-type Basis Sets for the Elements 1−118. *J. Comput. Chem.* **2003**, *24*, 1142−1156.
(33) van Lenthe, E.; van Leeuwen, R.; Baerends, E. J.; Snijders, J. G. Relativistic Regular Two-Component Hamiltonians. *Int. J. Quantum Chem.* **1996**, *57*, 281−293.
(34) Runge, E.; Gross, E. K. U. Density-Functional Theory for Time-Dependent Systems. *Phys. Rev. Lett.* **1984**, *52*, 997−1000.
(35) Petersilka, M.; Gossmann, U. J.; Gross, E. K. U. Excitation Energies from Time-Dependent Density-Functional Theory. *Phys. Rev. Lett.* **1996**, *76*, 1212−1215.
(36) Becke, A. D. Density Functional Thermochemistry. III. The role of Exact Exchange. *J. Chem. Phys.* **1993**, *98*, 5648−5652.
(37) Stephens, P. J.; Devlin, F. J.; Chabalowski, C. F.; Frisch, M. J. Ab initio Calculation of Vibrational Absorption and Circular Dichroism Spectra Using Density Functional Force Fields. *J. Phys. Chem.* **1994**, *98*, 11623−11627.
(38) Peach, M. J.; Tozer, D. J. Overcoming Low Orbital Overlap and Triplet Instability Problems in TDDFT. *J. Phys. Chem. A* **2012**, *116*, 9783−9789.
(39) Yanai, T.; Tew, D. P.; Handy, N. C. A New Hybrid Exchange−Correlation Functional Using the Coulomb-Attenuating Method (CAM-B3LYP). *Chem. Phys. Lett.* **2004**, *393*, 51−57.
(40) Daniel, C. Photochemistry and Photophysics of Transition Metal Complexes: Quantum Chemistry. *Coord. Chem. Rev.* **2015**, *282-283*, 19−32.
(41) Gourlaouen, C.; Daniel, C.; Durola, F.; Frey, J.; Heitz, V.; Sauvage, J.-P.; Ventura, B.; Flamigni, L. NIR Dual Luminescence from an Extended Porphyrin Spectroscopy, Photophysics and Theory. *J. Phys. Chem. A* **2014**, *118*, 3616−3624.
(42) Klamt, A.; Schüürmann, G. COSMO: a New Approach to Dielectric Screening in Solvents with Explicit Expressions for the Screening Energy and its Gradient. *J. Chem. Soc., Perkin Trans. 2* **1993**, *2*, 799−805.
(43) Klamt, A. Conductor-like Screening Model for Real Solvents: A New Approach to the Quantitative Calculation of Solvation Phenomena. *J. Phys. Chem.* **1995**, *99*, 2224−2235.
(44) Klamt, A.; Jonas, V. Treatment of the Outlying Charge in Continuum Solvation Models. *J. Chem. Phys.* **1996**, *105*, 9972−9981.
(45) Rosa, A.; Baerends, E. J.; van Gisbergen, S. J. A.; van Lenthe, E.; Groeneveld, J. A.; Snijders, J. G. Electronic Spectra of M(CO)$_6$ (M = Cr, Mo, W) Revisited by Relativistic TDDFT Approach. *J. Am. Chem. Soc.* **1999**, *121*, 10356−10365.
(46) Pye, C.; Ziegler, T. An Implementation of the Conductor-Like Screening Model of Solvation within the Amsterdam Density Functional Package. *Theor. Chem. Acc.* **1999**, *101*, 396−408.
(47) Gonzalez-Luque, R.; Garavelli, M.; Bernardi, F.; Merchan, M.; Robb, M. A.; Olivucci, M. Computational Evidence in Favor of a Two-State, Two-Mode Model of the Retinal Chromophore Photoisomerization. *Proc. Natl. Acad. Sci. U. S. A.* **2000**, *97*, 9379−9384.
(48) ADF, SCM, Theoretical Chemistry; Vrije Universiteit: Amsterdam, The Netherlands, 2013; https://www.scm.com/Downloads/2013.
(49) Kohout, M. *DGrid*, version 4.5; Springer: Radebeul, 2009.
(50) Záliš, S.; Farrell, I. R.; Vlček, A., Jr. The Involvement of Metal-to-CO Charge Transfer and Ligand-Field Excited States in the Spectroscopy and Photochemistry of Mixed-Ligand Metal Carbonyls. A Theoretical and Spectroscopic Study of [W(CO)$_4$(1,2-Ethylenediamine)] and [W(CO)$_4$(*N*,*N*′-Bis-alkyl-1,4-diazabutadiene)]. *J. Am. Chem. Soc.* **2003**, *125*, 4580−4592.
(51) Záliš, S.; Milne, C. J.; El Nahhas, A.; Blanco-Rodriguez, A. M.; van der Veen, R. M.; Vlček, A., Jr. Re and Br X-ray absorption near-edge structure study of the ground and excited states of [ReBr(CO)$_3$(bpy)] interpreted by DFT and TD-DFT calculations. *Inorg. Chem.* **2013**, *52*, 5775−5785.
(52) Schapiro, I.; Weingart, O.; Buss, B. Bicycle-Pedal Isomerization in a Rhodopsin Chromophore Model. *J. Am. Chem. Soc.* **2009**, *131*, 16−17.
(53) Szymczak, J. J.; Barbatti, M.; Lischka, H. Is the Photoinduced Isomerization in Retinal Protonated Schiff Base a Single- or Double-Torsional Process. *J. Phys. Chem. A* **2009**, *113*, 11907−11918.
(54) Dilger, J.; Musbat, L.; Sheves, M.; Bochenkova, A. V.; Clemmer, D. E.; Toker, Y. Direct Measurement of the Isomerization Barrier of the Isolated Retinal Chromophore. *Angew. Chem., Int. Ed.* **2015**, *54*, 4748−4752.
(55) Wang, W.; Nossoni, Z.; Berbasova, T.; Watson, C. T.; Yapici, I.; Lee, K. S. S.; Vasileiou, C.; Geiger, J. H.; Borhan, B. Tuning the Electronic Absorption of Protein-Embedded all-*trans*-Retinal. *Science* **2012**, *338*, 1340−1343.

DOI: 10.1021/acs.jpca.5b08047
J. Phys. Chem. A XXXX, XXX, XXX−XXX

Supplementary Information

Structural Properties and UV/visible Absorption Spectroscopy of Retinal-pyridyl-CN Re(I) Carbonyl Bipyridine Complex: a Theoretical Study

*Julien Eng and Chantal Daniel**

Laboratoire de Chimie Quantique, Institut de Chimie Strasbourg, UMR-7177 CNRS/Université de Strasbourg 1 Rue Blaise Pascal BP 296/R8, F-67008 STRASBOURG, France

Table S1. Cartesian coordinates corresponding to the fully optimized structures of the all-trans **a** and **1c**-**5c** cis conformers of $Re(CO)_3(bpy)(L)]^+$ (L = Ret-pyr-CN).

a				**1c**			
Re	-0.566338	-0.074696	-0.215917	Re	-0.656400	0.128270	-0.163292
C	-1.027259	-0.330212	-2.082247	C	-1.158296	0.059423	-2.035747
O	-1.300357	-0.477825	-3.202676	O	-1.456108	0.023575	-3.159331
C	-2.429095	-0.240043	0.244790	C	-2.509980	-0.066080	0.317434
O	-3.547879	-0.389592	0.538559	O	-3.624710	-0.234847	0.618150
C	-0.766318	1.830536	-0.432112	C	-0.841629	2.047674	-0.190226
O	-0.833574	2.986324	-0.568973	O	-0.899896	3.211687	-0.212992
N	1.559829	-0.195583	-0.691281	N	1.459229	0.037126	-0.693436
C	2.318245	0.867055	-1.041870	C	2.222578	1.122239	-0.952275
C	2.127793	-1.438169	-0.698616	C	2.014306	-1.203655	-0.831206
C	3.649547	0.748140	-1.419753	C	3.546577	1.029165	-1.362206
H	1.822831	1.835298	-1.018205	H	1.737888	2.087871	-0.825400
C	3.462655	-1.619059	-1.076907	C	3.340520	-1.358398	-1.249267
C	4.232826	-0.519958	-1.443756	C	4.116254	-0.235479	-1.519963
H	4.210253	1.640430	-1.695745	H	4.112678	1.939050	-1.557984
H	3.897638	-2.616000	-1.089748	H	3.764994	-2.353064	-1.366644
H	5.272043	-0.652027	-1.745804	H	5.149373	-0.346204	-1.850228
N	-0.030859	-2.173928	0.041891	N	-0.136473	-1.989273	-0.119395
C	-0.887840	-3.125916	0.472971	C	-0.994648	-2.970778	0.236102
C	1.247696	-2.536613	-0.270494	C	1.131410	-2.330769	-0.492487
C	-0.525016	-4.460779	0.602938	C	-0.644010	-4.315060	0.228218
H	-1.894493	-2.790468	0.712887	H	-1.992309	-2.650845	0.528989
C	1.668951	-3.866317	-0.162606	C	1.539964	-3.668502	-0.523822
C	0.777253	-4.840635	0.275125	C	0.646863	-4.672766	-0.163574
H	-1.259587	-5.184318	0.954547	H	-1.379255	-5.062670	0.523617
H	2.690232	-4.140709	-0.417724	H	2.552370	-3.925852	-0.827471
H	1.094889	-5.880035	0.360697	H	0.954466	-5.718416	-0.187141
N	-0.011397	0.197632	1.921293	N	-0.055302	0.186558	1.976858
C	1.115699	-0.320194	2.471644	C	1.103147	-0.346863	2.446187
C	-0.844615	0.859341	2.772386	C	-0.873214	0.749979	2.910606
C	1.442676	-0.208756	3.810238	C	1.469471	-0.345996	3.776915
H	1.780495	-0.865522	1.805209	H	1.764979	-0.801113	1.712014
C	-0.599054	0.996235	4.122800	C	-0.583080	0.782495	4.257733
H	-1.744492	1.283892	2.331756	H	-1.796719	1.189310	2.538732
C	0.576876	0.462476	4.702905	C	0.621343	0.226470	4.754871
H	2.343569	-0.703636	4.165522	H	2.413047	-0.817544	4.046008
H	-1.328968	1.520407	4.740273	H	-1.296953	1.246998	4.938535
C	0.803739	0.541372	6.138467	C	0.929722	0.244338	6.170094
C	-0.355953	0.780894	6.931990	C	-0.096049	0.702622	7.045802
N	-1.324172	0.984455	7.554671	N	-0.943655	1.083335	7.754788
C	2.014081	0.408862	6.820755	C	2.157047	-0.138401	6.715581
H	1.912661	0.359196	7.906259	H	2.939315	-0.422947	6.012088
C	3.320845	0.443327	6.303364	C	2.447582	-0.168229	8.085048
H	3.450701	0.703930	5.251040	H	1.628318	0.083789	8.764756
C	4.491883	0.291005	7.049939	C	3.674452	-0.480797	8.677562
C	5.736474	0.568119	6.420281	C	3.742368	-0.483646	10.094854
H	5.699793	0.907551	5.379820	H	2.810731	-0.272845	10.629057
C	6.971720	0.493860	7.036065	C	4.877376	-0.720102	10.850284
H	7.003590	0.142344	8.068488	H	5.817216	-0.905862	10.326964
C	8.189184	0.876805	6.432509	C	4.883549	-0.727501	12.260372

H	8.129292	1.268484	5.411350	H	3.916847	-0.570327	12.750173
C	9.450285	0.844051	7.015751	C	5.981165	-0.905424	13.095527
C	10.557770	1.357320	6.262304	C	5.753351	-0.890411	14.509931
H	10.313578	1.759363	5.278373	H	4.712548	-0.786372	14.816136
C	4.475170	-0.125914	8.498593	C	4.908966	-0.797723	7.872123
H	5.108722	-1.011894	8.650466	H	5.693122	-0.049284	8.061308
H	4.874660	0.675200	9.137977	H	5.317503	-1.778925	8.154074
H	3.473633	-0.381046	8.857185	H	4.721300	-0.809539	6.793785
C	9.685915	0.310629	8.404886	C	7.378471	-1.098419	12.567422
H	10.086609	1.099762	9.059205	H	7.809305	-2.037619	12.945078
H	8.776851	-0.080120	8.871402	H	7.418184	-1.128021	11.474516
H	10.426506	-0.502230	8.386733	H	8.034998	-0.282268	12.903850
C	11.844491	1.428091	6.732083	C	6.735770	-1.039790	15.456804
H	11.987919	1.091769	7.760804	H	7.738552	-1.226464	15.066892
C	13.035713	1.970948	6.107685	C	6.638192	-1.073272	16.901892
C	13.222632	2.036907	4.748233	C	5.619131	-0.484913	17.614491
C	12.303061	1.415491	3.730267	C	4.568460	0.414472	17.019956
H	11.735804	0.565314	4.127150	H	4.907226	0.931000	16.114160
H	11.582064	2.155475	3.342682	H	3.656039	-0.152364	16.767801
H	12.889377	1.074326	2.863600	H	4.265133	1.168307	17.761752
C	14.109001	2.473139	7.107076	C	7.796547	-1.827795	17.603266
C	14.419018	2.712030	4.127179	C	5.476003	-0.650788	19.105494
H	15.070151	1.925279	3.697880	H	5.720496	0.319253	19.581299
H	14.071076	3.295633	3.256250	H	4.406780	-0.811993	19.330764
C	15.216556	3.583321	5.089888	C	6.338068	-1.757605	19.699456
H	16.178890	3.866585	4.639417	H	6.348710	-1.685037	20.796595
H	14.671124	4.520171	5.286343	H	5.908209	-2.741147	19.451226
C	15.431270	2.814322	6.387296	C	7.747603	-1.637621	19.134497
H	15.964680	1.875221	6.157448	H	8.142920	-0.636959	19.382529
H	16.072071	3.378576	7.082833	H	8.427201	-2.368987	19.599338
C	14.437411	1.389863	8.158888	C	9.167642	-1.295098	17.129582
H	15.305951	1.715300	8.750896	H	9.960235	-1.738953	17.750643
H	13.616682	1.218883	8.869553	H	9.394980	-1.560800	16.087672
H	14.690967	0.432058	7.681305	H	9.227646	-0.201635	17.231119
C	13.570156	3.720405	7.840990	C	7.706864	-3.329534	17.255878
H	13.377179	4.549705	7.145189	H	6.773797	-3.777150	17.627349
H	12.624008	3.496391	8.357020	H	7.735786	-3.485357	16.166620
H	14.296633	4.062303	8.594714	H	8.554104	-3.874599	17.700766
2c				**3c**			
Re	-0.623546	0.231765	-0.243234	Re	-0.424056	0.343983	-0.373368
C	-1.093747	0.236984	-2.125173	C	-0.774170	0.322727	-2.280846
O	-1.374503	0.242139	-3.253486	O	-0.981957	0.312214	-3.424792
C	-2.487305	0.031162	0.203605	C	-2.321383	0.418826	-0.040401
O	-3.607070	-0.140692	0.479393	O	-3.468555	0.413136	0.168117
C	-0.799931	2.150098	-0.206965	C	-0.338525	2.269248	-0.422639
O	-0.854998	3.314909	-0.187811	O	-0.236674	3.430634	-0.449286
N	1.504805	0.152292	-0.715232	N	1.698385	-0.044777	-0.693950
C	2.282446	1.244197	-0.889727	C	2.629353	0.922683	-0.850638
C	2.057151	-1.082847	-0.902294	C	2.086054	-1.350686	-0.793847
C	3.618038	1.163760	-1.263098	C	3.963421	0.645120	-1.120430
H	1.799678	2.205462	-0.726613	H	2.273854	1.946812	-0.759273
C	3.395548	-1.224995	-1.284685	C	3.415115	-1.690084	-1.069974
C	4.185457	-0.094721	-1.470851	C	4.364398	-0.686867	-1.238567
H	4.194651	2.079011	-1.392751	H	4.668474	1.466972	-1.240162
H	3.818593	-2.215018	-1.440890	H	3.707131	-2.734420	-1.156769
H	5.227665	-0.194867	-1.774696	H	5.401271	-0.941123	-1.459828
N	-0.117917	-1.889912	-0.293853	N	-0.214484	-1.826956	-0.311539
C	-0.992606	-2.883344	-0.020098	C	-1.234605	-2.679182	-0.066653

C	1.155808	-2.220288	-0.659509	C	1.022065	-2.343214	-0.575040
C	-0.652716	-4.228090	-0.102694	C	-1.080317	-4.059852	-0.080615
H	-1.993838	-2.572004	0.269739	H	-2.199725	-2.222338	0.141452
C	1.552631	-3.557726	-0.767100	C	1.235808	-3.725489	-0.608124
C	0.643368	-4.573633	-0.488397	C	0.177778	-4.594982	-0.361456
H	-1.400168	-4.985477	0.130554	H	-1.939604	-4.697592	0.123753
H	2.568667	-3.805738	-1.066086	H	2.225027	-4.122357	-0.825720
H	0.942546	-5.618886	-0.570520	H	0.333485	-5.673772	-0.387198
N	-0.065446	0.210547	1.908543	N	-0.004676	0.348585	1.809820
C	0.959985	-0.522252	2.409766	C	0.897117	-0.472585	2.403692
C	-0.787045	0.929216	2.814146	C	-0.693935	1.181786	2.639227
C	1.301487	-0.557953	3.749093	C	1.148242	-0.489469	3.763442
H	1.527216	-1.120753	1.699869	H	1.434014	-1.161497	1.754781
C	-0.514539	0.939087	4.165778	C	-0.509762	1.216071	4.004979
H	-1.614301	1.513055	2.415096	H	-1.420564	1.839023	2.165401
C	0.568768	0.195411	4.694293	C	0.445501	0.377809	4.630577
H	2.106600	-1.219487	4.056894	H	1.851716	-1.223712	4.147726
H	-1.148068	1.532997	4.825044	H	-1.112113	1.903537	4.599362
C	0.836604	0.193997	6.124888	C	0.612263	0.397091	6.075433
C	-0.235040	0.648997	6.949791	C	-0.461576	0.982879	6.808795
N	-1.125616	1.032537	7.602667	N	-1.349106	1.478460	7.386154
C	2.011395	-0.162694	6.787622	C	1.697465	-0.053063	6.831519
H	1.923519	-0.142882	7.875441	H	1.531148	0.001319	7.908481
C	3.288920	-0.436791	6.267514	C	2.977800	-0.450273	6.411993
H	3.456419	-0.292719	5.200158	H	3.227245	-0.375565	5.352749
C	4.417217	-0.764361	7.031514	C	4.027490	-0.808503	7.267407
C	4.356102	-1.033567	8.423995	C	5.310449	-1.003291	6.677702
H	3.372209	-1.078889	8.896890	H	5.309868	-0.961691	5.584135
C	5.451571	-1.212053	9.249060	C	6.565823	-1.180550	7.248930
H	6.447816	-1.163655	8.805773	H	7.370180	-1.302735	6.519006
C	5.350107	-1.405349	10.643864	C	6.961717	-1.154076	8.606049
H	4.335977	-1.469246	11.052428	H	6.196429	-1.009966	9.366916
C	6.393172	-1.460982	11.560326	C	8.265936	-1.220246	9.089079
C	6.056791	-1.575463	12.949284	C	8.447877	-1.070503	10.503931
H	4.995503	-1.693802	13.166532	H	7.530300	-0.991326	11.087886
C	5.751698	-0.805618	6.327250	C	3.810414	-0.969012	8.748825
H	6.414853	-0.010637	6.700621	H	4.300377	-1.882604	9.110967
H	6.265622	-1.763086	6.493779	H	4.241493	-0.118286	9.299335
H	5.635144	-0.658819	5.246845	H	2.750627	-1.037274	9.013463
C	7.838932	-1.360693	11.149217	C	9.467200	-1.395246	8.199118
H	8.415916	-2.203429	11.557582	H	10.082851	-2.238699	8.545102
H	7.971511	-1.361796	10.062905	H	9.199139	-1.586867	7.155608
H	8.290929	-0.437376	11.541831	H	10.103332	-0.497433	8.225454
C	6.969946	-1.551337	13.973068	C	9.661865	-1.031175	11.141158
H	8.017210	-1.514750	13.665656	H	10.535675	-1.209269	10.510061
C	6.769452	-1.629496	15.406221	C	9.956310	-0.851415	12.549785
C	5.597671	-1.278728	16.035686	C	9.129169	-0.181356	13.421595
C	4.426518	-0.617819	15.358482	C	7.901376	0.591705	13.017014
H	4.716920	-0.019250	14.486661	H	7.939072	0.948330	11.980690
H	3.684775	-1.364178	15.026793	H	6.989785	-0.019002	13.135177
H	3.905777	0.034802	16.074806	H	7.776505	1.458965	13.683417
C	8.005378	-2.125655	16.199477	C	11.307035	-1.457977	13.008290
C	5.381177	-1.483992	17.513118	C	9.405333	-0.105342	14.901967
H	5.372721	-0.487352	17.996644	H	9.700281	0.936236	15.139226
H	4.358179	-1.874424	17.658094	H	8.450709	-0.255047	15.437622
C	6.414138	-2.381819	18.181716	C	10.471476	-1.076413	15.393681
H	6.327109	-2.313482	19.275743	H	10.774594	-0.820977	16.419783
H	6.225453	-3.433723	17.914299	H	10.060290	-2.098385	15.430300

C	7.802908	-1.958778	17.720747
H	7.954634	-0.897817	17.985952
H	8.587133	-2.529015	18.242514
C	9.264719	-1.311593	15.825155
H	10.082117	-1.577282	16.512168
H	9.625063	-1.520304	14.808113
H	9.082668	-0.230716	15.915035
C	8.262063	-3.609748	15.860905
H	7.419897	-4.247329	16.166368
H	8.404369	-3.748331	14.778225
H	9.169939	-3.965705	16.372501
4c			
Re	-0.655426	0.247487	-0.179912
C	-1.187712	0.227466	-2.045189
O	-1.503709	0.219984	-3.163949
C	-2.512318	0.178155	0.329238
O	-3.631161	0.085385	0.644610
C	-0.708868	2.174671	-0.191622
O	-0.688545	3.340300	-0.203962
N	1.442681	0.016774	-0.731170
C	2.275734	1.050474	-0.985265
C	1.909569	-1.256959	-0.891723
C	3.585045	0.872600	-1.413546
H	1.859802	2.045367	-0.841081
C	3.217718	-1.496726	-1.326485
C	4.064946	-0.425982	-1.593640
H	4.208988	1.744414	-1.606930
H	3.571996	-2.516437	-1.460797
H	5.083768	-0.602642	-1.939179
N	-0.283311	-1.901704	-0.166834
C	-1.204980	-2.826507	0.182038
C	0.952959	-2.325160	-0.562651
C	-0.950643	-4.191794	0.145323
H	-2.173952	-2.442368	0.493413
C	1.264905	-3.687570	-0.623413
C	0.306924	-4.632528	-0.269563
H	-1.733395	-4.891092	0.436765
H	2.252711	-4.010257	-0.945087
H	0.539155	-5.696708	-0.315949
N	-0.025380	0.250933	1.952964
C	1.031105	-0.457302	2.424633
C	-0.735403	0.956102	2.877594
C	1.410480	-0.485322	3.754528
H	1.591493	-1.042776	1.698651
C	-0.429443	0.967785	4.222126
H	-1.582480	1.526380	2.501345
C	0.681618	0.244709	4.719945
H	2.240007	-1.127247	4.040539
H	-1.058438	1.546105	4.899340
C	0.975492	0.229672	6.145753
C	-0.102710	0.614403	6.996581
N	-0.999735	0.943952	7.669681
C	2.178928	-0.080472	6.780799
H	2.107653	-0.096108	7.869408
C	3.461106	-0.262414	6.232266
H	3.598434	-0.110438	5.160606
C	4.622866	-0.492707	6.973101
C	5.876836	-0.458869	6.299287

C	11.662739	-1.018083	14.445316
H	12.041489	0.019329	14.417372
H	12.491289	-1.646718	14.807735
C	12.462480	-0.986612	12.095787
H	13.420033	-1.302544	12.536335
H	12.418594	-1.422916	11.087357
H	12.476442	0.109883	12.002025
C	11.219803	-2.998515	12.933630
H	10.452628	-3.395492	13.614992
H	10.960963	-3.330044	11.915876
H	12.188325	-3.448569	13.202679
5c			
Re	-0.491827	0.005902	-0.299725
C	-0.912476	-0.200669	-2.181182
O	-1.159163	-0.315930	-3.311356
C	-2.375980	-0.021591	0.093550
O	-3.513773	-0.092601	0.341731
C	-0.536623	1.923513	-0.501206
O	-0.507823	3.082158	-0.624221
N	1.629231	-0.281054	-0.730948
C	2.470069	0.714986	-1.089366
C	2.100729	-1.563475	-0.713277
C	3.792595	0.489050	-1.448677
H	2.049401	1.718230	-1.086701
C	3.421865	-1.851346	-1.072887
C	4.277903	-0.819952	-1.445829
H	4.422735	1.331295	-1.731877
H	3.778844	-2.878829	-1.067945
H	5.307308	-1.035435	-1.732982
N	-0.124175	-2.126355	-0.018768
C	-1.058618	-3.004952	0.406813
C	1.134114	-2.585159	-0.282235
C	-0.794137	-4.357647	0.582086
H	-2.046358	-2.594665	0.605500
C	1.458383	-3.937003	-0.126105
C	0.488241	-4.834912	0.308030
H	-1.587915	-5.018917	0.927463
H	2.465976	-4.287688	-0.338666
H	0.730509	-5.890540	0.432289
N	0.016723	0.215279	1.858156
C	1.144139	-0.302736	2.407809
C	-0.846038	0.822179	2.720073
C	1.441040	-0.246920	3.756657
H	1.835556	-0.799665	1.731150
C	-0.631558	0.900484	4.081049
H	-1.743985	1.251585	2.280766
C	0.541818	0.361782	4.660140
H	2.346075	-0.737090	4.108230
H	-1.384675	1.380858	4.706238
C	0.738483	0.369200	6.103194
C	-0.442643	0.523996	6.885558
N	-1.427712	0.664466	7.499151
C	1.941628	0.235018	6.795612
H	1.829780	0.113551	7.874439
C	3.251874	0.349424	6.296402
H	3.379992	0.693375	5.267896
C	4.420622	0.176749	7.039856
C	5.660639	0.546128	6.447375

H	5.856296	-0.311096	5.214429	H	5.619731	0.979150	5.442396
C	7.103635	-0.510315	6.929083	C	6.891754	0.452695	7.066527
H	7.104076	-0.623326	8.014118	H	6.930508	0.005169	8.061525
C	8.354290	-0.362472	6.285514	C	8.103115	0.944593	6.530464
H	8.339451	-0.274053	5.194589	H	8.053508	1.451106	5.560893
C	9.589348	-0.245584	6.916732	C	9.335579	0.893713	7.170286
C	9.718641	-0.315154	8.343949	C	10.446086	1.533800	6.511908
H	8.831437	-0.598058	8.905358	H	10.223548	1.857751	5.489401
C	4.599358	-0.722709	8.463828	C	4.406408	-0.357272	8.449388
H	5.190324	-1.611278	8.725800	H	5.060854	-1.237222	8.533078
H	5.041609	0.134879	8.994251	H	4.783691	0.397693	9.154842
H	3.590283	-0.876635	8.856731	H	3.409352	-0.665084	8.778017
C	10.809081	0.011195	6.070331	C	9.494939	0.141872	8.466148
H	11.594676	-0.732787	6.269727	H	9.163829	0.748767	9.323157
H	10.566060	-0.022555	5.001742	H	8.895719	-0.778031	8.460206
H	11.239953	1.000234	6.288934	H	10.542241	-0.123991	8.643882
C	10.869483	-0.057214	9.038992	C	11.731257	1.765007	6.924342
H	11.764614	0.135253	8.443403	H	12.393164	2.120154	6.127599
C	11.073484	-0.054874	10.477530	C	12.389597	1.605056	8.222914
C	10.077481	0.221785	11.382803	C	11.922533	2.199895	9.361844
C	8.698135	0.714757	11.024146	C	10.743534	3.133083	9.412935
H	8.662665	1.231847	10.058023	H	10.298740	3.335897	8.433398
H	7.971256	-0.115644	10.994507	H	9.958888	2.737421	10.078854
H	8.340896	1.403795	11.804543	H	11.058535	4.091111	9.858933
C	12.523932	-0.363831	10.925374	C	13.722258	0.816063	8.186408
C	10.285708	0.112575	12.872797	C	12.616626	2.052462	10.694707
H	10.289011	1.137794	13.292671	H	13.075918	3.026179	10.951694
H	9.392267	-0.367478	13.310603	H	11.845823	1.890605	11.468764
C	11.557611	-0.622577	13.276594	C	13.669161	0.950119	10.736038
H	11.756925	-0.477562	14.348303	H	14.287098	1.047640	11.640479
H	11.429673	-1.705982	13.122259	H	13.178751	-0.034861	10.796006
C	12.714936	-0.100731	12.434506	C	14.531274	1.033143	9.481763
H	12.807294	0.987458	12.597501	H	15.004938	2.029572	9.441671
H	13.670293	-0.548757	12.749268	H	15.348392	0.294892	9.512573
C	13.534801	0.537312	10.180986	C	14.607584	1.269237	7.005905
H	14.530609	0.408716	10.630858	H	15.595397	0.792733	7.092721
H	13.632555	0.282944	9.116185	H	14.190647	0.976376	6.032033
H	13.259602	1.599178	10.262772	H	14.756848	2.359414	7.011837
C	12.849000	-1.837768	10.599970	C	13.406029	-0.685329	8.002492
H	12.198633	-2.529024	11.155416	H	12.851484	-1.093924	8.860158
H	12.710811	-2.043927	9.527457	H	12.798889	-0.850506	7.099270
H	13.895396	-2.063133	10.858613	H	14.339785	-1.259539	7.896465

Table S2. TD-DFT transition energies (in eV), wavelength of absorption (in nm) and oscillator strengths f associated to the low-lying singlet excited states of $Re(CO)_3(bpy)(L)]^+$ cis **2c-5c** confomers in acetonitrile.

2c

State	One-electron excitation	%	Energie [eV]	Energie [nm]	f	Nature
T1	HOMO → LUMO	94	1.17	1060	-	IL_{ret}
S1	HOMO → LUMO	97	1.80	689	2.41	IL_{ret}
T2	HOMO − 1 → LUMO	70	2.09	593	0.00	IL_{ret}
	HOMO → LUMO + 2	16			-	IL_{ret}
T3	HOMO → LUMO + 1	98	2.20		-	$LLCT_{ret\rightarrow bpy}$
S2	HOMO → LUMO + 1	98	2.20	564	0.00	$LLCT_{ret\rightarrow bpy}$
T4	HOMO → LUMO + 2	67	2.52	492	-	IL_{ret}
	HOMO − 1 → LUMO	18			-	IL_{ret}
T5	HOMO − 2 → LUMO	38	2.82	440	-	$MLCT_{ret}$
	HOMO − 5 → LUMO	29				IL_{ret}
	HOMO − 1 → LUMO + 2	12				IL_{ret}
S3	HOMO − 1 → LUMO	91	2.82	440	0.36	IL_{ret}
T6	HOMO − 2 → LUMO + 1	49	2.90	428	-	$MLCT_{bpy}$
	HOMO − 1 → LUMO + 1	39				$LLCT_{ret\rightarrow bpy}$
S4	HOMO − 1 → LUMO + 1	60	3.01	412	0.01	$LLCT_{ret\rightarrow bpy}$
	HOMO − 2 → LUMO + 1	37			-	$MLCT_{bpy}$
S5	HOMO → LUMO + 2	89	3.06	405	0.12	IL_{ret}
T7	HOMO − 3 → LUMO + 1	94	3.10		-	$MLCT_{bpy}$
S6	HOMO − 2 → LUMO	94	3.18	390	0.11	$MLCT_{ret}$

3c

State	One-electron excitation	%	Energie [eV]	Energie [nm]	f	Nature
T1	HOMO $\rightarrow$ LUMO	95	1.12	1107	-	IL_{ret}
S1	HOMO $\rightarrow$ LUMO	97	1.77	700	2.54	IL_{ret}
T2	HOMO $-$ 1 $\rightarrow$ LUMO	75	2.07	599	0.00	IL_{ret}
	HOMO $\rightarrow$ LUMO + 2	11			-	IL_{ret}
T3	HOMO $\rightarrow$ LUMO + 1	98	2.18	569	-	$LLCT_{ret\rightarrow bpy}$
S2	HOMO $\rightarrow$ LUMO + 1	98	2.18	569	0.00	$LLCT_{ret\rightarrow bpy}$
T4	HOMO $\rightarrow$ LUMO + 2	72	2.55	486	-	IL_{ret}
	HOMO $-$ 1 $\rightarrow$ LUMO	13			-	IL_{ret}
S3	HOMO $-$ 1 $\rightarrow$ LUMO	93	2.77	448	0.23	IL_{ret}
T5	HOMO $-$ 2 $\rightarrow$ LUMO	47	2.82	440	-	$MLCT_{ret}$
	HOMO $-$ 5 $\rightarrow$ LUMO	25				IL_{ret}
	HOMO $-$ 1 $\rightarrow$ LUMO + 2	9				IL_{ret}
T6	HOMO $-$ 2 $\rightarrow$ LUMO + 1	52	2.90	428	-	$MLCT_{bpy}$
	HOMO $-$ 1 $\rightarrow$ LUMO + 1	36				$LLCT_{ret\rightarrow bpy}$
S4	HOMO $-$ 1 $\rightarrow$ LUMO + 1	57	3.01	412	0.01	$LLCT_{ret\rightarrow bpy}$
	HOMO $-$ 2 $\rightarrow$ LUMO + 1	40			-	$MLCT_{bpy}$
T7	HOMO $-$ 3 $\rightarrow$ LUMO + 1	63	3.10	400	-	$MLCT_{bpy}$
	HOMO $-$ 5 $\rightarrow$ LUMO	17				IL_{ret}
	HOMO $-$ 2 $\rightarrow$ LUMO	9				$MLCT_{ret}$
S5	HOMO $\rightarrow$ LUMO + 2	79	3.10	400	0.06	IL_{ret}
	HOMO $-$ 2 $\rightarrow$ LUMO	12				$MLCT_{ret}$
S6	HOMO $-$ 2 $\rightarrow$ LUMO	83	3.12	397	0.17	$MLCT_{ret}$
	HOMO $\rightarrow$ LUMO + 2	12				IL_{ret}

4c

State	One-electron excitation	%	Energie [eV]	Energie [nm]	f	Nature
T1	HOMO → LUMO	94	1.20	1033	-	IL_{ret}
S1	HOMO → LUMO	97	1.83	677	2.18	IL_{ret}
T2	HOMO − 1 → LUMO	73	2.10	590	-	IL_{ret}
	HOMO → LUMO + 2	11				IL_{ret}
	HOMO → 209	5				IL_{ret}
T3	HOMO → LUMO + 1	98	2.22	558	-	$LLCT_{ret\rightarrow bpy}$
S2	HOMO → LUMO + 1	98	2.23	556	0.00	$LLCT_{ret\rightarrow bpy}$
T4	HOMO → LUMO + 2	68	2.59	479	-	IL_{ret}
	HOMO − 1 → LUMO	14				IL_{ret}
	HOMO → 209	6				IL_{ret}
S3	HOMO − 1 → LUMO	95	2.80	443	0.35	IL_{ret}
T5	HOMO − 2 → LUMO	41	2.82	440	-	$MLCT_{ret}$
	HOMO − 5 → LUMO	25				IL_{ret}
	HOMO − 1 → LUMO + 2	11				IL_{ret}
	HOMO → 209	6				IL_{ret}
T6	HOMO − 2 → LUMO + 1	53	2.90	428	-	$MLCT_{bpy}$
	HOMO − 1 → LUMO + 1	36				$LLCT_{ret\rightarrow bpy}$
S4	HOMO − 1 → LUMO + 1	58	3.01	412	0.01	$LLCT_{ret\rightarrow bpy}$
	HOMO − 2 → LUMO + 1	39				$MLCT_{bpy}$
T7	HOMO − 3 → LUMO + 1	93	3.10	400	-	$MLCT_{bpy}$
S5	HOMO → LUMO + 2	53	3.13	396	0.05	IL_{ret}
	HOMO − 2 → LUMO	41				$MLCT_{ret}$
S6	HOMO − 2 → LUMO	53	3.16	392	0.21	$MLCT_{ret}$
	HOMO → LUMO + 2	40				IL_{ret}

5c

State	One-electron excitation	%	Energie [eV]	Energie [nm]	f	Nature
T1	HOMO $\rightarrow$ LUMO	94	1.17	1060	-	IL_{ret}
S1	HOMO $\rightarrow$ LUMO	96	1.86	667	2.51	IL_{ret}
T2	HOMO $-$ 1 $\rightarrow$ LUMO	73	2.18	569	-	IL_{ret}
	HOMO $-$ 5 $\rightarrow$ LUMO	9				IL_{ret}
	HOMO $\rightarrow$ LUMO + 2	7				IL_{ret}
T3	HOMO $\rightarrow$ LUMO + 1	97	2.22	558	-	$LLCT_{ret\rightarrow bpy}$
S2	HOMO LUMO + 1	99	2.23	556	0.00	$LLCT_{ret\rightarrow bpy}$
T4	HOMO $\rightarrow$ LUMO + 2	49	2.60	477	-	IL_{ret}
	HOMO $-$ 1 $\rightarrow$ LUMO	14				IL_{ret}
	HOMO $-$ 2 $\rightarrow$ LUMO	9				$MLCT_{ret}$
	HOMO $-$ 5 $\rightarrow$ LUMO	7				IL_{ret}
S3	HOMO $-$ 1 $\rightarrow$ LUMO	96	2.76	449	0.21	IL_{ret}
T5	HOMO $-$ 2 $\rightarrow$ LUMO	42	2.83	438	-	$MLCT_{ret}$
	HOMO $-$ 5 $\rightarrow$ LUMO	23				IL_{ret}
	HOMO $\rightarrow$ LUMO + 2	20				IL_{ret}
T6	HOMO $-$ 2 $\rightarrow$ LUMO + 1	58	2.92	425	-	$MLCT_{bpy}$
	HOMO $-$ 1 $\rightarrow$ LUMO + 1	26				$LLCT_{ret\rightarrow bpy}$
S4	HOMO $-$ 1 $\rightarrow$ LUMO + 1	47	3.04	408	0.01	$LLCT_{ret\rightarrow bpy}$
	HOMO $-$ 2 $\rightarrow$ LUMO + 1	46				$MLCT_{bpy}$
T7	HOMO $-$ 5 $\rightarrow$ LUMO	38	3.05	406	-	IL_{ret}
	HOMO $-$ 2 $\rightarrow$ LUMO	29				$MLCT_{ret}$
	HOMO $-$ 1 $\rightarrow$ LUMO	5				IL_{ret}
S5	HOMO $-$ 2 $\rightarrow$ LUMO	73	3.08	403	0.04	$MLCT_{ret}$
	HOMO $\rightarrow$ LUMO + 2	20				IL_{ret}
S6	HOMO $\rightarrow$ LUMO + 2	66	3.18	390	0.39	IL_{ret}
	HOMO $-$ 2 $\rightarrow$ LUMO	18				$MLCT_{ret}$
	HOMO $-$ 3 $\rightarrow$ LUMO	5				$MLCT_{ret}$

Scheme S1. Frontier Kohn-Sham orbitals of the cis **2c-5c** conformers of $Re(CO)_3(bpy)(L)]^+$ (L = Ret-pyr-CN) in acetonitrile.

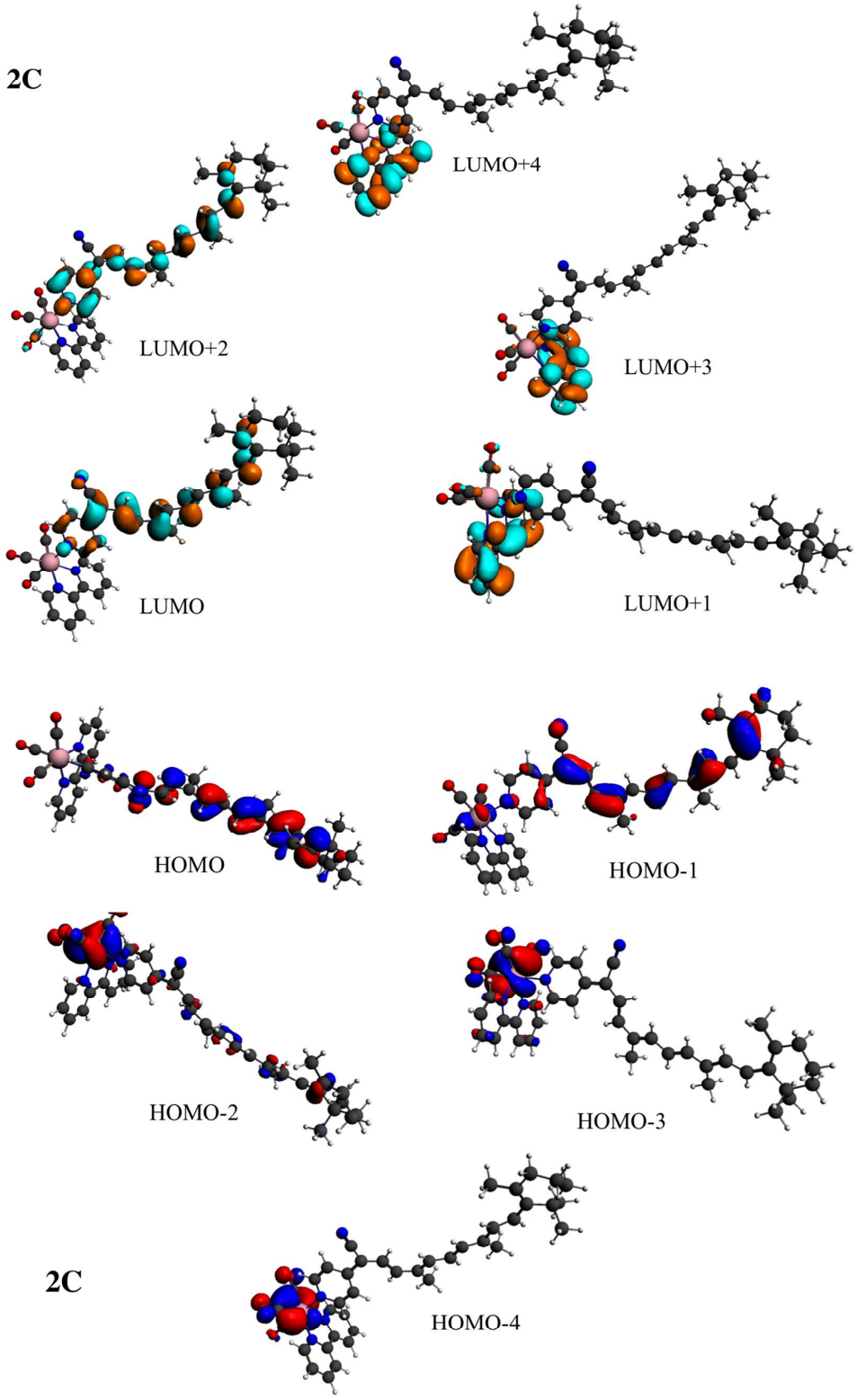

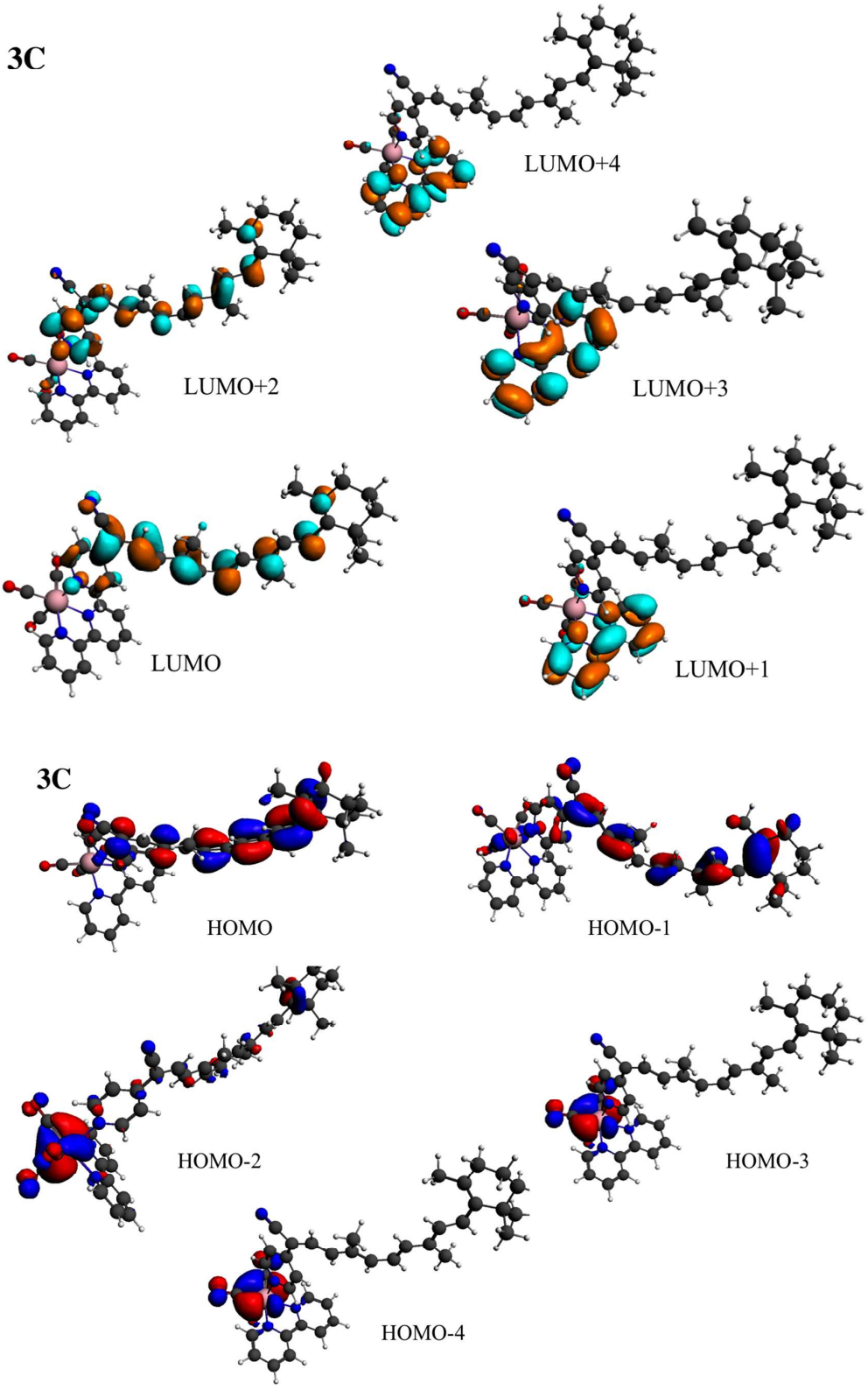
3C
LUMO+4
LUMO+2
LUMO+3
LUMO
LUMO+1
3C
HOMO
HOMO-1
HOMO-2
HOMO-3
HOMO-4

4C

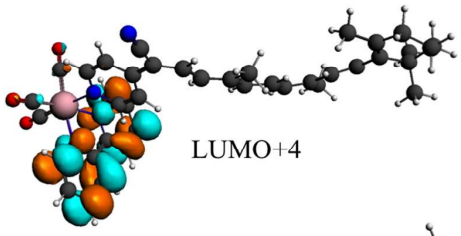

LUMO+4

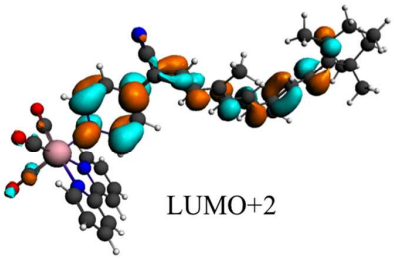

LUMO+2

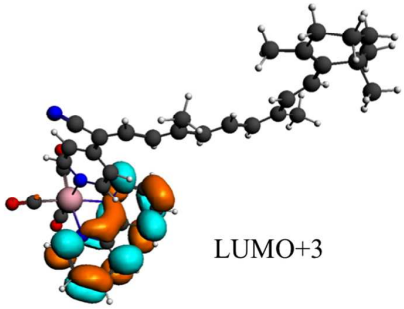

LUMO+3

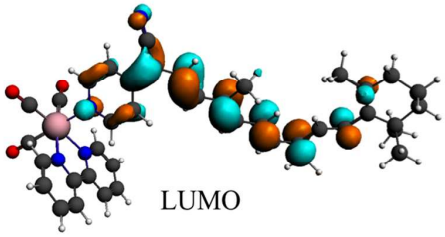

LUMO

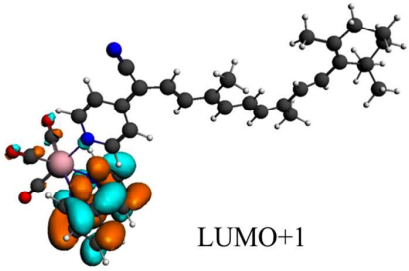

LUMO+1

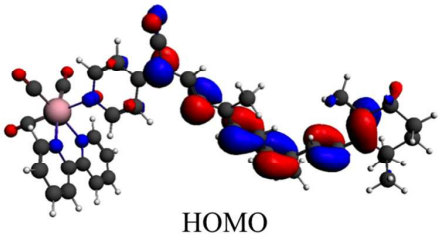

HOMO

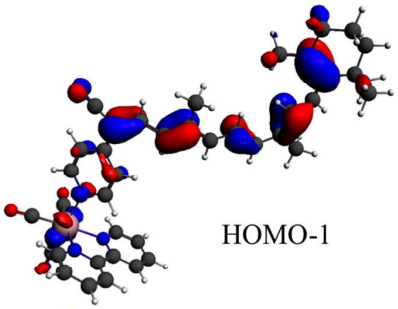

HOMO-1

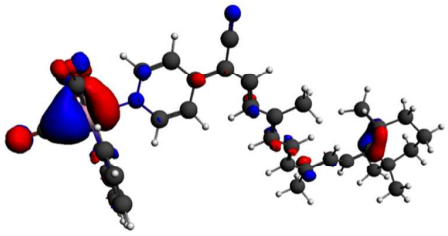

HOMO-2

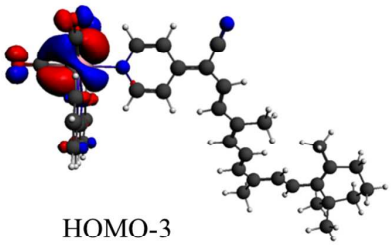

HOMO-3

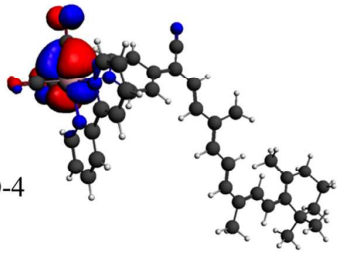

HOMO-4

4C

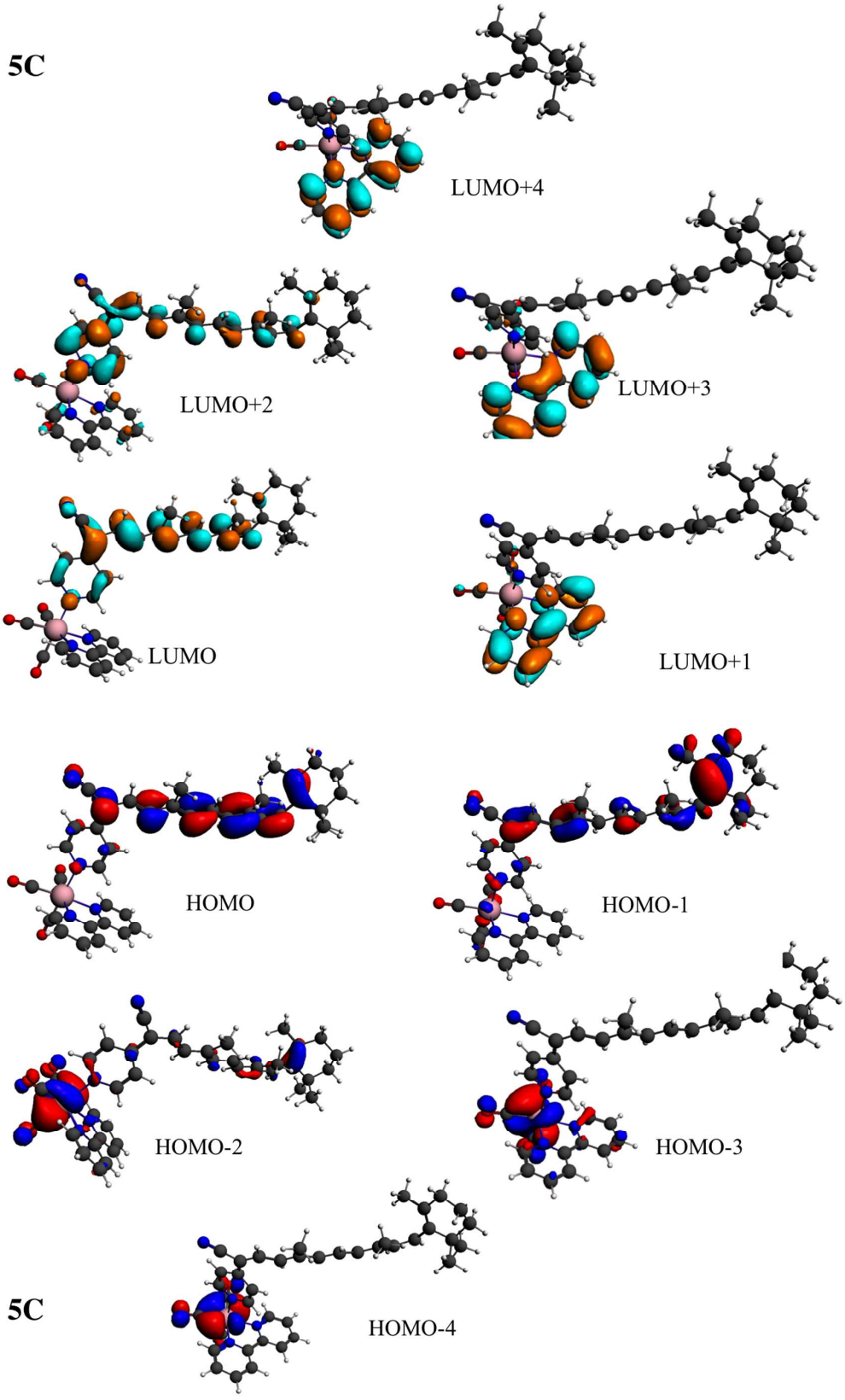
5C
LUMO+4
LUMO+2
LUMO+3
LUMO
LUMO+1
HOMO
HOMO-1
HOMO-2
HOMO-3
5C
HOMO-4

REFERENCES

[1] Köppel, H.; Domcke, W.; Cederbaum, L. S. *Adv. Chem. Phys.* **1984**, *57*, 59–245.

[2] Heydová, R.; Gindensperger, E.; Romano, R.; Sýkora, J.; Vlček, J., A.; Zálišš, S.; Daniel, C. *J. Phys. Chem. A* **2012**, *116*, 11319–11329.

[3] Cannizzo, A.; Blanco-Rodríguez, A. M.; Nahhas, A. E.; Šebera, J.; Zálišš, S.; Vlček, Jr., A.; Chergui, M. *J. Am. Chem. Soc.* **2008**, *130*, 8967–8974.

[4] Gozem, S.; Melaccio, F.; Lindh, R.; Krylov, A. I.; Granovsky, A. A.; Angeli, C.; Olivucci, M. *J. Chem. Theory Comput.* **2013**, *9*, 4495–4506.

[5] Gourlaouen, C.; Eng, J.; Otsuka, M.; Gindensperger, E.; Daniel, C. *J. Chem. Theory Comput.* **2015**, *11*, 99–110.

[6] Eisenstein, O.; Maron, L. *Journal of Organometallic Chemistry* **2002**, *647*, 190–197.

[7] Maseras, F.; Lledós, A.; Clot, E.; Eisenstein, O. *Chemical Reviews* **2000**, *100*, 601–636.

[8] Balcells, D.; Clot, E.; Eisenstein, O. *Chemical Reviews* **2010**, *110*, 749–823.

[9] Neese, F. *Coord. Chem. Rev.* **2009**, *253*, 526.

[10] Glaser, T.; Hoeke, V.; Gieb, K.; Schnak, J.; Schröder, C.; Müller, P. *Coord. Chem. Rev.* **2015**, *289-290*, 261–278.

[11] González, L.; Escudero, D.; Serrano-Andés. *Chem. Phys. Chem.* **2012**, *12*(886), 28–51.

[12] Vancoillie, S.; Zhao, H.; van Tran, T.; Hendrickx, E.; Pierloot, K. *J. Chem. Theory Comput.* **2011**, *7*, 3961–3977.

[13] Dreuw, A.; Head-Gordon, M. *Chem. Rev.* **2005**, *105*, 4009–4037.

[14] Adamo, C.; Jacquemin, D. *Chem. Soc. Rev.* **2013**, *42*, 845.

[15] Mennucci, B. *Wiley Interdisciplinary Reviews: Computational Molecular Science* **2012**, *2*(3), 386–404.

[16] Mennucci, B., Cammi, R., Eds. *Continuum Solvation MModel in Chemical Physics. From Theory to Applications;* John Wiley & Sons, Ltd, 2007.

[17] Monari, A.; Assfeld, X. In *Application of Computational Techniques in Pharmacy and Medicine*; Gorb, L., Kuz'min, V., Muratov, E., Eds., Vol. 17 of *Challenges and Advances in Computational Chemistry and Physics;* Springer Netherlands, 2014; pages 1–20.

[18] Lin, H.; Truhlar, D. G. *Theor. Chem. Acc.* **2007**, *117*, 185–199.

[19] Senn, H. M.; Thiel, W. *Angewandte Chemie International Edition* **2009**, *48*(7), 1198–1229.

[20] Pyykkö, P. *Annual Review of Physical Chemistry* **2012**, *62*, 45–64.

[21] Nanda, K.; Krylov, A. I. *J Chem. Phys. B* **2012**, *142*, 064118.

[22] Bergendhal, L. T.; Paterson, M. J. *J Phys. Chem. B.* **2012**, *116*, 11818–11828.

[23] Alam, M. M.; Chattopadhyaya, M.; Chakrabarti, S. *Phys. Chem. Chem. Phys.* **2012**, *14*, 1156–1165.

[24] Rivalta, I.; Nenov, A.; Weingart, O.; Cerullo, G.; Garavelli, M.; Mukamel, S. *J. Phys. Chem. B* **2014**, *118*, 8396–8405.

[25] Rivalta, I.; Nenov, A.; Cerullo, G.; Mukamel, S.; Garavelli, M. *Int. J. Quantum Chem.* **2014**, *114*(85-93).

[26] Wolf, T. J. A.; Kuhlman, T. S.; Schalk, O.; Martinez, T. J.; Møller, K. B.; Stolow, A.; Unterreiner, A.-N. *Phys. Chem. Chem. Phys.* **2014**, *16*, 11770.

[27] Martinez-Fernandez, J.; González-Vázquez, J.; González, L.; Corral, I. *J. Chem. Theory Comput.* **2015**, *11*(2), 406–414.

[28] González, L.; Marquetand, P.; Richter, M.; González-Vázquez, J.; Sola, I. In *Ultrafast Phenomena in Molecular Sciences*; de Nalda, R., Banares, L., Eds., Vol. 107

of *Springer Series in Chemical Physics;* Springer International Publishing, 2014; pages 145–170.

[29] González, L.; Stolow, A.; Vrakking, M. *Chem. Phys. Chem.* **2013**, *13*, 1299–1305.

[30] Auböck, G.; Chergui, M. *Nature Chemistry* **2015**, *7*, 629–633.

[31] Cho, H.; Strader, M. L.; Hong, K.; Jamula, L.; Gullikson, E. K.; Kim, T. K.; de Groot, F. M. F.; McCusker, J. K.; Schoenlein, R. W.; Huse, N. *Faraday Discuss.* **2012**, *157*, 463–474.

[32] McCusker, J. K. *Acc. Chem. Res.* **2003**, *36*, 876–887.

[33] Kayanuma, M.; Gindensperger, E.; Daniel, C. *Dalton Trans.* **2012**, *41*(42), 13191–13203.

[34] Kayanuma, M.; Daniel, C.; Köppel, H.; Gindensperger, E. *Coordination Chemistry Reviews* **2011**, *255*(21), 2693–2703.

[35] Kayanuma, M.; Daniel, C.; Gindensperger, E. *Can. J. Chem.* **2014**, *92*, 979–986.

[36] Cohen-Tanoudji, C.; Diu, B.; Laloë, F. *Quantum Mechanics*, Vol. 1; 1973.

[37] Baer, M. *Physics Reports* **2002**, *358*, 75–142.

[38] Worth, G. A.; Cederbaum, L. S. *Annu. Rev. Phys. Chem.* **2004**, *55*, 127.

[39] Born, M.; R., O. *Ann. Phys. (Leipzig)* **1927**, *84*, 457.

[40] Mead, C. A.; Truhlar, D. G. *J. Chem. Phys.* **1982**, *77*, 9060.

[41] Köppel, H.; Schubert, B. *Mol. Phys.* **2006**, *104*, 1069–1079.

[42] Köppel, H. *Faraday Discuss.* **2004**, *127*, 35–47.

[43] Köppel, H.; Gronki, J.; Mahapatra, S. *J. Chem. Phys.* **2001**, *115*, 2377.

[44] Groenhof, G.; Boggio-Pasqua, M.; Schäfer, L. V.; Robb, M. A.; 2010; chapter Computer Simulations of Photobiological Processes: The Effect of the Protein Environment, pages 181–212.

[45] Lluís, B.; Benjamin, L.; Bearpark, M. J.; Worth, G. A.; Robb, M. A.; Springer,

2009; chapter Second-Order Analysis of Conical Intersections: Applications to Photochemistry and Photophysics of Organic Molecules, pages 169–200.

[46] Yarkony, D. R.; 2004; Vol. 15; chapter Conical Intersections: Their Description and Consequences.; World scientific: Singapore ed.

[47] Toniolo, A.; Levine, B.; Thompson, A.; Quenneville, J.; Ben-Nun, M.; Owens, J.; Olsen, S.; Manohar, L.; Martinez, T. J.; 2005; chapter Photochemistry from First Principles and Direct Dynamics.; Marcel-dekker: New york ed.

[48] Mead, C. A. *J. Chem. Phys.* **1983**, *78*, 807.

[49] Paterson, M. J.; Bearpark, M. J.; Robb, M. A. *J. Chem. Phys.* **2004**, *121*(23), 11562.

[50] Renner, R. *Z. Phys.* **1934**, *92*, 172.

[51] Boggio-Pasqua, M.; Bearpark, M. J.; Hunt, P. A.; Robb, M. A. *J. Am. Chem. Soc.* **2002**, *124*, 1456.

[52] Groenhof, G.; Schäfer, L. V.; Boggio-Pasqua, M.; Goette, M.; Grubmüller, H.; Robb, M. A. *J. Am. Chem. Soc.* **2007**, *129*.

[53] Dirac, P. A. M. *Proc. Roy. Soc. Lond.* **1929**, *A123*, 714.

[54] Reiher, M. *Wiley Interdisciplinary Reviews: Computational Molecular Science* **2012**, *2*(1), 139–149.

[55] van Lenthe, E. R. v.; Baerends, E. J. G. S. *Int. J. Quantum Chem.* **1996**, *57*, 281.

[56] Roos, B. O.; Taylor, P. R.; Siegbahn, P. E. M. *Chem. Phys.* **1980**, *48*, 157.

[57] Ma, D.; Li Manni, G.; Gagliardi, L. *J. Chem. Phys.* **2011**, *135*(4), 044128.

[58] Ivanic, J. *J. Chem. Phys.* **2003**, *119*, 9364.

[59] Andersson, K.; Malmqvist, P.-A.; Roos, B. O.; Sadlej, A. J.; K., W. *J Phys Chem* **1990**, *94*, 5483.

[60] Andersson, K.; Malmqvist, P.-A.; Roos, B. O. *J. Chem. Phys.* **1992**, *96*, 1218.

[61] Hohenberg, P.; Kohn, W. *Phys. Rev.* **1964**, *136*, B864.

[62] Hohenberg, P.; Kohn, W. *Phys. Rev.* **1964**, *864*, B136.

[63] Kohn, W.; Sham, L. J. *Phys. Rev. A.* **1965**, *140*, 1133.

[64] Peverati, R.; Truhlar, D. G. *Phil. Trans. R. Soc.* **2014**, *A372*, 20120476.

[65] Kosloff, R.; Marcel Dekker, New York, 1996; chapter Dynamics of Molecules and Chemical Reactions, pages 185–230.

[66] Marquardt, R.; Quack, M.; Stohner, J.; Sutcliffe, E. *J. Chem. Soc.* **1986**, *Faraday Trans. 2*, 1173.

[67] Quack, M.; Sutcliffe, E. *QCOE Bull.* **1986**, *6*, 98.

[68] Marquardt, R. *ChemPhysChem* **2013**, *14*, 1350–1361.

[69] Krishna, B. M.; Lefèvre, J.; Marquardt, R.; Worth, G. A. *Int. J. Mass Spec.* **2014**, *365-366*, 121–127.

[70] Firmino, T.; Marquardt, R.; Gatti, F.; Dong, W. *J. Phys. Chem. Lett.* **2014**, *5*(24), 4270–4274.

[71] Füchsel, G.; Tremblay, J.-C.; Klamroth, T.; Saalfrank, P. *ChemPhysChem* **2013**, *14*(7), 1471–1478.

[72] Brunner, P.; Shapiro, M. *Chem. Phys. Lett.* **1986**, *126*, 541.

[73] Shapiro, M.; Brunner, P. *Principle of the quantum control of molecular processes;* John Wiley & Sons, hoboken nj ed., 2003.

[74] Tannor, D. J.; Rice, S. A. *J. Chem. Phys.* **1985**, *83*, 5013.

[75] Tannor, D. J.; Kosloff, R.; Rice, S. A. *J. Chem. Phys.* **1986**, *85*, 5805.

[76] Peirce, A. P.; Dahler, M. A.; Rabitz, H. *Phys. Rev. A* **1988**, *37*, 4950.

[77] Kosloff, R.; Rice, S. A.; Gaspard, P.; Tersigni, S.; Tannor, D. J. *Chem. Phys.* **1989**, *139*, 201.

[78] Daems, D.; Ruschhaupt, A.; Sugny, O.; Guérin, S. *Phys. Rev. Lett.* **2013**, *111*, 050404.

[79] Sala, M.; Saab, M.; Lasorne, B.; Gatti, F.; Guidoni, L. *J Chem. Phys.* **2014**, *140*, 194309.

[80] Saab, M.; Sala, M.; Guérin, S.; Lasorne, B.; Gatti, F. *J. Chem. Phys.* **2014**, *141*, 131114.

[81] Sala, M.; Gatti, F.; Guérin, S. *J. Chem. Phys.* **2014**, *141*, 164326.

[82] Meyer, H.-D.; Manthe, U.; Cederbaum, L. S. *Chem. Phys. Lett.* **1990**, *165*, 73.

[83] Beck, H. M.; Jăgle, A.; Worth, G. A.; Meyer, H.-D. *Phys. Rep.* **2000**, *324*, 1.

[84] Multidimensional quantum dynamics mctdh theory and applications. Meyer, H.-D.; Gatti, F.; Worth, G. A. Wiley-VCH: Weinheim, **2009**.

[85] Dirac, P. A. M. *Proc. Cambridge Philos. Soc.* **1930**, *26*, 376.

[86] Frenkel, J. *Wave Mechanics;* Clarendon Press, Oxford, 1934.

[87] Light, J. C.; Hamilton, I. P.; Lill, J. V. *J. Chem. Phys.* **1985**, *82*, 1400.

[88] Light, J. C.; Carrington, T. *Adv. Chem. Phys.* **2007**, page 263.

[89] Lamberti, V. E.; Fosdick, L. D.; Jessup, E. R.; Schauble, J. C. *J. Chem. Educ.* **2002**, *79*, 601–606.

[90] Blowey, J. F.; Craig, A. W.; Shardlow, T. *Frontiers in Numerical Analysis;* Springer, durham ed., 2003.

[91] Verlet, L. *Phys. Rev.* **1967**, *159*, 98–103.

[92] Verlet, L. *Phys. Rev.* **1968**, *165*, 201–204.

[93] Swope, W. C.; Andersen, H. C.; Berens, P. H.; Wilson, K. R. *The Journal of Chemical Physics* **1982**, *76*, 637–649.

[94] Tully, J. C.; Preston, R. K. *J. Chem. Phys.* **1971**, *37*, 55–562.

[95] Tully, J. C. *J. Chem. Phys.* **1990**, *37*, 93–1061.

[96] Granucci, G.; Persico, M. aPersico, M. A. *J. Chem. Phys.* **2010**, *133*, 134111.

[97] Aquilante, F.; Vico, L. D.; Ferré, N.; Ghigo, G.; Malmqvist, P.-A.; Neograd y, P.; Pedersen, T. B.; Pitonak, M.; Reiher, M.; Roos, B. O.; Serrano-Andés, L.; Urban, M.; Veryazov, V.; Lindh, R. *J. Comput. Chem.* **2010**, *31*, 224.

[98] Veryazov, V.; Widmark, P.-O.; Serrano-Andés, L.; Lindh, R.; Roos, B. O. *International journal of Quantum Chemistry* **2004**, *100*, 626.

[99] Karlström, G.; Lindh, R.; Malmqvist, P.-A.; Roos, B. O.; Ryde, U.; Veryazov, V.; Widmark, P.-O.; Cossi, M.; Schimmelpfennig, B.; Neogrady, P.; Seijo, L. *Computational Material Science* **2003**, *28*, 222.

[100] Sampath, A.; Rieke, F. *Neuron* **2004**, *41*, 431.

[101] Peteanu, L. A.; Schoenlein, R. W.; Wang, W.; Mathies, R. A.; Shank, C. V. *Proc. Natl. Acad. Sci. USA* **1993**, *90*, 11762–11766.

[102] Mathies, R. A.; Cruz, C. H. B.; Pollard, W. T.; Shank, C. V. *Science* **1988**, pages 777–779.

[103] Logunov, S. L.; El-Sayed, M. A.; Song, L.; Lanyi, J. K. *J. Phys. Chem.* **1996**, *100*, 2391–2398.

[104] Kim, J. E.; Tauber, M. J.; Mathies, R. A. *Biochemistry* **2001**, *40*, 13774–13778.

[105] Rohrig, U.; Guidoni, L.; Laio, A.; Frank, I.; Rothlisberger, U. *J. Am. Chem. Soc.* **2004**, *126*, 15328–15329.

[106] Becker, R. S.; Freedman, K. *J. Am. Chem. Soc.* **1985**, *107*, 1477–1485.

[107] Hendrickx, E.; Clays, K.; Persoons, A.; Dehu, C.; Bredas, J. L. *J. Am. Chem. Soc.* **1995**, *117*(12), 3547.

[108] Kukura, P.; McCamant, D. W.; Yoon, S.; Wandschneider, D. B.; Mathies, R. A. *Science* **2005**, *310*, 1006–1009.

[109] Meyer, C. K.; Böhme, M.; Ockenfels, A.; Gärtner, W.; Hofmann, K. P.; Ernst, O. P. *J. Bio. Chem.* **2000**, *275*(26), 19713.

[110] Patel, A. B.; Crocker, E.; Eilers, M.; Hirschfeld, A.; Sheves, M.; Smith, S. O. *Proc Natl Acad Sci* **2004**, *101*(27), 10048.

[111] Albeck, A.; Livnah, N.; Gottlieb, H.; Sheves, M. *J. Am. Chem. Soc.* **1997**, *114*, 2400–2411.

[112] Arnaboldi, M.; Motto, M. G.; Tsujimioto, K.; Balogh-Nair, V.; Nakanishi, K. *J. Am. Chem. Soc.* **1979**, *101*, 7082–7084.

[113] Froese, R. D. J.; Kromaroni, J.; Byun, K. S.; Morokuma, K. *Chem. Phys. Lett.* **1997**, *272*, 335–340.

[114] Buss, V.; Kolster, K.; Frank, T.; Vahrenhorst, R. *Angew. Chem., Int. Ed.* **1998**, *37*, 1893–1895.

[115] Rajamani, R.; Gao, J. *J. Comput. Chem.* **2002**, *23*, 96–105.

[116] Terstegen, F.; Buss, V. *J. Mol. Struct.* **1998**, *430*, 209–218.

[117] Garavelli, M.; Celani, P.; Bernardi, F.; Robb, M. A.; Olivucci, M. *J. Am. Chem. Soc.* **1997**, *119*, 6891–6901.

[118] Fantacci, S.; Migani, A.; Olivucci, M. *J. Phys. Chem. A* **2004**, *108*, 1208–1213.

[119] Conte, A. M.; Guidoni, L.; Sole, R. D.; Pulci, O. *Chem. Phys. Lett.* **2011**, *515*, 290–295.

[120] Huix-Rotllant, M.; Filatov, M.; Gozem, S.; Schapiro, I.; Olivucci, M.; Ferré, N. *J. Chem. Theory Comput.* **2013**.

[121] Gozem, S.; Krylov, A. I.; Olivucci, M. *J. Chem. Theory Comput.* **2013**, *9*, 284–292.

[122] Weingart, O.; Migani, A.; Olivucci, M.; Robb, M. A.; Buss, V.; Hunt, P. *J. Phys. Chem. A* **2004**, *108*, 4685–4693.

[123] Weingart, O. *Chem. Phys.* **2008**, *349*, 348–355.

[124] Weingart, O.; Altoè, P.; Stenta, M.; Bottoni, A.; Orlandi, G.; Garavelli, M. *Phys. Chem. Chem. Phys.* **2011**, *13*, 3645–3648.

[125] Ditchfield, R.; Hehre, W. J.; Pople, J. A. *J. Chem. Phys.* **1971**, *54*, 724.

[126] Hehre, W. J.; Ditchfield, R.; Pople, J. A. *J. Chem. Phys.* **1972**, *56*, 2257.

[127] Hariharan, P. C.; Pople, J. A. *Mol. Phys.* **1974**, *27*, 209.

[128] Gaussian 09 Revision D.01. Frisch, M. J.; Trucks, G. W.; Schlegel, H. B.; Scuseria, G. E.; Robb, M. A.; Cheeseman, J. R.; Scalmani, G.; Barone, V.; Mennucci, B.;

Petersson, G. A.; Nakatsuji, H.; Caricato, M.; Li, X.; Hratchian, H. P.; Izmaylov, A. F.; Bloino, J.; Zheng, G.; Sonnenberg, J. L.; Hada, M.; Ehara, M.; Toyota, K.; Fukuda, R.; Hasegawa, J.; Ishida, M.; Nakajima, T.; Honda, Y.; Kitao, O.; Nakai, H.; Vreven, T.; Montgomery, Jr., J. A.; Peralta, J. E.; Ogliaro, F.; Bearpark, M.; Heyd, J. J.; Brothers, E.; Kudin, K. N.; Staroverov, V. N.; Kobayashi, R.; Normand, J.; Raghavachari, K.; Rendell, A.; Burant, J. C.; Iyengar, S. S.; Tomasi, J.; Cossi, M.; Rega, N.; Millam, J. M.; Klene, M.; Knox, J. E.; Cross, J. B.; Bakken, V.; Adamo, C.; Jaramillo, J.; Gomperts, R.; Stratmann, R. E.; Yazyev, O.; Austin, A. J.; Cammi, R.; Pomelli, C.; Ochterski, J. W.; Martin, R. L.; Morokuma, K.; Zakrzewski, V. G.; Voth, G. A.; Salvador, P.; Dannenberg, J. J.; Dapprich, S.; Daniels, A. D.; Farkas, .; Foresman, J. B.; Ortiz, J. V.; Cioslowski, J.; Fox, D. J.

[129] Dgrid, version 4.5. Kohout, M. Springer: Radebeul, **2009**.

[130] Nakamichi, H. *Phase Transitions: A Multination Journal* **2004**, *77*(1-2), 21–29.

[131] Schapiro, I.; Ryazantev, M. N.; Frutos, L. M.; Ferré, N.; Lindh, R.; Olivucci, M. *J. Am. Chem. Soc.* **2011**, *133*, 3354–3364.

[132] Gozem, S.; Huntress, M.; Schapiro, I.; Lindh, R.; Granovsky, A. A.; Angeli, C.; Olivucci, M. *J. Chem. Theory Comput.* **2012**, *8*, 4069–4080.

[133] Weingart, O.; Schapiro, I.; Buss, V. *J. Phys. Chem. B* **2007**, *111*, 3782–3788.

[134] Weingart, O.; Schapiro, I.; Buss, V. *Journal of Molecular Modeling* **2006**, *12*, 713–721.

[135] Klaffki, N.; Weingart, O.; Garavelli, M.; Spohr, E. *Phys. Chem. Chem. Phys.* **2012**, *14*, 14299–14305.

[136] Ben-Nun, M.; Martinez, T. J. *Chem. Phys. Lett.* **1998**, *298*(1-3), 57–65.

[137] Quenneville, J.; Martinez, T. J. *J. Phys. Chem. A* **2003**, *107*, 829–837.

[138] Levine, B. G.; Martinez, T. J. *Annual Review of Physical Chemistry* **2007**, *58*, 613–634.

[139] González-Luque, R.; Garavelli, M.; Bernardi, F.; Merchán, M.; Robb, M. A. *Proceedings of the National Academy of Sciences* **2000**, *97*, 9379–9384.

[140] Vreven, T.; Bernardi, F.; Garavelli, M.; Olivucci, M.; Robb, M. A.; Schlegel, H. B. *J. Am. Chem. Soc.* **1997**, *119*, 12687–12688.

[141] Garavelli, M.; Vreven, T.; Celani, P.; Bernardi, F.; Robb, M. A.; Olivucci, M. *J. Am. Chem. Soc.* **1998**, *120*, 1285–1288.

[142] Garavelli, M.; Negri, F.; Olivucci, M. *J. Am. Chem. Soc.* **1999**, *121*, 1023–1029.

[143] Kaczmarski, M. S.; Ma, Y.; Rohlfing, M. *Phys. Rev. B* **2010**, *81*, 115433.

[144] Gatti, F.; Munñoz, C.; Iung, C. *J. Chem. Phys.* **2001**, *114*(19), 8275–8281.

[145] Kumar, A.; Sun, S.-S.; Lees, A. In *Photophysics of Organometallics*; Lees, A. J., Ed., Vol. 29 of *Topics in Organometallic Chemistry;* Springer Berlin Heidelberg, 2010; pages 37–71.

[146] Vlček, J., A. In *Photophysics of Organometallics*; Lees, A. J., Ed., Vol. 29 of *Topics in Organometallic Chemistry;* Springer Berlin Heidelberg, 2010; pages 115–158.

[147] Leonidova, A.; Gasser, G. *ACS Chem. Biol.* **2014**, *9*, 2180–2193.

[148] Kuninobu, Y.; Takai, K. *Chem. Rev.* **2011**, *111*, 1938–1953.

[149] Wenger, O. S. *Coord. Chem. Rev.* **2011**, *282-283*, 150–158.

[150] Lo, K. K.-W.; Louie, M.-W.; Sze, K.-S.; Lau, J. S.-Y. *Inorg. Chem.* **2008**, *47*, 602–611.

[151] Lo, K. K.-W.; Tsang, K. H.-K.; Sze, K.-S. *Inorg. Chem.* **2006**, *45*, 1714–1722.

[152] Choi, A. W.-T.; Louie, M.-W.; Li, S. P.-Y.; Liu, H.-W.; Chan, B. T.-N.; Lam, T. C.-Y.; Lin, A. C.-C.; Cheng, S.-H.; Lo, K. K.-W. *Inorg. Chem.* **2012**, *51*, 13289–13302.

[153] Louie, M.-W.; Fong, T. T.-H.; Lo, K. K.-W. *Inorg. Chem.* **2011**, *50*, 9465–9471.

[154] Chan, C. Y.; Pellegrini, P. A.; Greguric, I.; Banard, P. J. *Inorg. Chem.* **2014**, *53*, 10862–10873.

[155] Blanco-Rodriguez, A. M.; Di Biblio, A. J.; Shih, C.; Museth, A. K.; Clark, I. P.;

Towrie, M.; Cannizzo, A.; Sudhamsu, J.; Crane, B.; Sykora, J.; Winkler, J. R.; Gray, H. B.; Zálisš, S.; Vlček, J., A. *Chem. A Eur. J.* **2011**, *17*, 5350–5361.

[156] Blanco-Rodriguez, A. M.; Towrie, M.; Sykora, J.; Zálisš, S.; Vlček, J., A. *Inorg. Chem.* **2011**, *50*, 6122–6134.

[157] Blanco-Rodriguez, A. M.; Busby, M.; Graädinaru, C.; CrCrane, B.; Di Bilio, A. J.; Matousek, P.; Towrie, M.; Leigh, B. S.; Richards, J. H.; Vlček, J., A.; Gray, H. B. *J. Am. Chem. Soc.* **2006**, *128*, 4365–4370.

[158] Blanco-Rodriguez, A. M.; Busby, M.; Ronayne, K.; Towrie, M.; Grädinaru, C.; Sudhamsu, J.; Sykora, J.; Hof, M.; Zálisš, S.; Di Bilio, A. J.; Crane, B. R.; Gray, B.; Vlček, J., A. *J. Am. Chem. Soc.* **2006**, *128*, 4365–4370.

[159] Kirgan, R.; Sullivan, B.; Rillema, D. In *Photochemistry and Photophysics of Coordination Compounds II*; Balzani, V., Campagna, S., Eds., Vol. 281 of *Topics in Current Chemistry;* Springer Berlin Heidelberg, 2007; pages 45–100.

[160] McCusker, J. K. *Acc. Chem. Res.* **2003**, *36*, 896–887.

[161] Chergui, M. *Dalton Trans.* **2012**, *41*, 13022–13029.

[162] El Nahhas, A.; Consani, C.; Blanco-Rodriguez, A. M.; Lancaster, K. M.; Braem, O.; Cannizzo, A.; Towrie, M.; Clark, I. P. andZálisš, S.; Chergui, M.; Vlček, J., A. *Inorg. Chem.* **2011**, *50*, 2932–2943.

[163] Wenger, O. S.; Henling, L. M.; Day, M. W.; Winkler, J. R.; Gray, H. B. *Polyhedron* **2004**, *23*, 2955–2958.

[164] Busby, M.; Matousek, P.; Towrie, M.; Vlček, J., A. *J. Phys. Chem. A* **2005**, *109*, 3000–3008.

[165] Polo, A. S.; Itokazu, M. K.; Frin, K. M.; de Toledo Patrocinio, A. O.; Iha, N. Y. M. *Coordination Chemistry Reviews* **2006**, *250*, 1669–1680.

[166] Patrocinio, A. O. T.; Brennaman, M. K.; Meyer, T. J.; Iha, N. Y. M. *J. Phys. Chem. A* **2010**, *114*, 12129–12137.

[167] Gindensperger, E.; Köppel, H.; Daniel, C. *Chemical Communications* **2010**, *46*(43), 8225–8227.

[168] Bossert, J.; Daniel, C. *Chem. A Eur. J.* **2006**, *12*, 4835–4843.

[169] Vlček, J., A.; Busby, M. *Coord. Chem. Rev.* **2006**, *250*, 1755–1762.

[170] Cruz, A. J.; Kirgan, R. A.; Siam, K.; Islam, M. R.; Moore, C.; Rillema, D. P. In *Proceedings of the 3rd Annual GRASP Symposium, Wichita State Université*, 2007.

[171] Perdew, J. P.; Burke, K.; Ernzerhof, M. *Phys. Rev. Lett.* **1996**, *77*, 3865–3868.

[172] Grimme, S. *J. Comput. Chem.* **2006**, *27*, 1787–1799.

[173] van Lenthe, E.; Baerends, E. J. *J. Comput. Chem.* **2003**, *24*, 1142.

[174] Runge, E.; Gross, E. K. U. *Phys. Rev. Lett.* **1984**, *52*, 997.

[175] Petersilka, M.; Gossmann, U. J.; Gross, E. K. U. *Phys. Rev. Lett.* **1996**, *76*, 1212.

[176] Becke, A. D. *J. Chem. Phys.* **1993**, *98*, 5648.

[177] Stephens, P. J.; Devlin, F. J.; Chabalowski, C. F.; Frisch, M. J. *J. Phys. Chem.* **1994**, *98*, 11623.

[178] Peach, M. J.; Tozer, D. J. *J. Phys. Chem. A* **2012**, *116*, 9783.

[179] Yanai, T.; Twe, D. P.; Handy, N. C. A. *Chem. Phys. Lett.* **2004**, *393*, 51–57.

[180] Daniel, C. *Coord. Chem. Rev.* **2015**, *282-283*, 19–32.

[181] Gourlaouen, C.; Daniel, C.; Durola, F.; Frey, J.; Heitz, V.; Sauvage, J.-P.; Ventura, B.; Flamigni, L. *J Phys. Chem. A* **2014**, *118*, 3616–3624.

[182] Klamt, A.; Schüürmann, G. *J. Chem. Soc., Perkin Trans.* **1993**, *2*, 799.

[183] Klamt, A. *J. Phys. Chem.* **1995**, *99*, 2224.

[184] Klamt, A.; Jones, V. *J. Chem. Phys.* **1996**, *105*, 9972.

[185] Rosa, A.; Baerends, E. J.; van Gisbergen, S. J. A.; van Lenthe, E.; Groeneveld, J. A.; Snijders, J. G. *J. Am. Chem. Soc.* **1999**, *121*, 10356.

[186] Pye, C.; Ziegler, T. *Theor. Chem. Acc.* **1999**, *101*, 396.

[187] ADF, SCM, theoretical chemistry. Vrije Universitet: Amsterdam, T. N. `https://www.scm.com/Downloads/`, **2013**.

[188] Schapiro, I.; Weingart, O.; Buss, V. *J. Am. Chem. Soc.* **2009**, *131*, 16–17.

[189] Szymczak, J. J.; Barbatti, M.; Lischka, H. *J. Phys. Chem. A* **2009**, *113*, 11907–11918.

[190] Dilger, J.; Musbat, L.; Sheves, M.; Bochenkova, A. V.; Clemmer, D. E.; Toker, Y. *Angewandte Chemie International Edition* **2015**, *54*(16), 4748–4752.

[191] Wang, W.; Nossoni, Z.; Berbasova, T.; Watson, C. T.; Yapici, I.; Lee, K. S. S.; Vasileiou, C.; Geiger, J. H.; Borhan, B. *Science* **2012**, *338*(6112), 1340–1343.

[192] Fu, B.; Han, Y.-C.; Bowman, J. M.; Angelucci, L.; Balucani, N.; Leonori, F.; Casavecchia, P. *Proc Natl Acad Sci* **2012**, *109*(25), 9733–9738.

[193] Lim, E.; Laposa, J. *J Chem Phys* **1964**, *41*, 3257.

[194] Scott, D. R.; Maltenieks, O. *J Phys Chem* **1968**, *72*(9), 3354–3356.

[195] Chergui, M. *Dalton Transactions* **2012**, *41*, 13022–13029.

[196] Cannizzo, A.; van Mourik, F.; Gawelda, W.; Zgrablič, G.; Bressler, C.; Chergui, M. *Angew. Chem., Int. Ed.* **2006**, *45*, 3174.

[197] Gawelda, W.; Cannizzo, A.; Phan, V. T.; van Mourik, F.; Bressler, C.; Chergui, M. *J. Am. Chem. Soc.* **2007**, *129*, 8199.

[198] Yersin, H. *Top. Curr. Chem.* **2004**, *241*, 1.

[199] Manaa, M. R.; Yarkony, D. R. *J. Chem. Phys.* **1991**, *95*, 1808–1816.

[200] Merchán, M.; Serrano-Andés, L.; Robb, M. A.; Lluís, B. *J. Am. Chem. Soc.* **2005**, *127*, 1820–1825.

[201] Grimme, S.; Woeller, M.; Peyerimhoff, S. D. an Danovich, D.; Shaik, S. *Chem. Phys. Lett.* **1998**, *287*, 601.

[202] Tatchen, J.; Gilka, N.; Marian, C. M. *Phys. Chem. Chem. Phys.* **2007**, *9*, 5209.

[203] Etinski, M.; Tatchen, J.; Marian, C. M. *J Chem Phys* **2011**, *134*, 154105.

[204] Granucci, G.; Persico, M.; Spighi, G. *J Chem. Phys.* **2012**, *137*, 22A501.

[205] Favero, L.; Granucci, G.; Persico, M. *Phys. Chem. Chem. Phys.* **2013**, *15*, 20651–20661.

[206] Martinez-Fernández, L.; Corral, I.; Granucci, G.; Persico, M. *Chem. Sci.* **2014**, *5*, 1336.

[207] Richter, M.; Marquetand, P.; González-Vázquez, J.; Sola, I.; González, L. *J. Chem. Theory Comput.* **2011**, *7*(5), 1253–1258.

[208] Marquetand, P.; Richter, M.; González-Vázquez, J.; Sola, L.; González, L. *Faraday Discuss.* **2011**, *153*, 261–273.

[209] Mai, S.; Marquetand, P.; Richter, M.; González-Vázquez, J.; Gonzalez, L. *ChemPhysChem* **2013**, *14*(13), 2920–2931.

[210] Richter, M.; Marquetand, P.; González-Vázquez, J.; Sola, I.; González, L. *J. Phys. Chem. Lett.* **2012**, *3*(21), 3090–3095.

[211] Wilson, E.; Decius, J.; Cross, P. *Molecular Vibrations: The Theory of Infrared and Raman Vibrational Spectra*, Dover Books on Chemistry Series; Dover Publications, 1955.

[212] Eng, J.; Gourlaouen, C.; Gindensperger, E.; Daniel, C. *Acc. Chem. Res.* **2015**.

Julien ENG

Dynamics of Ultrafast Processes in Excited States of Organic and Inorganic Compounds

Résumé

Les travaux présentés dans cette thèse peuvent être divisés en deux parties.
Dans une première partie, nous avons étudié le processus de photoisomérisation dans plusieurs systèmes. Une analyse de structure électronique accompagnée d'un calcul préliminaire de dynamique semi-classique ont été appliqué à un modèle minimal du rétinal afin d'extraire les degrés de libertés les plus importants lors de l'isomérisation. Cela dans le but de construire des surfaces d'énergie potentielle diabatiques pour effectuer une étude de dynamique quantique. Une approche de type dynamique semi-classique a été appliquée à un modèle de moteur moléculaire dans le but d'étudier l'origine de l'uni-directionalité de sa rotation. Finalement, une étude de structure électronique d'un complexe de Rhénium contenant un ligand de type rétinal a été effectué pour étudier l'influence du métal sur la spectroscopie du ligand rétinal.
Dans une deuxième partie nous nous sommes intéressés à l'étude des croisements intersystème dans un complexe de Rhénium. Afin de pouvoir apporter une explication à un comportement contrintuitif de ce complexe, nous avons développé un Hamiltonien modèle capable de tenir compte des couplages vibroniques interétats et spin-orbit. Cet Hamiltonien a été testé sur ce-dit système, et nous a permis, grâce à une étude de structure électronique de proposer un mécanisme de relaxation différent de celui proposé expérimentalement.

MOTS-CLÉS : Dynamique quantique, construction de surfaces d'énergie potentielle diabatiques, photoisomérisation, PSB3, dynamique semi-classique, moteur moléculaire, complexe de Re(I), Hamiltonien modèle, couplages vibroniques, croisements intersystème.

Résumé en anglais

This thesis can be divided in two parts.
In the first one, we have studied the photoisomerization process in several systems. An electronic structure analysis mixed with a preliminary semi-classical dynamics investigation has been applied to a minimal model of the retinal chromophore in order to select the most important degrees of freedom involved in the process. The goal of this is to build diabatic potential energy surfaces in order to conduct quantum dynamics simulations. A semi-classical approach has also been applied to a molecular motor model to study the origin of the unidirectionality of its rotary motion. Finally, an electronic structure of a rhenium complex with a retinal-like ligand has been performed to study the effect of the coordination to a metallic atom on the spectroscopy of the retinal ligand.
In the second part, we have investigated the intersystem crossings in a rhenium complex. In order to bring an explanation to an experimentally observed conterintuitive behavior of this complex, we have developed a model Hamiltonian that includes both interstate vibronic coupling and spin-orbit coupling. This Hamiltonian has been tested on the said complex and, in complement to an electronic structure study, allowed us to formulate a decay mechanism different from the one proposed based on experiments.

KEYWORDS : Quantum dynamics, construction of diabatic potential energy surfaces,photoisomerization, PSB3, semi-classical dynamics, molecular motor, Re(I) complexes, model Hamiltonian, vibronic coupling, intersystem crossing.